STIMULI RESPONSIVE NANOPARTICLES FOR ANTI-CANCER THERAPY

EDITED BY: Saji Uthaman, In-Kyu Park, Kang Moo Huh, James J. Lai and Mitsuhiro Ebara

PUBLISHED IN: Frontiers in Bioengineering and Biotechnology and Frontiers in Molecular Biosciences

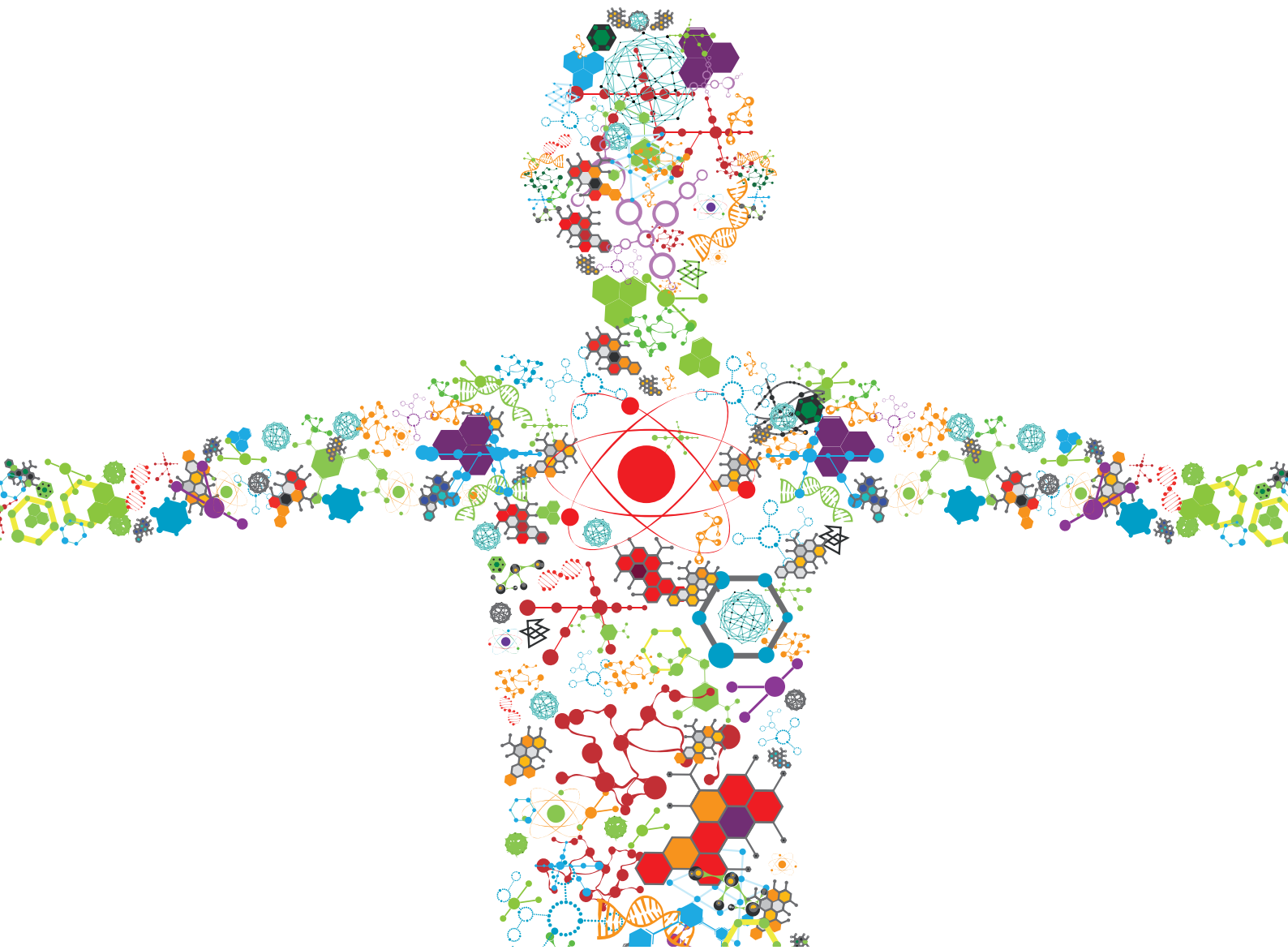

frontiers Research Topics

frontiers

ISSN 1664-8714
ISBN 978-2-88974-002-4
DOI 10.3389/978-2-88974-002-4

About Frontiers

Frontiers is more than just an open-access publisher of scholarly articles: it is a pioneering approach to the world of academia, radically improving the way scholarly research is managed. The grand vision of Frontiers is a world where all people have an equal opportunity to seek, share and generate knowledge. Frontiers provides immediate and permanent online open access to all its publications, but this alone is not enough to realize our grand goals.

Frontiers Journal Series

The Frontiers Journal Series is a multi-tier and interdisciplinary set of open-access, online journals, promising a paradigm shift from the current review, selection and dissemination processes in academic publishing. All Frontiers journals are driven by researchers for researchers; therefore, they constitute a service to the scholarly community. At the same time, the Frontiers Journal Series operates on a revolutionary invention, the tiered publishing system, initially addressing specific communities of scholars, and gradually climbing up to broader public understanding, thus serving the interests of the lay society, too.

Dedication to Quality

Each Frontiers article is a landmark of the highest quality, thanks to genuinely collaborative interactions between authors and review editors, who include some of the world's best academicians. Research must be certified by peers before entering a stream of knowledge that may eventually reach the public - and shape society; therefore, Frontiers only applies the most rigorous and unbiased reviews.
Frontiers revolutionizes research publishing by freely delivering the most outstanding research, evaluated with no bias from both the academic and social point of view. By applying the most advanced information technologies, Frontiers is catapulting scholarly publishing into a new generation.

What are Frontiers Research Topics?

Frontiers Research Topics are very popular trademarks of the Frontiers Journals Series: they are collections of at least ten articles, all centered on a particular subject. With their unique mix of varied contributions from Original Research to Review Articles, Frontiers Research Topics unify the most influential researchers, the latest key findings and historical advances in a hot research area! Find out more on how to host your own Frontiers Research Topic or contribute to one as an author by contacting the Frontiers Editorial Office: frontiersin.org/about/contact

STIMULI RESPONSIVE NANOPARTICLES FOR ANTI-CANCER THERAPY

Topic Editors:
Saji Uthaman, Iowa State University, United States
In-Kyu Park, Chonnam National University Medical School, South Korea
Kang Moo Huh, Chungnam National University, South Korea
James J. Lai, University of Washington, United States
Mitsuhiro Ebara, National Institute for Materials Science, Japan

Citation: Uthaman, S., Park, I.-K., Huh, K. M., Lai, J. J., Ebara, M., eds. (2021). Stimuli Responsive Nanoparticles for Anti-Cancer Therapy. Lausanne: Frontiers Media SA. doi: 10.3389/978-2-88974-002-4

Table of Contents

04 ***Editorial: Stimuli-Responsive Nanoparticles for Anti-cancer Therapy***
Saji Uthaman, In-Kyu Park, Kang Moo Huh, James Lai and Mitsuhiro Ebara

06 ***Zinc Oxide Nanocrystals and High-Energy Shock Waves: A New Synergy for the Treatment of Cancer Cells***
Luisa Racca, Tania Limongi, Veronica Vighetto, Bianca Dumontel, Andrea Ancona, Marta Canta, Giancarlo Canavese, Nadia Garino and Valentina Cauda

20 ***Nanotheranostics With the Combination of Improved Targeting, Therapeutic Effects, and Molecular Imaging***
Shin-Lei Peng, Chih-Ho Lai, Pei-Yi Chu, Jer-Tsong Hsieh, Yen-Chun Tseng, Shao-Chieh Chiu and Yu-Hsin Lin

35 ***Folic Acid–Functionalized Composite Scaffolds of Gelatin and Gold Nanoparticles for Photothermal Ablation of Breast Cancer Cells***
Huajian Chen, Xiuhui Wang, Linawati Sutrisno, Tianjiao Zeng, Naoki Kawazoe, Yingnan Yang and Guoping Chen

47 ***Near-Infrared Responsive Phase-Shifted Nanoparticles for Magnetically Targeted MR/US Imaging and Photothermal Therapy of Cancer***
Yan Xu, Wang Li, Sijie Chen, Biying Huang, Wenjing Pei and Chengcheng Niu

60 ***Recent Developments in Pathological pH-Responsive Polymeric Nanobiosensors for Cancer Theranostics***
E. K. Pramod Kumar, Wooram Um and Jae Hyung Park

77 ***Tumor Targeted Multifunctional Magnetic Nanobubbles for MR/US Dual Imaging and Focused Ultrasound Triggered Drug Delivery***
Zhen Jin, Jinlong Chang, Peipei Dou, Shang Jin, Min Jiao, Heyun Tang, Wenshuai Jiang, Wu Ren and Shaohui Zheng

90 ***Tumor Microenvironment-Stimuli Responsive Nanoparticles for Anticancer Therapy***
Reju George Thomas, Suchithra Poilil Surendran and Yong Yeon Jeong

105 ***External and Internal Stimuli-Responsive Metallic Nanotherapeutics for Enhanced Anticancer Therapy***
Adityanarayan Mohapatra, Saji Uthaman and In-Kyu Park

137 ***Plant Virus Nanoparticles for Anti-cancer Therapy***
Srividhya Venkataraman, Paul Apka, Erum Shoeb,Uzma Badar and Kathleen Hefferon

frontiers in Bioengineering and Biotechnology

EDITORIAL
published: 15 November 2021
doi: 10.3389/fbioe.2021.797619

Editorial: Stimuli-Responsive Nanoparticles for Anti-cancer Therapy

Saji Uthaman[1], In-Kyu Park[2]*, Kang Moo Huh[3]*, James Lai[4]* and Mitsuhiro Ebara[5]**

[1]Chemical and Biological Engineering, IOWA State University, Ames, IA, United States, [2]Department of Biomedical Sciences, Chonnam National University, Gwangju, South Korea, [3]Department of Polymer Science and Engineering, Chungnam National University, Daejeon, South Korea, [4]Department of Bioengineering, University of Washington, Washington, ME, United States, [5]International Center for Materials Nanoarchitectonic, National Institute for Materials Science, Tsukuba, Japan

Keywords: nanoparticle, drug delivery, photothermal therapy, molecular Imaging, ultra sound

Editorial on the Research Topic

Editorial: Stimuli-Responsive Nanoparticles for Anti-cancer Therapy

The Research topic entitled "Stimuli-Responsive Nanoparticles for Anti-Cancer Therapy" addresses the current advances in the stimuli-responsive nanoparticles for anti-cancer. This issue comprises nine selected peer-reviewed manuscripts (original research and review articles) discussing the latest updates on various stimuli-responsive nanoparticles used in oncology. Different types of nanoparticles, including activated polymeric delivery systems (Peng et al.), multifunctional magnetic nanobubbles (Jin et al.), folic acid functionalized gelatin–AuNPs composite scaffolds (Chen et al.), Zinc oxide nanocrystals (Racca et al.), and Near-Infrared responsive Phase-shifting nanoparticles (Xu et al.) are presented through original research works. These novel nanoparticles with tailor-made properties offer a universal approach for anti-cancer therapy as their responsiveness depends on the general physiological properties commonly found in all tumors.

The first example of external stimuli-responsive nanoparticles is presented by (Racca et al.). In this study, amino-propyl functionalized ZnO nanocrystals (ZnO NCs) combined with ultrasound shock waves (SW) were used to treat cancer cells. The ZnO NCs demonstrated synergism in combination with SW stimulus. In another study by Jin et al., multifunctional magnetic nanobubbles (MF-MNBs) comprising of poly (D, L-lactide-co-glycolide (PLGA) - polyethylene glycol–folate (PLGA-PEG-FA) polymer-based nanobubbles were evaluated as tumor-targeted ultrasound (US)/magnetic resonance (MR) imaging and focused ultrasound (FUS)-triggered drug delivery system. The MF-MNB exhibited ligand-receptor mediated tumor accumulation and focused ultrasound FUS-triggered drug delivery for efficient cancer treatment. Chen et al. have demonstrated photothermal ablation using near-infra-red irradiation as an external stimulus for killing cancer cells. This study synthesized folic acid (FA)-functionalized composite scaffold by hybridizing FA-conjugated gelatin and FA-modified AuNPs and using ice particulates as porogen material. *In vitro* and *In vivo* studies demonstrated that FA-functionalized gelatin–AuNPs composite scaffolds could elicit local photothermal ablation of breast cancer cells. Next, near-infrared responsive phase-shifted nanoparticles (NRPNs) have been designed by Xu et al. for magnetically targeted MR/US imaging and photothermal therapy of tumors. The near-infrared responsive phase-shifted nanoparticles (NRPNs) comprise PLGA nanoparticles encapsulated with indocyanine green (ICG), magnetic Fe_3O_4 nanoparticles, and perfluoro pentane (PFP). Upon irradiating with a NIR laser, the NRPNs, a phase-shifted expansion effect due to the quick conversion from light to heat by ICG and Fe_3O_4, can be used for ultrasound (US) imaging. In another study, Peng et al. have reported on an activated nanoparticle system comprising of poly (D, L-lactide-co-glycolide; PLGA)-containing iron oxide nanoparticles (IOs) for biological imaging, using fucoidan/hyaluronic acid (FU/HA) to achieve targeting activity and applying polyethylene glycol-modified gelatin

OPEN ACCESS

Edited and reviewed by:
Gianni Ciofani,
Italian Institute of Technology (IIT), Italy

****Correspondence:***
Saji Uthaman
suthaman@iastate.edu
In-Kyu Park
pik96@jnu.ac.kr
Kang Moo Huh
khuh@cnu.ac.kr
James Lai
jilai@uw.edu
Mitsuhiro Ebara
EBARA.Mitsuhiro@nims.go.jp

Specialty section:
This article was submitted to Nanobiotechnology, a section of the journal Frontiers in Bioengineering and Biotechnology

Received: *19 October 2021*
Accepted: *21 October 2021*
Published: *15 November 2021*

Citation:
Uthaman S, Park I-K, Huh KM, Lai J and Ebara M (2021) Editorial: Stimuli-Responsive Nanoparticles for Anti-cancer Therapy. Front. Bioeng. Biotechnol. 9:797619. doi: 10.3389/fbioe.2021.797619

(PG)-carrying a phytochemical, epigallocatechin gallate (EGCG) to eradicate prostate tumors. This study demonstrated that the combination of therapeutic and molecular imaging could effectively target prostate cancer cells.

Besides the original research articles, this research topic also has a series of review articles that summarized the recent advances in anti-cancer therapy using external and internal stimuli-responsive metallic nanoparticles (Mohapatra et al.), pathological pH-responsive polymeric nano biosensors (Kumar et al.), tumor microenvironment responsive nanoparticles (Thomas et al.), and plant virus nanoparticles (Hefferon et al.). As a starting example, Kumar et al. have summarized the recent developments in the design, preparation, and characterization of pH-responsive nanobiosensors and their ability to behave as efficient *in vivo* nano theranostics agents in acidic cancer environments. Thomas et al. have summarized the different types of internal (pH, redox, enzyme, ROS, hypoxia) stimuli-responsive nanoparticle drug delivery systems, Mohapatra et al., have outlined the role of different metallic nanotherapeutics in anti-cancer therapy, as well as their combinational effects with multiple stimuli for enhanced anti-cancer treatment. Finally, Hefferon et al. explore plant viruses as epitope-carrying nanoparticles and novel tools in cancer immunotherapy.

To summarize, we hope that this research topic will provide insights into the recent trends in nanomedicine, especially in oncology, using stimuli-responsive nanoparticles, providing insights into the development of targeted nanomedicine. The editors hope that the Research Topic "Stimuli-Responsive Nanoparticles for Anti-Cancer Therapy" will contribute to the progress of research and development activities in the field of nanomedicine, inspiring and offering a universal approach for anti-cancer therapy by taking advantage of the physiological properties commonly found in all tumors.

AUTHOR CONTRIBUTIONS

SU wrote the editorial, which was revised and proofed by IKP, and accepted by all the authors.

Conflict of Interest: The authors declare that the research was conducted in the absence of any commercial or financial relationships that could be construed as a potential conflict of interest.

Publisher's Note: All claims expressed in this article are solely those of the authors and do not necessarily represent those of their affiliated organizations, or those of the publisher, the editors and the reviewers. Any product that may be evaluated in this article, or claim that may be made by its manufacturer, is not guaranteed or endorsed by the publisher.

frontiers in Bioengineering and Biotechnology

ORIGINAL RESEARCH
published: 05 June 2020
doi: 10.3389/fbioe.2020.00577

Zinc Oxide Nanocrystals and High-Energy Shock Waves: A New Synergy for the Treatment of Cancer Cells

*Luisa Racca, Tania Limongi, Veronica Vighetto, Bianca Dumontel, Andrea Ancona, Marta Canta, Giancarlo Canavese, Nadia Garino and Valentina Cauda**

Department of Applied Science and Technology, Politecnico di Torino, Turin, Italy

OPEN ACCESS

Edited by:
In-Kyu Park, Chonnam National University, South Korea

Reviewed by:
Nanasaheb D. Thorat, University of Limerick, Ireland
Jae Young Lee, Gwangju Institute of Science and Technology, South Korea
Bhang Suk Ho, Sungkyunkwan University, South Korea

***Correspondence:**
Valentina Cauda
valentina.cauda@polito.it

Specialty section:
This article was submitted to Nanobiotechnology, a section of the journal Frontiers in Bioengineering and Biotechnology

Received: *16 February 2020*
Accepted: *12 May 2020*
Published: *05 June 2020*

Citation:
Racca L, Limongi T, Vighetto V, Dumontel B, Ancona A, Canta M, Canavese G, Garino N and Cauda V (2020) Zinc Oxide Nanocrystals and High-Energy Shock Waves: A New Synergy for the Treatment of Cancer Cells. Front. Bioeng. Biotechnol. 8:577. doi: 10.3389/fbioe.2020.00577

In the last years, different nanotools have been developed to fight cancer cells. They could be administered alone, exploiting their intrinsic toxicity, or remotely activated to achieve cell death. In the latter case, ultrasound (US) has been recently proposed to stimulate some nanomaterials because of the US outstanding property of deep tissue penetration and the possibility of focusing. In this study, for the first time, we report on the highly efficient killing capability of amino-propyl functionalized ZnO nanocrystals (ZnO NCs) in synergy with high-energy ultrasound shock waves (SW) for the treatment of cancer cells. The cytotoxicity and internalization of ZnO NCs were evaluated in cervical adenocarcinoma KB cells, as well as the safety of the SW treatment alone. Then, the remarkably high cytotoxic combination of ZnO NCs and SW was demonstrated, comparing the effect of multiple (3 times/day) SW treatments toward a single one, highlighting that multiple treatments are necessary to achieve efficient cell death. At last, preliminary tests to understand the mechanism of the observed synergistic effect were carried out, correlating the nanomaterial surface chemistry to the specific type of stimulus used. The obtained results can thus pave the way for a novel nanomedicine treatment, based on the synergistic effect of nanocrystals combined with highly intense mechanical pressure waves, offering high efficiency, deep and focused tissue penetration, and a reduction of side effects on healthy cells.

Keywords: zinc oxide, shock waves, anticancer therapy, acoustic cavitation, reactive oxygen species, ultrasound non-thermal effects

INTRODUCTION

Among various innovative new approaches to fight cancer, nanomedicine has attracted many interests (Shi et al., 2017). The application of nanomaterials for health and medicine can lead successful advancements in diagnosis and therapy (Zavaleta et al., 2017), particularly in the delivery of cargo molecules (Tran et al., 2017), or through their direct use to damage cancer cells (Chugh et al., 2018). Such nanotools indeed could be intrinsically toxic (Bisht and Rayamajhi, 2016), e.g., through the release of metal ions, or could be remotely activated to achieve cell death, as in the photothermal and photodynamic therapies (Lim et al., 2015). Zinc Oxide (ZnO) in particular has raised researchers' interest thanks to its biocompatibility and peculiar piezoelectric

and semiconductive properties (Jiang et al., 2018; Racca et al., 2018) useful for its exploitation for imaging (Jiang et al., 2011), biosensing (Sanginario et al., 2016; Shanmugam et al., 2017; Stassi et al., 2017), tissue engineering (Laurenti and Cauda, 2017) and drug delivery (Laurenti and Cauda, 2018; Martínez-Carmona et al., 2018) purposes. Remarkably, ZnO nanoparticles are also studied for their intrinsic anticancer properties thanks to their selective toxicity toward cancer cells (Bisht and Rayamajhi, 2016). ZnO cytotoxicity indeed is related to reactive oxygen species (ROS) production and Zn^{2+} ions release (Bisht and Rayamajhi, 2016; Jiang et al., 2018; Racca et al., 2018; Singh, 2019). Additionally, their toxic effects could be controlled and amplified through an external stimulation by their irradiation with ultraviolet light, as in the photodynamic therapy (PDT) (Ancona et al., 2018), producing ROS and exerting then a cytotoxic effect on cancer cells (Ancona et al., 2018; Kwiatkowski et al., 2018). However, the limited tissue penetration depth of UV light (less than 1 mm) reduces the ZnO-assisted PDT application to superficial cancers, i.e., melanomas. Otherwise, the light source has to be directly placed in the target tissue, as in the optic-fiber guided PDT (Mallidi et al., 2016; Baskaran et al., 2018).

An alternative therapeutic approach, namely the sonodynamic therapy (SDT), was also proposed (Shibaguchi et al., 2011). It is based on the activation through ultrasound (US) of an organic molecule, called sonosensitizer, to induce cells to death. US is a mechanical pressure wave with the outstanding properties of deep tissue penetration and focusing (Shibaguchi et al., 2011; Wan et al., 2016). The passage of an US wave through a tissue can exert two different consequences: thermal and non-thermal effects. Even though US thermal effects can be exploited to achieve tumor thermoablation, as in the high intensity focused US (HIFU) therapy, SDT investigations are generally based on the non-thermal ones (Canavese et al., 2018). Non-thermal effects consist in a vast group of phenomena. Among them, acoustic cavitation is probably the most studied (Canavese et al., 2018). The term "cavitation" refers to the formation and the oscillations of gas microbubbles in the medium under US stimulation. Indeed, US passage provokes compression and rarefaction cycles, in which gas bodies, already present in tissues, can form microbubbles that expand and shrink following wave cycles. Microbubbles can oscillate on their radius for several cycles, inducing a potential temperature increase, microstreamings, radiation forces and shear stress, in a situation of stable or non-inertial cavitation. Otherwise, microbubbles can collapse generating very high localized pressures and temperatures (Rosenthal et al., 2004), capable to induce the formation of several ROS and thus induce oxidative stress (Canavese et al., 2018). Microbubble collapse causes also mechanical stress, with the formation of microjets and shock waves (SW), and the emission of light. This state is described as inertial or transient cavitation (Canavese et al., 2018).

It is generally recognized that nanoparticles amplify US toxic effects (Canavese et al., 2018). It was experimentally observed indeed that nanoparticles addition decreases the US dose necessary to obtain acoustic cavitation, because nanoparticles carry gas pockets on their structure thanks to their surface roughness and/or porosity. This fact results in an improvement of the number of active microbubbles under the US irradiation (Sviridov et al., 2015).

Some groups proposed to employ high-energy SW to activate the organic molecular sonosentizer minimizing the US-related thermal effects, enhancing instead non-thermal ones (Wan et al., 2016). SW indeed are sonic pulses characterized by a first very rapid positive pressure phase (up to 100 MPa) that lasts for 0.5–3 μs, followed by a tensile wave characterized by a negative pressure (−10 MPa) for 2–20 μs, then recovering ambient values (Ogden et al., 2001; Wan et al., 2016). SW has been evaluated to enhance the intracellular drug delivery (Canaparo et al., 2008; Zhang et al., 2019) and for the activation of various porphyrin complexes (Canaparo et al., 2006, 2013; Serpe et al., 2011; Foglietta et al., 2015; Varchi et al., 2015). However, to our knowledge there are no investigations exploiting the non-thermal effect of SW assisted by solid nanoparticles. The combined use of SW with solid nanoparticles can induce the great above-mentioned advantages, i.e., improve the SW efficacy. This is achieved thanks to the enhanced cavitation effects produced by the presence of solid nanoparticles. Furthermore, the use of ZnO nanoparticles and SW to induce cancer cell death has not already been reported in the literature.

Herein, for the first time, we demonstrate the highly efficient killing capability of amino-propyl functionalized ZnO nanocrystals (ZnO NCs) in combination with SW for the treatment of cancer in an *in vitro* study. ZnO NCs were synthetized through a microwave-assisted solvothermal approach and chemically characterized. This synthetic strategy provides a high yield of ZnO NCs with spherical shape and very uniform nanosized distribution, allowing for their high colloidal stability. Our previous investigation indeed demonstrated the achievement of reproducible and reliable biological results with such ZnO NCs (Garino et al., 2019a). The cytotoxicity and internalization of ZnO NCs were evaluated in cervical adenocarcinoma KB cells, as well as the safety of the SW treatment alone. Then, the remarkably high cytotoxic combination of ZnO NCs and SW was demonstrated, comparing the effect of multiple (3 times/day) SW treatments to a single one. At last, preliminary tests to undertake the mechanism of the observed synergistic effect were carried out. The obtained results highlight the effective anticancer applicability of the proposed nanomedicine treatment, based on the synergistic effect of ZnO NCs and highly intense and focalized mechanical pressure waves.

MATERIALS AND METHODS

ZnO NCs Synthesis and Functionalization

ZnO NCs were synthesized by a microwave-assisted hydrothermal route, as previously described (Garino et al., 2019a). ZnO NCs surface was then decorated with amino-propyl functional groups and coupled with fluorescent Atto633-NHS ester dye (Thermofischer) when necessary. ZnO NCs were stored as ethanol colloidal suspensions.

ZnO NCs were characterized by X-Ray Diffraction (XRD) with a Cu-Kα source of radiation, operating at 40 kV and

30 mA in configuration θ–2θ Bragg-Brentano (Panalytical X'Pert diffractometer). For this analysis, several drops of the colloidal ZnO NCs solution were deposited on a silicon wafer and allowed to dry at room temperature (RT). The XRD spectrum was collected in the range of 20°–65° with a step size of 0.02° (2θ) and an acquisition time of 100 s.

High-resolution transmission electron microscopy (HRTEM) was used to characterize the morphological and structural features of the different materials. HRTEM was performed by using a FEI Titan ST microscope working at an acceleration voltage of 300 kV, equipped with a S-Twin objective lens, an ultra-bright field emission electron source (X-FEG) and a Gatan 2k × 2k CCD camera. All the ZnO NCs samples were diluted in ultrapure ethanol (99%) down to a concentration of 100 μg/mL. One drop of each sample was deposited on a holey carbon copper grid with 300-carbon mesh and left to dry overnight, prior to imaging.

Dynamic Light Scattering (DLS) and Z-Potential measurements were carried out with Zetasizer Nano ZS90 (Malvern Instruments). The size of pristine and amino-propyl functionalized ZnO NC was measured in both ethanol and double distilled (dd) water at a concentration of 100 μg/mL. Z-Potential measurements were performed in dd water at a concentration of 100 μ g/mL.

Cell Line

Cervical adenocarcinoma KB cell line (ATCC® CCL17TM) was grown in Eagle's Minimum Essential Medium (EMEM, Sigma) supplemented with 10% heath inactivated fetal bovine serum (FBS, Sigma), 100 units/mL penicillin and 100 μg/mL streptomycin (Sigma) and maintained at 37°C, 5% CO_2 atmosphere.

Cytotoxicity Tests

A 1.5 × 10^3 cells/well were plated in replicates (n = 4) into 96-well culture plates (TC-Treated, Corning) and incubated at 37°C, 5% CO_2. 24 h later, the culture medium was replaced with fresh medium containing different concentrations of ZnO NCs (5, 10, 15, 20, 25, 50 μg/mL). The ZnO NCs stock solution (1 mg/mL) was sonicated in a water bath (Labsonic LBS 2–10, Falc Instrument) at 40 kHz for 10 min before the preparation of the aliquots. After the incubation time, cell proliferation was assessed by the WST-1 cell proliferation assay. 10 μL of the WST-1 reagent (Roche) were added to each well and after 2 h incubation, the formazan absorbance was measured at 450 nm by the Multiskan GO microplate spectrophotometer (Thermo Fisher Scientific) using 620 nm as reference wavelength. Control values, represented by cells incubated with medium alone, were set at 100% viable and all values were expressed as a percentage of the control. Cell viability was measured after 5, 24, 48, and 72 h of incubation with ZnO NCs.

Internalization Assay

ZnO NCs uptake in KB cells was measured with a Guava Easycyte 6-2L flow cytometer (Merck Millipore). Briefly, cells were seeded into a 6-well TC treated culture plate (Corning) with cell culture medium 24 h before the assay (1 × 10^5 cells/well). Then, culture medium was replaced with freshly prepared medium containing ZnO NCs labeled with Atto633-NHS (10 μg/mL). A control well, containing untreated cells, was on the contrary filled with fresh medium without NCs. ZnO NCs progressive uptake was then measured at different time points (5–24 h). Cells were washed twice with phosphate saline buffer (PBS), trypsinized and centrifuged at 130 g for 5 min. Cell pellets were then re-suspended in 1 mL PBS and immediately analyzed with the flow cytometer. 1 × 10^4 gated events were considered excluding cellular debris, characterized by low forward scatter (FSC) and side scatter (SSC), with a flow rate of 0.59 μL/s. Results are shown as the percentage of positive events, analyzed with Incyte Software (Merck Millipore). In particular, a threshold of positivity upon control cell histogram was set. The percentage of events characterized by a shift in Red-R fluorescence intensity (emission filter 661/15 nm), due to the Atto633 attached on NCs surface, was thus measured. Representative histograms were then graphed with FCS Express Software (DeNovo Software).

Single SW Treatment

KB cells, seeded into a treated culture flask, in exponential growth phase, where trypsinized and 5 × 10^5 cells per well were plated in culture medium into a 96-well plate (Corning) for the SW treatment as described by others (Canaparo et al., 2008, 2013; Foglietta et al., 2017).

SW was administered by the high-energy focalized SW device PW^2 (R. Wolf, ELvation Medical). According with the previously mentioned literature, energy flux density ranges, corresponding to the energy at the focal point, were set, i.e., 0.15-0.22-0.3-0.4-0.52 mJ/mm^2, corresponding to positive peak pressures (PPP) of 29.1, 39.4, 50.3, 61.7, and 74.1 MPa. Furthermore, 500 or 1000 shots were given for each treatment (4 shots/s). The therapy source FB10G4, equipped with a 4 cm thick pad, was employed to give the SW treatment. The 96-well plate containing KB cells was directly put on the top of the cap covered by a thin layer of ultrasound gel (Stosswellen Gel 144 Bestelle, ELvation Medical) to minimize SW attenuation. Immediately after the treatment, 2 × 10^3 cells were seeded in 100 μL of culture medium in replicates (n = 4) in a 96-well culture plate for the WST-1 proliferation assay. Control wells containing the untreated cells, plated in the same conditions of the SW-treated samples, were also prepared. As before, the values kept from the untreated cells were set at 100% viability.

The experiments were then repeated, following the same protocol, preparing two flasks of KB and pre-incubating one with a freshly prepared solution of ZnO NCs (10 μg/mL per 24 h incubation) for the evaluation of the ZnO NCs-SW synergy. In this case, an additional control with KB cells, incubated with ZnO NCs but not irradiated with SW, was prepared.

Multiple SW Treatments

Since adherent cells bear multiple detachments, the protocol employed for the single treatment carried out from the literature was modified similarly to what reported by Marino et al. (2018,

2019) for the multiple treatments. Briefly, 1.5×10^3 cells were seeded into 100 μL of culture medium in a 96-well culture plate in replicates ($n = 4$). 24 h later, two wells were incubated with ZnO NCs (10 μg/mL) while the other two were re-filled with fresh medium. After 24 h, all the wells were washed with PBS and re-filled with 100 μL fresh culture medium. SW treatments were then performed (3 times/day, one every 4 h). 24 h after the last treatment, cell viability was carried out with the WST-1 proliferation assay.

ROS Scavenging Assay

The observed cell death upon the sonosensitizer activation is frequently related in the literature with the ROS production (Canavese et al., 2018; Vighetto et al., 2019). For this reason, the experiments with ZnO NCs and multiple SW treatments were repeated by pre-incubating KB cells with two different antioxidants in order to evaluate ROS involvement in cell proliferation upon ZnO NCs incubation and SW treatment. N-acetylcysteine (NAC, Sigma) and mannitol (MAN, Sigma) were chosen as ROS scavengers for this purpose.

It is reported that NAC could enhance cell antioxidant properties through increasing intracellular GSH and interacting with radicals such as H_2O_2 and OH• (Aruoma et al., 1989). MAN is instead an OH• scavenger (Goldstein and Czapski, 1984).

For NAC the successfully employed protocol by Brazzale et al. (2016) was followed. Briefly, 1 h before the first SW treatment, but already after the 24 h incubation with ZnO NCs, cell medium was replaced with a solution composed by culture medium with the addition of 5 mM NAC. This solution was discarded before the first SW treatment and cells were resuspended in culture medium (100 μL). Cell viability was measured with the WST-1 assay 24 h after the last treatment, as described before. In order to exclude potential toxic effects of the antioxidant alone, a well with untreated cells without NAC was also prepared.

For MAN the concentration was 0.1 M for 30 min incubation before the SW application (Yumita et al., 2010).

Kinetic Evaluation of Cell Death

The kinetic evaluation of cell apoptosis and necrosis was performed with the RealTime-Glo Annexin V Apoptosis and Necrosis Assay (Promega). Plate signals were collected with the microplate reader Glomax (Promega).

KB cells were plated in a black 96-well plate with clear bottom (Corning) following the same protocol already mentioned for the SW multiple treatments. Control wells were also prepared with culture medium to define the background of the luminescence and the fluorescence derived from the medium without cells. These values were subtracted from the test samples as recommended by the manufacturers.

The background of the samples was measured, then 100 μL of the reaction mix containing all the substrates for the reaction were added and immediately a second reading was performed. Then the signals were measured after each SW treatment and 24 h after the last one to have a comparison with the WST-1 viability tests.

Statistical Analysis

Measurement data were presented as mean ± standard error mean (SEM). Each assay was done at least in duplicate. One-way and two-way analysis of variance (ANOVA) were performed with the Sigmaplot software. $^{***}p < 0.001$, $^{**}p < 0.01$, and $^{*}p < 0.05$ were considered significant. A detailed report of the statistical analysis performed on each experiment is reported in the **Supplementary Material**.

RESULTS AND DISCUSSION

ZnO NCs, prior to the functionalization, were analyzed with XRD, shown in **Figure 1A**, and compared with the standard XRD pattern of ZnO (JCPDS card n. 36–1451) confirming that the pristine ZnO NCs showed the typical hexagonal wurtzite crystalline structure, with diffraction peaks corresponding to the Miller's index indicated in **Figure 1A**.

The HRTEM results (**Figures 1B,C**) additionally displayed that both the pristine and amino-functionalized NCs had a spherical morphology with size ranging from 15 to 25 nm and a single crystalline nature, in particular a wurtzite hexagonal structure, as already observed in our previous publication (Garino et al., 2019a).

The grafting of the amino-functional groups imparted to ZnO NCs a strong positive Z-potential in dd water (+22 mV), higher than the Z-potential recorded for pristine ZnO NCs (+15 mV), as shown in **Figure 1D**. DLS analyses were performed in both ethanol and dd water showing that amino-functionalized ZnO NCs hydrodynamic size was 79 nm in ethanol and 164 nm in dd water (**Figure 1F**), thus smaller than the hydrodynamic size of pristine ZnO NCs (91 nm in ethanol and aggregated in dd water, with 531 nm in size, **Figure 1E**). The positive charge of amino-functionalized ZnO NCs thus improves their colloidal stability in solution and can also possibly increase their uptake in cells, characterized mainly by negatively charged cell membranes (Albanese et al., 2012). Additionally, the amino functionalization allows the conjugation with different fluorescent dyes (Yu et al., 2014) for their further characterization at flow cytometry to test the internalization rate in cancer cells.

The viability of KB cancer cells after the incubation with different concentrations of ZnO NCs (5, 10, 15, 20, 25, 50 μg/mL) was assessed at different time points, as depicted in **Figure 2**, i.e., after 5, 24, 48, and 72 h. A dose dependent response was indeed observed, with a progressive decrease of cell viability increasing the concentration of ZnO NCs and confirming the previous results obtained at 24 h employing the same NCs (Garino et al., 2019a). ZnO NCs at the concentrations of 5 and 10 μg/mL resulted to be non-toxic for KB cells, while the mean percentages of cell viability progressively decreased starting from 15 μg/mL at all the considered time points. Moreover, the differences in cell viability between the safest conditions, i.e., 5–10 μg/mL, and the other ones continued to increase starting from 5 h of incubation. While a mild proliferative effect was observed at the lowest dosages at 48 h, cells incubated with 20-25-50 μg/mL of ZnO NCs never recovered and their viability drastically dropped after 24, 48, and 72 h. Interestingly, after 72 h a recovery of cells

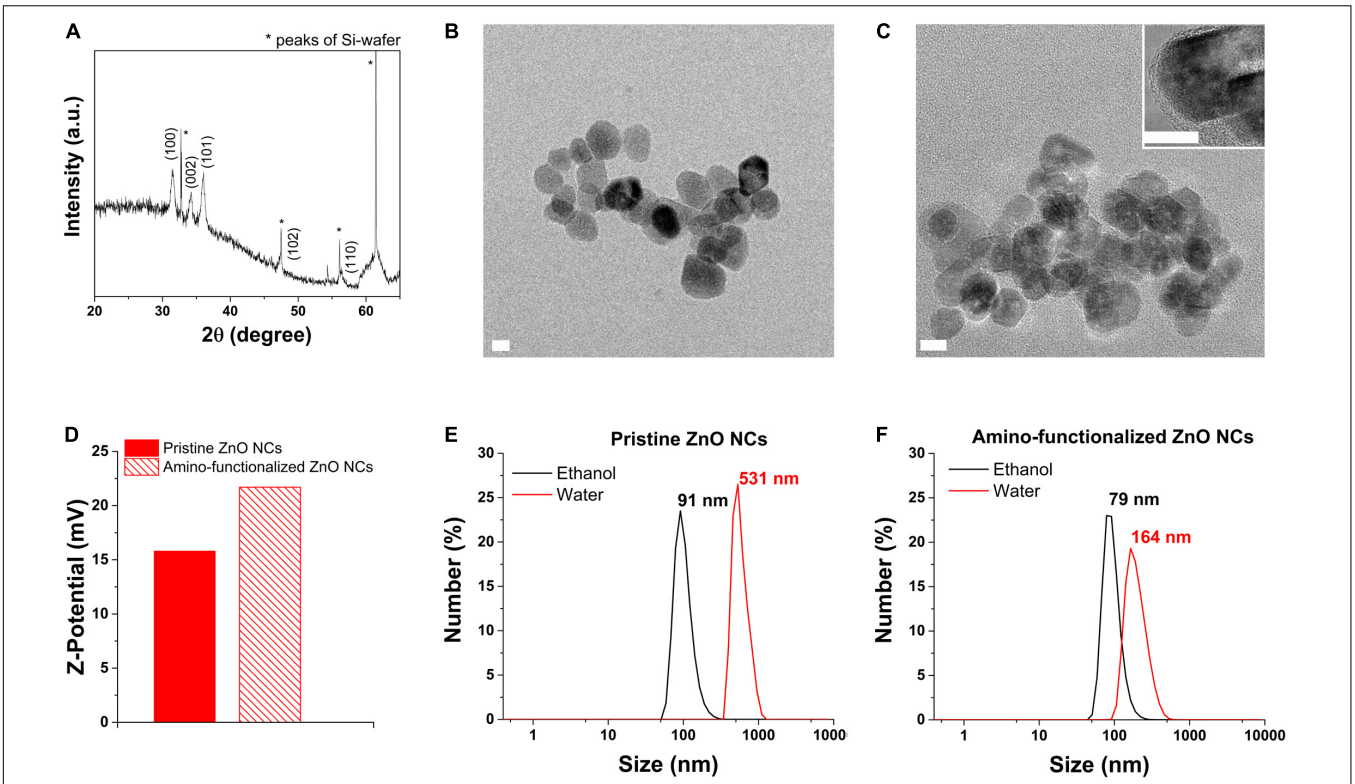

FIGURE 1 | ZnO NCs characterization. **(A)** XRD analysis. **(B)** HRTEM of pristine ZnO NCs and **(C)** amino-functionalized ZnO NCs, scale bar = 10 nm. The inset in C represents a higher magnification image of amino-functionalized ZnO NCs. **(D)** Z-potential of pristine and amino-functionalized ZnO NCs. DLS measurements of **(E)** pristine and **(F)** amino-functionalized ZnO NCs both in ethanol (black curve) and dd water (red curve).

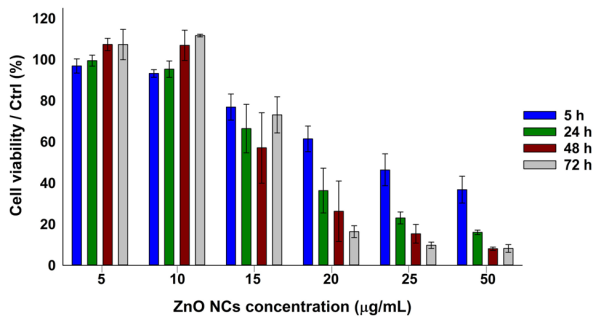

FIGURE 2 | ZnO NCs cytotoxicity on KB cells at different time points detected with the WST-1 assay. KB cells were incubated with different ZnO NCs concentrations (5, 10, 15, 20, 25, and 50 μg/mL). Cell viability was measured after 5, 24, 48, and 72 h. Bars represent mean ± SEM percentages of cell viability with respect to the control cells, $n = 3$.

incubated with 15 μg/mL was evidenced, with percentages of cell viability increasing from 57 ± 17% at 48 h up to 73 ± 9% at 72 h. The complete statistical analysis of these data is reported in the **Supplementary Material**.

ZnO NCs toxicity could be ascribed to two main events: the Zn^{2+} ions release and ROS production, as previously mentioned (Racca et al., 2018). The increase of NCs concentration exasperated both the reported effects, resulting in a marked decrease of cell growth.

The observed proliferative effect was also yet reported. Indeed, Zn^{2+} ions are involved in many cellular pathways, and thus a low dosage might enhance cell proliferation inducing key signal proliferation pathways (Liu et al., 2017).

Dedicated analyses of NC internalization were performed with the flow cytometry, detecting the Atto633 dye labeled ZnO NCs fluorescence inside the cells at progressive time points (5 and 24 h). In particular, the internalization of ZnO NCs-Atto633 at the concentration of 10 μg/mL was monitored, as it was the highest safe concentration in the previous cytotoxicity analysis. As it is possible to observe in **Figure 3**, a progressive increase of cells presenting a shift of the Red-R intensity, due to the NCs internalization, was recorded. A marked shift of the green curve, representing cells incubated with ZnO NCs-Atto633 for 5 h was also observed with respect to the black curve, corresponding to the untreated cells signal, suggesting that NCs internalization occurred quite rapidly. After 24 h of incubation, the percentage of cells internalizing the NCs increased, as noticeable from the orange curve, representing the signal of cells incubated with ZnO NCs-Atto633 at 10 μg/mL for 24 h. In particular, the percentage of positive events increased from 85 ± 3% at 5 h to 98.0 ± 0.4% at 24 h.

These results suggest that ZnO NCs were rapidly internalized in KB cells and, upon a longer incubation time, i.e., 24 h, almost

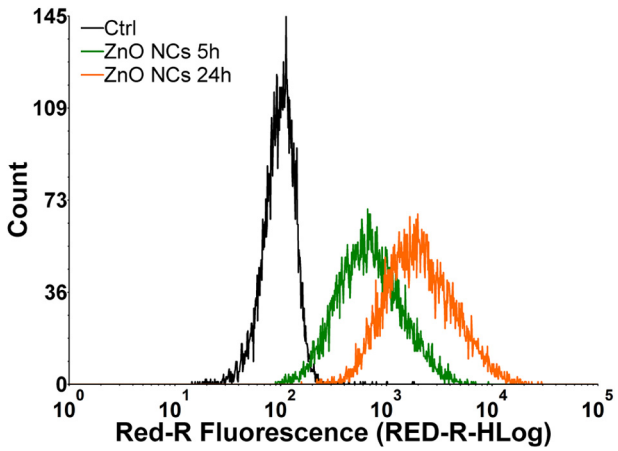

FIGURE 3 | Representative curves of ZnO NCs uptake in KB cells at different dosages and at different time point (5–24 h) of incubation. Black curve represents untreated cells signal (Ctrl), green curve regards signal generated by cells incubated with ZnO NCs 10 μg/mL for 5 h and orange one by the cells incubated with ZnO NCs 10 μg/mL for 24 h.

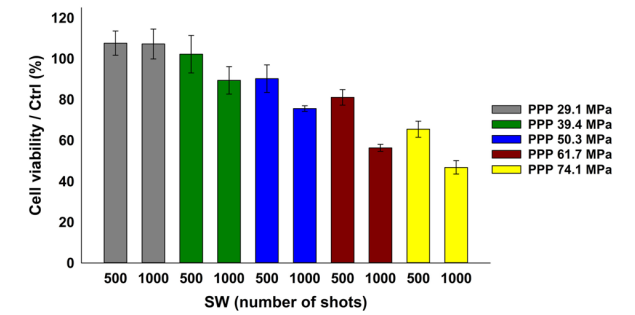

FIGURE 4 | KB cell viability upon SW treatment measured by the WST-1 proliferation assay. KB cells were treated with SW characterized by a different PPP and number of shots, as indicated in the bars legend. Results are shown as mean ± SEM percentage of cell viability with respect to control cells. $n = 3$.

all cells have internalized the highest amount of NCs. This result is indicated by the higher fluorescence intensity of these cells, as it is possible to observe in the pronounced shift of the orange curve with respect to the green one.

After the ZnO NCs characterization and the first tests to assess their cytotoxicity and internalization, the non-lethal dose of 10 μg/mL was identified as a safe condition for further investigations in combination with SW. In addition, 24 h seems to be a suitable incubation time, because almost all the considered cells presented a shift in fluorescence intensity due to NCs internalization at this time point.

For the tests in combination with SW, the effects of single toward multiple SW treatments were compared.

The analyses started looking for the safest conditions for KB cells under SW stimulation in absence of ZnO NCs. Based on the previous literature investigations (Canaparo et al., 2006, 2013; Serpe et al., 2011; Foglietta et al., 2017), a fixed number of shots (500 or 1000) was adopted, varying the PPP (29.1, 39.4, 50.3, 61.7, and 74.1 MPa). The cell viability decreased at increasing either the SW energies (from 29.1 MPa up to 74.1 MPa) or the number of shots (either 500 or 1000 shots), as evidenced in **Figure 4**. The related complete statistical analysis is reported in the **Supplementary Material**.

To prove the effective synergy between the SW and the ZnO NCs, the conditions where the cell viability were closest to 100 % with the sole stimulation (either SW alone or ZnO NC alone) were then selected. Cells were pre-incubated for 24 h with ZnO NCs at the concentration of 10 μg/mL and then treated with SW (ZnO NCs + SW). 24 h after the SW irradiation, cell viability was measured. The viabilities of untreated cells (Ctrl), cells incubated with ZnO NCs but not treated with SW (ZnO NCs) and cells treated only with SW in absence of ZnO NCs (SW) were also kept for comparison. The employed SW parameters were 29.1 MPa, 1000 shots (**Figure 5A**), 39.4 MPa, 500 shots (**Figure 5B**), 39.4 MPa, 1000 shots (**Figure 5C**) and 50.3 MPa, 500 shots (**Figure 5D**).

Interestingly, no differences in cell viability were evidenced between SW and ZnO NCs + SW cells, indicating that there was not a synergism between ZnO NCs and SW with the single treatment modality.

Multiple US treatments are routinely employed alone or in combination with drugs or nanoparticles in several *in vitro*, *in vivo* and in clinical trials studies (Ramirez et al., 1997; Hill et al., 2005; Wang et al., 2008; Ninomiya et al., 2012; Katiyar et al., 2014; Huang et al., 2018). Very recently, Marino et al. (2018, 2019) obtained positive results in terms of cell death combining barium titanate nanoparticles and multiple US treatments in an *in vitro* study. In these investigations, cells were treated 1 h/day for 4 consecutive days. This method was indeed applied here with some modifications and using ZnO NCs and SW on KB cells. The multiple SW dose was given by irradiating the KB cells three times in a day (a treatment every 4 h). 24 h after the last irradiation, cell viability was measured with the WST-1 assay as before.

As it is possible to observe in **Figure 6**, the cells incubated with ZnO NCs and subjected to multiple SW treatments always showed less viability than the control ones. In the first three cases, regarding cells treated with SW 29.1 MPa-1000 shots, 39.4 MPa-500 shots and 1000 shots (reported in **Figures 6A–C**, respectively), only those incubated with NCs and treated with SW were appreciably less viable than the controls. However, these results were not statistically different from the control experiments. Strikingly, the cells incubated with ZnO NCs and treated with SW with a PPP of 50.3 MPa and 500 shots (**Figure 6D**) resulted in a significant lower cell viability (47 ± 11%) not only with respect to the control or to the ZnO NCs cells w/o SW (100% of viability), but also with cells treated with only SW ($p < 0.01$ with a viability of 93 ± 9%) without NCs. Therefore, the anti-proliferative effect observed with the combination of ZnO NCs and multiple SW treatments was impressive and not found in the controls. These results suggest the existence of a powerful synergy between ZnO NCs and SW. While a single SW treatment is not able to induce a significant variation in ZnO NCs + SW cells, three consecutive SW treatments effectively result in a reduced cell viability.

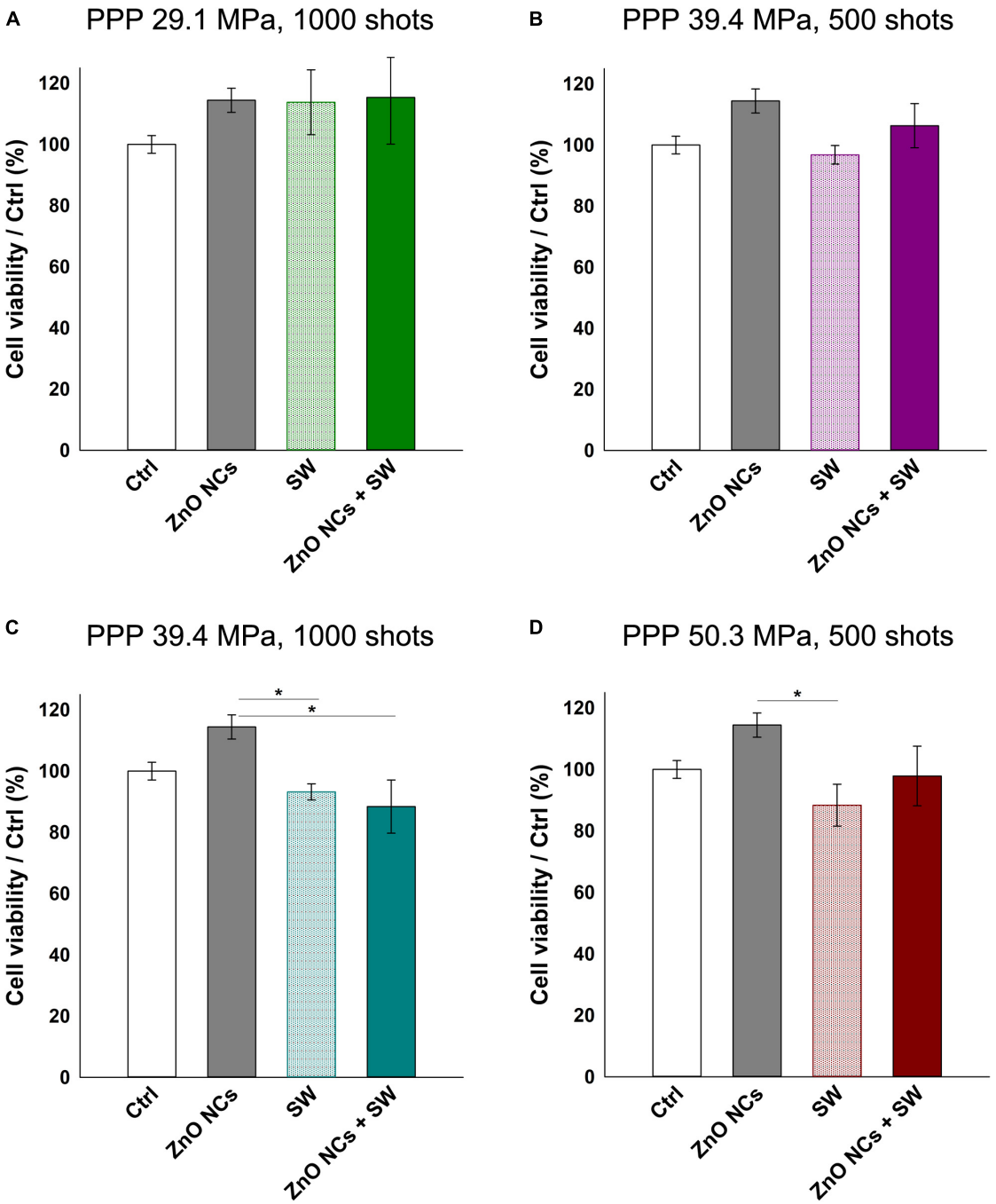

FIGURE 5 | Study on the possible synergistic effect of ZnO NCs and SW. Four different samples were prepared per assay. Control untreated cells (Ctrl), cells only incubated with 10 μg/mL ZnO NCs for 24 h (ZnO NCs), cells treated with SW (SW) and cells incubated with NCs and treated with SW (ZnO NCs + SW). Cells were treated with SW at: **(A)** 29.1 MPa, 1000 shots, **(B)** 39.4 MPa, 500 shots, **(C)** 39.4 MPa, 1000 shots, **(D)** 50.3 MPa, 500 shots. Cell viability was recorded 24 h after the SW treatment with the WST-1 proliferation reagent. Data are reported as the cell viability with respect to the control referred as the 100%. Results are shown as mean ± SEM. $n = 4$. $^*p < 0.05$.

Several SDT studies employ ROS scavengers to elucidate the ROS role in cell death upon the sonosensitizer activation (Brazzale et al., 2016; Canavese et al., 2018). In this regard, the experiments with ZnO NCs were repeated pre-incubating KB cells with two different antioxidants (NAC and MAN), using the experimental conditions where a significant difference between SW and ZnO NCs + SW cells was detected, i.e., with SW PPP 50.3 MPa, 500 shots, 3 treatments (**Figure 7**). Both NAC and MAN resulted to be non-toxic for KB cells in the chosen concentrations and times of incubation. Furthermore,

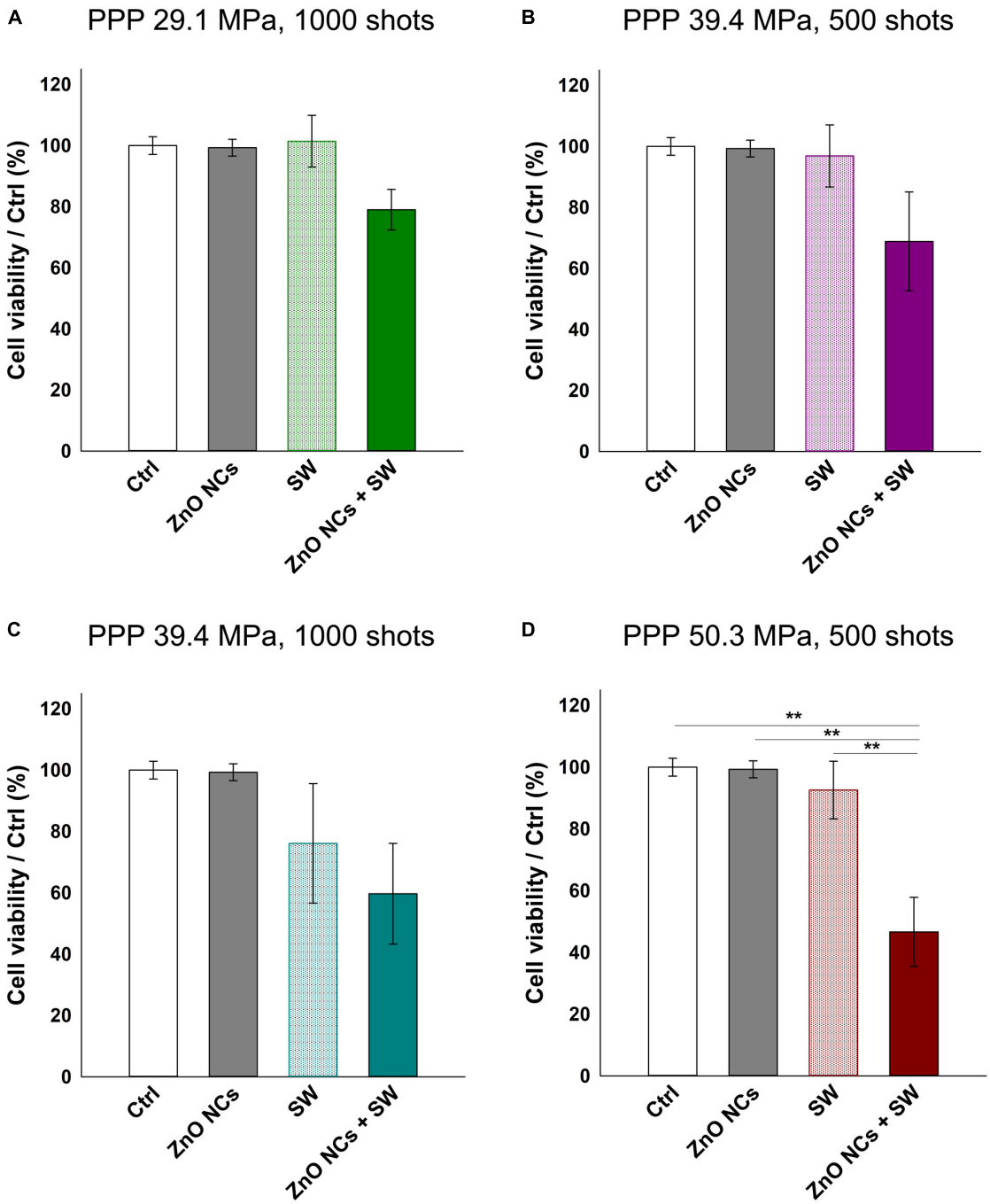

FIGURE 6 | Study of the possible synergistic effect of ZnO NCs and multiple SW treatments (3 times/day). Four different samples were prepared per assay. Control untreated cells (Ctrl), cells only incubated with 10 μg/mL ZnO NCs for 24 h (ZnO NCs), cells treated with SW (SW) and cells incubated with NCs and treated with SW (ZnO NCs + SW). Cells were treated with SW at: **(A)** 29.1 MPa, 1000 shots, **(B)** 39.4 MPa, 500 shots, **(C)** 39.4 MPa, 1000 shots, **(D)** 50.3 MPa, 500 shots. Cell viability was recorded 24 h after the SW treatment with the WST-1 proliferation reagent. Data are reported as the cell viability with respect to the control referred as the 100%. Results are shown as mean ± SEM. $n = 4$. $^{**}p < 0.01$.

the percentages of cell viability of ZnO NCs treated cells did not change with the addition of the antioxidants. Surprisingly, no cell viability recoveries were observed in ZnO NCs + SW samples, with both the scavengers. Furthermore, the presence of a scavenger seemed to already decrease the viability of SW-treated cells (in absence of ZnO NCs). In particular, only SW-treated cells percentage of viability shifted from 93 ± 9% (obtained from **Figure 6D**) to 58 ± 14% with NAC (**Figure 7A**) and to 59 ± 13% when pre-treated with MAN (**Figure 7B**). In contrast to the previous results, SW-treated cells resulted in a significant

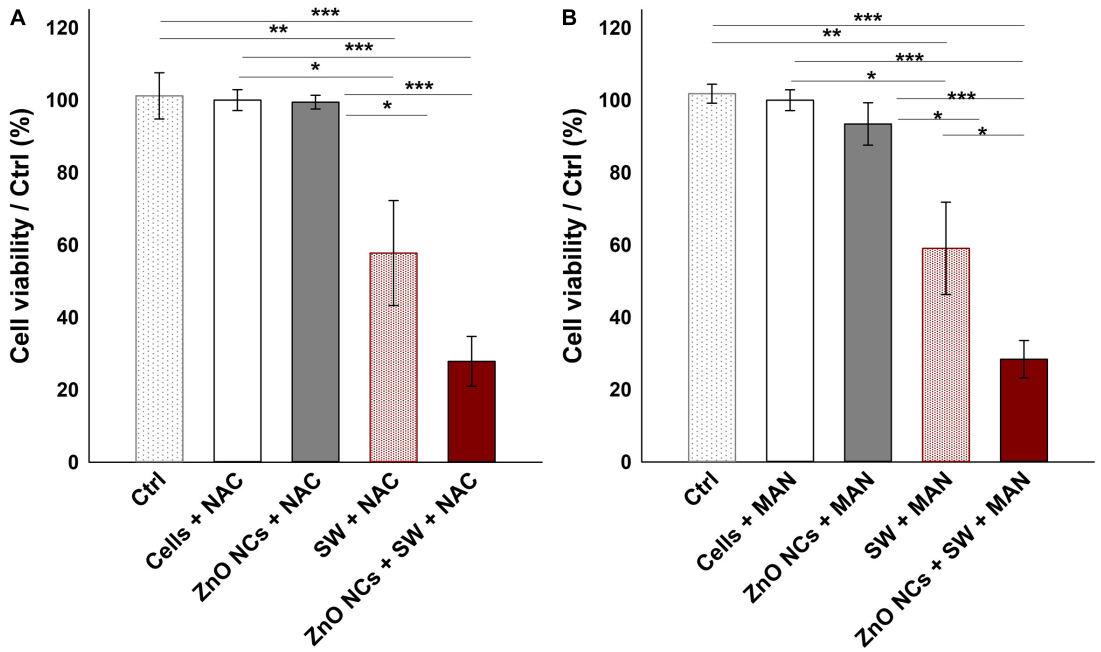

FIGURE 7 | Investigating the mechanism with ROS scavengers NAC **(A)** and MAN **(B)**. Five samples were prepared per assay. Ctrl were cells without the antioxidants; Cells+NAC and Cells+MAN were cells incubated with the antioxidants; ZnO NCs+NAC or MAN were cells incubated with 10 μg/mL ZnO NCs for 24 h and then with the antioxidants; SW+NAC or MAN were cells incubated with the antioxidants and treated with SW; and ZnO NCs+SW+NAC or MAN were cells incubated with NCs and the antioxidants, and then irradiated with SW PPP 50.3 MPa, 500 shots (3 treatments/day). Data are reported as the cell viability with respect to the control referred as the 100%. Results are shown as mean ± SEM. $n = 6$. $^{***}p < 0.001$, $^{**}p < 0.01$ and $^{*}p < 0.05$.

decreased viability with respect to control cells ($p < 0.01$ in both cases), to the cells with the antioxidants ($p < 0.05$ in both cases), and to the cells with ZnO NCs and the antioxidants ($p < 0.05$ in both cases). The same scenario was observed with the ZnO NCs + SW treated cells, where the percentage of cell viability shifted from 47 ± 11% (obtained from **Figure 6D**) down to 28 ± 7% with NAC (**Figure 7A**) and to 20 ± 6% with MAN (**Figure 7B**). Also in this case, significant differences were evidenced between these samples and the control cells, the cells with the antioxidants, and the cells with ZnO NCs and the antioxidants ($p < 0.001$ for all the comparisons and for both the antioxidants). Antioxidants pre-treatment seemed indeed to enhance SW cytotoxic power instead of allowing the recovery from SDT effects.

Actually, the ROS pivotal role on SDT is a debated question. From the one hand, many authors showed that the addition of an antioxidant molecule was able to protect cells from the SDT effects, thus claiming that ROS are strongly involved in the SDT mechanism of action (Li et al., 2012; Brazzale et al., 2016; Huang et al., 2018). On the contrary, other researchers proposed the mechanical stress as the main responsible of the observed cytotoxic effects (Canavese et al., 2018). Owing to these results, it seems here that ROS were not truly involved in the therapeutic effect recorded with SW. On the contrary, ROS showed to slight sustain cells proliferation, indeed their reduction with the addition of the two antioxidants resulted in a marked decrease of cell viability in both SW and ZnO NCs + SW samples. This could be explained remembering that ROS do not play always an anti-proliferative role. Instead, it is known and reported in the literature (Mittler, 2017) that ROS are essential for many cell functions, such as cell proliferation, innate immune responses and differentiation. Additionally, it is reported that ROS balance is strictly important to maintain cell homeostasis, because also faint imbalances could result in toxic consequences, thus their level is kept under control (Singh et al., 2018; Asadi-Samani et al., 2019).

In this context, it is probable that the imbalance of ROS levels caused by NAC and MAN addition followed by multiple SW treatments resulted to be more cytotoxic, suggesting that a certain level of ROS was perhaps necessary for KB cells to recover from SW induced damages.

In addition, the obtained results discourage the hypothesis of a ZnO NCs sonoluminescent activation. The production of light flash upon inertial acoustic cavitation is actually a debated issue. Some authors proposed the possibility of the organic sonosensitizer activation through sonoluminescence (Ninomiya et al., 2014; Brazzale et al., 2016; Beguin et al., 2019). In this case, an eventual light excitation of ZnO NCs has, as a result, the ROS overproduction with consequent cell death (Ancona et al., 2018). However, this phenomenon was not observed with the acoustic activation in our experiments, because a reduction in ROS burst was here associated with less cell viability and not with a recovery, as expected if the mechanism would be based on the light activation.

Here, the observed synergism possibly lies on a mechanical injury of the enhanced bubble cavitation. Indeed, the damage could derive from bubble oscillations under non-inertial

cavitation, or bubble implosion upon inertial cavitation (Izadifar et al., 2017). In this view, it is reasonable to suppose that the presence of ZnO NCs in cells subsequently irradiated with SW decreased the cavitation threshold improving the number of oscillating/imploding microbubbles, increasing the mechanical stress (Canavese et al., 2018). This effect was also previously reported by our research group using amino-functionalized ZnO NC in the presence of continuous ultrasound irradiation in water media (Vighetto et al., 2019).

In addition, the physical motion of nanoparticles internalized into cells upon US irradiation could also contribute to the cell death, even in absence of inertial cavitation, increasing locally the temperature and leading to mechanical destruction of the cells. This phenomenon is called "nanoscalpel effect," where nanoparticles physically alter organelles and nuclei (Osminkina et al., 2015).

A further possible mechanism, in concomitance to the above-mentioned ones, can be hypothesized based on the ZnO piezoelectric properties. Actually ZnO, due to its non-centrosymmetric crystal structure (Cauda et al., 2014; Racca et al., 2018) under a mechanical stimulation, is able to generate polar charges (Cauda et al., 2015; Laurenti et al., 2015, 2016). In this regard, the multiple and repetitive mechanical stimulation of ZnO NCs with the SW could also exert an electric stimulation in the cancer cells, resulting in a decrease of cell viability. This mechanism was also previously reported by Marino et al. with other piezoelectric nanomaterials (Marino et al., 2018, 2019).

To better elucidate the cell killing mechanism, the real-time measurement of both apoptotic and necrotic cells through luminescent and fluorescent signals was performed. In details, the used kit contains two annexin V fusion proteins associated with two complementary subunits of the luciferase enzyme. When the two subunits are in contact, during early apoptosis or secondary necrosis, the luciferase reacts with a substrate generating a luminescent signal. At the same time, a fluorescent intercalating DNA probe lets to precisely identify secondary necrosis. Thus, a sample negative for both signals indicates that cells are nor in apoptosis neither in necrosis. A sample positive for luminescence signal and not for fluorescence one indicates an early apoptosis, while a sample positive for both luminescence and fluorescence indicates the presence of secondary necrosis.

The recorded results of both luminescent and fluorescent signals are shown in **Figures 8A,B**, respectively. Before the addition of the reaction mix (pre mix) and immediately before the first SW treatment (post mix), the cell basal signal in both luminescence and fluorescence channels was very low. After the first SW irradiation, the SW and the ZnO NCs + SW treated cells immediately showed a marked increment of luminescence, while the recorded fluorescence reported a slight increase. After the second treatment, the SW and ZnO NCs + SW luminescence continued to increase, as well as the fluorescence of both samples. In contrast, after the third treatment, the recorded luminescence was more or less the same of the previous time point, while the fluorescence displayed a huge increase. In particular, the signal associated to the ZnO NCs + SW treated cells was more pronounced than the one related to only SW-treated cells (**Figure 8B**). After 24 h from the treatment, the luminescent signal dropped down and the four samples resulted to possess the same level of luminescence. The fluorescent signals also decreased, but to a less extend in comparison to the luminescent ones. In particular, the ZnO NCs + SW treated sample continued to possess a higher fluorescence signal than the one obtained from the cells treated with only SW. ZnO NCs-treated cells signal on the contrary showed the same trend of the control ones, indicating that ZnO NCs at the employed concentration and time of incubation did not induce any apoptosis nor necrosis.

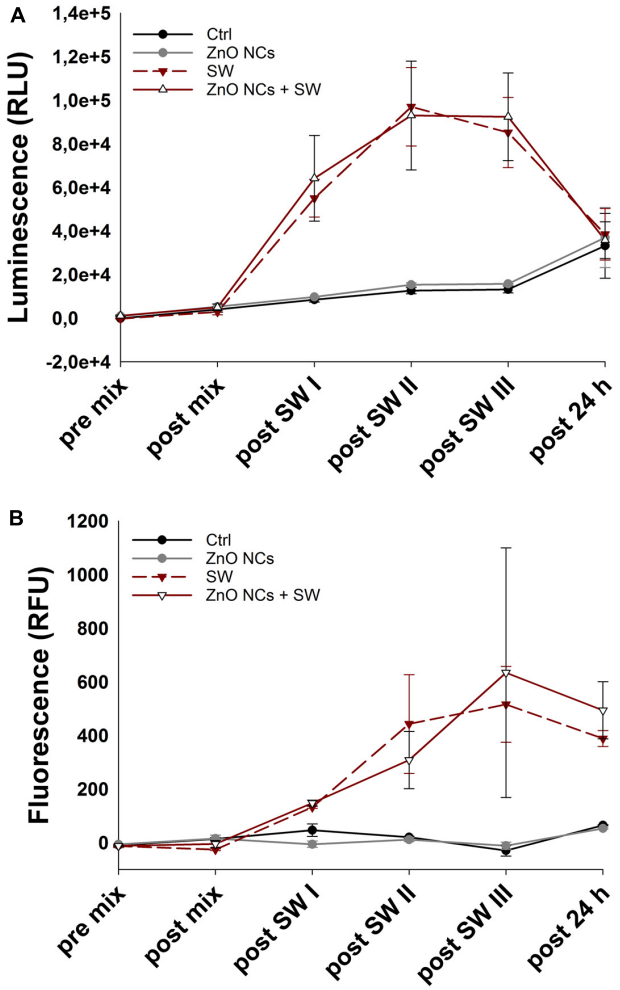

FIGURE 8 | Kinetic of cell death in the ZnO NCs + SW experiment. **(A)** luminescence, expressed as relative light units (RLU), and **(B)** fluorescence, expressed as relative fluorescence units (RFU), measurements. KB cells were considered alone (Ctrl), incubated with 10 μg/mL ZnO NCs for 24 h (ZnO NCs), treated with SW alone every 4 h for a total of 3 treatments in a day (SW), or incubated with ZnO NCs and then treated for three times (a treatment every 4 h) with SW (ZnO NCs + SW). Phosphatidylserine exposure (luminescence) and loss of the membrane integrity (fluorescence) were measured before the addition of the reaction mix (pre mix), after the addition but before SW treatment (post mix), after the first (post SW I), second (post SW II) and third (post SW III) SW treatment and 24 h after the last SW irradiation (post 24 h). $n = 2$.

Together, these results suggest that multiple treatments are required indeed to exert tumor cell death. The pro-apoptotic and necrotic effects of both SW and ZnO NCs + SW treated samples increased progressively after each treatment, achieving a peak in fluorescence after the third irradiation. Additionally, the fluorescent signals associated to ZnO NCs + SW treated cells showed a difference from the SW treated sample after the third treatment. This evidence agrees with the previous experiments, where no differences between SW and ZnO NCs + SW samples after a single SW treatment was evidenced. Here it was demonstrated that at least three treatments are required in order to obtain the desired synergistic effect.

Moreover, analyzing the trend of the two signals in **Figure 8**, the presence of an early apoptosis is highlighted after the first treatment, becoming, as expected, secondary necrosis in the next steps. The progressive increase of luminescence followed by an increase of the fluorescence signal is indeed typical of an apoptotic phenotype (Hassan et al., 2018). In this case, it is suggested that an apoptotic pathway is induced in both SW and ZnO + SW treated samples. However, the synergistic combination of the two stimuli resulted in a more pronounced cell death, as it was evidenced with the WST-1 tests of **Figure 6D**. The complete statistical analysis is reported in the **Supplementary Material**.

SW multiple treatments alone on KB cells were apparently able to first induce apoptosis and later, secondary necrosis. However, WST-1 results (**Figure 6D**) indicate that cancer cells recovered after 24 h from the last treatment, and thus the induced damages were reverted. This result is in accordance to what reported by Canaparo et al., who already observed that SW treatment was able to improve the percentage of cells in both apoptosis and necrosis (Canaparo et al., 2013).

Strikingly, the cells treated with ZnO NCs + SW were not able to recover, confirming that the synergistic action of ZnO NCs and SW induced irreversible consequences, resulting in a loss of cell viability.

The association between apoptosis and US is largely reported in the literature, even if the mechanism driving this event is not fully understood. US are indeed able to induce this type of cell death activating various pathways (Wan et al., 2016; Canavese et al., 2018; Huang et al., 2018).

Previous studies with SW associated with a photosensitizer, even if in a single dose, recorded a remarkable apoptosis and secondary necrosis caused by this synergy (Canaparo et al., 2006, 2013; Serpe et al., 2011). However, these estimations occurred at a single time point, while here we evaluated the trend over time at multiple SW stimulations.

Based on these results and the state of the art, it is thus hypothesized here that the apoptosis is caused by cell mechanical injury upon ZnO NCs and SW co-administration. Actually, it was previously observed that mechanical stress could result in DNA damage, with the activation of the apoptotic pathway (Furusawa and Kondo, 2017). Moreover, it was reported that SW mechanotransduction could exert an apoptotic pathway (d'Agostino et al., 2015), and the previously cited "nanoscalpel effect" is also related to apoptosis (Osminkina et al., 2015).

CONCLUSION

Herein the effects of amino-propyl functionalized ZnO NCs in combination with SW to treat cancer cells were investigated. Amino-propyl functionalized ZnO NCs were synthetized and characterized, confirming their single crystalline structure, with a spherical morphology and positive Z-potential, as previously reported (Garino et al., 2019a). Cytotoxicity tests let to identify the maximum non-lethal dose of the sole NCs. With internalization assays instead, the optimal incubation time to achieve a good internalization of ZnO NCs was undertaken.

After a preliminary phase dedicated to the study of the sole SW cytotoxicity, experiments involving both ZnO NCs and SW were carried out. It was discovered that a single treatment was not sufficient to achieve a significant difference in cells viability between SW and ZnO + SW stimulations. In contrast, multiple SW treatments (3 times/day) resulted to be highly cytotoxic and, strikingly, only for cells pre-incubated with ZnO NCs. Studies on the mechanism were then performed, finding that ROS role was controversial and seemed to be protective instead of being toxic. By exploring the kinetics of cell death, it was demonstrated that SW administration resulted in a pro-apoptotic stimulus. However, the ZnO NCs + SW stimuli led to high cell suffering, with an enhanced fluorescent signal associated with secondary necrosis and confirming what observed with the WST-1 viability assay. Additionally, it was highlighted that, only after the third treatment, an increase of ZnO NCs + SW fluorescent signals occurred with respect to the sole SW ones, suggesting the importance of the synergistic combination between ZnO NCs administration and SW stimulus.

Even if the elucidation of the exact mechanism of cell death is the focus of our current studies, we proposed here the combination of various effects, including the mechanical injury due to (i) the enhanced bubble cavitation and (ii) the so-called "nanoscalpel effect," as well as (iii) an electric change imbalance, potentially involving the piezoelectric behavior of ZnO.

Despite the previous report concerning the use of SW in presence or not with organic sonosensitizing molecules, this is the first time where a solid and dense nanomaterial, i.e., ZnO, results to be toxic in combination with SW. These results open the possibility of a future application of ZnO NCs and SW as an effective nanomedicine tool for cancer therapy.

FUTURE OVERVIEW

Further investigations about the mechanism of the observed synergy and cell death are required. In particular, dedicated quantitative and qualitative analysis could be performed to explain the synergy, such as gene expression to better understand the molecular mechanism (Foglietta et al., 2015), the evaluation of morphological modifications with a direct observation through fluorescence microscopy and transmission electron microscopy (Dai et al., 2014; Defour et al., 2014) and several

other tests to observe typical SW and ZnO nanoparticles related damages (Izadifar et al., 2017; Garino et al., 2019b). Moreover, the electric stimulation consequences could be measured, as suggested by other authors (Marino et al., 2018, 2019). Direct evaluation of intracellular ROS production, mechanical and electrical injuries are also further tests to be done for a better comprehension of the phenomenon. A different distribution of treatments and number of shots could also be tested in order to maximize the synergy. Since the ZnO specific toxicity toward cancer cells is reported in the literature (Racca et al., 2018; Dumontel et al., 2019), additional tests with ZnO NCs and SW on healthy cells could be performed to confirm the selectivity of the proposed anticancer approach before to proceed with *in vivo* investigations.

An additional enhancement could be generated by improving the colloidal dispersibility of ZnO NCs (Dumontel et al., 2019; Limongi et al., 2019). These interesting features could be successfully exploited for a future application of ZnO NCs and SW in *in vivo* investigations and clinic. An enhanced biostability can thus decrease the aggregation in biological fluids, improve the *in vivo* biodistribution and allow for future selective targeting to cancer cells, by anchoring targeting ligands.

DATA AVAILABILITY STATEMENT

The datasets generated for this study are available on request to the corresponding author.

AUTHOR CONTRIBUTIONS

All authors wrote the manuscript and gave approval to the final version of the manuscript.

FUNDING

This work has received funding from the European Research Council (ERC) under the European Union's Horizon 2020 Research and Innovation Program (Grant agreement No. 678151 – Project Acronym "TROJANANOHORSE" – ERC starting Grant), and also from the Politecnico di Torino and the Moschini Spa Company through a seed funding of Proof-of-Concept Grant No.16417.

ACKNOWLEDGMENTS

We wish to gratefully thank the ELvation Medical company for the supply free of charge of the PW^2 instrument (R. Wolf).

SUPPLEMENTARY MATERIAL

The Supplementary Material for this article can be found online at: https://www.frontiersin.org/articles/10.3389/fbioe.2020.00577/full#supplementary-material

REFERENCES

Albanese, A., Tang, P. S., and Chan, W. C. W. (2012). The effect of nanoparticle size, shape, and surface chemistry on biological systems. *Annu. Rev. Biomed. Eng.* 14, 1–16. doi: 10.1146/annurev-bioeng-071811-150124

Ancona, A., Dumontel, B., Garino, N., Demarco, B., Chatzitheodoridou, D., Fazzini, W., et al. (2018). Lipid-coated zinc oxide nanoparticles as innovative ROS-generators for photodynamic therapy in cancer cells. *Nanomaterials* 8:143. doi: 10.3390/nano8030143

Aruoma, O. I., Halliwell, B., Hoey, B. M., and Butler, J. (1989). The antioxidant action of N-acetylcysteine: its reaction with hydrogen peroxide, hydroxyl radical, superoxide, and hypochlorous acid. *Free Radic. Biol. Med.* 6, 593–597. doi: 10.1016/0891-5849(89)90066-X

Asadi-Samani, M., Farkhad, N., Mahmoudian-Sani, M., and Shirzad, H. (2019). "Antioxidants as a double-edged sword in the treatment of cancer," in *Antioxidants*, ed. E. Shalaby (London: IntechOpen).

Baskaran, R., Lee, J., and Yang, S.-G. (2018). Clinical development of photodynamic agents and therapeutic applications. *Biomater. Res.* 22, 25–25. doi: 10.1186/s40824-018-0140-z

Beguin, E., Shrivastava, S., Dezhkunov, N. V., McHale, A. P., Callan, J. F., and Stride, E. (2019). Direct evidence of multibubble sonoluminescence using therapeutic ultrasound and microbubbles. *ACS Appl. Mater. Interfac.* 11, 19913–19919. doi: 10.1021/acsami.9b07084

Bisht, G., and Rayamajhi, S. (2016). ZnO nanoparticles: a promising anticancer agent. *Nanobiomedicine* 3:9. doi: 10.5772/63437

Brazzale, C., Canaparo, R., Racca, L., Foglietta, F., Durando, G., Fantozzi, R., et al. (2016). Enhanced selective sonosensitizing efficacy of ultrasound-based anticancer treatment by targeted gold nanoparticles. *Nanomedicine* 11, 3053–3070. doi: 10.2217/nnm-2016-0293

Canaparo, R., Serpe, L., Catalano, M. G., Bosco, O., Zara, G. P., Berta, L., et al. (2006). High energy shock waves (HESW) for sonodynamic therapy: effects on HT-29 human colon cancer cells. *Anticancer Res.* 26, 3337–3342.

Canaparo, R., Serpe, L., Zara, G. P., Chiarle, R., Berta, L., and Frairia, R. (2008). High energy shock waves (HESW) increase paclitaxel efficacy in a syngeneic model of breast cancer. *Technol. Cancer Res. Treat.* 7, 117–124. doi: 10.1177/153303460800700204

Canaparo, R., Varchi, G., Ballestri, M., Foglietta, F., Sotgiu, G., Guerrini, A., et al. (2013). Polymeric nanoparticles enhance the sonodynamic activity of meso-tetrakis (4-sulfonatophenyl) porphyrin in an in vitro neuroblastoma model. *Int. J. Nanomed.* 8, 4247–4263. doi: 10.2147/IJN.S51070

Canavese, G., Ancona, A., Racca, L., Canta, M., Dumontel, B., Barbaresco, F., et al. (2018). Nanoparticle-assisted ultrasound: a special focus on sonodynamic therapy against cancer. *Chem. Eng. J.* 340, 155–172. doi: 10.1016/j.cej.2018.01.060

Cauda, V., Gazia, R., Porro, S., Stassi, S., Canavese, G., Roppolo, I., et al. (2014). "Nanostructured ZnO materials: synthesis, properties and applications," in *Handbook of Nanomaterials Properties*, eds B. Bhushan, D. Luo, S. Schricker, W. Sigmund, and S. Zauscher (Berlin: Springer), 137–177. doi: 10.1007/978-3-642-31107-9_32

Cauda, V., Stassi, S., Lamberti, A., Morello, M., Fabrizio Pirri, C., and Canavese, G. (2015). Leveraging ZnO morphologies in piezoelectric composites for mechanical energy harvesting. *Nano Ener.* 18, 212–221. doi: 10.1016/j.nanoen.2015.10.021

Chugh, H., Sood, D., Chandra, I., Tomar, V., Dhawan, G., and Chandra, R. (2018). Role of gold and silver nanoparticles in cancer nano-medicine. *Artif. Cells Nanomed. Biotechnol.* 46(suppl. 1), 1210–1220. doi: 10.1080/21691401.2018.1449118

d'Agostino, M. C., Craig, K., Tibalt, E., and Respizzi, S. (2015). Shock wave as biological therapeutic tool: from mechanical stimulation to recovery and healing, through mechanotransduction. *Int. J. Surg.* 24, 147–153. doi: 10.1016/j.ijsu.2015.11.030

Dai, S., Xu, C., Tian, Y., Cheng, W., and Li, B. (2014). In vitro stimulation of calcium overload and apoptosis by sonodynamic therapy combined with hematoporphyrin monomethyl ether in C6 glioma cells. *Oncol. Lett.* 8, 1675–1681. doi: 10.3892/ol.2014.2419

Defour, A., Sreetama, S. C., and Jaiswal, J. K. (2014). Imaging cell membrane injury and subcellular processes involved in repair. *J. Vis. Exp.* 85:e51106. doi: 10.3791/51106

Dumontel, B., Susa, F., Limongi, T., Canta, M., Racca, L., Chiodoni, A., et al. (2019). ZnO nanocrystals shuttled by extracellular vesicles as effective Trojan nanohorses against cancer cells. *Nanomedicine* 14, 2815–2833. doi: 10.2217/nnm-2019-0231

Foglietta, F., Canaparo, R., Francovich, A., Arena, F., Civera, S., Cravotto, G., et al. (2015). Sonodynamic treatment as an innovative bimodal anticancer approach: shock wave-mediated tumor growth inhibition in a syngeneic breast cancer model. *Discov. Med.* 20, 197–205.

Foglietta, F., Duchi, S., Canaparo, R., Varchi, G., Lucarelli, E., Dozza, B., et al. (2017). Selective sensitiveness of mesenchymal stem cells to shock waves leads to anticancer effect in human cancer cell co-cultures. *Life Sci.* 173, 28–35. doi: 10.1016/j.lfs.2017.01.009

Furusawa, Y., and Kondo, T. (2017). DNA damage induced by ultrasound and cellular responses. *Mol. Biol.* 6:2. doi: 10.4172/2168-9547.1000188

Garino, N., Limongi, T., Dumontel, B., Canta, M., Racca, L., Laurenti, M., et al. (2019a). A microwave-assisted synthesis of zinc oxide nanocrystals finely tuned for biological applications. *Nanomaterials* 9:212. doi: 10.3390/nano9020212

Garino, N., Sanvitale, P., Dumontel, B., Laurenti, M., Colilla, M., Izquierdo-Barba, I., et al. (2019b). Zinc oxide nanocrystals as a nanoantibiotic and osteoinductive agent. *RSC Adv.* 9, 11312–11321. doi: 10.1039/C8RA10236H

Goldstein, S., and Czapski, G. (1984). Mannitol as an $OH^{\cdot}$ scavenger in aqueous solutions and in biological systems. *Int. J. Radiat. Biol. Relat. Stud. Phys. Chem. Med.* 46, 725–729. doi: 10.1080/09553008414551961

Hassan, F., Ni, S., Arnett, T. C., McKell, M. C., and Kennedy, M. A. (2018). Adenovirus-mediated delivery of decoy hyper binding sites targeting oncogenic HMGA1 reduces pancreatic and liver cancer cell viability. *Mol. Ther. Oncol.* 8, 52–61. doi: 10.1016/j.omto.2018.01.002

Hill, G. E., Fenwick, S., Matthews, B. J., Chivers, R. A., and Southgate, J. (2005). The effect of low-intensity pulsed ultrasound on repair of epithelial cell monolayers in vitro. *Ultrasound Med. Biol.* 31, 1701–1706. doi: 10.1016/j.ultrasmedbio.2005.08.001

Huang, J., Liu, F., Han, X., Zhang, L., Hu, Z., Jiang, Q., et al. (2018). Nanosonosensitizers for highly efficient sonodynamic cancer theranostics. *Theranostics* 8, 6178–6194. doi: 10.7150/thno.29569

Izadifar, Z., Babyn, P., and Chapman, D. (2017). Mechanical and biological effects of ultrasound: a review of present knowledge. *Ultrasound Med. Biol.* 43, 1085–1104. doi: 10.1016/j.ultrasmedbio.2017.01.023

Jiang, H., Wang, H., and Wang, X. (2011). Facile and mild preparation of fluorescent ZnO nanosheets and their bioimaging applications. *Appl. Surf. Sci.* 257, 6991–6995. doi: 10.1016/j.apsusc.2011.03.053

Jiang, J., Pi, J., and Cai, J. (2018). The advancing of zinc oxide nanoparticles for biomedical applications. *Bioinorgan. Chem. Appl.* 2018:18. doi: 10.1155/2018/1062562

Katiyar, A., Duncan, R. L., and Sarkar, K. (2014). Ultrasound stimulation increases proliferation of MC3T3-E1 preosteoblast-like cells. *J. Ther. Ultrasound* 2:1. doi: 10.1186/2050-5736-2-1

Kwiatkowski, S., Knap, B., Przystupski, D., Saczko, J., Kędzierska, E., Knap-Czop, K., et al. (2018). Photodynamic therapy – mechanisms, photosensitizers and combinations. *Biomed. Pharmacother.* 106, 1098–1107. doi: 10.1016/j.biopha.2018.07.049

Laurenti, M., and Cauda, V. (2017). ZnO nanostructures for tissue engineering applications. *Nanomaterials* 7:374. doi: 10.3390/nano7110374

Laurenti, M., and Cauda, V. (2018). Gentamicin-releasing mesoporous ZnO structures. *Materials* 11:314. doi: 10.3390/ma11020314

Laurenti, M., Canavese, G., Stassi, S., Fontana, M., Castellino, M., Pirri, C. F., et al. (2016). A porous nanobranched structure: an effective way to improve piezoelectricity in sputtered ZnO thin films. *RSC Adv.* 6, 76996–77004. doi: 10.1039/C6RA17319E

Laurenti, M., Stassi, S., Lorenzoni, M., Fontana, M., Canavese, G., Cauda, V., et al. (2015). Evaluation of the piezoelectric properties and voltage generation of flexible zinc oxide thin films. *Nanotechnology* 26:215704. doi: 10.1088/0957-4484/26/21/215704

Li, Y., Wang, P., Zhao, P., Zhu, S., Wang, X., and Liu, Q. (2012). Apoptosis induced by sonodynamic treatment by protoporphyrin IX on MDA-MB-231 cells. *Ultrasonics* 52, 490–496. doi: 10.1016/j.ultras.2011.10.013

Lim, E.-K., Kim, T., Paik, S., Haam, S., Huh, Y.-M., and Lee, K. (2015). Nanomaterials for theranostics: recent advances and future challenges. *Chem. Rev.* 115, 327–394. doi: 10.1021/cr300213b

Limongi, T., Canta, M., Racca, L., Ancona, A., Tritta, S., Vighetto, V., et al. (2019). Improving dispersal of therapeutic nanoparticles in the human body. *Nanomedicine* 14, 797–801. doi: 10.2217/nnm-2019-0070

Liu, J., Kang, Y., Zheng, W., Song, B., Wei, L., Chen, L., et al. (2017). From the cover: ion-shedding zinc oxide nanoparticles induce microglial BV2 cell proliferation via the ERK and Akt signaling pathways. *Toxicol. Sci.* 156, 167–178. doi: 10.1093/toxsci/kfw241

Mallidi, S., Anbil, S., Bulin, A.-L., Obaid, G., Ichikawa, M., and Hasan, T. (2016). Beyond the barriers of light penetration: strategies, perspectives and possibilities for photodynamic therapy. *Theranostics* 6, 2458–2487. doi: 10.7150/thno.16183

Marino, A., Almici, E., Migliorin, S., Tapeinos, C., Battaglini, M., Cappello, V., et al. (2019). Piezoelectric barium titanate nanostimulators for the treatment of glioblastoma multiforme. *J. Colloid Interface Sci.* 538, 449–461. doi: 10.1016/j.jcis.2018.12.014

Marino, A., Battaglini, M., De Pasquale, D., Degl'Innocenti, A., and Ciofani, G. (2018). Ultrasound-activated piezoelectric nanoparticles inhibit proliferation of breast cancer cells. *Sci. Rep.* 8:6257. doi: 10.1038/s41598-018-24697-1

Martínez-Carmona, M., Gun'ko, Y., and Vallet-Regí, M. (2018). ZnO nanostructures for drug delivery and theranostic applications. *Nanomaterials* 8:268. doi: 10.3390/nano8040268

Mittler, R. (2017). ROS are good. *Trends Plant Sci.* 22, 11–19. doi: 10.1016/j.tplants.2016.08.002

Ninomiya, K., Noda, K., Ogino, C., Kuroda, S.-I., and Shimizu, N. (2014). Enhanced OH radical generation by dual-frequency ultrasound with TiO2 nanoparticles: its application to targeted sonodynamic therapy. *Ultrason. Sonochem.* 21, 289–294. doi: 10.1016/j.ultsonch.2013.05.005

Ninomiya, K., Ogino, C., Oshima, S., Sonoke, S., Kuroda, S.-I., and Shimizu, N. (2012). Targeted sonodynamic therapy using protein-modified TiO2 nanoparticles. *Ultrason. Sonochem.* 19, 607–614. doi: 10.1016/j.ultsonch.2011.09.009

Ogden, J. A., Tóth-Kischkat, A., and Schultheiss, R. (2001). Principles of shock wave therapy. *Clin. Orthop. Relat. Res.* 387, 8–17.

Osminkina, L. A., Nikolaev, A. L., Sviridov, A. P., Andronova, N. V., Tamarov, K. P., Gongalsky, M. B., et al. (2015). Porous silicon nanoparticles as efficient sensitizers for sonodynamic therapy of cancer. *Microporous Mesoporous Mater.* 210, 169–175. doi: 10.1016/j.micromeso.2015.02.037

Racca, L., Canta, M., Dumontel, B., Ancona, A., Limongi, T., Garino, N., et al. (2018). "12 – zinc oxide nanostructures in biomedicine," in *Smart Nanoparticles for Biomedicine*, ed. G. Ciofani (Amsterdam: Elsevier), 171–187.

Ramirez, A., Schwane, J., McFarland, C., and Starcher, B. (1997). The effect of ultrasound on collagen synthesis and fibroblast proliferation in vitro. *Med. Sci. Sports Exerc.* 29, 326–332. doi: 10.1249/00005768-199505001-00294

Rosenthal, I., Sostaric, J. Z., and Riesz, P. (2004). Sonodynamic therapy–a review of the synergistic effects of drugs and ultrasound. *Ultrason. Sonochem.* 11, 349–363. doi: 10.1016/j.ultsonch.2004.03.004

Sanginario, A., Cauda, V., Bonanno, A., Bejtka, K., Sapienza, S., and Demarchi, D. (2016). An electronic platform for real-time detection of bovine serum albumin by means of amine-functionalized zinc oxide microwires. *RSC Adv.* 6, 891–897. doi: 10.1039/C5RA15787K

Serpe, L., Canaparo, R., Berta, L., Bargoni, A., Zara, G. P., and Frairia, R. (2011). High energy shock waves and 5-aminolevulinic for sonodynamic therapy: effects in a syngeneic model of colon cancer. *Technol. Cancer Res. Treat.* 10, 85–93. doi: 10.7785/tcrt.2012.500182

Shanmugam, N. R., Muthukumar, S., and Prasad, S. (2017). A review on ZnO-based electrical biosensors for cardiac biomarker detection. *Future Sci. OA* 3, FSO196. doi: 10.4155/fsoa-2017-0006

Shi, J., Kantoff, P. W., Wooster, R., and Farokhzad, O. C. (2017). Cancer nanomedicine: progress, challenges and opportunities. *Nat. Rev. Cancer* 17, 20–37. doi: 10.1038/nrc.2016.108

Shibaguchi, H., Tsuru, H., Kuroki, M., and Kuroki, M. (2011). Sonodynamic cancer therapy: a non-invasive and repeatable approach using low-intensity ultrasound with a sonosensitizer. *Anticancer Res.* 31, 2425–2429.

Singh, K., Bhori, M., Kasu, Y. A., Bhat, G., and Marar, T. (2018). Antioxidants as precision weapons in war against cancer chemotherapy induced toxicity – exploring the armoury of obscurity. *Saudi Pharm. J.* 26, 177–190. doi: 10.1016/j.jsps.2017.12.013

Singh, S. (2019). Zinc oxide nanoparticles impacts: cytotoxicity, genotoxicity, developmental toxicity, and neurotoxicity. *Toxicol. Mech. Methods* 29, 300–311. doi: 10.1080/15376516.2018.1553221

Stassi, S., Chiadò, A., Cauda, V., Palmara, G., Canavese, G., Laurenti, M., et al. (2017). Functionalized ZnO nanowires for microcantilever biosensors with enhanced binding capability. *Anal. Bioanal. Chem.* 409, 2615–2625. doi: 10.1007/s00216-017-0204-2

Sviridov, A. P., Osminkina, L. A., Nikolaev, A. L., Kudryavtsev, A. A., Vasiliev, A. N., and Timoshenko, V. Y. (2015). Lowering of the cavitation threshold in aqueous suspensions of porous silicon nanoparticles for sonodynamic therapy applications. *Appl. Phys. Lett.* 107:123107. doi: 10.1063/1.4931728

Tran, S., DeGiovanni, P.-J., Piel, B., and Rai, P. (2017). Cancer nanomedicine: a review of recent success in drug delivery. *Clin. Transl. Med.* 6:44. doi: 10.1186/s40169-017-0175-0

Varchi, G., Foglietta, F., Canaparo, R., Ballestri, M., Arena, F., Sotgiu, G., et al. (2015). Engineered porphyrin loaded core-shell nanoparticles for selective sonodynamic anticancer treatment. *Nanomedicine* 10, 3483–3494. doi: 10.2217/nnm.15.150

Vighetto, V., Ancona, A., Racca, L., Limongi, T., Troia, A., Canavese, G., et al. (2019). The synergistic effect of nanocrystals combined with ultrasound in the generation of reactive oxygen species for biomedical applications. *Front. Bioeng. Biotechnol.* 7:374. doi: 10.3389/fbioe.2019.00374

Wan, G.-Y., Liu, Y., Chen, B.-W., Liu, Y.-Y., Wang, Y.-S., and Zhang, N. (2016). Recent advances of sonodynamic therapy in cancer treatment. *Cancer Biol. Med.* 13, 325–338. doi: 10.20892/j.issn.2095-3941.2016.0068

Wang, X. J., Mitchell, D., and Lewis, T. J. (2008). Primary clinical use of sonodynamic therapy (SDT) for advanced breast cancer. *J. Clin. Oncol.* 26, 12029–12029. doi: 10.1200/jco.2008.26.15_suppl.12029

Yu, S. Y., Jing, H., Cao, Z., and Su, H. Q. (2014). The luminescent properties and toxicity controllability investigation of novel ZnO quantum dots with schiff base complexes modification. *J. Nanosci. Nanotechnol.* 14, 3299–3304. doi: 10.1166/jnn.2014.7990

Yumita, N., Iwase, Y., Nishi, K., Ikeda, T., Umemura, S.-I., Sakata, I., et al. (2010). Sonodynamically induced cell damage and membrane lipid peroxidation by novel porphyrin derivative, DCPH-P-Na(I). *Anticancer Res.* 30, 2241–2246.

Zavaleta, C., Ho, D., and Chung, E. J. (2017). Theranostic nanoparticles for tracking and monitoring disease state. *SLAS Tech.* 23, 281–293. doi: 10.1177/2472630317738699

Zhang, J., Shrivastava, S., Cleveland, R. O., and Rabbitts, T. H. (2019). Lipid-mRNA nanoparticle designed to enhance intracellular delivery mediated by shock waves. *ACS Appl. Mater. Interfaces* 11, 10481–10491. doi: 10.1021/acsami.8b21398

Conflict of Interest: The authors declare that the research was conducted in the absence of any commercial or financial relationships that could be construed as a potential conflict of interest.

frontiers in Bioengineering and Biotechnology

ORIGINAL RESEARCH
published: 15 September 2020
doi: 10.3389/fbioe.2020.570490

Nanotheranostics With the Combination of Improved Targeting, Therapeutic Effects, and Molecular Imaging

Shin-Lei Peng[1†], Chih-Ho Lai[2†], Pei-Yi Chu[3], Jer-Tsong Hsieh[4], Yen-Chun Tseng[5], Shao-Chieh Chiu[6] and Yu-Hsin Lin[3,7,8]*

[1] Department of Biomedical Imaging and Radiological Science, China Medical University, Taichung, Taiwan, [2] Department of Microbiology and Immunology, Molecular Infectious Disease Research Center, Chang Gung University, Chang Gung Memorial Hospital, Taoyuan, Taiwan, [3] Faculty of Pharmacy, National Yang-Ming University, Taipei, Taiwan, [4] Department of Urology, University of Texas Southwestern Medical Center, Dallas, TX, United States, [5] Department of Biological Science and Technology, China Medical University, Taichung, Taiwan, [6] Center for Advanced Molecular Imaging and Translation, Chang Gung Memorial Hospital, Taoyuan, Taiwan, [7] Department of Medical Research, China Medical University Hospital, China Medical University, Taichung, Taiwan, [8] Institute of Biopharmaceutical Science, Department and Institute of Pharmacology, Center for Advanced Pharmaceutics and Drug Delivery Research, National Yang-Ming University, Taipei, Taiwan

OPEN ACCESS

Edited by:
Mitsuhiro Ebara,
National Institute for Materials Science, Japan

Reviewed by:
Nanasaheb D. Thorat,
University of Limerick, Ireland
Alessandra Quarta,
Institute of Nanotechnology (CNR), Italy

***Correspondence:**
Yu-Hsin Lin
ylhsin@ym.edu.tw

[†] These authors have contributed equally to this work

Specialty section:
This article was submitted to Nanobiotechnology, a section of the journal Frontiers in Bioengineering and Biotechnology

Received: 08 June 2020
Accepted: 27 August 2020
Published: 15 September 2020

Citation:
Peng S-L, Lai C-H, Chu P-Y, Hsieh J-T, Tseng Y-C, Chiu S-C and Lin Y-H (2020) Nanotheranostics With the Combination of Improved Targeting, Therapeutic Effects, and Molecular Imaging. Front. Bioeng. Biotechnol. 8:570490. doi: 10.3389/fbioe.2020.570490

There is an increasing interest in the design of targeted carrier systems with combined therapeutic and diagnostic modalities. Therapeutic modalities targeting tumors with single ligand-based targeting nanocarriers are insufficient for proficient delivery and for targeting two different surface receptors that are overexpressed in cancer cells. Here, we evaluated an activated nanoparticle delivery system comprising fucoidan/hyaluronic acid to improve therapeutic efficacy. The system comprised polyethylene glycol-gelatin-encapsulated epigallocatechin gallate (EGCG), poly (D,L-lactide-co-glycolide; PLGA), and stable iron oxide nanoparticles (IOs). The latter enables targeting of prostate cancers in their molecular images. We demonstrate the transfer of nanoparticles and their entry into prostate cancer cells through ligand-specific recognition. This system may prove the benefits of drug delivery that enhances the inhibition of cell growth through apoptosis induction. Moreover, the improved targeting of nanotheranostics significantly suppressed orthotopic prostate tumor growth and more accurately targeted tumors compared with systemic combination therapy. In the presence of nanoparticles with iron oxides, the hypointensity of the prostate tumor was visualized on a T2-weignted magnetic resonance image. The diagnostic ability of this system was demonstrated by accumulating fluorescent nanoparticles in the prostate tumor from the *in vivo* imaging system, computed tomography. It is suggested that theranostic nanoparticles combined with a molecular imaging system can be a promising cancer therapy in the future.

Keywords: targeting tumors, fucoidan, hyaluronic acid, molecular images, nanotheranostics

INTRODUCTION

Cancer is a heterogeneous group of diseases characterized by the generation of abnormal cells. Such cells proliferate uncontrollably, invading and destroying normal tissues (Salako et al., 2017; Gao et al., 2019; Roma-Rodrigues et al., 2019). Current cancer therapies may not achieve the optimum prognosis. Thus, effective and innovative targeted therapies are required (Leach et al., 2016; Yang et al., 2019). Moreover, single-target drug carriers may be unsatisfactory for selective and effective therapy. Therefore, carriers targeting different surface receptors overexpressed in tumor tissues have been studied (Kos et al., 2015; Gamper et al., 2019). Cancer cells usually present multiple surface antigens. For example, overexpression of fucosylated epitopes, such as type I and type II Lewis antigens, frequently occurs on the surface of cancer cells, and these molecules are highly expressed in association with high levels of Lewisy in localized and metastatic prostatic adenocarcinoma (Myers et al., 1995; Blanas et al., 2018). Fucosylation occurs when fucose residues are transferred to an oligosaccharide chain attached to a cell surface glycoprotein or glycolipid (Ma et al., 2006). Fucoidan (FU), a polysaccharide containing numerous L-fucose and sulfate ester residues, is a fucosylated agent binding material and has been considered as a binding agent of P-selectin (Preobrazhenskaya et al., 1997). The upregulation of P-selectin on tumor blood vessels has been demonstrated in a previous study (Preobrazhenskaya et al., 1997). Chung et al. (2020) used dendrimer-fucoidan polyionic nanocomplex specifically targets triple-negative breast cancer overexpressing P-selectin and tumor-related vasculature.

Prostate cancer cells can spread to other body parts, particularly the bone, where they adhere strongly to bone marrow endothelial cells that show high levels of membrane-associated CD44 (Draffin et al., 2004; van der Toom et al., 2016; Gao et al., 2018). Stem cell-like $CD44^+$ prostate cancer cells invade *in vitro* and metastasize *in vivo* (Draffin et al., 2004; Liu et al., 1999). The CD44 molecules expressed by cancer cells interact with hyaluronan (HA)-rich microenvironments, thereby affecting signaling pathways that induce malignant cells to invade and migrate, initiating metastatic tumor cell inflammation (Park et al., 2008; Chen et al., 2017). HA is a linear glycosaminoglycan comprising alternating disaccharide units of N-acetyl-D-glucosamine and D-glucuronic acid with $\beta(1 \rightarrow 4)$ interglycosidic linkages (Mizrahy et al., 2011). In addition, HA can be used as a targeting molecule toward cancer cells in nanoparticle (NP) delivery systems and increase the cellular uptake of NPs (Mattheolabakis et al., 2015). The numerous strategies that specifically target cancer stem cells have met with limited success (Krishnamurthy et al., 2015). NPs specifically and effectively target such cells (Bae et al., 2018; Deng et al., 2020). Poly (D,L-lactide-co-glycolide; PLGA) is commonly used in NPs employed in biomedical applications because of its excellent biocompatibility and is approved by the United States Food and Drug Administration (Sah and Sah, 2015). However, intravenously administered PLGA NPs, like other conventional colloidal carriers, are rapidly removed from the circulation by macrophages (Avgoustakis, 2004). Polyethylene glycol (PEG), a water-soluble polymer, can modify gelatin [PEG-gelatin (PG)] to decrease the cytotoxicity of doxorubicin significantly and increase the stability of NPs in cancer treatment (Lee et al., 2006). For example, Cao et al. (2016) used PEGylated PLGA NPs to prolong circulation time by preventing opsonin binding, which reduces the rapid uptake of NPs by the reticuloendothelial system.

The use of combination therapies targeting the metabolic and physiological properties of cancer cells reduces drug resistance. However, differences in their pharmacokinetics, inconsistency of drug uptake by tumor cells, and suboptimal drug concentrations *in vivo* limit their efficacy in cancer therapy (Park et al., 2008; Frohlich, 2012). Epigallocatechin gallate (EGCG), a phytochemical extracted from green tea, binds with high affinity to laminin receptors, which are overexpressed in prostate cancer cells. Furthermore, EGCG inhibits matrix metalloproteinases, which are associated with tumor invasion and metastasis, inducing apoptosis in prostate cancer cells and prostate cancer stem cells (Shukla et al., 2012; Zhou et al., 2016). EGCG has prompted increased interest in the design of nanoagents with combined therapeutic and diagnostic properties (Chung et al., 2014; Cheng et al., 2016; Du et al., 2016). Moreover, the design of targeting carrier systems by combining therapeutic and diagnostic modalities is gaining increasing attention. Smart platforms of hybrid nanostructures to release chemotherapeutic molecules/drugs in response to an external stimulus to perform remotely controlled therapeutics, diagnostics, and therapy monitoring in a variety of solid tumors, including brain cancer, breast cancer, and osteosarcoma, have been reported (Li et al., 2019; Min et al., 2019; Su et al., 2020; Thorat and Bauer, 2020). To develop nanoagents with diagnostic properties, iron oxide nanoparticles (IOs) can be used as magnetic resonance imaging (MRI) contrast agents to produce high-resolution and high-contrast images of tissues (Weissleder et al., 1990; Weinstein et al., 2010; Luong et al., 2017; Xu et al., 2019). Here, we specifically developed NPs comprising PLGA-containing IOs for biological imaging, using FU/HA to achieve targeting activity and applying PG-carrying EGCG to eradicate prostate tumors (**Figure 1**). Its efficacies were examined in cancer cells and in an orthotopic tumor mouse model.

MATERIALS AND METHODS

Materials

Hyaluronan and FU were purchased from Lifecore Biomedical, LLC (Chaska, MN, United States) and Chambio, Co., Ltd. (Taichung, Taiwan). Oleic-acid-coated IO nanoparticles (5 nm in diameter) dispersed in chloroform were obtained from AC Diagnostics, Inc. (Fayetteville, AR, United States). The N-hydroxylsuccinimide (NHS) functionalized methoxy polyethylene glycol (molecular weight 5,000 Da) was obtained from Nanocs, Inc. (New York, NY, United States). The VivoTag®-S 750 (VT750) is an amine reaction (NHS ester) near-infrared fluorochrome (excitation/emission at 750/775) purchased from PerkinElmer, Inc. (Waltham, MA, United States). Type A gelatin (molecular weight 25,000 Da), dimethyl sulfoxide,

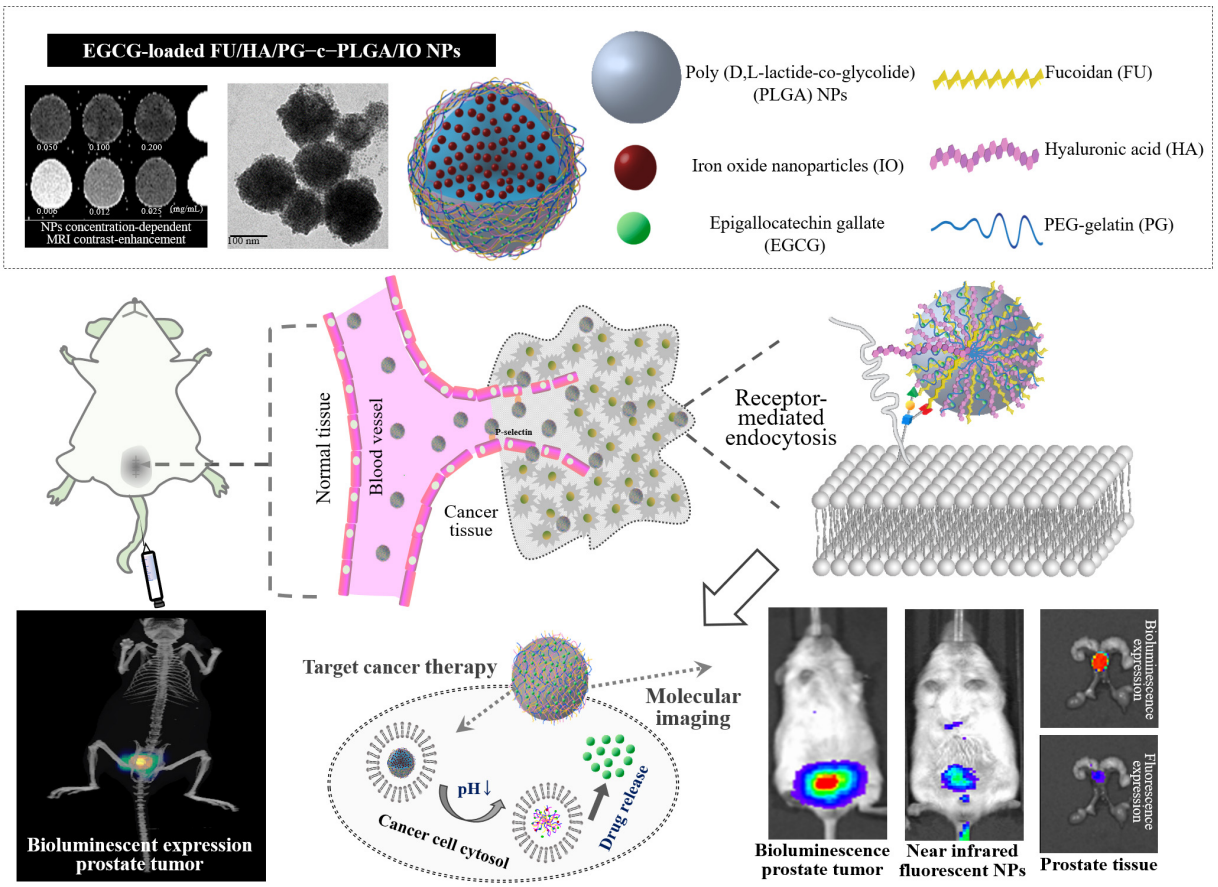

FIGURE 1 | Schematic representation of using an effective epigallocatechin gallate (EGCG)-loaded FU/HA/PG-coated [Poly (D,L-lactide-co-glycolide); PLGA] nanoparticles (NPs) targeting strategy and observation of their putative effects on prostate carcinoma cells.

3-(4,5-dimethylthiazol-2-yl)-2,5-diphenyltetrazolium bromide (MTT), rhodamine 6G (R6G), fluoresceinamine (FA), fluorescein isothiocyanate (FITC), 4′,6-diamidino-2-phenylindole (DAPI), phosphate-buffered saline (PBS), puromycin, EGCG, and Triton X-100 were purchased from Sigma-Aldrich (St Louis, MO, United States). Fetal bovine serum (FBS), Roswell Park Memorial Institute Medium, penicillin-streptomycin were from Gibco (Brooklyn, New York, United States). All other chemicals and reagents were of analytical grade.

Preparation and Characterization of FHP-c-PLGA NPs

Poly (D,L-lactide-co-glycolide) nanoemulsion particles were produced using a water-in-oil emulsification method employing homogenization using a rotating blade homogenizer (IKA Labortechnik, Germany). A 2.0 mL volume of D-α-tocopheryl polyethylene glycol succinate (TPGS) surfactant solution (30.0 mg/mL) was poured slowly into ethyl acetate containing 2.0 mL of PLGA solution (4.0 mg/mL). The mixture was homogenized at 15,000 rpm for 5 min at 4°C. The prepared PLGA NPs were centrifuged, then the pellets were washed with distilled water to remove the organic solvent, and then the precipitate was collected and suspended in deionized water for used the rest of the FHP–c–PLGA NPs study. The solution (1.0 mL) of polyvinyl alcohol surfactant (48.0 mg/mL) and different FU:HA:PG compositions (0.0:0.0:0.0, 1.2:1.2:1.2, 2.4:2.4:2.4, and 4.8:4.8:4.8 mg/mL) were mixed into the aqueous PLGA NPs solution (2.0 mg/mL, 1.0 mL) through a pipette tip with gentle stirring and then allowed to react for 2 h to form FU/HA/PG–coated PLGA NPs (FHP–c–PLGA NPs). The NPs were centrifuged and suspended in deionized water for Fourier-transform infrared spectroscopy (FTIR) analysis or placed onto a 400 mesh copper grid for scanning electron microscopy.

Characterization and Drug Release Profiles of EGCG-Loaded FHP-c-PLGA NPs

To study the release of EGCG from test NP samples, we prepared EGCG-loaded FHP–c–PLGA NPs. The EGCG solutions (0.0, 1.0, 2.0, 3.0 mg/mL; 1.0 mL) were each mixed with 1.0 mL of aqueous 2.0 mg/mL NPs and then stirred at room temperature. The NPs comprising PEG-gelatin were homogenized to form encapsulated EGCG. Gelatin is a water-soluble protein mixture derived from the natural polymer collagen (Boni et al., 2018; Chivere et al., 2020). Previous studies have shown that it can bind

polyphenols via hydrogen-bonding interactions among amino acids such as proline and the phenol ring of polyphenols (Shutava et al., 2009; Mi et al., 2018). The EGCG loaded NPs were collected by centrifugation, and the concentration of free EGCG in the supernatant was determined using high-performance liquid chromatography (HPLC). The drug loading efficiency and loading content of NPs were described in the literature and calculated according to the following equation:

$$\text{loading efficiency} = \frac{\text{total amount of EGCG} - \text{free EGCG in supernatant}}{\text{total amount of EGCG}} \times 100\% \quad (1)$$

$$\text{loading content} = \frac{\text{total amount of EGCG} - \text{free EGCG in supernatant}}{\text{weight of NPs}} \times 100\% \quad (2)$$

To investigate the stability of EGCG-loaded NPs, NPs were incubated at pH 7.4, 6.5 (10 mM PBS) and then at pH 5.0 (10 mM acetic acid/sodium acetate), simulating the pH values of physiological fluids, tumor tissues, and endosomal compartments (Qiu et al., 2008; Tian et al., 2013; Nehate et al., 2017). The EGCG-loaded NPs (2.0 mg/mL, 0.2 mL) were added to dialysis bags and dialyzed against 2.0 mL of these solutions. The dialysates (0.1 mL) were sampled and replenished with the same freshly prepared buffers to prevent drug saturation. The drugs released into the dialysate were detected using an HPLC system to determine the percentage of cumulative drug release. NP morphology was examined using transmission electron microscopy (TEM).

Cell Viability After Treatment With Only NPs and EGCG Solution or EGCG-Loaded NPs

For cytocompatibility studies, normal prostate epithelial cells (PZ-HPV7; ATCC® CRL-2221™) and human prostate cancer cells (PC3 cells; ATCC® CRL1435) were seeded in a 96-well plate at a density of 1.0×10^4 cells/well and maintained at 37°C and 5% CO_2 for overnight. The media containing different concentrations of only FHP-c-PLGA NPs and the cells were incubated for 2 h, and cells were washed twice with PBS and cultured in fresh growth medium for 22 h. Cells exposed to media only served as positive controls. The cell viability was determined at each time point using cell viability MTT assays. Moreover, the prostate cancer cells were allowed to adhere overnight and then treated with the EGCG solution or EGCG-loaded NPs containing different concentrations of EGCG for 2 h. Cell culture supernatants were gently removed, and cultured in fresh growth medium for 22 h prior to evaluation of cellular toxicity with MTT assays. Changes in cell morphology induced by EGCG-loaded FHP–c–PLGA NPs or only FHP–c–PLGA NPs and control samples were analyzed using an inverted microscope under phase-contrast illumination (10 × objective; Olympus, Japan).

Confocal Laser Scanning Microscopy Observation of Fluorescent-Labeled NP on Cancer Cells

To quantify the fluorescence signal of the NPs [R6G-FU/FA-HA/Cyanine 5 (Cy5)-PG–c–PLGA or Cy5-EGCG-loaded R6G-FU/FA-HA/PG–c–PLGA NPs] in cells, fluorescent FA-conjugated HA (FA-HA) was produced through reactions between FA (excitation/emission at 496/525) amine moieties and HA carboxylic acid groups based on earlier work carried out by Harada et al. (2006), with some modifications. R6G-FU was produced as R6G (excitation/emission at 515/555) in acetonitrile solution (1 mg/1 mL), added gently to FU in distilled water (100 mg/10 mL), and mixed with 1 mg of 1-ethyl-3-(3-dimethylaminopropyl) carbodiimide hydrochloride with continuous stirring for 12 h at 4°C. To eliminate unconjugated fluorescent R6G dye, R6G-FU was dialyzed against distilled water in the dark until no further fluorescence remained in the supernatant. The product was then lyophilized. Cy5-NHS or Cy5-hydrazide (excitation/emission at 646/662) was conjugated to PG or EGCG to prepare Cy5-PG or Cy5-EGCG, respectively. Cy5-NHS or Cy5-hydrazide in dimethyl sulfoxide (1 mg/mL) was prepared and added gradually to soluble PG or EGCG in distilled water (100 mg/10 mL) with continuous stirring for 12 h. To remove the unconjugated Cy5-NHS, Cy5-PG was dialyzed until fluorescence was undetectable in the supernatant. Cy5-EGCG was lyophilized using a freeze dryer, and lyophilized Cy5-EGCG was dissolved in distilled water. The precipitate was removed and subjected to repeated cycles of washing and centrifugation until the fluorescence of Cy5-hydrazide dye was undetectable in the precipitate. Cy5-PG and Cy5-EGCG were then lyophilized.

To detect the internalization of fluorescent NPs in PC3 cells, the cells were incubated on glass cover slip (3×10^5 cells/cm^2) for 1 day. Cells (2×10^5) were incubated with a Global Eukaryotic Microcarrier® (Global Cell Solutions, United States) in LeviTubes culture vessels at 37°C and 5% CO_2 for 7 days to track the NPs internalization of three-dimensional cancer cells. Test samples (0.4 mg/mL) were added to cells, incubated for 2 h, aspirated and washed with PBS, and fixed in 3.7% paraformaldehyde. The cells were permeabilized with 2 mg/mL Triton X-100 and stained with DAPI and observed using a confocal laser scanning microscope (CLSM).

Confocal Microscopy Observation of Apoptosis and Flow Cytometric Analysis of Cell Cycle

To analyze the EGCG-loaded NPs effects on apoptosis, FITC-Annexin V solution was used to detect apoptotic cells following the instructions provided by the manufacturer. The cells (3×10^5 cells/cm^2) were incubated on glass coverslips for 24 h. The test samples were put into cells for 2 h and were incubated in growth medium for further incubated 22 h. After washing with PBS and suspending in binding buffer, FITC-Annexin V was added to the cells and incubated for 15 min at 4°C, and stained cells were recorded by using confocal microscopy (excitation at 488 nm and emission at 525 nm; Gao et al., 2011). Subsequently, to examine the effects of EGCG-loaded NPs on cell cycle progression, PC3 cells were incubated with NP samples for 2 h, washed twice in PBS, and incubated in growth media for 22 h. Cells were washed with ice-cold PBS and then fixed in ice-cold 70% ethanol. After extensive washing, cells were suspended in hypotonic buffer and incubated at 37°C for 1 h. Propidium iodide (1.00 mg/mL, 0.01 mL) was added and then incubated for 0.5 h at 4°C in the dark. The propidium iodide and a BD FACSCanto

System (BD Biosciences, United States) were used to analyze the cell cycle phases.

Western Blotting Analysis of Apoptosis-Related Proteins

To evaluate the expression of apoptotic proteins, PC3 cells were subjected to western blotting analysis after treatment with EGCG-loaded NPs. For this purpose, cells were lysed using freeze/thaw cycles, and the cell lysates were centrifuged at 6,000 g at 4°C. Equal amounts of cell protein lysates were electrophoretically separated through sodium dodecyl sulfate (SDS) polyacrylamide gel, and the separated proteins were electrophoretically transferred onto polyvinylidene difluoride (PVDF) membranes, which were putted into PBS containing 5% (w/v) nonfat dry milk for 1 h and then probed with primary antibodies [i.e., rabbit poly-clonal anti-caspase-9 and anti-poly (ADP-ribose) polymerase (PARP)]; mouse monoclonal anti-caspase-8, anti-caspase-3 and anti-β-actin) overnight at 4°C. Membranes were incubated with horseradish peroxidase-conjugated secondary anti-bodies for 1 h, and immune complexes were detected enhanced chemiluminescence (Amersham Life Science, United States).

Mouse Model of Orthotopic Prostate Tumor

Animal care and use is in accordance with the 1996 revision of the Guide for the Care and Use of Laboratory Animals issued by the National Research Council Laboratory Animal Resources Institute. Severe combined immunodeficiency (SCID) 6-week-old males were used for xenografting. The mice were housed in the animal facility at least 1 week before injection with luminescent PC3 cells (Luc-PC3 cells) from Professor Jer-Tsong Hsieh (UT Southwestern Medical Center, Dallas, TX). After the abdomens of SCID mice were sterilized with alcohol, a transverse incision was made into the lower abdomen and bladder, and the seminal vesicles and prostate were removed from the abdominal cavity to expose the anterior prostate. Luc-PC3 cells (3×10^6/20 μL) were injected into the prostate gland. The bladder was replaced, and the muscle layer was closed using absorbable vicryl monofilament sutures. The skin layers were secured using sterile staples.

Magnetic Resonance Imaging (MRI) and *in vivo* Imaging System-Computed Tomography (IVIS Spectrum CT) Detection of NPs in Tumors

To achieve MR-based molecular imaging of the prostate tumor, the FHP–c–PLGA-encapsulated IO (FHP-c-PLGA/IO NPs) were produced according to the procedure described in previous section. The mean particle sizes and zeta potential values of the FHP-c-PLGA/IO NPs were measured with a Zetasizer instrument. MR-T2 relaxation times of FHP-c-PLGA/IO NPs were determined using a 7T MRI system (Bruker ClinScan 70/30, Germany). Samples were diluted with distilled water before adding them to 96-well microplates. Relaxivity was calculated by acquiring a multiecho spin echo sequence as follows: repetition time (TR) = 2000 ms; echo time (TE) = 7.2–230.4 ms (7.2 ms intervals); slice thickness = 1 mm; matrix size = 256 × 256; field of view (FOV) = 50 × 50 mm. The images were analyzed using custom Matlab scripts (The MathWorks, United States). Spin–spin T2 relaxation was estimated as follows: $M = M_0 e^{-TE/T2}$, where M_0 is the magnetic moment at equilibrium. For *in vivo* MR imaging of FHP–c–PLGA/IO NPs, eight SCID mice were used. A prostate tumor model was established by injecting cancer cells into the prostates of recipients. Four other mice served as controls. All MRI experiments were conducted using a 7T animal MRI scanner (gradient strength = 630 mT/m). The volume coil was used for signal excitation and the surface coil for signal detection. Mice were anesthetized with 4% isoflurane, which as reduced to 2.5% isoflurane for maintenance. A 30-gage needle connected to a 0.8 m polyethylene-30 tube was inserted into the tail vein for the injection of FHP–c–PLGA/IO NPs. A T2-weighted (T2W) fast spin echo sequence was used before and after one hour sample injection as follows: TR = 1,780 ms; TE = 69 ms; slice thickness = 0.8 mm; matrix size = 208 × 256; FOV = 36 × 45 mm.

To further observe the distribution of NPs in Luc-PC3 cells in xenografts, near-infrared fluorescent VT750-labeled NPs were injected through the tail vein into Luc PC3 tumor-bearing mice. Briefly, 0.1 mL of 1.0 mg/0.1 mL VT750 dye solution in dimethyl sulfoxide was added gradually to 5.0 mL of 10.0 mg/mL soluble PG in distilled water with continuous stirring for 12 h at 4°C. The unreacted dye was removed via dialysis, and the VT750-conjugated PG (VT750-PG) was lyophilized. The near-infrared fluorescent FU/HA/VT750-PG–c–PLGA NPs was prepared using the same protocol as for the preparation of NPs. Fluorescence imaging was performed using an *in vivo* imaging system (IVIS; excitation 710–760 nm; emission 810–875 nm). CT images were acquired using an IVIS Spectrum CT scanner (PerkinElmer, Inc., United States) with the settings as follows: 50 kV at 1 mA, 140 s acquisition and reconstruction times, and aluminum filter. We acquired 720 projections spaced 0.5° apart, and the CT volume was reconstructed using Living Image software with a FOV = 12.0 cm × 12.0 cm × 13.0 cm at 0.15 mm isotropic resolution.

Evaluations of Antitumor Activity, Bioluminescent Imaging, and Histological Analysis

To evaluate antitumor activity, the orthotopic luminescent prostate tumors were grown for 7 days. The SCID mice were then randomly divided into three groups of six mice each, which received different formulations of 0.1 mL of 15.0 mg EGCG/kg, EGCG-loaded FHP–c–PLGA NPs, and FHP–c–PLGA NPs (controls). Mice were injected in the tail vein every third day. Bioluminescent imaging *in vivo* was performed using an extremely sensitive charge-coupled device camera included with the IVIS Spectrum *in vivo* optical imaging system and viewed in real-time to measure total flux (pho-tons/s/cm^2/steradian). The condition and body weight of each mouse was determined. One day after the last bioluminescent observation, the mice were sacrificed and their tissues were removed for histological

examination. Tissue biopsies were performed with the aid of a visible-light microscope, and biopsies were stained with hematoxylin-eosin or subjected to immunohistochemistry using rabbit monoclonal antibodies against Ki-67 (Thermo Fisher Scientific, United States) and cleaved PARP (Cell Signaling Technology Inc., United States). Tissue inflammation and the microdistribution of stained tissue sections were detected at different magnifications using a visible light microscope.

Statistical Analysis

Statistical analysis to assess differences between groups was performed using one-way analysis of variance. The Statistical Analysis System was used to calculate the Confidence intervals. Data are presented as the mean ± standard deviation. The p values with an asterisk indicating $p < 0.05$ and two asterisks indicating $p < 0.01$ are considered statistically significant.

RESULTS

Preparation and Characterization of FHP-c-PLGA NPs

Poly (D,L-lactide-co-glycolide) nanoemulsion particles were prepared using a water-in-oil emulsification method with TPGS nonionic surfactant [hydrophile lipophilic balance (HLB) = 13.2]. Different concentrations of the FU/HA/PG mixture coated onto the PLGA NP solution were examined to find the optimal formulation for FU/HA/PG-coated PLGA NPs (FHP–c–PLGA NPs) preparation. As shown in **Table 1**, the mean particle size and polydispersity index of NPs were ranging from 158.64 ± 9.87 to 252.47 ± 19.76 nm and from 0.13 ± 0.04 to 0.43 ± 0.16, respectively. At a FU:HA:PG ratio of 1.2:1.2:1.2 mg/mL, NPs produced a particle size of 198.89 ± 12.56 nm with a negative zeta potential value of -33.75 ± 1.24 mV and had a significantly narrower distribution (0.22 ± 0.09). However, when the FU:HA:PG concentration was elevated to 2.4:2.4:2.4 mg/mL, the NP polydispersity index was increased to 0.4, indicating high heterogeneity. The polydispersity index is a parameter used to define particle size distribution and is a dimensionless number extrapolated from the autocorrelation function that ranges from 0 to 1. Values close to 0 indicate a homogeneous dispersion, while those greater than 0.3 indicate high heterogeneity. Therefore, the optimal FU:HA:PG concentrations were 1.2:1.2:1.2 mg/mL which therefore be used in subsequent experiments.

The FTIR analyses detected characteristic peaks of PLGA at 1,761 cm^{-1} and 2,937 cm^{-1} assigned to the stretching bands of C = O and C–H. The spectrum of FU showed stretching vibrations of O = S = O of sulfate esters at broad bands at approximately 1,244 cm^{-1}. Scissoring vibrations of CH_2 (galactose, xylose) or asymmetric bending vibrations of CH_3 (fucose, O-acetyls) were detected at 1,439 cm^{-1}, and HA exhibited C = O asymmetric stretching at 1,627 cm^{-1} and C–O symmetric stretching at 1,403 cm^{-1}, corresponding to carboxyl groups. Symmetrical PG peaks at 949 and 842 cm^{-1} corresponded to the reflected bending of C–O and C–C stretching vibrations, respectively, of PEG, and a characteristic band at 1,542 cm^{-1} represented the bending associated –NH stretching vibration of gelatin. The spectrum of the FHP–c–PLGA complex showed characteristic bands at 1,755 cm^{-1}, representing the C = O deformation band of PLGA and at 1,547 cm^{-1}, representing –NH bending of PG. Moreover, the characteristic C = O stretching at 1,627 cm^{-1} of HA and S = O stretching at 1,244 cm^{-1} of FU shifted to 1,635 and 1,229 cm^{-1}. These observations reflect intramolecular and intermolecular hydrogen bonding between –NH of PG to C = O of HA or PLGA (C = O···H–N) and S = O of FU (S = O···H–N; **Figure 2A**). Furthermore, PLGA, FU, HA, and PG complexes segregated into colloidal NPs (**Figure 1**).

Characterization of EGCG-Loaded FHP–c–PLGA NPs and Drug-Release Profiles

Epigallocatechin gallate-loaded FHP–c–PLGA NPs were produced by gelation of different concentrations of EGCG solution with aqueous FHP-c-PLGA NPs solution. The EGCG loading efficiencies and loading contents were as follows: 43.98 ± 7.87% and 9.87 ± 1.69% for EGCG (0.5 mg/mL); 47.86 ± 4.57% and 19.67 ± 2.48% for EGCG (1.0 mg/mL), and 37.96 ± 6.68% and 22.17 ± 3.98% for EGCG (1.5 mg/mL). Formation with EGCG concentration 1.0 mg/mL, the sizes of EGCG-loaded NPs were 217.19 ± 11.37 nm; zeta potential values were -35.75 ± 2.39 mV, and appreciably narrower distributions (0.25 ± 0.09), which formed a spherical and uniform matrix (**Table 2** and **Figure 2B**).

We next evaluated the pH-responsive property of EGCG-loaded NPs by using HPLC and TEM to determine drug release profiles and the morphologies of the NPs. At pH 7.4–6.5 (simulating the pH values of physiological fluids or the environment of tumor tissues), EGCG stably bound to PG to form hydrogen bonds, which generated spheres in the matrix. The percentages of EGCG released from NPs after 3 h incubation was 13.68 ± 1.73% at pH 7.4 and 18.41 ± 1.17% at pH 6.5. In contrast, at pH 5.0, $–COO^-$ groups were partially protonated in HA, affecting the negative electrostatic interaction between NPs. The structures of the NPs became unstable, accompanied with gradual increases of EGCG release from 30.25 ± 3.79% at 3 h to 71.12 ± 4.96% at 24 h (**Figure 3A**).

Cytotoxicities of Only FHP–c–PLGA NPs and EGCG Solution or EGCG-Loaded FHP–c–PLGA NPs

We investigated the effects of only FHP–c–PLGA NPs on the cytocompatibility of normal prostate epithelial cells (PZ-HPV7) and prostate cancer cells (PC3 cells). As shown in **Figure 3B**, cell viability was generally not all affected after treatment alone with FHP–c–PLGA NPs less than 3,200 mg/L. We next examined the effects of EGCG and EGCG-loaded NPs on the proliferation of prostate cancer cells. We then determined the cytotoxic effects of EGCG and EGCG-loaded FHP–c–PLGA NPs in cancer cell. Cell viability was not significantly affected by EGCG-loaded NPs and by EGCG alone at EGCG concentrations less than 40.0 mg/L and 80.0 mg/L. In contrast, both treatments significantly inhibited

TABLE 1 | Effect of different FU/HA/PG concentrations on particle sizes, polydispersity indices, and zeta potential values of the FHP-c-PLGA NPs (n = 5).

FU:HA:PG (mg/mL)	Mean Particle Size (nm)	Polydispersity Indices	Zeta Potential Value (mV)
0.0:0.0:0.0	158.64 ± 9.87	0.13 ± 0.04	−28.76 ± 2.47
0.6:0.6:0.6	177.57 ± 7.98	0.17 ± 0.06	−30.87 ± 1.78
1.2:1.2:1.2	198.89 ± 12.56	0.22 ± 0.09	−33.75 ± 1.24
2.4:2.4:2.4	252.47 ± 19.76	0.43 ± 0.16	−36.37 ± 3.87

PLGA, Poly (D,L-lactide-co-glycolide); NPs, nanoparticles.

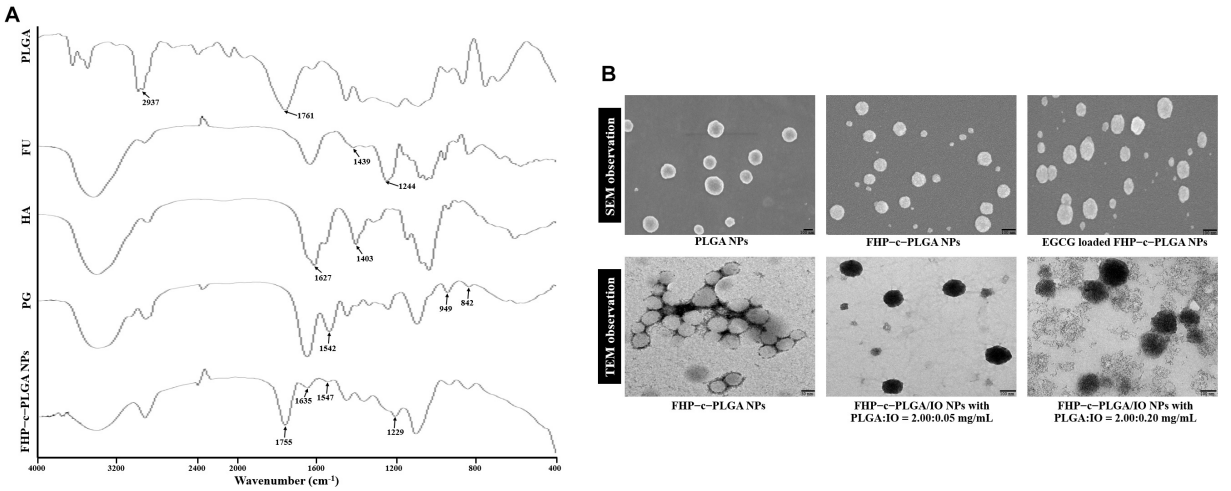

FIGURE 2 | (A) Fourier transform infrared analyses of PLGA, FU, HA, PG, and FHP–c–PLGA NPs. **(B)** Scanning electron microscopy (SEM) or transmission electron microscopy (TEM) micrographs of the different NP preparations.

TABLE 2 | Effect of different epigallocatechin gallate (EGCG) concentration on particle sizes, polydispersity indices, zeta potential values, and drug-loading efficiency of EGCG loaded FHP-c-PLGA NPs (n = 5).

EGCG (mg/mL)	Mean Particle Size (nm)	Polydispersity indices	Zeta Potential Value (mV)	Loading efficiency (%)	Loading content (%)
FU/HA/PG concentration at 1.2:1.2:1.2 (mg/mL)					
0.0	198.89 ± 12.56	0.22 ± 0.09	−33.75 ± 1.24	ND	ND
0.5	208.79 ± 8.78	0.24 ± 0.11	−34.89 ± 1.87	43.98 ± 7.87	9.87 ± 1.69
1.0	217.19 ± 11.37	0.25 ± 0.09	−35.75 ± 2.39	47.86 ± 4.57	19.67 ± 2.48
1.5	238.86 ± 13.27	0.29 ± 0.08	−34.97 ± 1.12	37.96 ± 6.68	22.17 ± 3.98

NPs, nanoparticles.

cell viabilities in a concentration-dependent manner. The 50% inhibitory concentration (IC50) of EGCG-loaded NPs was found to be 320.0 mg/L, in contrast to 560.0 mg/L for the EGCG solution. EGCG-loaded NPs presented better anti-cancer effects compared to EGCG alone (**Figure 3C**). To evaluate EGCG functions in EGCG-loaded FHP–c–PLGA NPs, the morphological changes were observed (**Figure 3D**). Control and FHP–c–PLGA NP-treated cells were oblong and firmly attached to the substratum in a flattened cobblestone arrangement. The cells had abundant cytoplasm and only occasional round, floating cells (dead) were observed in EGCG-loaded FHP–c–PLGA NPs treated culture. When cells were treated with EGCG-loaded NPs (EGCG 320.0 mg/mL and 480.0 mg/mL), more dramatic morphological changes were observed, and a higher percentage of cells were small. The more pronounced morphological changes (i.e., red arrows) and reduction in cell numbers were induced under these EGCG-loaded NPs treatments.

Cellular distribution of NP complexes and evaluation of apoptosis induced by EGCG-loaded NP. The distribution of NPs in PC3 cells were detected using CLSM analysis (**Figure 4A**). PC3 cells were incubated with fluorescent R6G-FU/FA-HA/Cy5-PG–c–PLGA NPs (R6G-FU: red spot; FA-HA: green spot; Cy5-PG: purple spot). Fluorescence of NPs were co-localized and remained intact (as indicated by superimposed red/green/purple spots, i.e., white arrows) when internalized into the cytoplasm. Cy5–EGCG subsequent fluorescence signals emitted by Cy5-EGCG-loaded R6G-FU/FA-HA/PG–c–PLGA NPs (R6G-FU: red spot; FA-HA: green spot; Cy5-EGCG: purple spot, i.e., white arrows) were in contact with PC3 cancer cells. More EGCG was released into cytoplasm compared to EGCG solution treatment.

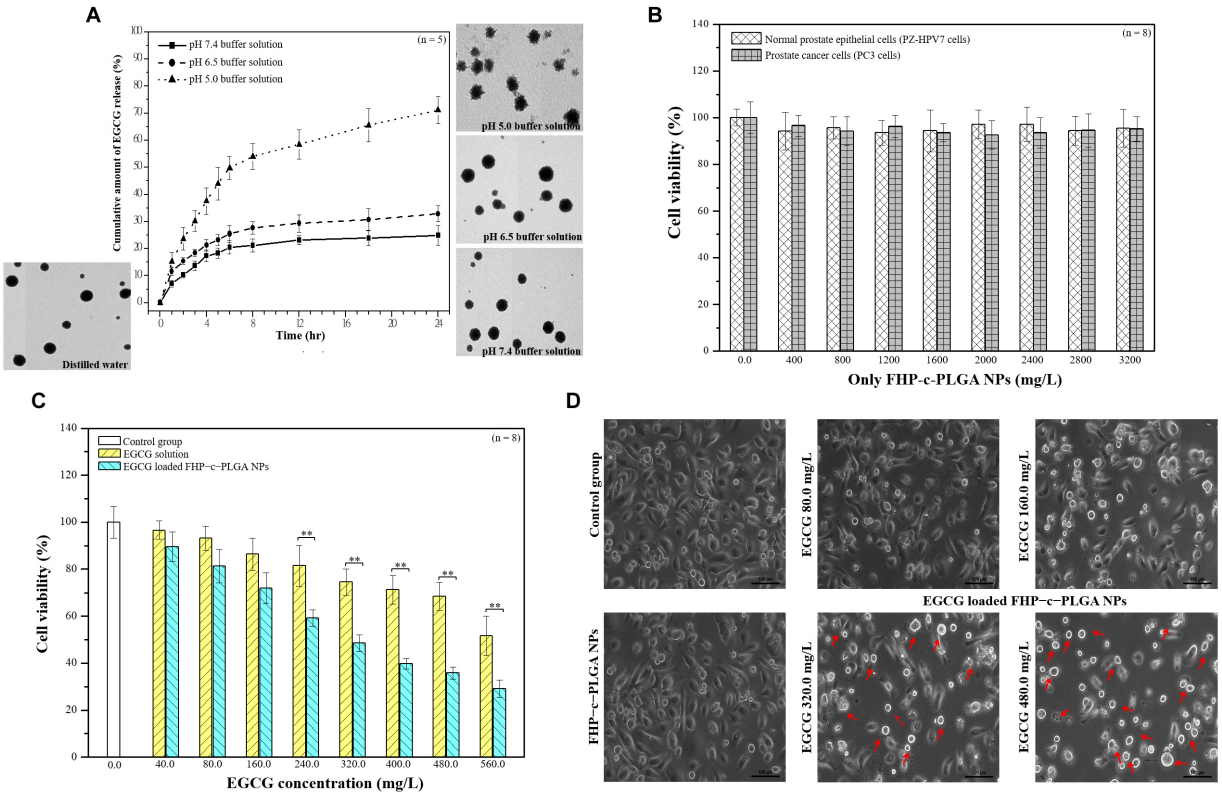

FIGURE 3 | (A) Transmission electron microscopy (TEM) micrographs and *in vitro* profiles of the release of epigallocatechin gallate (EGCG) from EGCG-loaded FHP–c–PLGA NPs in buffers differing in pH values at 37°C. **(B)** Cytocompatibility of normal prostate epithelial cells and prostate cancer cells after treated with different concentrations of only FHP–c–PLGA NPs. **(C)** Prostate cancer cell viability was determined using 3-(4,5-dimethylthiazol-2-yl)-2,5-diphenyltetrazolium bromide (MTT) assays after cells were treated with EGCG solution or EGCG-loaded FHP–c–PLGA NPs containing different concentrations of EGCG. Asterisk ** represents statistically a significant difference of p value < 0.01. **(D)** Microscopic observations of cells treated with different concentrations of EGCG in EGCG-loaded FHP–c–PLGA NPs, FHP–c–PLGA NPs, or controls.

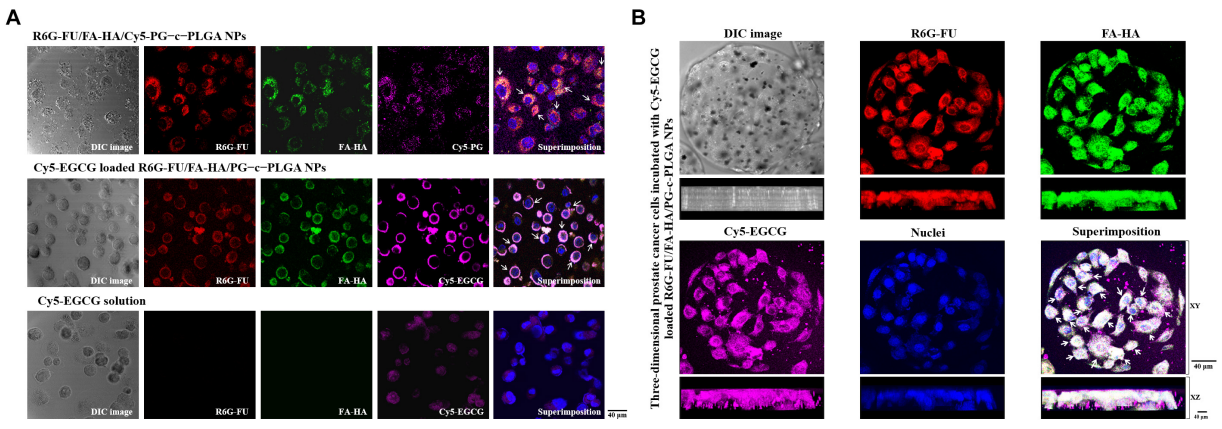

FIGURE 4 | (A) Confocal images of prostate cancer cells showing cellular distribution of the NP preparations. **(A)** Treatment with only R6G-FU/FA-HA/Cy5-PG–c–PLGA NPs or Cy5-epigallocatechin gallate (EGCG)-loaded R6G-FU/FA-HA/PG–c–PLGA NPs vs. Cy5-EGCG. **(B)** Three-dimensional analysis of fluorescent PC3 cells adhered to Matrigel-coated microcarriers incubated with fluorescent Cy5-EGCG-loaded R6G-FU/FA-HA/PG–c–PLGA NPs.

The three-dimensional PC3 cells were incubated with fluorescent EGCG-loaded NPs. CLSM analyses showed the superimposition of the images produced by Cy5-EGCG-loaded R6G-FU/FA-HA/PG-c-PLGA NPs (as indicated by superimposed green/red/purple spots, i.e., white arrows), which co-localized and interacted locally along with the *XY* plane and appeared

deep in the *XZ* plane (**Figure 4B**). Higher EGCG concentration of EGCG-loaded NPs treatment, significantly reduced cell viability and induced morphological changes from oblong to coccoid forms after 24 h, which correlated with FITC-Annexin V expression (i.e., green spots; **Figure 5A**). The binding of Annexin V is regarded as an apoptotic indicator according to the interaction of Annexin V to the inner cell membrane component phosphatidylserine. The fluorescence of FITC-Annexin V conjugate was undetectable in controls or FHP–c–PLGA NP-treated cells. In contrast, incubation of EGCG-loaded NPs led to induce the expression of green fluorescence at cell surfaces in a concentration-dependent manner.

Effects of EGCG-Loaded NPs on Cell Cycle Arrest and Apoptosis

To determine whether EGCG-loaded FHP-c-PLGA NPs arrest the cell cycle progression, we treated PC3 cells with propidium iodide following NP treatments with different concentrations of EGCG. EGCG induced a significant decrease of G0/G1 populations (decreased from 59.9 ± 1.34 to 41.13 ± 1.96%), an increase in cells undergoing S phase (increased from 13.04 ± 0.98 to 24.38 ± 2.31%), and the accumulation of cells in G2/M (increased from 27.87 ± 0.91 to 34.49 ± 2.87%; **Figure 5B**). To determine whether EGCG-loaded NPs induce apoptosis, we performed western blotting to determine the ratios of cleave-caspase-8, caspase-9, caspase-3, and PARP to their total (cleaved form plused proform) protein expressions. Twenty-four hours after EGCG-loaded NPs treatment, EGCG (480 mg/mL) increased the ratios of cleaved to total expressions of caspase-8 and -9 about 29% (caspase-8) and 15% (caspase-9) compared to the controls. The levels of cleaved caspase-3 and PARP in PC3 cells significantly increased in the presence of EGCG-loaded NPs compared with the controls ($p < 0.05$; **Figure 5C**).

Molecular Imaging of NPs in Tumor Xenografts

The effects of FHP–c–PLGA/IO NPs were visualized using MRI. FHP–c–PLGA/IO NPs were prepared with different concentrations of IO. The mean particle size, homogeneity/polydispersity indices were varied with IO concentrations (**Table 3**). The mean sizes of these NPs ranged from 230 to 600 nm, with homogeneity/polydispersity indices that varied relative to the concentrations of IO (**Table 3**). Furthermore, TEM observations revealed that single FHP–c–PLGA NPs were smooth and round. As expected, the FHP–c–PLGA/IO NPs obtained using PLGA:IO at a 2.00:0.20 mg/mL were unevenly disbursed and had a larger average diameter (598.90 ± 49.45 nm) compared to NPs obtained using PLGA:IO at 2.00:0.05 mg/mL, which exhibited an internal structure consisting with black granular IOs dispersed among gray NPs (**Figure 2B**).

The proportion of PLGA/IO at 2.00:0.05 produced the NPs with minimum mean particle size (232.64 ± 13.87 nm) and uniform polydispersity index (0.28 ± 0.04) and were therefore used for MRI analyses. FHP–c–PLGA/IO NPs achieved significant, concentration-dependent MRI contrast-enhancement (**Figure 1**). The MR imaging appeared hypointense as the IO concentration increased, i.e., the shorter T2-relaxation time. The MR images obtained using the T2W sequence before and after injection of mice with FHP–c–PLGA/IO-labeled NPs were shown in **Figures 6A,B**. The hypointensity of prostate tumor was clearly visualized in the T2W MR image because of the T2-shortening effect caused by the IOs (i.e., red arrows; **Figure 6A**). In contrast, in the control group, the MRI signals detected at the prostate were not significantly different before and after injection of sample (**Figure 6B**). Moreover, target-specific near infrared fluorescent VivoTag 750-labeled NPs were injected into the tail veins of Luc-PC3 tumor-bearing mice. The IVIS Spectrum CT images of Luc PC3 tumor-bearing mice were acquired after injection of VivoTag 750-labeled NPs. The axial image clearly showed the dominant accumulation of fluorescent NPs signals in the region of the prostate tumor (as indicated by superimposed green/red spots; i.e., yellow spots, white arrows; **Figure 6C**).

Assessment of Antitumor Activity and Histological Analysis

We next investigated the tumor-specific effects of EGCG-loaded NPs in the orthotopic mouse model of prostate cancer. The prostate tumor bioluminescence signals significantly increased with time by 3.08 ± 0.29- and 2.39 ± 0.21-fold at day 18 in mice treated with FHP–c–PLGA NPs and EGCG, respectively (**Figure 7A**). In contrast, the growth of prostate tumors was significantly inhibited in mice treated with EGCG-loaded FHP–c–PLGA NPs, with a lower relative photon flux compared with the other groups of treated mice. There was no significant difference in the loss of body weight between groups (**Figure 7B**). The survival rates of mice treated with EGCG-loaded NPs were significantly longer compared with controls, indicating significant antitumor activity (**Figure 7C**).

In the control group (treated with FHP–c–PLGA NPs), tumor-bearing prostate gland tissue had well-defined and unencapsulated margins, with the largest tumor range and foci of tumor cells in the surrounding stroma (i.e., black arrows, **Figure 8A**). Immunohistochemical examination revealed that the expression of cell proliferation marker Ki-67 was reduced and the expression of apoptotic marker (cleaved PARP) was increased in tumors treated with EGCG-loaded FHP–c–PLGA NPs (i.e., coffee dots, **Figure 8A**). Prostate cancer may induce in systemic inflammation *in vivo*. In the present study, the lung tissues of the normal mice were clear and intact, with no infiltration of inflammatory cells, bleeding, edema, or thickening of the alveolar wall. The mice with prostate tumors in control group had disorganized alveolar structures, significant exudation of inflammatory cells, red blood cells dispersed in multiple alveolar cavities, and interstitial pulmonary edema and thickening (i.e., black arrows, **Figure 8B**). The pathological damage was significantly milder in the EGCG-loaded NPs group that exhibited clear alveolar structures, insignificant interstitial pulmonary edema and thickening, and reduced inflammation (i.e., black arrows, **Figure 8B**). Hepatocyte

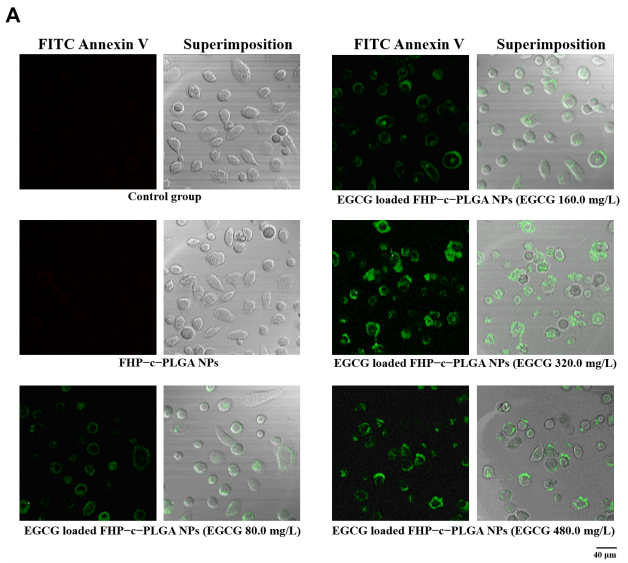

FIGURE 5 | (A) Fluorescence detection of apoptotic prostate cancer cells (PC3) cells after treatment with FHP–c–PLGA NPs loaded with different epigallocatechin gallate (EGCG) concentrations. Controls were labeled with FITC-Annexin V and analyzed using a con-focal laser scanning microscope. **(B)** The proportions of cells in the G0/G1, S, and G2/M phases after treatment with EGCG-loaded FHP-c-PLGA NPs are indicated. The cells were stained with propidium iodide, and the cell cycle distribution was analyzed using flow cytometry. **(C)** Western blotting analysis of apoptosis-related caspase-8, -9, -3, and poly (ADP-ribose) polymerase (PARP) in PC3 cells after incubation with EGCG-loaded FHP–c–PLGA NPs, and β-actin was used as an internal control. Asterisk * represents statistically a significant difference of p value < 0.05, as compared with the without sample treatment group.

TABLE 3 | Effect of different PLGA/IO concentrations on particle sizes, polydispersity indices, and zeta potential values of the FHP-c-PLGA/PLGA/IO NPs ($n = 5$).

PLGA:IO (mg/mL)	Mean Particle Size (nm)	Polydispersity indices	Zeta Potential Value (mV)
FU/HA/PG concentration at 1.2:1.2:1.2 (mg/mL)			
2.00:0.05	232.64 ± 13.87	0.28 ± 0.04	−36.76 ± 2.47
2.00:0.10	319.57 ± 19.68	0.39 ± 0.12	−38.52 ± 5.91
2.00:0.20	598.90 ± 49.45	0.72 ± 0.27	−37.52 ± 2.35

PLGA, poly (D,L-lactide-co-glycolide); NPs, nanoparticles.

swelling and neutrophil infiltration were decreased in liver tissues of mice treated with EGCG-loaded NPs compared to control mice. It is suggested that targeting NPs could not only significantly increase EGCG's antitumor activity against prostate tumors but also reduce the inflammatory reaction in the body.

DISCUSSION

Targeted therapy that delivers drugs to cancer cells is important for improving treatment efficacy and avoiding systemic toxicity (Li et al., 2020; Shen et al., 2020). In recent years, the focus on developing targeted therapy with NP delivery systems has increased (Swain et al., 2016; Genchi et al., 2017; Adekiya et al., 2020). Molecular targeting relying on binding between a targeting ligand and a cancer-specific receptor has been used extensively in nanomaterials techniques (Yao et al., 2016). In the present study, using a targeted NPs system, we detected significant increases in the fluorescence intensities of Rh6G-FU/FA-HA-complexed NPs, which emitted detectable fluorescence and did not interfere with each other when taken up by prostate cancer cells (**Figure 4**). FU represents a class of sulfated fucose-rich polysaccharides synthesized from brown algae. Prostate-specific membrane antigen, which contains fucosylated oligosaccharides, is an important marker of prostate cancer, and its level is increased many folds in prostate cancer and in the neovasculature of other tumors (Fitton et al., 2003; Ghosh and Heston, 2003; Synytsya et al., 2010). HA, which is a major component of the vertebrate extracellular matrix, efficiently targets CD44 through hydrogen bonds and van der Waals interactions (Banerji et al., 2007). We found that the EGCG-loaded NPs attached to PC3 cells. Furthermore, the carrier EGCG induced S phase or G2/M cell-cycle arrest, which is involved in inhibition of PC3 cell proliferation, and enhanced the expression of apoptosis-related proteins (**Figure 5**).

Integrated diagnosis and therapy systems that can offer effective cancer therapy are in high demand for personalized medicine. Molecular imaging techniques such MRI, CT, ultrasound, and fluorescence microscopy play important roles in medicine and biomedical research (Kherlopian et al., 2008; Thorat et al., 2019). Here, NPs containing IOs were

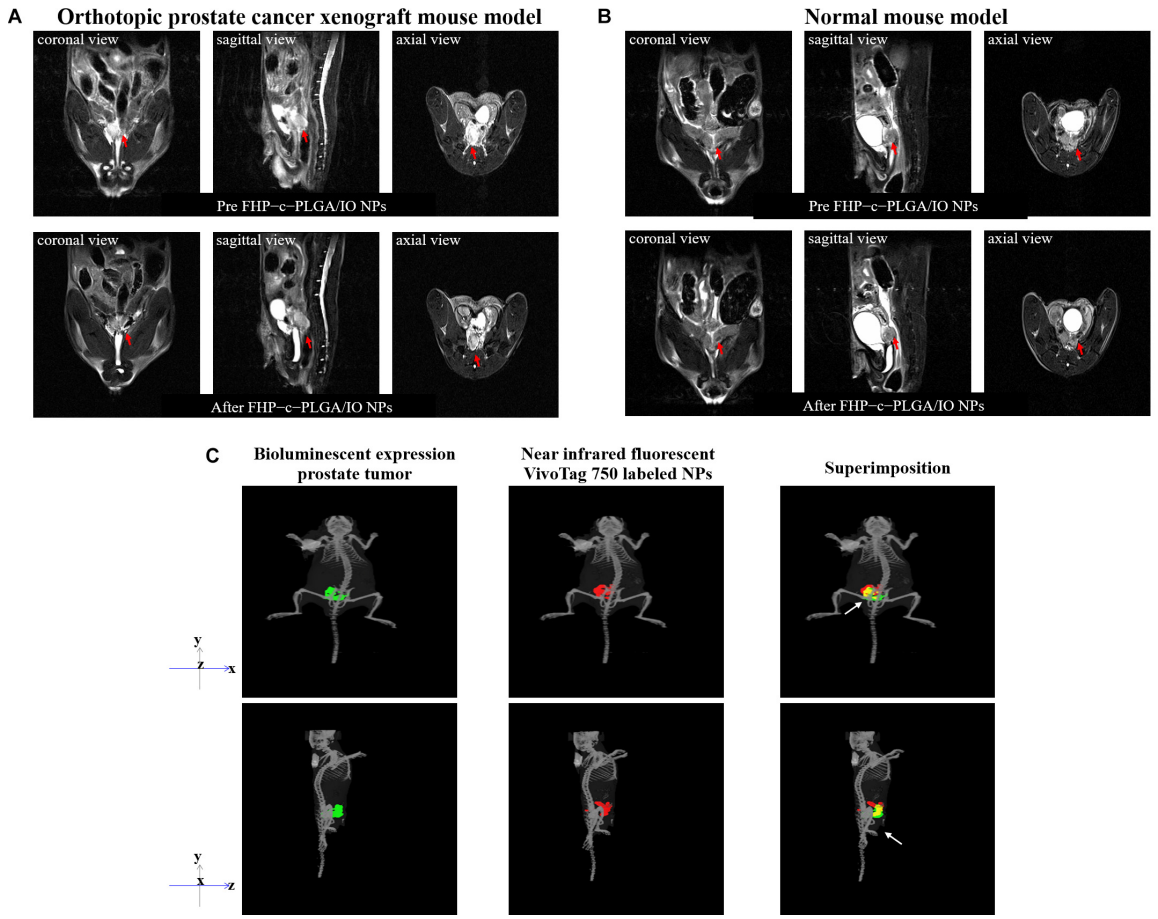

FIGURE 6 | *In vivo* T2-weighted axial MR images were acquired before and after injection of FHP–c–PLGA/IO NPs from untreated and xenografted mice. A decrease in signal intensity caused by FHP–c–PLGA/IO NPs was observed in prostate tumor tissue (red arrows) but not in normal prostate tissue. **(A)** Orthotopic prostate cancer xenograft mouse model. **(B)** Normal mouse model. **(C)** Three-dimensional bioluminescence or fluorescence optical tomography using *in vivo* imaging system (IVIS) Spectrum CT. The co-localization (yellow) of bio-luminescent prostate tumors (green) with VivoTag 750-labeled NPs (red) in the prostate tissue (white arrows).

intravenously injected into the tail veins of mice. MRI revealed that these NPs were retained at the site of prostate tumors compared with the control group, and there were no significant differences in T2W intensities between test and control mice (**Figures 6A,B**). In this study, we demonstrated that NPs containing IOs can be targeted to the prostate tumor instead of the normal prostate tissue. Every imaging technique has its own limitations, such as insufficient sensitivity, spatial resolution, data acquisition time, and complexity, which hinder the acquisition of accurate information. Multi-imaging modalities overcome these shortcomings (Zhao et al., 2018). For example, three-dimensional bioluminescence or fluorescence optical tomography using IVIS Spectrum CT clearly showed that VivoTag 750-labeled NPs mainly accumulated in the region of the prostate tumor and that NPs targeted the tumor with accurate detection (i.e., yellow spots, white arrows, **Figure 6C**).

Epigallocatechin gallate-loaded NPs with optimal pH responsiveness can improve the delivery and control the drug locally targeting to the tumor site. This type of NP delivery system is under intensive study. The pH value of tumor tissues (pH 6.5) differs from that of healthy tissues (pH 7.4). Furthermore, the pH value of intracellular endosomes and lysosomes ranges from pH 5.0 to 6.0. Endosomes and lysosomes trigger the drug's release from designed NPs into cancer cells. The EGCG-loaded NPs studied here were designed with a matrix structure for minimizing drug release into normal physiological environments such as blood and non-target tissues (pH 6.5–7.4). Such NPs facilitated the release of EGCG from late endosomes and lysosomes of tumor cells (cumulative release, 71.12 ± 4.96% at pH 5.0; **Figure 3A**). Specifically, *in vivo* experiments confirmed that significant enhancement of the inhibition of tumor growth was demonstrated by the lower bioluminescent intensity after intravenous EGCG-loaded NPs (15.0 mg/kg EGCG; **Figure 7**). Moreover, histological analyses demonstrated that the delivery of EGCG to tumors by NPs induce apoptosis in PC3 cells as indicated by increased levels of cleaved PARP accompanied by a reduction in inflammatory pulmonary lesions (**Figure 8**). Further preclinical and clinical studies will be of paramount importance to further enhance our understanding of the potential of such NPs as alternative anticancer treatments.

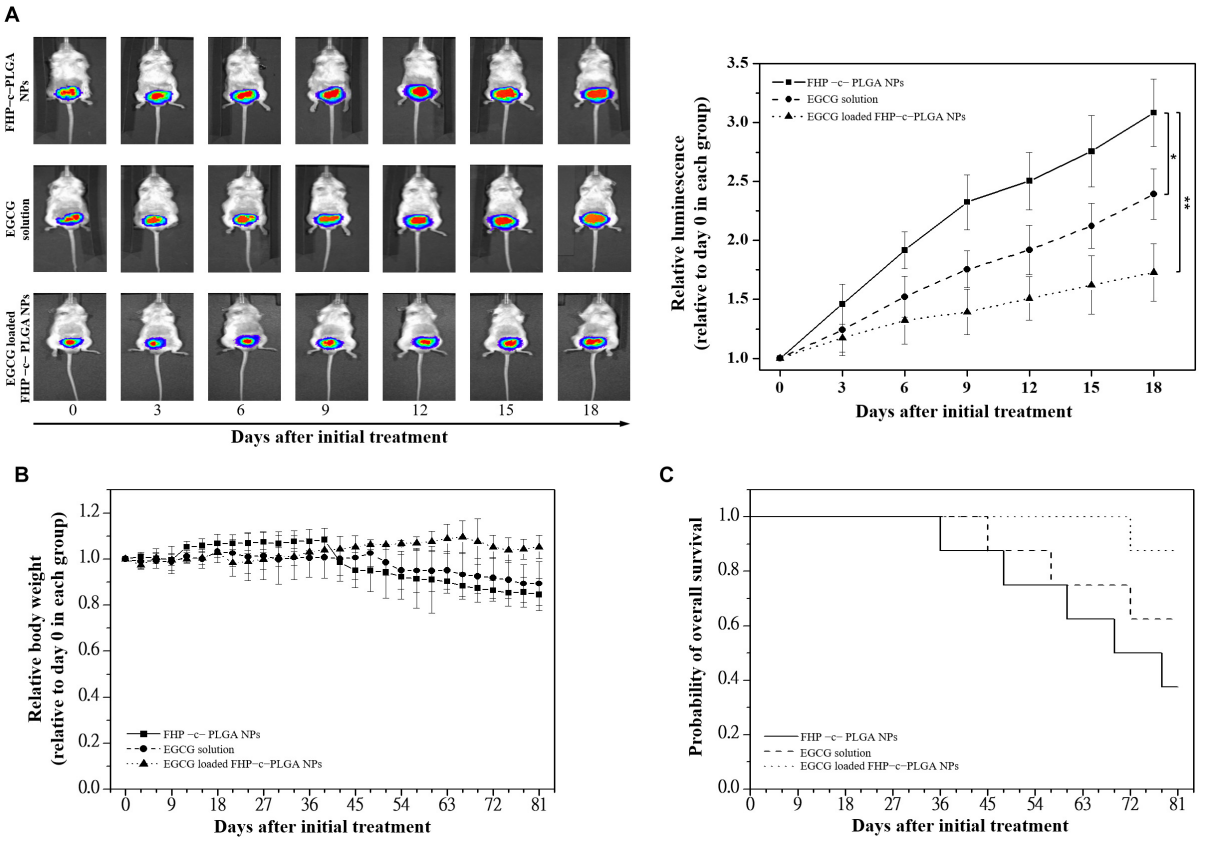

FIGURE 7 | Antitumor effects of epigallocatechin gallate (EGCG)-loaded FHP–c–PLGA NPs in orthotopic Luc prostate cancer cells (PC3) xenograft mice models. Mice were divided into three groups of six mice and were treated with only FHP–c–PLGA NPs (■), EGCG solution (●), or EGCG-loaded FHP–c–PLGA NPs (▲) every 3 days for 21 days. **(A)** Antitumor activities using a noninvasive *in vivo* imaging system. Asterisk *, ** represents statistically significant difference of p-value < 0.05, and p-value < 0.01, respectively. **(B)** Changes in relative body weight. **(C)** Kaplan–Meier survival curves of mice bearing orthotopic Luc-PC3 xenografts.

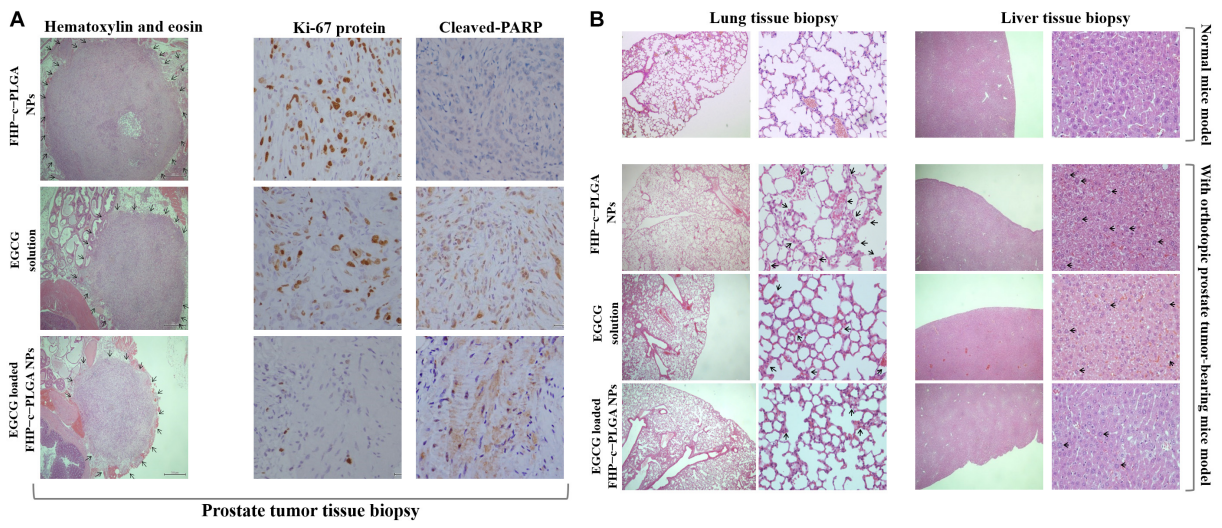

FIGURE 8 | Histological and immunohistochemical analyses of orthotopic prostate tumors treated with FHPŰcŰPLGA NPs, EGCG solution, or EGCG-loaded FHPŰcŰPLGA NPs. **(A)** Prostate biopsy. The black arrows indicate the tumor range. **(B)** Lung and liver biopsies. The black arrows indicate the inflammation.

CONCLUSION

The present study indicated that NPs with combined therapeutic and molecular imaging attributes can effectively target prostate cancers, leading to significant enhancement of anti-prostate tumor activity, as shown by the localization of tumors in an orthotopic mouse model of prostate cancer. These theranostic NPs have the potential to provide a delivery system for identifying alternative anticancer treatments and new diagnostic techniques that will facilitate clinical trials.

DATA AVAILABILITY STATEMENT

The original contributions presented in the study are included in the article/supplementary material, further inquiries can be directed to the corresponding author.

ETHICS STATEMENT

The animal study was reviewed and approved by Institutional Animal Care Use Committee (Approval No. 1061213), National Yang-Ming University, Taiwan.

AUTHOR CONTRIBUTIONS

S-LP, C-HL, and P-YC: conception or design of this work. S-CC: experimental study. J-TH and Y-CT: data analysis and interpretation. Y-HL: wrote the manuscript and obtained funding. All authors read and approved the manuscript.

FUNDING

This research was funded by Ministry of Science and Technology, grant number MOST 106-2314-B-010-051-MY3, MOST 107-2221-E-010-004-MY3, and MOST 107-2314-B-039-056-MY3.

ACKNOWLEDGMENTS

We thank the Laboratory of the iEGG and Animal Biotechnology Center at National Chung Hsing University for help with IVIS imaging. The Leica TSC SP2 confocal Spectral microscopy experiment and Malvern #ZS90 Zetasizer Nano apparatus supported by the Medical Research Core Facilities center, Office of Research and Development, China Medical University were gratefully acknowledged. We would also like to thank Enago (www.enago.tw), for the English language review.

REFERENCES

Adekiya, T. A., Kondiah, P. P. D., Choonara, Y. E., Kumar, P., and Pillay, V. (2020). A review of nanotechnology for targeted anti-schistosomal therapy. *Front. Bioeng. Biotechnol.* 8:32. doi: 10.3389/fbioe.2020.00032

Avgoustakis, K. (2004). Pegylated poly(lactide) and poly(lactide-co-glycolide) nanoparticles: preparation, properties and possible applications in drug delivery. *Curr. Drug Deliv.* 1, 321–333. doi: 10.2174/15672010433 34605

Bae, Y., Kim, G. J., Kim, H., Park, S. G., Jung, H. S., and Kang, S. (2018). Engineering tunable dual functional protein cage nanoparticles using bacterial superglue. *Biomacromolecules* 19, 2896–2904. doi: 10.1021/acs.biomac.8b00457

Banerji, S., Wright, A. J., Noble, M., Mahoney, D. J., Campbell, I. D., Day, A. J., et al. (2007). Structures of the Cd44-hyaluronan complex provide insight into a fundamental carbohydrate-protein interaction. *Nat. Struct. Mol. Biol.* 14, 234–239. doi: 10.1038/nsmb1201

Blanas, A., Sahasrabudhe, N. M., Rodriguez, E., van Kooyk, Y., and van Vliet, S. J. (2018). Fucosylated antigens in cancer: an alliance toward tumor progression, metastasis, and resistance to chemotherapy. *Front. Oncol.* 8:39. doi: 10.3389/fonc.2018.00039

Boni, R., Ali, A., Shavandi, A., and Clarkson, A. N. (2018). Current and novel polymeric biomaterials for neural tissue engineering. *J. Biomed. Sci.* 25:90. doi: 10.1186/s12929-018-0491-8

Cao, L. B., Zeng, S., and Zhao, W. (2016). Highly stable PEGylated poly(lactic-co-glycolic acid) (PLGA) nanoparticles for the effective delivery of docetaxel in prostate cancers. *Nanoscale Res. Lett.* 11:305. doi: 10.1186/s11671-016-1509-3

Chen, J., Ouyang, J., Chen, Q., Deng, C., Meng, F., Zhang, J., et al. (2017). EGFR and CD44 dual-targeted multifunctional hyaluronic acid nanogels boost protein delivery to ovarian and breast cancers in vitro and in vivo. *ACS Appl. Mater. Interfaces* 9, 24140–24147. doi: 10.1021/acsami.7b06879

Cheng, T., Liu, J., Ren, J., Huang, F., Ou, H., Ding, Y., et al. (2016). Green tea catechin-based complex micelles combined with doxorubicin to overcome cardiotoxicity and multidrug resistance. *Theranostics* 6, 1277–1292. doi: 10.7150/thno.15133

Chivere, V. T., Kondiah, P. P. D., Choonara, Y. E., and Pillay, V. (2020). Nanotechnology-based biopolymeric oral delivery platforms for advanced cancer treatment. *Cancers* 12:522. doi: 10.3390/cancers12020522

Chung, C. H., Lu, K. Y., Lee, W. C., Hsu, W. J., Lee, W. F., Dai, J. Z., et al. (2020). Fucoidan-based, tumor-activated nanoplatform for overcoming hypoxia and enhancing photodynamic therapy and antitumor immunity. *Biomaterials* 257:120227. doi: 10.1016/j.biomaterials.2020.120227

Chung, J. E., Tan, S., Gao, S. J., Yongvongsoontorn, N., Kim, S. H., Lee, J. H., et al. (2014). Self-assembled micellar nanocomplexes comprising green tea catechin derivatives and protein drugs for cancer therapy. *Nat. Nanotechnol.* 9, 907–912. doi: 10.1038/nnano.2014.208

Deng, Y., Zhang, X., Shen, H., He, Q., Wu, Z., Liao, W., et al. (2020). Application of the nano-drug delivery system in treatment of cardiovascular diseases. *Front. Bioeng. Biotechnol.* 7:489. doi: 10.3389/fbioe.2019.00489

Draffin, J. E., McFarlane, S., Hill, A., Johnston, P. G., and Waugh, D. J. (2004). CD44 potentiates the adherence of metastatic prostate and breast cancer cells to bone marrow endothelial cells. *Cancer Res.* 64, 5702–5711. doi: 10.1158/0008-5472.CAN-04-0389

Du, B., Cao, X. H., Zhao, F. F., Su, X. J., Wang, Y. H., Yan, X. S., et al. (2016). Multimodal imaging-guided, dual-targeted photothermal therapy for cancer. *J. Mater. Chem. B* 4, 2038–2050. doi: 10.1039/c6tb00215c

Fitton, J. H., Stringer, D. N., and Karpiniec, S. S. (2003). Therapies from fucoidan: an update. *Mar. Drugs* 13, 5920–5946. doi: 10.3390/md13095920

Frohlich, E. (2012). The role of surface charge in cellular uptake and cytotoxicity of medical nanoparticles. *Int. J. Nanomedicine* 7, 5577–5591. doi: 10.2147/IJN.S36111

Gamper, C., Spenle, C., Bosca, S., van der Heyden, M., Erhardt, M., Orend, G., et al. (2019). Functionalized tobacco mosaic virus coat protein monomers and oligomers as nanocarriers for anti-cancer peptides. *Cancers* 11:1609. doi: 10.3390/cancers11101609

Gao, L. L., Li, F. R., Jiao, P., Yang, M. F., Zhou, X. J., Si, Y. H., et al. (2011). Paris chinensis dioscin induces G2/M cell cycle arrest and apoptosis in human gastric cancer SGC-7901 cells. *World J. Gastroenterol.* 17, 4389–4395. doi: 10.3748/wjg.v17.i39.4389

Gao, P., Pan, W., Li, N., and Tang, B. (2019). Boosting cancer therapy with organelle-targeted nanomaterials. *ACS Appl. Mater. Interfaces* 11, 26529–26558. doi: 10.1021/acsami.9b01370

Gao, R., Li, D., Xun, J., Zhou, W., Li, J., Wang, J., et al. (2018). CD44ICD promotes breast cancer stemness via PFKFB4-mediated glucose metabolism. *Theranostics* 8, 6248–6262. doi: 10.7150/thno.28721

Genchi, G. G., Marino, A., Tapeinos, C., and Ciofani, G. (2017). Smart materials meet multifunctional biomedical devices: current and prospective implications for nanomedicine. *Front. Bioeng. Biotechnol.* 5:80. doi: 10.3389/fbioe.2017.00080

Ghosh, A., and Heston, W. D. W. (2003). Effect of carbohydrate moieties on the folate hydrolysis activity of the prostate specific membrane antigen. *Prostate* 57, 140–151. doi: 10.1002/pros.10289

Harada, H., Nakata, T., Hirota-Takahata, Y., Tanaka, I., Nakajima, M., and Takahashi, M. (2006). F-16438s, novel binding inhibitors of CD44 and hyaluronic acid. I. Establishment of an assay method and biological activity. *J. Antibiot.* 59, 770–776. doi: 10.1038/ja.2006.101

Kherlopian, A. R., Song, T., Duan, Q., Neimark, M. A., Po, M. J., Gohagan, J. K., et al. (2008). A review of imaging techniques for systems biology. *BMC Syst. Biol.* 2:74. doi: 10.1186/1752-0509-2-74

Kos, P., Lachelt, U., He, D., Nie, Y., Gu, Z., and Wagner, E. (2015). Dual-targeted polyplexes based on sequence-defined peptide-PEG-oligoamino amides. *J. Pharm. Sci.* 104, 464–475. doi: 10.1002/jps.24194

Krishnamurthy, S., Ke, X., and Yang, Y. Y. (2015). Delivery of therapeutics using nanocarriers for targeting cancer cells and cancer stem cells. *Nanomedicine* 10, 143–160. doi: 10.2217/nnm.14.154

Leach, J. C., Wang, A., Ye, K., and Jin, S. (2016). A RNA-DNA hybrid aptamer for nanoparticle-based prostate tumor targeted drug delivery. *Int. J. Mol. Sci.* 17, 380. doi: 10.3390/ijms17030380

Lee, G. Y., Park, K., Nam, J. H., Kim, S. Y., and Byun, Y. (2006). Anti-tumor and anti-metastatic effects of gelatin-doxorubicin and PEGylated gelatin-doxorubicin nanoparticles in SCC7 bearing mice. *J. Drug Target.* 14, 707–716. doi: 10.1080/10611860600935701

Li, D., He, S., Wu, Y., Liu, J., Liu, Q., Chang, B., et al. (2019). Excretable lanthanide nanoparticle for biomedical imaging and surgical navigation in the second near-infrared window. *Adv. Sci.* 6, 1902042. doi: 10.1002/advs.201902042

Li, Z., Zhu, L., Liu, W., Zheng, Y., Li, X., Ye, J., et al. (2020). Near-infrared/pH dual-responsive nanocomplexes for targeted imaging and chemo/gene/photothermal tri-therapies of non-small cell lung cancer. *Acta Biomater.* 107, 242–259. doi: 10.1016/j.actbio.2020.03.004

Liu, A. Y., True, L. D., LaTray, L., Ellis, W. J., Vessella, R. L., Lange, P. H., et al. (1999). Analysis and sorting of prostate cancer cell types by flow cytometry. *Prostate* 40, 192–199. doi: 10.1002/(sici)1097-0045(19990801)40:3<192::aid-pros7<3.0.co;2-f

Luong, D., Sau, S., Kesharwani, P., and Iyer, A. K. (2017). Polyvalent folate-dendrimer-coated iron oxide theranostic nanoparticles for simultaneous magnetic resonance imaging and precise cancer cell targeting. *Biomacromolecules* 18, 1197–1209. doi: 10.1021/acs.biomac.6b01885

Ma, B., Simala-Grant, J. L., and Taylor, D. E. (2006). Fucosylation in prokaryotes and eukaryotes. *Glycobiology* 16, 158R–184R. doi: 10.1093/glycob/cwl040

Mattheolabakis, G., Milane, L., Singh, A., and Amiji, M. M. (2015). Hyaluronic acid targeting of CD44 for cancer therapy: from receptor biology to nanomedicine. *J. Drug Target.* 23, 605–618. doi: 10.3109/1061186x.2015.1052072

Mi, F. L., Wang, L. F., Chu, P. Y., Peng, S. L., Feng, C. L., Lai, Y. J., et al. (2018). Active tumor-targeted co-delivery of epigallocatechin gallate and doxorubicin in nanoparticles for combination gastric cancer therapy. *ACS Biomater. Sci. Eng.* 4, 2847–2859. doi: 10.1021/acsbiomaterials.8b00242

Min, H., Wang, J., Qi, Y., Zhang, Y., Han, X., Xu, Y., et al. (2019). Biomimetic metal–organic framework nanoparticles for cooperative combination of antiangiogenesis and photodynamic therapy for enhanced efficacy. *Adv. Mater.* 31:e1808200. doi: 10.1002/adma.201808200

Mizrahy, S., Raz, S. R., Hasgaard, M., Liu, H., Soffer-Tsur, N., Cohen, K., et al. (2011). Hyaluronan-coated nanoparticles: the influence of the molecular weight on CD44-hyaluronan interactions and on the immune response. *J. Control. Release* 156, 231–238. doi: 10.1016/j.jconrel.2011.06.031

Myers, R. B., Srivastava, S., and Grizzle, W. E. (1995). Lewis Y antigen as detected by the monoclonal antibody BR96 is expressed strongly in prostatic adenocarcinoma. *J. Urol.* 153, 1572–1574. doi: 10.1016/s0022-5347(01)67464-0

Nehate, C., Moothedathu Raynold, A. A., and Koul, V. (2017). ATRP fabricated and short chain polyethylenimine grafted redox sensitive polymeric nanoparticles for codelivery of anticancer drug and siRNA in cancer therapy. *ACS Appl. Mater. Interfaces* 9, 39672–39687. doi: 10.1021/acsami.7b11716

Park, J. B., Kwak, H. J., and Lee, S. H. (2008). Role of hyaluronan in glioma invasion. *Cell Adh. Migr.* 2, 202–207. doi: 10.4161/cam.2.3.6320

Preobrazhenskaya, M. E., Berman, A. E., Mikhailov, V. I., Ushakova, N. A., Mazurov, A. V., Semenov, A. V., et al. (1997). Fucoidan inhibits leukocyte recruitment in a model peritoneal inflammation in rat and blocks interaction of P-selectin with its carbohydrate ligand. *Biochem. Mol. Biol. Int.* 43, 443–451. doi: 10.1080/15216549700204231

Qiu, L., Jing, N., and Jin, Y. (2008). Preparation and in vitro evaluation of liposomal chloroquine diphosphate loaded by a transmembrane pH-gradient method. *Int. J. Pharm.* 361, 56–63. doi: 10.1016/j.ijpharm.2008.05.010

Roma-Rodrigues, C., Pombo, I., Raposo, L., Pedrosa, P., Fernandes, A. R., and Baptista, P. V. (2019). Nanotheranostics targeting the tumor microenvironment. *Front. Bioeng. Biotechnol.* 7:197. doi: 10.3389/fbioe.2019.00197

Sah, E., and Sah, H. (2015). Recent trends in preparation of poly(lactide-co-glycolide) nanoparticles by mixing polymeric organic solution with antisolvent. *J. Nanomater.* 16:61. doi: 10.1155/2015/794601

Salako, O., Roberts, A. A., Isibor, V. I., Babatunde, O., Fatiregun, O., and Nwogu, C. N. (2017). Innovative breast cancer awareness and advocacy campaign. *J. Glob. Oncol.* 3, 169–176. doi: 10.1200/JGO.2016.003509

Shen, X., Li, T., Xie, X., Feng, Y., Chen, Z., Yang, H., et al. (2020). PLGA-based drug delivery systems for remotely triggered cancer therapeutic and diagnostic applications. *Front. Bioeng. Biotechnol.* 8:381. doi: 10.3389/fbioe.2020.00381

Shukla, R., Chanda, N., Zambre, A., Upendran, A., Katti, K., Kulkarni, R. R., et al. (2012). Laminin receptor specific therapeutic gold nanoparticles (198AuNP-EGCg) show efficacy in treating prostate cancer. *Proc. Natl. Acad. Sci. U.S.A.* 109, 12426–12431. doi: 10.1073/pnas.1121174109

Shutava, T. G., Balkundi, S. S., Vangala, P., Steffan, J. J., Bigelow, R. L., Cardelli, J. A., et al. (2009). Layer-by-layer-coated gelatin nanoparticles as a vehicle for delivery of natural polyphenols. *ACS Nano* 3, 1877–1885. doi: 10.1021/nn900451a

Su, Y. L., Kuo, L. W., Hsu, C. H., Chiang, C. S., Lu, Y. J., Chang, S. J., et al. (2020). Rabies virus glycoprotein-amplified hierarchical targeted hybrids capable of magneto-electric penetration delivery to orthotopic brain tumor. *J. Control. Release* 10, 159–173. doi: 10.1016/j.jconrel.2020.02.018

Swain, S., Sahu, P. K., Beg, S., and Babu, S. M. (2016). Nanoparticles for cancer targeting: current and future directions. *Curr. Drug Deliv.* 13, 1290–1302. doi: 10.2174/1567201813666160713121122

Synytsya, A., Kim, W. J., Kim, S. M., Pohl, R., Synytsya, A., Kvasnicka, F., et al. (2010). Structure and antitumor activity of fucoidan isolated from sporophyll of Korean brown seaweed *Undaria pinnatifida*. *Carbohydr. Polym.* 81, 41–48. doi: 10.1016/j.carbpol.2010.01.052

Thorat, N. D., and Bauer, J. (2020). Functional smart hybrid nanostructures based nanotheranostic approach for advanced cancer treatment. *Appl. Surf. Sci.* 527:146809. doi: 10.1016/j.apsusc.2020.146809

Thorat, N. D., Tofail, S. A. M., Rechenberg, B., Townley, H., Brennan, G., Silien, C., et al. (2019). Physically stimulated nanotheranostics for next generation cancer therapy: focus on magnetic and light stimulations. *Appl. Phys. Rev.* 6:041306. doi: 10.1063/1.5049467

Tian, J., Ding, L., Xu, H. J., Shen, Z., Ju, H., Jia, L., et al. (2013). Cell-specific and pH-activatable rubyrin-loaded nanoparticles for highly selective near-infrared photodynamic therapy against cancer. *J. Am. Chem. Soc.* 135, 18850–18858. doi: 10.1021/ja408286k

van der Toom, E. E., Verdone, J. E., and Pienta, K. J. (2016). Disseminated tumor cells and dormancy in prostate cancer metastasis. *Curr. Opin. Biotechnol.* 40, 9–15. doi: 10.1016/j.copbio.2016.02.002

Weinstein, J. S., Varallyay, C. G., Dosa, E., Gahramanov, S., Hamilton, B., Rooney, W. D., et al. (2010). Superparamagnetic iron oxide nanoparticles: diagnostic magnetic resonance imaging and potential therapeutic applications in neurooncology and central nervous system inflammatory pathologies, a review. *J. Cereb. Blood Flow Metab.* 30, 15–35. doi: 10.1038/jcbfm.2009.192

Weissleder, R., Elizondo, G., Wittenberg, J., Rabito, C. A., Bengele, H. H., and Josephson, L. (1990). Ultrasmall superparamagnetic iron oxide: characterization of a new class of contrast agents for MR imaging. *Radiology* 175, 489–493. doi: 10.1148/radiology.175.2.2326474

Xu, C., Udochukwu Akakuru, O. U., Zheng, J., and Wu, A. (2019). Applications of iron oxide-based magnetic nanoparticles in the diagnosis and treatment of bacterial infections. *Front. Bioeng. Biotechnol.* 7:141. doi: 10.3389/fbioe.2019.00141

Yang, Y., Wang, L., Wan, B., Gu, Y., and Li, X. (2019). Optically active nanomaterials for bioimaging and targeted therapy. *Front. Bioeng. Biotechnol.* 7:320. doi: 10.3389/fbioe.2019.00320

Yao, V. J., D'Angelo, S., Butler, K. S., Theron, C., Smith, T. L., Marchio, S., et al. (2016). Ligand-targeted theranostic nanomedicines against cancer. *J. Control. Release* 240, 267–286. doi: 10.1016/j.jconrel.2016.01.002

Zhao, J. H., Chen, J. W., Ma, S. N., Liu, Q. Q., Huang, L. X., Chen, X. N., et al. (2018). Recent developments in multimodality fluorescence imaging probes. *Acta Pharm. Sin. B.* 8, 320–338. doi: 10.1016/j.apsb.2018.03.010

Zhou, Y., Yu, Q., Qin, X., Bhavsar, D., Yang, L., Chen, Q., et al. (2016). Improving the anticancer efficacy of laminin receptor-specific therapeutic ruthenium nanoparticles (RuBB-loaded EGCG-RuNPs) via ROS-dependent apoptosis in SMMC-7721 cells. *ACS Appl. Mater. Interfaces* 8, 15000–15012. doi: 10.1021/acsami.5b02261

Conflict of Interest: The authors declare that the research was conducted in the absence of any commercial or financial relationships that could be construed as a potential conflict of interest.

frontiers in Bioengineering and Biotechnology

ORIGINAL RESEARCH
published: 04 November 2020
doi: 10.3389/fbioe.2020.589905

Folic Acid–Functionalized Composite Scaffolds of Gelatin and Gold Nanoparticles for Photothermal Ablation of Breast Cancer Cells

Huajian Chen[1,2†], Xiuhui Wang[1,3†], Linawati Sutrisno[1,2], Tianjiao Zeng[4], Naoki Kawazoe[1], Yingnan Yang[4] and Guoping Chen[1,2]*

[1] Research Center for Functional Materials, National Institute for Materials Science, Tsukuba, Japan, [2] Department of Materials Science and Engineering, Graduate School of Pure and Applied Sciences, University of Tsukuba, Tsukuba, Japan, [3] Institute of Translational Medicine, Shanghai University, Shanghai, China, [4] Graduate School of Life and Environmental Science, University of Tsukuba, Tsukuba, Japan

OPEN ACCESS

Edited by:
Kang Moo Huh,
Chungnam National University,
South Korea

Reviewed by:
Ramar Thangam,
Korea University, South Korea
Ali Shakeri-Zadeh,
Johns Hopkins University,
United States

***Correspondence:**
Guoping Chen
Guoping.CHEN@nims.go.jp

[†] These authors have contributed equally to this work

Specialty section:
This article was submitted to Nanobiotechnology, a section of the journal Frontiers in Bioengineering and Biotechnology

Received: 31 July 2020
Accepted: 24 September 2020
Published: 04 November 2020

Citation:
Chen H, Wang X, Sutrisno L, Zeng T, Kawazoe N, Yang Y and Chen G (2020) Folic Acid–Functionalized Composite Scaffolds of Gelatin and Gold Nanoparticles for Photothermal Ablation of Breast Cancer Cells. Front. Bioeng. Biotechnol. 8:589905. doi: 10.3389/fbioe.2020.589905

Photothermal therapy (PTT) has been developed as a useful therapeutic method for cancer treatment. Localization of PTT agents in cancer sites and targeting capacity are required to further increase therapeutic efficacy. In this study, gold nanoparticles (AuNPs) and gelatin were functionalized with folic acid (FA) and hybridized to prepare FA-functionalized gelatin–AuNPs composite scaffolds. AuNPs with rod and star shapes of three sizes (40, 70, and 110 nm) were used for the hybridization to investigate the influence of AuNPs shape and size. The composite scaffolds showed porous structures with good interconnectivity. Modification with FA increased capture capacity of the composite scaffolds. Hybridization with AuNPs rendered the composite scaffold a good photothermal conversion property under near-infrared (NIR) laser irradiation. Temperature change during laser irradiation increased with the laser power intensity and irradiation time. The shape and size of AuNPs also affected their photothermal conversion property. The composite scaffold of gold nanorods 70 (FA-G/R70) had the highest photothermal conversion capacity. Breast cancer cells cultured in the FA-G/R70 composite scaffold were killed under NIR laser irradiation. Mouse subcutaneous implantation further demonstrated the excellent photothermal ablation capability of FA-G/R70 composite scaffold to breast cancer cells. The FA-functionalized composite scaffolds were demonstrated a high potential for local PPT of breast cancer.

Keywords: photothermal therapy, folic acid, composite scaffolds, gold nanoparticles, cell targeting

INTRODUCTION

Breast cancer has high incident and mortality ratio and is a serious threat to human health (Bray et al., 2018; Ji et al., 2020). Surgery has widely used to cure breast cancer patients (Waks and Winer, 2019). However, complete elimination and prevention of local recurrence remain problematic for surgical resection of breast cancer (Laurberg et al., 2017; Niinikoski et al., 2019; Li et al., 2020). In recent years, many other therapeutic methods such as immunotherapy, gene therapy, photothermal therapy (PTT), and photodynamic therapy have been developed to overcome the limitations of

surgical resection (Bai et al., 2019; Nassa et al., 2019; Feng et al., 2020). Among them, PTT, which converts near-infrared (NIR) laser into hyperthermal effect for ablating cancer cells, has attracted broad attention due to its highly therapeutic effect (Kim et al., 2006; Li et al., 2015; Chen M.C. et al., 2016). A critical factor that realizes photothermal conversion is photothermal agents (Vines et al., 2019). Currently, various photothermal agents (PTT agents) have been studied. They include copper sulfide nanoparticles (Wang et al., 2015), carbon nanoparticles (Han et al., 2018), and gold nanoparticles (AuNPs) (Liu et al., 2015; Cheng et al., 2017; Alamzadeh et al., 2019; Wang et al., 2019a). AuNPs have been recognized as one of the most promising photothermal agents because of their good biocompatibility and high photothermal conversion efficiency (Deng et al., 2014). They have another advantage of tunable NIR absorbance due to their localized surface plasmon resonance (LSPR) (Ding et al., 2014; Eyvazzadeh et al., 2017), which means photothermal conversion capability of AuNPs can be controlled by adjusting their shapes and sizes (Hwang et al., 2014). Benefited from these features, optimal cancer therapeutic effect can be achieved by choosing the appropriate AuNPs (Mackey et al., 2014; Moustaoui et al., 2019).

Successful delivery of photothermal agents is important to realize photothermal therapeutic effect. AuNPs can be delivered through intravenous injection of free AuNPs or implantation with a combination of scaffolds (Blanco et al., 2015; Li et al., 2018; Wang et al., 2018, 2019b). Intravenous injection of free AuNPs has the problems of immunological clearance by host responses and unexpected accumulation in healthy tissues and organs (Attarilar et al., 2020). Recently, implantation of composite scaffolds of nanoparticles and biocompatible polymers or bioceramics has been reported to directly deliver PTT nanoparticles to the cancer tissues or the resected sites (Eivazzadeh-Keihan et al., 2019; Luo et al., 2019; Chen et al., 2020). The composite scaffolds can not only restrict unexpected diffusion of free nanoparticles, but also exhibit high local heating effect and repeat ablation effect (Abdelrasoul et al., 2015; Escudero-Duch et al., 2019). Furthermore, the composite scaffolds can have another function to induce regeneration of resected tissues (Chen S. et al., 2016). Except localization of nanoparticles in the expected sites, specific or selective capability to capture cancer cells is required to further increase the ablation efficiency. When the composite scaffolds are degraded, the nanoparticles are released and can be expected to be uptaken by cancer cells for long-term photothermal ablation. Targeting capacity of the released nanoparticles is required to further improve ablation efficiency. To achieve these effects, composite scaffolds and nanoparticles have been modified with ligands that have high affinity to their receptors on the surfaces of cancer cells (Li et al., 2015; Zhang et al., 2017b). Folic acid (FA) has been frequently used as targeting ligand in nanoparticles (Khademi et al., 2018; Montazerabadi et al., 2019), liposomes, and drugs to increase their targeting capacity. FA can specifically recognize and bind the FA receptors overexpressed by breast cancer cells (Li et al., 2017; He et al., 2019, 2020).

Therefore, in this study, AuNPs were hybridized with gelatin, which is biocompatible and broadly used for biomedical applications, to prepare composite scaffolds of AuNPs and gelatin. FA was bound to both gelatin and AuNPs to provide the composite scaffolds with targeting capacity to breast cancer cells. The composite scaffolds should have captured capacity for FA receptor–expressing breast cancer cells. Meanwhile, the released FA-modified AuNPs after scaffold degradation should have targeting capacity for breast cancer cells. The porous structure of the composite scaffolds was controlled by using pre-prepared ice particulates as a porogen material. The FA-functionalized gelatin–AuNPs composite scaffolds were used for culture of breast cancer cells. The targeting capacity and *in vitro* and *in vivo* photothermal ablation effects of the composite scaffolds were investigated.

MATERIALS AND METHODS

Materials

Folic acid, dimethyl sulfoxide (DMSO), 6 mol · L^{-1} hydrochloric acid (HCl) and sodium hydroxide, ethanol, acetic acid, trisodium citrate dihydrate, glycine, hydroquinone, hydrogen tetrachloroaurate tetrahydrate ($HAuCl_4 4H_2O$, 99.9%), dicyclohexylcarbodiimide (DCC), and *N*-hydroxysuccinimide (NHS) were purchased from Wako Pure Industries, Ltd., (Tokyo, Japan). Hexadecyltrimethylammonium bromide (CTAB), 2-(*N*-morpholino)ethanesulfonic acid (MES), Dulbecco modified eagle medium (DMEM), penicillin, streptomycin, L-glutamine, trypsin/EDTA, ascorbic acid (AA), sodium borohydride ($NaBH_4$), and silver nitrate ($AgNO_3$) were purchased from Sigma–Aldrich (St. Louis, MO, United States). Porcine gelatin was provided by Nitta Gelatin (Osaka, Japan). Collagenase type I was purchased from Worthington Biochemical Corporation (Lakewood, NJ, United States). All chemicals were used without further purification.

Synthesis of Folic Acid–Conjugated Gelatin

FA-conjugated gelatin was synthesized by activating carboxyl groups of FA and reacting with amino groups of the gelatin. At first, FA was activated to FA-NHS. Four hundred milligrams of FA was dissolved in 10 mL DMSO and mixed with 374 mg DCC dissolved in 10 mL DMSO and 84 mg NHS dissolved in 20 mL DMSO. The mixture was kept stirring for 6 h at room temperature to activate the carboxyl groups of FA. After activation, the mixture was centrifuged (12,000 rpm, 30 min) to remove extra DCU. The activated FA-NHS was precipitated by adding diethyl ether and acetone mixture solution (70:30, vol/vol) into the supernatant at −20°C and centrifuged (12,000 rpm, 10 min) at −2°C. The products were resolved in DMSO and repeated above two steps twice before dried in vacuum. Subsequently, the FA-NHS was dissolved in DMSO and added to gelatin aqueous solution that was prepared by dissolving gelatin in sodium carbonate buffer solution. The mixture solution was kept stirring overnight at room temperature. Finally, the mixture solution was dialyzed with DMSO–water mixture solvent having different volume ratio of DMSO and pure water (80:20, 70:30, 60:40, vol/vol) and pure water only (dialysis membrane

with a molecular weight cutoff of 3.5 kDa). FA-modified gelatin was obtained after lyophilization and stored at 4°C for following use.

Preparation of Folic Acid–Coated AuNPs With Different Shapes and Sizes

Au nanorods (AuNRs) with different sizes (around 40, 70, and 110 nm in length) and Au nanostars (AuNSs) with different sizes (around 40, 70, and 110 nm) were prepared by previously reported method (Zhang et al., 2017a). Briefly, the AuNRs (40 and 70 nm) were prepared by seed-growth method. With stabilization by CTAB, $HAuCl_4$ was quickly reduced by $NaBH_4$ and became Au seed. The AuNR40 (40 nm) and AuNR70 (70 nm) were prepared by adjusting the amount of $AgNO_3$ (0.44 and 2.20 mL of 10 mM $AgNO_3$, respectively) in the growth solution. The growth solution contained 10 mL of 0.01 M $HAuCl_4$, 4 mL of 1 M HCl, 1.6 mL of 0.1 M AA, 0.48 mL of Au seed, and 150 mL of 0.1 M CTAB. The AuNR110 (110 nm) was prepared by a one-pot method. Briefly, 7.6 mL of 0.01 M $HAuCl_4$, 2 mL of 0.02 M $AgNO_3$, and 1.6 mL of 0.62 M hydroquinone were mixed with 178 mL of 0.11 M CTAB solution. And then, 126 μL of 0.5 M $NaBH_4$ was added and the mixture was kept at 30°C for 24 h to obtain AuNR110. The AuNSs were also synthesized by seed-growth method with a little change of the aforementioned conditions for AuNRs preparation. The seed solution for AuNSs was prepared by using trisodium citrate to reduce $HAuCl_4$. The growth solution of AuNSs (40, 70, and 110 nm) consisted of 0.75 mL of 30 mg · mL^{-1} $HAuCl_4$, 0.3 mL of 5 mg · mL^{-1} $AgNO_3$, and 0.5 mL of 38 mg · mL^{-1} AA and Au seed (25, 5, and 1.1 mL, respectively). After AuNRs and AuNSs were prepared, they were mixed with 0.5% (wt/vol) of FA–gelatin solution and stirring at room temperature for 24 h. The FA-functionalized AuNPs were collected by centrifugation, washed with Milli-Q water, and redispersed in Milli-Q water for further use.

Preparation of FA-Functionalized Gelatin–AuNPs Composite Scaffolds

In order to control the porous structure of composite scaffolds, pre-prepared ice particulates were used as a porogen material as previously reported (Zhang et al., 2013). At first, ice particulates were prepared by spaying Milli-Q water into liquid nitrogen and sieving through mesh sieves with pore size ranging between 425 and 500 μm. Subsequently, the aqueous solution of FA-functionalized AuNPs was dropped into 8% (wt/vol) of FA-conjugated gelatin solution containing 70% of acetic acid. Seventy percent of acetic acid solution could protect freezing of the mixture solution during mixing with ice particulates. The final concentration of AuNPs was 2.0 mM. And then, the ice particulates were added to the FA–gelatin/AuNPs mixture solution at a ratio of 7:3 (wt/vol). The ice particulates/FA–gelatin/AuNPs mixture solution was added to a silicone mold at −4°C, followed with freezing at −20°C for 12 h and −80°C for 4 h. Finally, the frozen constructs were freeze-dried. After freeze-drying, the constructs were washed with ethanol and cross-linked with 50.0 mM EDC and 20.0 mM NHS dissolved in a mixture solution of ethanol and 0.1% (wt/vol) MES mixture solution at a series of ethanol–water ratio of 95/5, 90/10, and 85/5 (vol/vol), each for 8 h. After cross-linking, the composite scaffolds were washed with Milli-Q water for six times and immersed in 0.1 M glycine aqueous solution for 6 h to block the activated groups that were not reacted during cross-lining. The composite scaffolds were washed by Milli-Q water for six times and freeze-dried. Scaffolds of FA-functionalized gelatin, pristine gelatin without AuNPs, and pristine gelatin with bare AuR70 were prepared as controls by the same method described above. These scaffolds were denoted as FA-G (control), G (control), G/R70, FA-G/R40, FA-G/R70, FA-G/R110, FA-G/S40, FA-G/S70, and FA-G/S110, respectively.

Characterization of AuNPs and FA-Functionalized Gelatin–AuNPs Composite Scaffolds

Transmission electron microscopy (TEM; JEOL 2011F, Japan) was used for observation of AuNPs. An ImageJ software (National Institutes of Health, Bethesda, MD, United States) was used to measure the longitudinal length and transverse length of AuNRs and the distance between the two most distal points of AuNSs. Scanning electron microscopy (SEM; Hitachi S-4800, Japan) was used for observation of the porous structures of the composite scaffolds. UV-visible spectra of all the samples were measured by a UV-2600 UV-visible spectrophotometer (Shimadzu Corp., Japan).

Quantification of FA Amount in FA-Functionalized Gelatin–AuNPs Composite Scaffolds

Folic acid amount in each scaffold was measured by using a previously reported method (Escudero-Duch et al., 2019). At first, discs (φ 6 mm × H 1 mm) of the FA-functionalized gelatin–AuNPs composite scaffolds were dissolved in 2 mL of 6 M HCl solution for 24 h. And then, the solutions were centrifuged for excluding the influence of AuNPs, and pH of the solutions was adjusted to 13. Finally, UV-visible spectrophotometer was used to measure the absorbance of the supernatants at a wavelength of 365 nm, which was the specific absorbance peak of FA. FA concentration was calculated according to a standard curve. Every three samples were used for the measurement.

Cell Capture Experiment

MDA-MB231 breast cancer cells that express FA receptors on their membrane were used as FA receptor–positive cells for cell capture experiment (Soe et al., 2018). HT1080 cells that are FA receptor–negative cell line were used as a negative control (Stefflova et al., 2007). The two types of cells were subcultured in cell culture polystyrene flasks with DMEM supplemented with 10% fetal bovine serum, streptomycin (100 μg · mL^{-1}), and penicillin (100 U · mL^{-1}). The confluent cells were detached by treatment with 0.05% trypsin-EDTA, washed once with phosphate-buffered saline (PBS), and resuspended in serum-free

DMEM at a concentration of 2 × 10^5 cells/mL. Cell capture experiment was conducted in a flowing chamber that consisted of a silicone frame on a cell strainer. At first, a sterile silicone frame with a hole (φ 6 mm) was placed on a cell strainer (pore size was 70 μm). The sterilized scaffold discs (φ 6 mm × H 1 mm) were placed in the frame hole and on the cell strainer. The scaffold discs were pre-wetted with PBS and washed with serum-free DMEM by dropping medium on the scaffold discs. And then, the cell suspension solution in serum-free medium was added dropwise on the top of scaffold discs at a speed of 5 s per drop. After 5 mL (1 × 10^6 cells) of the cell solution was added, 30 μL of serum-free DMEM was added for three times to remove unadhered cells. Finally, the scaffold discs were digested with collagenase type I solution, and cell number in each scaffold disc was counted. Four types of scaffolds (G, G/R70, FA-G, FA-G/R70) were used for cell capture experiment. Every three samples were used for the measurement to calculate means and standard deviations.

In vitro Photothermal Property and Ablation Capacity of FA-Functionalized Gelatin–AuNPs Composite Scaffolds

The G, G/R70, and FA-G/R70 scaffolds were cut into discs (φ 6 mm × H 1 mm) and pregnant with 30 μL Milli-Q water. The hydrated scaffold discs were irradiated with 805-nm laser of different power intensities (1.3, 1.4, 1.5, and 1.6 W/cm^2) for 10 min, and temperature of the hydrated scaffold discs was recorded each 30 s by electronic thermometer during the irradiation. The laser beam spot size was 8 × 6 mm. For investigation of *in vitro* PTT ablation capacity, the scaffold discs were sterilized with 70% ethanol and washed with PBS for

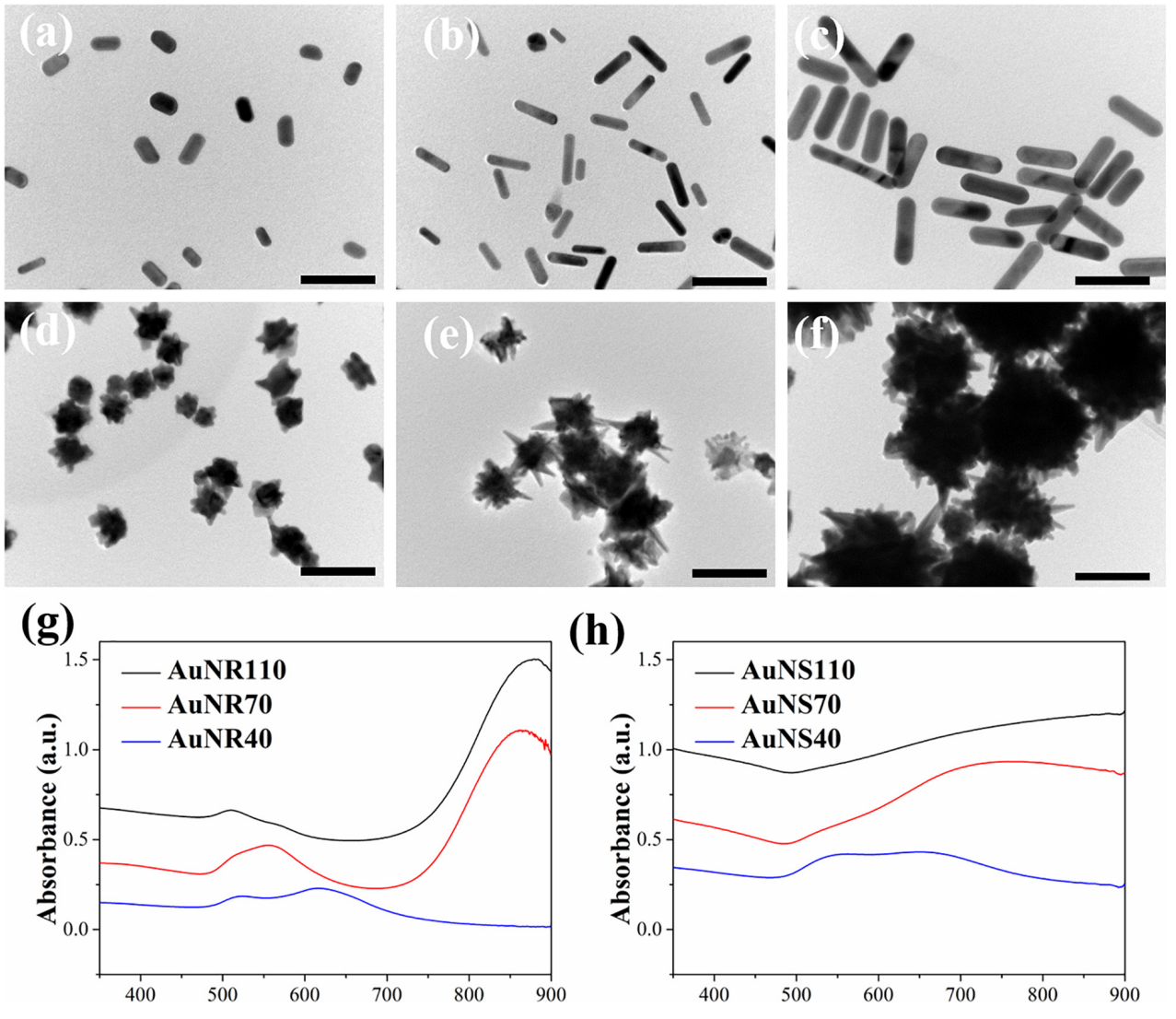

FIGURE 1 | TEM images of AuNPs: **(a)** AuNR40, **(b)** AuNR70, **(c)** AuNR110, **(d)** AuNS40, **(e)** AuNS70, **(f)** AuNS110. Scale bar: 100 nm. UV-visible spectra of AuNRs **(g)** and AuNSs **(h)**.

three times. DMEM serum medium was used for cell culture; 20 μL cell suspension solution (5×10^6 cells/mL) of MDA-MB231 cells was seeded on one side of the scaffold discs and cultured in DMEM serum medium for 6 h. After 6 h, the scaffold discs were turned upside down, and another side was seeded with another 20 μL cell suspension solution (5×10^6 cells/mL). After cell seeding, the cell/scaffold constructs were transferred into culture dish and incubated in DMEM serum medium for 1 day. And then, the cell/scaffold constructs were irradiated with 805-nm laser of two power intensities (1.3 and 1.6 W/cm^2) for 3 and 6 min. MDA-MB231 cells were also seeded and cultured in the FA-functionalized gelatin without AuNPs (control) and irradiated with NIR laser as described above. After NIR laser irradiation, cell/scaffold constructs were continuously cultured for 3 h. And then, cell viability was measured by WST-1 assay. A microplate reader (Benchmark Plus; Bio-Rad, Hercules, CA, United States) was used to measure the absorbance at 440 nm. Live/dead staining kit was used to visualize live and dead cells in the scaffolds with or without laser irradiation. The cell/scaffold constructs with or without NIR laser irradiation were washed by PBS and staining by calcein AM and propidium iodide in serum-free medium for 15 min.

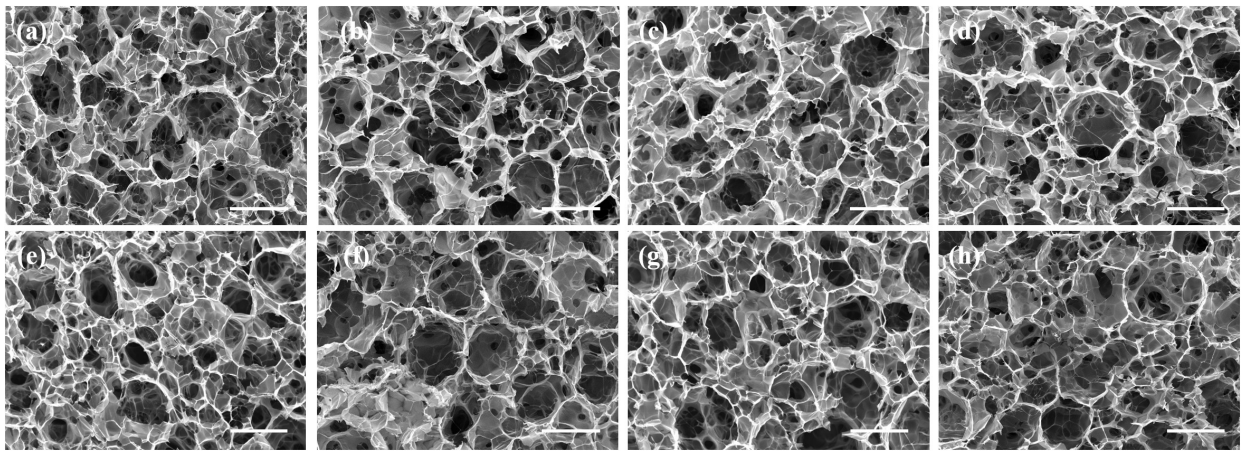

FIGURE 2 | SEM images of FA-functionalized gelatin–AuNPs composite scaffolds and FA-functionalized gelatin and gelatin control scaffold: **(a)** G (gelatin scaffold), **(b)** FA-G (FA-functionalized gelatin scaffold), **(c)** FA-G/R40, **(d)** FA-G/R70, **(e)** FA-G/R110, **(f)** FA-G/S40, **(g)** FA-G/S70, **(h)** FA-G/S110. Scale bar: 500 μm.

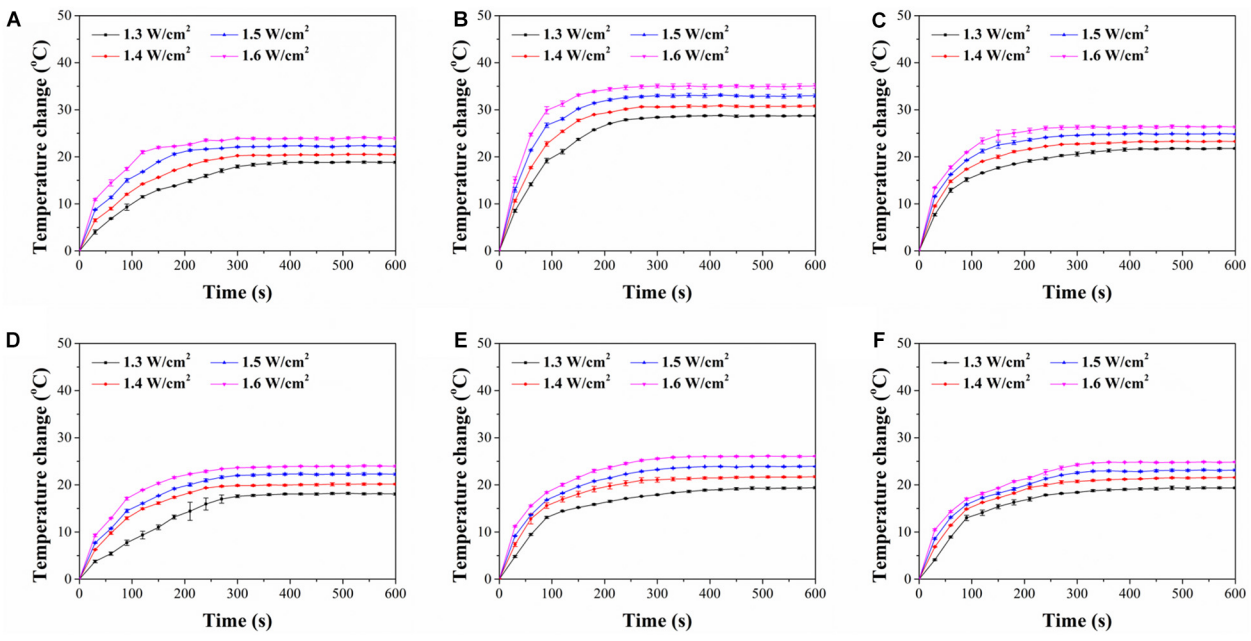

FIGURE 3 | Time course of temperature change of composite scaffolds during NIR laser irradiation with different laser power intensities of 1.3, 1.4, 1.5, and 1.6 W/cm^2 for 600 s: **(A)** FA-G/R40, **(B)** FA-G/R70, **(C)** FA-G/R110, **(D)** FA-G/S40, **(E)** FA-G/S70, **(F)** FA-G/S110.

The stained cells were observed with a fluorescence microscope (Olympus, Japan).

In vivo Photothermal Ablation Capacity of FA-Functionalized Gelatin–AuNPs Composite Scaffolds

The MDA-MB231-Luc cells were seeded in the G, G/R70, and FA-G/R70 scaffolds (φ 6 mm × H 1 mm) as described above and cultured in DMEM serum medium for 3 day. And then, the cell/scaffold constructs were subcutaneously implanted in 6-week-old female BALB/c nude mice. After implantation for 3 day, the implanted sites were irradiated with 805-nm laser at a power intensity of 1.6 W/cm^2 for 10 min, and the temperature change was detected by an infrared thermal imager. In order to evaluate PTT ablation capacity, an *in vivo* vision system (IVIS Lumina II, Japan) was used for detecting systemic bioluminescence of MDA-MB231-Luc cells. L-Luciferase solution was administered by intraperitoneal injection the next day after laser irradiation. After injection for 10 min, the IVIS imaging was used to detect the bioluminescence. Every three mice were used for each scaffold group. Systemic bioluminescence was examined before and after laser irradiation for each mouse. The animal experiment procedures were approved by the Animal Experiments Committee of National Institute for Materials Science, and the experiments were conducted according to the committee guidelines.

Statistical Analysis

All the quantitative experiments were repeated in triplicate (n = 3). All the results were expressed as mean ± standard deviation. The statistical analysis of experimental data was performed by using one-way analysis of variance statistical analysis. The p value was used to determine the level of significance: $^*P < 0.05$, $^{**}P < 0.01$, and $^{***}P < 0.001$.

RESULTS AND DISCUSSION

Characterization of AuNRs and AuNSs

Transmission electron microscopy images showed the rod- and star-shaped morphology of the AuNRs (**Figures 1a–f**). The AuNR40, 70, and 110 had a length × width dimension of (39.6 ± 5.7 nm) × (19.0 ± 2.6 nm), (68.3 ± 4.7 nm) × (14.2 ± 2.1 nm) and (113.8 ± 13.8 nm) × (25.6 ± 3.8 nm), respectively. The AuNS40, 70, and 110 had a dimension of 37.1 ± 2.9, 68.5 ± 10.2, and 113.9 ± 7.2 nm, respectively. UV-visible spectra of the AuNRs and AuNSs showed that the AuNR70 and AuNR110 had an absorbance peak at 833 and 880 nm, respectively. AuNR40 had an absorbance peak at 611 nm. AuNSs showed a broad absorbance peak around 800 nm. The difference of UV-visible absorbance spectra and absorbance peaks among these AuNRs and AuNRs could be attributed to LSPR effect of AuNPs (Zhao et al., 2009). By comparing the UV-visible spectra of all these AuNPs, AuNR70 had a relatively sharp and high absorbance peak in NIR area, suggesting AuNR70 should have the highest absorbance capability under NIR laser irradiation.

TABLE 1 | Temperature change (°C) of FA-G and FA-G/AuNPs composite scaffolds after 10-min laser irradiation. Data represent mean ± SD.

	1.3 W/cm^2	1.4 W/cm^2	1.5 W/cm^2	1.6 W/cm^2
FA-G	4.6 ± 0.2	5.8 ± 0.1	7.6 ± 0.2	9.0 ± 0.5
FA-G/R40	18.8 ± 0.2	20.4 ± 0.1	22.3 ± 0.2	23.9 ± 0.3
FA-G/R70	28.7 ± 0.1	30.8 ± 0.2	33.0 ± 0.3	35.1 ± 0.4
FA-G/R110	21.8 ± 0.1	23.3 ± 0.1	24.9 ± 0.5	26.3 ± 0.3
FA-G/S40	18.1 ± 0.3	20.1 ± 0.2	22.2 ± 0.3	24.0 ± 0.2
FA-G/S70	19.4 ± 0.3	21.7 ± 0.2	24.0 ± 0.1	26.1 ± 0.1
FA-G/S110	19.3 ± 0.1	21.6 ± 0.2	23.1 ± 0.2	25.0 ± 0.1

Preparation and Characterization of FA-Functionalized Gelatin–AuNPs Composite Scaffolds

UV-visible spectrum was used to confirm conjugation between FA and gelatin (Hao et al., 2018). Gelatin had no absorbance peak between wavelength of 300 and 900 nm, whereas FA had a sharp and strong absorbance peak at a wavelength of 365 nm (**Supplementary Figure S1**). FA–gelatin showed a broad absorbance around 365 nm. The results indicated that FA was conjugated with gelatin. FA amount in the FA-functionalized gelatin measured at 365 nm was 46.8 ± 5.1 μg/mg. UV-visible spectrum was also used for analyzing absorbance change of AuNR70 before and after modification with FA–gelatin (Mehdizadeh et al., 2014). FA–gelatin–coated AuNR70 showed an increased absorbance peak around 365 nm, suggesting modification of AuNR70 with FA (**Supplementary Figure S2**).

The FA-functionalized gelatin–AuNPs composite scaffolds were prepared by hybridizing FA–gelatin-coated AuNR40, 70, and 110 and AuNS40, 70, and 110 with FA-functionalized gelatin porous scaffolds, respectively. Pre-prepared ice particulates with a diameter between 425 and 500 μm were used as a porogen material to control the porous structures. Gelatin and FA-functionalized gelatin porous scaffolds were prepared as controls by the same method. Porous structures of the scaffolds were observed by SEM (**Figure 2**). All the scaffolds showed similar porous structures. There were many large spherical pores that were surrounded with small pores. The large spherical pores had identical sizes to the ice particulates (∼425–500 μm) and were well interconnected. The interconnected pores ensured that seeded cells could penetrate and distribute throughout the whole scaffold (Zhang et al., 2014).

In order to quantify the amount of FA in each composite scaffold, the scaffolds were dissolved in HCl solution, and absorbance of the solutions at 365 nm was measured to calculate FA amount. The FA amount in FA-G/R40, FA-G/R70, FA-G/R110, FA-G/S40, FA-G/S70, and FA-G/S110 was 47.3 ± 5.3, 46.8 ± 8.4, 47.4 ± 6.2, 48.4 ± 6.5, 50.3 ± 9.7, and 49.5 ± 7.5 μg/mg, respectively. FA amount was almost at the same levels for all the composite scaffolds because the same FA-conjugated gelatin was used for the preparation of all the composite scaffolds. The FA-functionalized AuNPs showed no evident influence on FA amount in the composite scaffolds.

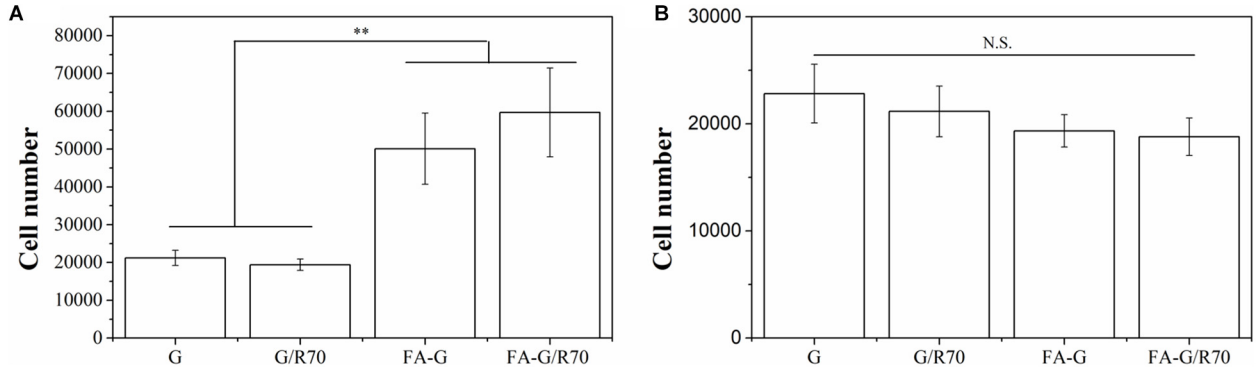

FIGURE 4 | Captured number of MDA-MB231 cells (FA receptor–positive cells) and HT1080 cells (FA receptor–negative cells) in G, G/R70, FA-G, and FA-G/R70 scaffolds: **(A)** MDA-MB231 cells, **(B)** HT1080. Data represent means ± SD (n = 3). $^{**}P < 0.01$; N.S., no significant difference.

Photothermal Conversion Property of FA-Functionalized Gelatin–AuNPs Composite Scaffolds

The photothermal conversion property of FA-functionalized gelatin–AuNPs composite scaffolds was investigated by irradiating the scaffolds with 805-nm laser at power intensity of 1.3, 1.4, 1.5, and 1.6 W/cm^2 (**Figure 3**). The results indicated that all composite scaffolds showed rapid temperature increase during the first 200-s NIR laser irradiation and then reached temperature plateau afterward. The magnitude of temperature change increased with NIR laser intensity. The six types of composite scaffolds had different magnitude of temperature change (**Table 1**). Among the composite scaffolds, FA-G/R70 showed the highest photothermal conversion property. The different photothermal conversion property should be attributed to the different absorbance capacity AuNPs under NIR laser irradiation as shown in **Figure 1**. The shape and size of AuNPs can LSPR absorption (Liu et al., 2011), which results in shift of UV-visible absorbance. The absorbance peak of AuNR70 was closest to the wavelength of NIR laser, and the sharp absorbance peak indicated specific absorbance to the NIR laser. Therefore, the composite scaffold FA-G/R70 was used for the following *in vitro* and *in vivo* cell culture experiments.

Capture Capability of Cancer Cell by FA-Functionalized Gelatin–AuNPs Composite Scaffolds

Instead of static cell culture in scaffolds (Escudero-Duch et al., 2019), a flowing cell capture method was used to evaluate cell capture capacity of the composite scaffolds. Two types, MDA-MB231 cells (FA receptor–positive cells) and HT1080 cells (FA receptor–negative cells), were used for cell culture to investigate the specific capture property of FA-functionalized composite scaffolds for FA receptor–positive cancer cells. The FA-functionalized composite scaffolds (FA-G/R70) and FA-functionalized gelatin (FA-G) captured significantly more MDA-MB231 cells than did the non-functionalized composite scaffold (G/R70) and gelatin scaffold (G) (**Figure 4A**). The number of captured MDA-MB231 cells in FA-G/R70 and FA-G had no significant difference. There was either no significant difference of captured number of MDA-MB231 cells in G/R70 and gelatin scaffolds. However, when HT1080 cells were cultured in the scaffolds, the number of captured cells in all the scaffolds had no significant difference (**Figure 4B**). The results indicated that the FA receptor–positive breast cancer cells could be efficiently captured by the FA-functionalized scaffolds. This should be due to the specific interaction between the FA molecules in the scaffolds and FA receptors on the cell membrane of MDA-MB231 cells. The incorporated AuNR70 in the composite scaffolds did not affect the cell capture capacity of the composite scaffolds because the AuNPs were coated with FA-conjugated gelatin and embedded in the pore walls of the scaffolds.

In vitro Photothermal Ablation of Cancer Cells by FA-Functionalized Gelatin–AuNPs Composite Scaffolds

MDA-MB231 cells were used for investigating *in vitro* photothermal ablation effect of the composite scaffold FA-G/R70. After cells were cultured in composite scaffolds for 1 day, the cell/scaffold constructs were irradiated with NIR laser. Two power densities of NIR laser were used for the irradiation. Cell viability before (0 min) and after irradiation (3 and 6 min) was measured (**Figures 5a,b**). The cells showed high cell viability both in FA-functionalized gelatin scaffold and FA-functionalized composite scaffold before laser irradiation. After irradiation with NIR laser, cell viability decreased. When irradiation time increased, cell viability in FA-G/R70 scaffold significantly decreased to 66.3% after 3-min and to 26.3% after 6-min irradiation with 1.3-W/cm^2 laser. When laser power intensity increased to 1.6 W/cm^2, cell viability decreased more rapidly than that irradiated with 1.3 W/cm^2. Cell viability decreased to 33.7% after 3-min and to 4.3% after 6-min irradiation with 1.6-W/cm^2 NIR laser.

Live/dead staining further demonstrated the hyperthermal ablation effect of the composite scaffolds (**Figures 5c–k**). After NIR laser irradiation, the live cells were stained in green

fluorescence, while dead cells in red fluorescence. Before NIR laser irradiation, almost all the MDA-MB231 cells were alive. However, after NIR irradiation, some of the cells were dead. The number of dead cells increased with laser power intensity and irradiation time. Under irradiation of a power intensity of 1.6 W/cm^2 for 6 min, almost all the cells were dead (**Figure 5k**). For control scaffold without AuNPs, no dead cells were observed even after NIR laser irradiation (**Figures 5d,e**). All the results indicated that the FA-G/R70 scaffold had a high photothermal ablation effect. The high ablation effect of the FA-G/R70 scaffold was due to its excellent PTT conversion property at the NIR laser irradiation wavelength. Cancer cell can be killed when temperature is higher than 42°C (Beqa et al., 2011). As shown in **Figure 3B**, when the FA-G/R70 scaffold was irradiated with NIR laser at a power intensity of 1.3 W/cm^2 for 3 and 6 min or 1.6 W/cm^2 for 3 and 6 min, the scaffold temperature increased 25.7, 28.6, 33.9, and 35.1°C over room temperature, respectively. The temperature after NIR laser irradiation was much higher than the tolerance temperature of the cancer cells, subsequently killing the cells.

In vivo Photothermal Ablation of Cancer Cells by FA-Functionalized Gelatin–AuNPs Composite Scaffolds

After confirmation of the *in vitro* photothermal ablation effect the FA-G/R70 scaffold, animal experiment was designed to further confirm its *in vivo* photothermal ablation property. The MDA-MB231-Luc cells cultured in the FA-G/R70 scaffold for

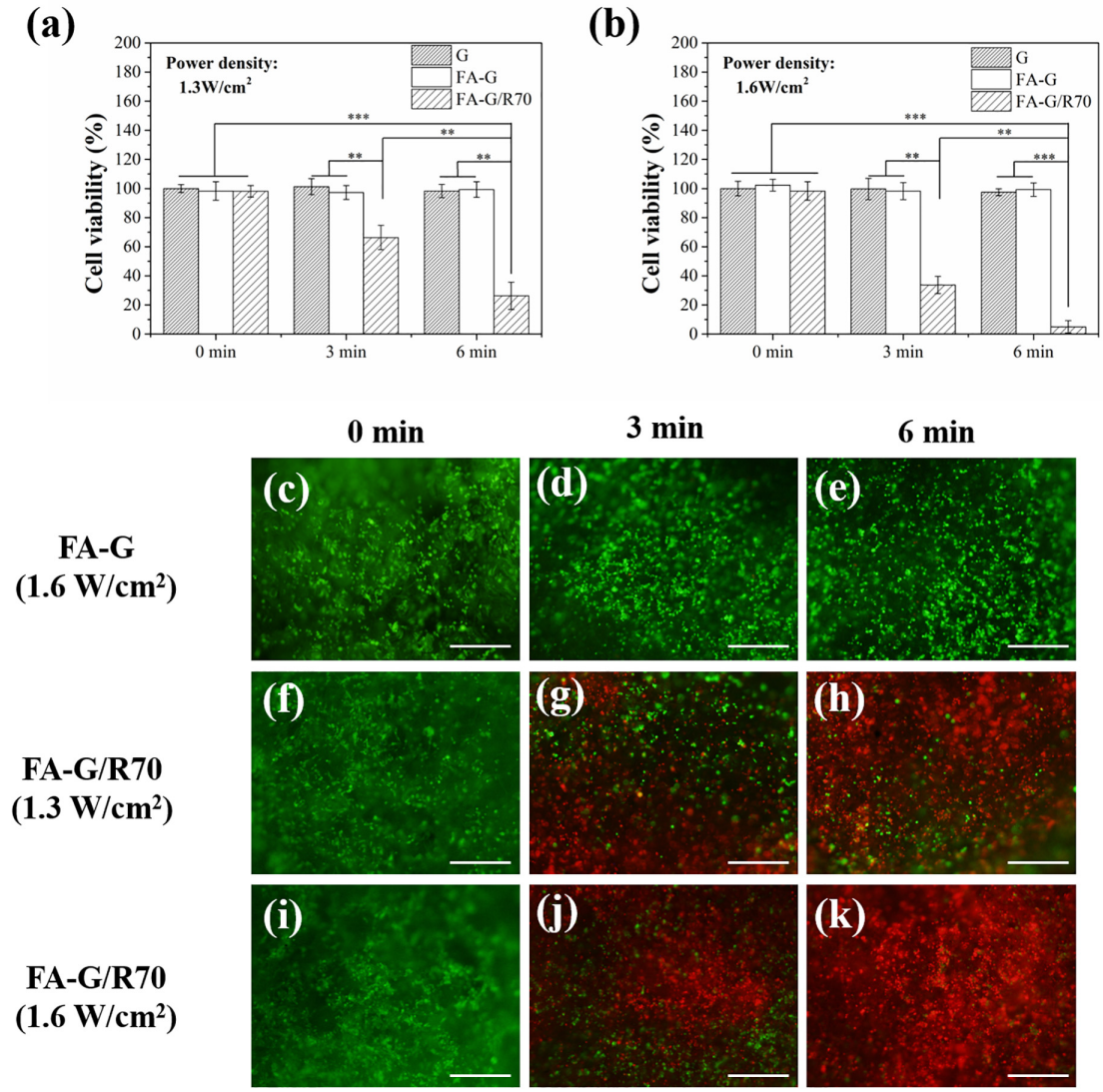

FIGURE 5 | Cell viability of MDA-MB231 cells in the G, FA-G, and FA-G/R70 scaffolds with different laser irradiation for 0, 3, and 6 min. **(a)** 1.3 W/cm^2 laser power intensity, **(b)** 1.6 W/cm^2 laser power intensity. **(c–k)** Live/dead staining of MDA-MB231 cells in FA-G and FA-G/AuNRs70 with laser irradiation for 0, 3, and 6 min. Scale bar: 100 μm. Data represent means ± SD (n = 3). $^{**}P < 0.01$; $^{***}P < 0.001$.

3 days, and then the cells/scaffold constructs were subcutaneously implanted in nude mice. After 3 days' implantation, the implantation sites were irradiated with NIR laser for 10 min. Gelatin and FA-functionalized gelatin scaffolds were used as controls. Temperature monitoring during NIR laser irradiation showed that the local temperature of the control G and FA-G scaffolds was kept almost unchanged during NIR laser irradiation (**Figure 6A**). However, the local temperature of the implantation sites of cells/FA-G/R70 constructs increased to 41.5, 44.5, and 47.5°C after irradiation for 3, 5, and 10 min, respectively, (**Figure 6A**). Whole-body bioluminescence imaging showed the *in vivo* photothermal ablation effect of the composite scaffolds (**Figure 6B**). All the mice implanted with the FA-G/R70 composite scaffold and G and FA-G control scaffolds showed strong luminescence imaging before NIR laser irradiation. The result indicated that the MDA-MB231-Luc cells were alive and survived after subcutaneous implantation in nude mice. After NIR laser irradiation for 10 min, the mice implanted with G and FA-G control scaffolds still showed strong luminescence, suggesting the MDA-MB231-Luc cells were still alive, not killed. On the other hand, no luminescence was detected in the mouse implanted with the FA-G/R70 composite scaffold after NIR laser irradiation. These results indicated that the FA-G/R70 composite scaffold could kill all the cancer cells under NIR laser irradiation because of its photothermal property. For future practical application in clinics, the composite scaffolds can be implanted after surgical resection of breast cancers. The composite scaffolds can be expected to target and capture remaining cancer cells and ablate them by repeating hyperthermal effect through laser irradiation. Therapeutic drugs can also be introduced in

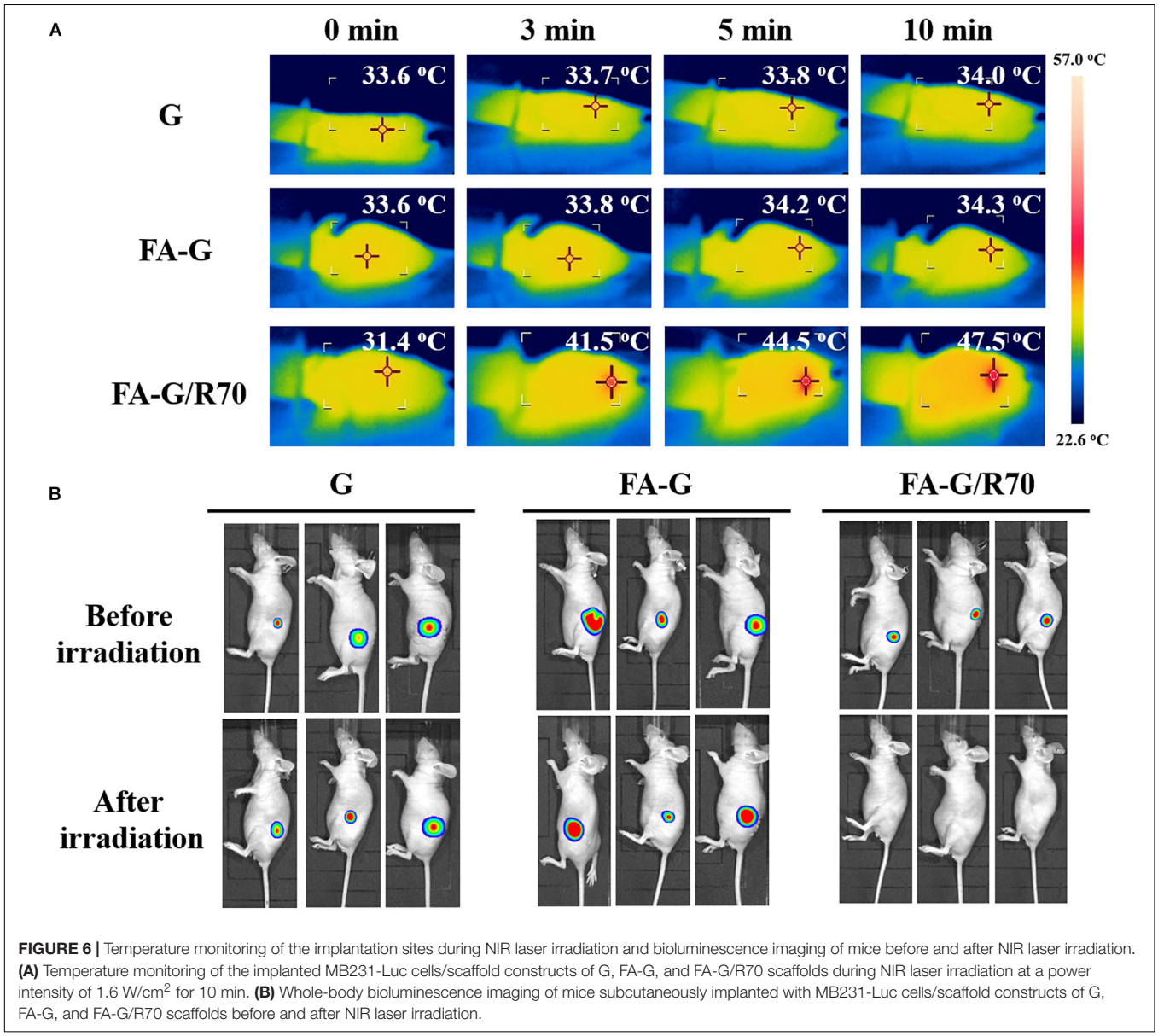

FIGURE 6 | Temperature monitoring of the implantation sites during NIR laser irradiation and bioluminescence imaging of mice before and after NIR laser irradiation. **(A)** Temperature monitoring of the implanted MB231-Luc cells/scaffold constructs of G, FA-G, and FA-G/R70 scaffolds during NIR laser irradiation at a power intensity of 1.6 W/cm^2 for 10 min. **(B)** Whole-body bioluminescence imaging of mice subcutaneously implanted with MB231-Luc cells/scaffold constructs of G, FA-G, and FA-G/R70 scaffolds before and after NIR laser irradiation.

the composite scaffolds to realize combination of PTT and chemical therapy.

CONCLUSION

FA-functionalized gelatin–AuNPs composite scaffolds were prepared by hybridizing FA-conjugated gelatin and FA-modified AuNPs and by using ice particulates as a porogen material. The composite scaffolds had the interconnected pore structures with large spherical pores surrounded with small pores. The composted scaffolds showed good photothermal properties and capture capacity for FA receptor–positive cancer cells. Temperature change of the composite scaffolds under NIR laser irradiation increased with laser power intensity and irradiation time. The FA-G/R70 composite scaffold showed the best photothermal property. *In vitro* cell culture and *in vivo* animal experiments demonstrated that the FA-G/R70 composite scaffold could kill cancers under NIR laser irradiation. The FA-functionalized gelatin–AuNPs scaffolds should be useful for local photothermal ablation of breast cancer cells for breast cancer therapy.

DATA AVAILABILITY STATEMENT

All datasets presented in this study are included in the article/**Supplementary Material**.

ETHICS STATEMENT

The animal study was reviewed and approved by Animal Experiments Committee of National Institute for Materials Science.

AUTHOR CONTRIBUTIONS

GC, NK, and YY designed the research. HC, XW, LS, and TZ did the experiments and analyzed experimental data. NK did the data analysis and figure revision. HC, YY, and GC wrote the manuscript. All authors contributed to the article and approved the submitted version.

FUNDING

This research was supported by JSPS KAKENHI Grant Number 19H04475.

SUPPLEMENTARY MATERIAL

The Supplementary Material for this article can be found online at: https://www.frontiersin.org/articles/10.3389/fbioe.2020.589905/full#supplementary-material

REFERENCES

Abdelrasoul, G. N., Farkas, B., Romano, I., Diaspro, A., and Beke, S. (2015). Nanocomposite scaffold fabrication by incorporating gold nanoparticles into biodegradable polymer matrix: synthesis, characterization, and photothermal effect. *Mater. Sci. Eng. C* 56, 305–310. doi: 10.1016/j.msec.2015.06.037

Alamzadeh, Z., Beik, J., Mahabadi, V. P., Ardekani, A. A., Ghader, A., Kamrava, S. K., et al. (2019). Ultrastructural and optical characteristics of cancer cells treated by a nanotechnology based chemo-photothermal therapy method. *J. Photochem. Photobiol. B Biol.* 192, 19–25. doi: 10.1016/j.jphotobiol.2019.01.005

Attarilar, S., Yang, J., Ebrahimi, M., Wang, Q., Liu, J., Tang, Y., et al. (2020). The toxicity phenomenon and the related occurrence in metal and metal oxide nanoparticles: a brief review from the biomedical perspective. *Front. Bioeng. Biotechnol.* 8:822. doi: 10.3389/fbioe.2020.00822

Bai, G., Yuan, P., Cai, B., Qiu, X., Jin, R., Liu, S., et al. (2019). Stimuli-responsive scaffold for breast cancer treatment combining accurate photothermal therapy and adipose tissue regeneration. *Adv. Funct. Mater.* 29:1904401. doi: 10.1002/adfm.201904401

Beqa, L., Fan, Z., Singh, A. K., Senapati, D., and Ray, P. C. (2011). Gold nano-popcorn attached SWCNT hybrid nanomaterial for targeted diagnosis and photothermal therapy of human breast cancer cells. *ACS Appl. Mater. Interf.* 3, 3316–3324. doi: 10.1021/am2004366

Blanco, E., Shen, H., and Ferrari, M. (2015). Principles of nanoparticle design for overcoming biological barriers to drug delivery. *Nat. Biotechnol.* 33:941. doi: 10.1038/nbt.3330

Bray, F., Ferlay, J., Soerjomataram, I., Siegel, R. L., Torre, L. A., and Jemal, A. (2018). Global cancer statistics 2018: GLOBOCAN estimates of incidence and mortality worldwide for 36 cancers in 185 countries. *CA Cancer J. Clin.* 68, 394–424. doi: 10.3322/caac.21492

Chen, B., Xiang, H., Pan, S., Yu, L., Xu, T., and Chen, Y. (2020). Advanced theragenerative biomaterials with therapeutic and regeneration multifunctionality. *Adv. Funct. Mater.* 30:2002621. doi: 10.1002/adfm.202002621

Chen, M. C., Lin, Z. W., and Ling, M. H. (2016). Near-infrared light-activatable microneedle system for treating superficial tumors by combination of chemotherapy and photothermal therapy. *ACS Nano* 10, 93–101. doi: 10.1021/acsnano.5b05043

Chen, S., Zhang, Q., Nakamoto, T., Kawazoe, N., and Chen, G. (2016). Gelatin scaffolds with controlled pore structure and mechanical property for cartilage tissue engineering. *Tissue Eng. Part C Methods* 22, 189–198. doi: 10.1089/ten.tec.2015.0281

Cheng, X., Sun, R., Yin, L., Chai, Z., Shi, H., and Gao, M. (2017). Light-triggered assembly of gold nanoparticles for photothermal therapy and photoacoustic imaging of tumors in vivo. *Adv. Mater.* 29:1604894. doi: 10.1002/adma.201604894

Deng, H., Zhong, Y., Du, M., Liu, Q., Fan, Z., Dai, F., et al. (2014). Theranostic self-assembly structure of gold nanoparticles for NIR photothermal therapy and X-Ray computed tomography imaging. *Theranostics* 4:904. doi: 10.7150/thno.9448

Ding, X., Liow, C. H., Zhang, M., Huang, R., Li, C., Shen, H., et al. (2014). Surface plasmon resonance enhanced light absorption and photothermal therapy in the second near-infrared window. *J. Am. Chem. Soc.* 136, 15684–15693. doi: 10.1021/ja508641z

Eivazzadeh-Keihan, R., Maleki, A., De La Guardia, M., Bani, M. S., Chenab, K. K., Pashazadeh-Panahi, P., et al. (2019). Carbon based nanomaterials for tissue engineering of bone: building new bone on small black scaffolds: a review. *J. Adv. Res.* 18, 185–201. doi: 10.1016/j.jare.2019.03.011

Escudero-Duch, C., Martin-Saavedra, F., Prieto, M., Sanchez-Casanova, S., Lopez, D., Sebastian, V., et al. (2019). Gold nanoparticles for the in situ polymerization

of near-infrared responsive hydrogels based on fibrin. *Acta Biomater.* 100, 306–315. doi: 10.1016/j.actbio.2019.09.040

Eyvazzadeh, N., Shakeri-Zadeh, A., Fekrazad, R., Amini, E., Ghaznavi, H., and Kamrava, S. K. (2017). Gold-coated magnetic nanoparticle as a nanotheranostic agent for magnetic resonance imaging and photothermal therapy of cancer. *Lasers Med. Sci.* 32, 1469–1477. doi: 10.1007/s10103-017-2267-x

Feng, B., Niu, Z., Hou, B., Zhou, L., Li, Y., and Yu, H. (2020). Enhancing triple negative breast cancer immunotherapy by ICG-templated self-assembly of paclitaxel nanoparticles. *Adv. Funct. Mater.* 30:1906605. doi: 10.1002/adfm.201906605

Han, B., Zhang, Y. L., Chen, Q. D., and Sun, H. B. (2018). Carbon-based photothermal actuators. *Adv. Funct. Mater.* 28:1802235. doi: 10.1002/adfm.201802235

Hao, C., Gao, J., Wu, Y., Wang, X., Zhao, R., Mei, S., et al. (2018). Design of folic acid based supramolecular hybrid gel with improved mechanical properties in NMP/H2O for dye adsorption. *React. Funct. Polym.* 122, 140–147. doi: 10.1016/j.reactfunctpolym.2017.11.003

He, J., Li, C., Ding, L., Huang, Y., Yin, X., Zhang, J., et al. (2019). Tumor targeting strategies of smart fluorescent nanoparticles and their applications in cancer diagnosis and treatment. *Adv. Mater.* 31:1902409. doi: 10.1002/adma.201902409

He, Z., Zhao, L., Zhang, Q., Chang, M., Li, C., Zhang, H., et al. (2020). An acceptor-donor-acceptor structured small molecule for effective nir triggered dual phototherapy of cancer. *Adv. Funct. Mater.* 30:1910301. doi: 10.1002/adfm.201910301

Hwang, S., Nam, J., Jung, S., Song, J., Doh, H., and Kim, S. (2014). Gold nanoparticle-mediated photothermal therapy: current status and future perspective. *Nanomedicine* 9, 2003–2022. doi: 10.2217/nnm.14.147

Ji, P., Gong, Y., Jin, M. L., Hu, X., Di, G. H., and Shao, Z. M. (2020). The burden and trends of breast cancer from 1990 to 2017 at the global, regional, and national levels: results from the global burden of disease study 2017. *Front. Oncol.* 10:650. doi: 10.3389/fonc.2020.00650

Khademi, S., Sarkar, S., Shakeri-Zadeh, A., Attaran, N., Kharrazi, S., Ay, M. R., et al. (2018). Folic acid-cysteamine modified gold nanoparticle as a nanoprobe for targeted computed tomography imaging of cancer cells. *Mater. Sci. Eng. C* 89, 182–193. doi: 10.1016/j.msec.2018.03.015

Kim, J., Park, S., Lee, J. E., Jin, S. M., Lee, J. H., Lee, I. S., et al. (2006). Designed fabrication of multifunctional magnetic gold nanoshells and their application to magnetic resonance imaging and photothermal therapy. *Angew. Chem.* 118, 7918–7922. doi: 10.1002/ange.200602471

Laurberg, T., Alsner, J., Tramm, T., Jensen, V., Lyngholm, C. D., Christiansen, P. M., et al. (2017). Impact of age, intrinsic subtype and local treatment on long-term local-regional recurrence and breast cancer mortality among low-risk breast cancer patients. *Acta Oncol.* 56, 59–67. doi: 10.1080/0284186X.2016.1246803

Li, J., Cai, R., Kawazoe, N., and Chen, G. (2015). Facile preparation of albumin-stabilized gold nanostars for the targeted photothermal ablation of cancer cells. *J. Mater. Chem. B* 3, 5806–5814. doi: 10.1039/C5TB00633C

Li, N., Sun, Q., Yu, Z., Gao, X., Pan, W., Wan, X., et al. (2018). Nuclear-targeted photothermal therapy prevents cancer recurrence with near-infrared triggered copper sulfide nanoparticles. *ACS Nano* 12, 5197–5206. doi: 10.1021/acsnano.7b06870

Li, S., Zhou, S., Li, Y., Li, X., Zhu, J., Fan, L., et al. (2017). Exceptionally high payload of the IR780 iodide on folic acid-functionalized graphene quantum dots for targeted photothermal therapy. *ACS Appl. Mater. Interf.* 9, 22332–22341. doi: 10.1021/acsami.7b07267

Li, Z., Wang, K., Shi, Y., Zhang, X., and Wen, J. (2020). Incidence of second primary malignancy after breast cancer and related risk factors—Is breast-conserving surgery safe? A nested case-control study. *Int. J. Cancer* 146, 352–362. doi: 10.1002/ijc.32259

Liu, S., Chen, G., Prasad, P. N., and Swihart, M. T. (2011). Synthesis of monodisperse Au, Ag, and Au-Ag alloy nanoparticles with tunable size and surface plasmon resonance frequency. *Chem. Mater.* 23, 4098–4101. doi: 10.1021/cm201343k

Liu, Y., Yuan, H., Fales, A. M., Register, J. K., and Vo-Dinh, T. (2015). Multifunctional gold nanostars for molecular imaging and cancer therapy. *Front. Chem.* 3:51. doi: 10.3389/fchem.2015.00051

Luo, Y., Wei, X., Wan, Y., Lin, X., Wang, Z., and Huang, P. (2019). 3D printing of hydrogel scaffolds for future application in photothermal therapy of breast cancer and tissue repair. *Acta Biomater.* 92, 37–47. doi: 10.1016/j.actbio.2019.05.039

Mackey, M. A., Ali, M. R., Austin, L. A., Near, R. D., and El-Sayed, M. A. (2014). The most effective gold nanorod size for plasmonic photothermal therapy: theory and in vitro experiments. *J. Phys. Chem. B* 118, 1319–1326. doi: 10.1021/jp409298f

Mehdizadeh, A., Pandesh, S., Shakeri-Zadeh, A., Kamrava, S. K., Habib-Agahi, M., Farhadi, M., et al. (2014). The effects of folate-conjugated gold nanorods in combination with plasmonic photothermal therapy on mouth epidermal carcinoma cells. *Lasers Med. Sci.* 29, 939–948. doi: 10.1007/s10103-013-1414-2

Montazerabadi, A., Beik, J., Irajirad, R., Attaran, N., Khaledi, S., Ghaznavi, H., et al. (2019). Folate-modified and curcumin-loaded dendritic magnetite nanocarriers for the targeted thermo-chemotherapy of cancer cells. *Artif. Cells Nanomed. Biotechnol.* 47, 330–340. doi: 10.1080/21691401.2018.1557670

Moustaoui, H., Saber, J., Djeddi, I., Liu, Q., Diallo, A. T., Spadavecchia, J., et al. (2019). Shape and size effect on photothermal heat elevation of gold nanoparticles: absorption coefficient experimental measurement of spherical and urchin-shaped gold nanoparticles. *J. Phys. Chem. C* 123, 17548–17554. doi: 10.1021/acs.jpcc.9b03122

Nassa, G., Salvati, A., Tarallo, R., Gigantino, V., Alexandrova, E., Memoli, D., et al. (2019). Inhibition of histone methyltransferase DOT1L silences ERα gene and blocks proliferation of antiestrogen-resistant breast cancer cells. *Sci. Adv.* 5:eaav5590. doi: 10.1126/sciadv.aav5590

Niinikoski, L., Leidenius, M. H., Vaara, P., Voynov, A., Heikkilä, P., Mattson, J., et al. (2019). Resection margins and local recurrences in breast cancer: comparison between conventional and oncoplastic breast conserving surgery. *Eur. J. Surg. Oncol.* 45, 976–982. doi: 10.1016/j.ejso.2019.02.010

Soe, Z. C., Thapa, R. K., Ou, W., Gautam, M., Nguyen, H. T., Jin, S. G., et al. (2018). Folate receptor-mediated celastrol and irinotecan combination delivery using liposomes for effective chemotherapy. *Coll. Surf. B Biointerf.* 170, 718–728. doi: 10.1016/j.colsurfb.2018.07.013

Stefflova, K., Li, H., Chen, J., and Zheng, G. (2007). Peptide-based pharmacomodulation of a cancer-targeted optical imaging and photodynamic therapy agent. *Bioconjug. Chem.* 18, 379–388. doi: 10.1021/bc0602578

Vines, J. B., Yoon, J. H., Ryu, N. E., Lim, D. J., and Park, H. (2019). Gold nanoparticles for photothermal cancer therapy. *Front. Chem.* 7:167. doi: 10.3389/fchem.2019.00167

Waks, A. G., and Winer, E. P. (2019). Breast cancer treatment: a review. *JAMA* 321, 288–300. doi: 10.1001/jama.2018.19323

Wang, S., Riedinger, A., Li, H., Fu, C., Liu, H., Li, L., et al. (2015). Plasmonic copper sulfide nanocrystals exhibiting near-infrared photothermal and photodynamic therapeutic effects. *ACS Nano* 9, 1788–1800. doi: 10.1021/nn506687t

Wang, X., Kawazoe, N., and Chen, G. (2019a). Interaction of immune cells and tumor cells in gold nanorod-gelatin composite porous scaffolds. *Nanomaterials* 9:1367. doi: 10.3390/nano9101367

Wang, X., Li, J., Kawazoe, N., and Chen, G. (2019b). Photothermal ablation of cancer cells by albumin-modified gold nanorods and activation of dendritic cells. *Materials* 12:31. doi: 10.3390/ma12010031

Wang, X., Zhang, J., Li, J., Chen, Y., Chen, Y., Kawazoe, N., et al. (2018). Bifunctional scaffolds for the photothermal therapy of breast tumor cells and adipose tissue regeneration. *J. Mater. Chem. B* 6, 7728–7736. doi: 10.1039/C8TB02325E

Zhang, J., Li, J., Kawazoe, N., and Chen, G. (2017a). Composite scaffolds of gelatin and gold nanoparticles with tunable size and shape for photothermal cancer therapy. *J. Mater. Chem. B* 5, 245–253. doi: 10.1039/C6TB02872A

Zhang, J., Li, J., Wang, X., Kawazoe, N., and Chen, G. (2017b). Targeting ligand-functionalized photothermal scaffolds for cancer cell capture and in situ ablation. *Biomater. Sci.* 5, 2276–2284. doi: 10.1039/C7BM00639J

Zhang, Q., Lu, H., Kawazoe, N., and Chen, G. (2013). Preparation of collagen porous scaffolds with a gradient pore size structure using ice particulates. *Mater. Lett.* 107, 280–283. doi: 10.1016/j.matlet.2013.05.070

Zhang, Q., Lu, H., Kawazoe, N., and Chen, G. (2014). Pore size effect of collagen scaffolds on cartilage regeneration. *Acta Biomater.* 10, 2005–2013. doi: 10.1016/j.actbio.2013.12.042

Zhao, W. B., Park, J., Caminade, A. M., Jeong, S. J., Jang, Y. H., Kim, S. O., et al. (2009). Localized surface plasmon resonance coupling in Au nanoparticles/phosphorus dendrimer multilayer thin films fabricated by layer-by-layer self-assembly method. *J. Mater. Chem.* 19, 2006–2012. doi: 10.1039/B814116A

Conflict of Interest: The authors declare that the research was conducted in the absence of any commercial or financial relationships that could be construed as a potential conflict of interest.

frontiers in Bioengineering and Biotechnology

ORIGINAL RESEARCH
published: 16 November 2020
doi: 10.3389/fbioe.2020.599107

Near-Infrared Responsive Phase-Shifted Nanoparticles for Magnetically Targeted MR/US Imaging and Photothermal Therapy of Cancer

*Yan Xu[1,2], Wang Li[1,2], Sijie Chen[1,2], Biying Huang[1,2], Wenjing Pei[1,2] and Chengcheng Niu[1,2]**

[1] Department of Ultrasound Diagnosis, The Second Xiangya Hospital, Central South University, Changsha, China, [2] Research Center of Ultrasonography, The Second Xiangya Hospital, Central South University, Changsha, China

OPEN ACCESS

Edited by:
Saji Uthaman,
Chungnam National University,
South Korea

Reviewed by:
Raghvendra Ashok Bohara,
National University of Ireland Galway,
Ireland
Puthusserickal Hassan,
Bhabha Atomic Research Centre
(BARC), India

***Correspondence:**
Chengcheng Niu
niuchengcheng@csu.edu.cn

Specialty section:
This article was submitted to
Nanobiotechnology,
a section of the journal
Frontiers in Bioengineering and
Biotechnology

Received: 26 August 2020
Accepted: 26 October 2020
Published: 16 November 2020

Citation:
Xu Y, Li W, Chen S, Huang B,
Pei W and Niu C (2020) Near-Infrared
Responsive Phase-Shifted
Nanoparticles for Magnetically
Targeted MR/US Imaging
and Photothermal Therapy of Cancer.
Front. Bioeng. Biotechnol. 8:599107.
doi: 10.3389/fbioe.2020.599107

Accurate diagnosis, providing guidance for early treatment, can greatly improve the survival rate of cancer patients. However, there are still some difficulties with the existing diagnostic technology and early treatment methods. Here, near-infrared responsive phase-shifted nanoparticles (NRPNs) have been designed for magnetically targeted MR/US imaging and photothermal therapy of tumors. In this study, we fabricated a multifunctional polymer nanoparticle encapsulating indocyanine green (ICG), magnetic Fe_3O_4 nanoparticles and perfluoropentane (PFP). Under laser irradiation, the NRPNs, which trigger a phase-shifted expansion effect due to the quick conversion from light to heat by ICG and Fe_3O_4, can be used for ultrasound (US) imaging. At the same time, such nanoparticles can kill cancer cells via photothermal therapy (PTT). As a kind of negative enhancement agent, magnetic Fe_3O_4 nanoparticles in NRPNs showed high spatial resolution in MR imaging. Moreover, with the help of the magnetic field, the NRPNs nanoparticles showed high cellular uptake and high tumor accumulation, indicating their magnetic targeting property without biosafety concerns. Therefore, we present a strategy for magnetically targeted MR/US imaging guided photothermal therapy for the accurate diagnosis and efficient treatment of tumors.

Keywords: magnetically targeted, MR/US imaging, perfluorocarbon, phase shifted, photothermal therapy

INTRODUCTION

Cancer is one of the major diseases associated with human mortality. With the increasing numbers of cancer patients worldwide, cancer has become a major public health problem threatening human health (Siegel et al., 2020). Earlier and more accurate diagnosis of cancer, to provide guidance for early treatment, can greatly improve the survival rate of cancer patients (Hussain and Nguyen, 2014). For more accurate biological details of the solid tumors, multimodal imaging, which integrates various of imaging techniques, such as ultrasound (US), magnetic resonance (MR), computed tomography (CT), positron emission tomography (PET) or optical imaging, has increasingly attracted much attention.

Recent studies have shown that liquid perfluorocarbon (PFC) could be used as a phase-shift enhancement agent encapsulated in nanoparticles (NPs) due to its low boiling point. These encapsulated PFC NPs could produce excellent contrast for US imaging by phase-transition of microbubbles via optical droplet vaporization (ODV) (Eric, 2011; Hannah et al., 2014; Santiesteban et al., 2017). In addition, owing to their small size (less than 700 nm), the encapsulated PFC NPs can accumulated in the tumor site by passing through the endothelial cells gaps in the blood vessels of tumors (Jian et al., 2014; Santiesteban et al., 2019). By encapsulating optical absorbing materials [i.e., organic (Zhu et al., 2018; Chen et al., 2019) and inorganic compounds (Li et al., 2018; Guan et al., 2019)] into the PFC NPs, the NPs can quickly transfer to microbubbles under NIR laser irradiation exposure induction. Once triggered into microbubbles, such NPs can produce excellent contrast-enhanced US imaging as well (Jian et al., 2014; Sun et al., 2014). Indocyanine green (ICG), a near infrared (NIR) organic dye, was approved by the US Food and Drug Administration (FDA) (Sheng et al., 2014) due to its very low rate of side effects (Sakka, 2007), and it can absorb light in the NIR region (Hu et al., 2016) and convert it into heat (Yan and Qiu, 2015; Li et al., 2016). This results in photothermal therapy (PTT) with the temperature exceeding 42°C, which can promote the death of cancer cells and inhibit tumor growth. However, ICG also suffers from several inherent drawbacks limiting its applications, such as its instability in aqueous solution (Saxena et al., 2003), rapid liver elimination (Ott, 1998), and temperature- and light-dependent optical properties (Ma et al., 2013). Moreover, ICG cannot actively target tumors (Yan and Qiu, 2015). Therefore, how to overcome these drawbacks and promote a targeting performance for enhancing the phototherapy of ICG is challenging work.

Magnetic iron oxide (Fe_3O_4) NPs have been widely studied for the treatment of cancer owing to their unique characteristics, such as acting as the magnetic hyperthermia or photothermal agents to increase temperature in response to magnetic induction or laser irradiation (Espinosa et al., 2016; Dadfar et al., 2019). Fe_3O_4 is typically used as an MR imaging contrast agent because of its typical darkening property due to the short transverse relaxation time (T2) of protons (Zeng et al., 2013; Wang et al., 2014). Moreover, Fe_3O_4 can be targeted to the tumor region with the help of a magnet, resulting in tissue-specific accumulation (Cheng et al., 2012; Zhu et al., 2013).

In this study, we synthesized near-infrared responsive phase-shifted nanoparticles (NRPNs) by incorporating ICG, PFP and Fe_3O_4 NPs into poly lactic-co-glycolic acid (PLGA) shells with a magnetic field for dual-modal enhancement of US/MR imaging via a phase-shift expansion and PTT treatment by NIR laser (**Figure 1**) based on the following considerations: (i) Previously, NRPNs were used as an effective therapeutic agent for tumor ablation via PTT (Niu et al., 2017). (ii) After NIR laser irradiation, Fe_3O_4 NPs and ICG can absorb NIR light and transfer it into heat, triggering the liquid-to-gas transition of PFP and developing a specific "nano-to-micro" phase-transformation strategy for contrast enhanced US (Xu et al., 2017; Wang et al., 2018). (iii) Dual-modal imaging of NRPNs, which integrates MR and US imaging, can offer imaging guidance for PTT of tumors. (iv) With the driving action of the magnetic field, more NRPNs can accumulate in the tumor region and will be more effective for the diagnosis and treatment of the tumor.

MATERIALS AND METHODS

Preparation of the NRPNs

The synthesis of the NRPNs followed the previous reports (Niu et al., 2017). First, 400 μL liquid PFP and 400 μL ICG solution (1 mg ICG dissolved in 100 μL of deionized water) were mixed, and then emulsified with an ultrasonic sonicator for 30 s. PLGA (100 mg) and Fe_3O_4 NPs (200 μL) were dissolved in 3 mL chloroform. Then, the PFP and ICG mixture was added into the chloroform with a second emulsification for 1 min. Subsequently, 15 mL cold 4% PVA was added to the above emulsified solution for a third emulsification for 2 min. The resulting emulsion was volatilized by evaporation for 2 h. At last, the NRPNs were washed with deionized water 3 times and stored at 4°C in the dark until further use. All of the operations were performed in an ice bath and in the dark. The same procedure was used to prepare the PLGA NPs without ICG, Fe_3O_4 and PFP, PFP/ICG/PLGA NPs without Fe_3O_4 and PFP/ICG/PLGA NPs without Fe_3O_4. These NPs were used as controls.

For cell uptake experiments, the fluorescent DiI labeled NRPNs was prepared. PLGA (100 mg), Fe_3O_4 NPs (200 μL) and 1 mg DiI were dissolved in 3 mL chloroform, 400 μL liquid PFP and 400 μL ICG solution (1 mg ICG dissolved in 100 μL of deionized water) were mixed, and then emulsified with an ultrasonic sonicator for 30 s. Then PFP and ICG mixture was added into to the chloroform with second emulsification for 1 min. Subsequently, 15 mL cold 4% PVA was added to the above emulsified solution with the third emulsification for 2 min. The resulting emulsion was volatilized by evaporation for 2 h. At last, the NRPNs was washed with deionized water 3 times and stored at 4°C in dark for further use.

Characterization

The morphological characteristics of the NRPNs was detected by scanning electron microscopy (SEM). Structural characterization and the existence of Fe_3O_4 NPs were measured using transmission electron microscopy (TEM). Size distributions and zeta potential were analyzed using a Malvern size analyzer. The encapsulated iron amount in the NRPNs was calculated by atomic absorption spectrometry. The UV–Vis-NIR absorption spectra of the NRPNs was detected by a UV–vis-NIR spectrophotometer to confirm the existence of ICG. The ICG encapsulation efficiency and loading content were calculated thus:

$$\text{Encapsulation efficiency (\%)} = \frac{\text{(Mass of all of the encapsulated ICG in the NRPNs)}}{\text{(Mass of all of the added ICG)}} \times 100\%$$

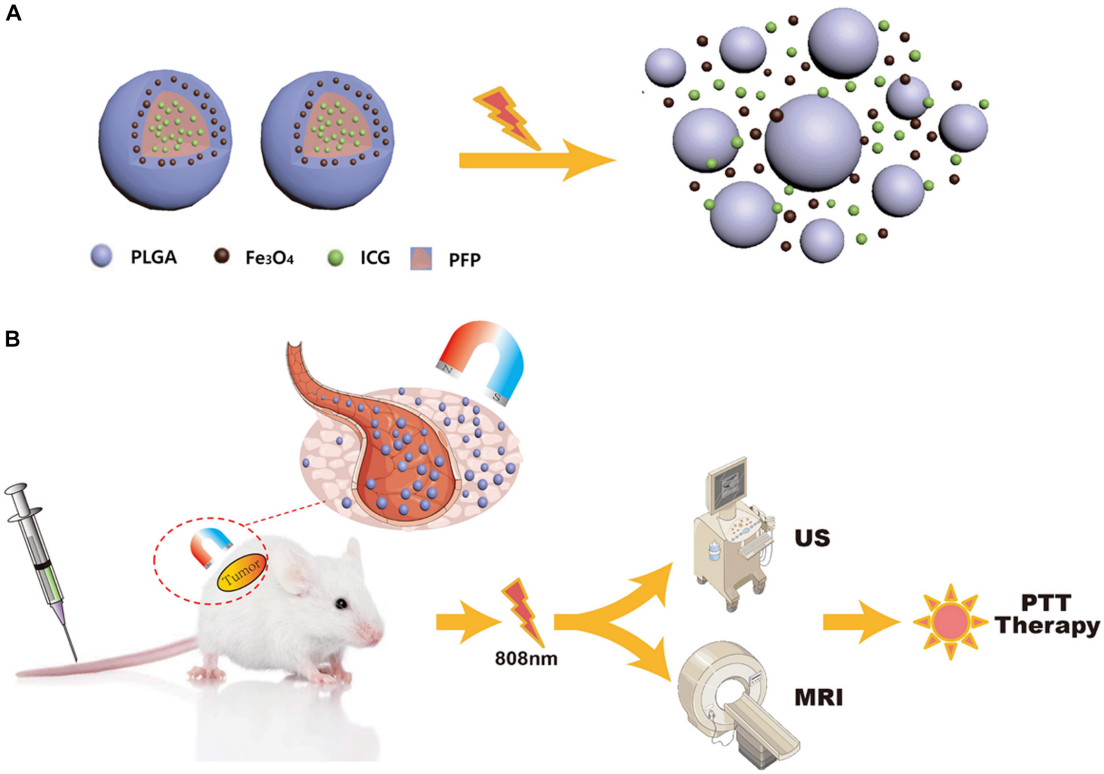

FIGURE 1 | (A) The optical droplet vaporization process of the NRPNs. **(B)** Schematic Illustration of the NRPNs used for magnetically targeted dual-modal imaging guided photothermal therapy of tumor.

$$\text{Loading content (\%)} = \frac{\text{(Mass of all of the encapsulated ICG in the NRPNs)}}{\text{(Mass of the NRPNs)}} \times 100\%$$

Temperature Elevation and NIR-Responsive Phase-Shift for US Imaging With NRPNs

Two hundred μL of various concentrations of the NRPNs (0, 2.5, 5.0, and 7.5 μg/mL ICG), ICG/PFP/PLGA NPs (5.0 μg/mL ICG), Fe_3O_4/PFP/PLGA NPs (the amount of Fe_3O_4 was equivalent to the NRPNs at 5.0 μg/mL ICG with a concentration of 8.0 μg/mL Fe) and PFP/PLGA were set in a 96-well plate and irradiated by an 808 nm NIR laser for 10 min. The power of the laser was 1 W/cm^2. The temperature of the NRPNs was measured under NIR laser irradiation by an infrared thermal imaging camera. The temperatures of the NPs were measured every 30 s. The phase-shift of the NRPNs was observed with TEM and an optical microscope.

To examine the vaporization process of US imaging, approximately 1 mL of the NRPNs suspension was injected into an agar-gel model. The NRPNs suspension was irradiated by a laser. The power of the laser was 1 W/cm^2. Then, an US apparatus was used to scan the suspension for B-mode and contrast-enhanced US (CEUS) mode imaging.

In vitro Stability Study of NRPNs

To access the stability of the nanoparticles, the experiments were conducted by measuring the DLS diameters of the NRPNs in PBS or 10% FBS (HyClone) at 37°C every 24 h for 7 days.

In vitro MR Imaging

To assess the *in vitro* MR imaging, different Fe_3O_4 concentrations (0.0, 0.1, 0.2, 0.3, 0.4, and 0.5 mg/mL) of the NRPNs suspension were added to 2 mL Eppendorf tubes for MR imaging using a 3.0 T MRI apparatus. The T2-weighted images (T2 WI) signal intensity (SI) at each concentration was measured.

Cell Experiments

For the *in vitro* magnetic targeting efficacy study of the NRPNs, a cellular uptake study was assessed by confocal laser scanning microscopy (CLSM). The MCF-7 cells (1×10^5) were planted into glass-bottomed Petri dishes and cultured with 200 μL serum-free medium containing the DiI labeled NRPNs nanoparticles (0.2 mg/mL) for 2 h with or without a magnet. Cells without nanoparticles were treated as control group. The maximum magnet strength was 6.0 Gs. The thickness of the petri dish was about 1 mm, and the depth of the liquid in each dish was 3 mm. For a distance of 1 mm from the magnet, the maximum magnetic field strength was 5.5 Gs. For a distance of 4 mm from the magnet, the maximum magnetic field strength was 4.8 Gs. Then, each well

was washed with PBS 3 times and the cells were stained with DAPI for 10 min before CLSM imaging.

Cell counting kit (CCK-8) assays were used to assess the *in vitro* cytotoxicity of the NRPNs and to inspect the photothermal efficiency under the magnetic field. MCF-7 cells (1×10^4 per well) were seeded onto 96-well plates and incubated for 24 h. Subsequently, the NRPNs with a serial concentration of 0, 200, 400, 600, 800, and 1000 μg/mL were incubated with the cells for 6 h with or without a magnet. The maximum magnet strength was 6.0 Gs. The thickness of the 96-well plate was about 1 mm, and the depth of the liquid in each well was 3 mm. For a distance of 1 mm from the magnet, the maximum magnetic field strength was 5.5 Gs. For a distance of 4 mm from the magnet, the maximum magnetic field strength was 4.8 Gs. Afterward, these wells continued to culture until 24 h, and then washed with PBS and irradiated by an NIR laser for 5 min. The power of the laser was 1.0 W/cm^2. Finally, a CCK-8 assay was used to measure the cell viability.

The apoptosis of MCF-7 cells was evaluated by Calcein-AM/PI double staining kit. Cells were seeded on a 6-well plate and then incubated with PBS or NRPNs for 2 h. The NRPNs groups were treated with or without a magnet and the concentration of NRPNs was 0.2 mg/mL in each well. The maximum magnet strength was 6.0 Gs. The thickness of the 6-well plate was about 1 mm, and the depth of the liquid in each well was 3 mm. For a distance of 1 mm from the magnet, the maximum magnetic field strength was 5.5 Gs. For a distance of 4 mm from the magnet, the maximum magnetic field strength was 4.8 Gs. After co-incubation with different treatments, the medium was removed and washed with PBS for 3 times. The laser irradiation was at the intensity of 1 W/cm^2 for 5 min. Then the Calcein-AM/PI double staining kit was added to each well in the dark at an appropriate concentration for 15 min at room temperature. After that, the cells were thoroughly washed and imaged through a fluorescence microscope.

Animal Studies

All animal experiments procedures were approved by the Ethics Committee of the Second Xiangya Hospital of Central South University. Female 4-week-old BALB/c mice were bred at the department of Laboratory Animals of Central South University. To establish the tumor model, the mice were injected subcutaneously with 1×10^6 4T1 cells into their right flanks. The size of the tumors was observed for 2 weeks. The volume of the tumors that achieved 60 mm^3 were used for the experiment.

In vivo Toxicity and Biodistribution Studies

For the *in vivo* biological toxicity, 200 μL of NRPNs solutions (20 mg/kg) was intravenously injected into 5 female BALB/c mice and 200 μL saline was intravenously injected into the other 5 female BALB/c mice as controls. These mice were sacrificed 14 days later. Then, the tissues of the brain, heart, liver, spleen, kidney and lung of each mouse were fixed with 4% formaldehyde solution and observed by H&E.

For assessment of the biodistribution and the magnetic targeting effect of the NRPNs, 200 μL of the NRPNs solutions (20 mg/kg) was intravenously injected into 10 tumor-bearing mice. Five mice were treated with magnetic targeting, the other 5 mice were treated without magnetic targeting. A magnet was placed next to the tumor region for 8 h for targeting. The maximum magnet strength was 6.0 Gs. At the 0, 1, 8, and 24 h time point, the fluorescence of each tumor was obtained with a Xenogen IVIS Spectrum *in vivo* imaging system. After 24 h, all of the tumors and major organs (brain, heart, liver, spleen, kidney, and lung) of the mice were *ex vivo* imaged by the fluorescence system.

In vivo MR Imaging

In the *in vivo* MRI experiments, 200 μL of the NRPNs solutions (20 mg/kg) was intravenously injected into 10 tumor-bearing mice. Five mice were treated with magnetic targeting, the other 5 mice were treated without magnetic targeting. A magnet was placed next to the tumor region for 8 h for the targeting. The maximum magnet strength was 6.0 Gs. The MRI images of the tumors were captured with a 3.0 T MRI Skyra scanner before and 24 h after injection. Finally, the SI within the ROI of the MRI images were measured.

In vivo US Imaging

In the *in vivo* US experiments, 200 μL of the NRPNs solutions (20 mg/kg) was intravenously injected into 10 tumor-bearing mice. Five mice were treated with magnetic targeting, the other 5 mice were treated without magnetic targeting. A magnet was placed next to the tumor for 8 h for targeting. The maximum magnet strength was 6.0 Gs. The mice were scanned by a Siemens S3,000 US scanner 24 h after injection. Then, the tumors were irradiated by an NIR laser for 6 min (808 nm, 1.0 W/cm^2). US images in B-mode and CEUS mode were obtained by a Siemens ultrasonography machine before and after laser irradiation.

In Vivo Anticancer Treatment Performance

Tumor-bearing mice were randomly divided into five groups (n = 3 for per group): (1) saline with laser irradiation, (2) only the NRPNs, (3) the NRPNs with laser irradiation but without magnetic targeting, (4) ICG/PFP/PLGA NPs with magnetic targeting and laser irradiation and (5) the NRPNs with magnetic targeting and laser irradiation. The dose of the NRPNs (20 mg/kg), saline or ICG/PFP/PLGA NPs (20 mg/kg) was 200 μL per mice by an intravenous injection. A magnet was placed next to the tumor for 8 h. The maximum magnet strength was 6.0 Gs. After 24 h, the tumors were subjected to laser irradiation for 10 min. The power of the laser was 1 W/cm^2. At the same time, the temperature of the tumor region was measured every 30 s. Tumor volumes were monitored by a caliper every 2 days. The tumor volume was calculated as: $V = \mathrm{L} \times \mathrm{W}^2/2$ (L = the length of the tumor and W = the width of the tumor), and 14 days after laser irradiation, the

tumors were collected and fixed with 4% formaldehyde solution for immunohistochemistry.

Statistical Analysis

All experimental data were expressed as the mean ± SD. Comparisons of two groups were analyzed by Student's *t*-test and multiple groups were analyzed by two-way analysis using SPSS 18.0. $p < 0.05$ was considered significant.

RESULTS AND DISCUSSION

Characterization

The NRPNs were produced using our group's previously published method with a different concentration of ICG (Niu et al., 2017). SEM images revealed that the NRPNs had a smooth and uniform spherical morphology (**Figure 2A**). The TEM images showed that the multiple Fe_3O_4 NPs were well encapsulated within the PLGA shells (**Figure 2B**). The nanoparticle average diameter was 315.29 ± 15.66 nm. The zeta potential was −21.1 ± 7.4 mV. The absorption spectra of the different components are shown in **Figure 2C**, revealing that ICG and Fe_3O_4 were successfully loaded onto the NRPNs. The EE of ICG was above 30.25 ± 5.13% and the LC of ICG was above 1.25 ± 0.52%. The Fe content was 97.30 ± 2.82 μg/mL.

A magnetic model was used to assess the magnetic response of the NRPNs. As shown in **Figure 2D**, the NRPNs were dispersed in water on the slide. A magnet was placed next to the slide. As the time increased, the solution of the NRPNs became increasingly colorless and most of the NRPNs were clustered together near the

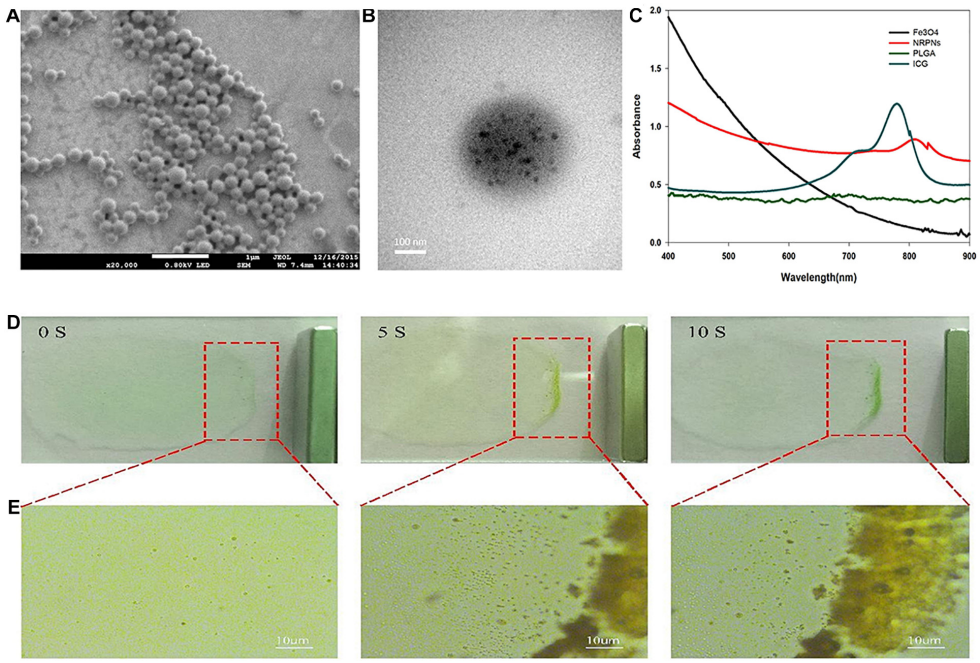

FIGURE 2 | (A) The SEM image of the NRPNs. **(B)** The TEM image shows the black Fe_3O_4 NPs embedded in the PLGA shell. **(C)** UV–vis–NIR absorption spectra of free Fe_3O_4, free ICG, PLGA NPs, and NRPNs. **(D)** Photograph, and **(E)** optical microscopy images of NRPNs solution (10 mg/mL) in a slide with an external magnetic field.

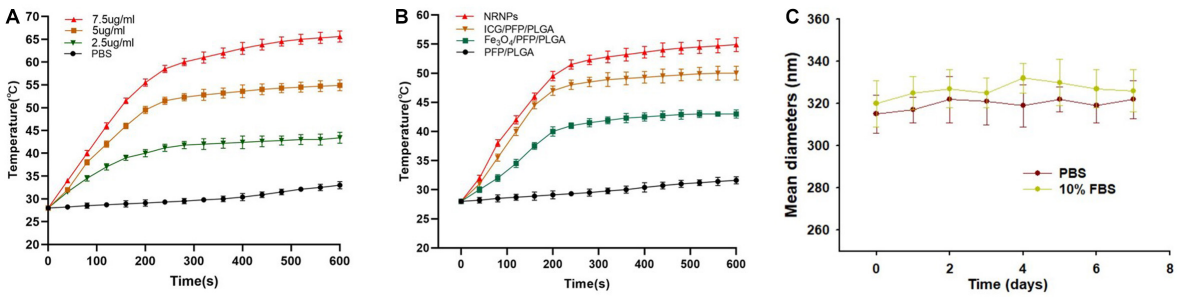

FIGURE 3 | (A) The temperature curves of the NRPNs with different concentration of laser irradiation at 1 W/cm^2. **(B)** The temperature curves of different nanoparticles with laser irradiation at 1 W/cm^2. **(C)** Size distributions of NRPNs in PBS or 10% FBS for 7 days.

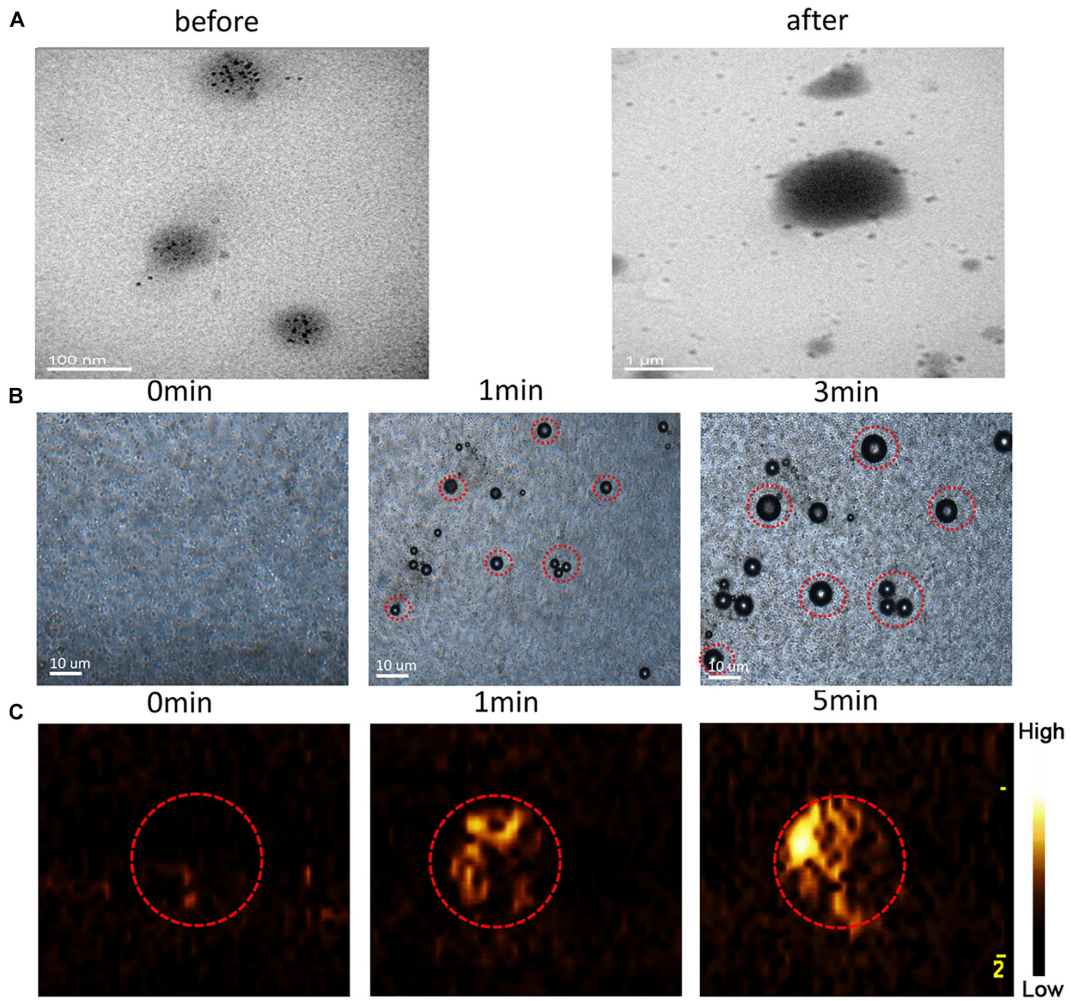

FIGURE 4 | (A) TEM images of the NRPNs under 808 nm NIR irradiation (1.0 W/cm^2, 5 min). **(B)** Images of phase-shift of the NRPNs with the laser irradiation by microscopy (1.0 W/cm^2, 3 min). **(C)** The CEUS imaging of the NRPNs under the laser irradiation (1.0 W/cm^2, 5 min).

magnet from 0 to 10 s. Under the light microscope, the NRPNs nanoparticles were observed to aggregate and move toward the magnet (**Figure 2E**).

Temperature Eelevation and Phase Transition Induced by NIR Laser Irradiation

To study the temperature elevation, an 808 nm NIR laser was used to irradiate the NRPNs for 10 min. With the laser irradiation, the temperature of the different concentrations of NRPNs increased rapidly from 43.4°C (at 2.5 mg/mL) to 65.6°C (at 7.5 mg/mL) (**Figure 3A**). This finding indicates that the temperature is positively correlated with the concentration of the NRPNs. As shown in **Figure 3B**, the temperature of the NRPNs (at 5.0 mg/mL) rapidly exceeded 54.9°C, while the PLGA/PFP/ICG NPs without Fe_3O_4 and the Fe_3O_4/PFP/PLGA NPs without ICG only achieved 50°C and 43°C, respectively. This finding indicates that the Fe_3O_4 and ICG worked together to produce the NIR-responsive temperature increase and that the NRPNs reached up to 42°C, which is the temperature point necessary for triggering cancer-cell damage. Meanwhile, with an increasing temperature up to 50°C, the liquid PFP of the PLGA nanoparticles could convert into a gaseous state with a phase-change. That was very important for US imaging.

The size distributions of NRPNs stored in PBS or 10% FBS at 37°C for 7 days were measured to investigate the colloidal stability. As shown in **Figure 3C**, there was no significant change in the particle size distribution over time. Therefore, the nanoparticles exhibited good colloidal stability and could be used in subsequent experiments.

Transmission electron microscopy analysis revealed the morphological and size changes of the NRPNs before and after laser irradiation (**Figure 4A**). After laser irradiation, the particle size increased significantly and Fe_3O_4 was released from the nanoparticles. The optical microscopy images further revealed that no microbubbles were observed before NIR irradiation (**Figure 4B**). After 1 min of irradiation, some of the NRPNs

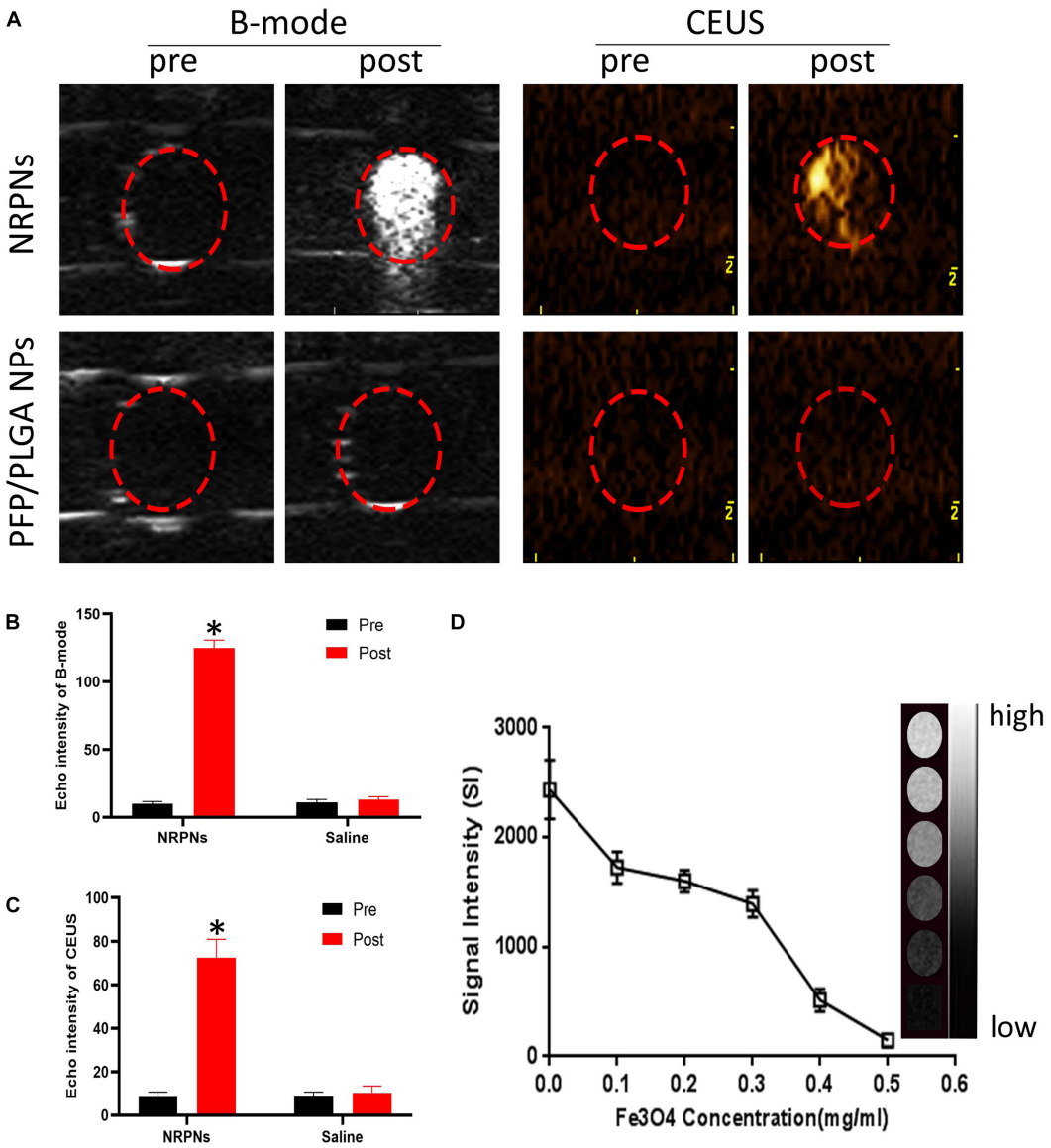

FIGURE 5 | (A) B-mode and CEUS imaging of the NPs with the laser irradiation (1 W/cm^2, 5 min). Echo intensity in B-mode **(B)** and CEUS **(C)** mode of NPs with the laser irradiation (1 W/cm^2, 5 min). **(D)** T2 WI SI curve of the NRPNs at different Fe_3O_4 concentrations. The right gray bar indicates the T2 MRI image at different Fe_3O_4 concentrations. The difference is statistically significant (*$p < 0.05$).

started to expand. When the time reached 3 min, the size of the NPs increased. A high efficiency of converting to microbubbles from the NRPNs after laser irradiation is important for US imaging. As the time increased, increasing number of microbubbles were produced, but we could not observe the same microbubbles changing since they moved to the upper level via their buoyancy.

At the same time, the NRPNs solutions were subjected to US imaging in CEUS mode (**Figure 4C**) at different times after laser irradiation. As the time increased under laser irradiation, the echo intensity of CEUS imaging became much stronger. These findings indicated that the size of the NRPNs was significantly increased after laser irradiation (1 W/cm^2, 5 min) and microbubble production resulting from the phase-change phenomenon was consistent with the strong CEUS echogenicity in the US imaging.

In vitro US/MR Imaging

To obtain more accurate biological details of solid tumors, dual-modality imaging has been studied widely. As shown in **Figure 5A**, there were no enhancement signals before and after NIR irradiation of the PFP/PLGA nanoparticles without ICG and Fe_3O_4. However, in the NRPNs group, when the NRPNs were irradiated by an 808 nm laser, significant enhancement in the B-mode and CEUS were observed. As shown in **Figures 5B,C**, the echo intensity of

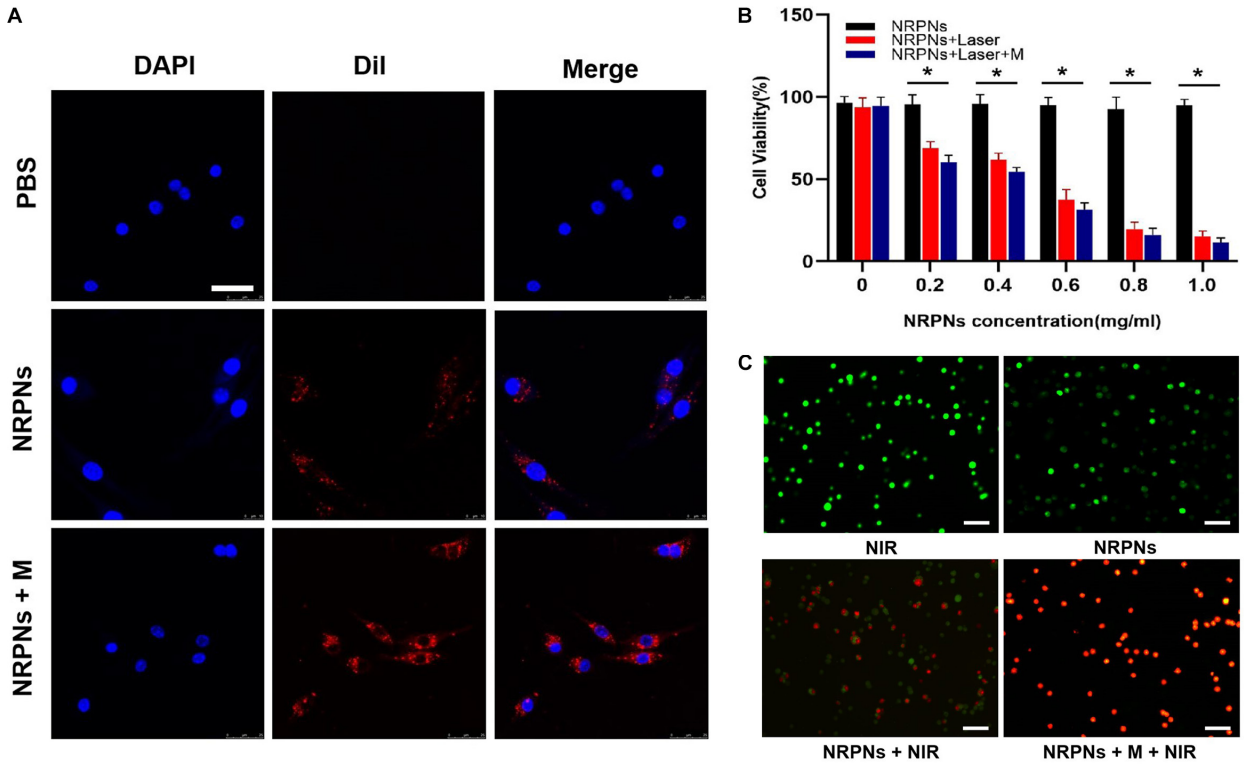

FIGURE 6 | (A) Cellular uptake of the NRPNs with or without a magnet (scale bar, 20 μm). **(B)** Cell viability of MCF-7 cells with different concentrations of the NRPNs after 808 nm laser irradiation (1 W/cm^2, 5 min) with or without a magnet. The difference is statistically significant (*$p < 0.05$). **(C)** calcein/PI staining of MCF-7 cells after different treatments: (1) NIR; (2) NRPNs; (3) NRPNs + NIR; (4) NRPNs + M + NIR (scale bar, 50 μm).

the B-mode and CEUS in the NRPNs group was significantly increased after laser irradiation compared to that in the PFP/PLGA nanoparticles group (*$p < 0.05$). These results further demonstrated that with the quick conversion from light energy to heat by ICG and Fe_3O_4, the PFP vaporization process was triggered, and then the NRPNs can be used for the enhancement of US imaging.

In the *in vitro* experiment, the MR imaging capabilities of the NRPNs were examined using a 3.0 T MR scanner. As shown in **Figure 5D**, the NRPNs negatively enhanced the T2 weighted MR images. The T2 weighted MR SI decreased with the increasing Fe_3O_4 concentration. These results indicated that in addition to US imaging, the NRPNs could also effectively serve as an MRI negative contrast agent.

The Magnetically Targeting Performance and Cytotoxicity in Cells

The magnetically targeting performance and cytotoxicity of the NRPNs were observed in cell experiments. The NRPNs were co-incubated with MCF-7 cells for 2 h, and divided into three groups: (1) PBS; (2) without the magnet (NRPNs) and (3) with the magnet (NRPNs + M). As shown in **Figure 6A**, a significantly red fluorescence appeared around the nucleus of the MCF-7 cells in the NRPNs + M group, only a little red fluorescence showed around the MCF-7 cells in the NRPNs, while no red fluorescence was observed in the PBS group. This finding demonstrated that with the help of a magnet, more NRPNs gathered around the cells, promoting their endocytosis.

Our previous experiments demonstrated low cytotoxicity and an excellent PTT effect of similar NPs (Niu et al., 2017). The same results were achieved in our current experiments. At the same NRPNs concentrations, the cell viability with laser irradiation was significantly reduced compared to that without irradiation (*$p < 0.05$). In addition, with magnetic targeting, more NRPNs were attracted around the cells. The MCF-7 cells with magnet targeting showed an obvious decrease in cell viability after irradiation, compared to non-magnetic targeting (**Figure 6B**, *$p < 0.05$). This finding demonstrated an excellent endocytosis ability of the NRPNs by MCF-7 cells and resulted in magnetically targeted PTT.

Then, the tumor killing effect of NRPNs was observed directly by using calcein/PI staining. The cells were divided into 4 groups: (1) NIR, (2) NRPNs, (3) NRPNs + NIR, (4) NRPNs + M + NIR. We stained live and dead with calcein (green fluorescence) and PI (red fluorescence) separately. As shown in **Figure 6C**, the MCF-7 cells of the NIR group (1) and NRPNs group (2), emitted pure green fluorescence. After the NIR irradiation, red fluorescence could be observed

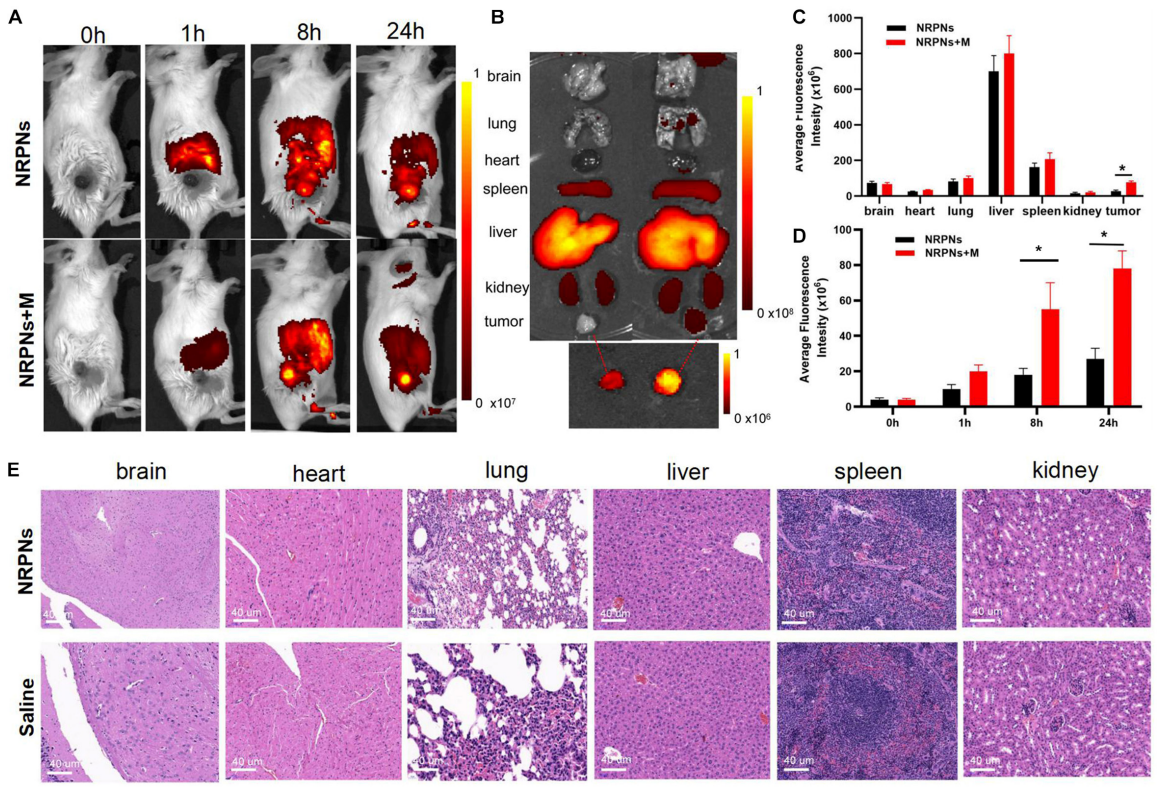

FIGURE 7 | (A) Biodistribution of NPs in tumor-bearing mice at different time points by *in vivo* fluorescent imaging. **(B)** Fluorescence imaging of major organs and tumors at 24 h after injection of the NRPNs. **(C)** Averaged fluorescence intensity of major organs and tumors at 24 h after injection of the NRPNs. **(D)** Averaged fluorescence intensity of tumors at different time points. **(E)** H&E-staining images of major organs collected from the NRPNs and saline groups. The difference is statistically significant (*$p < 0.05$).

to different extents. A lot of dead cells were observed in the NRPNs + NIR group (3), while almost all cells were dead in the NRPNs + M + NIR group, further suggesting that the tumor cells can be effectively killed by magnetic targeting, which promotes the cells to contact with more NPs and then uptake them.

In vivo Biodistribution Studies and Biotoxicity Evaluation

To quantify the biodistribution and the magnetically targeting performance of the NRPNs in tumor-bearing mice, fluorescence imaging was performed. With or without magnetic targeting, tumor fluorescence images were obtained at different times before and after injection with the NRPNs. As shown in **Figure 7A**, before administration, there were no red fluorescent signals in the tumor region or the major organs in tumor-bearing mice of the NRPNs + M group and the NRPNs group. The biodistribution of the fluorescent signals in the major organs and tumors were analyzed at 1, 8, and 24 h after injection of the NRPNs.

In the major organs, especially the reticuloendothelial system of the liver and spleen, accumulation of the NRPNs peaked at 8 h post injection, and the NRPNs content in these organs decreased after 24 h (**Figure 7A**). The NRPNs accumulation in the tumor region remained until 24 h post injection (**Figures 7B,C**), suggesting that with the help of a magnet, more NRPNs were clustered in the tumor. In the absence of the magnetic field, there were fewer red fluorescent signals of the NRPNs in the control group (**Figure 7D**, *$p < 0.05$), which means lower tumor accumulation in the tumor region. These findings indicated that magnet targeting provides a promising physical strategy for tumor targeting and the magnetically targeting NPs are a potential treatment platform for dual-model imaging and PTT of tumors.

In light of the biodistribution studies and the 24 h blood retention time *in vivo*, it was necessary to further assess the biotoxicity of the NRPNs *in vivo*. As shown in **Figure 7E**, there were no noticeable changes in inflammation or abnormal histomorphology in these major organs (heart, liver, spleen, lung, and kidney) of the mice after injection with the NRPNs, compared with the saline control group. These findings indicate that injection of the NRPNs was biosafe and they have low potential toxicity *in vivo*.

In vivo Targeting and MR/US Imaging Performance

Due to the excellent *in vitro* vaporization effect induced by laser irradiation, the NRPNs were used as an US enhancement

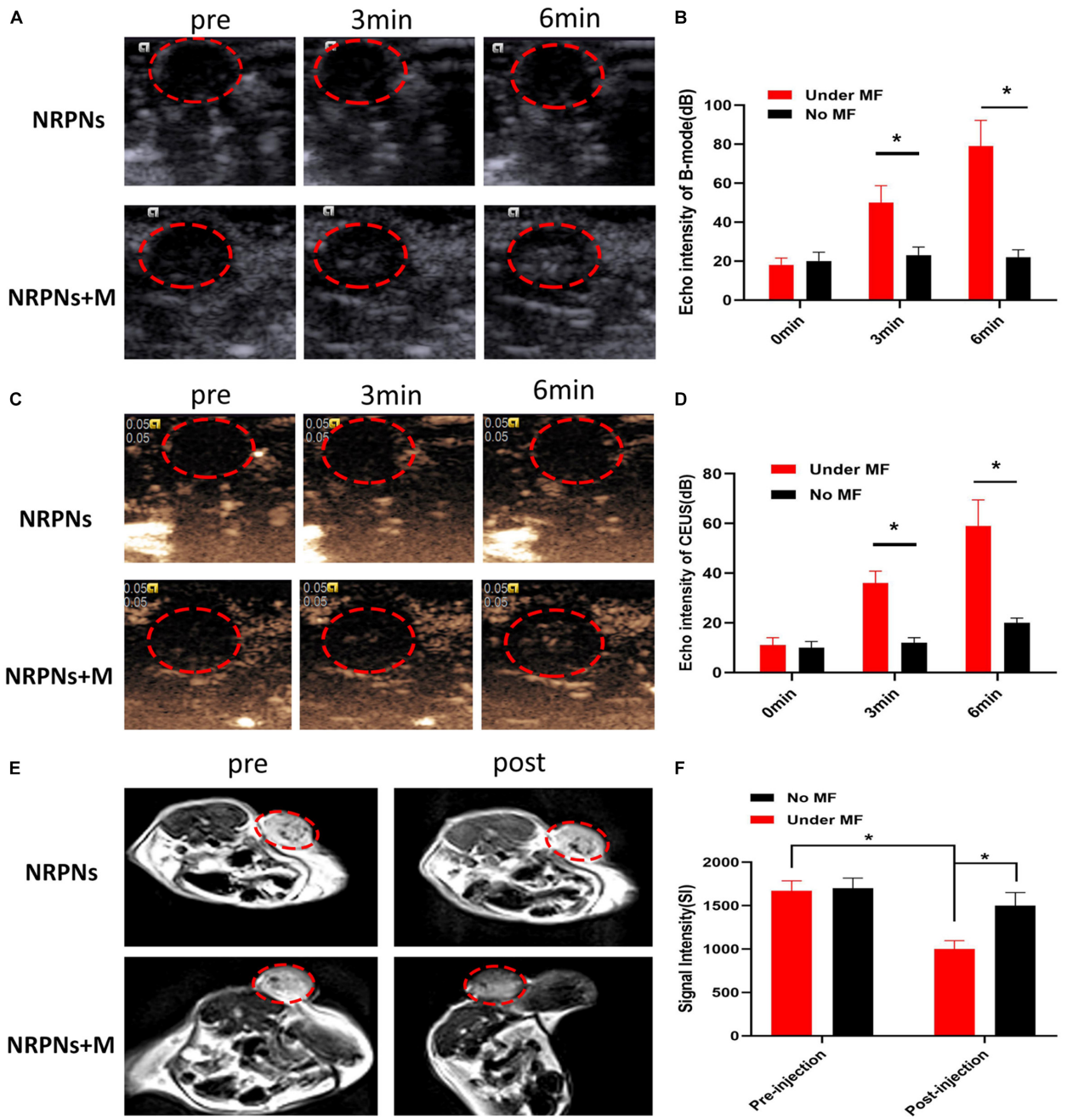

FIGURE 8 | (A) *In vivo* B-mode US images and **(B)** the echo intensities of the tumor regions after intravenous injection 24 h of the NRPNs under NIR laser irradiation with different irradiation time. **(C)** *In vivo* CEUS images and **(D)** the echo intensities of the tumor regions after intravenous injection 24 h of the NRPNs under NIR laser irradiation with different irradiation time. **(E)** *In vivo* T2-weighted MR image, and **(F)** the signal intensities of the tumor regions before and after intravenous injection 24 h of the NRPNs. The difference is statistically significant (*$p < 0.05$).

in vivo. After magnetic attraction for 8 h, the tumor region of the tumor-bearing mice was irradiated by a NIR laser at 24 h after injection. As shown in **Figure 8**, there was no or weak enhancement observed in B-mode (**Figures 8A,B**) and CEUS (**Figures 8C,D**) in the group without the magnet after NIR-laser irradiation. Some scholars have proven that the an enhanced permeability and retention (EPR) effect promotes the aggregation of NPs in the tumor region (Maeda et al., 2013). However, the amount of the NRPNs engulfed by tumor cells could not produce obvious changes in the US images while there was significant enhancement both in B-mode and CEUS mode as observed in the group with the magnet (*$p < 0.05$). With the help of the magnet, more NRPNs aggregated in the tumor region, demonstrating the excellent targeting ability of the NRPNs. Moreover, the ICG and

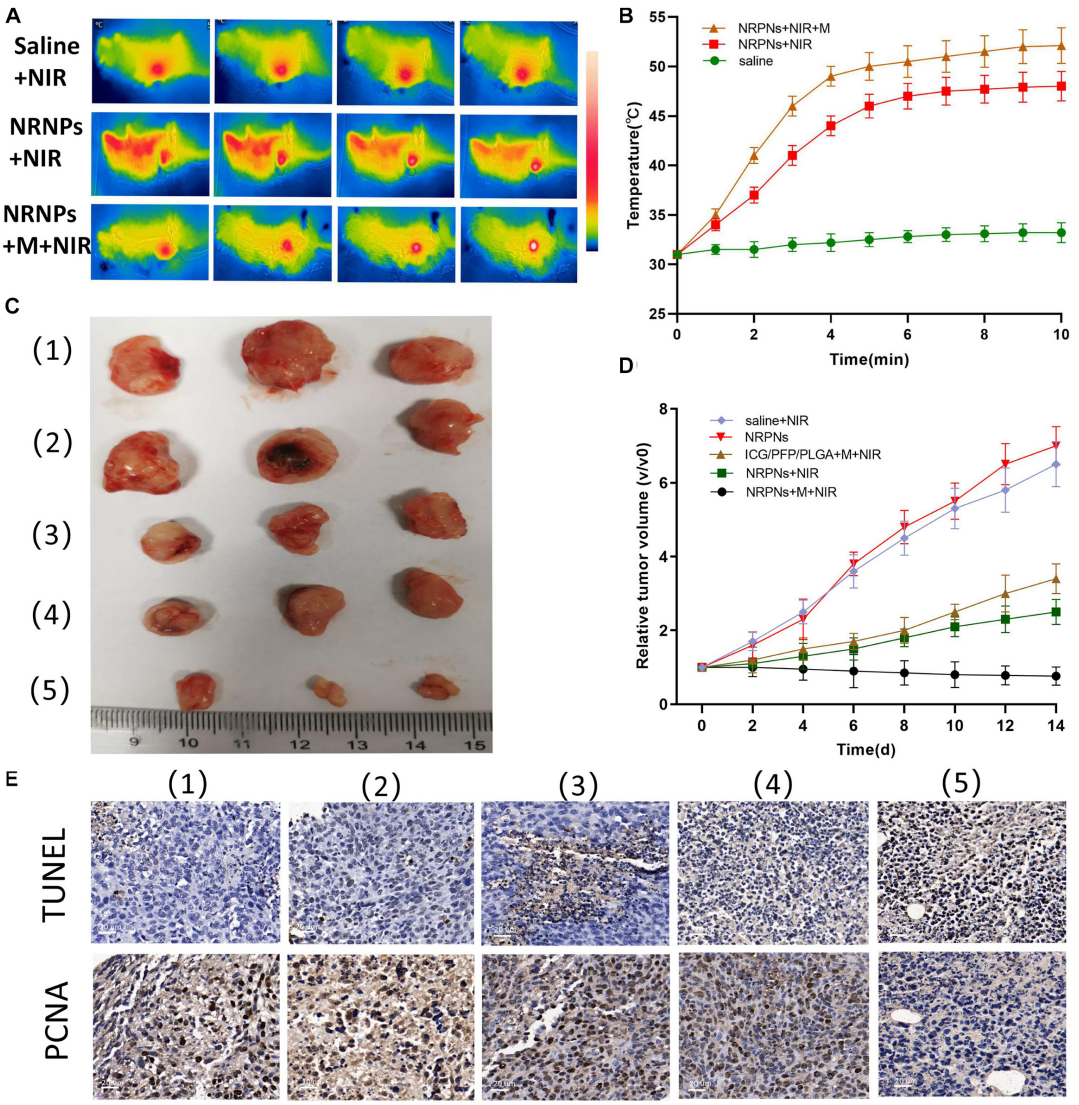

FIGURE 9 | (A) Infrared thermal images and **(B)** temperature variation of tumor-bearing mice injected with the saline or NRPNs with or without a magnet under 808 nm laser irradiation for 10 min (1 W/cm^2). **(C)** Photographs of tumors and **(D)** the relative tumor growth curves during the various treatments after 14 days. **(E)** Microscopy images of TUNEL and PCNA assays of stained tumor tissues at different treatments: (1) Saline, (2) NRPNs, (3) NRPNs + NIR laser, (4) ICG/PFP/PLGA NPs + M + NIR laser and (5) NRPNs + M + NIR laser.

Fe_3O_4 in the NRPNs absorbed the NIR light energy, transferred it to heat, triggered the PFP vaporization process, and induced more echo intensity generation. These results demonstrated the excellent US imaging ability of the NRPNs *in vivo*.

In light of the excellent MRI negative enhancement of the NRPNs *in vitro*, the ability of the NRPNs for use with MR imaging was studied in small animal experiments. T2-weighted MR imaging of the mouse tumor region was obtained after the injection of the NRPNs with and without magnetic targeting. As shown in **Figure 8E**, an obvious tumor darkening effect was observed in the tumor region at 24 h post injection of the NRPNs with the magnetic targeting field. However, there was no significant change observed in the group in the absence of magnetic targeting at 24 h post-injection of the NRPNs. Moreover, the decreased T2-weighted SI after NP injection with magnetic targeting was significantly lower than that without magnetic targeting (**Figure 8F**, $^*p < 0.05$). This finding also contributed to the magnetically targeted strategy of the NRPNs.

In vivo Anticancer Efficacy

After demonstrating that these NIR responsive phase-shifted nanoparticles can be ueed for MR/US dual model imaging, we then evaluated their PTT effect *in vivo*. Tumor-bearing mice were randomly divided into three groups: (1) saline with laser irradiation, (2) the NRPNs with laser irradiation but without magnetic targeting, and (3) the NRPNs with magnetic targeting and laser irradiation. As shown in **Figures 9A,B**, the temperature in the

tumors of the saline group and the NRPNs without the magnet group increased to 33°C and 48°C, respectively. The temperature increased rapidly to 52°C in the NRPNs with the magnet after laser irradiation, and this temperature is an appropriate temperature for killing tumor cells. Thus, the temperature of the other two groups were lower than that of the NRPNs with the magnet group ($^*p < 0.05$), indicating that with the help of the magnetic targeting field, more NPs accumulated into the tumor and then transferred light to heat, which increased to the local temperature.

Then, to evaluate the PTT therapeutic effect of the NRPNs after NIR laser irradiation with a magnet, the tumor growth was observed for 14 days after injection. Tumor-bearing mice were randomly divided into five groups ($n = 3$ for per group): (1) saline with laser irradiation, (2) only the NRPNs, (3) the NRPNs with laser irradiation but without magnetic targeting, (4) ICG/PFP/PLGA NPs with magnetic targeting and laser irradiation and (5) the NRPNs with magnetic targeting and laser irradiation. As shown in **Figures 9C,D**, in the only NRPNs group (2) and the saline with laser irradiation group (1), the tumor volumes increased significantly, up to seven-fold and 6.5-fold, respectively, compared to day 0, indicating NRPNs or NIR irradiation alone had no antitumor effect. As expected, the PTT effect using NRPNs (3) or ICG/PFP/PLGA NPs (4) showed a good antitumor effect with tumor volumes slowly increasing to 2.5-fold and 3.4-fold, respectively, compared with day 0. Compared with NRPNs without magnet targeting (3), the PTT effect using NRPNs with the magnet targeting group (5) displayed a better antitumor effect with decreased tumor volumes, demonstrating that with the help of magnetic targeting, the NRPNs could more effectively inhibit tumor growth through PTT treatment due to the high accumulation of the NPs in the tumors.

Finally, the PTT efficacy was further evaluated by TUNEL and PCNA immune-histochemical assays. As shown in **Figure 9E**, the proliferative cells with brown nuclear staining of the TUNEL assay in the NRPNs after laser irradiation group (3) and the ICG/PFP/PLGA with magnetic targeting and laser irradiation group (4) were higher than that in the only NRPNs group (2) and saline with laser irradiation (1), but they were lower than that in the NRPNs with a magnet after laser irradiation group (5). Opposite to the TUNEL expression pattern, the proliferative cells with brown nuclear staining of PCNA expression were the lowest in the NRPNs with a magnet after laser irradiation (5) compared to the other groups. These results showed that PTT combined with the enfolded ICG and Fe_3O_4 NPs could inhibit tumor growth and promote tumor apoptosis. With the help of magnetic targeting, PTT was a more efficient anticancer therapy.

CONCLUSION

In this study, we developed NRPNs, which improved the MRI and US diagnosis of cancer. The NRPNs showed excellent photothermal transformation capacity, higher ICG loading capacity, good liquid-gas phase transformation capabilities and amazing magnetic response abilities. Irradiation of the tumor site with a laser allowed them assimilate the NIR light rapidly and transform it into enormous heat energy, leading to superior tumor suppression. With a combination of simultaneous MRI and US diagnosis, this kind of multifunctional NPs guided by a magnetic field can be further applied for cancer theranostics.

DATA AVAILABILITY STATEMENT

The original contributions presented in the study are included in the article/supplementary materials, further inquiries can be directed to the corresponding author/s.

ETHICS STATEMENT

The animal study was reviewed and approved by the Ethics Committee of Central South University.

AUTHOR CONTRIBUTIONS

YX and CN: conceptualization and the data curation. YX and WL: methodology. SC, WL, WP, and BH: analysis and investigation. YX: writing original draft preparation. CN: writing-review, editing, and supervision. All authors contributed to the article and approved the submitted version.

FUNDING

This project was funded by the National Natural Science Foundation of China (Grant No. 81974267) and Hunan Provincial Health Commission Research Foundation Project (B2019166).

REFERENCES

Chen, R., Chen, Q., Qin, H., and Xing, D. (2019). A photoacoustic shockwave triggers the size shrinkage of nanoparticles to obviously improve tumor penetration and therapeutic efficacy. *Nanoscale* 11, 1423–1436. doi: 10.1039/c8nr08271e

Cheng, L., Yang, K., Li, Y., Zeng, X., Shao, M., Lee, S. T., et al. (2012). Multifunctional nanoparticles for upconversion luminescence/MR multimodal imaging and magnetically targeted photothermal therapy. *Biomaterials* 33, 2215–2222. doi: 10.1016/j.biomaterials.2011.11.069

Dadfar, S. M., Roemhild, K., Drude, N. I., von Stillfried, S., Knuchel, R., Kiessling, F., et al. (2019). Iron oxide nanoparticles: diagnostic, therapeutic and theranostic applications. *Adv. Drug Deliv. Rev.* 138, 302–325. doi: 10.1016/j.addr.2019.01.005

Eric, I. G. (2011). Strohm, Min rui, naomi matsuura,and michael kolios: vaporization of perfluorocarbon droplets using optical irradiation. *Biomed. Opt. Express* 2, 1432–1442.

Espinosa, A., Di Corato, R., Kolosnjaj-Tabi, J., Flaud, P., Pellegrino, T., and Wilhelm, C. (2016). Duality of iron oxide nanoparticles in cancer therapy:

amplification of heating efficiency by magnetic hyperthermia and photothermal bimodal treatment. *ACS Nano* 10, 2436–2446. doi: 10.1021/acsnano.5b07249

Guan, Q., Wang, C., Wu, D., Wang, W., Zhang, C., and Liu, J. (2019). Cerasome-based gold-nanoshell encapsulating L-menthol for ultrasound contrast imaging and photothermal therapy of cancer. *Nanotechnology* 30:015101. doi: 10.1088/1361-6528/aae6aa

Hannah, A., Luke, G., Wilson, K., Homan, K., and Emelianov, S. (2014). Indocyanine green-loaded photoacoustic nanodroplets: dual contrast nanoconstructs for enhanced photoacoustic and ultrasound imaging. *ACS Nano* 8, 250–259. doi: 10.1021/nn403527r

Hu, D., Zhang, J., Gao, G., Sheng, Z., Cui, H., and Cai, L. (2016). Indocyanine green-loaded polydopamine-reduced graphene oxide nanocomposites with amplifying photoacoustic and photothermal effects for cancer theranostics. *Theranostics* 6, 1043–1052.

Hussain, T., and Nguyen, Q. T. (2014). Molecular imaging for cancer diagnosis and surgery. *Adv. Drug Deliv. Rev.* 66, 90–100. doi: 10.1016/j.addr.2013.09.007

Jian, J., Liu, C., Gong, Y., Su, L., Zhang, B., and Wang, Z. (2014). India ink incorporated multifunctional phase-transition nanodroplets for photoacoustic/ultrasound dual-modality imaging and photoacoustic effect based tumor therapy. *Theranostics* 4, 1026–1038. doi: 10.7150/thno.9754

Li, W., Hou, W., Guo, X., Luo, L., Li, Q., and Zhu, C. (2018). Temperature-controlled, phase-transition ultrasound imaging-guided photothermal-chemotherapy triggered by NIR light. *Theranostics* 8, 3059–3073. doi: 10.7150/thno.23885

Li, Y., Zhou, Q., Deng, Z., Pan, M., Liu, X., Wu, J., et al. (2016). IR-780 dye as a sonosensitizer for sonodynamic therapy of breast tumor. *Sci. Rep.* 6:25968. doi: 10.1038/srep25968

Ma, Y., Tong, S., Bao, G., Gao, C., and Dai, Z. (2013). Indocyanine green loaded SPIO nanoparticles with phospholipid-PEG coating for dual-modal imaging and photothermal therapy. *Biomaterials* 34, 7706–7714. doi: 10.1016/j.biomaterials.2013.07.007

Maeda, H., Nakamura, H., and Fang, J. (2013). The EPR effect for macromolecular drug delivery to solid tumors: improvement of tumor uptake, lowering of systemic toxicity, and distinct tumor imaging in vivo. *Adv. Drug Deliv. Rev.* 65, 71–79. doi: 10.1016/j.addr.2012.10.002

Niu, C., Xu, Y., An, S., Zhang, M., Hu, Y., Wang, L., et al. (2017). Near-infrared induced phase-shifted ICG/Fe3O4 loaded PLGA nanoparticles for photothermal tumor ablation. *Sci. Rep.* 7:5490. doi: 10.1038/s41598-017-06122-1

Ott, P. (1998). Hepatic elimination of indocyanine green with special reference to distribution kinetics and the influence of plasma protein binding. *Pharmacol. Toxicol.* 83(Suppl. 2), 1–48. doi: 10.1111/j.1600-0773.1998.tb01945.x

Sakka, S. G. (2007). Assessing liver function. *Curr. Opin. Crit. Care* 13, 207–214. doi: 10.1097/MCC.0b013e328012b268

Santiesteban, D. Y., Dumani, D. S., Profili, D., and Emelianov, S. Y. (2017). Copper sulfide perfluorocarbon nanodroplets as clinically relevant photoacoustic/ultrasound imaging agents. *Nano Lett.* 17, 5984–5989. doi: 10.1021/acs.nanolett.7b02105

Santiesteban, D. Y., Hallam, K. A., Yarmoska, S. K., and Emelianov, S. Y. (2019). Color-coded perfluorocarbon nanodroplets for multiplexed ultrasound and photoacoustic imaging. *Nano Res.* 12, 741–747. doi: 10.1007/s12274-019-2279-x

Saxena, V., Sadoqi, M., and Shao, J. (2003). Degradation kinetics of indocyanine green in aqueous solution. *J. Pharm. Sci.* 92, 2090–2097.

Sheng, Z., Hu, D., Zheng, M., Zhao, P., Liu, H., and Gao, D. (2014). Smart human serum albumin-indocyanine green nanoparticles generated by programmed assembly for dual-modal imaging-guided cancer synergistic phototherapy. *ACS Nano* 8, 12310–12322. doi: 10.1021/nn5062386

Siegel, R. L., Miller, K. D., and Jemal, A. (2020). Cancer statistics, 2020. *CA Cancer J. Clin.* 70, 7–30. doi: 10.3322/caac.21590

Sun, Y., Wang, Y., Niu, C., Strohm, E. M., Zheng, Y., and Ran, H. (2014). Laser-activatible PLGA microparticles for image-guided cancer therapy in vivo. *Adv. Funct. Mater.* 24, 7674–7680. doi: 10.1002/adfm.201402631

Wang, G., Zhang, X., Skallberg, A., Liu, Y., Hu, Z., Mei, X., et al. (2014). One-step synthesis of water-dispersible ultra-small Fe3O4 nanoparticles as contrast agents for T1 and T2 magnetic resonance imaging. *Nanoscale* 6, 2953–2963. doi: 10.1039/c3nr05550g

Wang, L., Chen, S. J., Zhu, Y., Zhang, M. X., Tang, S. X., Li, J. Y., et al. (2018). Triple-modal imaging-guided chemo-photothermal synergistic therapy for breast cancer with magnetically targeted phase-shifted nanoparticles. *ACS Appl. Mater. Interfaces* 10, 42102–42114. doi: 10.1021/acsami.8b16323

Xu, Y., Niu, C. C., An, S. B., Tang, S. X., Xiao, P., Peng, Q. H., et al. (2017). Thermal-sensitive magnetic nanoparticles for dual-modal tumor imaging and therapy. *RSC Adv.* 7, 40791–40802. doi: 10.1039/c7ra07024a

Yan, L., and Qiu, L. (2015). Indocyanine green targeted micelles with improved stability for near-infrared image-guided photothermal tumor therapy. *Nanomedicine* 10, 361–373. doi: 10.2217/nnm.14.118

Zeng, L., Ren, W., Xiang, L., Zheng, J., Chen, B., and Wu, A. (2013). Multifunctional Fe3O4-TiO2 nanocomposites for magnetic resonance imaging and potential photodynamic therapy. *Nanoscale* 5, 2107–2113. doi: 10.1039/c3nr33978e

Zhu, H., Qin, D., Wu, Y., Jing, B., Liu, J., and Hazlewood, D. (2018). Laser-activated bioprobes with high photothermal conversion efficiency for sensitive photoacoustic/ultrasound imaging and photothermal sensing. *ACS Appl. Mater. Interfaces* 10, 29251–29259. doi: 10.1021/acsami.8b08190

Zhu, L., Wang, D., Wei, X., Zhu, X., Li, J., Tu, C., et al. (2013). Multifunctional pH-sensitive superparamagnetic iron-oxide nanocomposites for targeted drug delivery and MR imaging. *J. Control. Release* 169, 228–238. doi: 10.1016/j.jconrel.2013.02.015

Conflict of Interest: The authors declare that the research was conducted in the absence of any commercial or financial relationships that could be construed as a potential conflict of interest.

frontiers in Bioengineering and Biotechnology

REVIEW
published: 19 November 2020
doi: 10.3389/fbioe.2020.601586

Recent Developments in Pathological pH-Responsive Polymeric Nanobiosensors for Cancer Theranostics

*E. K. Pramod Kumar[1], Wooram Um[1] and Jae Hyung Park[1,2]**

[1] School of Chemical Engineering, College of Engineering, Sungkyunkwan University, Suwon, South Korea, [2] Biomedical Institute for Convergence at SKKU (BICS), Sungkyunkwan University, Suwon, South Korea

Polymeric nanobiosensors (PNBS) that respond to tumor-related factors, including pH, have shown great potential for disease detection owing to their selectivity and sensitivity. PNBS can be converted into theranostic polymeric nanobiosensors (TPNBS) by incorporating therapeutic cargo, thereby enabling concomitant diagnoses and therapy of targeted diseases. The polymeric compartments in TPNBS play a significant role in the development and therapeutic efficacy of nanobiosensors. Polymers enhance the stability, biocompatibility, and selective or effective accumulation of nanobiosensors at desired pathological sites. The intrinsic pH sensitivity of either the polymers in TPNBS or the TPNBS themselves provides integrated potentialities such as cogent accumulation of TPNBS at the tumor, augmented tumor penetration, cellular uptake, and theranostic activation, including enhanced bioimaging signals and controlled release of therapeutics. In this review, we summarize recent developments in the design, preparation, and characterization of pH-responsive TPNBS and their ability to behave as efficient *in vivo* nanotheranostic agents in acidic cancer environments.

Keywords: pH-responsive nanotheranostics, magnetic resonance imaging, ultrasound imaging, photoacoustic imaging, fluorescence imaging, photodynamic therapy, sonodynamic therapy, chemodynamic therapy

OPEN ACCESS

Edited by:
In-Kyu Park,
Chonnam National University,
South Korea

Reviewed by:
Shiyong Song,
Henan University, China
Ali Zarrabi,
Sabancı University, Turkey

****Correspondence:***
Jae Hyung Park
jhpark1@skku.edu

Specialty section:
This article was submitted to Nanobiotechnology, a section of the journal Frontiers in Bioengineering and Biotechnology

Received: *01 September 2020*
Accepted: *30 October 2020*
Published: *19 November 2020*

Citation:
Pramod Kumar EK, Um W and Park JH (2020) Recent Developments in Pathological pH-Responsive Polymeric Nanobiosensors for Cancer Theranostics. Front. Bioeng. Biotechnol. 8:601586. doi: 10.3389/fbioe.2020.601586

INTRODUCTION

Cancer is a major threat to human health worldwide. According to recent statistics, in 2020, the United States is projected to have 1,806,590 new cancer cases and 606,520 cancer-related deaths (Siegel et al., 2020). The cancer death rate increased until 1991 and then decreased continuously till 2017, resulting in an overall decrease of 29%. This was mainly attributed to the research and development in the field of cancer theranostics. Researchers have devoted significant efforts toward understanding the pathogenesis and properties of cancer in order to develop effective treatments for clinical applications. Compared to healthy tissues, the tumor microenvironment (TME),

Abbreviations: PNBS, polymeric nanobiosensors; TPNBS, theranostic polymeric nanobiosensors; TME, tumor microenvironment; ATP, adenosine triphosphate; ROS, reactive oxygen species; RES, reticuloendothelial system; EPR, enhanced permeability and retention; US, ultrasound; PTT, photothermal therapy; PDT, photodynamic therapy; SDT, sonodynamic therapy; CDT, chemodynamic therapy; MRI, magnetic resonance imaging; USI, ultrasound imaging; PAI, photoacoustic imaging; FI, fluorescence imaging; DOX, doxorubicin; HP, tumor-homing peptide; HA, hyaluronan; HAase, hyaluronidase.

which is composed of cancer-stromal-immune cells and the extracellular matrix, is characterized by uncontrolled cell proliferation. This high cell growth rate is associated with a modified metabolism and the abnormal development of tumor blood vessels. This results in a reduction in the transport of oxygen and nutrients (Vaupel and Harrison, 2004). Approaches for identifying such characteristics of cancer cells have contributed considerably toward the development of tumor-specific nanotheranostics.

Oxidative phosphorylation is a vital pathway of normal cell metabolism; it releases chemical energy from molecular oxygen bonds through the enzymatic oxidation of nutrients during adenosine triphosphate (ATP) synthesis (Da Poian et al., 2010). Oxygen and nutrient deficiency in tumor tissues urge cells to produce energy for survival through anaerobic glycolysis, which differs from oxidative phosphorylation (Vander Heiden et al., 2009). Warburg et al. (1927) studied the anaerobic glycolysis of glucose in tumor veins and arteries. They found more lactic acid and less glucose in tumor tissues than on the arteries, which served as evidence of the modified metabolism in tumor cells. In addition to lactic acid, tumor cells release chemical energy stored in the phosphoanhydride bonds of ATP via hydrolysis, along with the release of carbon dioxide and protons. Thus, the anaerobic glycolysis, or "Warburg effect," increases the acidity and lowers the pH of pathological sites compared to that in normal tissues. The extracellular pH values of healthy tissues and the late endosomes–lysosomes of normal cells are approximately 7.4 and 5–6.5, respectively, whereas those of the tumor tissue and the late endosomes–lysosomes of tumor cells are 6–7 and 4.5–6.5, respectively (Thews et al., 2006; Swietach et al., 2007; Kumar et al., 2014). These pH values may vary depending on the tumor; however, they are always lower than those of healthy tissues (Danhier et al., 2010). Given the acidic nature of the TME and the late endosomes–lysosomes of the cells, pH-sensitive cancer imaging and therapy using suitable theranostic nanomedicine agents have been developed (Webb et al., 2011).

Theranostic nanomedicine for cancer primarily involves the use of colloidal nanoparticles (NPs) ranging from 10 to 1000 nm in size (Muthu et al., 2014). Synthetic and natural polymers are vital constituents of these NPs, within which diagnostic and therapeutic agents (organic or inorganic theranostic agents) are encapsulated, conjugated, absorbed, or entrapped. The resulting theranostic polymeric nanobiosensors (TPNBS) simultaneously diagnose and treat cancer at the cellular level (Peng et al., 2015; Zhao et al., 2016). The polymer components improve aqueous stability and the delivery of theranostic cargoes associated with TPNBS (Kakkar et al., 2017; Kocak et al., 2017). An intravenously administered TPNBS may be sequestered by the reticuloendothelial-system (RES)-rich organs such as the liver and kidney. Research on theranostic nanomedicine allows for the development of TPNBS with a non-immunogenic polymer surface to increase their blood circulation half-life (Deepagan et al., 2013; Schöttler et al., 2016); this, in turn, improves their effective accumulation in leaky vasculature-containing tumors, which are associated with uncontrolled cell proliferation (the EPR effect) (Matsumura and Maeda, 1986). In addition to the passive accumulation of TPNBS in the tumor, resulting from the EPR effect, decorating its surface with tumor-specific targeting ligands, such as peptides, small molecules, antibodies, and aptamers, could further improve its targeted (active) accumulation through ligand–receptor interactions (Danhier et al., 2010; Rosenblum et al., 2018). However, the amount of administered TPNBS that can reach the tumor either via passive or active accumulation is still minimal (Wilhelm et al., 2016). This causes imaging and therapeutic functions to appear throughout the body rather than in the tumor alone, resulting in a poor signal-to-noise (S/N) ratio for imaging and an increased risk of systemic toxicity. Recent studies have focused on overcoming these issues by developing smart, stimuli-responsive TPNBS, which activate imaging and therapeutic functions only in response to endogenous stimuli (e.g., pH, enzymes, redox [glutathione (GSH)-reactive oxygen species (ROS), and hypoxia] or exogenous stimuli (e.g., ultrasound, light, microwave, radiofrequency, and magnetism) present or applied at targeted tumor sites (Feng Q.H. et al., 2018; Kang et al., 2018). Stimuli-responsive TPNBS are switched "on" only at the tumor tissues and afford the selective and sensitive enhancement of imaging and therapeutic efficacy. In contrast, they remain in the "off" state in normal tissues. These TPNBS with improved imaging and therapeutic efficiency provide valuable information, such as that required for detecting diseases, monitoring disease progression, and evaluating patient response to therapy, by performing simultaneous imaging and treatment.

Stimuli-sensitive nanotheranostics offer advantages over conventional passive or active tumor-targeting strategies. Therefore, different stimuli-responsive nanotheranostic agents have been developed (Alsehli, 2020; Gong et al., 2020; Mi, 2020; Parodi et al., 2020). pH-responsive nanotheranostic agents have gained popularity owing to their ability to activate theranostic functions in response to the pH difference among the normal cells, TME, and intracellular microenvironment of tumors. A large number of polymeric and polymer-coated inorganic nanomaterials exhibiting different physicochemical properties in response to changes in the pH have been employed for the preparation of acidic TMEs and intracellular microenvironment-responsive smart nanotheranostics (Feng Q.H. et al., 2018). pH-sensitive hydrophobic to hydrophilic transitional polymers featuring protonatable groups (Bazban-Shotorbani et al., 2017; Wu et al., 2018), pH-sensitive cleavable linkers containing polymers (Kanamala et al., 2016; Wu et al., 2018), pH-responsive charge and size convertible polymers (Yang et al., 2018; Dai et al., 2020), and pH-sensitive inorganic core-forming materials (Dong et al., 2016), among others, are being used to fabricate nanotheranostic agents (**Table 1**).

Conventional cancer treatment methods such as chemotherapy, surgery, and radiotherapy fail to cure cancer completely as they are associated with the impairment of the host immune system, adverse drug reactions, poor patient adherence, and low therapeutic efficiency (Nowak et al., 2002; Couzin, 2008; Chaffer and Weinberg, 2011). Thus far, several pH-responsive smart nanomaterials have been developed to overcome these limitations for chemotherapy. Additionally, several studies have convincingly summarized pH-sensitive drug delivery (Mura et al., 2013; Kanamala et al., 2016; Wang et al., 2018;

TABLE 1 | Summary of pH-responsive nanotheranostics.

Operational pH	Mechanism of pH sensitivity	pH-responsive chemical structure	Functions	References
~6.8	Cyclization-amide bond degradation (Kang et al., 2014)	DMMA-PEG	(1) Charge reversal (2) PDT, Immunotherapy	Yang et al., 2018; Peng et al., 2020
~6.8	Imine bonds	Benzoic-imine	(1) Charge reversal (2) PTT	Lei et al., 2017
~6.8	Boronate ester	PBA-Gal	(1) Ligand-reversible shielding (2) PDT	Cao et al., 2019
~6.0	Boronate ester	PBA-DA	(1) Charge reversal and size reduction (2) PTT, PDT, Chemo, PAI, FI	Cong et al., 2020
~6.8	Cyclization-amide bond degradation	DMMA-PEG	(1) Charge reverse and size reduction (2) Chemo and immunotherapy	Dai et al., 2020
~6.8	Peptide folding	Melittin peptide	(1) Morphology switching (2) PTT	Jia et al., 2019
~5.0–6.7	CaP degradation	CaP	(1) Contrast agent (T_1) release (2) MRI	Mi et al., 2016
~5.5–7.0	Structural transformation	i-Motif DNAs	(1) Contrast agent conversion (T_2 to T_1) (2) MRI	Lu et al., 2018
~5.0	Pore formation	FA-FRT-PFP	(1) Droplet vaporization (2) USI	Li et al., 2020
~5.5	Protonation	pH-BDP	(1) Ratiometric PAI of pH	Miao et al., 2016
~ < 7.0	Protonation	BSA–PANI	(1) Amplified PAI	Tian et al., 2019
~6.8	FRET	ANNA-$Cy_{5.5}$	(1) Dual ratiometric FI of pH	Ma et al., 2018
~4.5–5.0	Porosity, protonation	NEt_2Br_2BDP	(1) Amplified FI	Tian et al., 2015
~6.0–6.2	Protonation	mPEG-*b*-PDPA-$Cy_{7.5}$	(1) Augmented PDT and FI	Qi et al., 2019; Yang et al., 2019
~6.0	Cyclization-amide bond degradation	DEX-MMfu	(1) Enhanced permeability of TME (2) PAI, PDT, and Immunotherapy	Wang et al., 2019
~4.3–5.8	Degradation	$CaCO_3$	(1) Bursting effect (2) USI, SDT	Feng Q. et al., 2018
~6.8	Degradation	MnO_2	(1) O_2 release (2) MRI, SDT	Lin et al., 2020
~6.8	Degradation	MnS	(1) MRI and CDT agent release (2) H_2S release	He et al., 2020
~4.4–5.4	Degradation	MnO_x	(1) New mechanism of CDT (2) FI	Lu et al., 2020

Deirram et al., 2019). The development of minimally invasive or non-invasive therapeutic modalities [such as light, ultrasound (US), and endogenous ROS] and induced therapies [such as photothermal-photodynamic therapy (PTT-PDT) (Jaque et al., 2014; Lucky et al., 2015), sonodynamic therapy (SDT) (You et al., 2016), and chemodynamic therapy (CDT) (Tang et al., 2019)] are currently being used in theranostic nanomedicine for cancer treatment. These treatment protocols only damage cancer cells, while leaving normal cells unaffected and intact. The non-invasive therapeutic efficacy can be improved by developing pH-responsive nanotherapeutic agents.

In recent years, pH-responsive PNBS offering magnetic resonance imaging (MRI), photoacoustic imaging (PAI) fluorescence imaging (FI), ultrasound imaging (USI), and capabilities of improved signal-to-noise ratios in tumors have been developed (Kumar et al., 2013; Kaittanis et al., 2014; Ling et al., 2014; Søndergaard et al., 2015; Wang X. et al., 2015; Wang et al., 2017; Mi et al., 2016; Miao et al., 2016; Zhang et al., 2017b; Vidallon et al., 2020). Therapeutic cargo-incorporated PNBS (TPNBS), which are capable of simultaneous pH-responsive imaging and therapy, have also attracted significant research attention (Wang et al., 2013; Li et al., 2017; Feng Q.H. et al., 2018; Zhu et al., 2018; He et al., 2020). In this review, we evaluate how the development of pH-responsive multifunctional nanomaterials has contributed toward improvements in cancer treatment using the capabilities of these sensors to increase tumor accumulation, tumor penetration, cellular uptake, and theranostic functions. We summarize important recent developments in the design and fabrication of (1) pH-responsive charge and size convertible polymeric nanomaterials for augmented non-invasive cancer therapy, (2) pH-sensitive PNBS for disease detection and bioimaging, and (3) pH-responsive TPNBS for image-guided non-invasive cancer therapy.

pH-RESPONSIVE CHARGE AND SIZE CONVERTIBLE NPs FOR AUGMENTED NON-INVASIVE CANCER THERAPY

The treatment outcomes of theranostic nanomedicine primarily depends on prolonged *in vivo* blood circulation, intratumoral penetration, and the subsequent tumor cell internalization of the NPs (Alexis et al., 2008). Rapid clearance of circulating NPs during systemic delivery via RES is a critical issue in nanomedicine. Therefore, it is necessary to minimize the factors that reduce the blood circulation half-life and biodistribution of NPs while designing for theranostic applications. The NP–RES interactions are influenced by factors such as NP composition, size, surface charge, stability, and surface modifications (pegylation and targeting ligands). pH-responsive charge and size-tunable theranostic NPs have been developed to minimize interactions, thereby improving therapeutic efficacy in the tumor. These NPs enhance blood circulation time, selective tumor accumulation, penetration, and cellular internalizations.

pH-Responsive Charge Convertible NPs

It is well known that NPs with neutral or negatively charged surfaces prevent RES clearance and lengthen the blood

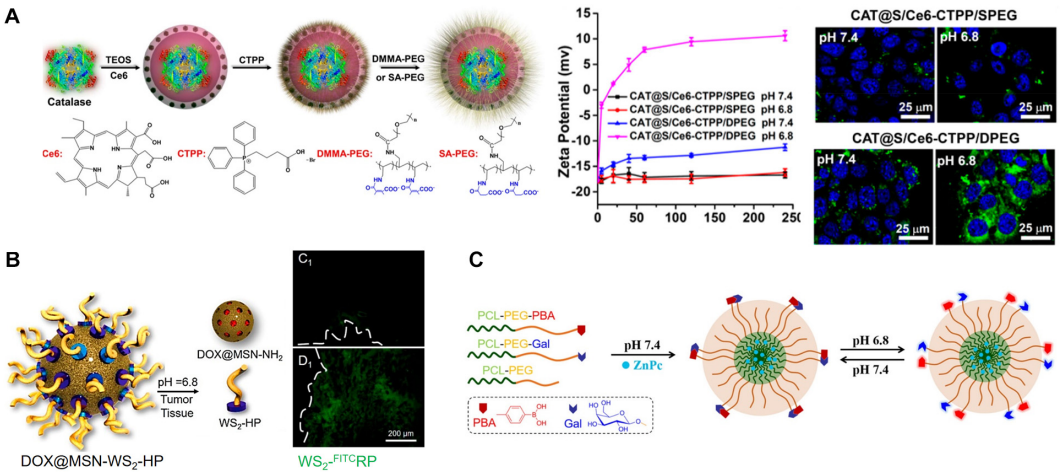

FIGURE 1 | (A) TME pH-responsive charge reversing NPs for enhanced intracellular mitochondrial targeting and improved PDT. Reproduced with permission from reference (Yang et al., 2018). Copyright 2018, American Chemical Society. **(B)** TME pH-responsive degradation cluster bomb and enhanced tumor penetration of the released WS_2 – ^{FITC}HP quantum dots compared to its control (WS_2 – ^{FITC}RP), confirmed via *ex vivo* imaging (the dotted line represents the edge of tumor sections). Reproduced with permission from reference (Lei et al., 2017). Copyright 2017, American Chemical Society. **(C)** pH-responsive ligand-reversible-shielding micelle for enhanced cellular uptake with the associated augmented PDT. Reproduced with permission from reference (Cao et al., 2019). Copyright 2019, American Chemical Society.

circulation half-life, leading to effective accumulation in tumor tissues owing to the EPR effect. However, a positive surface charge on the NPs would rapidly clear them from the blood through the RES (Yuan et al., 2012; Feng et al., 2014). This positive surface charge, however, facilitates intra-tumoral penetration and the ensuing tumor cell internalization of the NPs (Cho et al., 2009). Therefore, NPs with swappable surface charges that are neutral or negative during blood circulation and quickly convert to positive charges on reaching the acidic TME have recently been annotated as a promising strategy for pH-responsive augmentation in therapy (Han et al., 2016; Zhang et al., 2020).

The non-immunogenic polymer, such as polyethylene glycol (PEG), shielding on NPs creates an inert NP surface that enhances their blood circulation half-life and passive tumor accumulation (Fam et al., 2020). Although the dense PEG corona on NPs affords improved tumor accumulation, the PEGylated NPs exhibit reduced intratumoral penetration, succeeding tumor cell internalization, and endosomal escape (Mishra et al., 2004; Kong et al., 2019). Therefore, significant research efforts have devoted toward designing TME pH-responsive PEG corona deshielding NPs; the removal of the PEG corona converts surface charges into positive charges, thereby improving the intratumoral penetration and tumor cell internalization of these NPs. Yang et al. (2018) designed a pH-responsive PEG corona with smart nanoreactors for mitochondrial targeting and enhanced photodynamic-immuno combination therapy. Water-soluble, H_2O_2-decomposing, and oxygen-producing enzyme catalase (CAT)-encapsulated and photosensitizer (Ce6)-loaded hollow silica NPs (S) were prepared (**Figure 1A**). The NP surface was modified using the mitochondria-targeting molecule 3-carboxypropyl-triphenylphosphonium bromide (CTPP), and the resulting cationic surface was further modified with a pH-responsive charge convertible corona forming anionic PEG 2,3-dimethylmaleic amide (DMMA) polymer (PEG-DMMA) via electrostatic interaction. The obtained CAT@S/Ce6-CTPP/D-PEG featured a well-defined hollow structure with a negative surface charge at neutral pH because of the PEG shielding. After effective accumulation of the long-circulating NPs in the TME, due to the TME acidity, PEG was detached from the NPs owing to the pH-sensitive cyclization-induced degradation of the PEG-DMMA amide linkage. This detachment results in a CTPP-exposed cationic NP surface, enabling the effective intracellular targeting of mitochondria, thereby augmenting PDT-induced cancer cell destruction, in comparison with control NPs (CAT@S/Ce6-CTPP/S-PEG) with pH-inert PEG-succinic anhydride (SA-PEG). In the intracellular microenvironment, the catalase encapsulated within these NPs acts as a nanoreactor to trigger the decomposition of tumor-rich endogenous H_2O_2, production of O_2 used to relieve tumor hypoxia, and further augmentation of *in vivo* PDT efficacy. A combination of augmented PDT with checkpoint blockade immunotherapy and programmed death-ligand 1 (PD-L1) antibody significantly boosted the infiltration of cytotoxic T lymphocytes (CTLs) into remote tumors. It impeded their growth, demonstrating a robust abscopal effect encouraging metastasis inhibition. Similarly, pH-responsive charge reversing NPs featuring enhanced tumor targetability and mitochondrial accumulation for PD-immunotherapy were reported recently (Peng et al., 2020). Sequential-targeting positively charged micelles with a Ce6 loaded core were prepared from amphiphilic poly (beta-amino ester), composed of hydrophilic CTTP-PEG and hydrophobic thioketal polymer blocks. The micelles were coated with an anionic pH-responsive charge-transforming shell-forming polymer with tumor-targeting capability (BiotinPEG$_{4000}$-DMMA) using electrostatic interaction. Additionally, pH-responsive charge

conversion was used to augment mitochondrial targeting, thereby improving PDT efficacy.

Lei et al. (2017) prepared a TME pH-responsive "Cluster Bomb" composed of a drug (DOX) containing loaded mesoporous silica NPs (MSN) capped with tumor-homing or tumor-penetrating peptide tLyP-1-modified tungsten disulfide quantum dots (WS_2-HP), by using pH-sensitive benzoic-imine bonds for programmed tumor therapy. The prepared DOX@MSN-WS_2-HP with the surface-decorated peptide tLyP-1 promotes the tumor-homing ability of 4T1 (**Figure 1B**). The benzoic-imine bonds between MSN and the quantum dots remain stable during blood circulation. However, they become highly unstable when the TME pH is 6.8. Once the cluster bomb is accumulated in the TME, it breaks into two parts: DOX@MSN-NH_2 and tLyP-1weraing WS_2-HP. Charge-converted electropositive DOX@MSN-NH_2 enabled efficient chemotherapy on surface tumor cells. The deep tumor-penetrating WS_2-HP showed tumor suppression in the deep-seated tumor cells by near-infrared (NIR)-light-triggered PTT.

The Yuan group recently reported another interesting strategy of pH-sensitive "ligand-reversible-shielding micelle" for increased tumor accumulation associated with effective PDT (Cao et al., 2019). Phenylboronic acid-functionalized poly(ethylene glycol)-*b*-poly(ε-caprolactone) (PBA-PEG-PCL), and galactose-functionalized diblock polymer (Gal-PEG-PCL) were mixed to prepare dual-ligand micelles (PBA/Gal) to demonstrate this concept (**Figure 1C**). The PBA and Gal residues form boronate ester complexes at a pH of 7.4, which mutually shield their targeting function. In an acidic TME (pH 6.8), the binding affinity between the PBA and Gal is weakened, and the PBA prefers to bind with the sialic acid residues expressed on the tumor cell surface rather than the Gal on the micellar surface. Furthermore, the unbound Gal recovers its targeting ability toward the asialoglycoprotein receptor, leading to an enhancement in cellular uptake through receptor-mediated endocytosis. A photosensitizer, zinc phthalocyanine (ZnPc), was loaded onto the reversible-shielding micelle to augment the PDT, owing to its pH-responsive enhanced cellular uptake.

pH-Responsive Size Convertible NPs

It has been reported that NPs with a size of 10–100 nm and suitable surface modifications achieve efficient tumor accumulation during systemic administration via the EPR effect. NPs smaller than 10 nm have shown rapid clearance via renal excretion, resulting in reduced tumor accumulation (Cabral et al., 2011; Blanco et al., 2015; Hoshyar et al., 2016). However, compared to large NPs (10 nm<), small NPs (10 nm>) have shown improved capabilities of intratumoral penetration and subsequent tumor cell internalization (Blanco et al., 2015). Therefore, to solve the size-related conflict issues of NPs, TME or intracellular pH-responsive size swappable NPs have been developed (Sun et al., 2014; Wang J. et al., 2015). In acidic tumors, large NPs accumulated via the EPR effect could undergo a pH-responsive size shrinkage or degradation into smaller NPs. This size reduction improves tumor penetration and cell internalization, resulting in augmented therapeutic efficacy (Li et al., 2015; Li H.-J. et al., 2016).

Cong et al. (2020) reported hyaluronan (HA), stacked self-assembled NPs with folic acid (FA) and HA-mediated active targeting capabilities, upon pH-responsive intracellular transformations of size and surface charge. These transformations simultaneously augment tumor penetration, internalization, and intracellular drug release, as well as synergistic photo-chemo combination therapy. They prepared an amphiphilic hexadecapeptide decorated with three cholic acids (CA), one indocyanine green derivative (ICGD), and one 4-carboxy-3-fluorophenylboronic acid (PBA) (**Figure 2A**). This amphiphilic polypeptide was self-assembled into positively charged small and stable micelle NPs (<30 nm) (ICP NPs) that are loaded with the antineoplastic drug (SN-38) with a critical micelle concentration (CMC) value of 0.04 μM, indicating high thermodynamic stability. The ICP NPs were then stacked using dopamine (DA), and folic acid (FA) decorated with HA (HA-DA-FA). This resulted in the formation of large (130 nm), negatively charged hICP NPs formed through the development of pH-responsive boronate ester bonds between the DA of the HA-DA-FA and the PBA surface wearing the ICP NPs. Additionally, electrostatic interactions between the negatively charged HA and the positively charged ICP NP surface further strengthens NP stacking. The non-immunogenic HA surface provides improved blood circulation time for the hICP NPs and subsequently accumulates at the TME of subcutaneous B16 melanoma-bearing mice. The hICP NPs were taken up by cancer cells via HA- and FA-mediated endocytosis. At the intracellular level, the hICP NPs underwent size and surface charge transformations in the presence of the enzyme hyaluronidase (HAase) in an acidic pH in the endosomes/lysosomes; they released small ICP NPs and accelerated intracellular drug release. The transformed ICP NPs facilitated transcytosis-mediated penetration within the tumors. The ICGD in the ICP NPs not only provides NIR light-induced PDT-PTT but also photoacoustic and NIR imaging capabilities. Furthermore, synergistic augmentation of chemo-photo therapeutic efficacy was achieved owing to the pH-responsive size and charge transformation capabilities of the NPs.

Another type of pH-responsive size and charge transformable NPs was prepared and programmed by overcoming the delivery barrier for improved chemo-ido immunotherapy (Dai et al., 2020). The pH-responsive detachment of DMMA-PEG from a prodrug micelle converts its negative charge of −5.2 mV to a strongly positive charge of 20 mV and reduces its size from 85 nm to 42 nm. The transformed micelles, with reduced size and positive surface charge, enhance tumor penetration and improve endocytosis efficiency; they also synergistically inhibit melanoma growth through the combined effects of chemotherapy-induced antitumor immune response and IDO-blockade immunotherapy. The pH-responsive morphological switching of peptide-cyanine nanostructures, self-assembled by peptide melittin (MEL), and a NIR-absorbing photothermal cyanine dye, Cypate, which is further coated with an HA polymer for tumor targeting (termed MEL/Cypate@HA), has recently been reported (**Figure 2B**) (Jia et al., 2019). In an acidic TME, the MEL/Cypate@HA nanosphere, which transforms into net-like nanofibers, affords an inhibitory

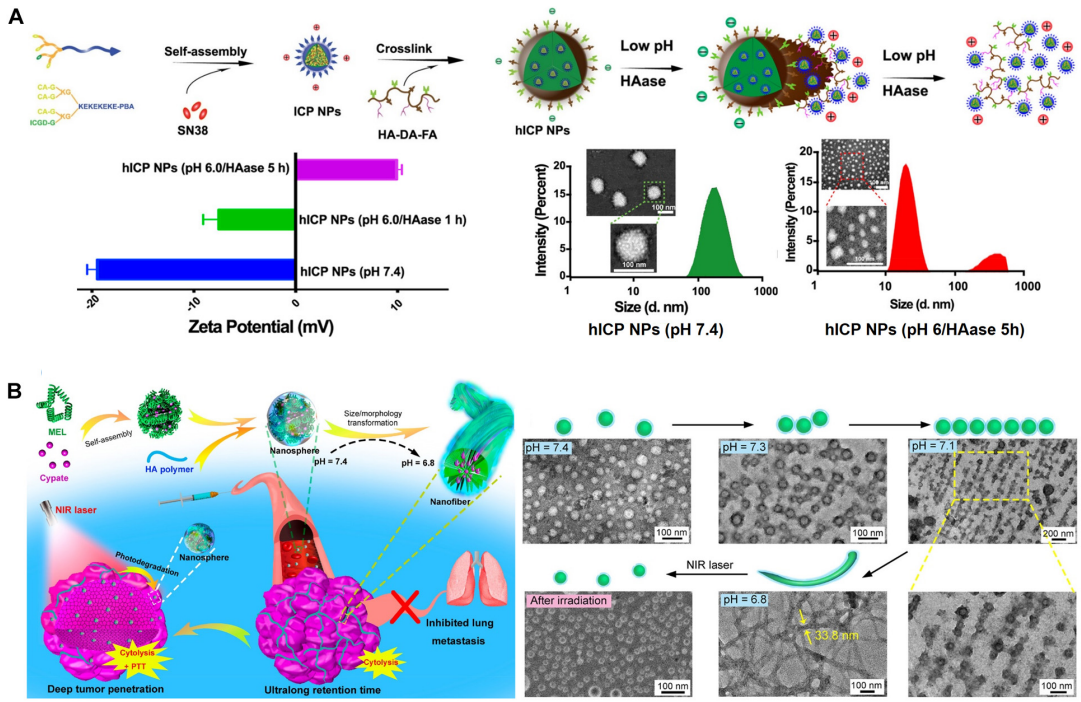

FIGURE 2 | (A) pH-responsive charge and size convertible hICP NPs. Reproduced with permission from reference (Cong et al., 2020). Copyright 2020, American Chemical Society. **(B)** pH-responsive morphological transformation of MEL/Cypate@HA nanospheres followed by their photodegradation into small nanospheres. Reproduced with permission from reference (Jia et al., 2019). Copyright 2019, American Chemical Society.

effect on tumor cell mobility and also increases its tumor retention time. The pH-responsive peptide sequence in MEL was found to be responsible for the morphological transformation. The nanofibers were photodegraded into small nanospheres (25 nm) via NIR laser irradiation during the cypate-mediated PTT, which further improved deep tumor penetration of the loaded MEL and the MEL-induced cytolysis.

pH-RESPONSIVE PNBS FOR TUMOR IMAGING

Imaging of heterogeneous tumors is essential for early detection, diagnoses, and precise treatment monitoring. The unique acidic characteristic of tumors enables the design of PNBS with a pH-responsive amplification of the signal-to-noise (S/N) ratio during tumor-specific imaging (Feng L. et al., 2018; Yang et al., 2020). Thus far, numerous pH-responsive smart PNBS have been reported for *in vivo* cancer imaging using techniques such as MRI, PAI, FI, and USI (Li Y. et al., 2016; Liu et al., 2017). In this section, we describe recent reports of pH-responsive imaging signal amplification in tumors and ratiometric imaging of pH in tumors.

pH-Responsive MRI

Non-invasive imaging techniques, such as MRI, provide a high spatial resolution and detailed three-dimensional anatomical images (Kircher and Willmann, 2012). During MRI, the magnetic field introduced by powerful magnets forces protons in the body to align with the magnetic field. A radiofrequency current is then pulsed through the patient, which stimulates the protons to spin out of equilibrium, causing strain against the pull of the magnetic field. Once the radiofrequency field is switched off, the protons relax back or realign with the magnetic field by releasing energy, which is detected using MRI sensors. The proton relaxation time, as well as the energy released during this process, depends on the chemical nature of the protons and their environments. Longitudinal or spin-lattice relaxation time (T_1) and transversal (T_2) or spin-spin relaxation times of protons are involved in MRI, where $T_2 \leq T_1$. The relaxation times (T_1 or T_2) of water protons in lesions can be sped up using an MRI contrast agent. The T_1 and T_2 contrast agents increase the S/N ratios or the contrast of the lesion for more accurate diagnoses of cancer-related pathological diseases. Therefore, the delivery of MR contrast agents to the tumor by using tumor acidity to improve the S/N of imaging has received significant research attention.

For example, a T_1 (longitudinal) MR contrast agent, releasing PNBS composed of MnO_2, has been extensively investigated for its ability to release Mn^{2+} ions in acidic tumors (Cai et al., 2019). Mi et al. (2016) prepared Mn^{2+}-doped calcium phosphate (CaP) NPs for the pH-responsive MRI contrast on-off system for signal amplification in subcutaneous C26 tumor-bearing mice. CaP NPs were prepared via the mineralization of poly(ethylene glycol)-*b*-poly(glutamic acid) [PEG-b-P(Glu)] block copolymers with Mn^{2+}, Ca^{2+}, and HPO_{42}^{-} in the aqueous phase, followed by hydrothermal treatment to improve the

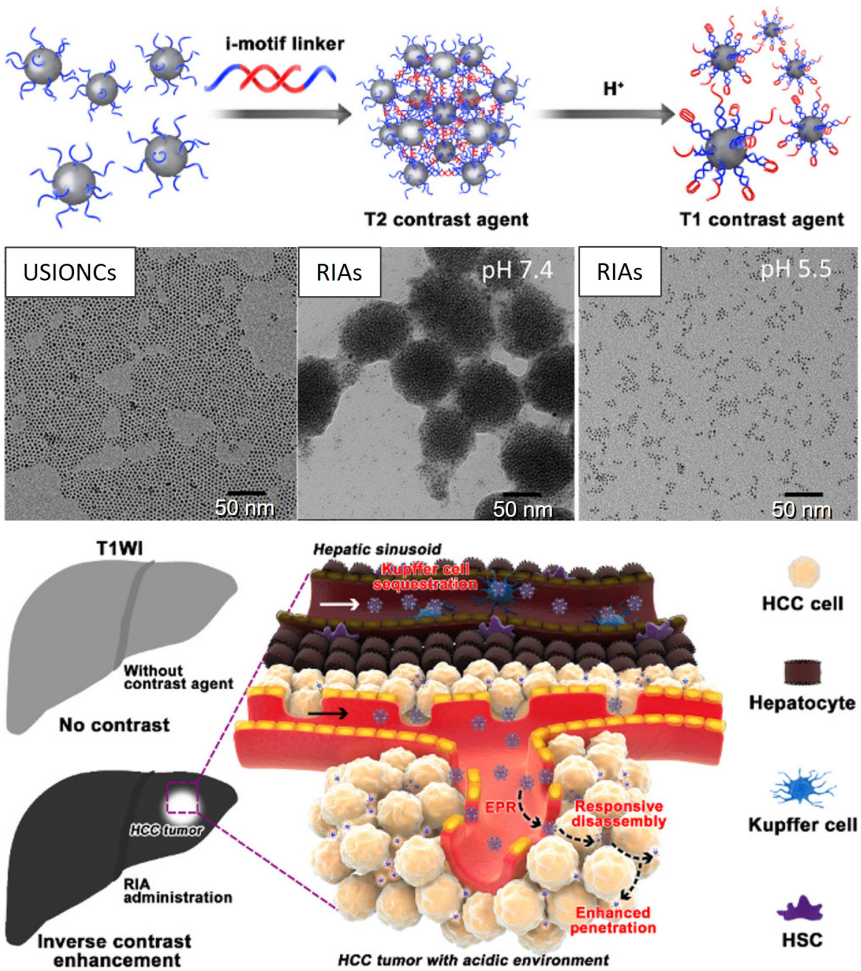

FIGURE 3 | pH-responsive conversion of the MRI contrast agent confirmed via TEM images, and used for inverse contrast enhancement for the detection of small hepatocellular carcinomas (HCCs). Reproduced with permission from reference (Lu et al., 2018). Copyright 2018, American Chemical Society.

mechanical strength of the CaP matrix. The PEG shell in the resulting PEGMnCaP helped maintain the size of the NPs at ~60 nm by preventing further expansion of the CaP core. The CaP core of accumulated PEGMnCaP NPs was dissolved in the acidic TME, thereby releasing Mn^{2+} ions. This Mn^{2+} readily interacted with surrounding proteins and slowly rotated the Mn-protein system, which enhanced the sharp contrast due to the increased T_1 relaxivity of Mn^{2+}. Additionally, the PEGMnCaP NPs rapidly and selectively brightened and detected hypoxic regions in solid tumors and detected invisible millimeter-sized metastatic tumors in the liver, owing to their pH-responsive signal amplification capabilities. According to another report, a T_2 contrast agent, such as Fe_3O_4 NPs, was loaded in the hydrophobic core of a pH-sensitive polymer (PEG-poly(β-amino ester) (PAE) micelle and was released and exposed to water molecules at the acidic tumor. Furthermore, a shortened water proton relaxation time T_2 responsible for contrast enhancement during MRI was reported (Gao et al., 2010). Recently, a pH-responsive conversion of i-motif DNA-assisted iron oxide nanocluster assemblies (RIAs) from a T_2 to a T_1 contrast agent for the detection of small hepatocellular carcinomas (HCCs) has been reported (**Figure 3**) (Lu et al., 2018). The i-Motif DNAs exhibit pH-responsive structural transformation from single-stranded to intercalated quadruple-helical structures. In the acidic TME, the T_2 contrast agent RIAs (120 nm), composed of the T_1 contrast agent ultrasmall iron oxide nanoclusters (USIONCs), is disassembled back to USIONCs. The pH-dependent detachment of the i-Motif cross-linker is responsible for this intelligent contrast agent transformation, resulting in bright HCCs and a healthy dark liver owing to the inverse contrast-enhancing imaging mode transformation.

pH-Responsive USI

Ultrasound imaging is portable, cost-effective, and enables real-time imaging. Despite these advantages, the low contrast in USI decreases its sensitivity, thereby limiting its diagnostic applications. Thus, contrast-enhanced US (CEUS), which utilizes 1–10-μm microbubbles (MBs) as the contrast agent, has been developed (Sun and Emelianov, 2019). However, these MBs cannot accumulate at disease sites via the EPR effect owing to

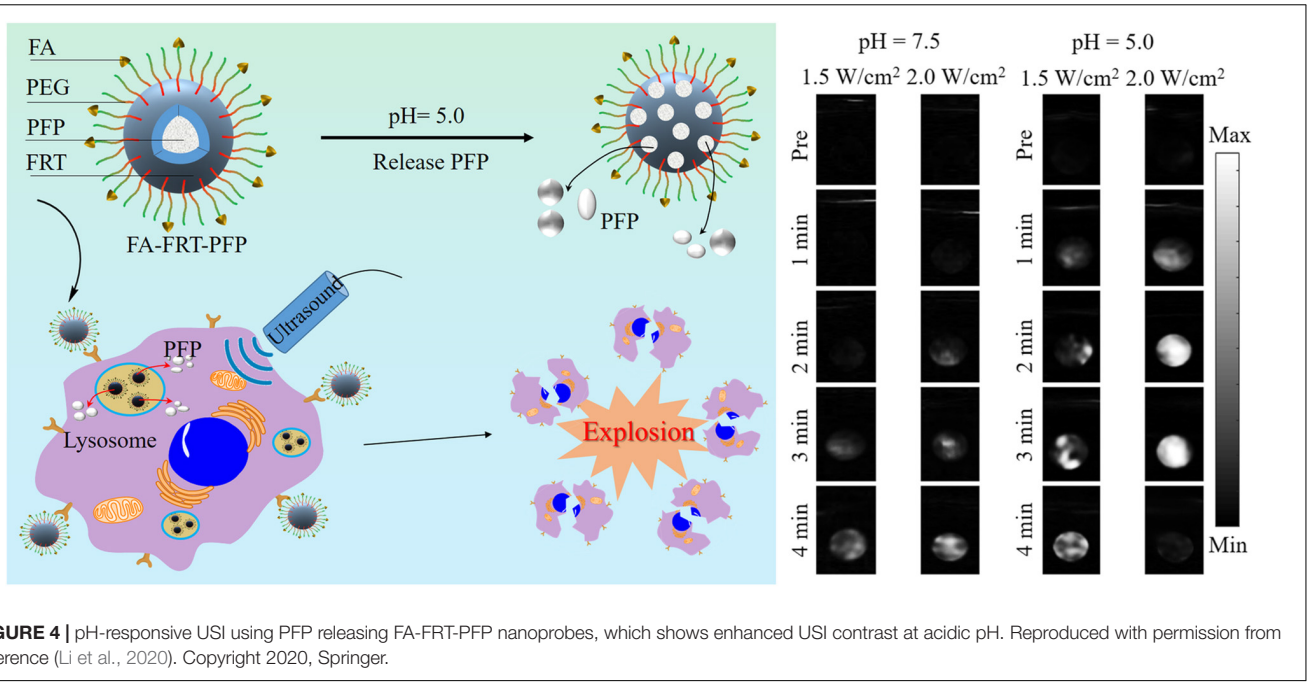

FIGURE 4 | pH-responsive USI using PFP releasing FA-FRT-PFP nanoprobes, which shows enhanced USI contrast at acidic pH. Reproduced with permission from reference (Li et al., 2020). Copyright 2020, Springer.

their large sizes, limiting their application *in vivo*. Thus, the size of contrast agents should be in the nanometer range in order to accumulate at disease sites. Therefore, reducing the size of MBs and transforming them into nanobubbles (NBs) appears as a straightforward solution. However, NBs have low stability and low echogenicity, and they are excessively small to efficiently scatter ultrasonic waves at the frequencies used in clinical applications. Gas-generating NPs are introduced as a contrast agent for US imaging to overcome these issues and generate sufficient USI contrast while maintaining the nanometer-scale size.

pH-sensitive release of carbon dioxide (CO_2) gas from mineralized calcium carbonate polymeric NPs (Min et al., 2015; Kim et al., 2018; Chen et al., 2019) or carbonate side chains containing polymer NPs (Kang et al., 2010) has been reported. These NPs exhibited strong echogenic signals with excellent echo persistence in tumoral acidic pH by producing CO_2 bubbles. Recently, Li et al. (2020) prepared a US therapeutic agent that encapsulates low boiling (bp = 29°C) perfluoropentane (PFP) into pH-sensitive cage protein ferritin (FRT) conjugated with the tumor-targeting molecule FA (FA-FRT-PFP) (Li et al., 2020). FRT disassembles at intracellular pH and releases PFP. A 3-min, low-intensity focused ultrasound (LIFU, 2 W/cm^2), which significantly enhances the US signal of the FA-FRT-PFP through the acoustic droplet vaporization (ADV) effect, is produced by the PFP (**Figure 4**). Additionally, the long duration (4 min) of LIFU irradiation at the lysosomal pH produced a physical shock wave due to the explosive release of PFP from the FA-FRT-PFP; this subsequently results in effective tumor cell destruction via necrosis. Another example of pH-responsive gas (O_2) generation for USI is the use of manganese dioxide (MnO_2) NPs that can aptly regulate TME oxygenation owing to their hydrogen peroxidase properties and favorable behavior of breaking-up in mildly acidic and H_2O_2-rich TMEs (Gao et al., 2017). The oxygen content in the tumor is elevated to 2.25 ± 0.07 times that in the absence of MnO_2, which demonstrates its potential for USI.

pH-Responsive PAI

Photoacoustic imaging is an emerging hybrid modality that combines optical excitation with ultrasonic detection. It allows for deeper tissue penetration and higher spatial resolution compared to traditional optical imaging techniques, owing to the involvement of deep tissue-penetrating ultrasound modalities (Miao and Pu, 2018). Endogenous (such as hemoglobin and melanin) and exogenous (such as NIR-emitting dyes, metallic NPs, carbon nanotubes, prophysomes, and 2D graphene analogs) PAI agents have been used for imaging applications. The PA signal depends on the difference in concentration between the healthy and diseased tissues. The poor accumulation and uptake of PAI agents could result in a poor S/N ratio in a complex pathological environment. Therefore, activatable PNBS that undergo intrinsic PAI signal amplification only in response to tumor-specific stimuli, including pH, and maintain a dormant state in the absence of pH can provide a high signal-to-noise ratio at the acidic tumor site. pH-sensitive activation provides a real-time correlation between PNBS states (activated vs. dormant) in pathological processes at the molecular level. This pH-responsive contrast enhancement has garnered significant research attention in recent years.

Miao et al. (2016) developed activated ultrasmall semiconducting oligomer nanoprobes (SONs) with amplified signals for the *in vivo* PAI of pH. The SONs are prepared via nanoprecipitation of a low-molecular-weight semiconducting oligomer (SO:F-DTS) as the inert PA matrix, doped with a pH indicator dye, boron-dipyrromethene (pH-BDP), and served

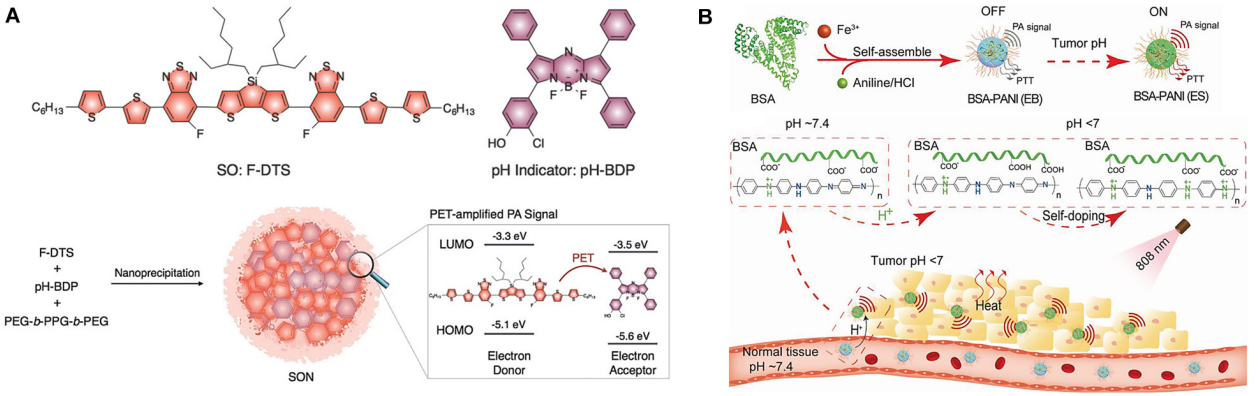

FIGURE 5 | (A) Nanoprobe design of PET-amplified PA imaging of pH. Reproduced with permission from reference (Miao et al., 2016). Copyright 2016, Wiley-VCH GmbH. **(B)** pH-responsive amplification of PAI using BSA–PANI nanoprobe. Reproduced with permission from reference (Tian et al., 2019). Copyright 2019, Wiley-VCH GmbH.

as a PA enhancer and amphiphilic triblock copolymer (PEG-*b*-PPG-*b*-PEG) as a coprecipitant (**Figure 5A**). The pH-BDP has a hydroxyl group on its backbone, which undergoes protonation upon acidification and imparts the pH-sensing ability of the SONs. Additionally, the electron affinity and ionization potential of the pH-BDP are lower than those of the SO:F-DTS. Thus, photoinduced electron transfer (PET) is favored between these binary optical partners, which results in the quenched fluorescence of SO:F-DTS; this, in turn, enhances the PA brightness of the SONs. Compared to the pH-inert non-doped SON (SON_0), the PA brightness of the 50 wt% pH-BDP-doped nanoprobe (SON_{50}) was substantially amplified by a factor of approximately 3.1 at 680 nm. Simultaneously, its ratiometric PA signal (PA_{680}/PA_{750}) increased by approximately 3.1 times on varying the pH from 7.4 to 5.5 *in vitro*. Systemic administration of SONs permits non-invasive real-time ratiometric PAI of the pH with the amplification of brightness in tumors of living mice. Another interesting example of pH-responsive PAI amplification was reported using a polyaniline (PANI)-based theranostic agent composed of bovine serum albumin (BSA) and PANI (**Figure 5B**) (Tian et al., 2019). The monomer aniline (ANI) polymerizes to PANI in the presence of BSA and Fe^{3+} ions, and the interaction between hydrophilic BSA and hydrophobic PANI self-assembles to BSA–PANI NPs. The strong BSA–PANI interaction leads to a pH-dependent self-doping effect through intermolecular acid-base reactions between the carboxyl groups of BSA and the imine moieties of the PANI backbone. This increases the degree of protonation of PANI and mediates its transformation from the emeraldine base (EB) to the emeraldine salt (ES) state in an acidic TME (pH < 7). Therefore, in healthy tissues (pH ~7.4), the BSA–PANI assemblies exhibit low PAI signals and PTT effects during blood circulation, whereas they exhibited amplified PAI and enhanced PTT in acidic TMEs.

pH-Responsive FI

Although FI is one of the most widely explored tumor imaging modalities, which also offers the advantages of ease of operation, high sensitivity, and multicolor imaging capabilities, its applications are limited owing to its low depth of light penetration in tissues and poor S/N ratio (Guo et al., 2014; Jin, 2019). The poor S/N in FI is attributed to the non-specific distribution of the imaging probe in tissues and background autofluorescence. pH-responsive fluorescence on-off PNBS are being developed to improve the S/N ratio, which can differentiate tumors from their surrounding normal tissue. The FI signal from PNBS is always turned off in the absence of tumor-specific stimuli (pH), providing pH-sensitive augmentation of FI at an acidic TME.

Lower pH in the TME and overexpressed matrix metalloproteases (MMPs) are two indicators of tumor-associated abnormalities. Quantitative and real-time detection of multiple TME factors through non-invasive multimodality imaging is highly informative. Non-invasive visualizations of these abnormality indicators are an effective approach for studying and confirming abnormal tumor signatures *in vivo*. A novel target-triggered dual-ratiometric fluorescent nanoprobe for simultaneous mapping of matrix metalloprotease-9 (MMP-9) activity and extracellular *in vivo* pH has been reported (Ma et al., 2018). The nanoprobe comprises a ratiometric pH-sensitive dye [(*N*-carboxyhexyl derivative of 3-amino-1,2,4-triazole fused 1,8-naphthalimide), ANNA], its fluorescence is quenched while being attached to the surface of an MRI agent (Fe_3O_4 NPs) using the peptide substrate of MMP-9, representing the "off" state (**Figure 6A**). The fluorescence of ANNA was quenched via Förster resonance energy transfer (FRET) between the dye and NPs. However, when the peptide was cleaved by MMP-9, the fluorescence of ANNA was activated ("on" state), allowing for *in vivo* pH mapping. This MMP-9 responsive nanoprobe was also co-labeled with a NIR reference dye (Cy5.5), which serves as an always "on" internal reference dye of the resulting secondary ratiometric fluorescent system. The MMP-9 dependent fluorescence emission from ANNA was compared with that of continually emitting Cy5.5 for quantitatively mapping proteases activity across the entire tumor. Extensive imaging studies using these dual-ratiometric probes in a mouse model of human colon cancer revealed

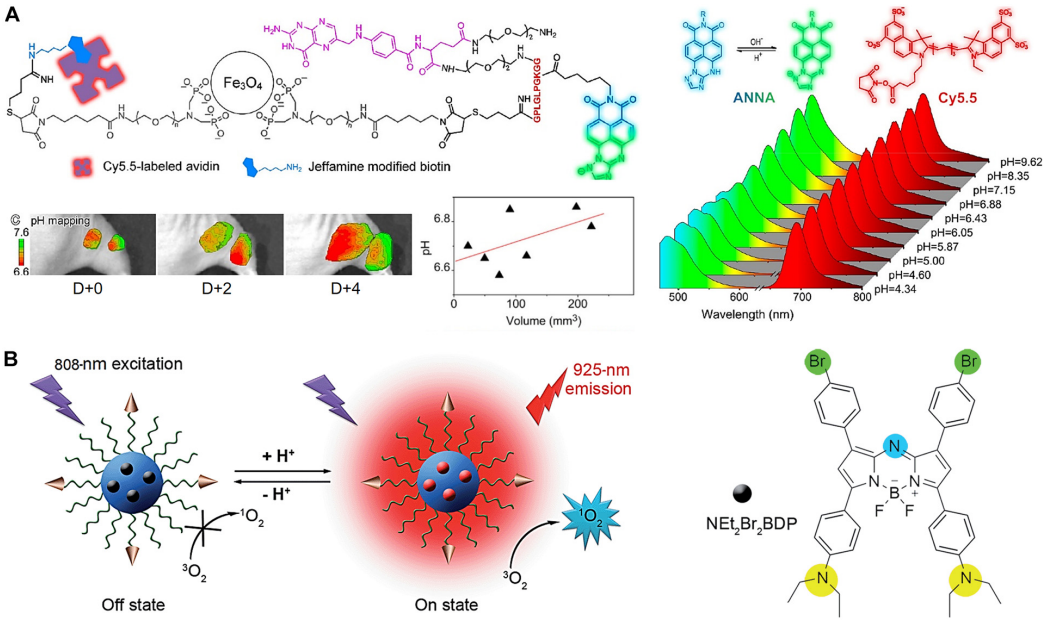

FIGURE 6 | (A) Dual-ratiometric fluorescent nanoprobe for *in vivo* pH mapping. Protonation-/deprotonation-induced structural transformation of ANNA combined with pH-insensitive $Cy_{5.5}$ yields two sets of fluorescence spectra recorded at different pH values excited at 455 and 675 nm, providing ratiometric pH monitoring capabilities. The intratumorally injected nanoprobes allow for TME pH mapping on different days and TME pH quantification. Reproduced with permission from reference (Ma et al., 2018). Copyright 2018, American Chemical Society. **(B)** pH-sensitive fluorescence on-off nanoprobe for FI. Reproduced with permission from reference (Tian et al., 2015). Copyright 2015, Royal Society of Chemistry.

that MMP-9 overexpression and abnormal TME pH have spatio-temporal correlations. Additionally, the synergistic effect of these two characteristics largely controls the heterogeneous invasion of malignant tumors. Another example is the use of the pH-sensitive fluorescence on-off nanoprobe to achieve highly selective tumor imaging (Tian et al., 2015). A pH-activatable fluorophore with an aza-boron-dipyrromethene structure substituted with diethylaminophenyl and bromophenyl groups (NEt_2Br_2BDP) and loaded in a nanomicelle composed of a cyclic RGD peptide-poly(ethylene glycol)-block-poly(lactic acid) (cRGD–PEG–PLA) unimers is used as a FI nanoprobe (**Figure 6B**). The fluorescence was quenched (off) in the nanomicelle at neutral pH (pH-7.4) owing to the photoinduced electron transfer from the diethylaminophenyl moiety to the excited fluorophore. In acidic tumors, the porosity of the nanoprobe increases due to its polymer composition, allowing protons to access the NEt_2 groups of the loaded NEt_2Br_2BDP. This protonation increases the fluorescence at 925 nm, resulting in an enhanced, pH-dependent NIR fluorescence (on).

pH-RESPONSIVE TPNBS FOR IMAGE-GUIDED THERAPY

pH-responsive TPNBS combine the functions of imaging and therapy in a single NP. Their pH-responsiveness selectively and sensitively activates imaging and therapeutic functions in pathological tissues. However, these functions remain inactive in normal tissues. The selective activation of theranostic functions improves the imaging (S/N ratio) and therapeutic efficacy in tumor tissues. Image-guided therapy using TPNBS enables disease detection, monitoring of disease progression, and evaluation of patient response to therapy. ROS-mediated cancer treatment methods, including light-induced PDT (Lucky et al., 2015), US-induced SDT (Qian et al., 2016), and endogenous ROS-induced CDT (Tang et al., 2019), have emerged as potential alternatives to conventional treatment methods such as chemotherapy and surgery, owing to their minimal or non-invasiveness and improved site-specific action. The efficacy of ROS-mediated PDT, SDT, and CDT depends on the ability of the method to produce an elevated level of cytotoxic intracellular ROS. Compared to neutral or less reactive hydrogen peroxide (H_2O_2) ROS, singlet oxygen ($^1O_2$), peroxy radicals ($\bullet O_2H$), and hydroxyl radicals ($\bullet OH$) are highly reactive or more cytotoxic to cancer cells. The overproduction of ROS damages lipid bilayers, proteins, and DNA associated with cancer cells and causes cell death (Yao et al., 2005; Trachootham et al., 2009).

pH-Responsive TPNBS in PDT

In PDT, light excites a photosensitizer from its ground state to a short-lived excited singlet state. The excited photosensitizer either decays back to the ground state by emitting fluorescence or undergoes intersystem crossing to a relatively long-lived triplet excited state with reversed electron spin. In the triplet excited state, the photosensitizer interacts directly with the substrate and cancer cell membrane, leading to proton or electron transfer and the production of radical cations and anions, which further

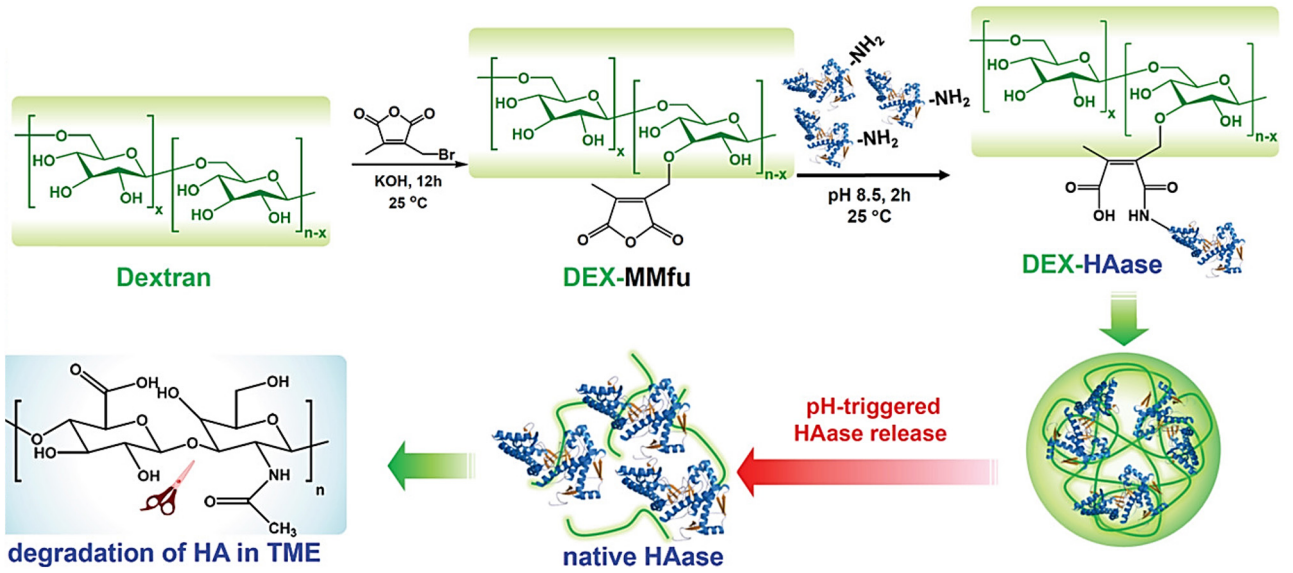

FIGURE 7 | pH-responsive loosening of the condensed extracellular matrix through enzymatic degradation for enhanced tumor permeability of oxygen and nanotheranostics. Reproduced with permission from reference (Wang et al., 2019). Copyright 2019, Wiley-VCH GmbH.

react with oxygen to produce ROS, such as superoxide anion radicals ($O_2^{-}\bullet$), •OH, and H_2O_2. Alternatively, a triplet excited photosensitizer can directly transfer its energy to molecular oxygen in its ground state ($^3O_2$) and convert it into powerful non-radical ROS, $^1O_2$. Therefore, in addition to light and photosensitizers, oxygen is also a key constituent that determines the success of PDT. In poorly oxygenated tumor tissues (tumor hypoxia), the efficacy of PDT is limited (Zhang et al., 2017a). The low depth of penetration of light into the tissue (<1 mm) is another parameter that limits the application of PDT in deep tumors (Lucky et al., 2015). Tumoral pH-responsive TPNBS were developed to improve the theranostic efficacy of TPNBS for PDT. The pH-responsive TPNBS could augment theranostic efficacy by providing prolonged blood circulation with reduced systemic toxicity, effective tumor accumulation, improved tissue penetration, tumor oxygenation, and tumoral pH-sensitive imaging signal and therapeutic efficacy enhancement.

Qi et al. (2019) reported a pH-responsive simultaneous activation of FI and PDT. Fluorescent dye (Cy7.5), labeled as a pH-responsive copolymer, poly(ethylene glycol)-*b*-poly(2-(isopropylamino) ethyl methacrylate) (mPEG-*b*-PDPA-Cy7.5) micelles were encapsulated with a mitochondria-targeted photosensitizer, triphenylphosphonium-conjugated pyropheophorbide-a (TPPa). The resulting NPs were represented as M-TPPa. The fluorescent signal and photoactivity of M-TPPa were completely switched off through the hetero-FRET from TPPa to Cy7.5 molecules. Hetero-FRET facilitated an amplified photodynamic effect in the tumor tissues and suppressed systemic adverse effects to normal tissues. M-TPPa is exposed to the acidic intracellular environment of human HO8910 ovarian cancer cells. The protonation of the tertiary amino groups of its unimers leads to micelle degradation, followed by the efficient early endosomal escape of TPPa owing to its small molecular structure and high permeability across the lipid membrane. Finally, cationic TPPa relocates into the mitochondria to kill the cancer cells through *in situ* ROS generation upon laser irradiation, providing robust antitumor efficacy with reduced systemic adverse effects. M-TPPa exhibited a 111-fold increase in the fluorescent signal and a 151-fold enhancement in singlet oxygen generation in acidic cancer cells.

In another study, the enzyme HAase was conjugated to a pH-sensitive traceless linker, 3-(bromomethyl)-4-methyl-2,5-furandione (MMfu), modified dextran (DEX), DEX-MMfu (**Figure 7**) (Wang et al., 2019). The obtained DEX-HAase NPs, with diminished immunogenicity compared to free HAase, showed enhanced passive tumor (4T1) accumulation owing to its prolonged blood circulation half-life after intravenous injection. The pH-sensitive release of HAase at the TME loosened the condensed extracellular matrix composed of cross-linked HA due to enzymatic degradation, which enhanced the penetration of oxygen and other therapeutic agents (e.g., liposomes). This improved permeability of the tumor, relieved its hypoxia, and enhanced the therapeutic effect of NP-based PDT, followed by the reversal of the immunosuppressive TME to boost cancer immunotherapy. PAI was used to monitor tumor oxygenation (oxygenated hemoglobin). Liposomes loaded with a photosensitizer, chlorine e6 (Ce6), were used as model nanotherapeutics to demonstrate enhanced PDT and immunotherapy as a result of the pH-sensitive augmentation in tumor permeability.

pH-Responsive TPNBS in SDT

In SDT, US-induced cavitation causes sonoluminescence or pyrolysis, which contributes to the production of ROS from sonosensitizers once it meets oxygen or water at the tumor tissues (Deepagan et al., 2016; Gong et al., 2019). Depending on the

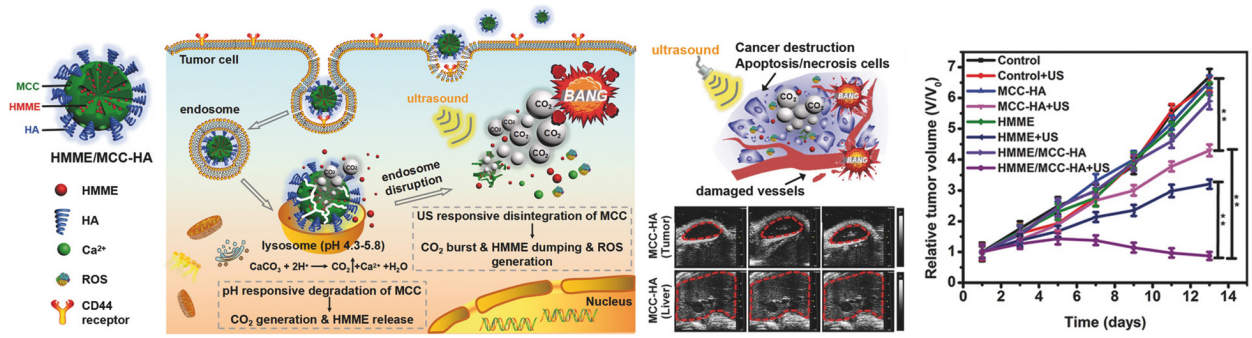

FIGURE 8 | CD44 receptor-mediated endocytosis of HMME/MCC-HA in a cancer cell, followed by the pH/ultrasound dual-responsive decomposition of MCC, CO_2 bubbling, HMME release, and ROS generation. The CO_2 burst release causes cancer destruction via cell apoptosis/necrosis and blood vessel destruction. *In vivo* therapeutic efficacy of NPs in MCF-7 tumor-bearing mice confirms effective tumor suppression. Compared to liver lesions with neutral pH, acidic tumor tissues exhibit US contrast enhancement, confirming the pH-responsive augmentation of USI. Reproduced with permission from reference (Feng Q. et al., 2018). Copyright 2018, Wiley-VCH GmbH.

frequency, US can be tightly focused, with a penetration of up to several tens of millimeters into soft tissue. Thus, SDT allows access to deeper-seated tumors than PDT (Bailey et al., 2003; Costley et al., 2015). PDT can only be used to treat superficial tumors or endoscopically reachable tumors such as skin cancer, owing to the low penetration depth of light. In PDT treatment, patients must avoid exposure to sunlight after being administered the photosensitizer to avoid light-induced toxicity. Owing to these limitations of PDT, in recent years, research on SDT-based cancer treatment has advanced more rapidly than that on PDT. The lack of an efficient sonosensitizer and poor quantum yield for ROS generation in existing sonosensitizer NPs (Qian et al., 2016) are the primary limitations of SDT. However, these limitations were overcome by developing stimuli-responsive TPNBS (Zhu et al., 2018; Gong et al., 2019). Particularly, a pH-responsive TPNBS for SDT would significantly negate potential side effects in normal tissues and enhance the theranostic efficacy in diseased tissues by providing pH-responsive augmentations in tumor oxygenation, tumor accumulation, tumor penetration, ROS generation, and the S/N ratio of imaging signals.

Feng Q. et al. (2018) reported the generation of mesoporous calcium carbonate (MCC) NPs for USI-guided cancer cell necrosis and apoptosis. MCC NPs were loaded with a sonosensitizer [hematoporphyrin monomethyl ether (HMME)], and their surface was decorated with CD44 receptors targeting HA. HA also served as the gatekeeper for the loaded HMME (**Figure 8**). After receptor-mediated endocytosis, the HMME/MCC-HA decomposed instantaneously via the co-stimulation of inherent tumoral acidic pH and US irradiation, followed by simultaneous HMME release and CO_2 generation. The degradation associated with the increase in osmotic pressure leads to the redistribution of TPNBS from the endosome to the cytoplasm. In addition to the endosomal escape, the bubbling and bursting of CO_2 under the US stimulus results in cavitation-mediated irreversible cell necrosis as well as the destruction of blood vessels to further obstruct blood supply, enabling a "bystander effect." The generation of ROS from HMME, triggered by US, causes cell apoptosis via SDT. Therefore, the same pH-responsive TPNBS are used for apoptosis and necrosis and to promote cell injury in a complementary manner. The generated CO_2 having the echogenic property, is an effective US contrast agent for the identification of cancerous tissues.

Manganese oxide (MnO_x) NPs can effectively regulate TME oxygenation owing to their hydrogen peroxidase properties and favorable breakup behavior in mildly acidic and H_2O_2-rich TMEs (Zhu et al., 2016). Additionally, MnO_x can breakup via an antioxidant (GSH) depletion reaction in mildly acidic pH (Deng et al., 2011); both of these pathways release Mn^{2+} ions, which is a T1-MRI agent. The combination of a sonosensitizer and MnOx can afford MRI-guided augmented SDT due to tumor oxygenation at a mildly acidic TME (Zhu et al., 2018). Similarly, via GSH depletion, sonosensitizer-MnO_x ensures the MRI-guided augmentation of SDT due to the depletion of ROS scavenging GSH in acidic cancer cells, resulting in the enhancement of intracellular oxidative stress (Lin et al., 2020).

pH-Responsive TPNBS in CDT

Chemodynamic therapy is a unique method for endogenously generating highly cytotoxic ROS (•OH) from TME-rich neutral ROS (H_2O_2) through a transition metal-ion catalyzed Fenton-like reaction (Chen and Schopfer, 1999; Tang et al., 2019). The released transition metal ions [Fe^{2+} (Li W.-P. et al., 2016), Mn^{2+} (Lin et al., 2020), Ti^{3+} (Wang et al., 2020), Cu^{+} (Ma et al., 2019), etc.] from pH-responsive degradable NPs can be used as CDT agents. Most importantly, as CDT involves ROS activation, compared with SDT or PDT, ROS generation via this process is independent of tumor oxygenation. However, novel TPNBS that follow oxygen-dependent CDT via a light-independent PDT mechanism at an acidic tumoral pH have been recently reported (Lu et al., 2020).

Tumoral pH-responsive theranostic NPs are being developed for imaging guided CDT. For example, a size-controllable, biodegradable, and metastable γ-phase MnS nanotheranostic (MnS@BSA) was prepared using BSA as a template for tumor pH-responsive T_1-weighted MRI-guided integrated CDT and gas

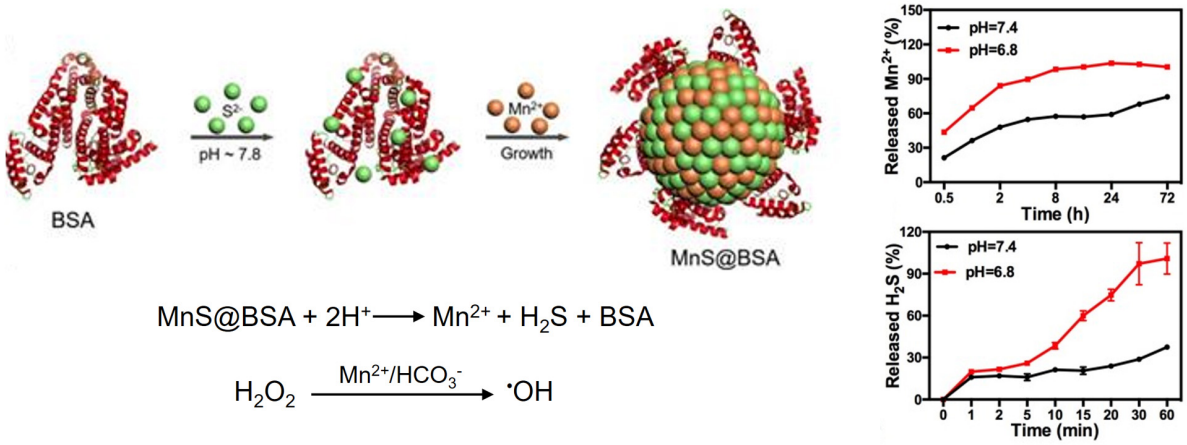

FIGURE 9 | pH-responsive MnS@BSA nanotheranostic for MRI-guided CDT and gas therapy. MnS@BSA enables a pH-responsive release of a CDT agent, Mn^{2+}, and H_2S gas. Reproduced with permission from reference (He et al., 2020). Copyright 2020, Wiley-VCH GmbH.

therapy (**Figure 9**) (He et al., 2020). BSA was used to regulate the size of MnS NPs by tuning the ratio of the proportion of BSA to that of Mn^{2+}. In an acidic TME, the as-prepared MnS@BSA underwent pH-responsive dissociation to simultaneously release the MRI or chemodynamic agent (Mn^{2+}) and H_2S gas. The anticancer effect of H_2S gas, together with the ROS production due to CDT, enables image-guided cancer therapy in 4T1-luciferase mammary tumor xenograft bearing BALB/c mice with significant suppression of tumor growth. Similarly, a pH-activatable chemodynamic system [ultrathin Mn-oxides MnO_x nanosheet $(Mn^{II})_1(Mn^{III})_{3.4}(Mn^{IV})_{2.8}O_{11.7}$] that can produce $^1O2$ under the trigger of acidity through a novel chemodynamic process has recently been developed (Lu et al., 2020). The $^1O2$ produced from MnO_x using this light-free process chemically reacts with thiophene units of semiconducting polymer (SP) NPs (SPNs); thus, the excited SPNs emit near-infrared (NIR) chemiluminescence through a process called chemical electron exchange luminescence (CIEEL). This process further amplifies the yield of $^1O2$ generation. In an acidic tumor environment, the MnOx-SPN system achieved satisfactory chemodynamic therapeutic outcomes *in vitro* and *in vivo* (4T1 female Balb/c mice). The output of $^1O2$ generation was calibrated using ratiometric imaging of chemiluminescence/fluorescence, which provides more accurate *in situ* monitoring of the chemodynamic treatment process.

CONCLUSION AND OUTLOOK

Owing to their unique physicochemical characteristics, pH-responsive NPs have been extensively investigated for cancer theranostics. The NPs, which exhibit pH-responsive behaviors such as charge conversion, size reduction, and shape changes, would facilitate theranostic efficacy via enhanced tumor accumulation, deep penetration, and/or cellular internalization. In this review, we summarized recent developments that demonstrated how the tumoral pH could be utilized in the design of intelligent NPs with the potential to enhance non-invasive cancer therapy, disease detection/diagnosis, and their combinations.

By utilizing the unique acidic characteristics of tumors, PNBS with pH-responsive amplification of the S/N ratio during tumor-specific imaging has been developed. Thus far, various pH-responsive smart PNBSs have been reported for *in vivo* cancer imaging using suitable techniques such as MRI, USI, PAI, and FI. MRI is a well-established non-invasive whole-body imaging technique owing to the deep tissue penetration of radiofrequency waves. A pH-responsive PNBS for MRI facilitates a tumoral pH-sensitive release of MRI contrast agents, enabling contrast enhancement of deep-seated tumors during diagnosis and treatment. USI is also available for deep-seated tumor imaging owing to the high tissue penetration depth of US. For instance, pH-responsive gas-generating PNBS with strong echogenic signals and excellent echo persistence has been prepared as the potential USI contrast agent. PAI is an emerging hybrid modality that combines optical excitation with ultrasonic detection. It offers deeper tissue penetration and higher spatial resolution than FI, ascribed to US involvement. PAI using a pH-responsive PNBS would allow for semi-quantitative *in vivo* pH sensing and mapping within tumors. Compared to clinically available MRI and USI, the PAI technique would be particularly suitable for *in vivo* pH imaging in small animal models to meet basic and preclinical research needs. *In vivo* applications of FI have limited by the low tissue penetration of light involved, making this approach unsuitable for deep-seated tumor imaging. Similar to PNBS for PAI, fluorescent PNBS are applied to quantitative detection of tumoral pH and tumor imaging in small animal models.

The TPNBS are intelligent, multifunctional nanosystems that combine the imaging and therapy functions into a single NP. Their pH-responsiveness affords selective activation of theranostic functions in pathological tissues, while being inactive in normal tissues. The selective activation of theranostic functions provides improved imaging (S/N ratio) and therapeutic

efficacy in acidic tumors with reduced systemic toxicity. Image-guided therapy using TPNBS enables disease detection, monitoring disease progression, and evaluating patients' responses to treatments. Numerous TPNBS with excellent theranostic functions have been reported recently in basic and preclinical research. These designs need to be relatively simple and biocompatible; most of them, however, are excessively complicated for their clinical translation. Until now, the tumor acidity has been mainly used for developing cancer theranostics. It should be emphasized that the tumor acidity plays a crucial role in tumor initiation, progression, and metastasis. Therefore, developing novel nanotheranostics that modulate tumor acidity would be a promising approach to overcome treatment resistance associated with the current TPNBS.

AUTHOR CONTRIBUTIONS

EP, WU, and JP reviewed and evaluated the literature and wrote the manuscript. All the authors contributed to the article and approved the submitted version.

FUNDING

This research was funded by the Basic Science Research Program (Grant Numbers 2018R1D1A1B07050867 and 2018R1A2B3006080) and the Korean Research Fellowship (Grant Number 2016H1D3A1909300) of the National Research Foundation (NRF), South Korea.

REFERENCES

Alexis, F., Pridgen, E., Molnar, L. K., and Farokhzad, O. C. (2008). Factors affecting the clearance and biodistribution of polymeric nanoparticles. *Mol. Pharm.* 5, 505–515. doi: 10.1021/mp800051m

Alsehli, M. (2020). Polymeric nanocarriers as stimuli-responsive systems for targeted tumor (cancer) therapy: recent advances in drug delivery. *Saudi Pharm. J.* 28, 255–265. doi: 10.1016/j.jsps.2020.01.004

Bailey, M., Khokhlova, V., Sapozhnikov, O., Kargl, S., and Crum, L. (2003). Physical mechanisms of the therapeutic effect of ultrasound (a review). *Acoust. Phys.* 49, 369–388. doi: 10.1134/1.1591291

Bazban-Shotorbani, S., Hasani-Sadrabadi, M. M., Karkhaneh, A., Serpooshan, V., Jacob, K. I., Moshaverinia, A., et al. (2017). Revisiting structure-property relationship of pH-responsive polymers for drug delivery applications. *J. Control. Release* 253, 46–63. doi: 10.1016/j.jconrel.2017.02.021

Blanco, E., Shen, H., and Ferrari, M. (2015). Principles of nanoparticle design for overcoming biological barriers to drug delivery. *Nat. Biotechnol.* 33:941. doi: 10.1038/nbt.3330

Cabral, H., Matsumoto, Y., Mizuno, K., Chen, Q., Murakami, M., Kimura, M., et al. (2011). Accumulation of sub-100 nm polymeric micelles in poorly permeable tumours depends on size. *Nat. Nanotechnol.* 6:815. doi: 10.1038/nnano.2011.166

Cai, X., Zhu, Q., Zeng, Y., Zeng, Q., Chen, X., and Zhan, Y. (2019). Manganese oxide nanoparticles as MRI contrast agents in tumor multimodal imaging and therapy. *Int. J. Nanomed.* 14, 8321–8344. doi: 10.2147/IJN.S218085

Cao, J., Gao, X., Cheng, M., Niu, X., Li, X., Zhang, Y., et al. (2019). Reversible shielding between dual ligands for enhanced tumor accumulation of ZnPc-loaded micelles. *Nano Lett.* 19, 1665–1674. doi: 10.1021/acs.nanolett.8b04645

Chaffer, C. L., and Weinberg, R. A. (2011). A perspective on cancer cell metastasis. *Science* 331, 1559–1564. doi: 10.1126/science.1203543

Chen, S., Xu, X.-L., Zhou, B., Tian, J., Luo, B.-M., and Zhang, L.-M. (2019). Acidic pH-activated gas-generating nanoparticles with pullulan decorating for hepatoma-targeted ultrasound imaging. *ACS Appl. Mater. Interfaces* 11, 22194–22205. doi: 10.1021/acsami.9b06745

Chen, S. X., and Schopfer, P. (1999). Hydroxyl-radical production in physiological reactions: a novel function of peroxidase. *Eur. J. Biochem.* 260, 726–735. doi: 10.1046/j.1432-1327.1999.00199.x

Cho, E. C., Xie, J., Wurm, P. A., and Xia, Y. (2009). Understanding the role of surface charges in cellular adsorption versus internalization by selectively removing gold nanoparticles on the cell surface with a I2/KI etchant. *Nano Lett.* 9, 1080–1084. doi: 10.1021/nl803487r

Cong, Z., Zhang, L., Ma, S.-Q., Lam, K. S., Yang, F.-F., and Liao, Y.-H. (2020). Size-transformable hyaluronan stacked self-assembling peptide nanoparticles for improved transcellular tumor penetration and photo–chemo combination therapy. *ACS Nano* 14, 1958–1970. doi: 10.1021/acsnano.9b08434

Costley, D., Mc Ewan, C., Fowley, C., Mchale, A. P., Atchison, J., Nomikou, N., et al. (2015). Treating cancer with sonodynamic therapy: a review. *Int. J. Hyperthermia* 31, 107–117. doi: 10.3109/02656736.2014.992484

Couzin, J. (2008). Can fasting blunt chemotherapy's debilitating side effects? *Science* 321, 1146–1147. doi: 10.1126/science.321.5893.1146a

Da Poian, A., Bacha, T., and Luz, M. (2010). Nutrient utilization in humans: metabolic pathways. *Nat. Educ.* 3:11.

Dai, L., Li, X., Yao, M., Niu, P., Yuan, X., Li, K., et al. (2020). Programmable prodrug micelle with size-shrinkage and charge-reversal for chemotherapy-improved IDO immunotherapy. *Biomaterials* 241:119901. doi: 10.1016/j.biomaterials.2020.119901

Danhier, F., Feron, O., and Préat, V. (2010). To exploit the tumor microenvironment: passive and active tumor targeting of nanocarriers for anti-cancer drug delivery. *J. Control. Release* 148, 135–146. doi: 10.1016/j.jconrel.2010.08.027

Deepagan, V., Thambi, T., Ko, H., Kang, Y. M., and Park, J. H. (2013). Amphiphilic polysialic acid derivatives: synthesis, characterization, and in-vitro cytotoxicity. *J. Nanosci. Nanotechnol.* 13, 7312–7318. doi: 10.1166/jnn.2013.8089

Deepagan, V. G., You, D. G., Um, W., Ko, H., Kwon, S., Choi, K. Y., et al. (2016). Long-circulating Au-TiO2 nanocomposite as a sonosensitizer for ROS-mediated eradication of cancer. *Nano Lett.* 16, 6257–6264. doi: 10.1021/acs.nanolett.6b02547

Deirram, N., Zhang, C., Kermaniyan, S. S., Johnston, A. P., and Such, G. K. (2019). pH-responsive polymer nanoparticles for drug delivery. *Macromol. Rapid Commun.* 40:1800917. doi: 10.1002/marc.201800917

Deng, R., Xie, X., Vendrell, M., Chang, Y.-T., and Liu, X. (2011). Intracellular glutathione detection using MnO2-nanosheet-modified upconversion nanoparticles. *J. Am. Chem. Soc.* 133, 20168–20171. doi: 10.1021/ja2100774

Dong, Z., Feng, L., Zhu, W., Sun, X., Gao, M., Zhao, H., et al. (2016). CaCO3 nanoparticles as an ultra-sensitive tumor-pH-responsive nanoplatform enabling real-time drug release monitoring and cancer combination therapy. *Biomaterials* 110, 60–70. doi: 10.1016/j.biomaterials.2016.09.025

Fam, S. Y., Chee, C. F., Yong, C. Y., Ho, K. L., Mariatulqabtiah, A. R., and Tan, W. S. (2020). Stealth coating of nanoparticles in drug-delivery systems. *Nanomaterials* 10:787. doi: 10.3390/nano10040787

Feng, L., Dong, Z., Tao, D., Zhang, Y., and Liu, Z. (2018). The acidic tumor microenvironment: a target for smart cancer nano-theranostics. *Natl. Sci. Rev.* 5, 269–286. doi: 10.1093/nsr/nwx062

Feng, L., Li, K., Shi, X., Gao, M., Liu, J., and Liu, Z. (2014). Smart pH-responsive nanocarriers based on nano-graphene oxide for combined chemo- and photothermal therapy overcoming drug resistance. *Adv. Healthc. Mater.* 3, 1261–1271. doi: 10.1002/adhm.201300549

Feng, Q., Zhang, W., Yang, X., Li, Y., Hao, Y., Zhang, H., et al. (2018). pH/ultrasound dual-responsive gas generator for ultrasound imaging-guided therapeutic inertial cavitation and sonodynamic therapy. *Adv. Healthc. Mater.* 7:1700957.

Feng, Q. H., Zhang, W. X., Yang, X. M., Li, Y. Z., Hao, Y. W., Zhang, H. L., et al. (2018). pH/ultrasound dual-responsive gas generator for ultrasound imaging-guided therapeutic inertial cavitation and sonodynamic therapy. *Adv. Healthc. Mater.* 7:1700957. doi: 10.1002/adhm.201700957

Gao, G. H., Im, G. H., Kim, M. S., Lee, J. W., Yang, J., Jeon, H., et al. (2010). Magnetite-nanoparticle-encapsulated pH-responsive polymeric micelle as an

MRI probe for detecting acidic pathologic areas. *Small* 6, 1201–1204. doi: 10.1002/smll.200902317

Gao, S., Wang, G., Qin, Z., Wang, X., Zhao, G., Ma, Q., et al. (2017). Oxygen-generating hybrid nanoparticles to enhance fluorescent/photoacoustic/ultrasound imaging guided tumor photodynamic therapy. *Biomaterials* 112, 324–335. doi: 10.1016/j.biomaterials.2016.10.030

Gong, F., Cheng, L., Yang, N., Betzer, O., Feng, L., Zhou, Q., et al. (2019). Ultrasmall oxygen-deficient bimetallic oxide MnWOX nanoparticles for depletion of endogenous gsh and enhanced sonodynamic cancer therapy. *Adv. Mater.* 31:1900730. doi: 10.1002/adma.201900730

Gong, F., Yang, N., Wang, X., Zhao, Q., Chen, Q., Liu, Z., et al. (2020). Tumor microenvironment-responsive intelligent nanoplatforms for cancer theranostics. *Nano Today* 32:100851. doi: 10.1016/j.nantod.2020.100851

Guo, Z., Park, S., Yoon, J., and Shin, I. (2014). Recent progress in the development of near-infrared fluorescent probes for bioimaging applications. *Chem. Soc. Rev.* 43, 16–29. doi: 10.1039/C3CS60271K

Han, K., Zhang, W. Y., Zhang, J., Lei, Q., Wang, S. B., Liu, J. W., et al. (2016). Acidity-triggered tumor-targeted chimeric peptide for enhanced intra-nuclear photodynamic therapy. *Adv. Funct. Mater.* 26, 4351–4361. doi: 10.1002/adfm.201600170

He, T., Qin, X., Jiang, C., Jiang, D., Lei, S., Lin, J., et al. (2020). Tumor pH-responsive metastable-phase manganese sulfide nanotheranostics for traceable hydrogen sulfide gas therapy primed chemodynamic therapy. *Theranostics* 10:2453. doi: 10.7150/thno.42981

Hoshyar, N., Gray, S., Han, H., and Bao, G. (2016). The effect of nanoparticle size on in vivo pharmacokinetics and cellular interaction. *Nanomedicine* 11, 673–692. doi: 10.2217/nnm.16.5

Jaque, D., Martínez Maestro, L., Del Rosal, B., Haro-Gonzalez, P., Benayas, A., Plaza, J. L., et al. (2014). Nanoparticles for photothermal therapies. *Nanoscale* 6, 9494–9530. doi: 10.1039/C4NR00708E

Jia, H.-R., Zhu, Y.-X., Liu, X., Pan, G.-Y., Gao, G., Sun, W., et al. (2019). Construction of dually responsive nanotransformers with nanosphere–nanofiber–nanosphere transition for overcoming the size paradox of anticancer nanodrugs. *ACS Nano* 13, 11781–11792. doi: 10.1021/acsnano.9b05749

Jin, T. (2019). Critical review—recent progress in NIR fluorophores emitting over 1000 nm for bioimaging. *ECS J. Solid State Sci. Technol.* 8:R9. doi: 10.1149/2.0111901jss

Kaittanis, C., Shaffer, T. M., Ogirala, A., Santra, S., Perez, J. M., Chiosis, G., et al. (2014). Environment-responsive nanophores for therapy and treatment monitoring via molecular MRI quenching. *Nat. Commun.* 5, 1–11. doi: 10.1038/ncomms4384

Kakkar, A., Traverso, G., Farokhzad, O. C., Weissleder, R., and Langer, R. (2017). Evolution of macromolecular complexity in drug delivery systems. *Nat. Rev. Chem.* 1, 1–17. doi: 10.1038/s41570-017-0063

Kanamala, M., Wilson, W. R., Yang, M., Palmer, B. D., and Wu, Z. (2016). Mechanisms and biomaterials in pH-responsive tumour targeted drug delivery: a review. *Biomaterials* 85, 152–167. doi: 10.1016/j.biomaterials.2016.01.061

Kang, E., Min, H. S., Lee, J., Han, M. H., Ahn, H. J., Yoon, I.-C., et al. (2010). Nanobubbles from gas-generating polymeric nanoparticles: ultrasound imaging of living subjects. *Angew. Chem. Int. Ed.* 49, 524–528. doi: 10.1002/anie.200903841

Kang, H., Hu, S., Cho, M. H., Hong, S. H., Choi, Y., and Choi, H. S. (2018). Theranostic nanosystems for targeted cancer therapy. *Nano Today* 23, 59–72. doi: 10.1016/j.nantod.2018.11.001

Kang, S., Kim, Y., Song, Y., Choi, J. U., Park, E., Choi, W., et al. (2014). Comparison of pH-sensitive degradability of maleic acid amide derivatives. *Bioorgan. Med. Chem. Lett.* 24, 2364–2367. doi: 10.1016/j.bmcl.2014.03.057

Kim, H., Sehgal, D., Kucaba, T. A., Ferguson, D. M., Griffith, T. S., and Panyam, J. (2018). Acidic pH-responsive polymer nanoparticles as a TLR7/8 agonist delivery platform for cancer immunotherapy. *Nanoscale* 10, 20851–20862. doi: 10.1039/C8NR07201A

Kircher, M. F., and Willmann, J. K. (2012). Molecular body imaging: MR imaging, CT, and US. Part I. principles. *Radiology* 263, 633–643. doi: 10.1148/radiol.12102394

Kocak, G., Tuncer, C., and Bütün, V. (2017). pH-Responsive polymers. *Polymer Chem.* 8, 144–176. doi: 10.1039/C6PY01872F

Kong, L., Campbell, F., and Kros, A. (2019). DePEGylation strategies to increase cancer nanomedicine efficacy. *Nanoscale Horizons* 4, 378–387. doi: 10.1039/C8NH00417J

Kumar, E. K. P., Feldborg, L. N., Almdal, K., and Andresen, T. L. (2013). Synthesis and characterization of a micelle-based pH nanosensor with an unprecedented broad measurement range. *Chem. Mater.* 25, 1496–1501. doi: 10.1021/cm302922d

Kumar, E. K. P., Søndergaard, R. V., Windschiegl, B., Almdal, K., and Andresen, T. L. (2014). Cross-linked self-assembled micelle based nanosensor for intracellular pH measurements. *J. Mater. Chem. B* 2, 6652–6659. doi: 10.1039/C4TB00446A

Lei, Q., Wang, S.-B., Hu, J.-J., Lin, Y.-X., Zhu, C.-H., Rong, L., et al. (2017). Stimuli-responsive "cluster bomb" for programmed tumor therapy. *ACS Nano* 11, 7201–7214. doi: 10.1021/acsnano.7b03088

Li, H.-J., Du, J.-Z., Liu, J., Du, X.-J., Shen, S., Zhu, Y.-H., et al. (2016). Smart superstructures with ultrahigh pH-sensitivity for targeting acidic tumor microenvironment: instantaneous size switching and improved tumor penetration. *ACS Nano* 10, 6753–6761. doi: 10.1021/acsnano.6b02326

Li, J., Ji, H., Jing, Y., and Wang, S. (2020). pH-and acoustic-responsive platforms based on perfluoropentane-loaded protein nanoparticles for ovarian tumor-targeted ultrasound imaging and therapy. *Nanoscale Res. Lett.* 15:31. doi: 10.1186/s11671-020-3252-z

Li, L., Sun, W., Zhong, J., Yang, Q., Zhu, X., Zhou, Z., et al. (2015). Multistage nanovehicle delivery system based on stepwise size reduction and charge reversal for programmed nuclear targeting of systemically administered anticancer drugs. *Adv. Funct. Mater.* 25, 4101–4113. doi: 10.1002/adfm.201501248

Li, W.-P., Su, C.-H., Chang, Y.-C., Lin, Y.-J., and Yeh, C.-S. (2016). Ultrasound-induced reactive oxygen species mediated therapy and imaging using a fenton reaction activable polymersome. *ACS Nano* 10, 2017–2027. doi: 10.1021/acsnano.5b06175

Li, X., Zheng, B.-Y., Ke, M.-R., Zhang, Y., Huang, J.-D., and Yoon, J. (2017). A tumor-pH-responsive supramolecular photosensitizer for activatable photodynamic therapy with minimal in vivo skin phototoxicity. *Theranostics* 7:2746. doi: 10.7150/thno.18861

Li, Y., Yang, H. Y., and Lee, D. S. (2016). Polymer-based and pH-sensitive nanobiosensors for imaging and therapy of acidic pathological areas. *Pharm. Res.* 33, 2358–2372. doi: 10.1007/s11095-016-1944-y

Lin, X., Liu, S., Zhang, X., Zhu, R., Chen, S., Chen, X., et al. (2020). An ultrasound activated vesicle of janus Au-MnO nanoparticles for promoted tumor penetration and sono-chemodynamic therapy of orthotopic liver cancer. *Angew. Chem. Int. Ed.* 59, 1682–1688. doi: 10.1002/anie.201912768

Ling, D., Park, W., Park, S.-J., Lu, Y., Kim, K. S., Hackett, M. J., et al. (2014). Multifunctional tumor pH-sensitive self-assembled nanoparticles for bimodal imaging and treatment of resistant heterogeneous tumors. *J. Am. Chem. Soc.* 136, 5647–5655. doi: 10.1021/ja4108287

Liu, J.-N., Bu, W., and Shi, J. (2017). Chemical design and synthesis of functionalized probes for imaging and treating tumor hypoxia. *Chem. Rev.* 117, 6160–6224. doi: 10.1021/acs.chemrev.6b00525

Lu, C., Zhang, C., Wang, P., Zhao, Y., Yang, Y., Wang, Y., et al. (2020). Light-free generation of singlet oxygen through manganese-thiophene nanosystems for pH-responsive chemiluminescence imaging and tumor therapy. *Chem* 6, 2314–2334. doi: 10.1016/j.chempr.2020.06.024

Lu, J., Sun, J., Li, F., Wang, J., Liu, J., Kim, D., et al. (2018). Highly sensitive diagnosis of small hepatocellular carcinoma using pH-responsive iron oxide nanocluster assemblies. *J. Am. Chem. Soc.* 140, 10071–10074. doi: 10.1021/jacs.8b04169

Lucky, S. S., Soo, K. C., and Zhang, Y. (2015). Nanoparticles in photodynamic therapy. *Chem. Rev.* 115, 1990–2042. doi: 10.1021/cr5004198

Ma, B., Wang, S., Liu, F., Zhang, S., Duan, J., Li, Z., et al. (2019). Self-assembled copper–amino acid nanoparticles for in situ glutathione "AND" H2O2 sequentially triggered chemodynamic therapy. *J. Am. Chem. Soc.* 141, 849–857. doi: 10.1021/jacs.8b08714

Ma, T., Hou, Y., Zeng, J., Liu, C., Zhang, P., Jing, L., et al. (2018). Dual-ratiometric target-triggered fluorescent probe for simultaneous quantitative visualization of tumor microenvironment protease activity and pH in Vivo. *J. Am. Chem. Soc.* 140, 211–218. doi: 10.1021/jacs.7b08900

Matsumura, Y., and Maeda, H. (1986). A new concept for macromolecular therapeutics in cancer chemotherapy: mechanism of tumoritropic accumulation of proteins and the antitumor agent smancs. *Cancer Res.* 46, 6387–6392.

Mi, P. (2020). Stimuli-responsive nanocarriers for drug delivery, tumor imaging, therapy and theranostics. *Theranostics* 10:4557. doi: 10.7150/thno.38069

Mi, P., Kokuryo, D., Cabral, H., Wu, H., Terada, Y., Saga, T., et al. (2016). A pH-activatable nanoparticle with signal-amplification capabilities for non-invasive imaging of tumour malignancy. *Nat. Nanotechnol.* 11:724. doi: 10.1038/nnano.2016.72

Miao, Q., Lyu, Y., Ding, D., and Pu, K. (2016). Semiconducting oligomer nanoparticles as an activatable photoacoustic probe with amplified brightness for in vivo imaging of pH. *Adv. Mater.* 28, 3662–3668. doi: 10.1002/adma.201505681

Miao, Q., and Pu, K. (2018). Organic semiconducting agents for deep-tissue molecular imaging: second near-infrared fluorescence, self-luminescence, and photoacoustics. *Adv. Mater.* 30:1801778. doi: 10.1002/adma.201801778

Min, K. H., Min, H. S., Lee, H. J., Park, D. J., Yhee, J. Y., Kim, K., et al. (2015). pH-controlled gas-generating mineralized nanoparticles: a theranostic agent for ultrasound imaging and therapy of cancers. *ACS Nano* 9, 134–145. doi: 10.1021/nn506210a

Mishra, S., Webster, P., and Davis, M. E. (2004). PEGylation significantly affects cellular uptake and intracellular trafficking of non-viral gene delivery particles. *Eur. J. Cell Biol.* 83, 97–112. doi: 10.1078/0171-9335-00363

Mura, S., Nicolas, J., and Couvreur, P. (2013). Stimuli-responsive nanocarriers for drug delivery. *Nat. Mater.* 12, 991–1003. doi: 10.1038/nmat3776

Muthu, M. S., Leong, D. T., Mei, L., and Feng, S.-S. (2014). Nanotheranostics? application and further development of nanomedicine strategies for advanced theranostics. *Theranostics* 4:660. doi: 10.7150/thno.8698

Nowak, A. K., Robinson, B. W., and Lake, R. A. (2002). Gemcitabine exerts a selective effect on the humoral immune response: implications for combination chemo-immunotherapy. *Cancer Res.* 62, 2353–2358.

Parodi, A., Rudzinska, M., Leporatti, S., Anissimov, Y., and Zamyatnin, A. A. (2020). Smart nanotheranostics responsive to pathological stimuli. *Front. Bioeng. Biotechnol.* 8:503. doi: 10.3389/fbioe.2020.00503

Peng, H., Liu, X., Wang, G., Li, M., Bratlie, K. M., Cochran, E., et al. (2015). Polymeric multifunctional nanomaterials for theranostics. *J. Mater. Chem. B* 3, 6856–6870. doi: 10.1039/C5TB00617A

Peng, N., Yu, H., Yu, W., Yang, M., Chen, H., Zou, T., et al. (2020). Sequential-targeting nanocarriers with pH-controlled charge reversal for enhanced mitochondria-located photodynamic-immunotherapy of cancer. *Acta Biomater.* 105, 223–238. doi: 10.1016/j.actbio.2020.01.005

Qi, T., Chen, B., Wang, Z., Du, H., Liu, D., Yin, Q., et al. (2019). A pH-Activatable nanoparticle for dual-stage precisely mitochondria-targeted photodynamic anticancer therapy. *Biomaterials* 213:119219. doi: 10.1016/j.biomaterials.2019.05.030

Qian, X., Zheng, Y., and Chen, Y. (2016). Micro/nanoparticle-augmented sonodynamic therapy (SDT): breaking the depth shallow of photoactivation. *Adv. Mater.* 28, 8097–8129. doi: 10.1002/adma.201602012

Rosenblum, D., Joshi, N., Tao, W., Karp, J. M., and Peer, D. (2018). Progress and challenges towards targeted delivery of cancer therapeutics. *Nat. Commun.* 9, 1–12. doi: 10.1038/s41467-018-03705-y

Schöttler, S., Becker, G., Winzen, S., Steinbach, T., Mohr, K., Landfester, K., et al. (2016). Protein adsorption is required for stealth effect of poly (ethylene glycol)- and poly (phosphoester)-coated nanocarriers. *Nat. Nanotechnol.* 11:372. doi: 10.1038/nnano.2015.330

Siegel, R. L., Miller, K. D., and Jemal, A. (2020). Cancer statistics, 2020. *CA Cancer J. Clin.* 70, 7–30. doi: 10.3322/caac.21590

Søndergaard, R. V., Christensen, N. M., Henriksen, J. R., Kumar, E. P., Almdal, K., and Andresen, T. L. (2015). Facing the design challenges of particle-based nanosensors for metabolite quantification in living cells. *Chem. Rev.* 115, 8344–8378. doi: 10.1021/cr400636x

Sun, I.-C., and Emelianov, S. (2019). Gas-generating nanoparticles for contrast-enhanced ultrasound imaging. *Nanoscale* 11, 16235–16240. doi: 10.1039/C9NR04471J

Sun, Q., Sun, X., Ma, X., Zhou, Z., Jin, E., Zhang, B., et al. (2014). Integration of nanoassembly functions for an effective delivery cascade for cancer drugs. *Adv. Mater.* 26, 7615–7621. doi: 10.1002/adma.201401554

Swietach, P., Vaughan-Jones, R. D., and Harris, A. L. (2007). Regulation of tumor pH and the role of carbonic anhydrase 9. *Cancer Metastasis Rev.* 26, 299–310. doi: 10.1007/s10555-007-9064-0

Tang, Z., Liu, Y., He, M., and Bu, W. (2019). Chemodynamic therapy: tumour microenvironment-mediated Fenton and Fenton-like reactions. *Angew. Chem. Int. Ed.* 58, 946–956. doi: 10.1002/anie.201805664

Thews, O., Gassner, B., Kelleher, D. K., Schwerd, G., and Gekle, M. (2006). Impact of extracellular acidity on the activity of P-glycoprotein and the cytotoxicity of chemotherapeutic drugs. *Neoplasia* 8, 143–152. doi: 10.1593/neo.05697

Tian, J., Zhou, J., Shen, Z., Ding, L., Yu, J.-S., and Ju, H. (2015). A pH-activatable and aniline-substituted photosensitizer for near-infrared cancer theranostics. *Chem. Sci.* 6, 5969–5977. doi: 10.1039/C5SC01721A

Tian, Q., Li, Y., Jiang, S., An, L., Lin, J., Wu, H., et al. (2019). Tumor pH-responsive albumin/polyaniline assemblies for amplified photoacoustic imaging and augmented photothermal therapy. *Small* 15:1902926. doi: 10.1002/smll.201902926

Trachootham, D., Alexandre, J., and Huang, P. (2009). Targeting cancer cells by ROS-mediated mechanisms: a radical therapeutic approach? *Nat. Rev. Drug Discov.* 8, 579–591. doi: 10.1038/nrd2803

Vander Heiden, M. G., Cantley, L. C., and Thompson, C. B. (2009). Understanding the Warburg effect: the metabolic requirements of cell proliferation. *Science* 324, 1029–1033. doi: 10.1126/science.1160809

Vaupel, P., and Harrison, L. (2004). Tumor hypoxia: causative factors, compensatory mechanisms, and cellular response. *Oncologist* 9, 4–9. doi: 10.1634/theoncologist.9-90005-4

Vidallon, M. L. P., Douek, A. M., Quek, A., Mcliesh, H., Kaslin, J., Tabor, R. F., et al. (2020). Gas-Generating, pH-responsive calcium carbonate hybrid particles with biomimetic coating for contrast-enhanced ultrasound imaging. *Particle Particle Syst. Charact.* 37:1900471. doi: 10.1002/ppsc.201900471

Wang, C., Cheng, L., Liu, Y., Wang, X., Ma, X., Deng, Z., et al. (2013). Imaging-guided pH-sensitive photodynamic therapy using charge reversible upconversion nanoparticles under near-infrared light. *Adv. Funct. Mater.* 23, 3077–3086. doi: 10.1002/adfm.201202992

Wang, C., Zhao, T., Li, Y., Huang, G., White, M. A., and Gao, J. (2017). Investigation of endosome and lysosome biology by ultra pH-sensitive nanoprobes. *Adv. Drug Deliv. Rev.* 113, 87–96. doi: 10.1016/j.addr.2016.08.014

Wang, H., Han, X., Dong, Z., Xu, J., Wang, J., and Liu, Z. (2019). Hyaluronidase with pH-responsive dextran modification as an adjuvant nanomedicine for enhanced photodynamic-immunotherapy of cancer. *Adv. Funct. Mater.* 29:1902440. doi: 10.1002/adfm.201902440

Wang, J., Mao, W., Lock, L. L., Tang, J., Sui, M., Sun, W., et al. (2015). The role of micelle size in tumor accumulation, penetration, and treatment. *ACS Nano* 9, 7195–7206. doi: 10.1021/acsnano.5b02017

Wang, X., Niu, D., Wu, Q., Bao, S., Su, T., Liu, X., et al. (2015). Iron oxide/manganese oxide co-loaded hybrid nanogels as pH-responsive magnetic resonance contrast agents. *Biomaterials* 53, 349–357. doi: 10.1016/j.biomaterials.2015.02.101

Wang, X., Zhong, X., Bai, L., Xu, J., Gong, F., Dong, Z., et al. (2020). Ultrafine titanium monoxide (TiO1+x) nanorods for enhanced sonodynamic therapy. *J. Am. Chem. Soc.* 142, 6527–6537. doi: 10.1021/jacs.9b10228

Wang, Z., Deng, X., Ding, J., Zhou, W., Zheng, X., and Tang, G. (2018). Mechanisms of drug release in pH-sensitive micelles for tumour targeted drug delivery system: a review. *Int. J. Pharm.* 535, 253–260. doi: 10.1016/j.ijpharm.2017.11.003

Warburg, O., Wind, F., and Negelein, E. (1927). The metabolism of tumors in the body. *J. Gen. Physiol.* 8, 519–530. doi: 10.1085/jgp.8.6.519

Webb, B. A., Chimenti, M., Jacobson, M. P., and Barber, D. L. (2011). Dysregulated pH: a perfect storm for cancer progression. *Nat. Rev. Cancer* 11, 671–677. doi: 10.1038/nrc3110

Wilhelm, S., Tavares, A. J., Dai, Q., Ohta, S., Audet, J., Dvorak, H. F., et al. (2016). Analysis of nanoparticle delivery to tumours. *Nat. Rev. Mater.* 1, 1–12. doi: 10.1038/natrevmats.2016.14

Wu, W., Luo, L., Wang, Y., Wu, Q., Dai, H.-B., Li, J.-S., et al. (2018). Endogenous pH-responsive nanoparticles with programmable size changes for targeted tumor therapy and imaging applications. *Theranostics* 8:3038. doi: 10.7150/thno.23459

Yang, G., Xu, L., Xu, J., Zhang, R., Song, G., Chao, Y., et al. (2018). Smart Nanoreactors for pH-responsive tumor homing, mitochondria-targeting, and enhanced photodynamic-immunotherapy of cancer. *Nano Lett.* 18, 2475–2484. doi: 10.1021/acs.nanolett.8b00040

Yang, H. Y., Jang, M.-S., Li, Y., Fu, Y., Wu, T. P., Lee, J. H., et al. (2019). Hierarchical tumor acidity-responsive self-assembled magnetic nanotheranostics for bimodal bioimaging and photodynamic therapy. *J. Control. Release* 301, 157–165. doi: 10.1016/j.jconrel.2019.03.019

Yang, H. Y., Li, Y., and Lee, D. S. (2020). Recent advances of pH-induced charge-convertible polymer-mediated inorganic nanoparticles for biomedical applications. *Macromol. Rapid Commun.* 2020:2000106. doi: 10.1002/marc.202000106

Yao, D., Shi, W., Gou, Y., Zhou, X., Aw, T. Y., Zhou, Y., et al. (2005). Fatty acid-mediated intracellular iron translocation: a synergistic mechanism of oxidative injury. *Free Radic. Biol. Med.* 39, 1385–1398. doi: 10.1016/j.freeradbiomed.2005.07.015

You, D. G., Deepagan, V., Um, W., Jeon, S., Son, S., Chang, H., et al. (2016). ROS-generating TiO 2 nanoparticles for non-invasive sonodynamic therapy of cancer. *Sci. Rep.* 6:23200. doi: 10.1038/srep23200

Yuan, Y. Y., Mao, C. Q., Du, X. J., Du, J. Z., Wang, F., and Wang, J. (2012). Surface charge switchable nanoparticles based on zwitterionic polymer for enhanced drug delivery to tumor. *Adv. Mater.* 24, 5476–5480. doi: 10.1002/adma.201202296

Zhang, C., Chen, W. H., Liu, L. H., Qiu, W. X., Yu, W. Y., and Zhang, X. Z. (2017a). An O2 self-supplementing and reactive-oxygen-species-circulating amplified nanoplatform via H2O/H2O2 splitting for tumor imaging and photodynamic therapy. *Adv. Funct. Mater.* 27:1700626. doi: 10.1002/adfm.201700626

Zhang, C., Ni, D., Liu, Y., Yao, H., Bu, W., and Shi, J. (2017b). Magnesium silicide nanoparticles as a deoxygenation agent for cancer starvation therapy. *Nat. Nanotechnol.* 12:378. doi: 10.1038/nnano.2016.280

Zhang, M., Chen, X., Li, C., and Shen, X. (2020). Charge-reversal nanocarriers: an emerging paradigm for smart cancer nanomedicine. *J. Control. Release* 319, 46–62. doi: 10.1016/j.jconrel.2019.12.024

Zhao, P., Zheng, M., Luo, Z., Fan, X., Sheng, Z., Gong, P., et al. (2016). Oxygen nanocarrier for combined cancer therapy: oxygen-boosted ATP-responsive chemotherapy with amplified ROS lethality. *Adv. Healthc. Mater.* 5, 2161–2167.

Zhu, P., Chen, Y., and Shi, J. (2018). Nanoenzyme-augmented cancer sonodynamic therapy by catalytic tumor oxygenation. *ACS Nano* 12, 3780–3795. doi: 10.1021/acsnano.8b00999

Zhu, W., Dong, Z., Fu, T., Liu, J., Chen, Q., Li, Y., et al. (2016). Modulation of hypoxia in solid tumor microenvironment with MnO2 nanoparticles to enhance photodynamic therapy. *Adv. Funct. Mater.* 26, 5490–5498. doi: 10.1002/adfm.201600676

Conflict of Interest: The authors declare that the research was conducted in the absence of any commercial or financial relationships that could be construed as a potential conflict of interest.

frontiers in Bioengineering and Biotechnology

ORIGINAL RESEARCH
published: 07 December 2020
doi: 10.3389/fbioe.2020.586874

Tumor Targeted Multifunctional Magnetic Nanobubbles for MR/US Dual Imaging and Focused Ultrasound Triggered Drug Delivery

*Zhen Jin[1], Jinlong Chang[1], Peipei Dou[2], Shang Jin[2], Min Jiao[2], Heyun Tang[2], Wenshuai Jiang[1], Wu Ren[1] and Shaohui Zheng[2]**

[1] College of Biomedical Engineering, Xinxiang Medical University, Xinxiang, China, [2] School of Medical Imaging, Xuzhou Medical University, Xuzhou, China

OPEN ACCESS

Edited by:
Saji Uthaman,
Chungnam National University,
South Korea

Reviewed by:
Lionel Fernel Gamarra,
Instituto do Cérebro, Hospital Israelita Albert Einstein, Brazil
Xiaoning Jiang,
North Carolina State University, United States
Johnson Vitharikunnil John,
University of Nebraska Medical Center, United States

***Correspondence:**
Shaohui Zheng
shaohui19910@163.com

Specialty section:
This article was submitted to Nanobiotechnology, a section of the journal Frontiers in Bioengineering and Biotechnology

Received: 24 July 2020
Accepted: 16 October 2020
Published: 07 December 2020

Citation:
Jin Z, Chang J, Dou P, Jin S, Jiao M, Tang H, Jiang W, Ren W and Zheng S (2020) Tumor Targeted Multifunctional Magnetic Nanobubbles for MR/US Dual Imaging and Focused Ultrasound Triggered Drug Delivery. Front. Bioeng. Biotechnol. 8:586874. doi: 10.3389/fbioe.2020.586874

The development of multifunctional nanoplatforms that are safe and have multiple therapeutic functions integrated with dual- or multi-imaging modality is one of the most urgent medical requirements for active cancer therapy. In our study, we prepared multifunctional magnetic nanobubbles (MF-MNBs) by co-encapsulating superparamagnetic iron oxide nanoparticles (SPIONs) and doxorubicin into polylactideco–glycolide–polyethylene glycol–folate (PLGA-PEG-FA) polymer-based nanobubbles for tumor-targeted ultrasound (US)/magnetic resonance (MR) imaging and focused ultrasound (FUS)-triggered drug delivery. Hydrophobic SPIONs were successfully embedded into MF-MNBs by a typical double emulsion process. The MF-MNBs were highly dispersed with well-defined spherical morphology and an average diameter of 208.4 ± 12.58 nm. The potential of MF-MNB as a dual-modal contrast agent for US and MR imaging was investigated via *in vitro* study, and the MF-MNB exhibits promising US/MR contrast ability. Moreover, tumor targeting ability was further enhanced by folate conjugation and assessed through *in vitro* cell test. Furthermore, FUS, as a non-invasive and remote-control technique, was adopted to trigger the release of doxorubicin from MF-MNB and generate the sonoporation effect to enhance drug release and cellular uptake of MF-MNBs. The 4T1 cell viability was significantly decreased by FA ligand-receptor-mediated targeting and FUS sonication. In addition, the developed MF-MNB also exhibits enhanced accumulation in tumor site by FA ligand-receptor-mediated tumor targeting, in which the accumulation of MF-MNB was further enhanced by FUS sonication. Hence, we believe that the MF-MNB could be a promising drug nanocarrier for US/MR-guided anticancer drug delivery to improve cancer treatment efficacy.

Keywords: multifunctional magnetic nanobubbles, US/MR imaging, tumor targeting, focused ultrasound controlled release, enhanced cellular uptake

INTRODUCTION

Cancer has been one of the leading causes of death in the world according to world cancer statistics (Zeng et al., 2019). Conventionally, cancer treatment mainly includes chemotherapy, radiotherapy, and clinical surgery. Although these therapeutic approaches can significantly inhibit cancer growth, they could be accompanied by severe side effects, such as systemic toxicity, recurrence, or physiologic dysfunction (Kievit and Zhang, 2011). Recently, the rapid development of nanotechnology has significantly influenced the strategy of cancer diagnosis and treatment. Various nanomaterials have been proposed as therapeutic drug carriers to achieve efficient therapy by enhancing the availability of therapeutic drugs and reducing side effects (Shi et al., 2017). Nanocarrier accumulation in solid tumor is generally based on the enhanced permeability and retention (EPR) effect, also called passive targeting (Maeda, 2010). However, the intravenously administered nanocarriers faced with physical and biological barriers [for example, intratumoral pressure, shear forces and binding-site effect, mononuclear phagocytic system (MPS) sequestration, and renal clearance] expected therapeutic outcomes that occur only if the nanocarriers could overcome the barriers to accumulate in tumor at a sufficiently high dosage (Rosenblum et al., 2018). Generally, the passive accumulation efficiency is highly heterogeneous and depends on the nanocarrier's property, tumor size, location, and progress state (Blanco et al., 2015). Therefore, extensive efforts have been devoted to develop multifunctional nanocarriers that combine therapeutic and diagnostic capabilities in a single probe to achieve imaging-guided cancer therapy (Kalidoss et al., 2019; Wang et al., 2020), which enables one to monitor the distribution and accumulation of nanocarriers and evaluate the treatment efficiency during and after therapy.

Furthermore, for accurate cancer imaging, it is meaningful to design multifunctional nanocarriers that afford dual- or multi-modal imaging as each imaging modality has its own limitations and advantages (Ju et al., 2019). Ultrasound (US) has been extensively used as a diagnostic tool in clinical application because of its non-invasiveness, high biosafety, and low cost. Moreover, US is also a promising external stimulus to trigger the drug release and enhance cellular uptake compared with other external stimuli, such as near-infrared (NIR) light, magnetic field, and electric field (Mura et al., 2013), because US is easy to focus and penetrates deeply into soft tissue in a non-invasive manner. However, US has also exhibited poor deep tissue discrimination ability ascribed to its low image resolution (Jain et al., 2018). In contrast, magnetic resonance (MR) imaging is a powerful, non-invasive technique to obtain real-time images containing morphological and functional information with high resolution (Li et al., 2015). Gas-filled microbubbles (MBs) and superparamagnetic iron oxide nanoparticles (SPIONs) are clinically used contrast agents for US and MR imaging, respectively (Geers et al., 2012; Li et al., 2015). For MR imaging, there are numerous promising design strategies for drug nanocarriers that can also act as MRI contrast agent (Zhu et al., 2017). However, effective ultrasonography generally requires enough large-sized MBs to obtain sufficient resonance reflection at the diagnostic US frequency. On the other hand, for effective anticancer drug delivery, it is essential to develop nanosized contrast agents that can efficiently penetrate through the leaky vasculature and accumulate inside tumors (the gaps range in tumor vasculature is 600 to 800 nm) (Blanco et al., 2015). Therefore, it remains a critical challenge to integrate the advantage of nanosized contrast agents with long circulation and EPR effect-induced accumulation in tumor sites and micrometer-sized MBs with effective US responsibility (Cui et al., 2019).

In the past decade, extensive efforts have been devoted to design nanocarriers to handle the above critical problem. For example, M.A. Malvindi et al. (2011) presented a magnetic iron oxide nanoparticle decorated silica nanocomposites that can enhance US imaging and T_2-weighted MR imaging signals. The authors found that the nanocomposites exhibited significant US backscatter enhancement and heightened T_2-weighted MR signal intensity. However, the low biodegrability, unclear biological effect, and long-term toxicity should be further addressed for clinical application. H. Tang et al. fabricated a liquid-formed PFH and SPIO-loaded PLGA nanoparticles for US and MR imaging. The phase of PFH could be changed from liquid to gas when the environment temperature elevated to 56°C by HIFU sonication (Tang et al., 2018). Therefore, the enhanced US imaging signal is only effective in the area upon HIFU sonication. Moreover, Prabhakar and Banerjee (2019) also illustrated submicron-sized nanobubble-paclitaxel liposome for US imaging and anticancer drug delivery. However, the soft and unstable structure of the liposome will result in easy dissolution of gas. Thus, the further modification of nanomaterials for MR imaging will be limited due to the complex structure. Recent studies have reported that the presence of SPIO nanoparticles in the bubble shell can alter the surface tension of bubbles, boost the acoustic impedance, and enhance the detectable backscatter, leading to enhanced US imaging signal (Huang et al., 2013). Sun et al. reported magnetite-loaded polypeptide-PLGA-iron MBs for dual-modal US/MR imaging for prostatic cancer (Sun et al., 2016). However, when used in diagnostic US, the MBs easily become trapped in the blood pool and are limited to the vascular system after intravenous injection attributed to their micro-scaled size, hindering their application in tumor-targeted therapy and imaging (Zhang et al., 2014). The ideal nanocarrier for US/MR imaging should be biocompatible and biodegradable, have a long circulation lifetime, and be smaller than a certain size to retain EPR effect and active tumor targeting.

Here, in this study, we presented novel multifunctional magnetic nanobubbles (MF-MNBs) that are biocompatible and biodegradable, and combined them with the functions of a MR/US dual image contrast agent, focused ultrasound (FUS)-triggered drug release, and FA ligand-receptor-mediated active tumor targeting, which was prepared by a one-pot double emulsion process. First, we synthesized the PLGA-PEG-FA copolymer using reported carbodimide reaction, in which the PEG chain could prolong the circulation half-life in the bloodstream and the folate ligand could enable active tumor targeting. Then, SPIO nanoparticles were fabricated with

a conventional chemical co-precipitated method with slight modification. Subsequently, MF-MNBs were prepared by co-encapsulating anticancer drugs DOX and SPIO in PLGA-PEG-FA nanobubbles with a one-pot double emulsion method and later filling them with perfluorocarbon gas. The MF-MNB exhibits promising US and MR image contrast capability due to the densely aggregated SPIO nanoparticles in the bubble shell to provide excellent magnetic property and enhance US signal. Moreover, significantly faster and higher DOX release from MF-MNBs was achieved by FUS triggering. In addition, the cellular uptake and cytotoxicity were dramatically enhanced by FA receptor-mediated targeting and FUS sonication. Moreover, the MF-MNB exhibits enhanced accumulation in tumor site by FA receptor-mediated tumor targeting, and it was then further enhanced by FUS sonication. Therefore, we believe that the developed MF-MNB could be a promising drug nanocarrier for US/MR dual-image guided drug delivery for efficiently treat cancer.

MATERIALS AND METHODS

Materials

Iron(II) chloride, iron(III) chloride, oleic acid, sodium hydroxide, chlorhydric acid, 4,6-diamidino-2-phenylindole (DAPI), 3-(4,5-dimethylthiazol-2-yl)-2,5-diphenyltetrazolium bromide) (MTT), polyvinylalcohol (PVA, MW = 30–70 kDa), poly(lacticco-glycolic acid) (PLGA, molar ratio of 50:50, MW = 7000–17,000), N-hydroxysuccinimide (NHS), dicyclohexyl carbodiimide (DCC), dichloromethane (DCM), dimethyl sulfoxide (DMSO), and folic acid were purchased from Sigma-Aldrich. Poly(ethylene glycol amine) (PEG-diamine, MW 3400) was received from Laysan Bio, Inc., Doxorubicin (DOX) was bought from Beijing HuaFeng United Technology Co., Ltd. Cell culture medium [Dulbecco's modified Eagle's medium (DMEM)], penicillin, streptomycin, and fetal bovine serum (FBS) were obtained from Gibco BRL (Annapolis, MD, United States). All chemicals were of analytical grade and used without further purification, and all aqueous solutions were prepared using ultrapure water from a Milli-Q system (Millipore, Billerica, MA, United States).

Synthesis of PLGA-PEG-FA Polymers

The fabrication of PLGA-PEG-FA was prepared with carbodimide reaction with the following two steps: coupling of PLGA and PEG, followed by FA conjugation (Jain et al., 2012). Briefly, PLGA was activated by DCC and NHS in DCM solvent for 24 h. Then, PEG-diamine was added in the resultant solution for 12 h. The product from the abovementioned reaction step was washed and purified with ice-cold diethyl ether, followed by completely drying under vacuum. Thereafter, the final PLGA-PEG product was dissolved in DMSO and dialyzed (MWCO: 3.5 kDa) against DI water for 2 days, and the product was freeze-dried for 2 days. For FA conjugation, FA was firstly activated with DCC for 2 h. Then, the PLGA-PEG-NH_2 dissolved in DMSO was added to activated FA solution in a dropwise manner (PLGA-PEG-NH_2:FA:DCC = 1:2:2.5). The reaction was performed under nitrogen gas protection at room temperature for 12 h. Then, the solution was dialyzed (MWCO: 3.5 kDa) against distilled water for 48 h to remove the unreacted FA and freeze-dried to obtain the PLGA-PEG-FA product.

Synthesis of Superparamagnetic Iron Oxide (SPIO) Nanoparticles

Hydrophobic SPIO was synthesized using a chemical co-precipitation method with slight modification (Schleich et al., 2013). Briefly, 10 mmol iron(III) chloride and 5 mmol iron(II) chloride were dissolved in 24 ml of HCl aqueous solution (1M). Then, the solution was added dropwise to an aqueous solution of NaOH (1M) under vigorous mechanical stirring for 60 min with the protection of dry nitrogen at room temperature. Then, 3 g of oleic acid was added and stirred for another 30 min at 80°C. Thereafter, the black precipitate was magnetically separated, washed thrice using anhydrous ethanol, and then dispersed in 20 ml of methylene chloride. The solution was then placed in an ultrasonic bath for 10 min and centrifuged (2000 rpm, 10 min) to remove the undispersed residue.

Synthesis of Multifunctional Magnetic Nanobubble (MF-MNB)

MF-MNB was fabricated by a double water/oil/water (W/O/W) emulsion solvent evaporation method (Sun et al., 2012). Briefly, 1 ml (0, 10, 20, 30, 40, and 50 mg/ml) of SPIO was mixed with the organic solution of the PLGA-PEG-FA solution (100 mg of polymer in 2 ml of methylene chloride). Then, 0.3 ml of DOX solution (10 mg of DOX dissolved in 0.3 ml of deionized water) was added to the previous organic phase. Thereafter, the mixture was emulsified by sonication for 1 min at 300 W (JY92-II, Ningbo Scientz Biotechnology Co., Ltd., China). Subsequently, 10 ml of poly(vinyl alcohol) (PVA) solution (5 wt%) was added to this resultant emulsion, and the mixture was then further sonicated in an ice bath for 5 min. The resultant double emulsion was diluted in 50 ml of PVA solution (0.5 wt%) under mechanical stirring at room temperature overnight to evaporate the residual methylene chloride from the prepared MF-MNBs. Then, the MF-MNB solution was centrifuged and washed thrice with DI water to obtain the pure MF-MNBs. Finally, the MF-MNBs were freeze-dried, filled with perfluorocarbon (C_3F_8) gas, and stored in a freezer at 4°C for further use. Moreover, the PLGA MNB and PLGA-PEG MNB were prepared with the same process for the negative control group test. The amount of SPIO encapsulated in the MF-MNB was measured by inductively coupled plasma optical emission spectroscopy (ICP-OES), and the amount of DOX was measured using a calibration curve of DOX at a wavelength of 480 nm. The DOX loading capacity was calculated as $W = W_{totoal\ DOX} - W_{DOX}$ in supernatant.

Characterizations of MF-MNBs

The structure and the percentage of the actual molar compositions of PLGA-PEG-FA were determined by ^1H

NMR analysis and the copolymer structures were confirmed by FT-IR using KBr disk (Thermo Nicolet Nexus 670, Ramsey, MN, United States). The morphology and structure of SPIO and MF-MNB were observed via a scanning electron microscope (SEM, SS-550; Shimadzu, Kyoto, Japan) and a transmission electron microscope (TEM, JEM-2100F, JEOL Ltd, Tokyo, Japan). The mean diameter, size distribution, and zeta potential of MF-MNB were measured by a DLS method in a Zetasizer nano ZS90 analyzer (Malvern Instruments Ltd., United Kingdom). The magnetization property was further evaluated using a vibrating sample magnetometer (VSM, Lake Shore Cryotronics 7404, Westerville, OH) at room temperature.

In vitro US and MR Imaging

In vitro US imaging was performed to evaluate the US contrast behavior of magnetic nanobubbles in 1% agarose gel mold, which was prepared with a casting method (Prabhakar and Banerjee, 2019). US images of air, degassed water, MF-MNB with different concentration of nanobubbles without SPIO loading, and MF-MNB with the same nanobubbles but different weight percent of SPIO were acquired by placing the samples in the holes of agarose phantom. An ultrasonic imaging system (alpinion medical system; E-CUBE-12R) with a 7.5-MHz US transducer was used as a transmitter and a receiver. All US images were acquired with the same instrument parameters (Mechanical Index, MI = 0.1; gain = 10 dB).

All MR imaging studies were performed on a Philips Achieva 3.0-T MRI scanner (Philips Achieva 3.0T TX, Philips Medical Systems, Netherlands). Magnetic nanobubbles were diluted to final iron concentrations of 0, 0.025, 0.05, 0.1, 0.2, 0.4, and 1.2 mM in PBS (pH 7.4) and placed in Eppendorf tubes of 1 cm in diameter. T_2-weighted (T_2 WI) images were obtained using the following parameters: repetition time (TR) = 72 ms, echo time (TE) = 9 ms, and slice thickness of 3.0 mm. The MRI signal intensity within the region of interest (ROI) was also measured.

FUS System Setup for Triggering Drug Release and Cell Test

The FUS system setup for triggering drug release and cell test was similar to our previous study (Zheng et al., 2016; Jin et al., 2017). Briefly, a single element US transducer (aperture diameter: 30 mm, focal length: 29.7 mm, frequency: 925 kHz) was employed to generate US, and a function generator (33210A, Agilent, Palo Alto Ca, United States) was applied to create burst signal. A power amplifier (HAS-4014, NF Corporation, Yokohama, Japan) was used to amplify the signal from the function generator, and a self-assembled external impedance matching circuit was used to match the electric impedance of the acoustic transducer with the output impedance of the amplifier. A needle-type polyvinylidene fluoride (PVDF) hydrophone with a sensing element of 0.2 mm (Precision Acoustics; Dorchester, United Kingdom) was adopted to measure the acoustic pressure in a tank filled with degassed and distilled water. The half-maximum pressure amplitude at the focal point of FUS has a diameter of 5.6 mm. All experiments were performed in a tank containing degassed water at 37°C. The FUS irradiation was applied at a frequency of 925 kHz, a pulse length of 1000 cycles, and a pulse repetition frequency (PRF) of 20 Hz.

FUS-triggered Drug Release

The *in vitro* DOX release from MF-MNB was investigated in the presence and absence of the FUS triggering. Briefly, 10 mg of MF-MNB with an SPIO weight percent of 17.6 wt% was dispersed in 5 ml of PBS solution (pH 7.4) and transferred to a dialysis bag (MWCO: 3500 Da). Then, the dialysis bag was placed in a sample holder in a test tube containing 50 ml of PBS in which the bottom wall is silicon membrane. After 3 min of FUS triggering, the sample was transferred to a shaking reservoir at 150 rpm at 37°C (Zhang et al., 2014). Thereafter, 1 ml of medium was removed from the samples and stored at −20°C for further analysis, and 1 ml of fresh PBS was added back to the tube to maintain a constant volume. The concentration of DOX in each sample was analyzed using a plate reader system. Then, the accumulative rates of the release DOX were calculated as a function of time. Controls were performed using the same setup and time scale, but without FUS triggering.

In vitro Cellular Uptake and Cellular Imaging

Enhanced intracellular uptake of MF-MNB mediated by folic acid and FUS irradiation was quantitatively analyzed by ICP-OES according to the analytical method. A total of 2×10^4 of 4T1 cells were seeded in 48-well plates and incubated overnight for cell attachment: a part of 4T1 cells were pretreated with a high dose of free FA for 4 h to block the FA receptors. Then, cells were incubated with MF-MNB for 4 h to allow cellular uptake, and the FUS was applied to the corresponding samples for 3 min to further enhance cellular uptake. Subsequently, cells were washed with ice-cold PBS (pH 7.4) thrice; 500 μl of radioimmunoprecipitation assay (RIPA) lysis and extraction buffer was added to each well and incubated for 30 min to allow lysate extraction from cells. The iron content in the cell lysates was analyzed by ICP-OES, and the protein content of cell lysates was measured according to the standard bovine serum albumin (BSA) assay performed.

The cellular uptake efficiency of the developed MF-MNB with FUS triggering was also evaluated. 4T1 cells were seeded on culture slides at a density of 10^5 cells per well (1.7 cm^2 of surface area per well) and incubated for 24 h at 37°C. Then, the medium was replaced with free DOX, blank MF-MNB, and DOX-loaded MF-MNB solutions. Then, certain groups were treated with FUS for 5 min and incubated for another 2 h at 37°C. The cells were washed with PBS (pH 7.4) and fixed with 4% formaldehyde solution for 10 min. Then, the samples were mounted after complete drying of the liquid with mounting medium with 4,6-diamidino-2-phenylindole (DAPI; H-1200, Vector Laboratories, Inc., CA, United States) to prevent fading. The slides were observed using confocal laser scanning microscopy (LSM510, Zeiss, Germany).

Cell Cytotoxicity Test

The cytotoxicity was determined by live and dead cell detection and a standard MTT cell proliferation assay. Briefly, 4T1 breast cancer cells were seeded at a density of 1×10^4 cell per well in 96-well plates and incubated for 24 h for cell attachment. Then, the used medium was replaced with free DOX, DOX-unloaded MN-MNB, and DOX loaded MF-MNB solutions (DOX concentration of 10 μg/ml). After 12 h, the cell wells were placed on a sample holder at 37°C and a certain group was triggered with FUS for 3 min. After further incubation for 6 h, supernatants were removed. Then, the cells were stained with calcein AM and PI, and the live and dead cells were observed with fluorescence microscope images (Nikon, United States). For the cell viability test, the cells were treated with the same drug formula mentioned above and a certain group was treated with FUS for 3 min. After further 12-h incubation, the wells were washed twice with PBS and incubated with DMEM containing MTT (5 mg/ml) for another 4 h. The MTT solution was removed and dimethyl sulfoxide (DMSO) was added to dissolve the cells for spectrum measurement. The absorbance at 570 nm was measured by a microplate reader (Thermo Scientific, Waltham, CA, United States).

In vivo Biodistribution and Pathological Analysis

For *in vivo* biodistribution test, 8-week old BALB/c mice bearing 4T1 breast cancer tumors were prepared. All animal care and procedures were conducted according to the protocols approved by the Xinxiang Medical University Animal Research Committee (Xinxiang, Henan, China). For the 4T1 tumor-bearing mouse model, 1×10^7 cells in 100 μl of serum free RMPI-1640 medium were subcutaneously injected onto the back side of each mouse. The mouse models were used when their tumor volumes approached 60–70 mm^3. To determine the *in vivo* biodistribution of MF-MNB, 4T1 tumor-bearing mice were i.v. injected with MF-MNB, and a certain group was sonicated with FUS for 3 min. Then, the mice were sacrificed at 4 and 24 h. Major tissues (heart, lung, liver, spleen, kidney, and tumor) from these mice were collected and weighted. Subsequently, the tissues were disrupted by TissueRuptor (QIAGEN) and digested using 6 ml of 65% HNO_3 and 4 ml of 30% H_2O_2 solution at 80°C. The digested samples were diluted with deionized water to a total volume of 25 ml. Thereafter, the iron concentration in each sample was evaluated by inductively coupled plasma optical spectrometry (ICP-OES). For the pathological analysis, the 4T1 tumor-bearing mice were sacrificed at 7 days and 21 days post injection of MF-MNB. Major organs were collected, fixed in 10% formalin solution, processed routinely into paraffin, sectioned at 8 μm, stained with hematoxylin–eosin, and examined with a digital microscope (Nikon United States).

Statistical Analysis

One-way ANOVA was performed to evaluate the significance of multiple groups. $p < 0.05$ was selected as the significance level, and the data were indicated (*) for $p < 0.05$, (**) for $p < 0.01$, and (***) for $p < 0.001$.

RESULTS

Synthesis and Characterization of MF-MNB

The fabrication process of MF-MNB is illustrated in **Figure 1A** for the synthesis of MF-MNB. First of all, the PLGA-PEG-FA copolymer was prepared by carbodiimide reaction. The conjugate structure of PLGA-PEG-FA was confirmed by ^{1}HNMR spectroscopy (**Supplementary Figure 1**). The principal peaks related to benzene of the folate moiety (δ = 6.7, 6.9, 7.7, and 7.9 ppm), the PEG (δ = 3.4 and 3.7 ppm), and the PLGA moiety (δ = 5.1 and 4.7 ppm) reveal the successful fabrication of the PLGA-PEG-FA copolymer. Then, SPIO nanoparticles were prepared with the traditional chemical co-precipitation method with slight modification. The size and morphology of SPIO were characterized using transmission election microscopy (TEM) (**Figure 1B**), and the TEM image of SPIO exhibits a spherical morphology with relatively uniform size ranging from 4 to 7 nm. Subsequently, MF-MNBs were prepared with the double emulsion method. The SEM image of MF-MNBs indicated that the MF-MNB revealed a uniform and spherical morphology without aggregation (**Figure 1C**). The presence of SPIO nanoparticles in the polymer shell of MF-MNB was determined by the enhanced contrast manifested as dark domains in the TEM image (**Figure 1D**). The polymer shell was also visible as gray areas surrounding black spots (SPIO). Moreover, the existence of Fe, O, and N elements in MF-MNB was further validated with EDS spectrum (**Figure 1E**). The mean hydrodynamic size of MF-MNB was 208.4 ± 12.58 nm, and the size ranged from 91.7 nm to 459 nm in PBS solution (**Figure 2A**). The zeta potential of PLGA-PEG MNB exhibits a higher negative value of −9.17 ± 1.95 mV than the value of PLGA MNB (−28.84 ± 1.82 mV), which may be attributed to the presence of an amine group in the PEG chains. In comparison, after FA conjugation, the value of MF-MNB was slightly decreased to −13.5 ± 0.762 mV, ascribed to the binding of FA on the amine group in the PEG chains (**Figure 2B**). Moreover, the synthesized MF-MNB exhibits excellent colloidal stability in PBS buffer (pH 7.4) and DMEM cell culture medium with a narrow size distribution for 24 h (**Supplementary Figure 8**). Then, the conjugate structure of MF-MNB was further confirmed using FTIR spectrum (**Figure 2C**). The strong absorption with vibration bands at 586 cm^{-1} and 1012 cm^{-1} could be attributed to Fe–O vibration mode. The peak at 1453 cm^{-1} and 1606 cm^{-1} is due to the stretching vibrations of C = C in the backbone of the aromatic ring of folic acid. The peak at 1622 cm^{-1} and 1568 cm^{-1} may be due to the presence of carbonyl (C = O) and amine (N–H) groups in amide (–CONH) linkage. The encapsulation efficiency of SPIO was higher than 57%, and it was not significantly affected by increasing the quantity of SPIO (**Supplementary Figure 2**); the weight percent of encapsulated SPIO in MF-MNB was 5.7 ± 0.54, 12.1 ± 1.22, 17.6 ± 1.39, 25.4 ± 2.13, and 31.2 ± 2.67wt%, respectively.

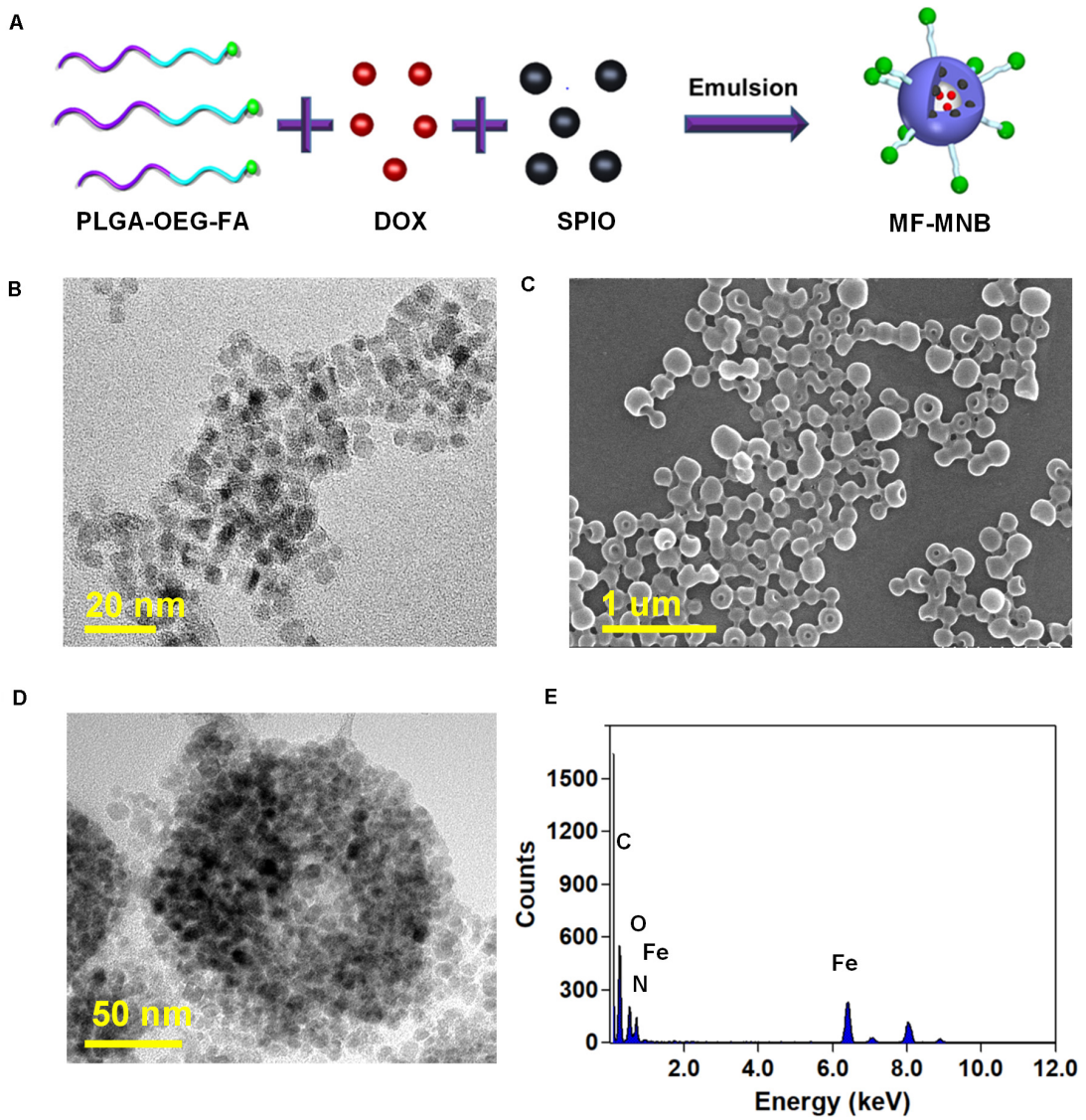

FIGURE 1 | Preparation of multifunctional magnetic nanobubbles (MF-MNBs). **(A)** Schematic illustration of the fabrication process of MF-MNB. **(B)** TEM image of SPIO nanoparticles. **(C,D)** SEM and TEM image of MF-MNB. **(E)** EDS spectrum curve of Fe, O, and N elements in MF-MNB.

In addition, as shown in the magnetization curve in **Figure 2D**, the magnetic property of MF-MNB was gradually increased to 22.1 emu/mg by increasing the SPIO weight percent to 17.6%; the high magnetic property may be attributed to the dense aggregation of SPIO in MF-MNB polymer shells. The results of these chemical and physical characterizations demonstrated the successful synthesis of MF-MNB.

Drug Loading and FUS-triggered Drug Release Test

The potential of the MF-MNB as a drug carrier was evaluated by its DOX loading efficiency. As revealed in **Supplementary Figure 3**, the high drug loading efficiency of MN-MNB (more than 61.5%) was not obviously affected by the SPIO encapsulation until the SPIO weight percentage increased to 17.6%. However, when the SPIO encapsulation was higher than 17.6 wt%, the drug loading capacity dramatically decreased, and the formation of MNF-MNB was affected by the large amount of SPIO, resulting in structure destruction of some MF-MNBs (**Supplementary Figure 4B**).

The drug release rate of MF-MNB (SPIO 17.6 wt%) with FUS sonication was investigated to evaluate the effects of FUS sonication on drug release. As shown in **Figure 3A**, the drug release rate was increased upon FUS treatment. In particular, when the pressure of FUS increased to 0.8 MPa, the drug release rate was enhanced to almost twofold in 0.6 MPa, and the drug release rate was further increased to 41% when the pressure was 1 MPa. The MF-MNB after FUS sonication was observed with TEM (**Supplementary Figure 5**), with most of the MF-MNBs

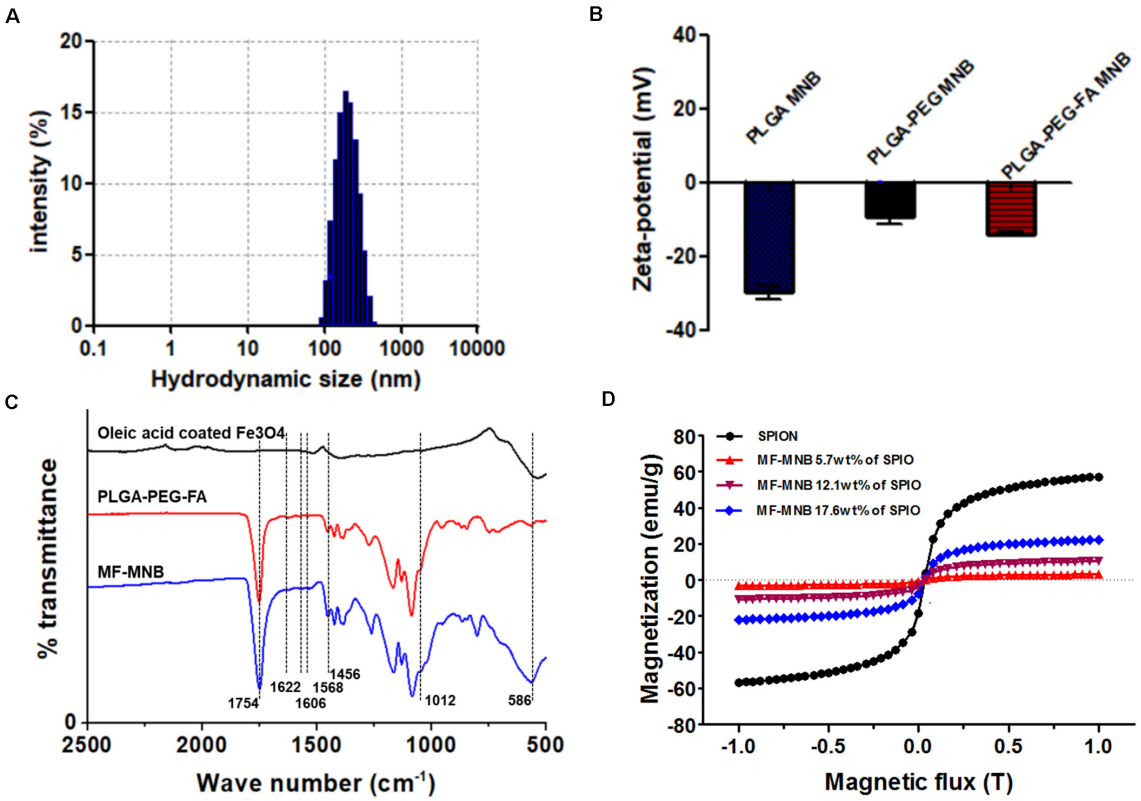

FIGURE 2 | Characterization of MF-MNB. **(A)** Hydrodynamic size of MF-MNB in PBS solution (pH 7.4). **(B)** Zeta potential of PLGA MNB, PLGA-PEG MNB, and PLGA-PEG-FA MNB (MF-MNB), respectively. **(C)** Fourier transform infrared (FTIR) spectrum curve of SPIO, PLGA-PEG-FA polymer and MF-MNB, respectively. **(D)** Magnetization curve of SPIO and MF-MNB with different encapsulation concentration of SPIO.

found to be destroyed or deformed, which could be due to the shear force from acoustic radiation force and cavitation effect (Cool et al., 2013). Moreover, the release of DOX from MF-MNB with/without FUS sonication was also evaluated for a 70-h period (**Figure 3B**). The results demonstrated that the release rate of DOX with FUS sonication was significantly enhanced when compared with that without FUS sonication, and approximately 92% of DOX was released in 2 days, while the MF-MNB without FUS sonication was less than 69% of the encapsulated DOX released. These results indicated that the DOX release from MF-MNB can be controllably triggered with FUS.

In vitro US and MR Imaging Evaluation of MF-MNB

The capability of MF-MNB as US and MR contrast agent was evaluated via *in vitro* phantom test. As shown in a US imaging test (**Figures 4A,B**), degassed and deionized water were used as the positive and negative control. The MF-MNB exhibits obvious contrast-enhanced US signal effect, in which the US signal intensity was increased by increasing MF-MNB concentration. Moreover, the US signal was further gradually enhanced to 129 (gray scale value) by increasing the SPIO content to 17.6 wt%. However, when the SPIO content was over 17.6 wt%, the US signal intensity steeply decreased due to the inability to form the bubble-like structure as well as decreased encapsulated amount of perfluorocarbon gas. In addition, the MF-MNB enables it as a promising candidate for T_2-weighted MR imaging due to the high magnetic property and excellent biocompatibility of MF-MNB. T_2-weighted MR imaging data revealed that the developed MF-MNB could weaken signal intensity of the MR images with the increasing Fe concentration (**Figure 4C**). Furthermore, the relaxation rate ($1/T_2$), also named as relaxivity r_2, was assessed to quantitatively evaluate the MR contrast ability of the MF-MNB. As indicated in **Figure 4D**, the T_2 relaxivity was calculated to be 109.18 mM^{-1} s^{-1}, which is enough for further animal MR imaging.

In vitro Cellular Uptake and Cytotoxicity

The subcellular localization of free DOX and MF-MNB in 4T1 cells and the FUS sonication-induced effect were observed using confocal microscope imaging (**Figure 5A**). Free DOX showed an obvious red fluorescence within cell nuclei, which may be due to the direct diffusion of small molecules like DOX into the cell. In contrast, 200-nm-sized MFMNBs have to undergo endocytosis process to enter the cells. Therefore, the DOX fluorescence from MF-MNB was mainly observed in the perinuclear cytoplasm. The MF-MNB-treated groups exhibited a much higher fluorescence signal when compared with the

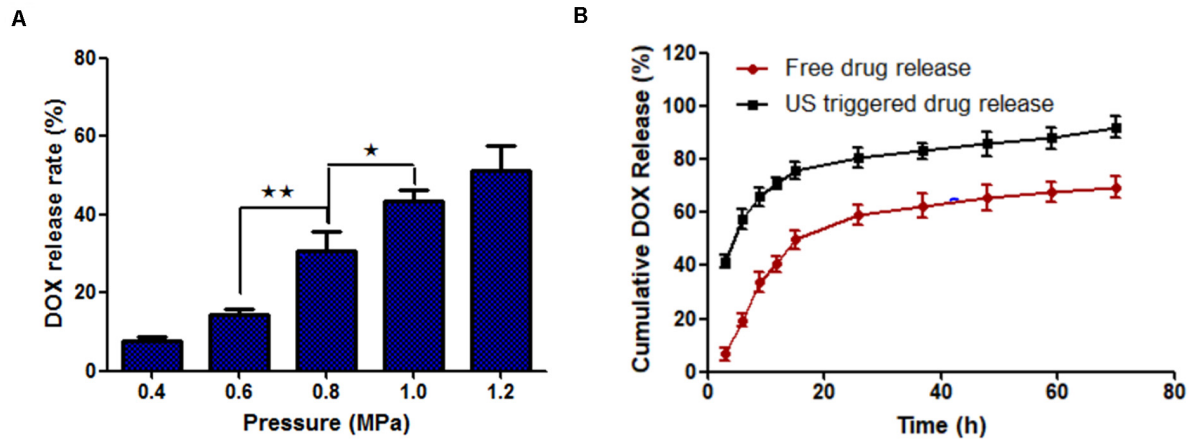

FIGURE 3 | FUS-triggered DOX release from MF-MNB. **(A)** Drug release rate depends on different FUS sonication powers of 0.4, 0.6, 0.8, 1.0, and 1.2 MPa. **(B)** Time-dependent DOX release profile with/without FUS sonication (*$p < 0.05$, **$p < 0.01$).

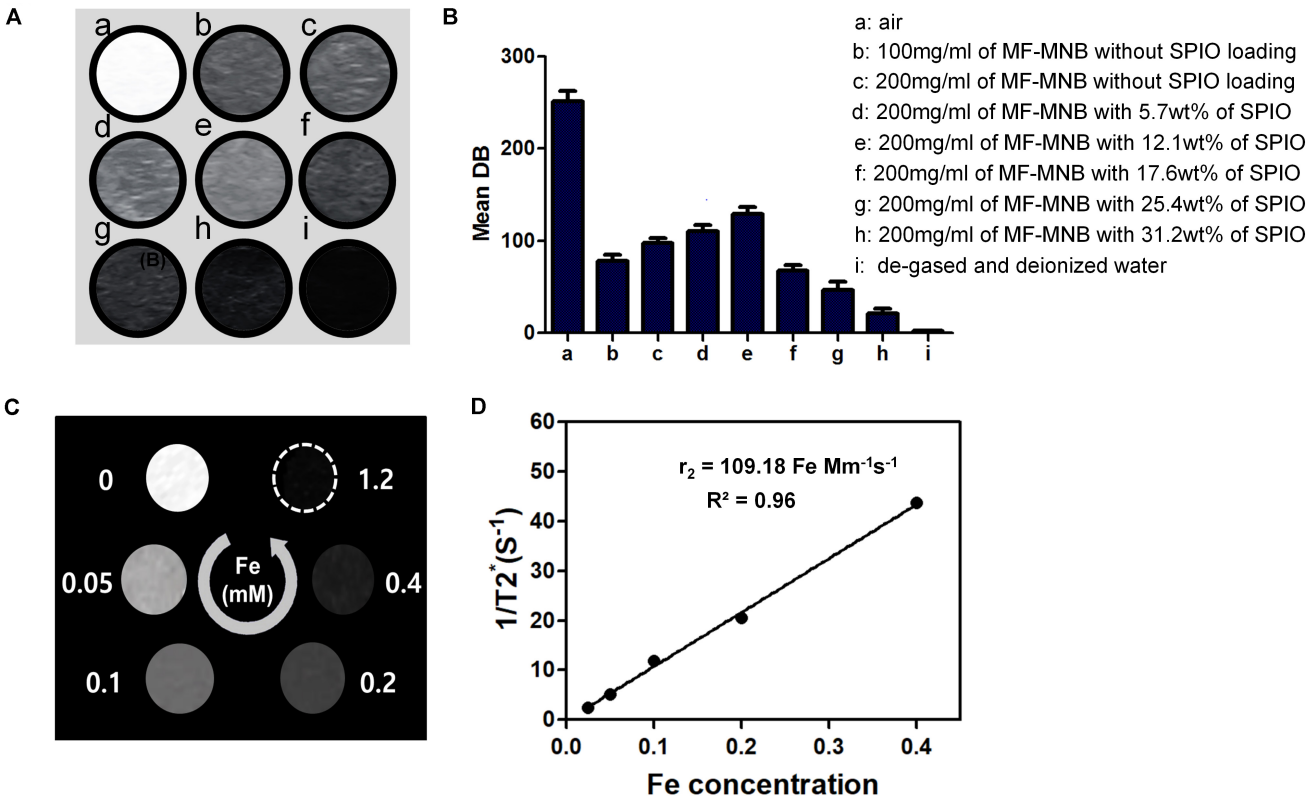

FIGURE 4 | US and MR image of MF-MNB. **(A,B)** US image and US signal intensity of **(a)** air, **(b and c)** 100 mg/ml and 200 mg/ml of MF-MNB without SPIO loading, **(d to h)** 200 mg/ml of MF-MNB with different SPIO weight percent of 5.7, 12.1, 17.6, 25.4, and 31.2, and **(i)** degassed and deionized water. **(C)** T_2-weighted MR image of MF-NRS in aqueous solution at different Fe concentration. **(D)** Relaxation rate *r*2 ($1/T_2$) of MF-NRS at different as a function of Fe concentrations.

MF-MNB with FA blocking treatment groups. These results demonstrated that MF-MNB targeted the 4T1 tumor through FA receptor-mediated targeting. After FUS sonication, a strong red fluorescence accumulated in the cytoplasm and nucleus attributed to the enhanced cellular uptake by the sonoporation effect and the rapid drug release upon FUS exposure. In addition, the enhanced cellular uptake of MF-MNB by FA receptor-mediated targeting and FUS sonication was further evaluated by quantifying the intracellular iron accumulation. As shown in **Figure 5C**, the significant enhanced cellular internalization

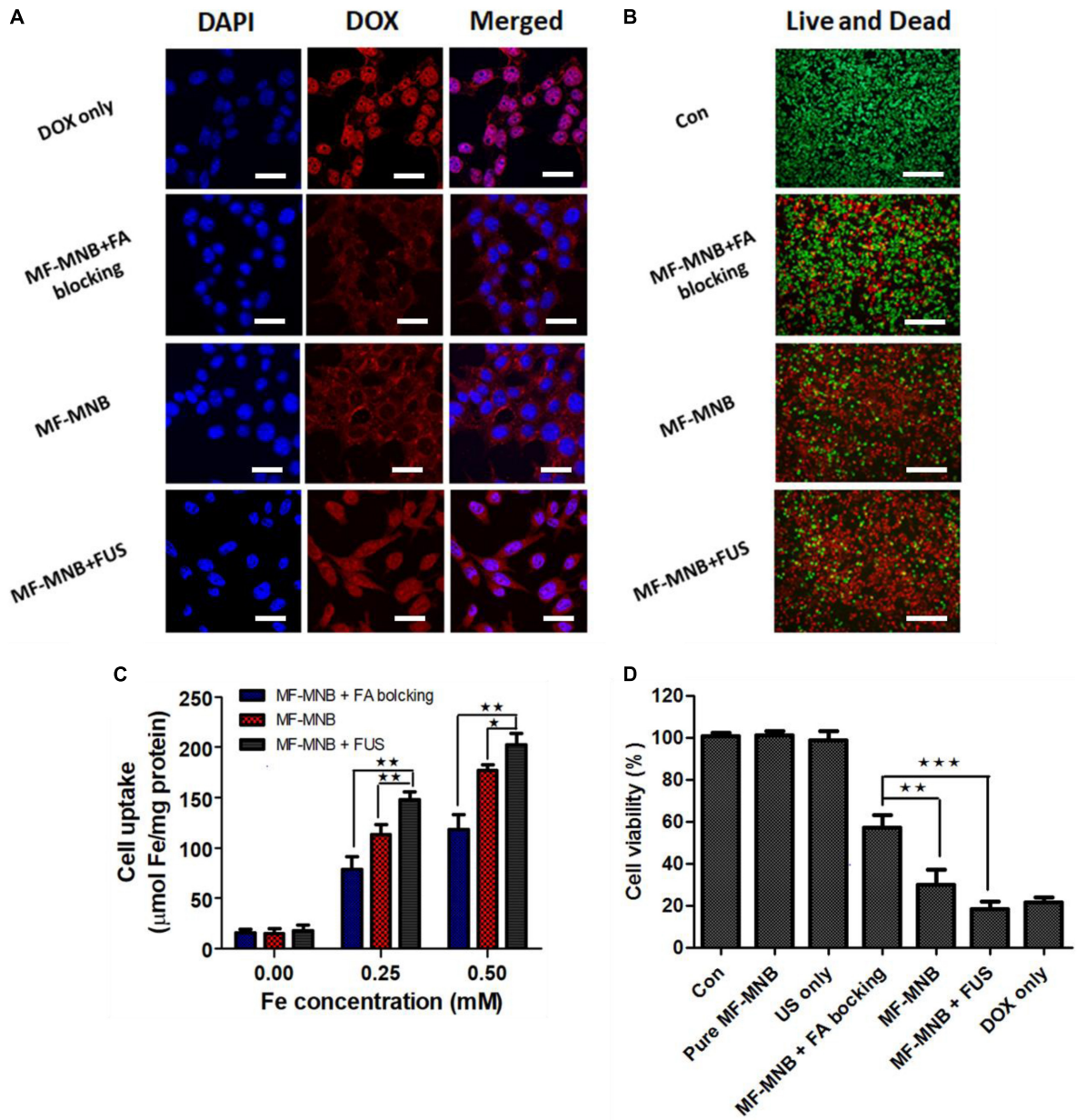

FIGURE 5 | *In vitro* cell test results. **(A)** Confocal microscopy images of live 4T1 cells treated with free DOX, MF-MNB with FA receptor blocking, MF-MNB, and MF-NRS with FUS sonication (blue fluorescence is associated with DAPI and the red fluorescence shows DOX). All scale bars are 30 μm. **(B)** Fluorescence microscopy images of live and dead 4T1 cells treated with PBS, MF-MNB with FA receptor blocking, MF-MNB, and MF-NRS with FUS sonication (green fluorescence is associated with calcein AM and the red fluorescence shows PI). All scale bars are 200 μm. **(C)** Quantification of iron concentration on 4T1 cells after treatment with MF-MNB with FA receptor blocking, MF-MNB, and MF-MNB with FUS sonication. **(D)** Viability of 4T1 cells after incubation for 24 h with the same treatment with those in the fluorescence images (*$p < 0.05$, **$p < 0.01$, ***$p < 0.001$).

of MF-MNB occurred with the FA receptor targeting; the iron concentration in 4T1 cells with MF-MNB reached 178 μmol/mg of protein, while that in FA receptor-blocked 4T1 cells was only 120 μmol/mg of protein. Moreover, the cellular uptake can be further enhanced to 202 μmol/mg of protein by FUS sonication ascribed to the enhanced permeability of tumor cell membrane (Mehier-Humbert et al., 2005]. Finally, the cell cytotoxicity of various formations was further evaluated by live and dead cell detection and MTT assay. **Figure 5B** and **Supplementary Figures 5**, **6** show the fluorescence microscopy images of live and dead cells; no obvious dead (red) cells were observed in the pure MF-MNB or FUS exposure group, indicating that pure MF-MNB and FUS sonication for 3 min did not induce obvious cytotoxicity to the cancer cells. However, part of the cells found to be dead in MF-MNB with FA receptor blocking cells and the number of dead cells in MF-MNB group were obviously increased, which

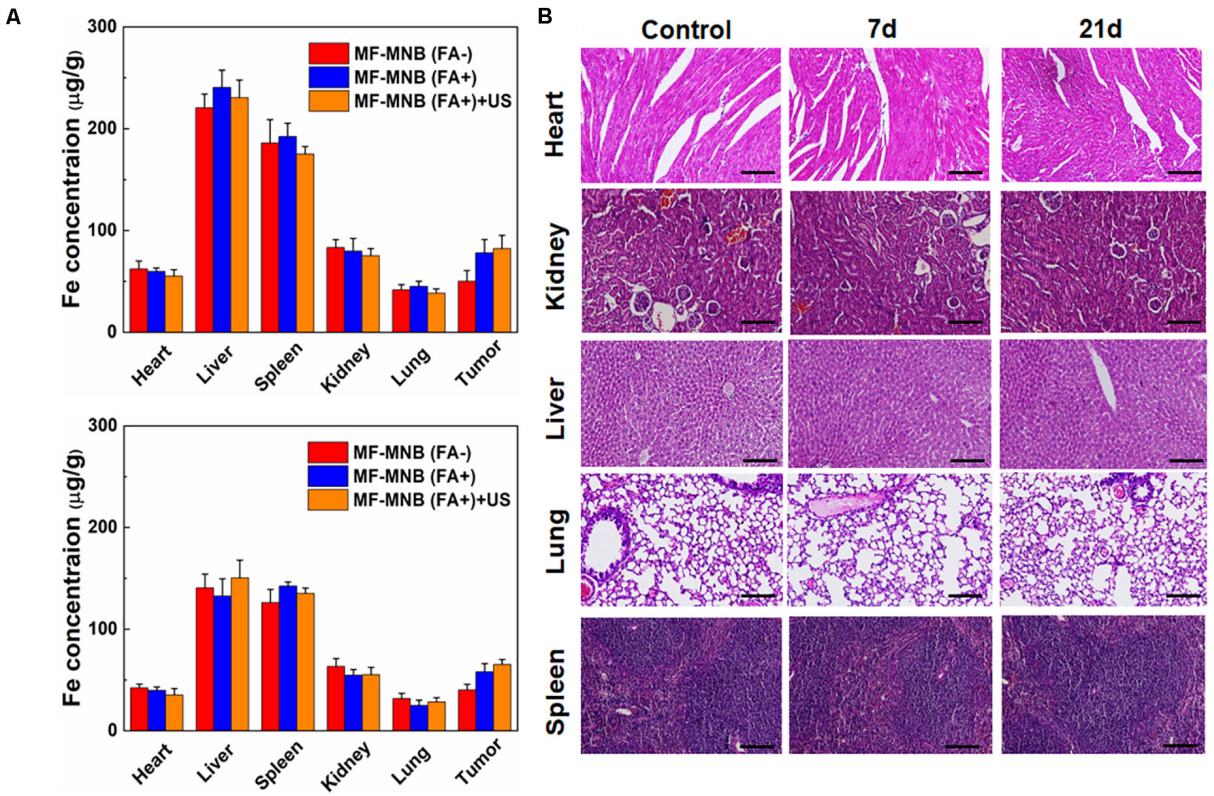

FIGURE 6 | Biodistribution and pathological analysis. **(A)** Biodistribution of MF-MNB without FA modification, MF-MNB, and MF-MNB with FUS sonication for 3 min, determined by ICP-OES (n = 3), in major tissues of mice bearing 4T1 tumors after 4 and 24 h. **(B)** H&E-stained images of major organs from untreated healthy mice and treated mice with MF-MNB injection and FUS sonication taken 7 days and 21 days. No noticeable abnormality was observed in major organs (liver, spleen, kidney, heart, and lung).

could be due to the enhanced cellular uptake of MF-MNB by FA ligand-receptor-mediated targeting. Then, the anticancer effect was further improved by FUS sonication. Moreover, the cytotoxicity was further evaluated with MTT assay, as shown in **Figure 5D**, and the cell viability had no obvious changes with pure MF-MNB or FUS sonication. MF-MNB showed an obvious heightened anticancer effect compared to MF-MNB with FA receptor blocking, and the cell viability was further decreased to 18.5% in 24 h with FUS sonication, attributed to the enhanced cellular uptake and rapid DOX release from MF-MNB. The cell viability was in accordance with the results from the live and dead cell detection test. All these results suggested that the fabricated MF-MNB could effectively kill the cancer cell with FA receptor-mediated tumor cell targeting and FUS sonication.

In vivo Targeted Biodistribution and Histological Analysis

In order to understand the *in vivo* targeted delivery of these NPs to the tumor sites, the 4T1 tumor-bearing mice were intravenously injected with MF-MNB with or without folic acid modification. US was also deployed to further enhance the deep penetration of the NPs inside the tumor. Then, the mice were sacrificed at 4 and 24 h to collect the major organs and subject to the ICP-OES analysis to evaluate the Fe amount in various major organs. As shown in **Figure 6A**, the MF-MNB NPs without FA indicated relatively low passive tumor accumulation in the tumor at both time points due to the EPR effect in cancerous tumors. In comparison, the accumulation of Fe was significantly increased for the mice after the injection of MF-MNB NPs coupled with FA. It revealed that FA modification could improve the targetability of the MF-MNB attributed to the high affinity of folic acid to the receptor on the 4T1 tumor cells. Furthermore, the US also exhibited slight facilitation to the uptake of MF-MNB NPs inside the tumors. It may be ascribed to the fact that the US could promote the permeability of vascular endothelial cells and ECM in tumor tissue, thus increasing the penetration distance of NPs inside the tumors. On the other hand, the injected NPs exhibited high accumulation reticuloendothelial systems (RES) such as, liver, spleen, and kidney at 4 h and then were gradually removed from these organs in 24 h.

Furthermore, we also carried out a histological analysis for the major organs from mice after the injection of MF-MNB for 7 and 21 days to evaluate the *in vivo* toxicity of the prepared NPs. As revealed in **Figure 6B**, the histological images indicated that no remarkable difference could be observed for organs of the control group and experiment groups. In addition, there were no obvious organ damage and inflammatory lesion in the major

organs post-injection. It suggested that the prepared MF-MNB could not cause any obvious toxicity in biological applications.

DISCUSSION

In this presented study, we fabricated a novel MF-MNB for tumor-targeted US/MR imaging and FUS-triggered drug delivery. A biocompatible and biodegradable polymeric material of PLGA-PEG-FA was designed and synthesized because the copolymer may enable excellent loading capacity of hydrophobic and hydrophilic drugs or moieties (for example, SPIO, gold nanoparticles, or other biomedical moieties) (Hao et al., 2013). The synthesized MF-MNB exhibits excellent biocompatibility and stability in PBS buffer and DMEM as shown in **Supplementary Figures 7, 8** with a hydrodynamic size of MF-MNB ranging from 91.7 nm to 459 nm, while the size range of the gaps in the leaky vasculature was reported as 600 nm to 800 nm. Furthermore, the PEG chain on the MF-MNB surface could form a flexible polymer brush layer that can prevent the absorption of opsonins (protein) on the MF-MNB surface, avoiding recognition by MPS, and thus prolong the circulation time. Therefore, the developed MF-MNB could efficiently pass through the leaky vasculature and accumulated in the tumor site.

Moreover, the presented MF-MNBs exhibits obvious enhanced cellular internalization and accumulation rate in the tumor site by the FA receptor-mediated tumor targeting, because the FA receptor (FR) is generally overexpressed in most types of tumors including ovarian, kidney, brain, breast, and liver (Maeng et al., 2010). However, before they can bind to the targeting tumor cells, the MF-MNBs also have to undergo the extravasation of blood vessels in tumors, penetrating deeply into the interstitium and crossing multiple cell layer processes together with various barriers, such as intratumoral pressure, shear force, binding-site effect, and multidrug resistance (Blanco et al., 2015; Miao et al., 2016). D.B. Kirpotin et al. reported that 100-nm-sized HER2-targeted liposomes accumulate to a higher extent in cancer cells than in macrophages, but do not achieve higher tumor concentrations (Kirpotin et al., 2006). The accumulation of MF-MNB with a mean diameter of 208 nm in tumor could also be limited. However, the aforementioned barriers could be properly overcome by employing FUS. The shear force and binding site effect could be overcome by enhancing the extravasation using the transient cavitation and acoustic radiation force generated by FUS sonication (Frenkel, 2008). Apfel and Holland (1991) calculated that US of 1 MHz can induce transient cavitation when the negative pressure is above 0.3 MPa, and the probability of cavitation occurrence increases as peak negative pressure increases and as frequency decreases. Moreover, acoustic streaming can be formed when the acoustic pressure and frequencies are on the order of MPa and MHz, which produce the translational force that pushes the nanocarriers against the blood vessel walls (Boissenot et al., 2016). In addition, the intratumoral pressure could also be overcome by acoustic streaming effect; the shear force created by FUS sonication can widen the intracellular space between endothelial cells and thus enhance the penetration of nanocarriers into solid tumor (Frenkel, 2008 and Couture et al., 2014). Consequently, the enhanced accumulation rate of MF-MNB in tumor by using FUS sonication (the results are shown in **Figure 6A**) is probably due to the transient cavitation and acoustic streaming effect as we used 925 kHz US with a peak negative pressure of 1 MPa.

In addition, the US imaging signal could be obviously enhanced by MF-MNB, in which the signal gradually increased with the increase in SPION loading quantity in MF-MNB shells. The US signal of the MF-MNB with 17.6 wt% SPIO loading was distinctly heightened more than 64% compared with MF-MNB without SPION loading because the densely imbedded SPIO in bubble shell leads to the MF-MNB not only being resonant with the US but also backscattering the US signal (Yang et al., 2009). The MF-MNB also exhibits promising MRI contrast effect with the T_2 relaxivity of 109.18 mM^{-1} s^{-1} attributed to the densely aggregated SPIO in the MF-MNB bubble shell. Therefore, the biodistribution and accumulation rates of intravenously administered MF-MNB could be precisely monitored with dual-modal US/MR imaging, in which the tumor progress after treatment could also be observed. These results will be absolutely meaningful to further design the treatment strategy.

Furthermore, after the proper accumulation of MF-MNB in the tumor site, the triggering DOX release with FUS sonication should be performed to lead the drug concentration in the tumor to rapidly reach the lethal dosage and thus effectively kill the cancer cells and avoid multidrug resistance, which could occur when the tumor cells are frequently exposed to sublethal drug dosage (Gottesman et al., 2002). The rapid DOX release could be achieved by the disruption or deformation of MF-MNB with the shear force from acoustic radiation force or acoustic cavitation, and there will be no thermal mechanisms due to the FUS exposure conducted in this study at about 2.1% duty cycles (the total operation time of FUS is about 21 ms in 1 s, and 979 ms is off). In addition, FUS exposure could further improve the dispersion of released drugs throughout the tumor cells and tissues attributed to the enhanced motion of fluid in the vicinity of the drug and the target tumor tissues by acoustic radiation force and transient cavitation bubble oscillations (Elkhodiry et al., 2016), thus enhancing the therapeutic efficiency.

CONCLUSION

In summary, we fabricated a folate receptor-targeted MF-MNB for US and MR imaging and FUS-triggered drug delivery. The MF-MNB can stably entrap more than 17.6 wt% of SPIO nanoparticles into the polymer shell and load drug with an efficiency of more than 64% into the core. Moreover, the MF-MNB exhibits a promising US and MR imaging contrast effect due to the densely aggregated SPIO nanoparticles in the bubble shell, providing excellent magnetic property and enhancing US signal. In addition, an almost threefold faster drug release time and 22% increased DOX release from MF-MNB in 2 days were achieved by FUS triggering. Furthermore, the cellular uptake was enhanced more than 100% by FA receptor targeting and FUS sonication. Moreover, the cell cytotoxicity

of MF-MNB with FA ligand and FUS sonication was evaluated with MTT assay, and a significantly decreased cell viability of 18.5% in 24 h was achieved. In addition, the accumulation of MF-MNB was enhanced by FA ligand-receptor-mediated tumor targeting and FUS sonication. Hence, we believe that the fabricated MF-MNB is a promising drug nanocarrier for US/MR imaging-guided and FUS-triggered drug delivery for efficient cancer treatment.

DATA AVAILABILITY STATEMENT

All datasets presented in this study are included in the manuscript/**Supplementary Material**.

AUTHOR CONTRIBUTIONS

ZJ investigation, validation, and writing the manuscript. JLC, PD, SJ, MJ, and HT investigation and validation. WSJ and WR writing review and editing. SZ funding acquisition, project administration, and writing review and editing. All authors contributed to the article and approved the submitted version.

FUNDING

This work was supported by the National Natural Science Foundation of China (81901798), the Natural Science Fund for Colleges and Universities in Jiangsu Province (19KJB310025), the Startup Fund for Youth Talent in Xuzhou Medical University (D2019022), and the Science and Technology Development Program of Xuzhou (KC19141).

SUPPLEMENTARY MATERIAL

The Supplementary Material for this article can be found online at: https://www.frontiersin.org/articles/10.3389/fbioe.2020.586874/full#supplementary-material

Supplementary Figure 1 | ^{1}HNMR spectrum of PLGA-PEG-FA polymer.

Supplementary Figure 2 | SPIO encapsulation efficiency with different weight percent of SPIO to PLGA-PEG-FA polymer.

Supplementary Figure 3 | DOX loading efficiency in MF-MNB with different weight percent of SPIO in MF-MNB.

Supplementary Figure 4 | TEM images of MF-MNB with **(A)** 5.7wt% of SPIO and **(B)** 25.4wt% of SPIO.

Supplementary Figure 5 | TEM image of MF-MNB after treated with FUS for 3 min.

Supplementary Figure 6 | Fluorescence microscopy images of **(A)** live and dead 4T1 cells treated with FUS sonication for 3 min, **(B)** pure MF-MNB and **(C)** free DOX (green fluorescence is associated with Calcein AM and the red fluorescence shows PI). All scale bars are 200 μm.

Supplementary Figure 7 | Biocompatibility test of MF-MNB. **(A,B)** Viability of NIH3T3 and 4T1 cells incubated for 24 h with DOX unloaded MF-MNB.

Supplementary Figure 8 | Stability test of MF-MNB in PBS buffer (pH 7.4), black line is the size distribution of MF-MNB in PBS at the time of 0 h, red line is the size distribution of MF-MNB at the time of 24 h.

REFERENCES

Apfel, R. E., and Holland, C. K. (1991). Gauging the likelihood of cavitation from short-pulse, low-duty cycle diagnostic ultrasound. *Ultrasound Med. Biol.* 17, 179–185. doi: 10.1016/0301-5629(91)90125-G

Blanco, E., Shen, H., and Ferrari, M. (2015). Principles of nanoparticle design for overcoming biological barriers to drug delivery. *Nat. Biotechnol.* 33, 941–951. doi: 10.1038/nbt.3330

Boissenot, T., Bordat, A., Fattal, E., and Tsapis, N. (2016). Ultrasound-triggered drug delivery for cancer treatment using drug delivery systems: from theoretical considerations to practical applications. *J. Control. Release* 241, 144–163. doi: 10.1016/j.jconrel.2016.09.026

Cool, S. K., Geers, B., Roels, S., Stremersch, S., Vanderperren, K., Saunders, J. H., et al. (2013). Coupling of drug containing liposomes to microbubbles improves ultrasound triggered drug delivery in mice. *J. Control. Release* 172, 885–893. doi: 10.1016/j.jconrel.2013.09.014

Couture, O., Foley, J., Kassell, N. F., Larrat, B., and Aubry, J. F. (2014). Review of ultrasound mediated drug delivery for cancer treatment: updates from pre-clinical studies. *Transl Cancer Res.* 3, 494–511. doi: 10.3978/j.issn.2218-676X.2014.10.01

Cui, X., Han, X., Yu, L., Zhang, B., and Chen, Y. (2019). Intrinsic chemistry and design principle of ultrasound-responsive nanomedicine. *Nano Today* 28:100773. doi: 10.1016/j.nantod.2019.100773

Elkhodiry, M. A., Momah, C. C., Suwaidi, S. R., Gadalla, D., Martins, A. M., Vitor, R. F., et al. (2016). Synergistic nanomedicine: passive, active, and ultrasound-triggered drug delivery in cancer treatment. *J. Nanosci. Nanotechnol.* 16, 1–18. doi: 10.1166/jnn.2016.11124

Frenkel, V. (2008). Ultrasound mediated delivery of drugs and genes to solid tumors. *Adv. Drug Deliv. Rev.* 60, 1193–1208. doi: 10.1016/j.addr.2008.03.007

Geers, B., Dewitte, H., De Smedt, S. C., and Lentacker, I. (2012). Crucial factors and emerging concepts in ultrasound-triggered drug delivery. *J. Control. Release* 164, 248–255. doi: 10.1016/j.jconrel.2012.08.014

Gottesman, M. M., Fojo, T., and Bates, S. E. (2002). Multidrug resistance in cancer: role of ATP–dependent transporters. *Nat. Rev. Cancer* 2, 48–58. doi: 10.1038/nrc706

Hao, S., Wang, Y., Wang, B., Deng, J., Liu, X., and Liu, J. (2013). Rapid preparation of pH-sensitive polymeric nanoparticle with high loading capacity using electrospray for oral drug delivery. *Mater. Sci. Eng. C* 33, 4562–4567. doi: 10.1016/j.msec.2013.07.009

Huang, H.-Y., Hu, S.-H., Hung, S.-Y., Chiang, C.-S., Liu, H.-L., Chiu, T.-L., et al. (2013). SPIO nanoparticle-stabilized PAA-F127 thermosensitive nanobubbles with MR/US dual-modality imaging and HIFU-triggered drug release for magnetically guided in vivo tumor therapy. *J. Control. Release* 172, 118–127. doi: 10.1016/j.jconrel.2013.07.029

Jain, A., Tiwari, A., Verma, A., and Jain, S. K. (2018). Ultrasound-based triggered drug delivery to tumors. *Drug Deliv. Transl. Res.* 8, 150–164. doi: 10.1007/s13346-017-0448-6

Jain, S., Rathi, V. V., Jain, A. K., Das, M., and Godugu, C. (2012). Folate-decorated PLGA nanoparticles as a rationally designed vehicle for the oral delivery of insulin. *Nanomedicine* 7, 1311–1337. doi: 10.2217/nnm.12.31

Jin, Z., Choi, Y., Ko, S. Y., Park, J. O., and Park, S. (2017). Experimental and simulation studies on focused ultrasound triggered drug delivery. *Appl. Biochem. Biotechnol.* 64, 134–142. doi: 10.1002/bab.1453

Ju, Y., Dong, B., Yu, J., and Hou, Y. (2019). Inherent multifunctional inorganic nanomaterials for imaging-guided cancer therapy. *Nano Today* 26, 108–122. doi: 10.1016/j.nantod.2019.03.006

Kalidoss, M., Yunus Basha, R., Doble, M., and Sampath Kumar, T. (2019). Theranostic calcium phosphate nanoparticles with potential for multimodal imaging and drug delivery. *Front. Bioeng. Biotechnol.* 7:126. doi: 10.3389/fbioe.2019.00126

Kievit, F. M., and Zhang, M. (2011). Surface engineering of iron oxide nanoparticles for targeted cancer therapy. *ıAcc. Chem. Res.* 44, 853–862. doi: 10.1021/ar2000277

Kirpotin, D. B., Drummond, D. C., Shao, Y., Shalaby, M. R., Hong, K., Nielsen, U. B., et al. (2006). Antibody targeting of long-circulating lipidic nanoparticles does not increase tumor localization but does increase internalization in animal models. *Cancer Res.* 66, 6732–6740. doi: 10.1158/0008-5472.CAN-05-4199

Li, J., Hu, Y., Yang, J., Wei, P., Sun, W., Shen, M., et al. (2015). Hyaluronic acid-modified Fe3O4@ Au core/shell nanostars for multimodal imaging and photothermal therapy of tumors. *Biomaterials* 38, 10–21. doi: 10.1016/j.biomaterials.2014.10.065

Maeda, H. (2010). Tumor-selective delivery of macromolecular drugs via the EPR effect: background and future prospects. *Bioconjug. Chem.* 21, 797–802. doi: 10.1021/bc100070g

Maeng, J. H., Lee, D. H., Jung, K. H., Bae, Y. H., Park, I. S., Jeong, S., et al. (2010). Multifunctional doxorubicin loaded superparamagnetic iron oxide nanoparticles for chemotherapy and magnetic resonance imaging in liver cancer. *Biomaterials* 31, 4995–5006. doi: 10.1016/j.biomaterials.2010.02.068

Malvindi, M. A., Greco, A., Conversano, F., Figuerola, A., Corti, M., Bonora, M., et al. (2011). Magnetic/silica nanocomposites as dual-mode contrast agents for combined magnetic resonance imaging and ultrasonography. *Adv. Funct. Mater.* 21, 2548–2555. doi: 10.1002/adfm.201100031

Mehier-Humbert, S., Bettinger, T., Yan, F., and Guy, R. H. (2005). Plasma membrane poration induced by ultrasound exposure: implication for drug delivery. *J. Control. Release* 104, 213–222. doi: 10.1016/j.jconrel.2005.01.007

Miao, L., Newby, J. M., Lin, C. M., Zhang, L., Xu, F., Kim, W. Y., et al. (2016). The binding site barrier elicited by tumor-associated fibroblasts interferes disposition of nanoparticles in stroma-vessel type tumors. *ACS Nano* 10, 9243–9258. doi: 10.1021/acsnano.6b02776

Mura, S., Nicolas, J., and Couvreur, P. (2013). Stimuli-responsive nanocarriers for drug delivery. *Nat. Mater.* 12, 991–1003. doi: 10.1038/nmat3776

Prabhakar, A., and Banerjee, R. (2019). Nanobubble liposome complexes for diagnostic imaging and ultrasound-triggered drug delivery in cancers: a theranostic approach. *ACS Omega* 4, 15567–15580. doi: 10.1021/acsomega.9b01924

Rosenblum, D., Joshi, N., Tao, W., Karp, J. M., and Peer, D. (2018). Progress and challenges towards targeted delivery of cancer therapeutics. *Nat. Commun.* 9:1410. doi: 10.1038/s41467-018-03705-y

Schleich, N., Sibret, P., Danhier, P., Ucakar, B., Laurent, S., Muller, R. N., et al. (2013). Dual anticancer drug/superparamagnetic iron oxide-loaded PLGA-based nanoparticles for cancer therapy and magnetic resonance imaging. *Int. J. Pharm.* 447, 94–101.

Shi, J., Kantoff, P. W., Wooster, R., and Farokhzad, O. C. (2017). Cancer nanomedicine: progress, challenges and opportunities. *Nat. Rev. Cancer* 17, 20–37. doi: 10.1038/nrc.2016.108

Sun, Y., Zheng, Y., Ran, H., Zhou, Y., Shen, H., Chen, Y., et al. (2012). Superparamagnetic PLGA-iron oxide microcapsules for dual-modality US/MR imaging and high intensity focused US breast cancer ablation. *Biomaterials* 33, 5854–5864. doi: 10.1016/j.biomaterials.2012.04.062

Sun, Y., Zhu, Y., Huang, C., Li, R., Chen, Y., and Duan, Y. (2016). Magnetite loaded Polypeptide-PLGA multifunctional microbubbles for dual-mode US/MR imaging. *Contrast Media Mol. Imaging* 11, 146–153. doi: 10.1002/cmmi.1675

Tang, H., Guo, Y., Peng, L., Fang, H., Wang, Z., Zheng, Y., et al. (2018). In vivo targeted, responsive, and synergistic cancer nanotheranostics by magnetic resonance imaging-guided synergistic high-intensity focused ultrasound ablation and chemotherapy. *Appl. Mater. Interfaces* 10, 15428–15441. doi: 10.1021/acsami.8b01967

Wang, Y., Wang, Z., Sun, X., Huang, T., and Song, J. (2020). A Sandwitch Nanostructure of Gold Nanoparticle Coated Reduced Graphene Oxide for Photoacoustic Imaging-Guided Photothermal Therapy in the Second NIR Window. *Front. Bioeng. Biotechnol.* 8:655. doi: 10.3389/fbioe.2020.00655

Yang, F., Li, Y., Chen, Z., Zhang, Y., Wu, J., and Gu, N. (2009). Superparamagnetic iron oxide nanoparticle-embedded encapsulated microbubbles as dual contrast agents of magnetic resonance and ultrasound imaging. *Biomaterials* 30, 3882–3890. doi: 10.1016/j.biomaterials.2009.03.051

Zeng, J. Y., Wang, X. S., Song, W. F., Cheng, H., and Zhang, X. Z. (2019). Metal-organic framework mediated multifunctional nanoplatforms for cancer therapy. *Adv. Ther.* 2:1800100. doi: 10.1002/adtp.201800100

Zhang, X., Zheng, Y., Wang, Z., Huang, S., Chen, Y., Jiang, W., et al. (2014). Methotrexate-loaded PLGA nanobubbles for ultrasound imaging and synergistic targeted therapy of residual tumor during HIFU ablation. *Biomaterials* 35, 5148–5161. doi: 10.1016/j.biomaterials.2014.02.036

Zheng, S., Jin, Z., Han, J., Cho, S., Ko, S. Y., Park, J.-O., et al. (2016). Preparation of HIFU-triggered tumor-targeted hyaluronic acid micelles for controlled drug release and enhanced cellular uptake. *Colloids Surf. B* 143, 27–36. doi: 10.1016/j.colsurfb.2016.03.019

Zhu, L., Zhou, Z., Mao, H., and Yang, L. (2017). Magnetic nanoparticles for precision oncology: theranostic magnetic iron oxide nanoparticles for image-guided and targeted cancer therapy. *Nanomedicine* 12, 73–87. doi: 10.2217/nnm-2016-0316

Conflict of Interest: The authors declare that the research was conducted in the absence of any commercial or financial relationships that could be construed as a potential conflict of interest.

frontiers in Molecular Biosciences

REVIEW
published: 18 December 2020
doi: 10.3389/fmolb.2020.610533

Tumor Microenvironment-Stimuli Responsive Nanoparticles for Anticancer Therapy

Reju George Thomas[1,2], *Suchithra Poilil Surendran*[1,2] *and Yong Yeon Jeong*[1,2]*

[1] Department of Radiology, Chonnam National University Hwasun Hospital, Hwasun, South Korea, [2] BioMolecular Theranostics (BiT) Laboratory, Department of Biomedical Sciences, Chonnam National University Medical School, Chonnam National University Hwasun Hospital, Gwangju, South Korea

Cancer is a disease that affects a large number of people all over the world. For treating cancer, nano-drug delivery system has been introduced recently with objective of increasing therapeutic efficiency of chemotherapeutic drug. The main characteristics of this system are the encapsulation of the insoluble chemotherapeutic cargo, increasing the period of circulation in the body, as well as the delivery of the drug at that specific site. Currently, the nano-drug delivery system based on the stimuli response is becoming more popular because of the extra features for controlling the drug release based on the internal atmosphere of cancer. This review provides a summary of different types of internal (pH, redox, enzyme, ROS, hypoxia) stimuli-responsive nanoparticle drug delivery systems as well as perspective for upcoming times.

Keywords: stimuli, nanoparticle, tumor microenvironment, cancer, drug release

OPEN ACCESS

Edited by:
Saji Uthaman, Chungnam National University, South Korea

Reviewed by:
Jayakumar Rangasamy, Amrita Vishwa Vidyapeetham University, India
Afeesh Rajan Unnithan, University of Birmingham, United Kingdom

***Correspondence:**
Yong Yeon Jeong
yjeong@jnu.ac.kr

Specialty section:
This article was submitted to Nanobiotechnology, a section of the journal Frontiers in Molecular Biosciences

Received: *26 September 2020*
Accepted: *23 November 2020*
Published: *18 December 2020*

Citation:
Thomas RG, Surendran SP and Jeong YY (2020) Tumor Microenvironment-Stimuli Responsive Nanoparticles for Anticancer Therapy. Front. Mol. Biosci. 7:610533. doi: 10.3389/fmolb.2020.610533

INTRODUCTION

Cancer is a common cause of death in humans. To overcome cancer, the general strategies used in chemotherapy still have some specific limits, such as adverse side effects because of unintentional drug accumulation in normal cells and not cancer cells. The discovery of nanomedicine, which is quite impactful for treating cancer, has created a new stage for targeted therapeutics. The featured mechanism of nanoparticles for targeting the tumor region is the enhanced permeation and retention (EPR) effect (Cheng et al., 2014; Shi et al., 2017). The capability of nanoparticles to accumulate at the tumor site through the effect of EPR is determined by the shape, size, and surface chemistry of the nanoparticles (Blanco et al., 2015). Additionally, some other aspects lead to the uptake of nanoparticles by tumor cells as well as consequent drug release at the tumor site. Stimuli-responsive nanoparticulate systems can deliver molecules of therapeutic drugs without affecting the regions near the tumor site (Ruttala et al., 2018). These stimuli-responsive particles used in chemotherapy for treating cancer have become very popular, along with the evolution of nanotechnology, nanomedicine, and material chemistry (Mura et al., 2013; Torchilin, 2014).

Stimuli responsive nanoparticles systems are divided into 2 classes: internal (pH, enzyme, ROS, hypoxia, redox) and external (radiation, electromagnetic, thermal) stimuli depending upon the method of inducing the delivery of the drug (**Figure 1**) (Taghizadeh et al., 2015; Yao et al., 2016). A vital role is also played by the design, material, and nanoparticle chemistry for spatiotemporally controllable delivery of the drug in addition to some of the stimuli-inducing factors (Crucho, 2015; Du et al., 2015; Ding et al., 2016; Wang S. et al., 2016). Rapid and controllable release of the drug through tuning the features of nanoparticles are the two main benefits of stimuli-responsive nanoparticle systems (Liao et al., 2015). Although there are few disadvantages of external stimuli-responsive materials, they are limited in terms of their tumor targeting capability to induce

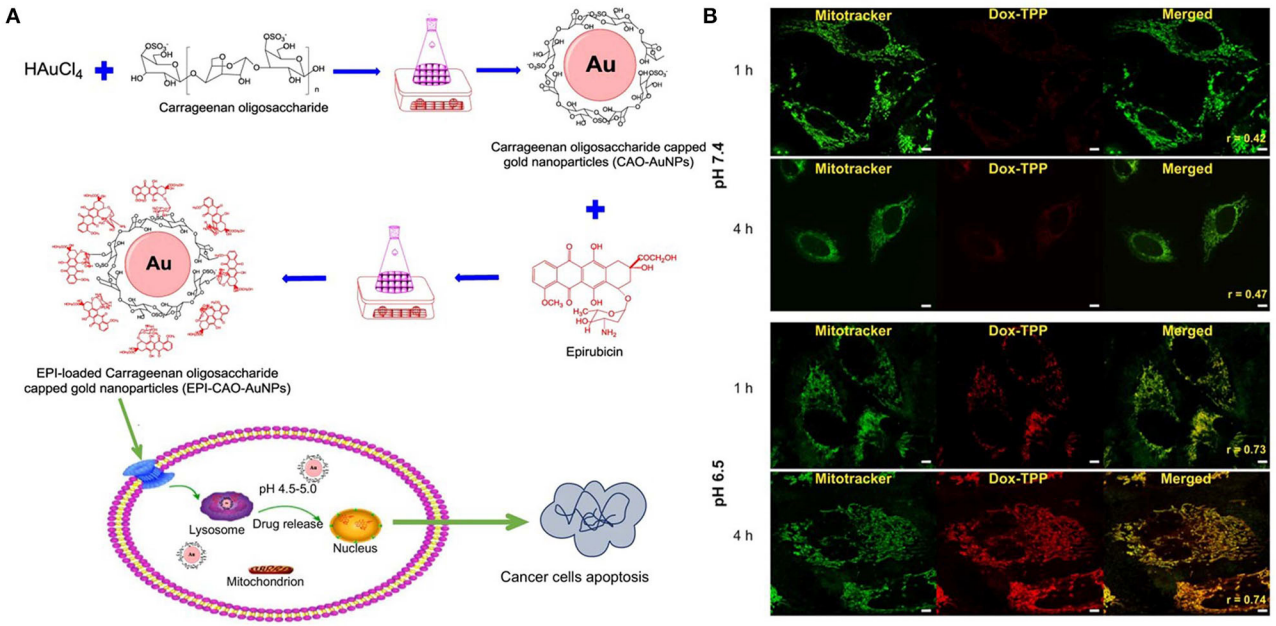

FIGURE 1 | pH stimuli responsive system of **(A)** epirubicin loaded Carrageenan oligosaccharide capped gold nanoparticle. **(B)** Drug release from the Dox-TPP nanoparticle was observed at lower pH (6.5) in the intracellular compartment of cell whereas at 7.5 pH minimal release was observed after 4 h. Reprinted with permission from Chen X. et al. (2019) and Palanikumar et al. (2020). Copyright © 2017 OMICS International.

the proper release of the drug. An internal stimulus at the site of the tumor could address this issue. In this review, we summarize the current strategies to achieve tumor microenvironment (TME)-responsive nanoparticle drug release (**Scheme 1**). We also cover the nanoparticle properties required to respond to internal stimuli, such as pH, enzyme, ROS, hypoxia, and redox conditions, in detail.

INTERNAL STIMULI-RESPONSIVE SYSTEM

pH-Responsive System

Compared to the other methods of drug release, the release of the drug from the nanoparticles in response to the pH can be considered the most efficient method. This particular mechanism for releasing drugs based on the slightly acidic microenvironment of the tumor as well as extremely acidic intracellular compartments with a pH value of 5.5 is known as pH-responsive release mechanism (Yu J. et al., 2014). The microenvironment of a tumor is acidic because of the built-up lactic acid formed during the division of the tumor cells. This specific phenomenon is called the Warburg effect (Vander Heiden et al., 2009; Liberti and Locasale, 2016). Nanoparticles with pH sensitivity in this acidic environment trigger a stimuli-responsive action, which consequently changes the chemistry of the material and induces the drug release (Gao et al., 2010) (**Table 1**).

To produce pH-responsive nanoparticles, both organic and inorganic materials are used (Gisbert-Garzaran et al., 2017). The pH-sensitive systems are prepared with polymer-based nanoparticles because their pH-induced changes, such as changes in volume or conformation and solubility, can be easily obtained. Polymer systems with pH-based linkers will experience a change in their properties based on charge reversal when the pK value of the polymer changes. Cationic polymers change from being hydrophobic to hydrophilic, whereas anionic polymers change from hydrophilic to hydrophobic. Examples of pH-responsive cationic polymers are poly(histidine), poly(4-vinyl pyridine), poly(β-amino ester), and poly[2-(diisopropylamino) ethyl methacrylate]. Similarly, anionic polymers change to hydrophobic from hydrophilic when exposed to a lower pH. Examples of anionic polymers are sulfonamide-based polymers, poly(aspartic acid) (PAsp), and poly(methacrylic acid) (PMAA). Another strategy of achieving a pH-induced release mechanism is the inclusion of linkers which hydrolyze at low pH and therefore become unstable. The linkers commonly used in cancer drug delivery systems are β-thiopropionate moieties, orthoesters, cis-aconityl groups, acetal/ketal groups, imine, and hydrazine (Deirram et al., 2019).

Doxorubicin-loaded phospholipid-linked polyurethane nanoparticles were prepared with acetal linkers, which were responsible for the particle degradation in acidic conditions. The molecular dynamics of these micelles revealed a compact core with surface-attached polymer chains and encapsulated doxorubicin (John et al., 2016). Doxorubicin-loaded polyethylene glycol (PEG) methyl ether-block-poly(ε-caprolactone) nanomicelles were prepared using different β-carboxylic amide amounts to improve the acid-labile properties of the polyester moieties (Deng et al., 2014). β-carboxylic amides were exposed at a low pH of 6.0 to induce their hydrolysis, leading

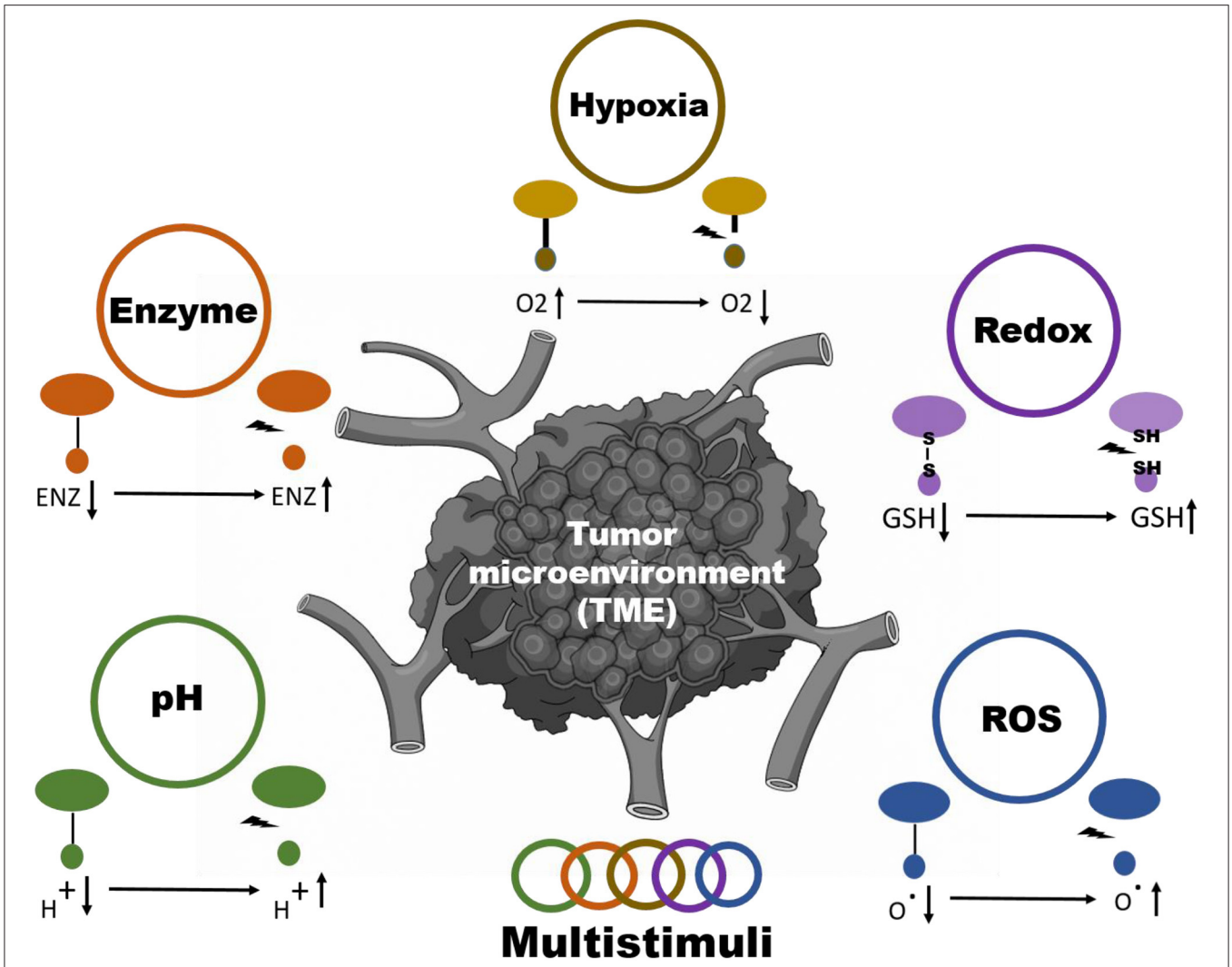

SCHEME 1 | Schematic illustration for internal stimuli-responsive drug delivery systems.

to a charge reversal from negative to positive of the polymeric micelles. Another benefit of the charge reversal is the increased uptake by the tumor cells, which has been previously shown with the HepG2 liver cancer cell line. The same kind of charge reversal method was employed in another study with β-carboxylic amide. Tat peptide was amidated to produce succinyl chloride [Tat (SA)] by click chemistry. PLLeu–PLL (DMA)–Tat (SA) nanomicelles were prepared with the nuclei-targeting Tat peptide (Han et al., 2015).

Bis-norbornene, as an acid-labile linker in the ring-opening metathesis polymerization, is used for preparing a polymer-drug conjugate of doxorubicin (DOX) and PEG (Gao et al., 2014; Yu Y. et al., 2014). Another method for releasing the drug from a nanoparticle used self-assembled hyaluronic acid (HA) mineralized by calcium phosphate, resulting in the formation of hydroxyapatite nanoparticles loaded with DOX. When the pH was low, the mineral dissolved; thus, the drug was released into the microenvironment of the tumor (Han et al., 2013). HA pH-responsive lipid membrane mesoporous silica nanoparticles (MSNs) have been utilized as a $CD44^{+}$-based targeting system for cancer therapy. DOX was loaded into these pH-sensitive MSNs, which were unstable in acidic conditions, thus releasing DOX from the MSN cage. This particular system is considered very biocompatible due to the use of silica, biocompatible lipids, and HA (Wang Z. et al., 2016). A dual pH-responsive zirconia ceramic nanosystem was prepared. The dual pH-mediated sensitivity was attributed to the hollow mesoporous zirconia nanospheres releasing the DOX payload through a molecular switching function (Wang M. et al., 2016).

In another system based on gold nanoparticles, carrageenan oligosaccharide (CAO) was used as a reducing agent to synthesize CAO-coated gold nanoparticles (AuNPs) (**Figure 1**). Epirubicin (EPI) was loaded into the nanoparticles as an anticancer drug. The *in vitro* release of EPI induced the apoptosis of HCT-116 and HepG2 cells (Chen X. et al., 2019). DOX-triphenylphosphonium (DOX-TPP) was loaded inside BSA-PLGA nanoparticles, and

TABLE 1 | pH stimuli responsive nanoparticle for anti-cancer drug release.

Nanoparticular components	Mechanism	Payload	References
Phospholipid, polyurethane	Acetal link destabilization	Doxorubicin	Deng et al., 2014
Polyethelene glycol, polycaprolactone	β-carboxylic amides link hydrolyzation	Doxorubicin	Gao et al., 2014
Poly-L-Leucine, poly-L-Lysine	β-carboxylic amides link hydrolyzation	Doxorubicin	Han et al., 2015
Poly-l-Arginine, polydopamine	bis-norbornene as acid-labile linker destabilization	Doxorubicin	Yu Y. et al., 2014
Polyethelene glycol, hyaluronic acid	Calcium phosphate dissolution	Doxorubicin	Han et al., 2013
Hyaluronic acid	pH stimuli sensitive lipids	Doxorubicin	Wang Z. et al., 2016
Zirconia	Molecular switching	Doxorubicin	Wang M. et al., 2016
Gold	pH stimuli responsive coating	Epirubucin	Chen X. et al., 2019
Polylactic glycolic acid	Acidity triggered rational membrance destabilization	Doxorubicin	Palanikumar et al., 2020

TABLE 2 | Redox stimuli responsive nanoparticle for anti-cancer drug release.

Nanoparticular components	Mechanism	Payload	References
Poly(3-caprolactone), poly(N,N-dimethylamino-2-ethylmethacrylate)	Disulphide link destabilization	Doxorubicin	Qu et al., 2017
Au, mesoporous silica	Host-guest interaction system release of the hydrophilic Fc+	Doxorubicin	Li et al., 2015
Mesoporous silica	Disulphide link destabilization	Doxorubicin	Xiao et al., 2015
Mesoporous silica	Disulphide link destabilization	Doxorubicin	Li et al., 2020
Polyethylene glycol	Ditelluride link destabilization	Doxorubicin	Pang et al., 2020
Polydopamine	Disulphide link destabilization	Doxorubicin	Tian and Lei, 2019

ATRAM was conjugated to induce tumor targeting capabilities. The pH-responsive effect was attributed to the ester bond hydrolysis in PLGA, which resulted in drug release (Palanikumar et al., 2020).

In the low-pH environment of tumors, a supersensitive polymer material, poly(2-ethyl-2-oxazoline)-poly(methacryloyl sulfadimethoxine), was synthesized (PEOz-*b*-PSD). PEOz-*b*-PSD and polyamidoamine/DOX can form nanoparticles at the physiological environment. This nanoparticles were protonated and underwent a charge reversal resulting in the detachment of PEOz-b-PSD, which formed ultrafine nanoparticles with improved accumulation in tumors. The ultrasensitive nanoparticles in the tumor microenvironment showed to be beneficial for enhancing the treatment efficacy of DOX in solid tumors (Jia et al., 2020). An innovative nanorobot was developed based on iron oxide nanoparticles (Fe_3O_4) chemically conjugated to carbon nanotube loaded with doxorubicin and anti-epithelial cell adhesion molecule antibody for targeting to colorectal cancer. This nanoparticle system provided mechanism whereby Fe_3O_4 moeity opening facilitated doxorubicin release from carbon nanotube. The therapeutic effect wqs tested in colon cancer spheroids (HCT116) and found to have sufficient anti-cancer effect (Andhari et al., 2020).

Redox-Responsive Systems

Compared to normal cells in our body, cancer cells have a higher redox potential with nearly 100–1,000-fold upsurge. Glutathione (GSH) is responsible for the destabilization of the redox-mediated disulfide linkage. The variation in the level of GSH in the blood as well as the environment of the tumor is nearly 500-fold, which can be utilized for efficient internal stimuli-responsive drug release. Redox-responsive nanoparticles have a disulfide bond-linked removable shell, which can easily be shed in the presence of the GSH enzyme, resulting in the release of the drug (Bauhuber et al., 2009; Jhaveri and Torchilin, 2014). Two main types of redox-responsive bonds are utilized in redox-responsive delivery systems: delivery systems with disulfide bonds and diselenium bonds. These disulfide bonds are cleaved to form sulfhydryl groups from glutathione, which indirectly results in the breakdown of the polymer system containing these bonds, thereby releasing the drug. In a similar manner, diselenium bonds can be cleaved more efficiently than disulfide bonds because their bond energy is lower than that of disulfide bonds (Gunawan et al., 2014; Guo et al., 2018) (**Table 2**).

A redox-sensitive PEGylated liposome with orthoester linkages was prepared. The poly-e-benzyloxycarbonyl-L-lysine (PzLL) as the lipid portion is responsible for the formation of micelles of DOX-loaded mPEG-SS-PzLL nanomicelles. A special

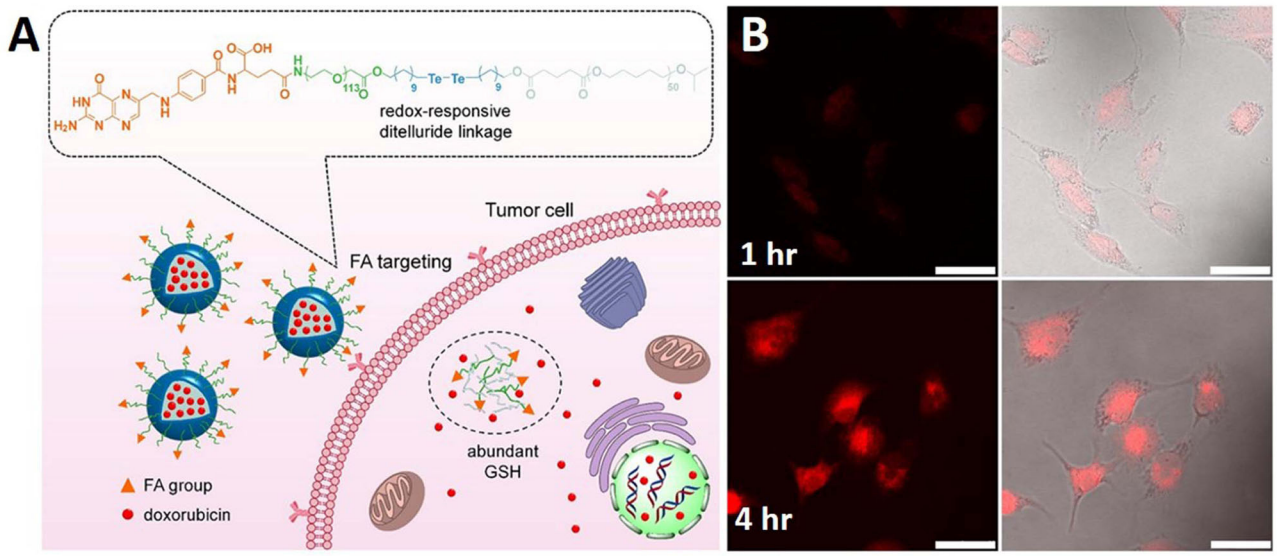

FIGURE 2 | Schematic illustration of **(A)** redox sensitive NPs with disulfide linked PEG shell which can respond to tumor intracellular GSH microenvironments for controlled release of therapeutic agents. **(B)** PDA@PMAA nanoparticles kept for 1 h and 4 h time period. Reprinted with permission from Pang et al. (2020) and Tian and Lei (2019). Copyright © 2020 Frontiers Media S.A.

property of this nanomicelle is its ability to shed its PEG shell at an increased level of GSH, which is accompanied with DOX release (Wen et al., 2011). This particular strategy for detaching the shell was utilized in disulfide-linked poly(3-caprolactone)-b-poly(N,N-dimethylamino-2-ethylmethacrylate), which showed a GSH-dependent release of DOX along with the gene. These positively charged nanoparticles could bind DNA and could be taken up by cells (Li et al., 2014).

MSNs incorporate redox responsiveness with AuNP-like gatekeepers (Qu et al., 2017). Here, rather than the conventional GSH reactive disulfide linkage, a host-guest interaction system was used, which involved cyclodextrin-modified AuNPs bound to the MSN for drug release. The role of the host was played by the molecules of ferrocene (Fc), which were bound to the cyclodextrin (guest) and responded to the redox conditions by releasing hydrophilic Fc+, thus opening the gate for the subsequent release of the drug from the cavities. Another MSN system used Arg-Gly-Asp (RGD) peptide as a capping agent. RGD as the capping agent functioned as a targeting moiety in redox-sensitive peptide-functionalized MSNs (DOX@MSN-S-S-RGD). This system showed improved cellular uptake in the COS-7 cells as well as improved DOX release (Li et al., 2015).

A redox-responsive MSN was developed as a drug nanocarrier by non-covalent functionalization of MSNs with amphiphilic peptides containing the RGD ligand. After the internalization of MSNs by cancer cells *via* the receptor-mediated endocytosis, the surface amphiphilic peptides and alkyl chain of redox responsive MSN/DOX were removed to induce rapid drug release intracellularly after the cleavage of the disulfide bond triggered by GSH (Xiao et al., 2015). The protein capping and the drug release strategy were also studied for transferrin-capped MSNs (DOX@MSNs-S-S-Tf), which showed cancer-targeting effects and released DOX through uncapping transferrin because of disulfide link destabilization. This specific system claims the slower release of the drug without GSH and rapid release in an intracellular state (Li et al., 2020). DOX-releasing nanoparticles were developed with MSNs coated with disulfide linkers to regulate the drug release in response to varying redox conditions.

In another study, GSH-responsive ditelluride bonds were utilized to synthesize nanoparticles releasing loaded doxorubicin in cancer cells. Compared to the S-S bond, the detelluride bond has a lower bond energy. PEGylated folic acid (FA) and redox responsive ditelluride linkage created an ambiphilic system capable of loading doxorubicin (F-TeNP$_{DOX}$). An *in vivo* tumor treatment study showed significant tumor reduction in the F-TeNPDox nanoparticle-injected group compared to the other groups. A redox labile coating of disulfide-crosslinked poly(methacrylic acid) (PMAA) was coated onto polydopamine (PDA) nanoparticles prepared by the precipitation polymerization method. In addition to redox-responsiveness, PDA induced responsiveness to photothermal stimuli. Through the dual stimuli-responsive mechanism of the PDA@PMAA nanoparticles, 86% DOX release was achieved. This nanoparticles were found to be highly toxic in response to both stimuli (redox and photothermal) (**Figure 2**) (Pang et al., 2020). Nanoparticles based on poly(methacrylic acid) with disulfide crosslinkers were synthesized to load drugs and release them in response to redox stimuli. The nanoparticle core consisted of PDA, which has a very high photothermal efficiency. This nanoparticle simultaneously acted as a chemotherapeutic and photothermal agent (Tian and Lei, 2019).

TABLE 3 | Enzyme stimuli responsive nanoparticle for anti-cancer drug release.

Nanoparticlular components	Mechanism	Payload	References
Polyethylene glycol	Enzyme responsive linker glycylphenyl-lananylleucy glycine tetrapeptide	Paclitaxel	Li et al., 2017
L-lysine polyurethanes	Nanoparticle degradation by lysosomal esterase enzyme	Doxorubicin	Joshi et al., 2019
Poly(ester-urethane)	Enzyme responsive amphiphilic poly(ester-urethanes)	Camptothecin	Joshi et al., 2019
Mesoporous silica	Chitosan with an azo bond destabilization	Doxorubicin	Cai et al., 2020
Hyaluronic acid	HAase enzyme mediated destabilization of nanoparticle	Doxorubicin	Naz et al., 2019

Enzyme-Responsive Systems

An ailing condition, such as cancer, can lead to changed enzyme expression, which can cause higher levels of matrix metalloproteinases (MMPs), cathepsin, hyaluronidase, trypsin, thrombin, proteinase K, etc. The upregulated enzymes can be utilized for the controlled release of cargos from nanocarriers, breakage of polymer backbones, physical disruption of the nanocarriers and cleavage of bonds between the drug and the carrier in the tumor microenvironment (Mi, 2020). The biorecognition and catalytic function of enzymes can be used for the destabilization of nanoparticles. The major classifications of enzymes include hydrolase (protease, trypsin, elastase, lipase, glycosidase) and oxidoreductase (glucose oxidase, peroxidase, azoreductase, glutathione reductase) (**Table 3**). Hydrolase enzymes are capable of cleaving chemical bonds by the addition of water molecules; oxidoreductase enzymes are capable of catalyzing oxidation/reduction reactions, resulting in the destruction of the nanoparticles (Rabiee, 2019).

Paclitaxel (PTX) was delivered using Janus PEGylated peptide dendrimer nanoparticles for the treatment of breast cancer. The tumor microenvironment enzyme-responsive linker glycyl phenylalanine leucyl glycine tetrapeptide was incorporated into the nanoparticles for effective release of PTX. The nanoparticles were destabilized in the presence of enzyme capthepsin B overexpressed in breast cancer, which acts as a lysosomal cysteine protease. The cell uptake and PTX release study also indicated the effectiveness of the nanoparticle in delivering PTX and the release of the drug into the tumor microenvironment using an enzyme degradable linker (Li et al., 2017).

Polyurethanes have been used as an enzyme stimuli-responsive carrier system for delivering cargos to the tumor microenvironment. In the related study, L-lysine-based amphiphilic enzymes and thermosensitive nanocarriers were designed, which were capable of delivering the drug DOX to the intracellular region of the cancer tissue at physiological temperature. The cumulative DOX release was studied in the presence and absence of intracellular esterase enzyme, which showed that a considerable amount of the drug was released in the presence of the enzyme. All the *in vitro* studies showed effective drug release in the presence of enzyme at a temperature of 42°C, which indicated the dual responsive characteristics of the nanoparticles. Overall, the utilization of L-lysine polyurethanes as a dual sensitive drug delivery system for delivering anticancer drugs could be a useful tool for cancer treatment (Joshi et al., 2019). Another study used polyurethanes containing DOX and camptothecin (CPT). In this study, enzyme-responsive amphiphilic poly(ester-urethanes) were synthesized by polycondensation of L-tyrosine amino acid moieties and hydrophilic PEG. Enzyme-dependent cumulative release of both DOX and CPT was observed when biological amounts of esterase enzyme were present. The amphiphilic polyurethanes showed no toxicity toward the normal cell lines, but they were toxic to the cancer cell lines when treated with the anticancer drugs DOX and CPT (Aluri and Jayakannan, 2017).

Hollow mesoporous silica spheres (HMSS) for drug delivery have been studied widely. In one study, HMSS was modified using chitosan with an azo bond responsive to the enzyme activity in the TME. DOX was encapsulated in the hollow cavity, which was released in the presence of colon enzyme. The drug release profile of the HMSS/DOX was investigated, and a sustained release of the drug in the presence of the enzyme was found when compared to the release in the absence of enzyme. The *in vitro* results supported the drug release studies, which showed the ability of the nanoparticles to release the drug at the TME (**Figure 3**) (Cai et al., 2020).

Other enzyme-responsive MSN was modified with triphenylphosphine (TPP) for mitochondria targeting, DOX for anticancer activity and HA capping for CD44 targeting. The enzyme-responsive drug release was studied over time in the presence and absence of the HAase enzyme, which showed significant release of the drug from the nanoparticle when treated with the enzyme. The DOX-loaded final nanoparticle showed toxicity to stomach cancer MGC-803 cells. A live/dead assay was conducted to understand more about the cytotoxicity of the nanoparticles (**Figure 4**) (Naz et al., 2019).

ROS-Responsive Systems

The generation and persistence of higher amounts of ROS was observed in cancer cells compared to normal cells due to the stimulation of different oncogenes, inflammation and mitochondrial damage (Li et al., 2020). A number of strategies have been developed for the design of ROS-responsive nanoparticle systems for cancer therapy by utilizing their physiochemical characteristics. The utilization of ROS-cleavable bonds in cargos for effective and sustained drug release in the presence of different hydroxyl radicals ($^{\bullet}OH$), hydrogen peroxides (H_2O_2), superoxide anions (O_2^-), and peroxynitries ($ONOO^-$) is an emerging field of research interest (Tao and He, 2018; Aggarwal et al., 2019). A number of studies have been reported that make use of

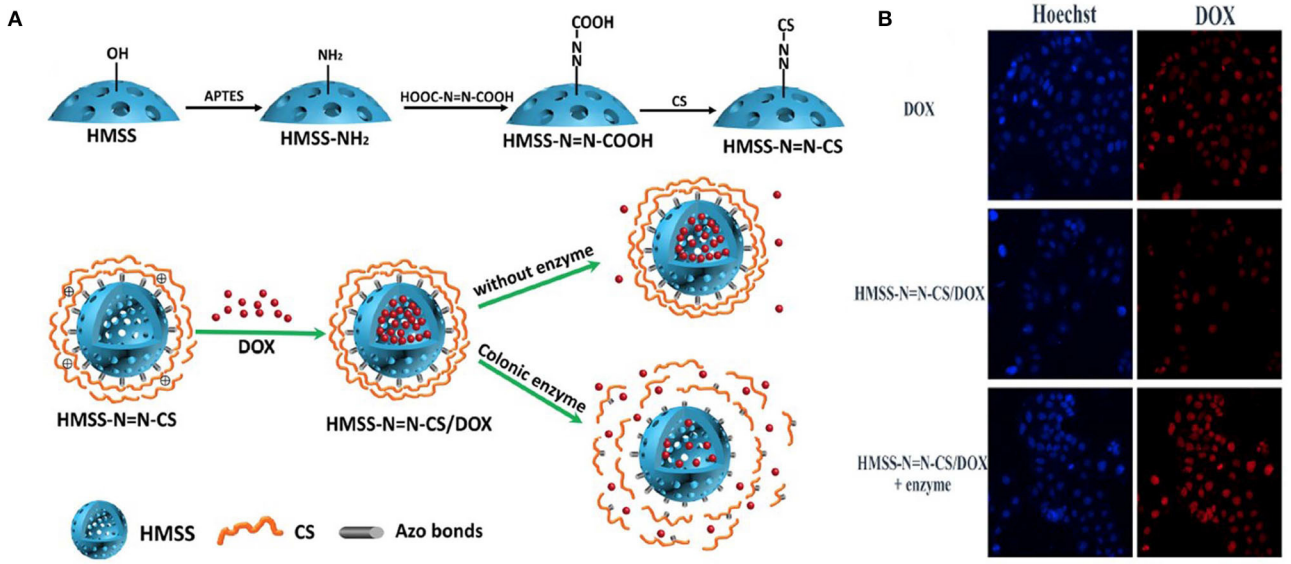

FIGURE 3 | Schematic illustration of preparation of HMSSN=N-CS. **(A)** Drug loading and colon enzyme responsive release of DOX from HMSS-N=N-CS, CLMS of Caco-2 cells incubated with HMSS/DOX in presence and absence of enzyme compared with DOX only. **(B)** MFI of DOX, HMSS/DOX, and HMSS/DOX +Enzyme using FCM analysis. Reprinted with permission from Cai et al. (2020). This article is licensed under a Creative Commons Attribution 4.0 International License.

different linkages for ROS-responsive drug release. The major types of the currently used linkers are thioethers, selenides, arylboronic esters, thioketals, aminoacrylates, oligoprolines, peroxalate esters, mesoporous silicons, etc. Drug release from the nanoparticles depends on the chemical structure and reaction mechanism of the linkers. The major parameters in the drug release mechanisms are ROS-induced dissolution of the carrier system, ROS-induced carrier breakage and prodrug breakage (Tao and He, 2018) (**Table 4**).

Nanoparticles with thioketal (tk) linkers, which are sensitive to ROS stimuli, as well as the tumor-targeting peptide RGD with anticancer epothilone B (Epo B) showed an effective anticancer effect both *in vitro* and *in vivo*. Self-assembly of RGD-tk-EpoB resulted in a stable nanoparticle structure, which can undergo degradation via the tk group at the biological ROS level, which in turn leads to the release of the EpoB drug. An RGD targeted internalization and cell apoptosis study with PC-3 cells showed the efficacy of the nanoparticles to target the cells followed by induction of apoptosis (Xia et al., 2020). In another study, micelles were synthesized using the stimuli-responsive amphiphilic diblock copolymer prodrug, and the side chain contained poly(methacrylate) conjugated with the thioketal linker CPT. The final micellar particle GR-BCP exhibited a spherical morphology with ROS-responsive drug release when treated with biological amounts of H_2O_2 (Bertoni et al., 2020). The use of lipids as well as liposomes for drug delivery has been studied for different cancer treatments. The development of a tumor microenvironment ROS-responsive nanoparticle system using polyphatidylcholines S-PCs and liposomes loaded with doxorubicin DOX was studied. The thioether bond present in the final formulation is oxidized in the presence of ROS, which in turn results in drug release (Yin et al., 2020).

Another strategy for the release of drugs from the nanoparticles uses spacer chemistry to destabilize the nanoparticles in the TME. Novel ready-to-use amphiphilic block polymer-modified polymersomes (PS) were synthesized for the release of DOX. The tunable site-specific release of the drug was achieved through incorporation of a hydrophobic boronic ester-based ROS sensor into the backbone of the polymer. In addition, the reaction of ROS results in the production of hydrophilic carboxylic acid or phenol, which can destabilize DOX-loaded PS. Cumulative release of the drug also indicated the time-dependent sustained release of DOX (Du et al., 2019). Mitochondrial ROS can be used for the stimuli-responsive release of drugs for cancer therapy. Here, endogenous mitochondrial ROS was utilized to release the cellular respiration inhibitor CPT from dual targeting polydrug nanoreactors. This CPT can be used for the mitochondrial ROS burst. Cumulative drug release from the carrier nanoparticle was found to be increased after treatment with H_2O_2, indicating ROS-responsive drug release (Zhang W. et al., 2019). Celastrol is a water insoluble naturally derived anticancer drug found effective against ovarian cancer. For effective targeting and delivery of drug a thioketal ROS responsive linker based nanoparticle was developed with folic acid ovarian cancer targeting ability. Thioketal linker was added between PLGA and PEG polymer moiety. In final preparation a water in oil emulsion of celestrol containing nanoparticle containing PLGA-Tk-PEG and PVA was developed. Effective ROS stimulated breaking of thioletal linker was obtained and subsequent release of celastrol caused therapeutic effect in ovarian cancer (Niu et al., 2020).

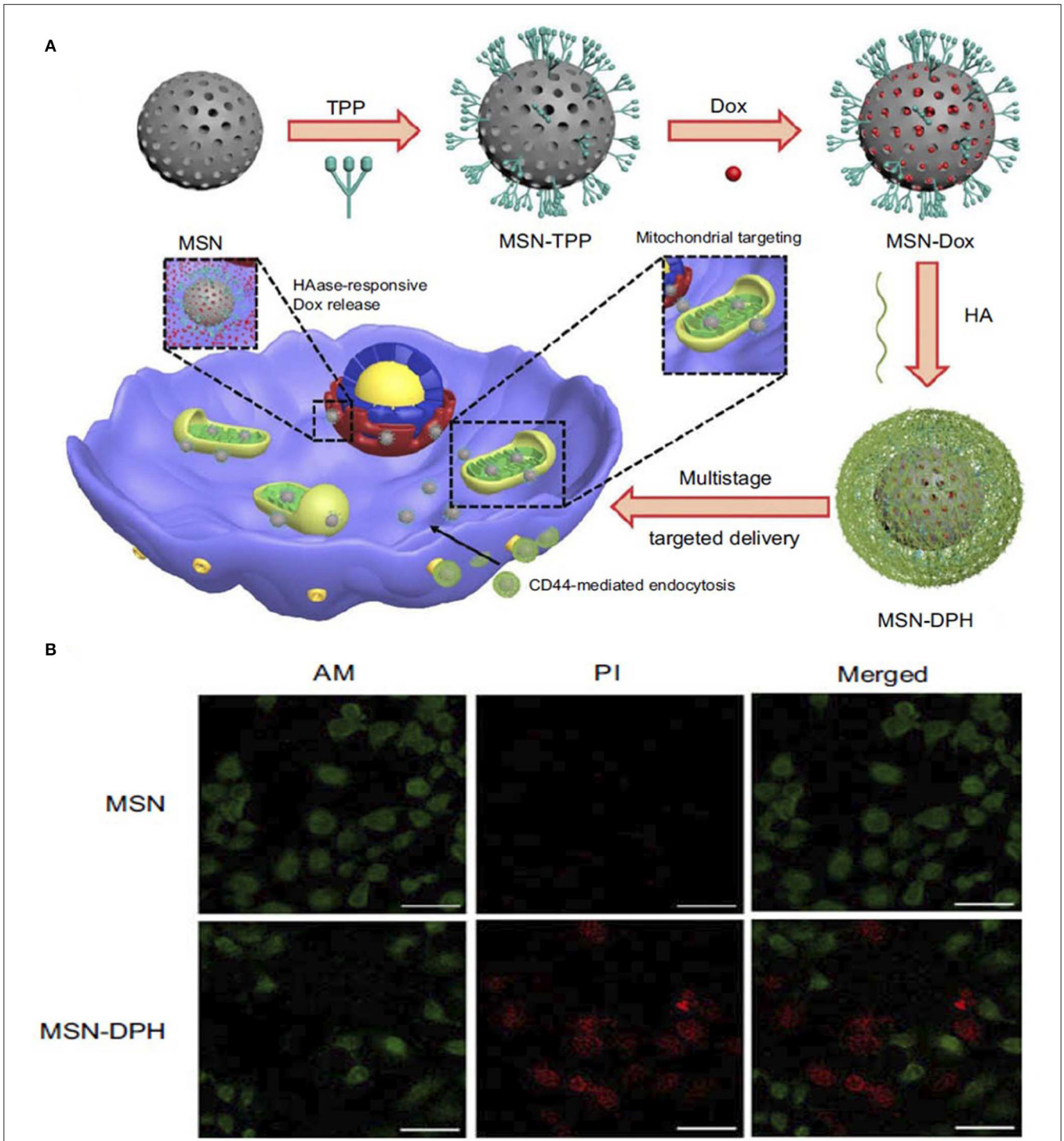

FIGURE 4 | Schematic illustration of synthesis and application of **(A)** MSN-DPH nanoparticles, Cumulative DOX release from MSN-DOX, MSN-DPH, and MSN-DPH+HAase. **(B)** Live/dead images of MGC-803 cells incubated with MSN and MSN-DPH nanoparticles. Reprinted with permission from Naz et al. (2019). This work is published and licensed by Dove Medical Press Limited and incorporate the Creative Commons Attribution—Non-Commercial (unported, v3.0) License (http://creativecommons.org/licenses/by-nc/3.0/).

The interaction between curcumin and phenylboronic acid (PBA) can be used to fabricate ROS-responsive nanoparticles. Curcumin can be used to regulate growth inhibition and apoptosis in cancer cells. In a related study, a biocompatible PBA modified with PEG-grafted poly(acrylic acid) was used to synthesize TME ROS-responsive nanoparticles with encapsulated curcumin for effective delivery of curcumin to the target site. The H_2O_2-triggered curcumin release was

TABLE 4 | ROS stimuli responsive nanoparticle for anti-cancer drug release.

Nanoparticular components	Mechanism	Payload	References
Arginylglycylaspartic acid	Degradation of thioketal group under the biological ROS level	EpothiloneB	Bertoni et al., 2020
Polyphatidylcholines	Degradation of thioether group under the biological ROS level	Doxorubicin	Yin et al., 2020
Poly([N-(2-hydroxypropyl)] methacrylamide	Degradation of boronic ester linker under the biological ROS level	Doxorubicin	Du et al., 2019
Polydimethylsiloxane	Mitochondrial ROS mediated destabilization	Camptothecin	Zhang W. et al., 2019
PEG grafted poly(acrylic acid)	Mitochondrial ROS mediated destabilization	Curcumin	Luo et al., 2017
PEG grafted poly glycolic acid	Degradation of thioketal group under the biological ROS level	Celastrol	Niu et al., 2020

investigated to understand the release pattern of the drug in the presence and absence of ROS (**Figure 5**) (Luo et al., 2017). Although ROS-responsive nanoparticle systems are a promising tool for delivering therapeutic cargos to the tumor site, the synergistic effect of ROS with temperature, enzymes, hypoxia, etc. could be used as an efficient method of treatment.

Hypoxia-Responsive Systems

The TME plays a major role in causing hypoxia and in turn promoting cancer progression. Hypoxia is a phenomenon in tumors attributed to an insufficient amount of oxygen reaching the cells due to the blood supply disruption, usually in deeper parts of tumors. The hypoxic level in cells is defined as an oxygen threshold level of 2% or less from a normal oxygen level of 9% (Muz et al., 2015). Hypoxia is expressed in the majority of tumors and is also considered to be a prognostic factor associated with tumor progression (Jing et al., 2019). Utilizing hypoxia to enable nanoparticles to change their physiochemical properties to release drugs has been the subject of many studies. Similar to other stimuli release mechanisms, hypoxia-mediated release also depends on certain degradation mechanisms. The main mechanism requires reducible functional groups in the material, which can receive electrons and change the material physical properties, such as hydrophobicity, in the presence of hypoxia. Approximately three types of moieties are responsible for hypoxia-responsive release; azo linkers, nitrobenzyl alcohol, and nitroimidazoles. Nitroimidazole possesses bioreductive groups, which undergo reduction under hypoxic conditions and generate intermediates causing polymers to change their physiochemical properties, allowing the drug to be released. Nitrobenzyl alcohol induces electron transfer, and derivatives of nitrobenzyl are degraded by the 1–6 elimination reaction. Azobenzene also undergoes electron transfer and is reduced to aniline, which reduces the stability of the polymer structure and initiates drug release (Thambi et al., 2016) (**Table 5**).

A hypoxia-sensitive polymer based on a hydrophobic p-nitrobenzyl derivative, 4-nitrobenzyl (3-azidopropyl) carbamate (AP-NC) conjugated to methoxy PEG-b-poly(γ-propargyl-L-glutamate) (PPLG) copolymers self-assembled into micelles was developed to load DOX. The DOX release was enhanced in the hypoxic environment when the amino groups in the mPEG-PPLG-NC side chain were liberated after conversion of the p-aminobenzyl group. The p-nitrobenzyl derivative of AP-NC is sensitive to hypoxia and forms a reduced p-aminobenzyl group due to the overexpression of nitroreductase in a hypoxic environment (**Figure 6**) (Zhang et al., 2020). In a similar kind of application, an amphiphilic block copolymer, composed of PEG as the hydrophilic block and poly(ε-(4-nitro)benzyloxycarbonyl-L-lysine) as the hydrophobic block, was prepared for DOX. The DOX-loaded micelles exhibited rapid intracellular release of DOX under the hypoxic condition, implying high potential as a drug carrier for cancer therapy (Thambi et al., 2016). In another study, a hypoxia-sensitive azo-bond containing black hole quencher 3 was conjugated to carboxymethyl dextran to form nanoparticles with loaded DOX. *In vitro* cytotoxicity study revealed that this nanopartilces showed higher toxicity under hypoxic conditions than normoxic conditions (Son et al., 2018). Azobenzene-based nanoparticles linking PEG and PEI-DOPE (PAPD) were synthesized to load siRNA. In a hypoxic environment, the azobenzene linker is cleaved, and PEI-DOPE/siRNA is exposed and taken up by cells. Hypoxia-induced gene silencing was observed in the *in vitro* analysis (Perche et al., 2014). Human serum albumin (HSA)-based nanoparticles were prepared with a hypoxia-sensitive azobenzene linker connecting chlorin-e6 and oxaliplatin to HSA (Yang et al., 2019).

The dissociated particles of HC (HSA+chlorin e6) and HO (HSA+oxaliplatin) enhanced the anticancer effect through photodynamic and chemotherapeutic mechanisms. The release of chorine 6 due to hypoxic-mediated release was measured indirectly by fluorescence, which showed a periodic increase in fluorescence in the nanoparticle formulation. This nanoparticle was tested in terms of cell uptake and response to hypoxic conditions, under which it showed enhanced release of doxorubicin compared with normoxic conditions. NP study showed the presence of DOX in the deep regions of spheroids/tumors due to hypoxic conditions enabling azobenzene linker disruption (Li Z. et al., 2018). Breast cancer have overexpressing 17β-Estradiol (E2) cells that provide unique opportunity for breast tumor targeting for drug delivery. Polymerosome loaded with doxorubicin was developed with estradiol targeting for hypoxic stimuli responsive breast cancer. Hypoxia environment (2% oxygen) stimulated release of almost 90% of drug release compared to 30% release of DOX (21% oxygen) (Mamnoon et al., 2020).

Multistimuli-Responsive Systems

Multistimuli-responsive nanoparticle systems use a combination of internal tumor stimuli to release drugs from the nanoparticles (**Figure 7**). Compared to release in response to a single stimulus, drugs can be released from multistimuli nanoparticles in a

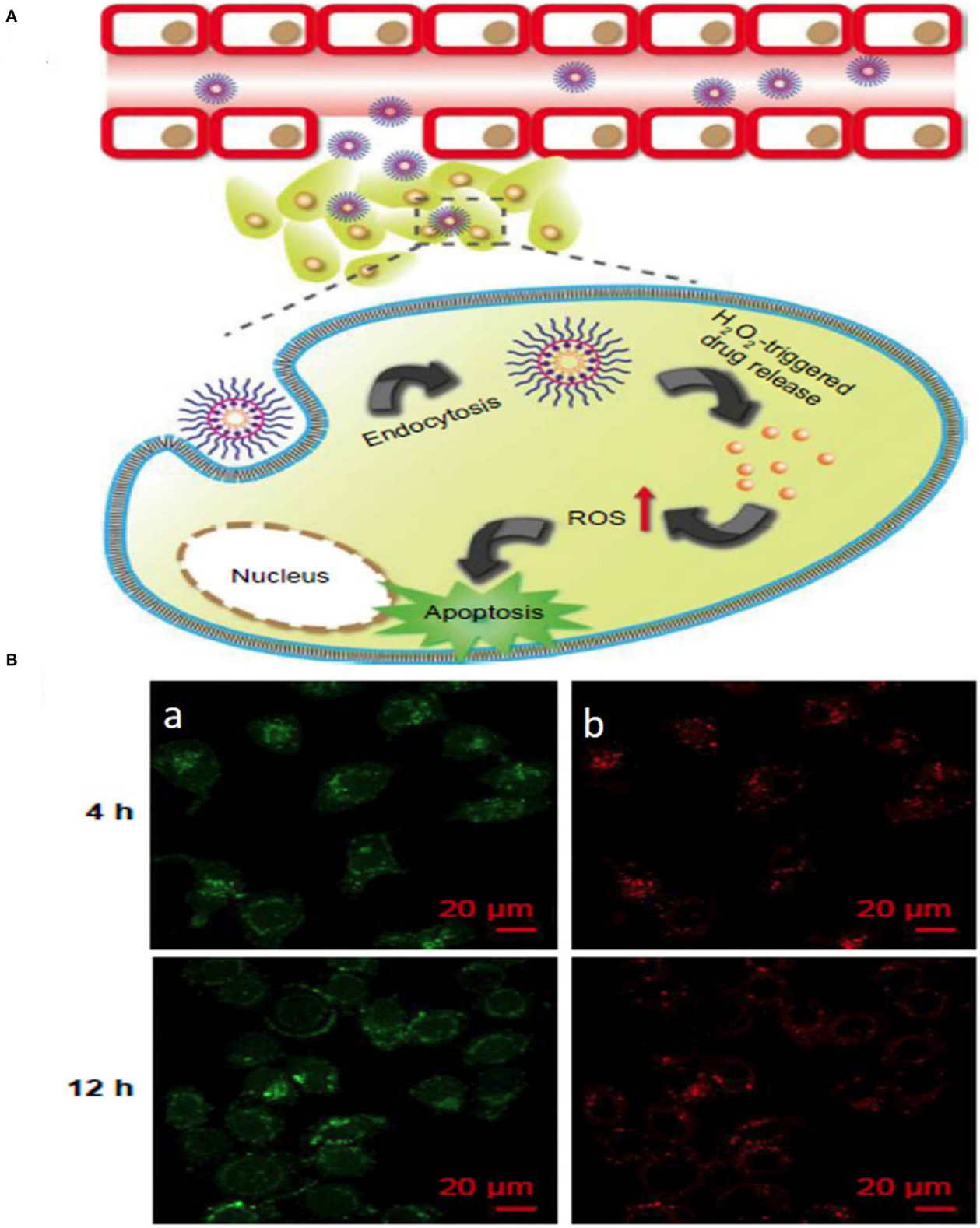

FIGURE 5 | Schematic illustration of **(A)** ROS stimuli responsive delivery of PPHC nanoparticles, schematic representation of ROS triggered intracellular drug delivery followed by apoptosis. **(B)** Confocal microscopic images of intracellular localization of PPHC nanoparticles in A549 cells at 4 h and 12 incubation [(a) PPHC channel, (b) lysotracker red channel. Reprinted with permission from Luo et al. (2017). This work is published and licensed by Dove Medical Press Limited. The full terms of this license are available at https://www.dovepress.com/terms.php and incorporate the Creative Commons Attribution].

TABLE 5 | Hypoxia stimuli responsive nanoparticle for anti-cancer drug release.

Nanoparticular components	Mechanism	Payload	References
Polyethyleneglycol	Hypoxia sensitive p-nitrobenzyl derivative destabilization	Doxorubicin	Zhang et al., 2020
Poly-L-Lysine	Hypoxia sensitive nitrobenzyl chlorformate moiety destabilization	Doxorubicin	Thambi et al., 2016
Carboxymethyl dextran	Hypoxia sensitive azo bon destabilization	Doxorubicin	Son et al., 2018
Poly(N-isopropylacrylamide	Hypoxia sensitive azobenzene linker destabilization	Gemcitabine	Kulkarni et al., 2016
Human serum albumin	Hypoxia sensitive azobenzene linker destabilization	Oxaliplatin	Yang et al., 2019
Poly(lactic-co-glycolic acid)	Hypoxia sensitive azobenzene linker destabilization	Doxorubicin	Li Z. et al., 2018
Polyethyleneglycol, polylactic acid	Hypoxia sensitive azobenzene linker destabilization	Doxorubicin	Mamnoon et al., 2020

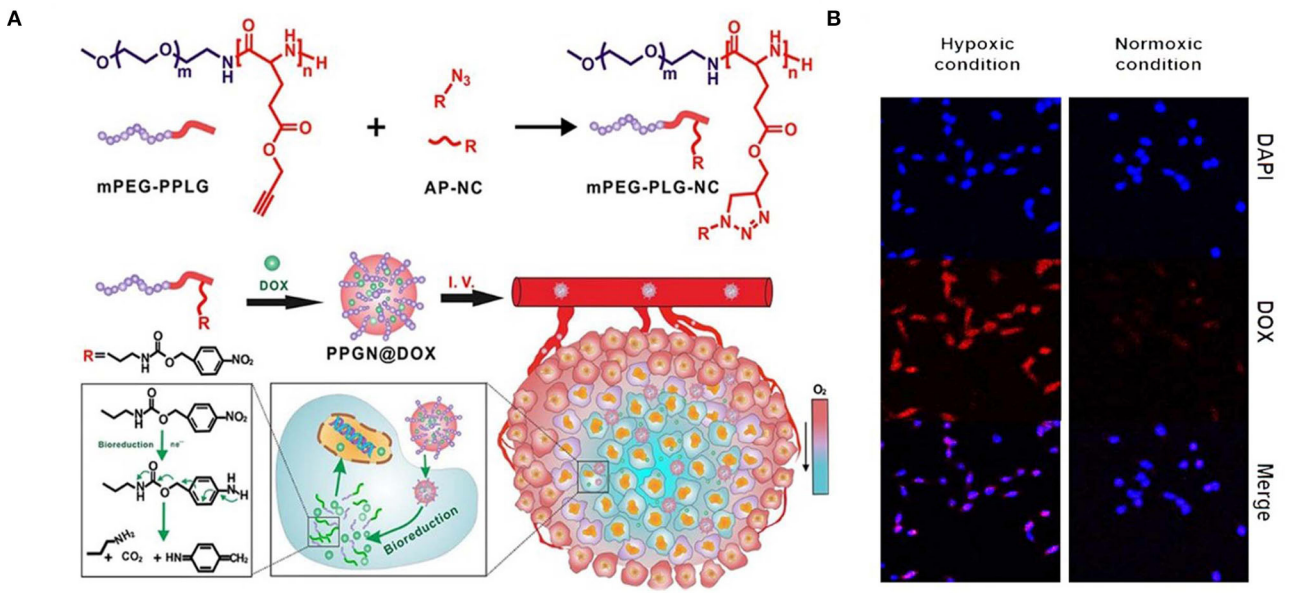

FIGURE 6 | Schematic illustration of synthesis and intracellular hypoxia stimuli responsive delivery of PPGN@DOX nanoparticles. **(A)** Schematic representation of hypoxia triggered intracellular drug delivery. **(B)** Confocal microscopic images of intracellular localization of PPGN@DOX nanoparticles in cells at Hypoxa and Normoxia condition. Reprinted with permission from Zhang et al. (2020). Copyright © 2020 American Chemical Society.

programmed manner (Cheng et al., 2013) (**Table 6**). A triple stimuli-responsive system (pH/GSH/enzyme) was developed with keratin and DOX by an ionic gelation method. The release increased at low pH due to protonation of keratin and DOX. In a similar manner, GSH-based release was observed at GSH concentrations of 10 and 50 mM. Trypsin is overexpressed in the tumor microenvironment and therefore very useful as an enzyme stimulus for drug release. With the combined stimuli action of pH, GSH and trypsin, the cumulative release obtained was very high compared with that obtained through a single stimulus. Keratin DOX nanoparticles (KDNPs) have the potential to release nitric oxide (NO) in the presence of GSH. Overall, KDNPs are effective multistimuli platforms for the release of DOX and NO (Li Y. et al., 2018).

Random copolymers of (PNIPAM-co-AA-co-NIA) and poly(isopropylacryamide-co-acrylic acid-co-2-nitroimidazole acrylate) were self-assembled into spherical micelles at room temperature by EDC and RAFT reactions. The copolymers contained different levels of the 2-nitroimidazole (NI) group, which responds to hypoxic conditions by being transformed into an amino imidazole group (hydrophobic to hydrophilic transition), thereby releasing the drug. In addition, the temperature-sensitive property of PNIPAM can further facilitate the release of the drug. The cumulative release of DOX was found to be almost 55% in both hypoxic and high-temperature conditions and nearly 20% in normoxic and low-temperature conditions (Ji et al., 2020).

A pH- and thermal-based stimuli-responsive system was synthesized with PMAA and PNIPAM coated onto a silica core to form SiO_2-PMAA-b-PNIPAM nanoparticles. The particle size was 15 nm, which was very small, enabling the incorporation of more drug and facilitating the deep penetration into the tissue. Apart from pH- and temperature-based release, the nanoparticles also possessed the ability to precipitate in acidic conditions at an increased temperature, which facilitated the accumulation of nanoparticles in the tumor tissue. *In vitro* studies were conducted with HeLa cells and revealed the uptake of the particles and drug release ability (Zheng et al., 2017). The stimuli-responsive

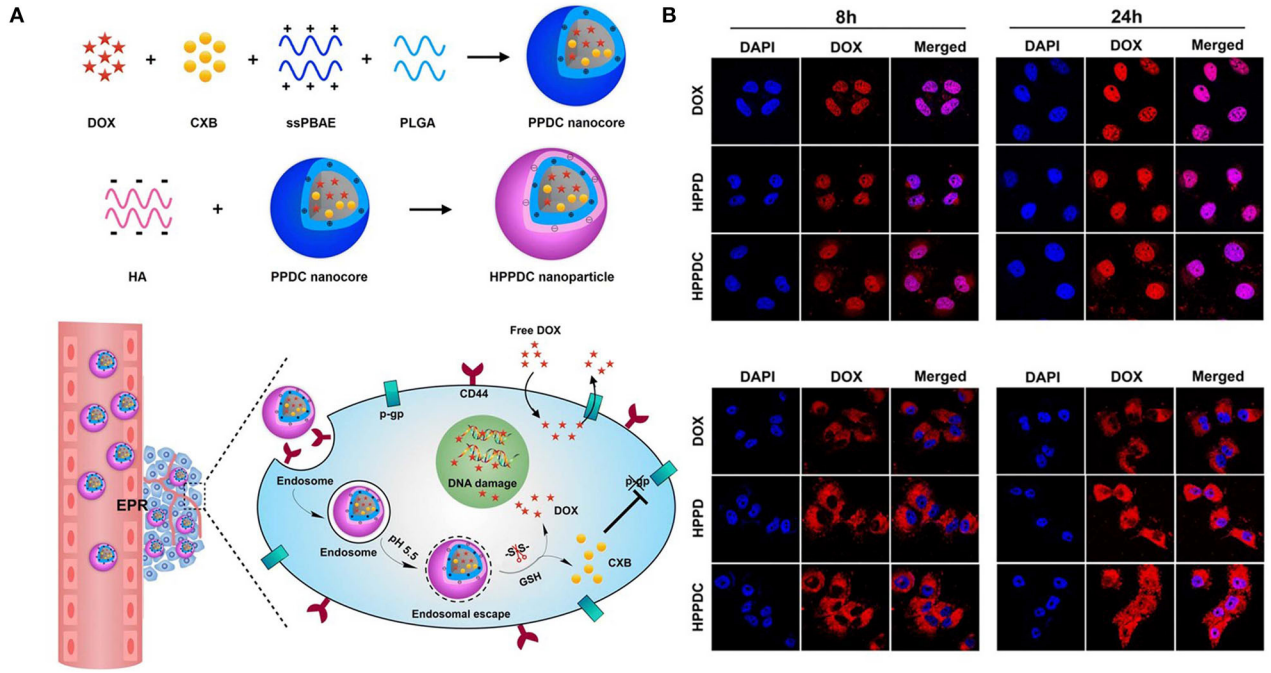

FIGURE 7 | Schematic illustration of **(A)** synthesis and intracellular pH and ROS stimuli responsive delivery of HPPDC nanoparticles **(B)** Confocal microscopic images of intracellular localization of HPPDC nanoparticles in MCF7/ADR cells at (a) 8 h and (b) 24 h incubation. Reprinted with permission from Zhang S. et al. (2019). This work is published and licensed by Springer Nature under the terms of Creative Commons license.

behavior of the nanoparticles was utilized to treat lung metastasis of colorectal cancer cells using methoxy poly(ethylene glycol)-grafted chitosan crosslinked to selenocystine-acetyl histidine (Ac-histidine) conjugates (PL NPs). An *in vivo* study was performed in a pulmonary metastasis model using the CT-26 cell line. Lung metastasis in the PL NP-treated group was inhibited (Lee et al., 2018).

In another study, MSN-based redox/pH-responsive nanoparticles were developed with carbon dots, HA and chitosan as capping agents. This nanoparticle released the loaded DOX via a simple mechanism, which involved the destabilization of HA through the breakage of disulfide bonds to uncover chitosan and release the drug in response to the redox environment in the tumor (Chen Y. et al., 2019). pH/redox-responsive dox-loaded polymeric micelles were developed using poly(2- methacryloyloxyethyl phosphorylcholine) 25-block-poly(L-histidine) n (p[MPC])25-b-p[His]n, with p[His] as the pH-responsive element and p[MPC] as a redox-responsive block (John et al., 2017). A charge reversible pullulan derivative was used to develop a pH- and redox-responsive nanoparticle. Methotrexate, a cancer drug, was conjugated to an amino-modified poly(β-amino ester) amino ester. The nanoparticles could also load plasmid DNA coding for cancer therapeutic effects (Zhang et al., 2018). A pH-responsive zwitterionic poly(2-methacryloyloxyethyl phosphorylcholine)50-block-poly(L-aspartic acid)n (p(MPC)50–b–p(AA)n) was synthesized with a disulfide linker for dual stimuli-induced drug release of DOX. DOX release also seemed to be very high, when incubated in 4T1 cells at pH 5.5 (Johnson et al., 2017). Hyaluronic acid based nanoparticles were synthesized for loading multi drug resistance (MDR) blocking drug (Cyclooxygenase 2) and doxorubicin to treat against MDR resistant tumor. This nanoparticle contain core of sPBAE, PLGA Cyclooxygenase 2 (CXB) and doxorubicin (Zhang S. et al., 2019).

Internal stimuli in combination with external stimuli, such as light, temperature, or mechanical stimuli can enhance the release of the drug. In most cases, the TME itself may provide one kind of stimulus to facilitate drug release, but this approach might not be sufficient for the drug release from certain kinds of nanoparticles. Therefore, external stimuli can provide an additional push to reach the maximum release potential of the drug. However, a disadvantage of external stimuli-responsive materials is their inability to reach the site of the tumor to induce the appropriate release of the drug. For instance, photodynamic or photothermal stimuli can diffuse inside the body before reaching the active site. Regarding future use, there is a need to combine polymers, inorganic materials, and lipids to design multistimuli responsive anticancer drug delivery systems (An et al., 2016).

SUMMARY AND FUTURE DIRECTIONS

The main characteristic of stimuli-responsive drug delivery systems compared to the direct delivery of small-molecule anticancer drugs is their ability to release the drug in a stimuli-responsive manner, high drug loading capability and biocompatibility. The internal stimuli are activated inside the

TABLE 6 | Multi-stimuli responsive nanoparticle for anti-cancer drug release.

Nanoparticular components	Mechanism	Payload	References
Keratin	pH stimuli release by protonation of keratin/GSH/enzyme stimuli release by trypsin overexpression in TME	Doxorubicin	Li Y. et al., 2018
Poly(N-isopropylacrylamide	Hypoxia sensitive nitroimidazole (NI) group conversion to amino imidazole group/Temperature sensitive polymer PNIPAM	Doxorubicin	Ji et al., 2020
Poly(methacrylic acid), poly(N-isopropylacrylamide	pH sensitive PMAA/Temperature sensitive PNIPAM	Doxorubicin	Zheng et al., 2017
Poly(ethylene glycol)	Redox/pH sensitive selenocystine-acetyl histidine (Ac-histidine)	Piperlongumine	Lee et al., 2018
Mesoporous silica	Redox responsiveness from disulfide bond/pH sensitiveness from chitosan shell	Doxorubicin	Chen Y. et al., 2019
Poly(2- methacryloyloxyethyl phosphorylcholine, poly(L-histidine)	Redox sensitive p[MPC]/pH sensitive poly(L-histidine)	Doxorubicin	John et al., 2017
Poly(2-methacryloyloxyethyl phosphorylcholine, poly(L-aspartic acid	Redox responsiveness from disulfide bond/pH sensitive poly(β-amino ester)	Methotrexate	Zhang et al., 2018
Poly(2-methacryloyloxyethyl phosphorylcholine, poly(L-aspartic acid	Redox/pH responsive zwitterionic poly(2-methacryloyloxyethyl phosphorylcholine)50-block-poly(L-aspartic acid)n (p(MPC)50–b–p(AA)n)	Doxorubicin	Johnson et al., 2017
Poly(lactic-co-glycolic acid), poly(β-amino ester)	Redox responsiveness from disulfide bond/pH sensitive poly(β-amino ester)	Doxorubicin	Zhang S. et al., 2019

tumor. An internal stimuli-responsive system depends on the variation of stimuli, such as enzymatic variations, GSH level, pH, and ROS in the TME. This capability of internal stimuli release systems needs further development to gain more value than external stimuli responsive systems. In the field of nanotechnology, the new findings have paved a way for exclusive designs of polymeric nanosystems along with the capability for tuning their chemistry based on the surface and characterization of their physical nature, such as shape and size, to induce stimuli-responsiveness. Clinical translation of external stimuli responsive nanoparticles is conducted worldwide. But there are only limited clinical trial studies on internal stimuli responsive nanoparticle system such as pH responsive polymeric micelle loaded with epirubicin (NCT03168061) which is undergoing phase 1 and phase 2 trials. Another one is cisplatin loaded liposomal system (NCT01861496) which is internally activated by secretory phospholipase undergoing phase 1 and phase 2 trials (Mi, 2020).

An internal stimuli-responsive system should be developed which can respond to biochemical signals in the TME at very low concentrations in the range of nanomoles. This system would ensure a higher drug release efficacy of the nanoparticle system. This system would also open the possibility for incorporating a programmed multistage drug release mechanism involving biological processes. Overall, the future of internal stimuli-responsive systems depends on programmable and smart nanoparticle carriers, which can load and release drugs at the target site with maximum efficiency (An et al., 2016).

AUTHOR CONTRIBUTIONS

RT and SS wrote the manuscript. YJ wrote and edited the manuscript. All authors contributed to the article and approved the submitted version.

FUNDING

This work was supported by the Technology Innovation Program (or Industrial Strategic Technology Development Program-Development of Core Industrial Technology) (20003822, Development of Navigation System Technologies of MicroNano Robots with Drug for Brain Disease Therapy) funded by the Ministry of Trade, Industry & Energy (MOTIE, Korea).

REFERENCES

Aggarwal, V., Tuli, H. S., Varol, A., Thakral, F., Yerer, M. B., Sak, K., et al. (2019). Role of reactive oxygen species in cancer progression: molecular mechanisms and recent advancements. *Biomolecules* 9:735. doi: 10.3390/biom9110735

Aluri, R., and Jayakannan, M. (2017). Development of l-tyrosine-based enzyme-responsive amphiphilic poly(ester-urethane) nanocarriers for multiple drug delivery to cancer cells. *Biomacromolecules* 18, 189–200. doi: 10.1021/acs.biomac.6b01476

An, X., Zhu, A., Luo, H., Ke, H., Chen, H., and Zhao, Y. (2016). Rational design of multi-stimuli-responsive nanoparticles for precise cancer therapy. *ACS Nano* 10, 5947–5958. doi: 10.1021/acsnano.6b01296

Andhari, S. S., Wavhale, R. D., Dhobale, K. D., Tawade, B. V., Chate, G. P., Patil, Y. N., et al. (2020). Self-propelling targeted magneto-nanobots for deep tumor

penetration and pH-responsive intracellular drug delivery. *Sci. Rep.* 10:4703. doi: 10.1038/s41598-020-61586-y

Bauhuber, S., Hozsa, C., Breunig, M., and Göpferich, A. (2009). Delivery of nucleic acids via disulfide-based carrier systems. *Adv. Mater.* 21, 3286–3306. doi: 10.1002/adma.200802453

Bertoni, S., Machness, A., Tiboni, M., Bartolo, R., and Santos, H. A. (2020). Reactive oxygen species responsive nanoplatforms as smart drug delivery systems for gastrointestinal tract targeting. *Biopolymers* 111:e23336. doi: 10.1002/bip.23336

Blanco, E., Shen, H., and Ferrari, M. (2015). Principles of nanoparticle design for overcoming biological barriers to drug delivery. *Nat. Biotechnol.* 33, 941–951. doi: 10.1038/nbt.3330

Cai, D., Han, C., Liu, C., Ma, X., Qian, J., Zhou, J., et al. (2020). Chitosan-capped enzyme-responsive hollow mesoporous silica nanoplatforms for colon-specific drug delivery. *Nanoscale Res. Lett.* 15:123. doi: 10.1186/s11671-020-03351-8

Chen, X., Han, W., Zhao, X., Tang, W., and Wang, F. (2019). Epirubicin-loaded marine carrageenan oligosaccharide capped gold nanoparticle system for pH-triggered anticancer drug release. *Sci. Rep.* 9:6754. doi: 10.1038/s41598-019-43106-9

Chen, Y., Wang, Y.-F., He, L., Wang, Z., Shen, Y.-Q., Cong, H.-L., et al. (2019). Redox and pH double stimulus-responsive mesoporous silica nanoparticles for drug delivery. *Ferroelectrics* 549, 1–11. doi: 10.1080/00150193.2019.1592538

Cheng, R., Meng, F., Deng, C., Klok, H. A., and Zhong, Z. (2013). Dual and multi-stimuli responsive polymeric nanoparticles for programmed site-specific drug delivery. *Biomaterials* 34, 3647–3657. doi: 10.1016/j.biomaterials.2013.01.084

Cheng, W., Gu, L., Ren, W., and Liu, Y. (2014). Stimuli-responsive polymers for anti-cancer drug delivery. *Mater. Sci. Eng. C Mater. Biol. Appl.* 45, 600–608. doi: 10.1016/j.msec.2014.05.050

Crucho, C. I. C. (2015). Stimuli-responsive polymeric nanoparticles for nanomedicine. *ChemMedChem* 10, 24–38. doi: 10.1002/cmdc.201402290

Deirram, N., Zhang, C., Kermaniyan, S. S., Johnston, A. P. R., and Such, G. K. (2019). pH-responsive polymer nanoparticles for drug delivery. *Macromol. Rapid Commun.* 40:1800917. doi: 10.1002/marc.201800917

Deng, H., Liu, J., Zhao, X., Zhang, Y., Liu, J., Xu, S., et al. (2014). PEG-b-PCL copolymer micelles with the ability of pH-controlled negative-to-positive charge reversal for intracellular delivery of doxorubicin. *Biomacromolecules* 15, 4281–4292. doi: 10.1021/bm501290t

Ding, C., Tong, L., Feng, J., and Fu, J. (2016). Recent advances in stimuli-responsive release function drug delivery systems for tumor treatment. *Molecules* 21:1715. doi: 10.3390/molecules21121715

Du, J., Lane, L. A., and Nie, S. (2015). Stimuli-responsive nanoparticles for targeting the tumor microenvironment. *J. Control. Release* 219, 205–214. doi: 10.1016/j.jconrel.2015.08.050

Du, Y., He, W., Xia, Q., Zhou, W., Yao, C., and Li, X. (2019). Thioether phosphatidylcholine liposomes: a novel ROS-responsive platform for drug delivery. *ACS Appl. Mater. Interfaces* 11, 37411–37420. doi: 10.1021/acsami.9b08901

Gao, A. X., Liao, L., and Johnson, J. A. (2014). Synthesis of acid-labile PEG and PEG-doxorubicin-conjugate nanoparticles via brush-first ROMP. *ACS Macro Lett.* 3, 854–857. doi: 10.1021/mz5004097

Gao, W., Chan, J. M., and Farokhzad, O. C. (2010). pH-Responsive nanoparticles for drug delivery. *Mol. Pharm.* 7, 1913–1920. doi: 10.1021/mp100253e

Gisbert-Garzaran, M., Manzano, M., and Vallet-Regi, M. (2017). pH-responsive mesoporous silica and carbon nanoparticles for drug delivery. *Bioengineering* 4:3. doi: 10.3390/bioengineering4010003

Gunawan, S. T., Liang, K., Such, G. K., Johnston, A. P. R., Leung, M. K. M., Cui, J., et al. (2014). Engineering enzyme-cleavable hybrid click capsules with a pH-sheddable coating for intracellular degradation. *Small* 10, 4080–4086. doi: 10.1002/smll.201400450

Guo, X., Cheng, Y., Zhao, X., Luo, Y., Chen, J., and Yuan, W.-E. (2018). Advances in redox-responsive drug delivery systems of tumor microenvironment. *J. Nanobiotechnol.* 16:74. doi: 10.1186/s12951-018-0398-2

Han, H. S., Lee, J., Kim, H. R., Chae, S. Y., Kim, M., Saravanakumar, G., et al. (2013). Robust PEGylated hyaluronic acid nanoparticles as the carrier of doxorubicin: mineralization and its effect on tumor targetability *in vivo*. *J. Controll. Release* 168, 105–114. doi: 10.1016/j.jconrel.2013.02.022

Han, S. S., Li, Z. Y., Zhu, J. Y., Han, K., Zeng, Z. Y., Hong, W., et al. (2015). Dual-pH sensitive charge-reversal polypeptide micelles for tumor-triggered targeting uptake and nuclear drug delivery. *Small* 11, 2543–2554. doi: 10.1002/smll.201402865

Jhaveri, A. M., and Torchilin, V. P. (2014). Multifunctional polymeric micelles for delivery of drugs and siRNA. *Front. Pharmacol.* 5:77. doi: 10.3389/fphar.2014.00077

Ji, C., Deng, Y., Yuan, H., Wu, Y., and Yuan, W. (2020). Hypoxia and temperature dual-stimuli-responsive random copolymers: facile synthesis, self-assembly and controlled release of drug. *N. J. Chem.* 44, 10229–10238. doi: 10.1039/D0NJ02114H

Jia, N., Li, W., Liu, D., Wu, S., Song, B., Ma, J., et al. (2020). Tumor microenvironment stimuli-responsive nanoparticles for programmed anticancer drug delivery. *Mol. Pharm.* 17, 1516–1526. doi: 10.1021/acs.molpharmaceut.9b01189

Jing, X., Yang, F., Shao, C., Wei, K., Xie, M., Shen, H., et al. (2019). Role of hypoxia in cancer therapy by regulating the tumor microenvironment. *Mol. Cancer* 18:157. doi: 10.1186/s12943-019-1089-9

John, J. V., Thomas, R. G., Lee, H. R., Chen, H., Jeong, Y. Y., and Kim, I. (2016). Phospholipid end-capped acid-degradable polyurethane micelles for intracellular delivery of cancer therapeutics. *Adv. Healthc. Mater.* 5, 1874–1883. doi: 10.1002/adhm.201600126

John, J. V., Uthaman, S., Augustine, R., Manickavasagam Lekshmi, K., Park, I.-K., and Kim, I. (2017). Biomimetic pH/redox dual stimuli-responsive zwitterionic polymer block poly(L-histidine) micelles for intracellular delivery of doxorubicin into tumor cells. *J. Polymer Sci. A Polymer Chem.* 55, 2061–2070. doi: 10.1002/pola.28602

Johnson, R. P., Uthaman, S., Augustine, R., Zhang, Y., Jin, H., Choi, C. I., et al. (2017). Glutathione and endosomal pH-responsive hybrid vesicles fabricated by zwitterionic polymer block poly(l -aspartic acid) as a smart anticancer delivery platform. *React. Func. Polymers* 119, 47–56. doi: 10.1016/j.reactfunctpolym.2017.07.010

Joshi, D. C., Saxena, S., and Jayakannan, M. (2019). Development of l-lysine based biodegradable polyurethanes and their dual-responsive amphiphilic nanocarriers for drug delivery to cancer cells. *ACS Appl. Polymer Mater.* 1, 1866–1880. doi: 10.1021/acsapm.9b00413

Kulkarni, P., Haldar, M. K., You, S., Choi, Y., and Mallik, S. (2016). Hypoxia-responsive polymersomes for drug delivery to hypoxic pancreatic cancer cells. *Biomacromolecules* 17, 2507–2513. doi: 10.1021/acs.biomac.6b00350

Lee, H. L., Hwang, S. C., Nah, J. W., Kim, J., Cha, B., Kang, D. H., et al. (2018). Redox- and pH-responsive nanoparticles release piperlongumine in a stimuli-sensitive manner to inhibit pulmonary metastasis of colorectal carcinoma cells. *J. Pharm. Sci.* 107, 2702–2712. doi: 10.1016/j.xphs.2018.06.011

Li, N., Cai, H., Jiang, L., Hu, J., Bains, A., Hu, J., et al. (2017). Enzyme-sensitive and amphiphilic PEGylated dendrimer-paclitaxel prodrug-based nanoparticles for enhanced stability and anticancer efficacy. *ACS Appl. Mater. Interfaces* 9, 6865–6877. doi: 10.1021/acsami.6b15505

Li, R., Peng, F., Cai, J., Yang, D., and Zhang, P. (2020). Redox dual-stimuli responsive drug delivery systems for improving tumor-targeting ability and reducing adverse side effects. *Asian J. Pharm. Sci.* 15, 311–325. doi: 10.1016/j.ajps.2019.06.003

Li, Y., Lei, X., Dong, H., and Ren, T. (2014). Sheddable, degradable, cationic micelles enabling drug and gene delivery. *RSC Adv.* 4, 8165–8176. doi: 10.1039/c3ra46756b

Li, Y., Lin, J., Zhi, X., Li, P., Jiang, X., and Yuan, J. (2018). Triple stimuli-responsive keratin nanoparticles as carriers for drug and potential nitric oxide release. *Mater. Sci. Eng. C Mater. Biol. Appl.* 91, 606–614. doi: 10.1016/j.msec.2018.05.073

Li, Z., Wu, M., Bai, H., Liu, X., and Tang, G. (2018). Light-enhanced hypoxia-responsive nanoparticles for deep tumor penetration and combined chemo-photodynamic therapy. *Chem. Commun.* 54, 13127–13130. doi: 10.1039/C8CC08445A

Li, Z.-Y., Hu, J.-J., Xu, Q., Chen, S., Jia, H.-Z., Sun, Y.-X., et al. (2015). A redox-responsive drug delivery system based on RGD containing peptide-capped mesoporous silica nanoparticles. *J. Mater. Chem. B* 3, 39–44. doi: 10.1039/C4TB01533A

Liao, J., Li, W., Peng, J., Yang, Q., Li, H., Wei, Y., et al. (2015). Combined cancer photothermal-chemotherapy based on doxorubicin/gold nanorod-loaded polymersomes. *Theranostics* 5, 345–356. doi: 10.7150/thno.10731

Liberti, M. V., and Locasale, J. W. (2016). The warburg effect: how does it benefit cancer cells? *Trends Biochem. Sci.* 41, 211–218. doi: 10.1016/j.tibs.2015.12.001

Luo, C. Q., Xing, L., Cui, P. F., Qiao, J. B., He, Y. J., Chen, B. A., et al. (2017). Curcumin-coordinated nanoparticles with improved stability for

reactive oxygen species-responsive drug delivery in lung cancer therapy. *Int. J. Nanomed.* 12, 855–869. doi: 10.2147/IJN.S122678

Mamnoon, B., Feng, L., Froberg, J., Choi, Y., Sathish, V., and Mallik, S. (2020). Hypoxia-responsive, polymeric nanocarriers for targeted drug delivery to estrogen receptor-positive breast cancer cell spheroids. *Mol. Pharm.* 17, 4312–4322. doi: 10.1021/acs.molpharmaceut.0c00754

Mi, P. (2020). Stimuli-responsive nanocarriers for drug delivery, tumor imaging, therapy and theranostics. *Theranostics* 10, 4557–4588. doi: 10.7150/thno.38069

Mura, S., Nicolas, J., and Couvreur, P. (2013). Stimuli-responsive nanocarriers for drug delivery. *Nat. Mater.* 12, 991–1003. doi: 10.1038/nmat3776

Muz, B., De La Puente, P., Azab, F., and Azab, A. K. (2015). The role of hypoxia in cancer progression, angiogenesis, metastasis, and resistance to therapy. *Hypoxia* 3, 83–92. doi: 10.2147/HP.S93413

Naz, S., Wang, M., Han, Y., Hu, B., Teng, L., Zhou, J., et al. (2019). Enzyme-responsive mesoporous silica nanoparticles for tumor cells and mitochondria multistage-targeted drug delivery. *Int. J. Nanomed.* 14, 2533–2542. doi: 10.2147/IJN.S202210

Niu, W., Wang, J., Wang, Q., and Shen, J. (2020). Celastrol loaded nanoparticles with ROS-response and ROS-inducer for the treatment of ovarian cancer. *Front. Chem.* 8:574614. doi: 10.3389/fchem.2020.574614

Palanikumar, L., Al-Hosani, S., Kalmouni, M., Nguyen, V. P., Ali, L., Pasricha, R., et al. (2020). pH-responsive high stability polymeric nanoparticles for targeted delivery of anticancer therapeutics. *Commun. Biol.* 3:95. doi: 10.1038/s42003-020-0817-4

Pang, Z., Zhou, J., and Sun, C. (2020). Ditelluride-bridged PEG-PCL copolymer as folic acid-targeted and redox-responsive nanoparticles for enhanced cancer therapy. *Front. Chem.* 8:156. doi: 10.3389/fchem.2020.00156

Perche, F., Biswas, S., Wang, T., Zhu, L., and Torchilin, V. P. (2014). Hypoxia-targeted siRNA delivery. *Angew. Chem. Int. Edn.* 53, 3362–3366. doi: 10.1002/anie.201308368

Qu, H., Yang, L., Yu, J., Dong, T., Rong, M., Zhang, J., et al. (2017). A redox responsive controlled release system using mesoporous silica nanoparticles capped with Au nanoparticles. *RSC Adv.* 7, 35704–35710. doi: 10.1039/C7RA04444E

Rabiee, M. (2019). Enzyme-responsive nanomaterials. *Nanoscale* 6, 12273–12286. doi: 10.1088/2053-2571/aafb0cch5

Ruttala, H. B., Ramasamy, T., Madeshwaran, T., Hiep, T. T., Kandasamy, U., Oh, K. T., et al. (2018). Emerging potential of stimulus-responsive nanosized anticancer drug delivery systems for systemic applications. *Arch. Pharm. Res.* 41, 111–129. doi: 10.1007/s12272-017-0995-x

Shi, J., Kantoff, P. W., Wooster, R., and Farokhzad, O. C. (2017). Cancer nanomedicine: progress, challenges and opportunities. *Nat. Rev. Cancer* 17, 20–37. doi: 10.1038/nrc.2016.108

Son, S., Rao, N. V., Ko, H., Shin, S., Jeon, J., Han, H. S., et al. (2018). Carboxymethyl dextran-based hypoxia-responsive nanoparticles for doxorubicin delivery. *Int. J. Biol. Macromol.* 110, 399–405. doi: 10.1016/j.ijbiomac.2017.11.048

Taghizadeh, B., Taranejoo, S., Monemian, S. A., Salehi Moghaddam, Z., Daliri, K., Derakhshankhah, H., et al. (2015). Classification of stimuli-responsive polymers as anticancer drug delivery systems. *Drug Deliv.* 22, 145–155. doi: 10.3109/10717544.2014.887157

Tao, W., and He, Z. (2018). ROS-responsive drug delivery systems for biomedical applications. *Asian J. Pharm. Sci.* 13, 101–112. doi: 10.1016/j.ajps.2017.11.002

Thambi, T., Son, S., Lee, D. S., and Park, J. H. (2016). Poly(ethylene glycol)-b-poly(lysine) copolymer bearing nitroaromatics for hypoxia-sensitive drug delivery. *Acta Biomater.* 29, 261–270. doi: 10.1016/j.actbio.2015.10.011

Tian, Y., and Lei, M. (2019). Polydopamine-based composite nanoparticles with redox-labile polymer shells for controlled drug release and enhanced chemo-photothermal therapy. *Nanoscale Res. Lett.* 14:186. doi: 10.1186/s11671-019-3027-6

Torchilin, V. P. (2014). Multifunctional, stimuli-sensitive nanoparticulate systems for drug delivery. *Nat. Rev. Drug Discov.* 13, 813–827. doi: 10.1038/nrd4333

Vander Heiden, M. G., Cantley, L. C., and Thompson, C. B. (2009). Understanding the warburg effect: the metabolic requirements of cell proliferation. *Science* 324, 1029–1033. doi: 10.1126/science.1160809

Wang, M., Gong, G., Feng, J., Wang, T., Ding, C., Zhou, B., et al. (2016). Dual pH-mediated mechanized hollow zirconia nanospheres. *ACS Appl. Mater. Interfaces* 8, 23289–23301. doi: 10.1021/acsami.6b07603

Wang, S., Huang, P., and Chen, X. (2016). Stimuli-responsive programmed specific targeting in nanomedicine. *ACS Nano* 10, 2991–2994. doi: 10.1021/acsnano.6b00870

Wang, Z., Tian, Y., Zhang, H., Qin, Y., Li, D., Gan, L., et al. (2016). Using hyaluronic acid-functionalized pH stimuli-responsive mesoporous silica nanoparticles for targeted delivery to CD44-overexpressing cancer cells. *Int. J. Nanomed.* 11, 6485–6497. doi: 10.2147/IJN.S117184

Wen, H. Y., Dong, H. Q., Xie, W. J., Li, Y. Y., Wang, K., Pauletti, G. M., et al. (2011). Rapidly disassembling nanomicelles with disulfide-linked PEG shells for glutathione-mediated intracellular drug delivery. *Chem. Commun.* 47, 3550–3552. doi: 10.1039/c0cc04983b

Xia, X., Yang, X., Huang, P., and Yan, D. (2020). ROS-responsive nanoparticles formed from RGD-epothilone B Conjugate for targeted cancer therapy. *ACS Appl. Mater. Interfaces* 12, 18301–18308. doi: 10.1021/acsami.0c00650

Xiao, D., Jia, H.-Z., Ma, N., Zhuo, R.-X., and Zhang, X.-Z. (2015). A redox-responsive mesoporous silica nanoparticle capped with amphiphilic peptides by self-assembly for cancer targeting drug delivery. *Nanoscale* 7, 10071–10077. doi: 10.1039/C5NR02247A

Yang, G., Phua, S. Z. F., Lim, W. Q., Zhang, R., Feng, L., Liu, G., et al. (2019). A hypoxia-responsive albumin-based nanosystem for deep tumor penetration and excellent therapeutic efficacy. *Adv. Mater. Weinheim.* 31:e1901513. doi: 10.1002/adma.201901513

Yao, J., Feng, J., and Chen, J. (2016). External-stimuli responsive systems for cancer theranostic. *Asian J. Pharm. Sci.* 11, 585–595. doi: 10.1016/j.ajps.2016.06.001

Yin, W., Ke, W., Lu, N., Wang, Y., Japir, A., Mohammed, F., et al. (2020). Glutathione and reactive oxygen species dual-responsive block copolymer prodrugs for boosting tumor site-specific drug release and enhanced antitumor efficacy. *Biomacromolecules* 21, 921–929. doi: 10.1021/acs.biomac.9b01578

Yu, J., Chu, X., and Hou, Y. (2014). Stimuli-responsive cancer therapy based on nanoparticles. *Chem. Commun.* 50, 11614–11630. doi: 10.1039/C4CC03984J

Yu, Y., Chen, C. K., Law, W. C., Weinheimer, E., Sengupta, S., Prasad, P. N., et al. (2014). Polylactide-graft-doxorubicin nanoparticles with precisely controlled drug loading for pH-triggered drug delivery. *Biomacromolecules* 15, 524–532. doi: 10.1021/bm401471p

Zhang, P., Yang, H., Shen, W., Liu, W., Chen, L., and Xiao, C. (2020). Hypoxia-responsive polypeptide nanoparticles loaded with doxorubicin for breast cancer therapy. *ACS Biomater. Sci. Eng.* 6, 2167–2174. doi: 10.1021/acsbiomaterials.0c00125

Zhang, S., Guo, N., Wan, G., Zhang, T., Li, C., Wang, Y., et al. (2019). pH and redox dual-responsive nanoparticles based on disulfide-containing poly(β-amino ester) for combining chemotherapy and COX-2 inhibitor to overcome drug resistance in breast cancer. *J. Nanobiotechnol.* 17:109. doi: 10.1186/s12951-019-0540-9

Zhang, S., Wang, D., Li, Y., Li, L., Chen, H., Xiong, Q., et al. (2018). pH- and redox-responsive nanoparticles composed of charge-reversible pullulan-based shells and disulfide-containing poly(ss-amino ester) cores for co-delivery of a gene and chemotherapeutic agent. *Nanotechnology* 29:325101. doi: 10.1088/1361-6528/aac4b5

Zhang, W., Hu, X., Shen, Q., and Xing, D. (2019). Mitochondria-specific drug release and reactive oxygen species burst induced by polyprodrug nanoreactors can enhance chemotherapy. *Nat. Commun.* 10:1704. doi: 10.1038/s41467-019-12198-2

Zheng, Y., Wang, L., Lu, L., Wang, Q., and Benicewicz, B. C. (2017). pH and thermal dual-responsive nanoparticles for controlled drug delivery with high loading content. *ACS Omega* 2, 3399–3405. doi: 10.1021/acsomega.7b00367

Conflict of Interest: The authors declare that the research was conducted in the absence of any commercial or financial relationships that could be construed as a potential conflict of interest.

frontiers in Molecular Biosciences

REVIEW
published: 11 January 2021
doi: 10.3389/fmolb.2020.597634

External and Internal Stimuli-Responsive Metallic Nanotherapeutics for Enhanced Anticancer Therapy

Adityanarayan Mohapatra[1], *Saji Uthaman*[2] *and In-Kyu Park*[1]*

[1] Department of Biomedical Sciences, Chonnam National University Medical School, Jeollanam-do, South Korea,
[2] Department of Polymer Science and Engineering, Chungnam National University, Daejeon, South Korea

Therapeutic, diagnostic, and imaging approaches based on nanotechnology offer distinct advantages in cancer treatment. Various nanotherapeutics have been presented as potential alternatives to traditional anticancer therapies such as chemotherapy, radiotherapy, and surgical intervention. Notably, the advantage of nanotherapeutics is mainly attributable to their accumulation and targeting ability toward cancer cells, multiple drug-carrying abilities, combined therapies, and imaging approaches. To date, numerous nanoparticle formulations have been developed for anticancer therapy and among them, metallic nanotherapeutics reportedly demonstrate promising cancer therapeutic and diagnostic efficiencies owing to their dense surface functionalization ability, uniform size distribution, and shape-dependent optical responses, easy and cost-effective synthesis procedure, and multiple anti-cancer effects. Metallic nanotherapeutics can remodel the tumor microenvironment by changing unfavorable therapeutic conditions into therapeutically accessible ones with the help of different stimuli, including light, heat, ultrasound, an alternative magnetic field, redox, and reactive oxygen species. The combination of metallic nanotherapeutics with both external and internal stimuli can be used to trigger the on-demand release of therapeutic molecules, augmenting the therapeutic efficacies of anticancer therapies such as photothermal therapy, photodynamic therapy, magnetic hyperthermia, sonodynamic therapy, chemodynamic therapy, and immunotherapy. In this review, we have summarized the role of different metallic nanotherapeutics in anti-cancer therapy, as well as their combinational effects with multiple stimuli for enhanced anticancer therapy.

Keywords: metallic nanotherapeutics, internal-stimuli, external-stimuli, phototherapy, sonodynamic therapy, magnetic hyperthermia, immunotherapy, clinical status

OPEN ACCESS

Edited by:
Weien Yuan,
Shanghai Jiao Tong University, China

Reviewed by:
David J. Lundy,
Taipei Medical University, Taiwan
Koichiro Uto,
National Institute for Materials Science, Japan

***Correspondence:**
In-Kyu Park
pik96@jnu.ac.kr

Specialty section:
This article was submitted to Nanobiotechnology, a section of the journal Frontiers in Molecular Biosciences

Received: *21 August 2020*
Accepted: *30 November 2020*
Published: *11 January 2021*

Citation:
Mohapatra A, Uthaman S and Park I-K (2021) External and Internal Stimuli-Responsive Metallic Nanotherapeutics for Enhanced Anticancer Therapy. Front. Mol. Biosci. 7:597634. doi: 10.3389/fmolb.2020.597634

INTRODUCTION

Nanotherapeutics can be the potential alternatives to standard cancer therapies such as chemotherapy, surgery, and radiation, and is an expanding sector of nanotechnology that combines nanoscience, biological science, material science, and pharmaceutical science, to develop novel anticancer therapeutics (Wang et al., 2020b). Nanoparticles (NPs) can regulate the pharmacokinetic

and pharmacodynamic profiles of chemotherapeutic drugs to prolong therapeutic activity. Owing to the nanoscale size, nanoparticles take advantage of leaky tumor vasculature and defective lymphatic drainage system to enhance their accumulation and retention time inside tumors, which is mediated by the enhanced permeability and retention (EPR) effect (Martin et al., 2020). Multiple nanotherapeutics based on the EPR effect mechanism have reached clinical trials such as Doxil™, Abraxane™, Marqibo™, DaunoXome™, Onivyde™, Myocet™, Mepact™, Genexol-PM™, and SMANCS™ (Shi et al., 2017). Although most of these nanotherapeutics have only improved the solubility and pharmacokinetic profile of the anticancer drugs, few of them have improved the survival rate in clinical studies (Rosenblum et al., 2018). Passively targeted nanotherapeutics result in the non-uniform accumulation inside the tumor vasculature due to various physiological barriers like the heterogenicity of the EPR effect, variable endothelial gaps, poor tumor penetration ability, hypoxic condition, and inefficient endosomal escape (Anselmo and Mitragotri, 2016). Moreover, nanoparticles can be functionalized with different moieties and ligands to actively target the tumor through overexpressed receptor binding and enhanced targeted cell uptake (Haider et al., 2020). To enhance the therapeutic efficacy of actively targeted nanotherapeutics, it needs a broad understanding of tumor microenvironment interactions with nanotherapeutics. Classical nanomedicine incorporates two vital components, a therapeutic agent and a drug delivery carrier. Nanomedicines can accommodate chemotherapeutic drugs, nucleotides such as DNA and RNA, immunomodulatory agents, photothermal and photodynamic agents, and radioisotopes to exert potent anticancer effects (Martin et al., 2020). To develop appropriate anticancer nanotherapeutics for specific cancer types, multiple nanoparticle properties have been reported, which need to be considered and prioritized according to the therapeutic requirements. Firstly, nanotherapeutics can conquer the solubility dilemma presented by hydrophobic chemotherapeutic drugs, enhancing their systemic stability. Secondly, nano-sized drug carriers protect anticancer drugs from biodegradation or elimination through the excretory and immune systems, establishing their biocompatible nature. Thirdly, nanomedicines can be functionalized with targeting ligands and stimuli-responsive moieties for site-specific, controlled drug delivery. Moreover, premature drug release into normal tissues can be prevented, enhancing the bioavailability of nanomedicines (Ahmad et al., 2010). These characteristics need to be considered during nanomedicine formulation to magnify the therapeutic potency of anticancer drugs and avoid adverse side effects.

Metallic nanotherapeutics are novel multifunctional units with potential application to biomedical processes such as diagnosis, imaging, and the delivery of therapeutically active agents (**Figure 1**). Nanoscale metallic nanoparticles (MNPs) range in size from between 10 and 100 nanometers and can be modified during their synthesis using different strategies according to the requirements of the particular biomedical application (Mody et al., 2010). Notably, the use of MNPs is gaining attention owing to their unique thermal, magnetic, optical, catalytic, and electrical properties (Venkatesh et al., 2018). Biological fluids maintain high ionic strength, causing the destabilization and aggregation of lipids, proteins, and polymeric nanoparticles within the body (Jurašin et al., 2016). Unlike lipid-, polymeric-, and protein-based nanoparticles, MNPs can overcome stability issues in different biological environments due to their lower agglomeration tendency and facile surface functionalization (Jurašin et al., 2016). The production of MNPs is easy and cost-effective. Moreover, MNPs can be tuned into different sizes and shapes, such as nanospheres, nanorods, nanostars, nanocages, and nanotriangles, to achieve maximal therapeutic efficacy. Notably, the size and shape of MNPs can alter cellular uptake and induce immune responses against cancer (Xie et al., 2017). The high surface-to-volume ratio of metallic nanotherapeutics enables a wide range of surface functionalization with antibodies, targeting ligands, drugs, and nucleotides in cancer therapy (Conde et al., 2012). Surface modifications of MNPs can enhance cellular internalization and incorporate stealth properties against the biological milieu (Conde et al., 2012). Surface-functionalized metallic nanotherapeutics potentiate the preferential transport of anticancer drugs into cancer cells, thereby diminishing side effects to the normal tissues. MNPs facilitate imaging and diagnostic modalities, including computed tomography (CT), magnetic resonance imaging (MRI), positron emission tomography (PET), photoacoustic imaging (PA), ultrasound (US), and surface-enhanced Raman scattering (SERS) (**Table 1**; Sharma et al., 2018).

Typically, anticancer prodrugs are designed with a specific balance of hydrophilic and lipophilic moieties (Zhang et al., 2017). After administration, the prodrugs are rapidly distributed throughout the body, irrespective of targeted and non-targeted tissues, followed by fast metabolization and subsequent excretion through the liver and kidneys. For example, liposomal and polymeric nanoparticles tend to initially accumulate in the liver, followed by excretion through the reticuloendothelial system (RES). Therefore, elaborate modifications in size, shape, and surface functionalization on nanoparticles can be beneficial in cancer therapeutics for controlling nanoparticle escape from the mononuclear phagocytic system (MPS) and enhancing circulation time. Thus, the rational design of metallic nanotherapeutics should primarily consider the biological barriers encountered during systemic circulation and the pharmacokinetic profiles of the nanotherapeutic. The surface functionalization of MNPs using hydrophilic polymers enhances their solubility and protects them from the MPS, extending the blood-retention time (Mohapatra et al., 2019). For example, passive targeting using polyethylene glycol (PEG)-coated gold nanorods significantly increased the retention time in the systemic circulation up to 19 h compared to non-PEGylated particles, which underwent rapid clearance within 15 min after administration (Lankveld et al., 2011). For metallic nanotherapeutics, active targeting involves communication between receptors overexpressed by cancer cells and a ligand conjugated on the surface of the MNPs. Hence, targeting ligand modifications on the surface of MNPs should be considered to establish receptor-mediated cellular internalization, which

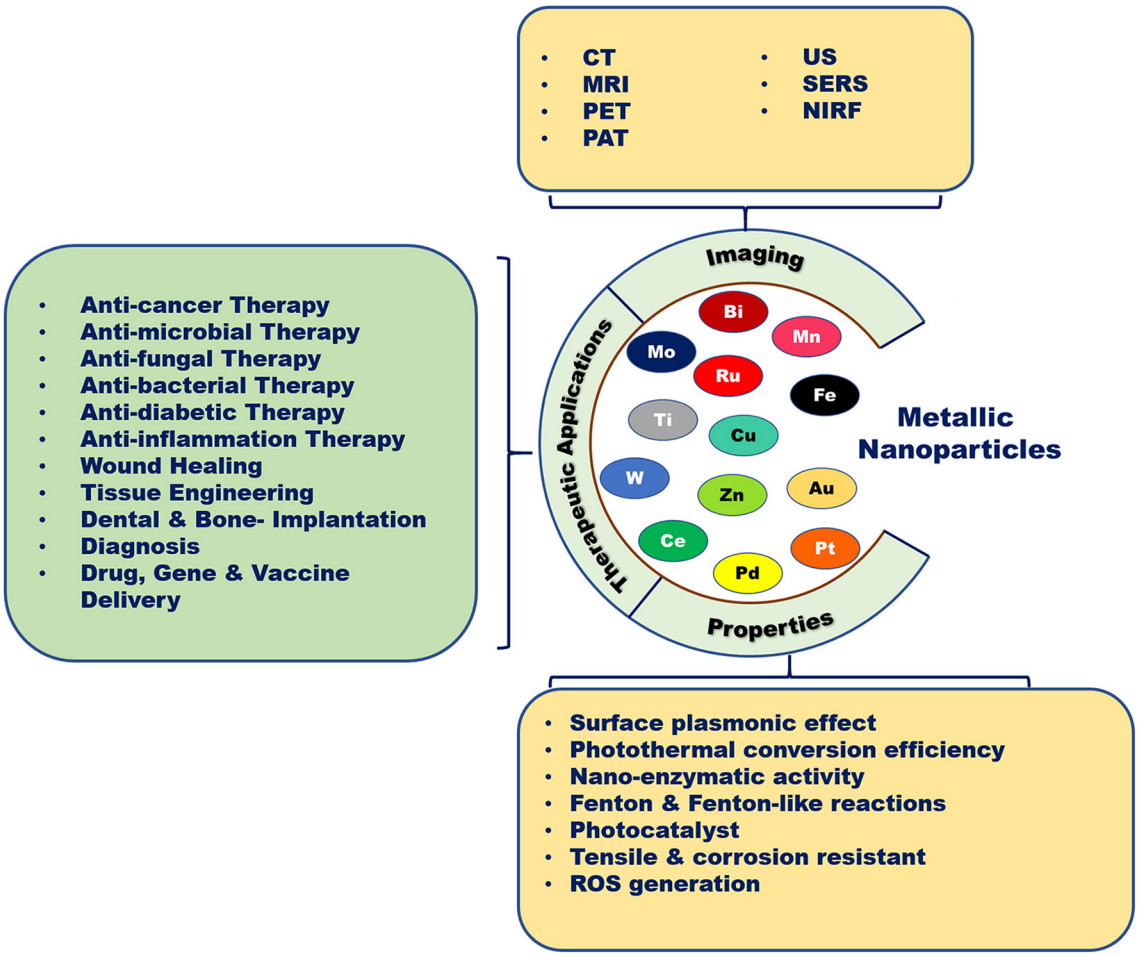

FIGURE 1 | Biomedical applications of metallic nanoparticles. Metallic nanoparticles are used as potent candidates for different types of diseases due to their unique properties and imaging characteristics.

can enhance tumor targeting as well as therapeutic activities. However, all the reported experiments based on metallic nanotherapeutics have investigated in small animal models and laboratory experiments only which is not comparable against established traditional therapies but, expanding sector of metallic nanotherapeutics is a future leading technology and it can compete after successful clinical trials.

Metallic nanotherapeutics are termed as theranostic mediators owing to their dual applications for therapeutic and imaging purposes (**Figure 2**) (Silva et al., 2019). For example, light-irradiated gold nanoparticles have used in both photothermal treatment as well as CT and PA dual imaging (Xuan et al., 2019). Similarly, superparamagnetic iron oxide nanoparticles (SPIONs) have established as excellent MRI contrast agents and these are used for radiotherapy sensitization and hyperthermia treatment (Winter et al., 2020). MNPs can be combined with various stimuli, including light, an alternative magnetic field (AMF), and US, to potentiate anticancer therapeutic efficacy. Stimuli-triggered metallic nanotherapeutics have been utilized in various cancer therapies such as photothermal therapy (PTT), photodynamic therapy (PDT), magnetic hyperthermia (MHT), sonodynamic therapy (SDT), and chemodynamic therapy (CDT) to eradicate tumor tissues (Huang et al., 2020a). These therapies are associated with multiple immunogenic responses against cancer cells by inducing immunogenic cell death (ICD) and releasing tumor antigens. The release of tumor antigens into the tumor microenvironment (TME) by tumor remodeling whereby cold tumors are changed to hot tumors, modulates the infiltration of cytotoxic T cells (Huang et al., 2020a). The TME is biologically abnormal, with lower pH, hypoxia, and higher lactate and glutathione levels, which hinder therapeutic outcomes. Modulating the hypoxic and redox levels of tumors using different types of MNPs can enhance the therapeutic action. The TME can be suppressed by various tumor-suppressive agents, including myeloid-derived suppressor cells (MDSC), M2 tumor-associated macrophages (TAMs), and regulatory T cells (Tregs) within the tumor region, suppressing immune activity against cancer (Yang et al., 2017). A combination of therapies that include metallic nanotherapeutics can manipulate tumor-suppressive agents and potentiate immune activities against

TABLE 1 | General properties and therapeutic applications of metallic nanotherapeutics.

Metal	Types of nanoparticle	Properties	Therapeutic outcome	Imaging	References
Iron (Fe)	Fe_2O_3, Fe_3O_4	High magnetization, negative MRI contrast, nano-enzymatic activities, Fenton reaction	Hyperthermia, drug delivery, biosensing of biological molecules, chemodynamic therapy, antimicrobial activity	MRI, CT, PET	Pham et al., 2013, 2017; Cortajarena et al., 2014; Arakha et al., 2015; Shen et al., 2018; Piehler et al., 2020
Gold (Au)	Rod, star, shell, triangle, spherical-shaped Au NPs	Surface plasmon resonance effect, high electrical and heat conductivity, radioactivity and high X-ray absorption coefficient, photothermal conversion, catalytic activity, photosensitization	Plasmonic biosensing, diagnosis, photothermal therapy, photodynamic therapy, sonodynamic therapy, drug, and gene delivery	CT, PET, SERS, NIRF, PAT	Xie et al., 2017; Singh et al., 2018; Park et al., 2019; Shanei and Akbari-Zadeh, 2019; Xuan et al., 2019; Kang et al., 2020
Copper (Cu)	CuO, CuS, CuI	Magnetic properties, electrical conductivity, catalytic activity, photothermal conversion efficiency	Radiotherapy, photothermal therapy, photodynamic therapy, Fenton-like reaction, antimicrobial, antifungal therapy, wound healing, biosensing of glucose, peroxidase, antigen, and biomolecules	PET, PAT, NIRF, MRI	Hessel et al., 2011; Pham et al., 2013; Ma et al., 2018; Jiang et al., 2019b;Tao et al., 2019; Sun et al., 2020b
Bismuth (Bi)	Bi_2O_3, Bi_2Se_3, Bi2S3, BFO, Bi2Te3, BiPO4	Large X-ray attenuation coefficient, high K-edge value, chemically stable compound in biological environments, ROS production, ATP depletion	Radiotherapy, photothermal therapy, photodynamic therapy, biosensing, antimicrobial therapy, tissue engineering and implantation	CT, MRI, infrared thermography, PA, ultrasonography	Chen et al., 2019b; Badrigilan et al., 2020; El-Batal et al., 2020; Feng et al., 2020; Shahbazi et al., 2020
Platinum (Pt)	Pt-NP	Excellent catalytic agent used in various chemical reactions, platinum-catalyzed hydrogenation reactions are required for fat and vitamin production, platinum interferes with oxidation reactions used for the industrial production of organic acids, surface plasmonic resonance activity, radical scavenger, and peroxidase dismutation	Chemotherapy, photothermal therapy, radiotherapy, antibacterial and antifungal activity, cosmetic production, anti-inflammation effects, Diagnosis of tumor markers, glucose, peroxidase, proteins, and bacteria	CT	Spain et al., 2016; Barman et al., 2018; Samadi et al., 2018; Jiang et al., 2019a; Li et al., 2019d; Eramabadi et al., 2020; Fu et al., 2020
Palladium (Pd)	Pd-NP. Pd-nanosheet,	Thermal stability, photothermal stability, photocatalytic activity, optical properties, electric conductivity, ROS generator, Pro-drug activation in the TME	Chemodynamic therapy, photothermal therapy, drug and gene delivery, biosensing, anti-bacterial therapy, wound healing	PA	Dumas and Couvreur, 2015; Yan et al., 2018; Sivamaruthi et al., 2019; Yang et al., 2019c; Jiang et al., 2020; Murugesan et al., 2020; Phan et al., 2020
Molybdenum (Mo)	MoS_2, MoO_2, MoO	Localized surface plasmon resonance, photothermal conversion efficacy, catalytic activity, optical properties, good conductivity	Photothermal therapy, peroxidase scavenging, biosensing	PA, NIRF, CT	Liu et al., 2018; Zhan et al., 2018; Li et al., 2019a, 2020a; Sun et al., 2019
Manganese (Mn)	MnO_2, Mn_3O_4, $MnCO_3$, Mn-sheet, MnO_x	Excellent catalytic activities, fluorescence quencher, T1-contrast, paramagnetic properties, pH and GSH-responsive disintegration, photothermal conversion efficiency	Chemodynamic therapy, photothermal and photodynamic therapy, radiotherapy, sonodynamic therapy, drug and gene delivery	MRI, PA, US	Casula et al., 2016; Cho et al., 2017; Wu et al., 2019b; Zhang and Ji, 2019; Chen et al., 2020; Gorgizadeh et al., 2020; Gupta and Sharma, 2020; Zhou et al., 2020b
Cerium(Ce)	Ce-NP, CeO	Strong X-ray attenuation, intracellular ROS generation, higher interconversion rate (Augustine et al., 2019; Kobyliak et al., 2019; Li et al., 2020b; Naha et al., 2020; Shin and Sung, 2020) of Ce3+/Ce4+, SOD mimetic activity, pH-sensitive pro-oxidant activity, attenuation of the pro-inflammatory cytokines and NF-kB transcription factor expression, nitric oxide scavenging	Anti-inflammation, anti-diabetic, anti-cancer, drug/gene delivery, antibacterial activity, tissue regeneration, ocular oncology	MRI, CT	Celardo et al., 2011; Dhall and Self, 2018; Inbaraj and Chen, 2019; Jia et al., 2019; Abuid et al., 2020

(Continued)

TABLE 1 | Continued

Metal	Types of nanoparticle	Properties	Therapeutic outcome	Imaging	References
Ruthenium (Ru)	RuNP	Catalytic activity, luminescent property, photothermal conversion efficiency, antioxidant activity	Anti-inflammation, photothermal therapy, biosensing, antibacterial activity	Fluorescence imaging	Liu et al., 2019c, 2020; Xu et al., 2019a; Jayakumar et al., 2020
Tungsten (W)	WO_3, WO_{3-x}, M_xWO3	Local SPR, suitable for multiple doping, strong electrical conductivity, higher X-ray absorption coefficient, pyroelectricity properties, NIR-shielding, photocatalyst, water oxidation, carbon dioxide reduction	Photothermal therapy, photodynamic therapy, anti-bacterial therapy, antimicrobial activity	CT, PET	Zhou et al., 2014; Duan et al., 2019; Levin et al., 2019; Wu et al., 2019a; Matharu et al., 2020
Titanium (Ti)	TiO_2, TiO_{1+x}	Photocatalytic activity, high tensile strength, high corrosion resistance, biological environment resistant	Antibacterial activity, tissue engineering, dental and bone implantation, drug delivery, sonodynamic therapy, photodynamic therapy	CT	Bogdan et al., 2017; Wang et al., 2017, 2020d; Azzawi et al., 2018; Çeşmeli and Biray Avci, 2019; Thomas and Kwan, 2019; Kim et al., 2020

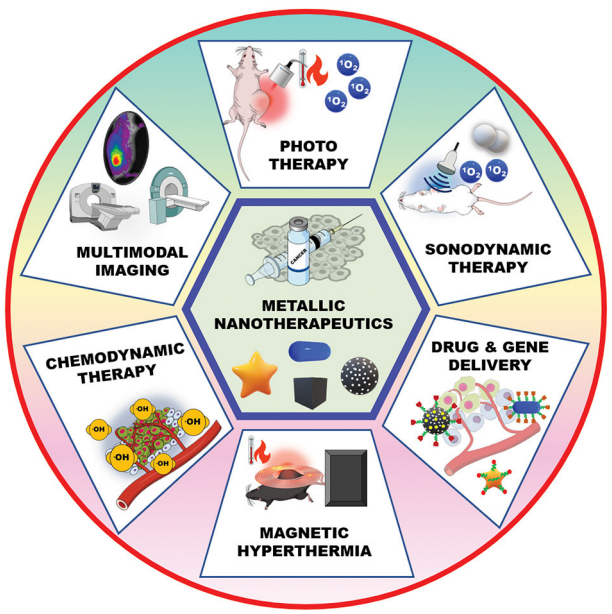

FIGURE 2 | Metallic nanotherapeutic applications in cancer theranostics. Metallic nanotherapeutics are used for different types of anticancer therapies and multimodal imaging.

cancer. In this review, we detailed the stimuli that can trigger metallic nanotherapeutics to deregulate immune barriers, like MDSCs, TAMs, and Tregs, as well as combinational treatments for cancer theranostics.

GENERAL OVERVIEW OF INTERNAL AND EXTERNAL STIMULI

The mechanism of stimuli-triggered cancer therapeutics is based on the function of nanomaterials modulated by stimuli from outside and within the tumor. After administration, nanoparticles accumulate inside the tumor either via passive targeting through the EPR effect and leaky vasculature or active targeting with targeting moieties functionalization. Drug delivery or other therapeutic programs can be activated by specific or multiple stimuli triggers (Rajendrakumar et al., 2018b). Stimuli triggers can be promoted from the inner or outer part of the body. The internal stimuli include pH, redox, hypoxia, and enzymes, and the external stimuli include light, temperature, AMF, and US (Rajendrakumar et al., 2018b). Internal stimuli are local stimuli that are present inside the TME, whereas external stimuli are externally applied to trigger the therapeutic modality.

Internal stimulants are widely used for safe and efficient drug delivery applications in cancer therapies. Firstly, the difference in pH between healthy and tumor cells is an important aspect for a controlled drug delivery system. Tumor tissues require a high amount of energy for cellular growth, which involves increasing glucose catabolism and the concentration of lactate and hydrogen ions. Hence, the TME becomes more acidic, with a pH of 6.5 or less (Wu et al., 2018). These pH differences are extensively used in cancer drug delivery applications owing to site-specific and controllable release features (Wu et al., 2018). Secondly, glutathione (GSH) plays a significant role in cellular growth, and its concentration is higher in the cytosol and nucleus than in the intracellular and extracellular fluids. Thus, it protects cells and hinders cellular apoptosis by oxidizing reactive oxygen species (ROS) (Li et al., 2019b). Moreover, higher concentrations of GSH are detected (2–20 mM) in cancer cells compared to healthy cells which is responsible for tumor growth (Li et al., 2019b). Hence, these remarkable variations in redox concentrations promote redox-responsive nanocarriers to deliver cargoes to the targeted tumor sites (Cherukula et al., 2018). Redox-responsive linkages such as disulfide and diselenide are widely used for designing smart nano-drugs. Tumor cell-secreted enzymes, including matrix

metalloproteinase (MMP) and other proteolytic enzymes, are responsible for cancer cell proliferation by triggering metabolic activity and tumor metastasis (Zhou et al., 2018). Targeting these dysregulated enzymes can enhance therapeutic activity. Enzymes are an ideal substitute for catalyzing chemical reactions under mild environments, including low temperature and neutral pH and promote biological triggers for drug release. The integration of enzyme-triggered moieties into nanotherapeutics can accomplish efficient drug release without compromising specificity. Alternatively, ROS can play a greater stimulant role during cancer nanotherapeutics. Peroxide (H_2O_2) is an abundant ROS present in cancer cells, promoting cancer cell proliferation, angiogenesis, apoptotic resistance, and tumor metastasis (Lopez-Lázaro, 2007). H_2O_2 can induce hypoxia-inducible factor- 1 (HIF-1) and genetic alternations, which are hallmarks of cancer cell invasion and metastasis (Lopez-Lázaro, 2007). Several investigations have confirmed that cancer cells possess high levels of H_2O_2 compared to normal cells (Revuri et al., 2019). Hence, ROS-responsive nanotherapeutics can scavenge peroxide and promote drug delivery. Manganese oxide, cerium oxide, and other MNPs are the best examples for possessing H_2O_2–scavenging activity and are additionally used for imaging during cancer treatment (Revuri et al., 2019; Abuid et al., 2020).

Compared to internal stimuli, external stimuli are more suitable in the field of drug delivery and cancer therapeutics. The TME varies depending upon the patient, types of cancer and pathological conditions (Wang et al., 2014). External stimuli are more feasible in controlled and disciplined manner during treatment (Wang et al., 2014) and can be manually controlled and modulated based on individual requirements. Externally stimuli triggered nanoparticles provide upgraded site-specific drug delivery, as well as constant and rapid payload release (Yao et al., 2016). However, external triggering systems necessitate the utilization of several types of specialized equipment and techniques to achieve specific stimulations. Various external stimulants was applied in cancer nanotherapeutics, including light, temperature, AMF, and US (Yao et al., 2016). AMF-induced hyperthermia and radiotherapy have been used extensively and demonstrated both positive and negative effects. Ultra-small iron oxide nanoparticles (IONPs) are considered as appropriate theranostic agents for MRI and anticancer therapy by hyperthermia and radiotherapy (Cherukula et al., 2019a; Pillarisetti et al., 2019). Recently, light-triggered phototherapy, which elevates the cellular temperature to kill cancer cells, was further investigated. Phototherapy significantly ablated tumors, inducing ICD, and reactivating cytotoxic immune cells against cancer (Rajendrakumar et al., 2018a; Cherukula et al., 2019a,b). Additionally, ultrasonic waves have been used to generate ROS and microbubbles, which interfere with cellular reactions and induce cancer cell death (Thomas and Kwan, 2019). Reportedly, various MNPS can be stimulated by both external and internal stimuli for advanced cancer therapy (**Table 2**). Herein, we discuss different stimuli trigger MNPs those are used in cancer therapy.

EXTERNAL STIMULI-RESPONSIVE METALLIC NANOTHERAPEUTICS

Thermo/Near-Infrared Light-Sensitive Nanoparticles

MNPs are the most effective light-sensitive vectors for temperature- elevated tumor ablation. Unlike other organic dyes and photosensitizers, MNPs are thermally stable over multiple irradiations. Following multi-ligand functionalization on the surface, MNPs have been extensively investigated for combinational therapies. Multiple metallic and bimetallic nanoparticles, metal oxides, and metal hybrids have been utilized for light-irradiated, combined PTT and PDT (Bao et al., 2016b).

Gold Nanoparticles

Recently, gold nanoparticles (GNPs) have gained attention because of their potential cancer theranostic applications. GNPs are potential photothermal and photodynamic transducers that may be evaluated in future clinical trials (Singh et al., 2018). Free electrons present on the surface of the GNPs are excited upon external light irradiation owing to the collective oscillation of metal conduction band electrons at a similar frequency (Kim et al., 2019). This phenomenon is termed as surface plasmon resonance (SPR). This SPR energy is transferred to the conduction band electrons, resulting in photoemission and local heating (Kim et al., 2019). The SPR property of GNPs depends on the size and shape of the nanoparticles (Huang et al., 2008). Surface plasmon absorption shifts to the near-infrared (NIR) region with increasing size or nanoparticle aggregation (Huang et al., 2008). When GNPs change from spherical to rod-shaped, the absorption band splits into a longer wavelength band in the NIR region due to longitudinal oscillation, and a shorter wavelength in the visible region, attributed to transverse oscillation (Huang et al., 2008). GNPs can be converted into different shapes such as nanorods, nanostars, nanocages, or nanoshells, which provide a wide NIR absorption range for plasmon photothermal therapy (Park et al., 2019). Gold nanostars (GNS) are a type of nanostructures possessing multiple sharp tips and have been investigated using SERS. Owing to the presence of multiple sharp tips, GNS provide tip-enhanced plasmonic properties and a wide NIR absorption range, suggesting their suitability for PTT (Park et al., 2019). Gold nanoshells have been widely investigated for NIR light-triggered PTT and PDT. Nanoshell structures have been developed using a degradable spherical template, which later forms hollow gold nanoshells (Park et al., 2019). Gold nanoshells are easy to load with surface medications and carry different types of payloads to deliver drugs upon NIR light irradiation, which promotes both cancer drug delivery and PTT. The green synthesis of GNPs using natural substrates such as citrate, chitosan, mannose, other plant-based substrates, and various biological organism-based sources improves biocompatibility and biomedical properties useful in antimicrobial and anticancer applications. Both the NIR and visible spectrum absorption of GNPs indicate several

TABLE 2 | Stimuli-triggered metallic nanotherapeutics for multiple anticancer therapies.

Types of metal	Metallic nanotherapeutics	Stimuli	Applications	References
Gold	AuNSs@PDA-PEG	NIR Laser (808 nm, 0.9 W/cm^2)	Photothermal therapy, apoptosis, and autophagy	Li et al., 2019c
	GNR@Mem	NIR laser (980 nm, 0.5 W cm^{-2}) and X-Ray (4Gy)	Photothermal therapy and radiosensitization induced apoptosis	Sun et al., 2020a
	ANS-Mas	NIR laser (810 nm, 14 W/cm^2)	Photothermal therapy	Kang et al., 2020
	FA-AuNPs	638 nm Laser (1.56 W cm^{-2})	Photothermal and photodynamic therapy	Guerrero-Florez et al., 2020
	FA-PEG-GNP	Ultrasound (1.8 MHz, 8 × 10^{-6} J cm^{-2})	Sonodynamic therapy	Brazzale et al., 2016
	Au-MnO JNP Ves	Ultrasound (1.0 MHz, 2.0 W cm^{-2}) and Redox	Chemodynamic therapy by Fenton-like reaction and sonodynamic therapy	Lin et al., 2020
Copper	CuS@MSN-TAT-RGD	NIR Laser (980 nm, 2 W/cm^2)	Photothermal therapy	Li et al., 2018
	CuS NPs-PEG-Mal	NIR laser (808 nm, 2 W/cm^2)	Photothermal therapy and immunotherapy	Wang et al., 2019c
	IONF@CuS	AMF (471 kHz of frequency and 18 mT) and NIR laser (1,064 nm, 0.3 W/cm^2)	Photothermal therapy, photodynamic therapy, and magnetic hyperthermia	Curcio et al., 2019
	Cu-Cys NPs	Redox and ROS	Chemodynamic therapy	Ma et al., 2018
Molybdenum	MoO_2 NPs	NIR laser (980 nm laser)	Photothermal therapy	Liu et al., 2018
	MoS2-ss@SiO2	NIR laser (808 nm, 1.5 W/cm^2), Redox	Photothermal therapy, photodynamic therapy	Li et al., 2019a
Iron	USPIONs	AMF (15.92 mT at 200 kHz)	Magnetic hyperthermia	Sánchez-Cabezas et al., 2019
	Fe_3O_4@HA NPs	AMF 10 kA/m, 120 kHz)	Magnetic hyperthermia	Soleymani et al., 2020
	IONF@CuS	AMF (471 kHz of frequency and 18 mT) and NIR laser (1,064 nm, 0.3 W/cm^2)	Magnetic hyperthermia, photodynamic therapy	Curcio et al., 2019
	Fe3O4-C and RLR NPs	NIR laser (808 nm, 1.5 W/cm^2), Redox, and ROS	Photothermal therapy, chemodynamic therapy	Wang et al., 2019d
	BSO-FeS_2 NPs	NIR laser (808 nm), redox	ROS generation, photothermal therapy, and chemodynamic therapy	Xiao et al., 2020
	Gd-Fe_3O_4	AMF (f = 370 kHz, amplitude 500 Oe)	Magnetic hyperthermia	Thorat et al., 2016
Titanium	PEG–TiO_{1+x}	Ultrasound (40 kHz, 3.0 W/cm^2)	Sonodynamic therapy	Wang et al., 2020d
	CCM-HMTNPs/HCQ	Ultrasound (1 W cm−2)	Ultrasound responsive drug delivery, sonodynamic therapy, and chemotherapy	Feng et al., 2019
	Nd:UCNPs@H-TiO_2	NIR laser (808 nm, 4.7 W/cm^2)	Photothermal therapy	Hou et al., 2019b
	BTiO_2-COS	NIR laser (808 nm, 1.5 W/cm^2)	Photothermal therapy, macrophage polarization, and immunotherapy	Zhang et al., 2019b
Palladium	FePd NPs	NIR laser (1,064 nm, 1.0 W cm^{-2})	Photothermal therapy and magnetic hyperthermia	Yang et al., 2019c
Platinum	PEG@Pt/DOX	NIR laser (808 nm, 1.5 W/cm^2)	Photothermal therapy, NIR laser-triggered drug delivery and chemotherapy	Fu et al., 2020
Manganese	HSA-MnO_2-Ce6 NPs	ROS, PDT laser (660 nm, 5 mW/cm^2)	Tumor microenvironment modulation via oxygen generation and photodynamic therapy	Lin et al., 2018
	H-$MnCO_3$/Ce6-PEG	ROS, PDT laser (660 nm, 5 mW/cm^2)	Photodynamic therapy and chemodynamic therapy	Wang et al., 2019b
	Mn(ox)-LDH NPs	NIR laser (808 nm, 1 W/cm^2)	Photothermal therapy and cell apoptosis	Xie et al., 2020
Bismuth	CD47-PEG-Bi_2Se_3	NIR laser (808 nm, 1 W/cm^2)	Photothermal therapy	Guo et al., 2019
	Bi@SiO_2_CQ	NIR laser (808 nm, 1 W/cm^2)	Photothermal therapy	Chen et al., 2019a
	BFO NCs	Ultrasound (3 W/cm^2, 40 kHz,), ROS	Ultrasound-triggered chemodynamic therapy	Feng et al., 2020
Cerium	UCNPs@mCeO_x	NIR laser (980 nm laser irradiation (0.72 W cm^{-2}), ROS	Oxygen generation, photodynamic therapy, and chemodynamic therapy	Jia et al., 2019

possible applications, including NIR light-triggered PTT, PDT, and imaging (Park et al., 2019).

Plasmonic nanoparticles such as GNPs can generate explosive nanobubbles upon laser irradiation which is an interesting therapeutic model for cancer therapy (Lapotko, 2011). During laser irradiation with sufficient energy, GNPs induce thermal ablation above the evaporation threshold for the NP environment which results in nanoscale boiling with surrounding medium and vapor nanobubble formation. Further, this nanobubble expands within the thin layer of the surrounding medium and collapses within a very short time. These nanobubbles generation through laser irradiation is termed as plasmonic nanobubbles (PNB). Compared to other vapor bubbles which are generated through high temperature and ultrasound irradiation, PNB can thermally

insulate the outer membrane of the NPs to reduce the side effects by thermal damaging. Localization of PNB is determined in a nanoscale area surrounded by the plasmonic NPs: PNB cannot generate in an NP -free area which significantly enhances the external control and therapeutic performances (Huang et al., 2020b). Formation of PNB can be personalized by the power sources and it can be optically monetarized through different probes. PNB can be utilized for the detection and elimination of cancer cells with different combinational anticancer therapy (Huang et al., 2020b).

Bismuth Nanoparticles

Bismuth nanoparticles have gained momentum in cancer nanotherapeutics owing to their excellent X-ray attenuation coefficient and strong NIR absorption (Shahbazi et al., 2020). As an ideal theranostic agent, they are well-suited for CT and PA imaging and present excellent photothermal capability. Bismuth-based nanoparticles such as bismuth selenide (Bi2Se3) and bismuth sulfide (Bi2S3) are mostly used as biocompatible and cost-effective NIR agents for PTT (Chen et al., 2019b; Ding et al., 2019; Yang et al., 2019a). Bismuth rods, quantum dots, and bismuth urchins are considerably more popular agents for bimodal imaging and PTT, presenting high photothermal conversions of more than 60% (Li et al., 2017; Yang et al., 2019a). As bismuth nanoparticles lack adequate tumor-targeting capacities, various surface functionalization, cell membrane coatings, as well as cell-mediated delivery systems, have been recently investigated (Chen et al., 2019b). Platelet membrane-coated bismuth nanoparticles had prolonged circulation time and tumor-homing capability, and effective PTT was achieved (Chen et al., 2019b). Bi_2Se_3 nanosheet delivery with macrophage cells showed high cell targetability, whereas blank nanoparticles demonstrated poor targeting abilities (Li et al., 2017). Moreover, the high photothermal conversion efficiency presented by bismuth nanoparticles successfully eradicated tumor tissue upon NIR light irradiation.

Palladium Nanoparticles

Palladium nanoparticles provide excellent physiochemical properties including catalytic activities, optical properties, as well as strong thermal and chemical stability (Phan et al., 2020). Currently, palladium nanoparticles are used in dental applications, and needle-shaped palladium nanoparticles are clinically utilized for prostate and melanoma treatment (Phan et al., 2020). Typically, spherical palladium nanoparticles demonstrate poor NIR absorption efficiency and limited SPR activity. Hence, modified structures like palladium sheets and porous palladium nanoparticles have demonstrated significant photothermal abilities and have been extensively investigated (Kang et al., 2018). Moreover, ultra-thin palladium nanosheets have been developed, which produce significant heat to the tumor region upon NIR light exposure (Dumas and Couvreur, 2015). Controlled synthesis generated porous-structured palladium nanoparticles exhibiting strong NIR absorption and remarkable photothermal conversion efficiency similar to that of gold nanoparticles (Xiao et al., 2014). Furthermore, porous palladium nanoparticles exhibit superior biocompatibility compare to spherical palladium nanoparticles which have been used in several applications such as drug carriers and PTT agents (Xiao et al., 2014). Both nanosheet and porous nanoparticles have large surface areas, allowing further modifications for generating an ideal agent for cancer therapy.

Platinum Nanoparticles

Platinum nanoparticles are biocompatible materials, widely used because of their catalytic activity and ROS-scavenging property (Cheng and Liu, 2017). Platinum nanoparticles demonstrated strong NIR absorbance properties, emerging as prominent thermo-plasmonic light-to-heat converters (Cheng and Liu, 2017). Spherical platinum nanoparticles demonstrated photothermal efficiency similar to gold nanoshells (Wang et al., 2015a). Gold nanoparticles have been coated with platinum to potentiate NIR-irradiated PTT and ROS-scavenging (Wang et al., 2015a). Although different biosynthetic processes for platinum nanoparticles provide adequate biocompatibility, platinum ions released in the cancer cell environment induced cancer cell death and ROS generation (Cheng and Liu, 2017). However, the SPR effect of platinum nanoparticles can be achieved by treatment in the UV region, resulting in lower photothermal conversion efficiency than in other metallic nanotherapeutics (Cheng and Liu, 2017). Manikandan et al. confirmed that the modulation of nanoparticle synthesis within 1–21 nm could enhance the PTT effect, killing cancer cells (Manikandan et al., 2013). Platinum nanoparticles <6 nm in size are non-toxic but can cause cancer cell death following NIR irradiation (Manikandan et al., 2013). Typically, platinum nanoparticles are combined with other MNPs, such as Au and Fe, as a bimetallic platform to stimulate therapeutic efficacy (Samadi et al., 2018).

Copper Nanoparticles

Copper nanoparticles have been established as an excellent candidate for therapeutic purposes owing to their strong NIR absorption property, molar extinction coefficient, and optical imaging properties (Zha et al., 2013). Copper oxide nanoparticles are highly toxic compared to other nanoparticles as they induce greater ROS generation (Benguigui et al., 2019). The role of copper oxide nanoparticles against various cancers has been investigated in preclinical studies. However, copper selenide and copper sulfide nanoparticles demonstrated strong NIR absorbance between 800 and 900 nm. The NIR absorption property of copper nanoparticles is acquired from the d-d transition of copper ions, whereas gold demonstrates a surface plasmon effect (Li et al., 2010). Furthermore, the absorption property of copper nanoparticles, involving the d-d transitions of copper ions, differed from free-electron oscillation in the conduction band but was similar to the trapped excitation of doped metals (Li et al., 2010). Hence, the absorption range was not highly affected by the size and shape of the particles, unlike other MNPs (Li et al., 2010). Hessel et al. investigated the NIR-triggered PTT effect of copper nanoparticles that demonstrated NIR absorption with a high molar extinction efficiency and a 22% thermal transduction ability, similar to gold nanoparticles (Hessel et al., 2011). Multifunctional copper

nanoparticles are highly efficient for NIR-based PTT and PA imaging for cancer theranostics.

Molybdenum Nanoparticles

Molybdenum nanoparticles have been widely utilized in biomedicine for imaging, therapeutic, and biosensing purposes. Primarily, molybdenum disulfide (MoS_2) nanoparticles have been explored for theranostic approaches as 2D-nanosheets, quantum dots, and nanocages. MoS_2 nanoparticles belong to the transition metal dichalcogenides (TMDs), demonstrating an X-M-X layered construction, where M is the transition metal (Mo, W, Ti) and X represents the chalcogenides (S, Se, Te), with atoms covalently bonded to each other within a single layer, and multiple layers attached together (Yadav et al., 2019). MoS_2 nanostructure properties are dependent upon the arrangement of atoms and the crystallinity of the material. MoS_2 nanoparticles have shown significant catalytic activities, photothermal conversion efficiency with an extinction coefficient of 29.2 $L{\cdot}mol^{-1}{\cdot}cm^{-1}$ at 800 nm laser irradiation, and multipurpose optical properties (Liu and Liu, 2018). MoS_2 nanoparticles are reportedly suitable as NIR laser-triggered drug delivery agents that can trigger payload release upon external NIR stimuli. These NPs are easily degraded under physiological conditions. However, owing to a large surface area, these nanoparticles can be modified into a potential therapeutic model. Chen et al. reported that hyaluronic acid functionalization on MoS_2 nanoparticles improved the stability, tumor-targeting ability, and NIR-triggered drug release, as well as application in PTT (Zhang et al., 2019a). Oxygen-deficient molybdenum oxide nanoparticles have been investigated for their strong NIR absorption property and pH-dependent degradability (Bao et al., 2016a). The intervalence charge-transfer transition between Mo elements and sufficient oxygen deficiency can cause a stronger SPR effect, resulting in a significant photothermal conversion ability (Bao et al., 2016a). Zhan et al. developed surfactant-free molybdenum oxide nanoparticles by tuning the reaction time and different phases, modulating the SPR property of the nanoparticles from the visible to the NIR range and thus, producing an adequate photothermal conversion ability (Zhan et al., 2018).

Tungsten Nanoparticles

Tungsten-based nanoparticles are a type of transition metal oxide exhibiting a strong localized SPR, widely used for PTT (Fernandes et al., 2020). These nanoparticles consist of perovskite units and a large band gap regulating SPR activity (Fernandes et al., 2020). Oxygen vacancy generation has been introduced in tungsten oxide nanoparticles, resulting in the alteration of the oxidation states and the formation of a new electronic state, with an appropriate number of oxygen vacancies and a narrow band gap (Wu et al., 2019a). Furthermore, the non-stochiometric property of tungsten nanoparticles is considered suitable for introducing multiple doping systems, which increases the free electrons in the conduction band (Wu et al., 2019a). However, these oxygen-deficient and doping systems can adjust the SPR activity and improve the electrical conductivity of tungsten oxide nanoparticles, resulting strong photothermal conversion efficiency. Tungsten nanoparticles exhibit a higher X-ray absorption coefficient (4.438 cm^2/kg at 100 keV) than iodine, allowing theranostic applications of tungsten nanoparticles (Zhou et al., 2014). Zhiguo et al. developed a tungsten oxide nanorod (WO2.9) 13 nm in length and 4 nm in width. Further surface modification of WO2.9 by PEGylation enhanced the biocompatibility and potential for cancer PTT and CT imaging (Zhou et al., 2014). The synthesis of tungsten oxide nanoparticles is mostly based on a high-temperature pyrolysis process. Upon NIR laser (980 nm) irradiation, WO2.9 nanoparticles exhibited significant photothermal efficiency owing to a strong SPR effect (Zhou et al., 2014).

Alternative Magnetic Field (AMF)-Responsive Nanoparticles

Magnetic nanoparticles (MNPs) have gained momentum in biomedical applications due to their strong diagnostic capability in MRI imaging. MNPs are efficient drug delivery vehicles that can deliver therapeutic moieties to tumors through passive, active, and magnetic targeting. External AMF exposure can cause non-invasive magnetic hyperthermia, resulting in cell apoptosis and irreversible changes in tumors. The drug delivery process can be altered by AMF exposure, which can be externally controlled to maintain adequate delivery to the tumors. IONPs are the most frequently investigated magnetic models for AMF-responsive cancer therapy.

Iron Oxide Nanoparticles

IONPs are an appealing agent for cancer diagnosis and therapy because of their superparamagnetic behavior that enables a wide range of activities. SPIONs with a 10-nm size have been established as a potential candidate for cancer theranostic due to their inherent magnetic property, convenient synthesis, and surface fabrication with multiple biomolecules for biomedical applications. Iron oxide has been explored as an MRI contrast agent for cancer diagnosis as well as for tracking therapeutic activity within the body. The biodegradability of IONPs has drawn massive attention because iron degraded from IONPs can accumulate as natural iron stores in the body. Several IONPs, such as Ferridex I.V.® and Ferumoxytol®, are currently in clinical use. The surface functionalization of IONPs enhanced plasma half-life and bioavailability. In comparison to other nanotherapeutics used for tumor targeting, IONPs are one step ahead as they allow passive and active targeting as well as external targeting with strong magnets. IONPs can induce local hyperthermia when exposed to AMF. AMF-induced hyperthermia can trigger cell apoptosis, protein degradation, and cell membrane destabilization, rendering cancer cells more susceptible to chemotherapy. Hence, IONPs are prominent candidates for combinational hyperthermia and chemotherapy. AMF-triggered drug delivery has an additional advantage during cancer treatment. Sami et al. reported that AMF-triggered drug release could destroy artificial 3D tumor spheroids. The macrophage-based delivery of silica nanoparticles embedded with IONPs demonstrated effective drug delivery, with the drug covalently linked to silica-coated IONPs using a thermosensitive linker. AMF triggering could significantly raise the temperature,

resulting in drug release and destruction of the 3D spheroids. Combinational hyperthermia and AMF-triggered chemotherapy can induce cancer cell toxicity and avoid non-specific delivery, which is essential for cancer therapy.

Hybrid Ferrite Nanoparticles

Different nanosized (10–100 nm) IONPs, including magnetite (Fe_3O_4), maghemite (γ-Fe_2O_3), and hematite (α-Fe_2O_3), reportedly induced magnetic hyperthermia and have been utilized for MRI imaging in cancer theranostics (Can et al., 2012). Researchers have adjusted the intrinsic properties of IONPs by doping with multiple transition metal ions. A small number of zinc (Zn^{2+}) substitutions in IONPs alters their magnetic properties. Zn^{2+}, a diamagnetic cation possessing zero magnetic moments, can substitute for the iron cations in the tetrahedral and octahedral sites and weaken antiferromagnetic coupling, resulting in stronger magnetization saturation (Hadadian et al., 2019). Doping with an appropriate amount of Zn^{2+} strongly affected the *Curie* temperature (Tc) and hyperthermia performance of IONPs, where large amount of doping resulted in a canted spin and decreased magnetization (Hadadian et al., 2019). Furthermore, doping with various magnetic nanoparticles can reduce the size of the hybrid IONPs, which assists in immune system escapes and prolonged circulation. Similarly, doping with cobalt ions resulted in smaller-sized cobalt ferrite nanoparticles (size $<$ 12 nm), demonstrating stronger hyperthermia efficiency and MRI contrast than IONPs of similar size (Fantechi et al., 2015). However, bare cobalt ferrite nanoparticles are toxic. Surface functionalization with biocompatible polymers and adjusting the doping content of the cobalt ions can avoid these issues and potentiate the biocompatibility of the particles without compromising performance (Fantechi et al., 2015). Ruby et al. have reported hybrid IONPs with manganese doping could enhance AMF-induced hyperthermia with T1 and T2 dual-mode MRI for anticancer therapy (Gupta and Sharma, 2020). Water-soluble and easily synthesized Mn-doped IONPs possessed similar morphology and intrinsic magnetic properties (Casula et al., 2016). Along with cobalt and manganese ions, various studies have utilized copper, nickel, bismuth, and gadolinium ions for doping IONPs to enhance MRI contrast efficiency and magnetic hyperthermia. These hybrid nanoparticles are the future of AMF-triggered cancer therapy, presenting better applications compared to single nanoparticles.

Ultrasound (US)-Responsive Nanoparticles

US is a mechanical sound wave with a frequency $>$20 kHz, which is higher than the hearing range of humans. Compared to other external stimuli, US possesses a significant advantage, with stronger tissue penetration due to its non-radiative and low tissue-attenuation properties (You et al., 2016). US mediates both thermal and non-thermal effects, which can be used in treatment. Alterations in the frequency, scattering, and absorption can modulate the generation of cavitation, which renders it useful in imaging and drug-release applications. High-intensity focused US (HIFU) has been clinically established for cancer treatment as well as diagnostic purposes. Various sonosensitizers, which include both organic and inorganic materials, have been investigated in US-based cancer therapy and imaging. Reportedly, metallic sonosensitizers demonstrate greater efficacy than other sonosensitizers in generating ultrasonic cavitation-based microbubbles and toxic radicals to adequately kill cancer cells.

Titanium Oxide Nanoparticles

Titanium dioxide (TiO_2) nanoparticles are chemically inert and stable in physiological environments and considered as biocompatible models for therapy (Ninomiya et al., 2012; Canavese et al., 2018). TiO_2 nanoparticles have two different crystal structures, anatase, and rutile. Rutile TiO_2 nanoparticles are fine-structure nanoparticles, whereas anatase possesses a crystal structure (Bogdan et al., 2017). The crystal structure allows anatase TiO_2 NPs to generate ROS and the NPs have been used as a photocatalyst. Rutile TiO_2 nanoparticles are fine in structure and chemically inert. However, smaller-sized TiO_2 nanoparticles possess a larger surface and cause toxicity (Bogdan et al., 2017). The larger surface area of TiO_2 nanoparticles, compared to that of microparticles, allows for the absorption of UV radiation, enhancing the excellent photocatalyst properties of TiO_2 nanoparticles (Bogdan et al., 2017). The surface modification of TiO_2 nanoparticles can modulate therapeutic behavior and systemic toxicity. TiO_2 nanoparticles belong to the semiconductor metal oxide group, consisting of an electron-enriched valence band and an electron-free conduction band (Bogdan et al., 2017). The bandwidth gap of TiO_2 nanoparticles is reportedly 3.20 eV and excited in the UV radiation range. During irradiation, the electron transfer from the valency bond to the conduction band creates electron excitation. Excited electrons can reduce molecular oxygen to superoxide radicals, while the positive ions oxidize water molecules to generate hydroxyl radicals and H_2O_2. Several investigations have reported the excitation of TiO_2 nanoparticles under sonoexcitation in aqueous solution (Çeşmeli and Biray Avci, 2019). In aqueous conditions, sonoexcitation under US waves induces a temporary dilution from the loss of pressure, which causes the cavitation of bubbles and thickening of the liquid, resulting in the collapse of the bubbles (**Figure 3**). This phenomenon is termed acoustic cavitation, which acts as a sonocatalyst, generating toxic effects and emitting sonoluminescence during cavity collision (Çeşmeli and Biray Avci, 2019). Furthermore, the shape of TiO_2 nanoparticles can affect cavitation and ROS formation during treatment. Reju et al. reported that nanocone-structured TiO_2 nanoparticles accelerated the inertial cavitation process and enhanced cell penetration under US exposure (Thomas and Kwan, 2019). Surface-modified hydrophilic TiO_2 nanoparticles have shown prolonged blood circulation and a high level of ROS upon US irradiation (You et al., 2016). US-triggered SDT can upregulate pro-inflammatory cytokines within the tumor and destroy the tumor microvasculature (You et al., 2016). Multiple anti-tumor therapeutic effects are the key feature of SDT, which can be utilized in future clinical applications.

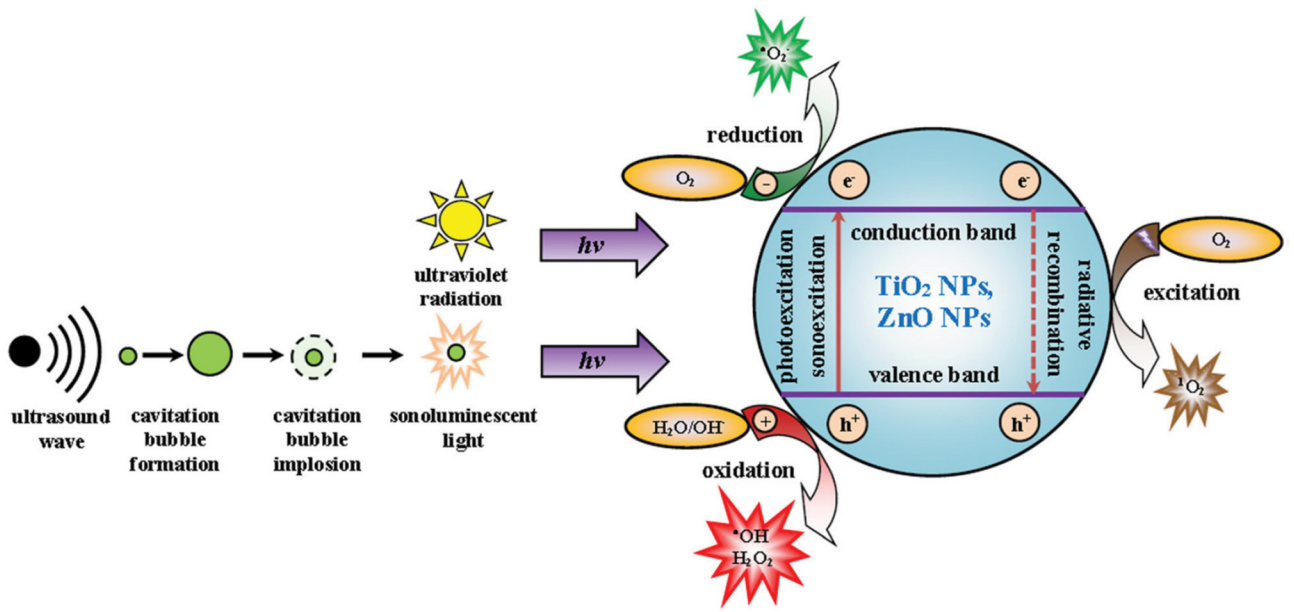

FIGURE 3 | Mechanism of cavitation and ROS production by TiO_2 and ZnO nanoparticles. Reproduced with permission (Bogdan et al., 2017) *Copyright © 2017, Springer Nature*.

Gold Nanoparticles

GNPs are extensively used in cancer therapy owing to their unique optical properties. GNPs are appropriate models to induce PTT and PDT effects upon laser irradiation. In tumors, laser light absorption by GNPs results in the production of vapor cavities around the nanoparticles (Shanei and Sazgarnia, 2019). This cavitation ability introduces a strong SDT effect and improves US imaging (Shanei and Sazgarnia, 2019). HIFU is a potential cancer therapy technique to target a small focused region in the body and penetrate soft tissue to induce thermal ablation (Shanei and Sazgarnia, 2019). In tumors, the surrounding liquid provides a nucleation site for GNPs to achieve acoustic cavitation and bubble formation, with the surface roughness causing bubble collisions under HIFU irradiation (Shanei and Sazgarnia, 2019). Notably, folic acid-conjugated GNPs selectively target breast cancer cells. Low-intensity US irradiation results in marked ROS production, whereas high-intensity US irradiation causes both ROS production and hyperthermia (Serpe et al., 2020). US irradiation causes thermal and mechanical effects and produces singlet oxygen and toxic hydroxyl radicals by reacting with the surrounding liquid (Serpe et al., 2020). Lin et al. developed gold-manganese oxide nanoparticles that decomposed in the TME to initiate a Fenton-like reaction and generate additional hydroxyl radicals (Lin et al., 2020). US-triggering improved the efficacy of the Fenton reaction and stimulated ROS generation (Lin et al., 2020). Ahmad et al. investigated the combination of radiosensitization and sonodynamic effects in cervical cancer cells (Shanei and Akbari-Zadeh, 2019). US irradiation enhanced the radiosensitivity of cancer cells and combination therapy increased the cytotoxic effect from low-intensity US waves by up to 95.8% (Shanei and Akbari-Zadeh, 2019).

INTERNAL STIMULI-RESPONSIVE METALLIC NANOTHERAPEUTICS

ROS and GSH-Responsive Nanoparticles

ROS is considered the most crucial factor associated with cellular physiological processes such as cell growth, cell proliferation, cell signaling, and pathological activities. ROS is endogenously produced during cellular respiration when oxidase receives the electrons released from membrane carriers, including ubiquinone and cytochrome c, and converts them into superoxide ions. In the cytosol and mitochondria, superoxide ions are rapidly converted to H_2O_2 by superoxide dismutase (SOD) and xanthine oxidase. Other functions inducing ROS generation include NADPH oxidase reactions, the β-oxidation of fatty acids, flavin oxidase reactions in the peroxisomes, and the protein oxidation process. Notably, H_2O_2 has a longer lifespan inside cells compared to other ROS. Oxidative stress results in H_2O_2 overproduction and induces pro-inflammatory cytokines and cellular apoptosis. The scavenging ability of H_2O_2-responsive nanomaterials is used in drug delivery to inhibit hypoxic conditions by generating oxygen. Various MNPS have demonstrated H_2O_2 degradation and oxygen regeneration to reduce ROS levels, hypoxic conditions, and undesirable side effects. H_2O_2 can stimulate the generation of toxic radicals such as hydroxyl radicals and peroxide ions to induce cellular apoptosis.

Manganese Oxide Nanoparticles

The physical and chemical properties of manganese oxide (MnO_2) nanoparticles have made them vital MNPs for biomedical applications. MnO_2 nanoparticles demonstrate

greater optical properties, potent oxidizing capability, and strong absorption, enhancing their utility in cancer applications (Wu et al., 2019b). MnO_2 nanoparticle compositions such as MnO, Mn_5O_8, Mn_2O_3, Mn_3O_4, and MnO_2 have been investigated in cancer therapy. Various MnO_2 nanoparticle compositions have been synthesized using different protocols, allowing broad applications such as imaging, phototherapy, catalytic activity, and drug delivery (Wu et al., 2019b). Furthermore, MnO_2 nanoparticles possess remarkable oxidizing properties that can improve the hypoxic tumor environment. In cancer cells, the main function of MnO_2 nanoparticles involves interacting with endogenous H_2O_2 and O_2 by reacting with reduced-state oxygen to reduce hypoxia, as well as reducing acidosis by interacting with various ions (Chen et al., 2020). Owing to the lack of oxygen inside the TME, PDT agents tend to generate fewer ROS, resulting in unsuccessful PDT. MnO_2 nanoparticles react with TME-based H_2O_2 and generate Mn^+ ions, water, and O_2. Reoxygenation of the TME modulates the therapeutic effects as PDT laser irradiation converts the regenerated O_2 molecule into singlet oxygen, causing cancer cell death (Chen et al., 2020). Released Mn^+ ions are used for T1 contrast-based MRI imaging, enabling the theranostic application of MnO_2 nanoparticles (Chen et al., 2020). The hypoxic environment of cancer cells is induced by insufficient oxygen delivery and the rapid cell proliferation of tumor tissue cells. Furthermore, hypoxia induces HIF-1 protein, which is responsible for aggressive tumor development i.e., three times more resistant to therapy (Vaupel and Mayer, 2007; Devarasetty et al., 2020). Alleviation of the hypoxic environment downregulates hypoxic markers in cells, including HIF-1α, which promotes multidrug resistance (MDR) and reoxygenates the tumor environment to promote therapeutic efficacy. Lin et al. reported that oxygen-producing HAS-MnO_2-Ce6 nanoparticles relieved hypoxia and treated bladder cancer (Lin et al., 2018). Albumin protein-biomineralized MnO_2 nanoparticles were shown to re-oxygenate the TME and double the PDT efficacy following PDT laser irradiation (**Figure 4**). Biocompatible materials modified MnO_2 nanoparticles demonstrated excellent therapeutic activity without any side effects. Radiation therapy produces ROS (•OH) by the radiolysis of water molecules in the tumor, which can cause cancer cell death. However, high concentrations of intracellular GSH neutralize intracellular ROS to protect the cell, limiting the effects of radiotherapy (Cho et al., 2017). Reportedly, MnO_2 nanoparticles oxidize GSH to glutathione disulfide (GSSG), reducing GSH levels in the tumor, promoting radiotherapy effects, and enhancing ROS activity against cancer cells (Cho et al., 2017). Yang et al. developed attractive hollow MnO_2 nanoparticles for TME-specific on-demand drug delivery and imaging. The MnO_2 nanoparticles modulated the hypoxic TME conditions and significantly improved the antitumor responses. The hollow template allows for the co-loading of MnO_2 nanoparticles with Ce6 (photosensitizer) and doxorubicin (DOX) for synergistic anticancer effects. MnO_2 nanoparticles reduce the hypoxic environment via the generation of molecular oxygen through intracellular H_2O_2 reactions. Adequate oxygen generation improved Ce6 activity, demonstrating significant ROS generation and DOX activity against cancer cells (Yang et al., 2017).

Cerium Oxide Nanoparticles

In recent years, cerium oxide nanoparticles have been investigated for biomedical applications. CeO_2 nanoparticles demonstrate diverse advantages such as strong redox ability, low toxicity, and significant catalytic activity (Dhall and Self, 2018). Additionally, these nanoparticles possess a unique mixture of both Ce^{3+} and Ce^{4+} ions on their surface, where the ratio of Ce^{3+} and Ce^{4+} affects the nanoparticle size. The size of CeO_2 nanoparticles depends on the Ce^{3+} composition. Increasing the Ce^{3+} concentration can reduce particle diameters and enhance oxygen deficiency (Dhall and Self, 2018). Additionally, these nanoparticles are incorporated with a fluorite crystalline lattice structure, resulting in a higher reactive surface area to scavenge free radicals. Owing to a lower redox potential (=1.52 v), CeO_2 nanoparticles can shift between Ce^{3+} and Ce^{4+}, depending upon the experimental conditions, a key feature for using CeO_2 nanoparticles as an antioxidant carrier (Siposova et al., 2019). Furthermore, the redox property of CeO_2 nanoparticles has been widely utilized against ROS-based tissue damage. A higher Ce^{3+}-to-Ce^{4+} ratio allows superoxide reduction as Ce^{3+} is easily oxidized to Ce^{4+}. The oxidation and reduction processes between Ce^{3+} and Ce^{4+} are reversible reactions, which spontaneously react with H_2O_2 to produce Ce^{3+} and molecular O_2 (Celardo et al., 2011). The ROS-scavenging activity of CeO_2 nanoparticles is a spontaneous, recyclable reaction. CeO_2 nanoparticles react with superoxide ions and are reduced to H_2O_2 and Ce^{4+}, with the regenerated Ce^{4+} ions again oxidizing H_2O_2 to oxygen molecules (Celardo et al., 2011). This spontaneous reaction cycle can scavenge H_2O_2 and superoxide simultaneously and protect from the paradoxical effect of SOD and catalase activities. Based on previous reports, lower Ce^{3+}-to-Ce^{4+} ratios in CeO_2 nanoparticles demonstrated nitric oxide radical scavenging, whereas higher ratios scavenged peroxide and toxic hydroxyl radicals (Inbaraj and Chen, 2019).

Iron Oxide Nanoparticles

IONPs are unique MNPs used extensively in biomedical applications and are superior theranostic agents in MRI and radiotherapy against cancer. IONPs have been widely investigated for oxidase-like behavior in the Fenton reaction as well as for peroxidase-like activity for H_2O_2 scavenging. During the Fenton reaction, Fe^{2+} reacts with surrounding H_2O_2, which is excessively produced by the aerobic processes of cancer cells, generating toxic radicals (•OH) by oxidizing Fe^{2+} to Fe^{3+} (Ranji-Burachaloo et al., 2018). The toxic radicals generated via the iron-based Fenton reaction induced non-apoptotic cell death, which was termed ferroptosis by Dixon et al. (2012). Among the various IONPs, Fe_3O_4 and αFe_2O_3 IONPs react with endogenous H_2O_2 in low pH conditions to advance Fenton reactions and generate (•OH) radicals and those hydroxyl radicals are highly reactive and possess biological activity (Ranji-Burachaloo et al., 2018).

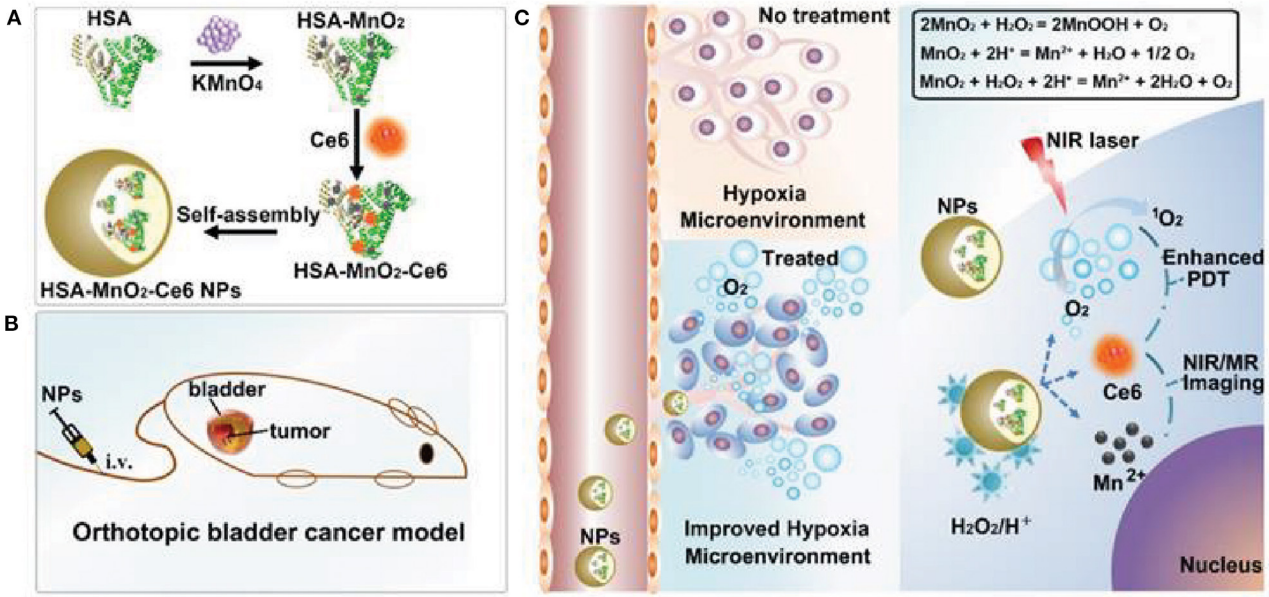

FIGURE 4 | Schematic representation of self-assembled MnO_2 nanoparticles modified with photosensitizer for photodynamic therapy (PDT) **(A)**. Application of MnO_2 nanoparticles catalyze endogenous peroxidase to oxygen and water and enhance the PDT efficacy upon laser exposure **(B,C)**. Reproduced with permission (Lin et al., 2018) under *copyright Creative Commons Attribution 4.0 International License (CC-BY license)*.

Hence, IONPs ar used for CDT in combination with other therapies such as PTT, PDT, and immune therapy. To overcome the limited solubility of IONPs, a photodynamic photosensitizer (Ce6) was incorporated on the surface of SPION nanoclusters (Ce6-SCs) by preparing an oil-in-water emulsion (Amirshaghaghi et al., 2019). The therapeutic performance of the Ce6-SCs was evaluated by the systemic administration to tumor-bearing mice. Hybrid IONPs produced excess O_2 with H_2O_2 scavenging, which altered PDT efficacy (Amirshaghaghi et al., 2019).

Copper Nanoparticles

Under acidic conditions, the redox-active catalytic property of copper nanoparticles (CuNPs) induces Fenton-like reactions. The Cu^+-based Fenton-like reaction demonstrated the highest reaction rate, approximately 160 times higher than that in IONPs (Yang et al., 2020b). Hence, it is a popular H_2O_2-responsive Fenton catalyst used in cancer therapy. Unlike Fe-based Fenton reactions, Cu-based Fenton-like reactions are independent of pH, with its catalytic activity achieved in circumneutral pH (6.5–7.5). Both Cu^+ and Cu^{2+} are highly reactive toward H_2O_2, where Cu^+ is responsible for the generation of hydroxyl radicals (Pham et al., 2013). Moreover, the Cu-based Fenton-like reaction and H_2O_2-scavenging property suggested a broad range of possibilities for therapeutic approaches. In the human body, copper is a cofactor for several enzymatic redox reactions, shifting between the two states of Cu^{2+} and Cu^+, with bioactive copper associated with proteins and their functions (Ma et al., 2018). However, excess free copper ions induce harsh side effects and systemic toxicity. Therefore, researchers have designed CuNPs containing Cu^{2+} ions, which are stable in the physiological environment but reduced to Cu^+ by tumor-specific reductive stimuli. CuNPs demonstrated a stronger coordination capability with sulfhydryl groups. Hence, Baojin et al. developed cystine-modified CuNPs (Cu-Cys). Cu-Cys nanoparticles can oxidize intracellular GSH to GSSG and simultaneously reduce Cu^{2+} to Cu^+ ions, then Cu^+ can react with H_2O_2 to generate hydroxyl radicals (shown in the **Figure 5**; Ma et al., 2018). Thus, amino acid modified CuNPs can be triggered by both intracellular GSH and peroxide stimuli. Owing to the Fenton-like activity, Cu-Cys nanoparticles can scavenge both GSH and H_2O_2 and produce adequate hydroxyl radicals, causing lipid peroxidation, DNA damage, and cellular apoptosis (Ma et al., 2018). Amino acid-fabricated Cu-Cys nanoparticles are highly stable in physiological conditions, limiting the unnecessary reduction process, and protecting other organs from systemic toxicity. Similarly, tetrakis (4-carboxyphenyl) porphyrin CuNPs (TCPP-Cu) revealed significant singlet oxygen generation within the TME by scavenging both GSH and H_2O_2 (Wang et al., 2019a). In the acidic TME, TCPP-Cu efficiently oxidized H_2O_2 to peroxyl radicals and Cu^{2+} ions (Wang et al., 2019a). Furthermore, peroxyl radicals spontaneously generate singlet oxygen via a recombination reaction with Cu^{2+} ions. GSH acts as an antioxidant and high concentrations protect cells from ROS-mediated ferroptosis. TCPP-Cu depletes intracellular GSH, inhibiting ROS consumption, and improving PDT efficacy (Wang et al., 2019a). Cu-Cys nanoparticles oxidize intracellular GSH and generate an adequate amount of ROS to induce ferroptosis (Ma et al., 2018). Finally, CuNPs are

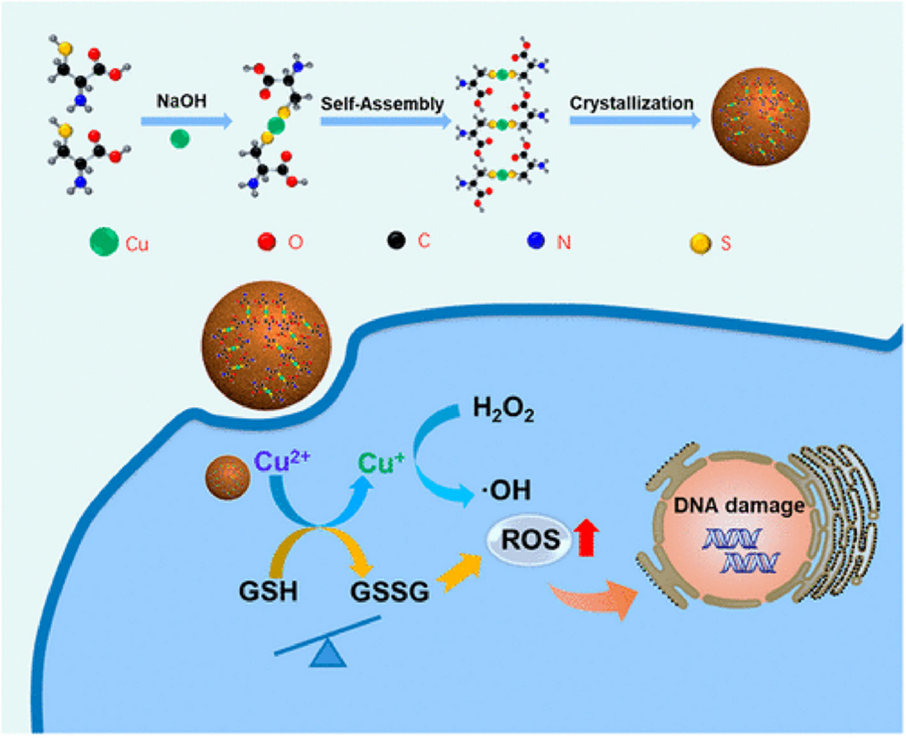

FIGURE 5 | Amino acid-modified copper nanoparticles (CuNPs) induce anticancer effects. CuNPs oxidize glutathione (GSH) to glutathione disulfide (GSSG) and generate Cu^{+} ions, further reacting with endogenous peroxidase to generate hydroxyl radicals to kill cancer cells. Reproduced with permission (Ma et al., 2018) *Copyright © 2019, American Chemical Society*.

popularly considered metallic nanotherapeutics to undergo Fenton reactions with additional advantages and efficacies.

APPLICATION OF STIMULI-TRIGGERED METALLIC NANOTHERAPEUTICS IN CANCER THERAPIES

In cancer therapy, the therapeutic application of MNPs are potentiated by the combination of multiple internal and external stimuli. The controllable anticancer behavior of metallic nanotherapeutics can be achieved by stimuli modulation based on the therapeutic purposes. The surface modification of metallic nanotherapeutics with appropriate moieties can enhance the specificity and reduce the off-site attack against healthy cells, whereas external stimulation can trigger therapeutic activities, resolving the drawbacks of current therapies, and providing a new direction for advanced treatment techniques in cancer therapy (Morales-Cruz et al., 2019; Yoo et al., 2019). Each stimulus affords specific activity, which can be considered during nanomedicine formulation. Here, we discussed the role of metallic nanotherapeutics triggered with external and internal stimuli in multiple anticancer techniques, including PT, CDT, SDT, magnetic hyperthermia, and immune therapy (**Figure 6**). Some metallic nanotherapeutics have demonstrated responsiveness to multiple stimuli, and diverse anticancer properties, rendering them more applicable in cancer therapy.

Chemodynamic Therapy

The side effects associated with traditional chemotherapeutic drugs, as well as their efficacy during treatment, cannot be avoided. Therefore, several investigations have focused on nanotechnology-based therapeutic approaches. The TME is highly complex, with hypoxic conditions owing to lower oxygen supply, pH imbalance, and GSH overproduction, as well as the expression of inhibitory proteins, which suppress traditional chemotherapeutic drug efficacy inside the cells, introducing the MDR effect. CDT, an enhanced therapeutic technique involving the generation of hydroxyl radicals (•OH) via the Fenton reaction and Fenton-like reactions, can cause lipid peroxidation, DNA damage, and apoptosis (Liu et al., 2019a). During CDT, metal nanoparticles catalyze H_2O_2 to generate hydroxyl radicals (•OH) and molecular oxygen. The main advantages of CDT include GSH depletion and reduced hypoxic conditions in the TME, which are deemed the main source of the MDR effect (Liu et al., 2019a). CDT is based on hydroxyl radical (•OH) generation via an iron oxide-induced Fenton reaction, as well as Fenton-like reactions induced by other metallic nanotherapeutics (CuNPs, MnO2, and GNPs) (Wang et al., 2020c). Hydroxyl radicals are highly reactive, allowing CDT to be

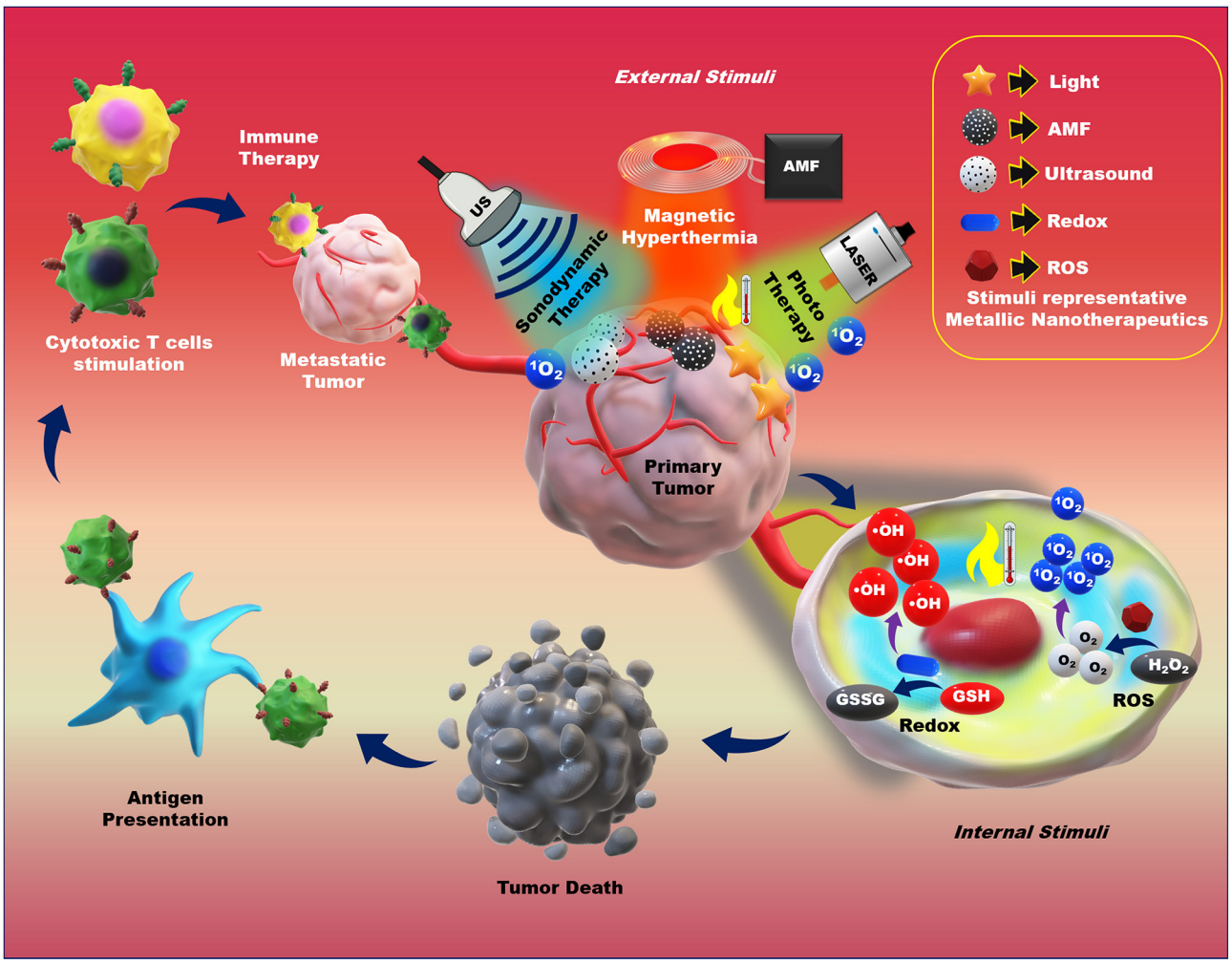

FIGURE 6 | Application of external and internal stimuli-triggered metallic nanotherapeutics for cancer therapy. Different stimuli such as light, an alternative magnetic field (AMF), ultrasound (US), redox, and reactive oxygen species (ROS) trigger metallic nanotherapeutics to exert their anticancer activities. External stimuli such as light, AMF, and US induce phototherapy, magnetic hyperthermia, and sonodynamic therapy, whereas internal stimuli such as redox and ROS promote toxic radical production, resulting in tumor death. Antigens are released upon tumor death and captured by antigen-presenting cells, which further trigger cytotoxic immune cell activation against metastatic tumors.

extensively investigated for cancer treatment and combinational cancer treatments, enhancing the efficacy of PDT, PTT, and chemotherapy (Hou et al., 2019a). IONPs are the main source, inducing non-apoptotic programmed cell death through iron-dependent ROS generation, i.e., ferroptosis (Dixon et al., 2012). In cancer theranostics, one main research frontier has explored the triggering of *in situ* chemical reactions via endogenous H_2O_2 stimuli to produce more toxic hydroxyl radicals via the Fenton reaction (Dixon et al., 2012). SPIONs are ultra-small IONPs widely investigated in cancer therapy and MRI imaging. SPIONs are metabolized in the acidic environment of cancer cells, resulting in the formation of iron ions (Fe^{3+} and Fe^{2+}) and undergo endo/lysosomal transportation into the cytosol through divalent metal transporter 1 (Huang et al., 2013). Furthermore, iron ions generate ROS inside the cells via intracellular oxidation-reduction reactions with peroxidase. The combination of SPION-based micelles with the exogenous ROS generator, β-lapachone, catalyzed by overexpressed NAD(P)H:quinone oxidoreductase 1 (NQO1) produced massive amounts of superoxide and H_2O_2, elevating antitumor activity by Fenton reaction-based ROS production (Huang et al., 2013). The amount of endogenous H_2O_2 is insufficient for the Fenton reaction to generate an adequate amount of ROS to eradicate cancer cells. Shengdi et al. reported that artemisinin (ART) and its derivative, which contains a peroxy group accelerating the Fenton reaction with iron or copper ions, were loaded into MNPs to enhance the cytotoxic effect (Guo et al., 2020a). MNPs are degraded in acidic tumor conditions to release Fe^{2+} ions that induce the Fenton reaction. Under acidic conditions (pH 5.0), the iron content is 10.45 μg/mL, 10 times higher than that in the normal physiological condition of 1.61 μg/mL (Guo et al., 2020a). MNP

degradation accelerates the release of ART and its derivatives, generating significant additional peroxidase to enhance the Fenton reaction inside cells. The surface modification of IONPs can achieve specific targeting to brain tumors and cross the blood-brain barrier (BBB) (Shen et al., 2018). Zheyu et al. developed cisplatin (CDDP)-loaded Fe_3O_4/Gd_2O_3 hybrid nanoparticles with lactoferrin (LF) and RGD dimer surface modifications to treat brain tumors (Shen et al., 2018). The LF functionalization promoted LF receptor-mediated transcytosis through the BBB, with the RGD dimer accelerating cellular endocytosis to transport the FeGd-HN@Pt cargo efficiently. The successful delivery of FeGd-HN@Pt into the brain tumor modulated the release of Fe^{3+}, Fe^{2+}, and CDDP owing to the acidic environment (shown in **Figure 7**). Then, CDDP was involved in the NADPH oxidation process, converting NADPH to $NADP^+$ by releasing excess superoxide ions and H_2O_2, accelerating ferroptosis activity in the brain tumor (Shen et al., 2018).

Sonodynamic Therapy

For the last two decades, SDT has been established as a non-invasive targeted cancer therapy (Canavese et al., 2018). The principle of SDT is similar to that of PDT and can be used with low-intensity US and a sonosensitizer to generate toxic free radicals (Canavese et al., 2018). As discussed in section Ultrasound (US)-Responsive Nanoparticles, US is a form of mechanical waves that can penetrate deep tissues to activate sonosensitizers (Canavese et al., 2018) and is deemed superior to visible and NIR light-triggered PT because of its enhanced deep tissue penetration property. The SDT mechanism is dependent upon the experimental procedure, biological models, the sonosensitizer type, and the US exposure guidelines including the intensity and frequency used. Various possible principles have been reported for SDT, including free radical generation, ultrasonic cavitation-induced microbubbles, US-induced cell apoptosis, and singlet oxygen production (Mchale et al., 2016). Ultrasonic cavitation is a physical phenomenon induced by immediate pressure changes in the surroundings, resulting in microscopic bubbles in tissues (Mchale et al., 2016). Microscopic tissue bubbles can oscillate, expand, and finally collapse violently in the tissue. Furthermore, ultrasonic cavitation can cause sonoluminescence and generate various sonochemical species such as free radicals and singlet oxygen molecules (Mchale et al., 2016). Ultrasonic sonosensitizer-derived free radicals are generated by reacting with H^+ and OH^- ions produced during the thermolysis of water. These free radicals can react with oxygen and produce peroxyl and alkoxyl radicals, leading to lipid peroxidation and cell death. During SDT, sonosensitizers excite and return to the ground state by releasing energy. The surrounding oxygen molecules accept the released energy and become excited singlet oxygen molecules, which are highly reactive and trigger oxidation reactions inside tumor cells, as well as sufficient singlet oxygen species to initiate various biological activities, including DNA fragmentation, the shrinkage of cytoskeletal filaments, and chromatin condensation to induce cellular apoptosis (Mchale et al., 2016). Reportedly, HIFU can ablate tumors at temperatures up to 80°C, causing thermal toxicity and irreversible cell damage.

Various porphyrin-based organic sonosensitizers are utilized for SDT against cancer. However, organic sonosensitizers are quickly degraded by ROS. Hence, TiO_2 nanoparticles are considered biocompatible MNPs as they are chemically inert and highly stable in the physiological environment (You et al., 2016). As a potential alternative to PDT, carboxymethyl dextran (CMD)-modified hydrophilic TiO_2 ($HTiO_2$) has been investigated for US-triggered SDT (You et al., 2016). CMD modification provides a unique stealth characteristic to TiO_2 nanoparticles, enhancing the blood circulation time (You et al., 2016). CMD-coated $HTiO_2$ demonstrated a hydrodynamic size of 198 nm, with a negative surface charge and good stability in the physiological environment (pH 7.4) for 5 days (You et al., 2016). $HTiO_2$ nanoparticles caused significant *in vitro* and *in vivo* ROS generation under US exposure in a dose-dependent manner, elevating the ROS level sufficiently to destroy tumor blood vessels and suppress tumor growth. Furthermore, $HTiO_2$ nanoparticle-based SDT upregulated the levels of pro-inflammatory cytokines such as interleukin (IL)-1β, IL-6, and tumor necrosis factor (TNF)-α within the tumor, increasing the immune response against the tumor. Additionally, the hollow mesoporous structure possesses an additional function, i.e., carrying therapeutic cargoes inside for combinational drug delivery and SDT (Feng et al., 2019). During cancer treatment, SDT is involved in both apoptosis and autophagy mechanisms. During SDT, autophagy acts as a double-edged sword, suppressing tumor growth in the early stage, but inducing tumor cell progression and suppressing SDT-mediated apoptosis in the later stage (Feng et al., 2019). Feng et al. developed hollow mesoporous titanium dioxide nanoparticles (HMTNPs) loaded with hydroxychloroquine (HCQ), an autophagy inhibitor, for autophagy-suppressed SDT (Feng et al., 2019). Furthermore, HMTNPs were coated with cancer cell membrane (CCM) to induce biomimetic behavior, which can safeguard against macrophage phagocytes and tumor homing activities. In the tumor, ultrasonic stimuli triggered HCQ release and suppressed autophagy by blocking the damaged tissue-derived nutrient supply to cancer cells, promoting SDT resistance (Feng et al., 2019). Subsequently, CCM-HMTNPs/HCQ demonstrated strong ROS generation and SDT sensitivity against a breast cancer model with US triggering. However, TiO_2 nanoparticles exhibit a low quantum yield for ROS generation. Hence, hybrid titanium-based sonosensitizers have been investigated for cancer SDT (Feng et al., 2019). Wang et al. reported nanorod-shaped titanium monoxide nanoparticles (TiO_{1+x}), which exhibited potent US-triggered ROS generation owing to an oxygen-deficient arrangement (Wang et al., 2020d). An oxygen-deficient structure provides a charge trap to reduce the band gap and limit electron-hole recombination, resulting in elevated ROS generation during US exposure (Wang et al., 2020d). PEGylated TiO_{1+x} nanorods (PEG- TiO_{1+x} NRs) demonstrated a horseradish peroxidase-like nanozyme activity, generating hydroxyl radicals (•OH) by reacting with H_2O_2 via a Fenton-like reaction. Reportedly, the intravenous administration of PEG-TiO_{1+x} NRs to a 4T1 tumor mouse model enhanced ROS generation under US

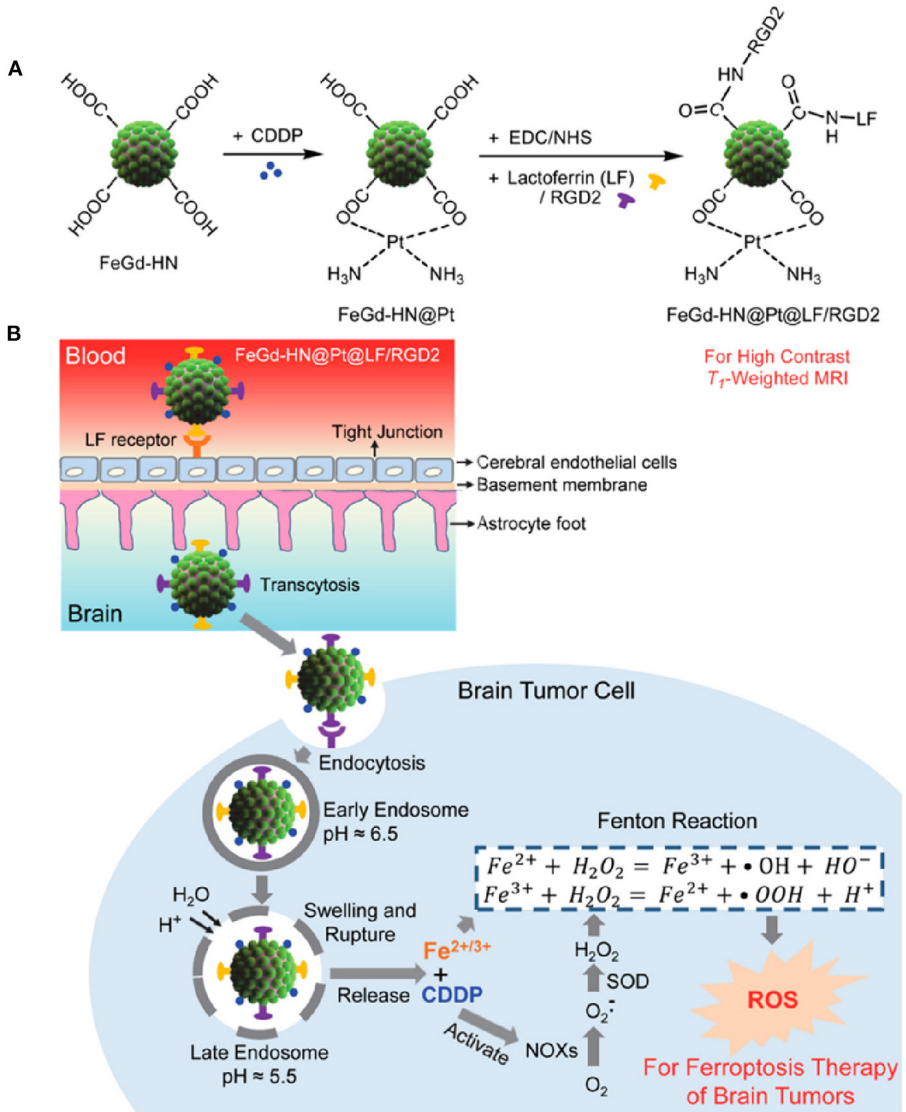

FIGURE 7 | Synthesis procedure of magnetic nanoparticle **(A)**. Mechanism of Brain tumor targeted IONP application in cancer cells via the Fenton reaction **(B)**. Reproduced with permission (Shen et al., 2018). *Copyright © 2018, American Chemical Society*.

irradiation (40 kHz, 3.0 W/cm^2) for 5 min. ROS generation via SDT and hydroxyl radical (•OH) generation by the Fenton-like reaction (**Figure 8**) successfully inhibited tumor growth, which was superior to TiO_2-based nanoparticle treatment (Wang et al., 2020d). Mitochondria are considered the powerhouse of cells and produce ROS to regulate cellular metabolism. An imbalance in ROS in the mitochondria leads to mitochondrial dysfunction and cancer cell apoptosis. Cao et al. reported that mitochondrial-targeted TiO_2 nanosheets efficiently inhibited tumor growth (Cao et al., 2019). TiO_2 nanosheets consist of highly reactive facets, decorated with Au crystals, and modified with a cancer cell-targeting aptamer (AS_{1411}) and triphenylphosphine (TPP) to target mitochondria inside the cells. These TiO_2 nanosheets induced Au crystal growth, limiting the fast recombination of excited electrons and holes (Cao et al., 2019). Furthermore, Au crystals present on the surface-mediated interfacial electron transfer to promote a high ROS quantum yield under US exposure. Dual-targeting Au-TiO_2-A-TPP nanosheets have demonstrated complete tumor regression without tumor relapse (Cao et al., 2019).

Magnetic Hyperthermia

Magnetic nanoparticle-induced hyperthermia is aimed at raising the tumor tissue temperature up to 40–43°C, inducing protein and DNA impairment, and resulting in cancer cell death (Chang et al., 2018). MNPs convert magnetic energy to thermal energy upon AMF exposure owing to the loss of heat during the reversal of the magnetization process. Three major mechanisms are involved, hysteresis loss, eddy current, and Néel and Brownian relaxation mechanisms, which conduct the heat loss process and

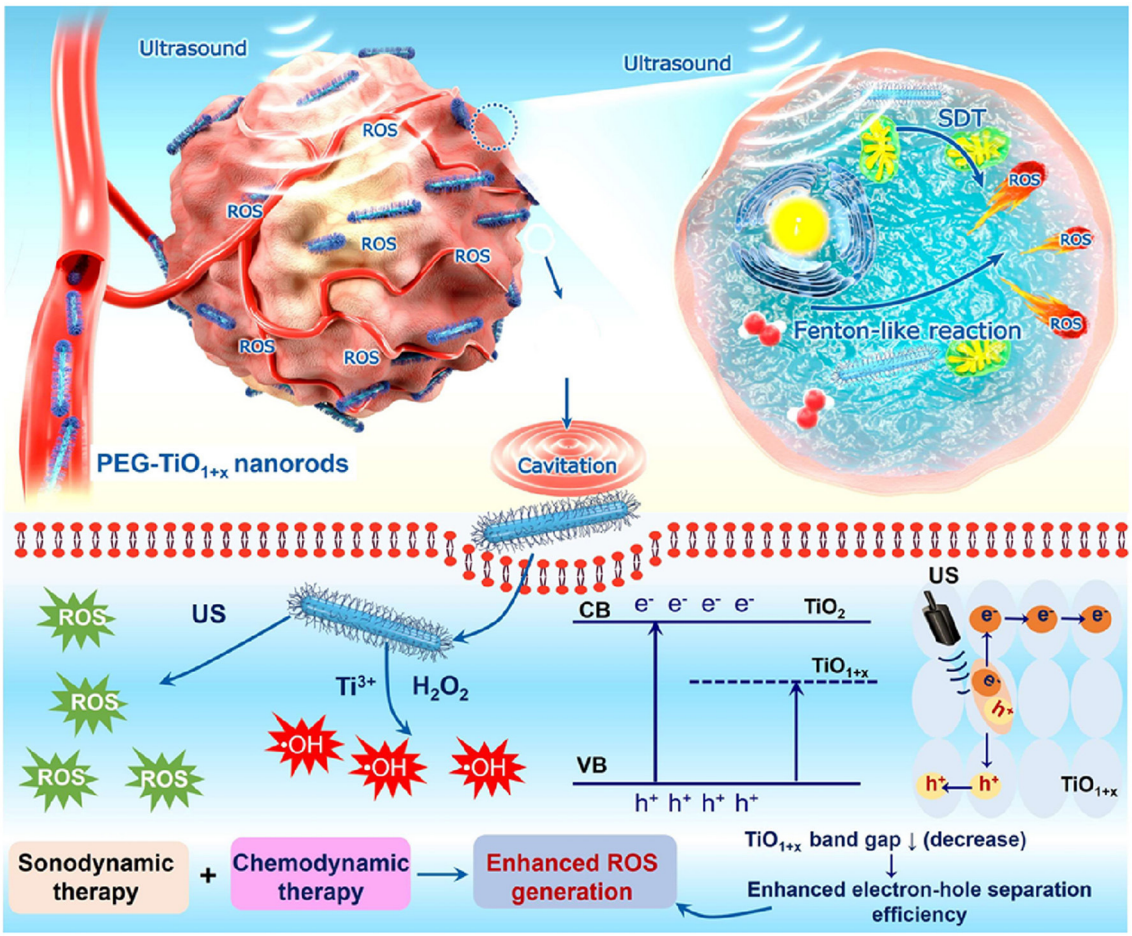

FIGURE 8 | Application of PEGylated titanium monoxide nanorods (TiO_2 NRs) in sonodynamic therapy. Oxygen-deficient TiO_2 NRs have shown higher reactive oxygen species (ROS) generation upon ultrasound irradiation. Reproduced with permission (Wang et al., 2020d) *Copyright © 2020, American Chemical Society*.

thermal energy production following AMF exposure (Hervault and Thanh, 2014). Magnetic heating based on hysteresis loss is developed using multi-domain MNPs, i.e., ferromagnetic or ferrimagnetic nanoparticles, 100 nm in size. The ferromagnetic material is incorporated with a uniform magnetic domain aligned in one direction, whereas ferrimagnetic material contains magnetic domains aligned opposite to each other. Following the application of an external magnetic field, the magnetic domain magnetizes in the same direction during the positive half-cycle, demagnetizing during the negative half-cycle. Withdrawal of the applied magnetic fields does not revert the magnetization to zero, for which the external intensity of the magnetic field is required. The sequence of the magnetization presents as a non-linear curve, which is termed the hysteresis loop, with the curve representing the magnetic strength of the MNPs (Hervault and Thanh, 2014). Superparamagnetic MNPs are small (10–20 nm) and contain only a single domain. During withdrawal of the magnetic field, superparamagnetic MNPs do not retain any magnetization and dissipate heat through relaxation loss based on Néel and Brownian relaxations (Hervault and Thanh, 2014). Depending upon the temperature and duration of hyperthermia, AMF-induced hyperthermia can cause cancer cell death. Hyperthermia is involved in various changes observed within cells such as protein denaturation and aggregation, as well as the regulation of several downstream pathways involved in the synthesis of cellular proteins, cell growth, and DNA repair. Elevated temperatures induce blood vessel perfusion, resulting in increased blood circulation, as well as the delivery of oxygen and chemotherapeutic moieties (Chang et al., 2018). Similarly, AMF-induced magnetic hyperthermia provokes an immune response inside tumors through cytotoxic immune cell infiltration, as well as pro-inflammatory cytokine production within cancer cells (Chang et al., 2018). Folic acid-modified PEGylated SPIONs (Mag-PEG-FA) are suitable candidates to target cancer cells overexpressing folic acid receptors (Piazza et al., 2020). Mag-PEG-FA NPs, with a hydrodynamic size of 94 nm, are highly stable in various physiological conditions (Piazza et al., 2020), demonstrating the highest surface absorption rate (SAR) of 21.6 W g^{-1} following an increase in temperature to 42°C upon 80 s of AMF exposure (Piazza et al., 2020). To

achieve combined magnetic hyperthermia and chemotherapy, Sivakumar et al. used SPIONs and curcumin, an anticancer drug, encapsulated within poly(lactic-co-glycolic acid) (PLGA) nanoparticles with a surface modification using the pancreatic cancer-specific AS1411 aptamer (Sivakumar et al., 2017). SPION nanocomposites are excellent material for T2 contrast-based MRI and PA imaging, introducing a theranostic approach. Following the induction of hyperthermia, pancreatic cancer cell-targeted nanoparticles effectively unloaded the anticancer drug within the cells (Sivakumar et al., 2017). MNPs are considered an efficient drug delivery agent for site-specific on-demand delivery. Kondareddy et al. developed magnetic field-inducible drug-eluting nanoparticles (MIDENs) for the delivery of DOX dual cancer therapy. DOX and SPIONs were loaded into a temperature-responsive PLGA nanoparticle (T_g = 42–45°C) (Thirunavukkarasu et al., 2018). Following AMF exposure, the MIDENs elevated the temperature above 45°C, which facilitated the transition of the PLGA polymer matrix from a glassy to a rubbery state, resulting in the release of DOX inside colon cancer cells (Thirunavukkarasu et al., 2018). A significant release of DOX delivered by MIDENs can be promoted upon AMF stimulation and control non-specific toxicity within the body. AMF-induced combinational magnetic hyperthermia and chemotherapy is a potential anticancer strategy to eradicate tumors and enable *in vivo* tracking by MRI (Thirunavukkarasu et al., 2018).

Superparamagnetic MNPs possess properties leading to aggregation, with weaker magnetization hysteresis loops suitable for biomedical applications, but lower magnetic power than larger MNPs. However, larger-sized MNPs can provide higher magnetic power but tend to aggregate following AMF exposure (Pardo et al., 2020). Hence, modifying the magnetic property of MNPs by tailoring their morphology and composition is an important aspect that needs consideration. Recently, hybrid ferrite nanoparticles were developed by substitution with other magnetic atoms, including cobalt (Co), manganese (Mn), nickel (Ni), gadolinium (Gd), and yttrium (Yt), onto the tetrahedral A and octahedral B sites of the spinal structure of magnetite, modulating the magnetic behavior and thermal ablation properties (Pardo et al., 2020). Elvira et al. reported that the controlled doping of Co(II) into ferrite nanoparticles significantly enhanced the magnetic hyperthermia efficiency (Fantechi et al., 2014). Human ferritin (HFt) is a protein involved in iron homeostasis in the body and can be safely assembled into a cage-like structure, with a 12-nm outer layer and an 8-nm inner cavity. HFt can be easily functionalized with diverse moieties and acts as a favorable template for the biomineralization of various MNPs (Fantechi et al., 2014). A small amount of Co (5%) doping in HFt-based ferrite nanoparticles reportedly enhanced the SAR value and hyperthermia effect (Fantechi et al., 2014). Furthermore, the therapeutic performance of co-doped ferrite nanoparticles has been investigated following AMF exposure under physiological tolerance for 30 min, demonstrating significant cytotoxic behavior compared to undoped HFt nanoparticles in melanoma cancer cells (Fantechi et al., 2014). Hasan et al. reported that Co and Mn-doped hexagonal structured IONPs demonstrated 3.6-times higher SAR values than those of spherical IONPs (CoMn-IONP, 1718.0 W/g; IONP, 475.3 W/g) (Albarqi et al., 2019). For intravenous administration, CoMn-IONPs are coated with a poly(ethylene glycol)-b poly(ε-caprolactone) (PEG–PCL)-based polymer for undisturbed tumor targeting and biocompatibility. Compared to commercially available IONPs, CoMn-IONPs demonstrated high heating efficiency under AMF exposure (frequency, 420 kHz; magnetic field strength, 26.9 kA/m). In this process, the temperature of the CoMn-IONPs increased to 40°C within 10 min, whereas the temperature of spherical IONPs only increased to 20°C (Albarqi et al., 2019). Additionally, the anticancer effect of CoMn-IONPs was evaluated in ovarian cancer cells with a non-toxic concentration of 50 μg/mL for 24 h. Under AMF exposure, CoMn-IONPs increased the temperature up to 46°C, inducing 99% cell toxicity, whereas spherical IONPs caused a 10% reduction in cell viability (Albarqi et al., 2019). Similarly, shape modulations can regulate the SAR value of MNPs and effectively contribute to magnetic hyperthermia. Liu et al. developed ferrimagnetic vortex-domain iron oxide nanorings (FVIOs) that attained a markedly high SAR value (3,000 W/g), twelve times higher than that of the FDA-approved IONPs (Liu et al., 2019b). Under AMF exposure, PEGylated FVIOs have demonstrated a significant cell death of 38.42% during early apoptosis and 48.96% in late apoptosis. Furthermore, mild hyperthermia induces calreticulin (CRT) expression, transmitting an "eat-me" signal to immune cells, further activating ICD, and resulting in effective immune therapy (**Figure 9**; Liu et al., 2019b). AMF-treated FVIOs demonstrated significantly higher CRT expression than that of the non-treated group, as well as the production of multiple pro-inflammatory cytokines. Furthermore, ICD-induced immune reactions revealed enhanced cytotoxic T lymphocyte (CTL) infiltration, including CD8+ and CD4+ cells, into the tumor site. AMF treatment combined with programmed death-1 (PD-1) ligand 1 (PD-L1) checkpoint blockade eradicated both primary and secondary tumors in the abscopal 4T1 model, as well as lung metastasis in a metastatic model (Liu et al., 2019b).

Phototherapy

PTT is a minimally invasive and prominent therapeutic approach, involving a photosensitizer that can absorb light energy and generate heat and ROS, which is triggered using electromagnetic radiation such as NIR or visible light. In the cellular environment, heat causes hyperthermia, resulting in protein denaturation and protein aggregation, cell lysis, and cytosol evaporation, which leads to cancer cell death. PTT activates programmed cell death following a specific temperature rise within the cell but avoids necrotic cell death, hindering antitumor activities. Similar to PTT, PDT relies on the generation of various ROS, including hydroxyl radicals, singlet oxygen, and superoxide ions. PDT-induced ROS interacts with various cellular chemical reactions and pathways, resulting in cancer cell death. Photosensitizers like organic dyes, semiconducting polymers, and MNPs have been investigated in phototherapy. Among the available photosensitizers, MNPs are potent agents as they can be stimulated multiple times to generate heat and ROS, whereas photosensitizing dyes are degraded by single irradiation.

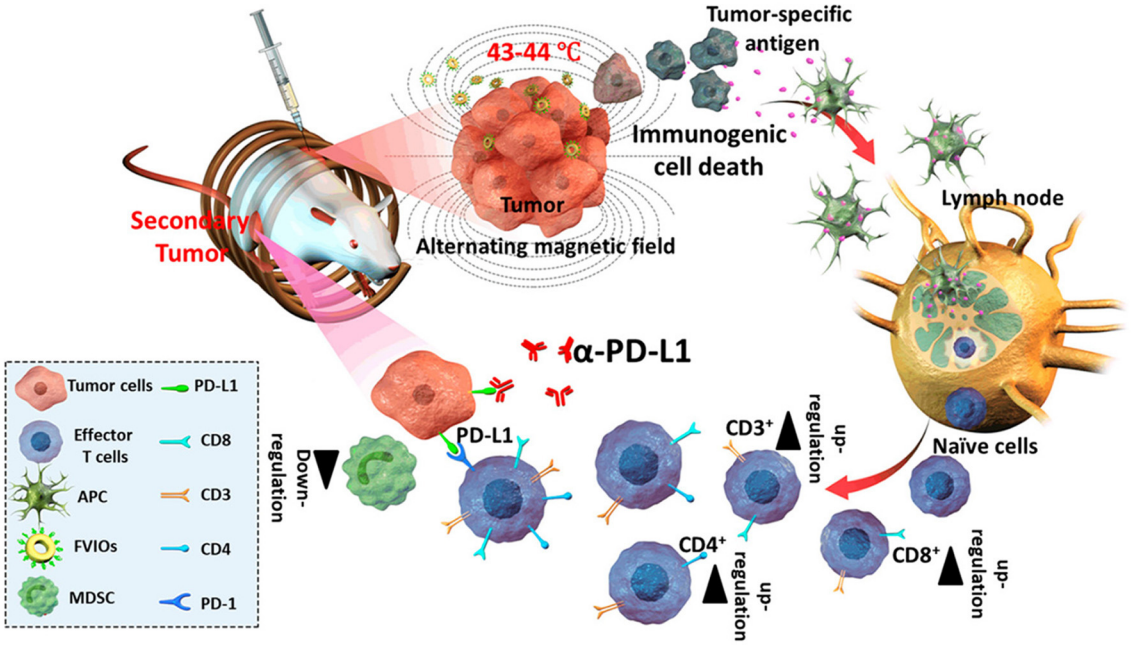

FIGURE 9 | Alternative magnetic field (AMF)-induced hyperthermia and immune therapy. AMF-induced heat triggers immunogenic cell death (ICD) and antigen release in tumors, which further induces cytotoxic T lymphocyte activation, and the combination with checkpoint blockade activates antitumor immune therapy. Reproduced from Liu et al. (2019b) *Copyright © 2019, American Chemical Society*.

GNPs are widely used for cancer theranostic applications and as anti-angiogenic agents. GNPs interfere with angiogenesis-based signaling pathways through vascular endothelial growth factor (VEGF) binding with the sulfur or amine groups of amino acids present in the heparin-binding domain, thus initiating the inhibition of angiogenesis in the tumor tissue (You et al., 2019). Huang et al. reported that GNS, featuring multiple sharp tips, induced tip-enhanced plasmonic effects and high photothermal conversion efficiency in PTT (You et al., 2019). Furthermore, the polydopamine coating of GNS enabled DOX loading through electrostatic or π-π stacking interactions, accelerating photothermal efficiency (**Figure 10**). Surface modification with folic acid-tethered thiol polyethylene glycol (HS-PEG-FA) resulted in specific targeting to MCF-7 breast cancer cells for dual chemo-PTT. In response to NIR (808 nm, 0.9 W/cm^2) laser irradiation, GNS generated a strong PTT effect and triggered drug release. Combined chemo-PTT showed marked efficacy in MCF cells, a breast cancer model, and the drug-resistant MCF-7/ADR tumor model (You et al., 2019). Furthermore, folic acid-modified GNS successfully inhibited VEGF-mediated angiogenesis and reduced the levels of CD31 and pVEGFR2 in tumor xenograft tissues (You et al., 2019). Lee et al. demonstrated that gold nanoshells were efficient drug carriers and strongly absorbed in the NIR region (Lee and Shieh, 2020). In colorectal cancer, platinum (II) drug-loaded gold nanoshells ablated the tumor region under NIR laser exposure at a mild power density (1W/cm^2), triggering drug release in chemo-PTT combinational treatment (Lee and Shieh, 2020). Similarly, Weijun et al. developed NIR/pH dual-responsive gold nanorod-based nanotherapeutics for combined chemo-PTT in a breast cancer model (Xu et al., 2019b). GNRs have been modified with dopamine-functionalized hyaluronic acid via Au-catechol binding. Additionally, DOX was anchored on hyaluronic acid and modified with hydroxyethyl chitosan, a pH-dependent cationic polysaccharide that modulated the GNR-HA^{DOX}CH-based nanotherapeutic surface charge from negative to positive in the acidic tumor environment. Under NIR laser (2.0 W/cm^2) irradiation for 10 min, GNR-HA^{DOX}CH elevated the temperature up to 55°C and triggered a 60% drug release, which was 1.8-fold higher than that in the non-irradiated group (Xu et al., 2019b). Dual pH/NIR-responsive GNR-HA^{DOX}CH revealed a higher cellular accumulation owing to CD44-based targeting and surface charge reversal, demonstrating a significant cytotoxic effect.

Other than GNPs, copper sulfide-based nanoparticles are gaining significant attention owing to their combinational PTT and PDT efficacies. Wang et al. demonstrated that copper-deficient copper sulfide nanoparticles ($Cu_{2-x}S$) combined with different metal domains were superior photothermal conversion agents owing to their SPR property (Wang et al., 2015b). NIR-triggered $Cu_{2-x}S$ could convert light to heat energy, simultaneously generating ROS (Wang et al., 2015b). PEGylated $Cu_{2-x}S$ nanocrystals were intratumorally injected into B16 tumor-bearing mice to measure the PTT effect. Following irradiation with an NIR laser for 100 s, $Cu_{2-x}S$ nanocrystals elevated the tumor temperature to 47.1°C, which was sufficient to kill tumor cells (Wang et al., 2015b). The photothermal efficiency was evaluated through heat shock protein 70 (Hsp70) expression, as it can be activated by

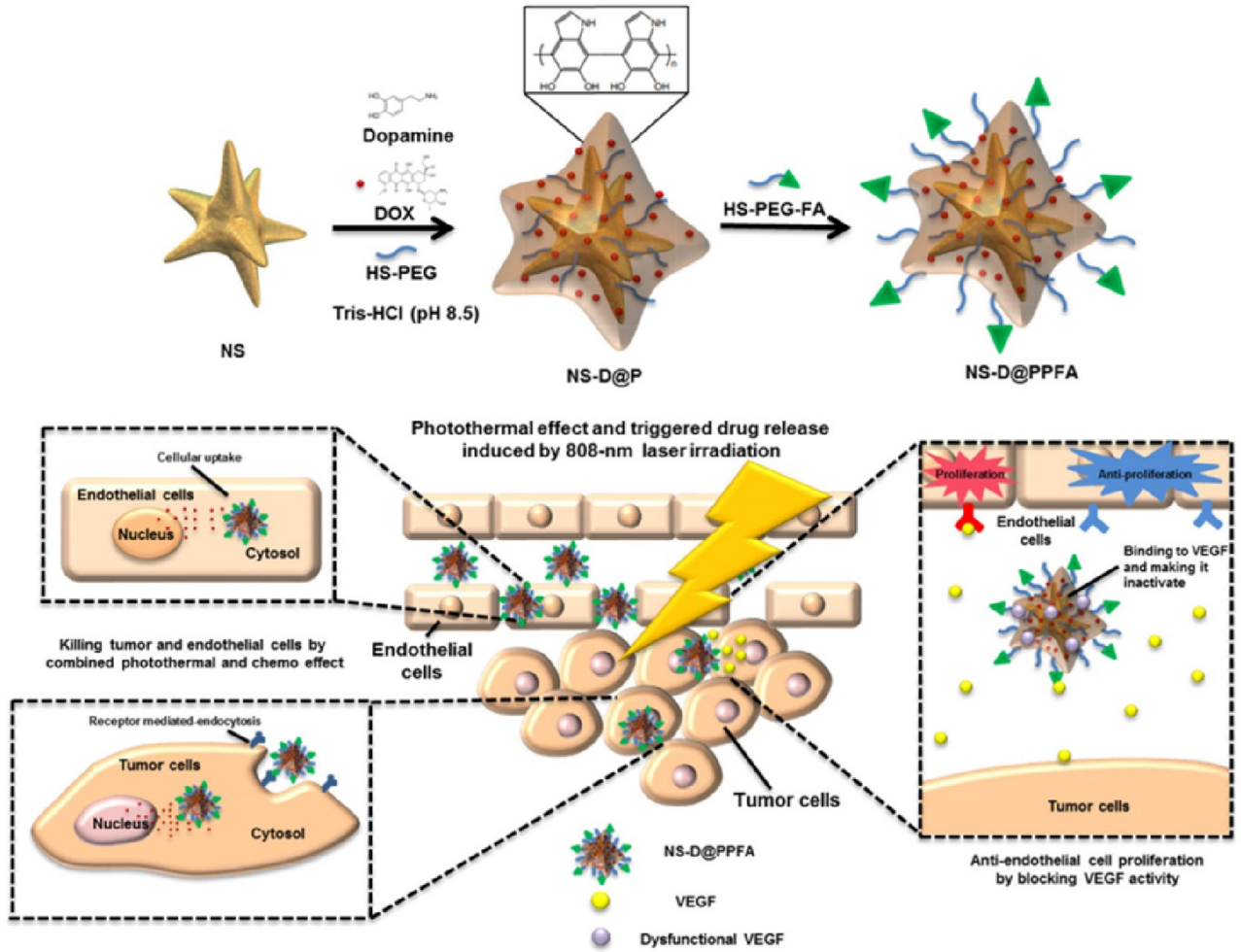

FIGURE 10 | Gold nanostars (GNS) modified with folic acid and thiolated polyethylene glycol (PEG) for targeted cancer therapy. GNS coated with dopamine can facilitate doxycycline (DOX)-loading and are modified with targeting ligands for near-infrared (NIR)-triggered drug release and photothermal chemotherapy. Reproduced with permission from You et al. (2019) under *copyright Creative Commons Attribution 4.0 International License (CC-BY license)*.

temperature and environmental stress. The laser-irradiated $Cu_{2-x}S$ nanocrystal group demonstrated significantly higher Hsp70 expression than that in the non-irradiated group. Moreover, dichlorofluorescein (DCFDA) and electron-spin resonance (ESR) spectral analysis confirmed ROS generation under laser irradiation. Hence, the combined PDT and PTT efficiency of copper MNPs can be further investigated for cancer therapy (Wang et al., 2015b). Alberto et al. developed iron oxide nanoflower-based copper shell-like nanoparticles (IONF@CuS) for PA and MRI imaging and combined PTT, PDT, and magnetic hyperthermia (Curcio et al., 2019). IONFs with copper shells demonstrated photothermal efficiency, acting as a bimodal nano-heater under AMF and NIR irradiation. Tri-therapeutic strategies have successfully eliminated tumors both *in vitro* and *in vivo* (Curcio et al., 2019). Similarly, other MNPs, including Mo, Pd, Pt, Mn, and Bi nanoparticles, have been extensively investigated as excellent phototherapy and imaging agents, which can be used in clinical studies based on their biocompatible behaviors (Badrigilan et al., 2020; Guo et al., 2020b; Jiang et al., 2020; Qian et al., 2020).

Combinational Immunotherapy

The mechanism of cancer immunotherapy is based on the therapeutic activity of the body's immune system against cancer to eradicate tumor cells (Yang et al., 2020a). During cancer cell death, the released tumor antigens are captured by antigen-presenting cells (APCs) such as immature dendritic cells (iDC) and infiltrate tumor-draining lymph nodes (Park et al., 2018). In the lymph nodes, the antigens are exposed to T cells through major histocompatibility complex (MHC) I or II through mature DCs. APCs activate naive T cells via MHC binding to T cell receptors and costimulatory molecules like CD80 and CD86 on APCs bind to the CD28 receptor on T cells, releasing cytokines that stimulate T cells. Activated T cells are divided into two subpopulations, CD4+ T cells and CD8+ T cells. CD4+ T cells differentiate into T helper cells (Th I or Th II) and

stimulate natural killer cells (NK cells) and macrophages that eliminate tumor cells and release pro-inflammatory cytokines to initiate the inflammatory process. CD8+ T cells are divided into CTLs and memory cells to induce potent anticancer immunity. However, various obstacles limit immune activity against cancer. During cancer cell elimination, dead cancer cells release immune suppressive factors such as IL-10, transforming growth factor (TGF)-β, and sphingosine-1-phosphate (S1P), which reduce the M1 macrophage population inside the tumor by polarizing M1 cells to M2 cells (Park et al., 2018). Apoptotic cancer cells recruit monocytes inside the tumor by secreting chemo attractants, which further differentiate into TAMs. The infiltration of MDSCs and TAMs into the tumor simultaneously suppresses the immune response. Furthermore, T cell activity is hindered owing to the expression of tumor-suppressive molecules such as PD-L1 and PD-L2 on cancer cells and CTLA-4 and PD-1 on T cells, which camouflage tumor cells from the immune system, and ultimately limit anticancer immunity. To overcome this barrier, scientists have developed nano-sized vehicles to deliver antigens and adjuvants successfully, which remodel the TME and induce cytotoxic activities and a pro-inflammatory process (Park et al., 2018). MNPs are perceptive agents that can be modified with various ligands to induce specific targeting and delivery (Evans et al., 2018). Stimuli-responsive MNPs can achieve successful antigen and adjuvant delivery, performing diverse therapeutic activities to stimulate antigen release (Evans et al., 2018).

Stimuli-triggered metallic nanotherapeutics like CDT, SDT, PTT/PDT, and RT provide cancer therapy in association with immune therapy directly or indirectly by promoting ICD, which releases antigens, or in combination with various immune stimulatory molecules and immune-suppressive inhibitors (Park et al., 2018). Kang et al. reported size-dependent GNP-based vaccine delivery to lymph nodes, inducing immune response activity (Kang et al., 2017). Ovalbumin (OVA), a primary antigen, conjugated to GNPs (OVA-GNPs) of different sizes such as 10 nm, 22 nm, and 33 nm, demonstrated size-dependent DC uptake and T cell presentation (Kang et al., 2017). OVA-GNPs with sizes of 22 nm and 33 nm demonstrated higher antigen delivery to lymph nodes than 10 nm-sized OVA-GN. Furthermore, 22 nm-sized OVA-GNPs induced a stringent antitumor response and CD8+ T cell infiltration into tumors (Kang et al., 2017). Nanoparticle-based PTT ablated the tumor, and induced ICD and tumor-associated antigens (TAA) to remodel cold tumors into hot tumors and promote T cell infiltration. Wang et al. developed gold nanostar (AuNSs)-encapsulated selenium nanoparticles (Au@Se nanoparticles) via gold-selenium coordination for PTT-induced immunotherapy (Wang et al., 2020a). Selenium coordination on the AuNSs enhanced the photothermal conversion effect through AuNSs plasmonic coupling, and NIR induced heat-activated SeNP activities, promoting cellular secondary metabolism and apoptosis (Wang et al., 2020a). During NIR irradiation, the Au@Se nanoparticles upregulated HSP 70 and TAA expression to induce CTL infiltration by antigen cross presentation (Wang et al., 2020a). Furthermore, Au@Se nanoparticles reprogrammed TAMs from M2 to M1 types, accelerating pro-inflammatory activities inside the tumors, and re-challenged distant tumor growth. Au@Se nanoparticle-induced PTT could introduce an efficient strategy to remodel the immunosuppressive TME to an immune-supportive TME through infiltrating CTLs and pro-inflammatory cytokine secretion such as IL-12p40 and TNF-α (Wang et al., 2020a). Inhibiting the activities of immunosuppressive Tregs through checkpoint blockade therapy can reinforce the CTL performance against cancer cells and suppress metastatic behavior. However, the lack of deep tissue penetration and nanoparticle accumulation limits PTT efficacy, generating ineffective PTT that further upregulates PD-1 or HSP proteins, and reduces the antitumor immune response (Yang et al., 2019b). Hence, the active targeting of nanoparticles to cancer cells can potentiate the PTT effect, and the combination with checkpoint blockade therapy (PD-1/PD-L1) can suppress the immunosuppressive activity of immune cells inside the TME. Hu et al. presented copper-doped covalent organic polymerized-*p*-phenylenediamine-5,10,15,20-tetra-(4-aminophenyl)porphyrin nanoparticles (Cu-PPT) for enhanced photo-chemodynamic therapy (Hu et al., 2020). Copper-doping induces catalytic activity, including peroxidase-mimicking and Fenton-like activity, to stimulate the CDT effect. Irradiation with both 650 nm and 808 nm laser achieved synergistic PTT and PDT activity. Combinational therapy augmented tumor-associated antigen release and antitumor immunity stimulation (**Figure 11**; Hu et al., 2020). Moreover, PD-1/PD-L1 checkpoint blockade therapy restricted immune tolerance and T cell stimulation against tumors (Hu et al., 2020). Yang et al. developed matrix metalloproteinase-2 (MMP2)-responsive peptide-modified Au@Pt NPs for tumor homing photo-immunotherapy (Yang et al., 2019b). A tumor-targeting linear peptide sequence (LyP-1) was designed with a PD-L1 antagonist (^{D}PPA-1) through an MMP-2 switch, which could trigger PD-L1 antagonist peptide release inside the tumor and expose the LyP-1 peptide on the nanoparticle surface, targeting P32 overexpressed protein on the tumor cell surface. MMP-responsive cleavage of the ^{D}PPA-1 sequence allowed binding to the PD-L1 receptor on tumors and prevented PD-1/PD-L1 checkpoint activation, which reduced T cell antitumor activity (Yang et al., 2019b). The PTT treated group revealed significant PD-L1 and MMP expression. Hence, the MMP-responsive ^{D}PPA-1 and LyP-1 peptide-modified Au@Pt NP (Au@Pt-LM^{D}P)-treated group showed significant tumor inhibition with 100% survival after treatment (Yang et al., 2019b). The Au@Pt-LC^{D}P-treated (MMP-responsive switch absent) group showed uncontrolled tumor growth of both the primary and distant tumors after 2 weeks of PTT treatment, attributed to the unsuccessful release of the PD-L1 antagonist (^{D}PPA-1), justifying the efficacy of combinational PD-L1 peptide-based immunotherapy and PTT (Yang et al., 2019b). In the previous section, we explained that mild hyperthermia induced by an AMF could trigger ICD and an antitumor response. Upon AMF exposure, the intratumorally delivery of nano-adjuvants and IONPs modulated the immune response and DC maturation (Chao et al., 2019). The delivery of R837 (TLR 7 agonist) stimulated antigen presentation and CTL infiltration inside the tumor (Chao et al., 2019). Combined therapy with AMF exposure triggered mild hyperthermia, and the

adjuvant-based treatment successfully initiated a strong immune response against cancer (**Figure 12**). Reportedly, the systemic administration of a checkpoint antibody (anti-CTLA4) inhibited the immune suppressive molecules that heavily influence the immune response against cancer cells (Chao et al., 2019).

A combination of antigen and adjuvant delivery to the tumor site can elicit significant DC maturation and an antitumor immune response. Zhou et al. demonstrated that the co-delivery of OVA antigen and R837 with PEGylated $MnFe_2O_4$ nanoparticles successfully induced *in vitro* and *in vivo* immune responses (Zhou et al., 2020a). Additionally, NIR irradiation comprehensively inhibited primary tumor growth and suppressed lung metastasis in an orthotopic breast cancer model (Zhou et al., 2020a). Chang et al. proposed multifunctional hollow mesoporous Cu_2MoS_4 (CMS) loaded with glucose oxidase (GOx) nanoparticles to modulate the TME for combined CDT, PTT, starvation therapy, and immune therapy (Chang et al., 2019). The hollow mesoporous CMS accommodated an enormous range of cavities to carry GOx, which catalyzed glucose to H_2O_2 to induce glucose starvation inside the tumor and regenerated H_2O_2 to assist the Cu and Mo ions in performing Fenton-like reactions. The presence of Cu^+/Cu^{2+} and Mo^{4+}/Mo^{6+} redox couples in CMS facilitated the significant production of hydroxyl radicals (•OH) to induce ferroptosis. The combination of NIR-irradiated cell death and ferroptosis-based cell death promoted TAA production and a robust immune response (Chang et al., 2019). Additional checkpoint blockade with anti-CTL antigen-4 (CTLA4) treatment effectively eliminated the primary and metastatic tumors (Chang et al., 2019). Therefore, the combination of immunotherapy with other therapeutic modalities has demonstrated a significant antitumor response, with robust immune activation against cancer cells for successful eradication without reoccurrence.

BIOSAFETY OF METALLIC NANOTHERAPEUTICS

The biosafety of metallic nanotherapeutics is an important aspect to assure that the toxic effects of these agents do not surpass their advantages during treatment. The toxicity of metallic nanotherapeutics is determined by their cellular and subcellular localization properties (Su et al., 2018). Moreover, the size of metallic nanotherapeutics is a key factor in determining cellular uptake. Metallic nanotherapeutics are transported through endocytosis and largely localized in lysosomes, cytoplasm, and the nucleus (Su et al., 2018). Bulk materials lack high cellular uptake and are easily cleared from the body by the liver (Su et al., 2018). Similarly, the shape of nanoparticles can play a critical role in cellular internalization (Xie et al., 2017). Lin et al. reported that triangle-shaped, rod-shaped, and star-shaped Au MNPs demonstrated different endocytosis rates (Xie et al., 2017). Triangle-shaped Au MNPs showed the highest cellular uptake, followed by rod-shaped, and then star-shaped Au MNPs (Xie et al., 2017). The toxicity of metallic nanotherapeutics depends on its biodegradability, the chemical meltability nature, and surface adsorption capacity. In the case of metallic nanotherapeutics, a larger surface per unit mass can induce the higher adsorption of proteins, nutrients, and growth factors, affecting the toxicity of the agent (Yao et al., 2019). However, the surface modification of metallic nanotherapeutics with biocompatible moieties can avoid unnecessary accumulation in different organs and protein adsorption, thereby reducing toxicity and side effects. Edward et al. reported that transferrin-modified Au nanoparticles demonstrated higher uptake in MDA-MB-435 cancer cells, whereas PEG-coated Au nanoparticles penetrated the tumors more deeply with a slower adsorption rate (Sykes et al., 2014). The surface modification of metallic nanotherapeutics enhances the biocompatibility of these agents by enabling an appropriate amount of absorption into the body without any side effects during treatment. MNPs tend to release metal ions when exposed to aqueous solutions or biological media (Yao et al., 2019). Furthermore, the toxicity of metallic nanotherapeutics depends upon the released metal ions, as well as their behavior and interaction with cellular organelles. The catalytic activities of metallic nanotherapeutics can induce ROS production, releasing a large number of metal ions inside the cells. Hence, the type of metallic nanotherapeutics, dosage, and its systemic behavior should be considered during treatment (Yao et al., 2019). Biosafety is an important aspect of nanotherapeutics, which needs to be prioritized during cancer therapy to reduce unnecessary side effects.

CLINICAL STATUS

Ongoing and completed clinical trials have reported the application of MNPs in cancer therapy. Aurimune (CYT-6091) using 27-nm gold nanoparticles modified with thiolated PEG and recombinant human TNF-α (rhTNF-α) completed a phase I clinical trial in 2010 (Libutti et al., 2010). The delivery of rhTNF-α to cancer cells stimulated CD4+ and CD8+ cells and reduced regulatory T cell infiltration. PEGylated gold nanoparticles are an ideal candidate that successfully delivered rhTNF-α, and were cleared from the body after 120 days without any unnecessary damage to other tissues (Libutti et al., 2010). A silica-coated gold nanoshell, termed an AuroShell, was investigated in phase I clinical trials with 14 patients (Staves, 2010). For the treatment of head and neck cancer, a 120-nm silica nanoparticle with a 15-nm gold shell layer was modified with 5 kDa PEG for NIR laser (808 nm, 4 W/cm^2)-irradiated PTT (Staves, 2010). AuroShell was administered intravenously at a dose of 24–31 mg/kg to the patients. Fourteen hours after treatment, the patient was exposed to an NIR laser (Staves, 2010). Following NIR irradiation, AuroShell treatment elevated the temperature and caused tissue damage within 6 min. AuroLase®, a nanoshell structed gold nano particle, was developed by Nano spectra biosciences company for photo thermal ablation of prostate cancer therapy. AuroLase® clinical trial has updated in August 2014 (NCT00848042) with 11 patients for Head and Neck cancer. In the follow-up trial, AuroLase® was investigated for thermal ablation of the targeted tumor with different doses like 4.5, 7.5 ml/kg, and different power. All the participants have experienced

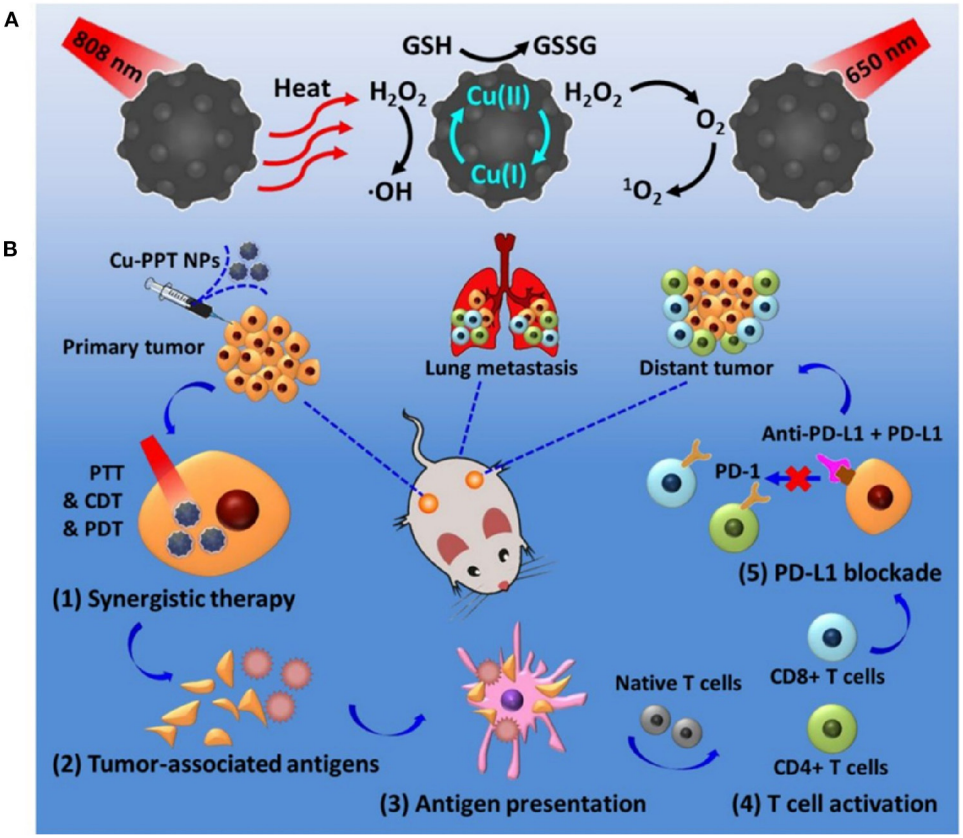

FIGURE 11 | Schematic representation of Cu-PPT based synergistic anticancer effect with photothermal therapy, photodynamic therapy, and chemodynamic therapy **(A)**. Mechanism of Synergistic therapy triggers the release of tumor-associated antigens and PD-1/PD-L1 combination induced a robust antitumor immunity **(B)**. Reproduced with permission from Hu et al. (2020) under *Copyright © 2020, American Chemical Society*.

an adverse effect during the treatments and the study was continued for 6 months. Another clinical trial is active in the investigation of primary and metastatic lung cancer. AMF-based hyperthermia was investigated in phase I clinical trials in 2015 with an iron nanoparticle called Magnablate (NCT02033447). This study was conducted using 12 prostate cancer patients as an early phase I trial and the results are yet to be published (Staves, 2010). Various IONPs under phase I and phase II clinical trials with AMF induced magnetic hyperthermia owing to the favorable systemic tolerability of IONPs (Cortajarena et al., 2014). Ferumoxytol is a super paramagnetic iron oxide coated with carbohydrates and it is often used for iron deficiency anemia disease. Ferumoxytol is being investigated in various clinical trials for MR imaging of numerous cancers. One clinical trial is ongoing from 2015 with 90 patients for steady-state blood volume maps by using Ferumoxytol non-stoichiometric magnetite MR imaging in glioblastoma patients (NCT02359097). The primary objective of this trial is to investigate the steady-state cerebral blood volume (CBV) maps that are better than dynamic susceptibility contrast CBV maps in brain tumor blood vessel visualizations. The secondary objective of the trial is to quantitate CBV estimation, therapeutic response and survival assessment, correlation of relative CBV, and performance of Ferumoxytol administration in different stages of cancer. However, there is slow progress in metallic nanoparticle translation into the clinical stage. The significant challenge facing by MNPs from entering the clinical stage is insufficient optimization of physical properties to achieve maximum functionality. Multiple preclinical studies have been reported that by modulating the size and shape of MNPs can tune the therapeutic performances. These investigations should be carried out at the biological level to prove the widely adopted physical modifications of MNPs for successful anticancer therapy. Another major drawback is that many preclinical studies have been investigated in small animal models which complicate the accurate representation of therapeutic activity into the human model. Currently IONPs and GNPs are investigated for drug delivery and thermal ablation in cancer treatment. However, these MNPs are limited toward local treatment and solid tumors. The long-term toxicity of MNPs is another major concern because if these MNPs are not cleared through the kidney or their accumulation in different organs for a long time can causes severe side effects. So, these are the main concerns that obstruct the clinical progress of MNPs. Moreover, sufficient investigation is needed to understand the function

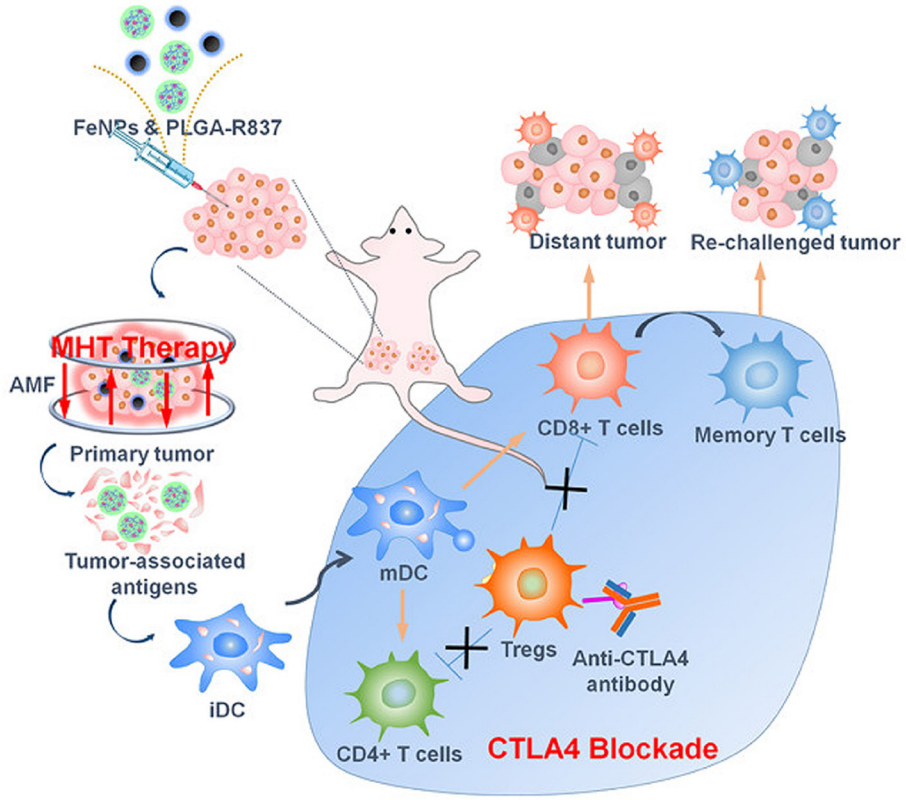

FIGURE 12 | Mechanism of toll-like receptor (TLR)-7 agonist-based iron oxide nanoparticle (IONP) delivery with a checkpoint blockade antibody for alternative magnetic field (AMF)-induced magnetic hyperthermia and immune therapy. Reproduced from Chao et al. (2019) *Copyright © 2019, American Chemical Society*.

of MNPs against our biological systems and how the physical modifications can impact its performances during preclinical stages to amplify future MNPs clinical translation.

FUTURE PERSPECTIVES AND CONCLUSION

MNPs for cancer therapy have faced significant hurdles for FDA approval and very few of them have approved for clinical trials. There are several concerns about the MNPs such as toxicity, biodegradability, biodistribution inside the body, immunogenicity, and clearance from the body, that should be investigated more in detail before the clinical trials. Various MNPs have shown acute and chronic toxicities which limit their translation into clinical settings. Notably, MNPs synthesized biologically by using multiple biological sources such as plants and microbes might overcome this toxicity issue. Biosynthesized MNPs have shown less serum protein adsorption in the blood favorable for the *in vivo* stability. The size and shape of the MNPs affect the *in vivo* toxicity, pharmacokinetics, and clearance from the body. Extremely small MNPs can be easily cleared from the body through our excretion system where the larger MNPs can be accumulated in different major organs and further induce some systemic toxicity. So, the ideal size and shape of the MNPs are essential to determine the longer circulation and higher accumulation inside the tumor. MNPs exhibiting excellent catalytic activity like manganese, iron, copper, cerium, etc. can be degraded into ionic forms in the presence of intracellular stimuli like lower pH, GSH, and peroxidase and generate toxic radicals and ROS. Intracellular degradation of MNPs into ionic form can be cleared easily after the treatment, thereby it can reduce the long-term toxicity. Modification of MNPs with biocompatible polymers and biomolecules can affect systemic toxicity and cellular uptake. So, detailed and careful studies are required to understand the therapeutic potential of biocompatible MNPs. Multiple stimuli responsive MNP can be a suitable candidate to manipulate the TME for personalized anticancer therapy. Although the role of MNPs in tumor site accumulation, systemic toxicity, biodegradability, and systemic clearance are uncertain, the potential anticancer response demonstrated by the combination of stimuli and MNPs can be considered as a possible alternative in near future.

Developments in the field of nanomedicine, specifically metallic nanotherapeutics, present immense potential for cancer theranostics. In cancer nanomedicine, MNPs contribute to various functions, from treatment to imaging purposes, which can be easily made available for future therapeutic procedures. General requirements for designing potential MNPs are based on their size, shape, surface modifications, therapeutic competence,

and toxicity profile. Based on the desired application, metal nanotherapeutics can be fine-tuned to the required size, shape, and morphology. Surface modification is essential to minimize systemic toxicity and active site accumulation. The higher surface area of metallic nanotherapeutics presents a great advantage and can be modified with biological molecules and ligands to strengthen its applicability toward treatment by targeting cancer cells and transporting multiple drugs. Small-sized MNPs can be easily degraded inside the body and cleared by our clearance system. The optical properties of metallic nanotherapeutics introduce a tremendous opportunity for *in vivo* imaging such as PA, CT, SERS, US, and MRI to track the MNPs delivery. Simultaneously, different stimuli can enhance the therapeutic ability of metallic nanotherapeutics. Multiple stimuli-triggered metallic nanotherapeutics, as well as their therapeutic activities, have been discussed in this review. Stimuli-triggering can alter the on-demand drug delivery at targeted sites, which can be controlled externally, a key point for advanced research. Internal stimuli-triggered metallic nanotherapeutics have been shown to modulate the TME by reducing hypoxic conditions and decreasing GSH concentrations to induce a favorable environment for treatment. External stimuli are superior options to modulate the activities of metallic nanotherapeutics to control treatment procedures. For example, light-triggered metallic nanotherapeutics can elevate the TME temperature, which can be controlled to induce ICD for enhanced immune therapy. Similarly, US-triggered metallic nanotherapeutics can penetrate deep tissues for ROS generation, which can be further investigated for clinical use. Currently, various IONPs and GNPs are used clinically for radiotherapy and hyperthermia but warrant advanced research to verify their therapeutic behavior, as well as the toxicity of metallic nanotherapeutics. However, various MNPs have demonstrated unwanted toxicities, and intensive research can overcome this barrier by modifying the size, shape, and surface functionalization with biocompatible molecules to generate a favorable therapeutic agent. Stimuli triggers can induce multiple therapeutic activities inside a tumor, a beneficial feature for therapy, and can control the drug dose concentrations. Although there are some limitations, metallic nanotherapeutics combined with stimuli-triggering can be developed as proficient therapeutic agents for anticancer therapy.

AUTHOR CONTRIBUTIONS

AM contributed to conceptualization, writing the manuscript, and drawing figures. SU and I-KP edited and revised the manuscript. All authors contributed to the article and approved the submitted version.

FUNDING

This work was financially supported by the Bio & Medical Technology Development Program (No. NRF-2017M3A9E2056372) through the National Research Foundation of Korea (NRF) funded by the Korean government, MSIP. This work was also supported by the National Research Foundation of Korea (NRF) grant funded by the Korea government (MSIT) (No. 2020R1A2C2005620, 2018R1A5A2024181, and NRF-2019M3E5D1A02068082).

REFERENCES

Abuid, N. J., Gattás-Asfura, K. M., Lashoto, D. J., Poulos, A. M., and Stabler, C. L. (2020). "Biomedical applications of cerium oxide nanoparticles: a potent redox modulator and drug delivery agent," in Chung EJ, Leon L, Rinaldi C editors. *Nanoparticles for Biomedical Applications,* (Elsevier), 283–301.

Ahmad, M. Z., Akhter, S., Jain, G. K., Rahman, M., Pathan, S. A., Ahmad, F. J., et al. (2010). Metallic nanoparticles: technology overview & drug delivery applications in oncology. *Expert Opin. Drug Deliv.* 7, 927–942. doi: 10.1517/17425247.2010.498473

Albarqi, H. A., Wong, L. H., Schumann, C., Sabei, F. Y., Korzun, T., Li, X., et al. (2019). Biocompatible nanoclusters with high heating efficiency for systemically delivered magnetic hyperthermia. *ACS Nano* 13, 6383–6395. doi: 10.1021/acsnano.8b06542

Amirshaghaghi, A., Yan, L., Miller, J., Daniel, Y., Stein, J. M., Busch, T. M., et al. (2019). Chlorin e6-coated Superparamagnetic Iron Oxide Nanoparticle (SPION) nanoclusters as a theranostic agent for dual-mode imaging and photodynamic therapy. *Sci. Rep.* 9:2613. doi: 10.1038/s41598-019-39036-1

Anselmo, A. C., and Mitragotri, S. (2016). Nanoparticles in the clinic. *Bioeng. Transl. Med.* 1, 10–29. doi: 10.1002/btm2.10003

Arakha, M., Pal, S., Samantarrai, D., Panigrahi, T. K., Mallick, B. C., Pramanik, K., et al. (2015). Antimicrobial activity of iron oxide nanoparticle upon modulation of nanoparticle-bacteria interface. *Sci. Rep.* 5:14813. doi: 10.1038/srep14813

Augustine, R., Hasan, A., Patan, N. K., Dalvi, Y. B., Varghese, R., Antony, A., et al. (2019). Cerium oxide nanoparticle incorporated electrospun poly (3-hydroxybutyrate-co-3-hydroxyvalerate) membranes for diabetic wound healing applications. *ACS Biomater. Sci. Eng.* 6, 58–70. doi: 10.1021/acsbiomaterials.8b01352

Azzawi, Z. G. M., Hamad, T. I., Kadhim, S. A., and Naji, G. A.-H. (2018). Osseointegration evaluation of laser-deposited titanium dioxide nanoparticles on commercially pure titanium dental implants. *J. Mater. Sci. Mater. Med.* 29:96. doi: 10.1007/s10856-018-6097-6

Badrigilan, S., Choupani, J., Khanbabaei, H., Hoseini-Ghahfarokhi, M., Webster, T. J., and Tayebi, L. (2020). Bismuth-based nanomaterials: recent advances in tumor targeting and synergistic cancer therapy techniques. *Adv. Healthc. Mater.* 9:1901695. doi: 10.1002/adhm.201901695

Bao, T., Yin, W., Zheng, X., Zhang, X., Yu, J., Dong, X., et al. (2016a). One-pot synthesis of PEGylated plasmonic MoO3–x hollow nanospheres for photoacoustic imaging guided chemo-photothermal combinational therapy of cancer. *Biomaterials* 76, 11–24. doi: 10.1016/j.biomaterials.2015.10.048

Bao, Z., Liu, X., Liu, Y., Liu, H., and Zhao, K. (2016b). Near-infrared light-responsive inorganic nanomaterials for photothermal therapy. *Asian J. Pharm. Sci.* 11, 349–364. doi: 10.1016/j.ajps.2015.11.123

Barman, S. C., Hossain, M. F., and Park, J. Y. (2018). Soft surfactant-assisted uniformly dispersed platinum nanoparticles for high performance electrochemical non-enzymatic glucose sensing platform. *J. Electroanal. Chem.* 824, 121–127. doi: 10.1016/j.jelechem.2018.07.028

Benguigui, M., Weitz, I. S., Timaner, M., Kan, T., Shechter, D., Perlman, O., et al. (2019). Copper oxide nanoparticles inhibit pancreatic tumor growth primarily by targeting tumor initiating cells. *Sci. Rep.* 9:12613. doi: 10.1038/s41598-019-48959-8

Bogdan, J., Pławińska-Czarnak, J., and Zarzyńska, J. (2017). Nanoparticles of titanium and zinc oxides as novel agents in tumor treatment: a review. *Nanoscale Res. Lett.* 12:225. doi: 10.1186/s11671-017-2007-y

Brazzale, C., Canaparo, R., Racca, L., Foglietta, F., Durando, G., Fantozzi, R., et al. (2016). Enhanced selective sonosensitizing efficacy of ultrasound-based anticancer treatment by targeted gold nanoparticles. *Nanomedicine* 12, 3053–3070. doi: 10.2217/nnm-2016-0293

Can, M. M., Coşkun, M., and Firat, T. (2012). A comparative study of nanosized iron oxide particles; magnetite (Fe3O4), maghemite (γ-Fe2O3) and hematite

(α-Fe2O3), using ferromagnetic resonance. *J. Alloys Compd.* 542, 241–247. doi: 10.1016/j.jallcom.2012.07.091

Canavese, G., Ancona, A., Racca, L., Canta, M., Dumontel, B., Barbaresco, F., et al. (2018). Nanoparticle-assisted ultrasound: a special focus on sonodynamic therapy against cancer. *Chem. Eng. J.* 340, 155–172. doi: 10.1016/j.cej.2018.01.060

Cao, Y., Wu, T., Dai, W., Dong, H., and Zhang, X. (2019). TiO2 nanosheets with the Au nanocrystal-decorated edge for mitochondria-targeting enhanced sonodynamic therapy. *Chem. Mater.* 31, 9105–9114. doi: 10.1021/acs.chemmater.9b03430

Casula, M. F., Conca, E., Bakaimi, I., Sathya, A., Materia, M. E., Casu, A., et al. (2016). Manganese doped-iron oxide nanoparticle clusters and their potential as agents for magnetic resonance imaging and hyperthermia. *Phys. Chem. Chem. Phys.* 18, 16848–16855. doi: 10.1039/C6CP02094A

Celardo, I., Pedersen, J. Z., Traversa, E., and Ghibelli, L. (2011). Pharmacological potential of cerium oxide nanoparticles. *Nanoscale* 3, 1411–1420. doi: 10.1039/c0nr00875c

Çeşmeli, S., and Biray Avci, C. (2019). Application of titanium dioxide (TiO2) nanoparticles in cancer therapies. *J. Drug Target.* 27, 762–766. doi: 10.1080/1061186X.2018.1527338

Chang, D., Lim, M., Goos, J. A., Qiao, R., Ng, Y. Y., Mansfeld, F. M., et al. (2018). Biologically targeted magnetic hyperthermia: potential and limitations. *Front. Pharmacol.* 9:831. doi: 10.3389/fphar.2018.00831

Chang, M., Wang, M., Wang, M., Shu, M., Ding, B., Li, C., et al. (2019). A Multifunctional cascade bioreactor based on hollow-structured cu2mos4 for synergetic cancer chemo-dynamic therapy/starvation therapy/phototherapy/immunotherapy with remarkably enhanced efficacy. *Adv. Mater.* 31:1905271. doi: 10.1002/adma.201905271

Chao, Y., Chen, G., Liang, C., Xu, J., Dong, Z., Han, X., et al. (2019). Iron nanoparticles for low-power local magnetic hyperthermia in combination with immune checkpoint blockade for systemic antitumor therapy. *Nano Lett.* 19, 4287–4296. doi: 10.1021/acs.nanolett.9b00579

Chen, T., Cen, D., Ren, Z., Wang, Y., Cai, X., Huang, J., et al. (2019a). Bismuth embedded silica nanoparticles loaded with autophagy suppressant to promote photothermal therapy. *Biomaterials* 221:119419. doi: 10.1016/j.biomaterials.2019.119419

Chen, Y., Cong, H., Shen, Y., and Yu, B. (2020). Biomedical application of manganese dioxide nanomaterials. *Nanotechnology* 31:202001. doi: 10.1088/1361-6528/ab6fe1

Chen, Y., Zhao, G., Wang, S., He, Y., Han, S., Du, C., et al. (2019b). Platelet-membrane-camouflaged bismuth sulfide nanorods for synergistic radio-photothermal therapy against cancer. *Biomater. Sci.* 7, 3450–3459. doi: 10.1039/C9BM00599D

Cheng, Q., and Liu, Y. (2017). Multifunctional platinum-based nanoparticles for biomedical applications. *Wiley Interdiscip. Rev. Nanomed. Nanobiotechnol.* 9:e1410. doi: 10.1002/wnan.1410

Cherukula, K., Bae, W. K., Lee, J. H., and Park, I.-K. (2018). Programmed 'triple-mode'anti-tumor therapy: improving peritoneal retention, tumor penetration and activatable drug release properties for effective inhibition of peritoneal carcinomatosis. *Biomaterials* 169, 45–60. doi: 10.1016/j.biomaterials.2018.03.051

Cherukula, K., Park, M. S., Sontyana, A. G., Mathew, A. P., Vijayan, V., Bae, W. K., et al. (2019a). Role of immunosuppressive microenvironment in acquiring immunotolerance post-photothermal therapy. *J. Korean Med. Sci.* 34:e272. doi: 10.3346/jkms.2019.34.e272

Cherukula, K., Uthaman, S., and Park, I.-K. (2019b). "Navigate-dock-activate" anti-tumor strategy: tumor micromilieu charge-switchable, hierarchically activated nanoplatform with ultrarapid tumor-tropic accumulation for trackable photothermal/chemotherapy. *Theranostics* 9, 2505–2525. doi: 10.7150/thno.33280

Cho, M. H., Choi, E.-S., Kim, S., Goh, S.-H., and Choi, Y. (2017). Redox-responsive manganese dioxide nanoparticles for enhanced MR imaging and radiotherapy of lung cancer. *Front. Chem.* 5:109. doi: 10.3389/fchem.2017.00109

Conde, J., Doria, G., and Baptista, P. (2012). Noble metal nanoparticles applications in cancer. *J. Drug Deliv.* 2012:751075. doi: 10.1155/2012/751075

Cortajarena, A. L., Ortega, D., Ocampo, S. M., Gonzalez-García, A., Couleaud, P., Miranda, R., et al. (2014). Engineering iron oxide nanoparticles for clinical settings. *Nanobiomedicine* 1:2. doi: 10.5772/58841

Curcio, A., Silva, A. K., Cabana, S., Espinosa, A., Baptiste, B., Menguy, N., et al. (2019). Iron oxide nanoflowers@ CuS hybrids for cancer tri-therapy: interplay of photothermal therapy, magnetic hyperthermia and photodynamic therapy. *Theranostics* 9, 1288–1302. doi: 10.7150/thno.30238

Devarasetty, M., Forsythe, S. D., Shelkey, E., and Soker, S. (2020). *In vitro* modeling of the tumor microenvironment in tumor organoids. *Tissue Eng. Regen. Med.* 17, 759–771. doi: 10.1007/s13770-020-00258-4

Dhall, A., and Self, W. (2018). Cerium oxide nanoparticles: a brief review of their synthesis methods and biomedical applications. *Antioxidants* 7:97. doi: 10.3390/antiox7080097

Ding, K., Zheng, C., Sun, L., Liu, X., Yin, Y., and Wang, L. (2019). NIR light-induced tumor phototherapy using ICG delivery system based on platelet-membrane-camouflaged hollow bismuth selenide nanoparticles. *Chin. Chem. Lett.* 5, 1168–1172. doi: 10.1016/j.cclet.2019.10.040

Dixon, S. J., Lemberg, K. M., Lamprecht, M. R., Skouta, R., Zaitsev, E. M., Gleason, C. E., et al. (2012). Ferroptosis: an iron-dependent form of nonapoptotic cell death. *Cell* 149, 1060–1072. doi: 10.1016/j.cell.2012.03.042

Duan, G., Chen, L., Jing, Z., De Luna, P., Wen, L., Zhang, L., et al. (2019). Robust antibacterial activity of tungsten oxide (WO3-X) nanodots. *Chem. Res. Toxicol.* 32, 1357–1366. doi: 10.1021/acs.chemrestox.8b00399

Dumas, A., and Couvreur, P. (2015). Palladium: a future key player in the nanomedical field? *Chem. Sci.* 6, 2153–2157. doi: 10.1039/C5SC00070J

El-Batal, A. I., Nada, H. G., El-Behery, R. R., Gobara, M., and El-Sayyad, G. S. (2020). Nystatin-mediated bismuth oxide nano-drug synthesis using gamma rays for increasing the antimicrobial and antibiofilm activities against some pathogenic bacteria and Candida species. *RSC Adv.* 10, 9274–9289. doi: 10.1039/C9RA10765G

Eramabadi, P., Masoudi, M., Makhdoumi, A., and Mashreghi, M. (2020). Microbial cell lysate supernatant (CLS) alteration impact on platinum nanoparticles fabrication, characterization, antioxidant and antibacterial activity. *Mater. Sci. Eng. C* 117:111292. doi: 10.1016/j.msec.2020.111292

Evans, E. R., Bugga, P., Asthana, V., and Drezek, R. (2018). Metallic nanoparticles for cancer immunotherapy. *Mater. Today* 21, 673–685. doi: 10.1016/j.mattod.2017.11.022

Fantechi, E., Innocenti, C., Albino, M., Lottini, E., and Sangregorio, C. (2015). Influence of cobalt doping on the hyperthermic efficiency of magnetite nanoparticles. *J. Magn. Magn. Mater.* 380, 365–371. doi: 10.1016/j.jmmm.2014.10.082

Fantechi, E., Innocenti, C., Zanardelli, M., Fittipaldi, M., Falvo, E., Carbo, M., et al. (2014). A smart platform for hyperthermia application in cancer treatment: cobalt-doped ferrite nanoparticles mineralized in human ferritin cages. *ACS Nano* 8, 4705–4719. doi: 10.1021/nn500454n

Feng, L., Gai, S., He, F., Yang, P., and Zhao, Y. (2020). Multifunctional bismuth ferrite nanocatalysts with optical and magnetic functions for ultrasound enhanced tumor theranostics. *ACS Nano* 6, 7245–7258. doi: 10.1021/acsnano.0c02458

Feng, Q., Yang, X., Hao, Y., Wang, N., Feng, X., Hou, L., et al. (2019). Cancer cell membrane-biomimetic nanoplatform for enhanced sonodynamic therapy on breast cancer via autophagy regulation strategy. *ACS Appl. Mater. Interfaces* 11, 32729–32738. doi: 10.1021/acsami.9b10948

Fernandes, N., Rodrigues, C. F., Moreira, A. F., and Correia, I. J. (2020). Overview of the application of inorganic nanomaterials in cancer photothermal therapy. *Biomater. Sci.* 8, 2990–3020. doi: 10.1039/D0BM00222D

Fu, B., Dang, M., Tao, J., Li, Y., and Tang, Y. (2020). Mesoporous platinum nanoparticle-based nanoplatforms for combined chemo-photothermal breast cancer therapy. *J. Colloid Interface Sci.* 570, 197–204. doi: 10.1016/j.jcis.2020.02.051

Gorgizadeh, M., Behzadpour, N., Salehi, F., Daneshvar, F., Vais, R. D., Nazari-Vanani, R., et al. (2020). A MnFe2O4/C nanocomposite as a novel theranostic agent in MRI, sonodynamic therapy and photothermal therapy of a melanoma cancer model. *J. Alloys Compd.* 816:152597. doi: 10.1016/j.jallcom.2019.152597

Guerrero-Florez, V., Mendez-Sanchez, S. C., Patrón-Soberano, O. A., Rodríguez-González, V., Blach, D., and Martínez, F. (2020). Gold nanoparticle-mediated generation of reactive oxygen species during plasmonic photothermal therapy: a comparative study for different particle sizes, shapes, and surface conjugations. *J. Mater. Chem. B* 8, 2862–2875. doi: 10.1039/D0TB00240B

Guo, S., Yao, X., Jiang, Q., Wang, K., Zhang, Y., Peng, H., et al. (2020a). Dihydroartemisinin-loaded magnetic nanoparticles for

enhanced chemodynamic therapy. *Front. Pharmacol.* 11:226. doi: 10.3389/fphar.2020.00226

Guo, Y., Li, Y., Zhang, W., Zu, H., Yu, H., Li, D., et al. (2020b). Insights into the deep-tissue photothermal therapy in near-infrared II region based on tumor-targeted MoO 2 nanoaggregates. *Sci. China Mater.* 63, 1085–1098. doi: 10.1007/s40843-019-1272-0

Guo, Z., Liu, Y., Zhou, H., Zheng, K., Wang, D., Jia, M., et al. (2019). CD47-targeted bismuth selenide nanoparticles actualize improved photothermal therapy by increasing macrophage phagocytosis of cancer cells. *Colloids Surf. B Biointerfaces* 184:110546. doi: 10.1016/j.colsurfb.2019.110546

Gupta, R., and Sharma, D. (2020). Manganese-doped magnetic nanoclusters for hyperthermia and photothermal glioblastoma therapy. *ACS Appl. Nano Mater.* 3, 2026–2037. doi: 10.1021/acsanm.0c00121

Hadadian, Y., Ramos, A. P., and Pavan, T. Z. (2019). Role of zinc substitution in magnetic hyperthermia properties of magnetite nanoparticles: interplay between intrinsic properties and dipolar interactions. *Sci. Rep.* 9:18048. doi: 10.1038/s41598-019-54250-7

Haider, N., Fatima, S., Taha, M., Rizwanullah, M., Firdous, J., Ahmad, R., et al. (2020). *Nanomedicines in diagnosis and treatment of* cancer: an update. *Curr. Pharm. Design.* 26, 1216–1231. doi: 10.2174/1381612826666200318170716

Hervault, A., and Thanh, N. T. K. (2014). Magnetic nanoparticle-based therapeutic agents for thermo-chemotherapy treatment of cancer. *Nanoscale* 6, 11553–11573. doi: 10.1039/C4NR03482A

Hessel, C. M., Pattani, V. P., Rasch, M., Panthani, M. G., Koo, B., Tunnell, J. W., et al. (2011). Copper selenide nanocrystals for photothermal therapy. *Nano Lett.* 11, 2560–2566. doi: 10.1021/nl201400z

Hou, H., Huang, X., Wei, G., Xu, F., Wang, Y., and Zhou, S. (2019a). Fenton reaction-assisted photodynamic therapy for cancer with multifunctional magnetic nanoparticles. *ACS Appl. Mater. Interfaces* 11, 29579–29592. doi: 10.1021/acsami.9b09671

Hou, Z., Deng, K., Wang, M., Liu, Y., Chang, M., Huang, S., et al. (2019b). Hydrogenated titanium oxide decorated upconversion nanoparticles: facile laser modified synthesis and. 808 nm near-infrared light triggered phototherapy. *Chem. Mater.* 31, 774–784. doi: 10.1021/acs.chemmater.8b03762

Hu, C., Cai, L., Liu, S., Liu, Y., Zhou, Y., and Pang, M. (2020). Copper-doped nanoscale covalent organic polymer for augmented photo-/chemodynamic synergistic therapy and immunotherapy. *Bioconjug. Chem.* 31, 1661–1670 doi: 10.1021/acs.bioconjchem.0c00209

Huang, G., Chen, H., Dong, Y., Luo, X., Yu, H., Moore, Z., et al. (2013). Superparamagnetic iron oxide nanoparticles: amplifying ROS stress to improve anticancer drug efficacy. *Theranostics* 3, 116–126. doi: 10.7150/thno.5411

Huang, T.-Y., Huang, G.-L., Zhang, C.-Y., Zhuang, B.-W., Liu, B.-X., Su, L.-Y., et al. (2020a). Supramolecular photothermal nanomedicine mediated distant tumor inhibition via PD-1 and TIM-3 blockage. *Front. Chem.* 8:1. doi: 10.3389/fchem.2020.00001

Huang, W.-T., Chan, M.-H., Chen, X., Hsiao, M., and Liu, R.-S. (2020b). Theranostic nanobubble encapsulating a plasmon-enhanced upconversion hybrid nanosystem for cancer therapy. *Theranostics* 10, 782–796. doi: 10.7150/thno.38684

Huang, X., Jain, P. K., El-Sayed, I. H., and El-Sayed, M. A. (2008). Plasmonic photothermal therapy (PPTT) using gold nanoparticles. *Lasers Med. Sci.* 23, 217–228. doi: 10.1007/s10103-007-0470-x

Inbaraj, B. S., and Chen, B.-H. (2019). An overview on recent *in vivo* biological application of cerium oxide nanoparticles. *Asian J. Pharm. Sci.* 15, 558–575. doi: 10.1016/j.ajps.2019.10.005

Jayakumar, T., Huang, H.-C., Hsia, C.-W., Fong, T.-H., Khamrang, T., Velusamy, M., et al. (2020). Ruthenium derivatives attenuate LPS-induced inflammatory responses and liver injury via suppressing NF-κB signaling and free radical production. *Bioorg. Chem.* 96:103639. doi: 10.1016/j.bioorg.2020.103639

Jia, T., Xu, J., Dong, S., He, F., Zhong, C., Yang, G., et al. (2019). Mesoporous cerium oxide-coated upconversion nanoparticles for tumor-responsive chemo-photodynamic therapy and bioimaging. *Chem. Sci.* 10, 8618–8633. doi: 10.1039/C9SC01615E

Jiang, Y.-W., Gao, G., Hu, P., Liu, J.-B., Guo, Y., Zhang, X., et al. (2020). Palladium nanosheet-knotted injectable hydrogels formed via palladium–sulfur bonding for synergistic chemo-photothermal therapy. *Nanoscale* 12, 210–219. doi: 10.1039/C9NR08454A

Jiang, Y.-W., Gao, G., Jia, H.-R., Zhang, X., Zhao, J., Ma, N., et al. (2019b). Copper oxide nanoparticles induce enhanced radiosensitizing effect via destructive autophagy. *ACS Biomater. Sci. Eng.* 5, 1569–1579. doi: 10.1021/acsbiomaterials.8b01181

Jiang, H., Xing, L., and Yang, C. (2019a). *Amphiphilic Nonsteroid Anti-Inflammatory Platinum Nanoparticles and Preparation Methods Therefor*. Nanjing: Google Patents.

Jurašin, D. D., Curlin, M., Capjak, I., Crnković, T., Lovrić, M., Babič, M., et al. (2016). Surface coating affects behavior of metallic nanoparticles in a biological environment. *Beilstein J. Nanotechnol.* 7, 246–262. doi: 10.3762/bjnano.7.23

Kang, S., Ahn, S., Lee, J., Kim, J. Y., Choi, M., Gujrati, V., et al. (2017). Effects of gold nanoparticle-based vaccine size on lymph node delivery and cytotoxic T-lymphocyte responses. *J. Controll. Release* 256, 56–67. doi: 10.1016/j.jconrel.2017.04.024

Kang, S., Shin, W., Kang, K., Choi, M.-H., Kim, Y.-J., Kim, Y.-K., et al. (2018). Revisiting of Pd nanoparticles in cancer treatment: all-round excellence of porous Pd nanoplates in gene-thermo combinational therapy. *ACS Appl. Mater. Interfaces* 10, 13819–13828. doi: 10.1021/acsami.8b01000

Kang, S. H., Lee, Y. K., Park, I. S., Park, I.-K., Hong, S. M., Kwon, S. Y., et al. (2020). Biomimetic gold nanoshell-loaded macrophage for photothermal biomedicine. *Biomed Res. Int.* 2020:5869235. doi: 10.1155/2020/5869235

Kim, M., Lee, J. H., and Nam, J. M. (2019). Plasmonic photothermal nanoparticles for biomedical applications. *Adv. Sci.* 6:1900471. doi: 10.1002/advs.201900471

Kim, S., Im, S., Park, E.-Y., Lee, J., Kim, C., Kim, T.-I., et al. (2020). Drug-loaded titanium dioxide nanoparticle coated with tumor targeting polymer as a sonodynamic chemotherapeutic agent for anti-cancer therapy. *Nanomedicine* 24:102110. doi: 10.1016/j.nano.2019.102110

Kobyliak, N., Abenavoli, L., Kononenko, L., Kyriienko, D., and Spivak, M. (2019). Neuropathic diabetic foot ulcers treated with cerium dioxide nanoparticles: a case report. *Diabetes Metab. Syndr.* 13, 228–234. doi: 10.1016/j.dsx.2018.08.027

Lankveld, D. P., Rayavarapu, R. G., Krystek, P., Oomen, A. G., Verharen, H. W., Van Leeuwen, T. G., et al. (2011). Blood clearance and tissue distribution of PEGylated and non-PEGylated gold nanorods after intravenous administration in rats. *Nanomedicine* 6, 339–349. doi: 10.2217/nnm.10.122

Lapotko, D. (2011). Plasmonic nanobubbles as tunable cellular probes for cancer theranostics. *Cancers* 3, 802–840. doi: 10.3390/cancers3010802

Lee, S.-Y., and Shieh, M.-J. (2020). Platinum (II) drug-loaded gold nanoshells for chemo-photothermal therapy in colorectal cancer. *ACS Appl. Mater. Interfaces* 12, 4254–4264. doi: 10.1021/acsami.9b18855

Levin, T., Sade, H., Binyamini, R. B.-S., Pour, M., Nachman, I., and Lellouche, J.-P. (2019). Tungsten disulfide-based nanocomposites for photothermal therapy. *Beilstein J. Nanotechnol.* 10, 811–822. doi: 10.3762/bjnano.10.81

Li, N., Sun, Q., Yu, Z., Gao, X., Pan, W., Wan, X., et al. (2018). Nuclear-targeted photothermal therapy prevents cancer recurrence with near-infrared triggered copper sulfide nanoparticles. *ACS Nano* 12, 5197–5206. doi: 10.1021/acsnano.7b06870

Li, P., Liu, L., Lu, Q., Yang, S., Yang, L., Cheng, Y., et al. (2019a). Ultrasmall MoS2 nanodots-doped biodegradable SiO2 nanoparticles for clearable FL/CT/MSOT imaging-guided PTT/PDT combination tumor therapy. *ACS Appl. Mater. Interfaces* 11, 5771–5781. doi: 10.1021/acsami.8b18924

Li, R., Peng, F., Cai, J., Yang, D., and Zhang, P. (2019b). *Redox dual-stimuli responsive drug delivery systems for improving tumor-targeting ability and reducing adverse side effects. Asian J. Pharm. Sci.* 15, 311–325. doi: 10.1016/j.ajps.2019.06.003

Li, Y., Lu, W., Huang, Q., Li, C., and Chen, W. (2010). Copper sulfide nanoparticles for photothermal ablation of tumor cells. *Nanomedicine* 5, 1161–1171. doi: 10.2217/nnm.10.85

Li, Y., Miao, Z., Shang, Z., Cai, Y., Cheng, J., and Xu, X. (2020a). A visible-and NIR-light responsive photothermal therapy agent by chirality-dependent MoO3–x nanoparticles. *Adv. Funct. Mater.* 30:1906311. doi: 10.1002/adfm.201906311

Li, Y., Sun, H., Yin, Z., Guo, X., and Yan, J. (2020b). Anti-Inflammatory effects of cerium dioxide nanoparticles on peritonitis in rats induced by staphylococcus epidermidis infection. *Adv. Polymer Technol.* 2020:3591508. doi: 10.1155/2020/3591508

Li, Y., Wang, X., Yang, D., Hu, P., Gao, L., Chen, D., et al. (2019c). Polydopamine-coated gold nanostars for near-infrared cancer photothermal

therapy by multiple pathways. *J. Mater. Sci.* 54, 12036–12048. doi: 10.1007/s10853-019-03774-4

Li, Y., Yun, K.-H., Lee, H., Goh, S.-H., Suh, Y.-G., and Choi, Y. (2019d). Porous platinum nanoparticles as a high-Z and oxygen generating nanozyme for enhanced radiotherapy *in vivo*. *Biomaterials* 197, 12–19. doi: 10.1016/j.biomaterials.2019.01.004

Li, Z., Shao, J., Luo, Q., Yu, X.-F., Xie, H., Fu, H., et al. (2017). Cell-borne. 2D nanomaterials for efficient cancer targeting and photothermal therapy. *Biomaterials* 133, 37–48. doi: 10.1016/j.biomaterials.2017.04.012

Libutti, S. K., Paciotti, G. F., Byrnes, A. A., Alexander, H. R., Gannon, W. E., Walker, M., et al. (2010). Phase I and pharmacokinetic studies of CYT-6091, a novel PEGylated colloidal gold-rhTNF nanomedicine. *Clin. Cancer Res.* 16, 6139–6149. doi: 10.1158/1078-0432.CCR-10-0978

Lin, T., Zhao, X., Zhao, S., Yu, H., Cao, W., Chen, W., et al. (2018). O2-generating MnO2 nanoparticles for enhanced photodynamic therapy of bladder cancer by ameliorating hypoxia. *Theranostics.* 8, 990–1004. doi: 10.7150/thno.22465

Lin, X., Liu, S., Zhang, X., Zhu, R., Chen, S., Chen, X., et al. (2020). An ultrasound activated vesicle of janus au-mno nanoparticles for promoted tumor penetration and sono-chemodynamic therapy of orthotopic liver cancer. *Angew. Chem. Int. Edn.* 59, 1682–1688. doi: 10.1002/anie.201912768

Liu, M., Liu, B., Liu, Q., Du, K., Wang, Z., and He, N. (2019a). Nanomaterial-induced ferroptosis for cancer specific therapy. *Coord. Chem. Rev.* 382, 160–180. doi: 10.1016/j.ccr.2018.12.015

Liu, T., and Liu, Z. (2018). 2D MoS2 nanostructures for biomedical applications. *Adv. Healthc. Mater.* 7:1701158. doi: 10.1002/adhm.201701158

Liu, W., Li, X., Li, W., Zhang, Q., Bai, H., Li, J., et al. (2018). Highly stable molybdenum dioxide nanoparticles with strong plasmon resonance are promising in photothermal cancer therapy. *Biomaterials* 163, 43–54. doi: 10.1016/j.biomaterials.2018.02.021

Liu, X., Zheng, J., Sun, W., Zhao, X., Li, Y., Gong, N., et al. (2019b). Ferrimagnetic vortex nanoring-mediated mild magnetic hyperthermia imparts potent immunological effect for treating cancer metastasis. *ACS Nano* 13, 8811–8825. doi: 10.1021/acsnano.9b01979

Liu, Y., Lin, A., Liu, J., Chen, X., Zhu, X., Gong, Y., et al. (2019c). Enzyme-responsive mesoporous ruthenium for combined chemo-photothermal therapy of drug-resistant bacteria. *ACS Appl. Mater. Interfaces* 11, 26590–26606. doi: 10.1021/acsami.9b07866

Liu, Z., Qiu, K., Liao, X., Rees, T. W., Chen, Y., Zhao, Z., et al. (2020). Nucleus-targeting ultrasmall ruthenium (iv) oxide nanoparticles for photoacoustic imaging and low-temperature photothermal therapy in the NIR-II window. *Chem. Commun.* 56, 3019–3022. doi: 10.1039/C9CC09728G

Lopez-Lázaro, M. (2007). Dual role of hydrogen peroxide in cancer: possible relevance to cancer chemoprevention and therapy. *Cancer Lett.* 252, 1–8. doi: 10.1016/j.canlet.2006.10.029

Ma, B., Wang, S., Liu, F., Zhang, S., Duan, J., Li, Z., et al. (2018). Self-assembled copper–amino acid nanoparticles for in situ glutathione "AND" H2O2 sequentially triggered chemodynamic therapy. *J. Am. Chem. Soc.* 141, 849–857. doi: 10.1021/jacs.8b08714

Manikandan, M., Hasan, N., and Wu, H.-F. (2013). Platinum nanoparticles for the photothermal treatment of Neuro. 2A cancer cells. *Biomaterials* 34, 5833–5842. doi: 10.1016/j.biomaterials.2013.03.077

Martin, J. D., Cabral, H., Stylianopoulos, T., and Jain, R. K. (2020). Improving cancer immunotherapy using nanomedicines: progress, opportunities and challenges. *Nat. Rev. Clin. Oncol. 17,* 251–26. doi: 10.1038/s41571-019-0308-z

Matharu, R. K., Ciric, L., Ren, G., and Edirisinghe, M. (2020). Comparative study of the antimicrobial effects of tungsten nanoparticles and tungsten nanocomposite fibres on hospital acquired bacterial and viral pathogens. *Nanomaterials* 10:1017. doi: 10.3390/nano10061017

Mchale, A. P., Callan, J. F., Nomikou, N., Fowley, C., and Callan, B. (2016). "Sonodynamic therapy: concept, mechanism and application to cancer treatment," in Escoffre J-M, Bouakaz A editors. *Therapeutic Ultrasound*. (Cham: Springer), 429–450.

Mody, V. V., Siwale, R., Singh, A., and Mody, H. R. (2010). Introduction to metallic nanoparticles. *J. Pharm. Bioallied Sci.* 2, 282–289. doi: 10.4103/0975-7406.72127

Mohapatra, A., Uthaman, S., and Park, I.-K. (2019). "Polyethylene glycol nanoparticles as promising tools for anticancer therapeutics," in Kesharwani P,Paknikar KM, Gajbhiye V editors. *Polymeric Nanoparticles as a Promising Tool for Anti-cancer Therapeutics*. (Elsevier), 205–231.

Morales-Cruz, M., Delgado, Y., Castillo, B., Figueroa, C. M., Molina, A. M., Torres, A., et al. (2019). Smart targeting to improve cancer therapeutics. *Drug Des. Devel. Ther.* 13, 3753–3772. doi: 10.2147/DDDT.S219489

Murugesan, B., Pandiyan, N., Arumugam, M., Sonamuthu, J., Samayanan, S., Yurong, C., et al. (2020). Fabrication of palladium nanoparticles anchored polypyrrole functionalized reduced graphene oxide nanocomposite for antibiofilm associated orthopedic tissue engineering. *Appl. Surf. Sci.* 510:145403. doi: 10.1016/j.apsusc.2020.145403

Naha, P. C., Hsu, J. C., Kim, J., Shah, S., Bouch,é, M., Si-Mohamed, S., et al. (2020). *Dextran coated cerium oxide* nanoparticles: a computed tomography contrast agent for imaging the gastrointestinal tract and inflammatory bowel disease. *ACS Nano*. 14, 10187–10197. doi: 10.1021/acsnano.0c03457

Ninomiya, K., Ogino, C., Oshima, S., Sonoke, S., Kuroda, S.-I., and Shimizu, N. (2012). Targeted sonodynamic therapy using protein-modified TiO2 nanoparticles. *Ultrason. Sonochem.* 19, 607–614. doi: 10.1016/j.ultsonch.2011.09.009

Pardo, A., YáÑEz, S., Piñeiro, Y., Iglesias-Rey, R. N., Al-Modlej, A., Barbosa, S., et al. (2020). Cubic anisotropic Co-and Zn-substituted ferrite nanoparticles as multimodal magnetic agents. *ACS Appl. Mater. Interfaces* 12, 9017–9031. doi: 10.1021/acsami.9b20496

Park, H., Lim, D.-J., Vines, J. B., Yoon, J.-H., and Ryu, N.-E. (2019). Gold nanoparticles for photothermal cancer therapy. *Front. Chem.* 7:167. doi: 10.3389/fchem.2019.00167

Park, W., Heo, Y.-J., and Han, D. K. (2018). New opportunities for nanoparticles in cancer immunotherapy. *Biomater. Res.* 22:24. doi: 10.1186/s40824-018-0133-y

Pham, A. N., Xing, G., Miller, C. J., and Waite, T. D. (2013). Fenton-like copper redox chemistry revisited: hydrogen peroxide and superoxide mediation of copper-catalyzed oxidant production. *J. Catal.* 301, 54–64. doi: 10.1016/j.jcat.2013.01.025

Pham, T. N., Lengkeek, N. A., Greguric, I., Kim, B. J., Pellegrini, P. A., Bickley, S. A., et al. (2017). Tunable and noncytotoxic PET/SPECT-MRI multimodality imaging probes using colloidally stable ligand-free superparamagnetic iron oxide nanoparticles. *Int. J. Nanomedicine* 12, 899–909. doi: 10.2147/IJN.S127171

Phan, T. T. V., Huynh, T.-C., Manivasagan, P., Mondal, S., and Oh, J. (2020). An up-to-date review on biomedical applications of palladium nanoparticles. *Nanomaterials* 10:66. doi: 10.3390/nano10010066

Piazza, R. D., Viali, W. R., Dos Santos, C. C., Da Silva, E. N., Marques, R. F. C., De Morais, P. C., et al. (2020). *PEGlatyon-SPION surface functionalization with folic acid for magnetic hyperthermia applications. Mater. Res. Express.* 7:1591–2053. doi: 10.1088/2053-1591/ab6700

Piehler, S., Dähring, H., Grandke, J., Göring, J., Couleaud, P., Aires, A., et al. (2020). Iron oxide nanoparticles as carriers for DOX and magnetic hyperthermia after intratumoral application into breast cancer in mice: impact and future perspectives. *Nanomaterials* 10:1016. doi: 10.3390/nano10061016

Pillarisetti, S., Uthaman, S., Huh, K. M., Koh, Y. S., Lee, S., and Park, I.-K. (2019). Multimodal composite iron oxide nanoparticles for biomedical applications. *Tissue Eng. Regen. Med. 16,* 451–465. doi: 10.1007/s13770-019-00218-7

Qian, X., Han, X., Yu, L., Xu, T., and Chen, Y. (2020). Manganese-based functional nanoplatforms: nanosynthetic construction, physiochemical property, and theranostic applicability. *Adv. Funct. Mater.* 30:1907066. doi: 10.1002/adfm.201907066

Rajendrakumar, S. K., Chang, N.-C., Mohapatra, A., Uthaman, S., Lee, B.-I., Tsai, W.-B., et al. (2018a). A lipophilic ir-780 dye-encapsulated zwitterionic polymer-lipid micellar nanoparticle for enhanced photothermal therapy and nir-based fluorescence imaging in a cervical tumor mouse model. *Int. J. Mol. Sci.* 19:1189. doi: 10.3390/ijms19041189

Rajendrakumar, S. K., Cherukula, K., Park, H. J., Uthaman, S., Jeong, Y. Y., Lee, B.-I., et al. (2018b). Dual-stimuli-responsive albumin-polyplex nanoassembly for spatially controlled gene release in metastatic breast cancer. *J. Control. Release* 276, 72–83. doi: 10.1016/j.jconrel.2018.02.039

Ranji-Burachaloo, H., Gurr, P. A., Dunstan, D. E., and Qiao, G. G. (2018). Cancer treatment through nanoparticle-facilitated Fenton reaction. *ACS Nano* 12, 11819–11837. doi: 10.1021/acsnano.8b07635

Revuri, V., Cherukula, K., Nafiujjaman, M., Vijayan, V., Jeong, Y. Y., Park, I.-K., et al. (2019). *In situ* oxygenic nanopods targeting tumor adaption to hypoxia potentiate image-guided photothermal therapy. *ACS Appl. Mater. Interfaces* 11, 19782–19792. doi: 10.1021/acsami.9b03889

Rosenblum, D., Joshi, N., Tao, W., Karp, J. M., and Peer, D. (2018). Progress and challenges towards targeted delivery of cancer therapeutics. *Nat. Commun.* 9:1410. doi: 10.1038/s41467-018-03705-y

Samadi, A., Klingberg, H., Jauffred, L., Kjær, A., Bendix, P. M., and Oddershede, L. B. (2018). Platinum nanoparticles: a non-toxic, effective and thermally stable alternative plasmonic material for cancer therapy and bioengineering. *Nanoscale* 10, 9097–9107. doi: 10.1039/C8NR02275E

Sánchez-Cabezas, S., Montes-Robles, R., Gallo, J., Sancenón, F., and Martínez-Máñez, R. (2019). Combining magnetic hyperthermia and dual T 1/T 2 MR imaging using highly versatile iron oxide nanoparticles. *Dalton Trans.* 48, 3883–3892. doi: 10.1039/C8DT04685A

Serpe, L., Brazzale, C., Racca, L., Durando, G., Caliceti, P., Salmaso, S., et al. (2020). "Targeted gold nanoparticles as nanosonosensitizers: a new challenge for the sonodynamic treatment of cancer," in *Ultrasonics*, (Lisbon: Bioscope Group), 1–1.

Shahbazi, M.-A., Faghfouri, L., Ferreira, M. P., Figueiredo, P., Maleki, H., Sefat, F., et al. (2020). The versatile biomedical applications of bismuth-based nanoparticles and composites: therapeutic, diagnostic, biosensing, and regenerative properties. *Chem. Soc. Rev.* 49, 1253–1321. doi: 10.1039/C9CS00283A

Shanei, A., and Akbari-Zadeh, H. (2019). Investigating the sonodynamic-radiosensitivity effect of gold nanoparticles on hela cervical cancer cells. *J. Korean Med. Sci.* 34:e243. doi: 10.3346/jkms.2019.34.e243

Shanei, A., and Sazgarnia, A. (2019). An overview of therapeutic applications of ultrasound based on synergetic effects with gold nanoparticles and laser excitation. *Iran J. Basic Med. Sci.* 22, 848–855. doi: 10.22038/ijbms.2019.29584.7142

Sharma, A., Goyal, A. K., and Rath, G. (2018). Recent advances in metal nanoparticles in cancer therapy. *J. Drug Target.* 26, 617–632. doi: 10.1080/1061186X.2017.1400553

Shen, Z., Liu, T., Li, Y., Lau, J., Yang, Z., Fan, W., et al. (2018). Fenton-reaction-acceleratable magnetic nanoparticles for ferroptosis therapy of orthotopic brain tumors. *ACS Nano* 12, 11355–11365. doi: 10.1021/acsnano.8b06201

Shi, J., Kantoff, P. W., Wooster, R., and Farokhzad, O. C. (2017). Cancer nanomedicine: progress, challenges and opportunities. *Nat. Rev. Cancer* 17, 20–37. doi: 10.1038/nrc.2016.108

Shin, S.-M., and Sung, A. (2020). Effects on the physical properties of ophthalmic hydrogels containing. 4-chlorostyrene and cerium oxide nanoparticles with ultraviolet blocking ability. *J. Nanosci. Nanotechnol.* 20, 6871–6876. doi: 10.1166/jnn.2020.18812

Silva, C. O., Pinho, J. O., Lopes, J. M., Almeida, A. J., Gaspar, M. M., and Reis, C. (2019). Current trends in cancer nanotheranostics: metallic, polymeric, and lipid-based systems. *Pharmaceutics* 11:22. doi: 10.3390/pharmaceutics11010022

Singh, P., Pandit, S., Mokkapati, V., Garg, A., Ravikumar, V., and Mijakovic, I. (2018). Gold nanoparticles in diagnostics and therapeutics for human cancer. *Int. J. Mol. Sci.* 19:1979. doi: 10.3390/ijms19071979

Siposova, K., Huntosova, V., Shlapa, Y., Lenkavska, L., Macajova, M., Belous, A., et al. (2019). Advances in the study of cerium oxide nanoparticles: new insights into antiamyloidogenic activity. *ACS Appl. Bio Mater.* 2, 1884–1896. doi: 10.1021/acsabm.8b00816

Sivakumar, B., Aswathy, R. G., Romero-Aburto, R., Mitcham, T., Mitchel, K. A., Nagaoka, Y., et al. (2017). Highly versatile SPION encapsulated PLGA nanoparticles as photothermal ablators of cancer cells and as multimodal imaging agents. *Biomater. Sci.* 5, 432–443. doi: 10.1039/C6BM00621C

Sivamaruthi, B. S., Ramkumar, V. S., Archunan, G., Chaiyasut, C., and Suganthy, N. (2019). Biogenic synthesis of silver palladium bimetallic nanoparticles from fruit extract of *Terminalia chebula–in vitro* evaluation of anticancer and antimicrobial activity. *J. Drug Deliv. Sci. Technol.* 51, 139–151. doi: 10.1016/j.jddst.2019.02.024

Soleymani, M., Velashjerdi, M., Shaterabadi, Z., and Barati, A. (2020). One-pot preparation of hyaluronic acid-coated iron oxide nanoparticles for magnetic hyperthermia therapy and targeting CD44-overexpressing cancer cells. *Carbohydr. Polym.* 237:116130. doi: 10.1016/j.carbpol.2020.116130

Spain, E., Gilgunn, S., Sharma, S., Adamson, K., Carthy, E., O'kennedy, R., et al. (2016). Detection of prostate specific antigen based on electrocatalytic platinum nanoparticles conjugated to a recombinant scFv antibody. *Biosens. Bioelectron.* 77, 759–766. doi: 10.1016/j.bios.2015.10.058

Staves, B. (2010). Pilot study of AurolaseTM therapy in refractory and/or recurrent tumors of the head and neck. *ClinicalTrials.gov Identifier: NCT00848042.*

Su, H., Wang, Y., Gu, Y., Bowman, L., Zhao, J., and Ding, M. (2018). Potential applications and human biosafety of nanomaterials used in nanomedicine. *J. Appl. Toxicol.* 38, 3–24. doi: 10.1002/jat.3476

Sun, G., Yang, S., Cai, H., Shu, Y., Han, Q., Wang, B., et al. (2019). Molybdenum disulfide nanoflowers mediated anti-inflammation macrophage modulation for spinal cord injury treatment. *J. Colloid Interface Sci.* 549, 50–62. doi: 10.1016/j.jcis.2019.04.047

Sun, Q., Wu, J., Jin, L., Hong, L., Wang, F., Mao, Z., et al. (2020a). *Cancer cell membrane-coated gold nanorods for photothermal therapy and radiotherapy on oral squamous cancer. J. Mater. Chem. B* 8, 7253–7263. doi: 10.1039/D0TB01063D

Sun, T., Xia, N., Yuan, F., Liu, X., Chang, Y., Liu, S., et al. (2020b). A colorimetric method for determination of the prostate specific antigen based on enzyme-free cascaded signal amplification via peptide-copper (II) nanoparticles. *Microchim. Acta.* 187:116. doi: 10.1007/s00604-019-4074-5

Sykes, E. A., Chen, J., Zheng, G., and Chan, W. C. (2014). Investigating the impact of nanoparticle size on active and passive tumor targeting efficiency. *ACS Nano* 8, 5696–5706. doi: 10.1021/nn500299p

Tao, B., Lin, C., Deng, Y., Yuan, Z., Shen, X., Chen, M., et al. (2019). Copper-nanoparticle-embedded hydrogel for killing bacteria and promoting wound healing with photothermal therapy. *J. Mater. Chem. B* 7, 2534–2548. doi: 10.1039/C8TB03272F

Thirunavukkarasu, G. K., Cherukula, K., Lee, H., Jeong, Y. Y., Park, I.-K., and Lee, J. Y. (2018). Magnetic field-inducible drug-eluting nanoparticles for image-guided thermo-chemotherapy. *Biomaterials* 180, 240–252. doi: 10.1016/j.biomaterials.2018.07.028

Thomas, R. G., and Kwan, J. J. (2019). Gas stabilizing titanium dioxide nanocones against desmoplastic cancer by ultrasound cavitation induced tumor penetration and sonodynamic therapy. *J. Acoust. Soc. Am.* 145, 1892–1892. doi: 10.1121/1.5101855

Thorat, N. D., Bohara, R. A., Yadav, H. M., and Tofail, S. A. (2016). Multi-modal MR imaging and magnetic hyperthermia study of Gd doped Fe. 3 O 4 nanoparticles for integrative cancer therapy. *RSC Adv.* 6, 94967–94975. doi: 10.1039/C6RA20135K

Vaupel, P., and Mayer, A. (2007). Hypoxia in cancer: significance and impact on clinical outcome. *Cancer Metastasis Rev.* 26, 225–239. doi: 10.1007/s10555-007-9055-1

Venkatesh, N., Bhowmik, H., and Kuila, A. (2018). Metallic nanoparticle: a review. *Biomed. J. Sci. Techn. Res.* 4, 3765–3775. doi: 10.26717/BJSTR.2018.04.0001011

Wang, C., Cai, X., Zhang, J., Wang, X., Wang, Y., Ge, H., et al. (2015a). Trifolium-like platinum nanoparticle-mediated photothermal therapy inhibits tumor growth and osteolysis in a bone metastasis model. *Small* 11, 2080–2086. doi: 10.1002/smll.201403315

Wang, C., Cao, F., Ruan, Y., Jia, X., Zhen, W., and Jiang, X. (2019a). Specific generation of singlet oxygen through the russell mechanism in hypoxic tumors and GSH depletion by Cu-TCPP nanosheets for cancer therapy. *Angew. Chem. Int. Edn.* 58, 9846–9850. doi: 10.1002/anie.201903981

Wang, G., Jin, W., Qasim, A. M., Gao, A., Peng, X., Li, W., et al. (2017). Antibacterial effects of titanium embedded with silver nanoparticles based on electron-transfer-induced reactive oxygen species. *Biomaterials* 124, 25–34. doi: 10.1016/j.biomaterials.2017.01.028

Wang, J., Chang, Y., Luo, H., Jiang, W., Xu, L., Chen, T., et al. (2020a). Designing immunogenic nanotherapeutics for photothermal-triggered immunotherapy involving reprogramming immunosuppression and activating systemic antitumor responses. *Biomaterials* 255:120153. doi: 10.1016/j.biomaterials.2020.120153

Wang, J., Zhang, B., Sun, J., Wang, Y., and Wang, H. (2020b). Nanomedicine-enabled modulation of tumor hypoxic microenvironment for enhanced cancer therapy. *Adv. Therapeutics* 3:1900083. doi: 10.1002/adtp.201900083

Wang, P., Liang, C., Zhu, J., Yang, N., Jiao, A., Wang, W., et al. (2019b). Manganese-based nanoplatform as metal ion-enhanced ROS generator for combined chemodynamic/photodynamic therapy. *ACS Appl. Mater. Interfaces* 11, 41140–41147. doi: 10.1021/acsami.9b16617

Wang, R., He, Z., Cai, P., Zhao, Y., Gao, L., Yang, W., et al. (2019c). Surface-functionalized modified copper sulfide nanoparticles enhance checkpoint blockade tumor immunotherapy by photothermal therapy and antigen capturing. *ACS Appl. Mater. Interfaces* 11, 13964–13972. doi: 10.1021/acsami.9b01107

Wang, S., Riedinger, A., Li, H., Fu, C., Liu, H., Li, L., et al. (2015b). Plasmonic copper sulfide nanocrystals exhibiting near-infrared photothermal and photodynamic therapeutic effects. *ACS Nano* 9, 1788–1800. doi: 10.1021/nn506687t

Wang, S., Yang, L., Cho, H.-Y., Chueng, S.-T. D., Zhang, H., Zhang, Q., et al. (2019d). Programmed degradation of a hierarchical nanoparticle with redox and light responsivity for self-activated photo-chemical enhanced chemodynamic therapy. *Biomaterials* 224:119498. doi: 10.1016/j.biomaterials.2019.119498

Wang, W., Jin, Y., Xu, Z., Liu, X., Bajwa, S. Z., Khan, W. S., et al. (2020c). Stimuli-activatable nanomedicines for chemodynamic therapy of cancer. *Wiley Interdiscip. Rev. Nanomed. Nanobiotechnol. 12:e*1614. doi: 10.1002/wnan.1614

Wang, X., Zhong, X., Bai, L., Xu, J., Gong, F., Dong, Z., et al. (2020d). Ultrafine titanium monoxide (TiO1+ x) nanorods for enhanced sonodynamic therapy. *J. Am. Chem. Soc.* 142, 6527–6537. doi: 10.1021/jacs.9b10228

Wang, Y., Shim, M. S., Levinson, N. S., Sung, H. W., and Xia, Y. (2014). Stimuli-responsive materials for controlled release of theranostic agents. *Adv. Funct. Mater.* 24, 4206–4220. doi: 10.1002/adfm.201400279

Winter, A., Kowald, T., Engels, S., and Wawroschek, F. (2020). Magnetic resonance sentinel lymph node imaging and magnetometer-guided intraoperative detection in penile cancer, using superparamagnetic iron oxide nanoparticles: first results. *Urol. Int.* 104, 177–180. doi: 10.1159/000502017

Wu, C.-M., Naseem, S., Chou, M.-H., Wang, J.-H., and Jian, Y.-Q. (2019a). Recent advances in tungsten-oxide-based materials and their applications. *Front. Mater.* 6:49. doi: 10.3389/fmats.2019.00049

Wu, M., Hou, P., Dong, L., Cai, L., Chen, Z., Zhao, M., et al. (2019b). Manganese dioxide nanosheets: from preparation to biomedical applications. *Int. J. Nanomed.* 14:4781. doi: 10.2147/IJN.S207666

Wu, W., Luo, L., Wang, Y., Wu, Q., Dai, H.-B., Li, J.-S., et al. (2018). Endogenous pH-responsive nanoparticles with programmable size changes for targeted tumor therapy and imaging applications. *Theranostics* 8, 3038–3058. doi: 10.7150/thno.23459

Xiao, J.-W., Fan, S.-X., Wang, F., Sun, L.-D., Zheng, X.-Y., and Yan, C.-H. (2014). Porous Pd nanoparticles with high photothermal conversion efficiency for efficient ablation of cancer cells. *Nanoscale* 6, 4345–4351. doi: 10.1039/C3NR06843A

Xiao, S., Lu, Y., Feng, M., Dong, M., Cao, Z., Zhang, X., et al. (2020). Multifunctional FeS2 theranostic nanoparticles for photothermal-enhanced chemodynamic/photodynamic cancer therapy and photoacoustic imaging. *Chem. Eng. J. 396:*125294. doi: 10.1016/j.cej.2020.125294

Xie, W., Guo, Z., Gao, Q., Wang, D., Liang, K., Gu, Z., et al. (2020). *Manganese-doped layered double* hydroxide: a biodegradable theranostic nanoplatform with tumor microenvironment response for magnetic resonance imaging-guided photothermal therapy. *ACS Appl. Bio Mater.* 9, 5845–5855. doi: 10.1021/acsabm.0c00564

Xie, X., Liao, J., Shao, X., Li, Q., and Lin, Y. (2017). The effect of shape on cellular uptake of gold nanoparticles in the forms of stars, rods, and triangles. *Sci. Rep.* 7:3827. doi: 10.1038/s41598-017-04229-z

Xu, M., Wen, Y., Liu, Y., Tan, X., Chen, X., Zhu, X., et al. (2019a). Hollow mesoporous ruthenium nanoparticles conjugated bispecific antibody for targeted anti-colorectal cancer response of combination therapy. *Nanoscale* 11, 9661–9678. doi: 10.1039/C9NR01904A

Xu, W., Wang, J., Qian, J., Hou, G., Wang, Y., Ji, L., et al. (2019b). NIR/pH dual-responsive polysaccharide-encapsulated gold nanorods for enhanced chemo-photothermal therapy of breast cancer. *Mater. Sci. Eng. C* 103:109854. doi: 10.1016/j.msec.2019.109854

Xuan, Y., Zhang, R.-Y., Zhao, D.-H., Zhang, X.-S., An, J., Cheng, K., et al. (2019). Ultrafast synthesis of gold nanosphere cluster coated by graphene quantum dot for active targeting PA/CT imaging and near-infrared laser/pH-triggered chemo-photothermal synergistic tumor therapy. *Chem. Eng. J.* 369, 87–99. doi: 10.1016/j.cej.2019.03.035

Yadav, V., Roy, S., Singh, P., Khan, Z., and Jaiswal, A. (2019). 2D MoS2-based nanomaterials for therapeutic, bioimaging, and biosensing applications. *Small* 15:1803706. doi: 10.1002/smll.201803706

Yan, T., Zhu, L., Ju, H., and Lei, J. (2018). DNA-walker-induced allosteric switch for tandem signal amplification with palladium nanoparticles/metal–organic framework tags in electrochemical biosensing. *Anal. Chem.* 90, 14493–14499. doi: 10.1021/acs.analchem.8b04338

Yang, F., Shi, K., Jia, Y.-P., Hao, Y., Peng, J.-R., and Qian, Z.-Y. (2020a). Advanced biomaterials for cancer immunotherapy. *Acta Pharmacol. Sin.* 41, 911–927. doi: 10.1038/s41401-020-0372-z

Yang, G., Xu, L., Chao, Y., Xu, J., Sun, X., Wu, Y., et al. (2017). Hollow MnO 2 as a tumor-microenvironment-responsive biodegradable nano-platform for combination therapy favoring antitumor immune responses. *Nat. Commun.* 8:902. doi: 10.1038/s41467-017-01050-0

Yang, H., Zhang, Y., Song, J., Wang, M., Yu, S., Chen, L., et al. (2019a). Boosting phototherapeutic efficiency with single NIR laser-activated ultrasmall bismuth sulfide quantum dots. *Chem. Eng. J.* 375:121941. doi: 10.1016/j.cej.2019.121941

Yang, N., Xiao, W., Song, X., Wang, W., and Dong, X. (2020b). Recent advances in tumor microenvironment hydrogen peroxide-responsive materials for cancer photodynamic therapy. *Nano-Micro Lett.* 12:15. doi: 10.1007/s40820-019-0347-0

Yang, Q., Peng, J., Shi, K., Xiao, Y., Liu, Q., Han, R., et al. (2019b). Rationally designed peptide-conjugated gold/platinum nanosystem with active tumor-targeting for enhancing tumor photothermal-immunotherapy. *J. Control. Release* 308, 29–43. doi: 10.1016/j.jconrel.2019.06.031

Yang, Y., Lyu, M., Li, J.-H., Zhu, D.-M., Yuan, Y.-F., and Liu, W. (2019c). Ultra-small bimetallic iron–palladium (FePd) nanoparticle loaded macrophages for targeted tumor photothermal therapy in NIR-II biowindows and magnetic resonance imaging. *RSC Adv.* 9, 33378–33387. doi: 10.1039/C9RA05649A

Yao, J., Feng, J., and Chen, J. (2016). External-stimuli responsive systems for cancer theranostic. *Asian J. Pharm. Sci.* 11, 585–595. doi: 10.1016/j.ajps.2016.06.001

Yao, Y., Zang, Y., Qu, J., Tang, M., and Zhang, T. (2019). The toxicity of metallic nanoparticles on liver: the subcellular damages, mechanisms, and outcomes. *Int. J. Nanomedicine.* 14, 8787–8804. doi: 10.2147/IJN.S212907

Yoo, J., Park, C., Yi, G., Lee, D., and Koo, H. (2019). Active targeting strategies using biological ligands for nanoparticle drug delivery systems. *Cancers* 11:640. doi: 10.3390/cancers11050640

You, D. G., Deepagan, V., Um, W., Jeon, S., Son, S., Chang, H., et al. (2016). ROS-generating TiO 2 nanoparticles for non-invasive sonodynamic therapy of cancer. *Sci. Rep.* 6:23200. doi: 10.1038/srep23200

You, Y.-H., Lin, Y.-F., Nirosha, B., Chang, H.-T., and Huang, Y.-F. (2019). Polydopamine-coated gold nanostar for combined antitumor and antiangiogenic therapy in multidrug-resistant breast cancer. *Nanotheranostics* 3, 266–283. doi: 10.7150/ntno.36842

Zha, Z., Zhang, S., Deng, Z., Li, Y., Li, C., and Dai, Z. (2013). Enzyme-responsive copper sulphide nanoparticles for combined photoacoustic imaging, tumor-selective chemotherapy and photothermal therapy. *Chem. Commun.* 49, 3455–3457. doi: 10.1039/c3cc40608c

Zhan, Y., Liu, Y., Zu, H., Guo, Y., Wu, S., Yang, H., et al. (2018). Phase-controlled synthesis of molybdenum oxide nanoparticles for surface enhanced Raman scattering and photothermal therapy. *Nanoscale* 10, 5997–6004. doi: 10.1039/C8NR00413G

Zhang, C., Zhang, D., Liu, J., Wang, J., Lu, Y., Zheng, J., et al. (2019a). Functionalized MoS 2-erlotinib produces hyperthermia under NIR. *J. Nanobiotechnol.* 17:76. doi: 10.1186/s12951-019-0508-9

Zhang, X., Li, X., You, Q., and Zhang, X. (2017). Prodrug strategy for cancer cell-specific targeting: a recent overview. *Eur. J. Med. Chem.* 139, 542–563. doi: 10.1016/j.ejmech.2017.08.010

Zhang, Y., Sha, W., Zhang, X., Cheng, M., Wu, Q., Wang, W., et al. (2019b). Zwitterionic chitooligosaccharide-modified ink-blue titanium dioxide nanoparticles with inherent immune activation for enhanced photothermal therapy. *Biomater. Sci.* 7, 5027–5034. doi: 10.1039/C9BM01170F

Zhang, Z., and Ji, Y. (2019). Mesoporous manganese dioxide coated gold nanorods as a multiresponsive nanoplatform for drug delivery. *Ind. Eng. Chem. Res.* 58, 2991–2999. doi: 10.1021/acs.iecr.8b05331

Zhou, B., Wu, Q., Wang, M., Hoover, A., Wang, X., Zhou, F., et al. (2020a). Immunologically modified MnFe2O4 nanoparticles to synergize photothermal therapy and immunotherapy for cancer treatment. *Chem. Eng. J. 396:*125239. doi: 10.1016/j.cej.2020.125239

Zhou, J., Shi, L., Liu, Q., Zhang, H., Liu, X., Han, F., et al. (2020b). Porous lanthanum-doped manganese oxide nanoparticles for enhanced sonodynamic cancer therapy. *Part. Part. Syst. Charact.* 37:2000143. doi: 10.1002/ppsc.202000143

Zhou, L., Wang, H., and Li, Y. (2018). Stimuli-responsive nanomedicines for overcoming cancer multidrug resistance. *Theranostics* 8, 1059–1074. doi: 10.7150/thno.22679

Zhou, Z., Kong, B., Yu, C., Shi, X., Wang, M., Liu, W., et al. (2014). Tungsten oxide nanorods: an efficient nanoplatform for tumor CT imaging and photothermal therapy. *Sci. Rep.* 4:3653. doi: 10.1038/srep03653

Conflict of Interest: SU and I-KP declare that they are the topic editors of this special issue "Stimuli responsive nanoparticles for anti-cancer therapy."

The remaining author declares that the research was conducted in the absence of any commercial or financial relationships that could be construed as a potential conflict of interest.

frontiers in Bioengineering and Biotechnology

REVIEW
published: 15 December 2021
doi: 10.3389/fbioe.2021.642794

Plant Virus Nanoparticles for Anti-cancer Therapy

Srividhya Venkataraman[1], *Paul Apka*[2,3]*, *Erum Shoeb*[1,4], *Uzma Badar*[1,4] and *Kathleen Hefferon*[1]

[1]Department of Cell and Systems Biology, University of Toronto, Toronto, ON, Canada, [2]Theranostics and Drug Discovery Research Group, Faculty of Pharmaceutical Sciences, University of Nigeria, Nsukka, Nigeria, [3]Department of Pharmaceutics, Faculty of Pharmaceutical Sciences, University of Nigeria, Nsukka, Nigeria, [4]Department of Genetics, University of Karachi, Karachi, Pakistan

Plant virus nanoparticles (VNPs) are inexpensive to produce, safe, biodegradable and efficacious as treatments. The applications of r plant virus nanoparticles range from epitope carriers for vaccines to agents in cancer immunotherapy. Both VNPs and virus-like particles (VLPs) are highly immunogenic and are readily phagocytosed by antigen presenting cells (APCs), which in turn elicit antigen processing and display of pathogenic epitopes on their surfaces. Since the VLPs are composed of multiple copies of their respective capsid proteins, they present repetitive multivalent scaffolds which aid in antigen presentation. Therefore, the VLPs prove to be highly suitable platforms for delivery and presentation of antigenic epitopes, resulting in induction of more robust immune response compared to those of their soluble counterparts. Since the tumor microenvironment poses the challenge of self-antigen tolerance, VLPs are preferrable platforms for delivery and display of self-antigens as well as otherwise weakly immunogenic antigens. These properties, in addition to their diminutive size, enable the VLPs to deliver vaccines to the draining lymph nodes in addition to promoting APC interactions. Furthermore, many plant viral VLPs possess inherent adjuvant properties dispensing with the requirement of additional adjuvants to stimulate immune activity. Some of the highly immunogenic VLPs elicit innate immune activity, which in turn instigate adaptive immunity in tumor micro-environments. Plant viral VLPs are nontoxic, inherently stable, and capable of being mass-produced as well as being modified with antigens and drugs, therefore providing an attractive option for eliciting anti-tumor immunity. The following review explores the use of plant viruses as epitope carrying nanoparticles and as a novel tools in cancer immunotherapy.

Keywords: nanoparticles, plant virus-like particles, therapeutics, imaging, cancer 2

OPEN ACCESS

Edited by:
In-Kyu Park,
Chonnam National University,
South Korea

Reviewed by:
Kai Xiao,
Sichuan University, China
Renjith P. Johnson,
Yenepoya University, India

***Correspondence:**
Paul Apka
paulapka275@gmail.com

Specialty section:
This article was submitted to Nanobiotechnology, a section of the journal Frontiers in Bioengineering and Biotechnology

Received: *16 December 2020*
Accepted: *27 August 2021*
Published: *15 December 2021*

Citation:
Venkataraman S, Apka P, Shoeb E, Badar U and Hefferon K (2021) Plant Virus Nanoparticles for Anti-cancer Therapy. Front. Bioeng. Biotechnol. 9:642794. doi: 10.3389/fbioe.2021.642794

INTRODUCTION

Nanomedicine is an emerging area of multidisciplinary research that has already shown promise of transforming into a disruptive innovative development (Farokhzad et al., 2008). Already, there are dozens of products in clinical trials and even some on the shelf in some pharmacies across the world though users are relatively few because of the rather prohibitive price tags of these innovative products (Park, 2019). It is pertinent to state that while a lot has been proposed in terms of the

anticipated efficacy of nanomedicines, opinions tend to vary when it comes to the stage of a critical cost-benefit- analysis for the availability of nanomedicines for use in the treatment of cancer and other ailments (FDA Drug Reports, 2017).

Nanomedicines includes a wide array of nanomaterials with particle size ranging from 1nm to more than 400 nm and are a remarkably diverse group of materials (Zhang et al., 2008; Zhou et al., 2012). They may be made up of entirely of a metal as in the case of Gold and Silver nanoparticles (Paviolo and Stoddart, 2017), or a combination of liquids or a ternary system composed of an assortment of several compatible materials giving rise in most cases to a multifunctional entity often possessing stimuli responsive attributes enabling it to respond to minute changes in factors such as pH and temperature variations (Moreira et al., 2016). Additionally, nanoparticles can be prepared with simple polymeric materials such as cellulose and chitosan (Steinmetz and Manchester, 2009).

Immunotherapy in cancer treatment simply refers to a strategy with the objective of galvanizing the immune system of the patient to resist the implanting of cancerous cells. There are several approaches to achieve the desired end. One approach involves the use of drugs known as "Immune checkpoint inhibitors, to block immune checkpoints (Byun et al., 2017). The checkpoints are a typical part of the immune system and serve to modulate the immune response so that it does not come as too strong. The net effect of this treatment modality is that the blocking of these checkpoints makes it possible for the immune cells to respond more strongly to cancer.

Plant virus-based nanoparticles (VNPs) have been explored as a unique class of nanocarriers for biomedical applications (Pitek et al., 2016). In addition to their ease of production and quality control maintenance, plant virus VNPs offer a logical alternative to synthetic nanoparticles as they are inexpensive to produce, nontoxic and biodegradable (Rybickie, 2020). Plant virus nanoparticles have been further improved for their performance in terms of stimuli-responsivity (Brun, Gomez, and Suh 2017).

Plant virus nanoparticles tend to be either rod shaped, such as Tobacco mosaic virus (TMV) and Potato virus X (PVX), or icosahedral shaped, such as Cowpea mosaic virus (CPMV). Different shaped viruses respond differently as nanoparticles *in vivo*. Tobacco mosaic virus can assemble into VLPs without requiring its RNA genome carry a drug payload on the surface or to a limited extent, within the inner channel of the nanoparticle. Potato virus X, cannot self-assemble in the absence of its RNA genome, and thus can only carry a payload on the outer surface. Cowpea mosaic virus can be made to self-assemble into empty virus like particles in the absence of its RNA genome and can thus carry a payload both inside and outside of its protein shell (Sainsbury et al., 2010). In this review, we provide a series of examples to discuss how plant virus architecture contributes to their applications in cancer diagnostics and therapy (Wen et al., 2015a; Wen et al., 2015b). We discuss the architecture of plant viruses, how they came to be used as nanoparticles in various medical applications, and how they may be employed in the future as novel cancer immunotherapies (Shahgolzari et al., 2021).

Architecture of Plant Virus Nanoparticles

Viruses are composed of outer protein shells which encapsulate the genomic material. The multiple copies of coat proteins that form the virus outer shell of viruses are collectively known as the capsid (Liu et al., 2016). Primarily, the capsid occurs in different shapes and sizes and is meant to protect the genomic material to keep viruses safe under extreme environments (Pokorski and Steinmetz 2011). The immense diversity with respect to the shape and size of plant viruses enables them to be tailored for specific applications. The structural integrity of viruses remains intact even when surface properties have been altered through chemical and genetic modification; this allows control over targeting ligands, drugs and contrast agents for imaging (Rong et al., 2011). Various chemical and genetic approaches are reported to control the virus surface properties without affecting structural integrity, and allow control on the attachment sites of drug molecules or contrast agents on the virus surface (Rong et al., 2011). Plant-virus capsid pores are also reported to be employed to encapsulate small therapeutic molecules (Zeng et al., 2013).

Plant viruses have been used as virus like particles (VLPs) and virus nanoparticles (VNPs) as epitope display systems for vaccine production. VLPs are a subset of the VNPs but lack any nucleic acid genome, thus making them non-infectious. VNPs and VLPs based on plant viruses are both non-pathogenic to humans and biodegradable (Steinmetz, 2010). VNPs and VLPs are advantageous due to their ability to be generated quickly while serving as highly versatile molecular scaffolds (Young et al., 2008; Steinmetz and Evans, 2007]. Examples of plant viruses utilized as VLPs include Cowpea mosaic virus (CPMV) and Tobacco mosaic virus (TMV). An example of a plant virus utilized as a VNP is Potato virus X (PVX). These are listed in **Figure 1**.

Tobacco mosaic virus (TMV) is the most well-studied plant virus and was initially characterized in the 19th century. TMV can be easily produced and purified in bulk amounts and can be manipulated genetically due to its relatively simple particle structure and genome organization. The rod-shaped virus particle measures 300 nm in length and 18 nm in diameter and contains a 6.7 kb viral RNA genome that is encapsulated by 2,130 identical copies of the capsid protein assembled in a helical arrangement. At neutral pH and in the absence of RNA, the CP assembles itself into an 18 nm double disk, a 20S aggregate or nano-ring containing two layers of 17 CP molecules which can serve as a nanoscale scaffold.

Potato virus X (PVX) is a member of the family Alphaflexiviridae, genus Potexvirus, an important plant pathogen of the family Solanaceae, and specifically infects potato, tomato and tobacco (Adams et al., 2004) (Massumi et al., 2014). It has a 6.4-kb positive-stranded RNA genome (Park et al., 2008). Multiple copies of CP assemble around the genomic RNA to form the capsid. PVX can carry large payloads due to its flexible and filamentous structure, making it possible to use for pharmaceutical and imaging applications (Roder, Dickmeis, and Commandeur 2019).

The PVX particle is 515 × 14.5 nm in dimension and comprised of 1,270 subunits of CP, (Parker et al., 2002). The C-terminus of each CP subunit is located internally and the

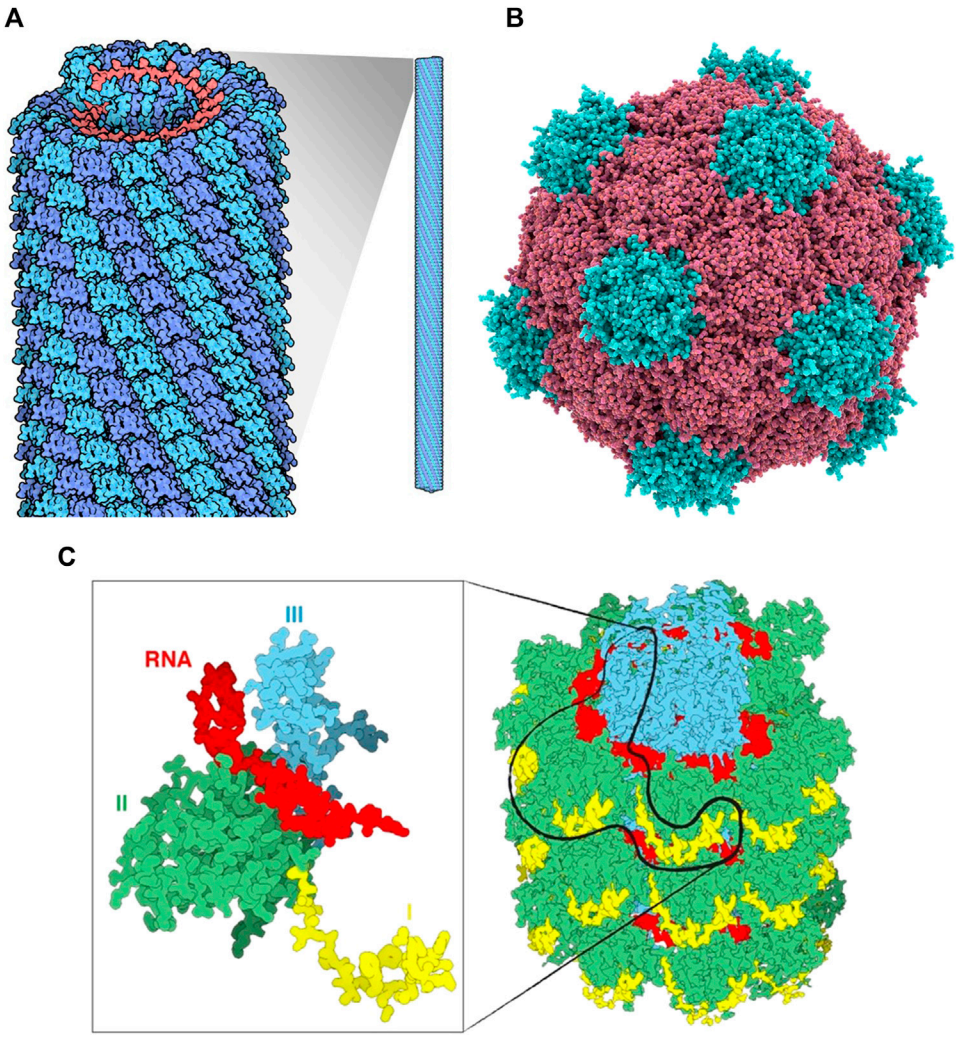

FIGURE 1 | (A) Tobacco mosaic virus structure, RNA is in red, protein subunits in blue Source: https://pdb101.rcsb.org/motm/109. **(B)** Cowpea mosaic virus structure, Protein subunits in red and blue Source: fineartamerica. com. **(C)** An overview of a portion of the PVX virus **(right)**. The three domains of the protein are shin in yellow, green and cyan, the RNA in red. The magnification on the left displays only one single CP with a fragment of RNA.

N-terminus projected externally to the assembled particle, which provides a suitable site for modification (Nemykh et al., 2008). Unlike other reported viruses, the assembly of PVX CP subunits into filamentous VLP, *in vivo* or *in vitro*, is not possible in the absence of genomic RNA. This reflects the unique connection between virus RNA and CP (Kwon et al., 2005).

The plant pathogen Cowpea mosaic virus (CPMV) belongs to the Comovirus genus. CPMV is an icosahedral shaped virus with a diameter of approximately 27 nm. It is composed of RNA-1 and RNA-2 of 6 and 3.5 kb, respectively packed in 60 copies each of Large and Small coat protein (Singh et al., 2007). CPMV is one of the most developed VNPs for biomedical and nanotechnology applications due to its ability to target specific tissues and act as an efficient drug delivery system. It is also reported to be well-adapted for the attachment of a variety of molecules to the coat protein. Five reactive lysine residues of CPMV coat protein provide sites to chemically conjugate to various compounds such as fluorescent dyes (Steinmetz, 2010). CPMV can be produced as empty virus like particles (eVLPs) Meshcheriakova et al. (2017). eVLPs are non-infectious and could be loaded with heterologous material, has increased the number of possible applications for CPMV-based particles.

Biomedical Applications

VLPs can act as strong vaccine candidates as they simulate the conformations of native viruses, utilizing their intrinsic immunogenicity without compromising their safety. VLPs evoke effectual immune responses as they are readily internalized by antigen presenting cells (APCs) and are ideal platforms for antigen processing and epitope presentation to immune cells. VLPs are composed of multiple copies of their capsid (coat) proteins, which when assembled appear as repetitive, multivalent molecular scaffolds. As a result, the multiple copies of coat protein can facilitate the multivalent

presentation of antigens fused to their surface. Therefore, VLP vaccines afford superior immunogenicity compared to antigens in their soluble states. Additionally, plant viral VLPs and VNPs possess inherent adjuvant properties dispensing with the use of additional adjuvants to evoke strong immune responses (**Table 1**).

TMV VLPs have been utilized as epitope display systems in a variety of settings, with a first example being a polio vaccine by Haynes et al. (1986). Later, TMV was used as an epitope display vehicle for a malaria vaccine and others, including foot and mouth disease virus, human papillomavirus, norovirus, hepatitis B virus, influenza virus and human immunodeficiency virus (Turpen et al., 1995; Nooraei et al., 2021). Röder et al. (2017), were able to fuse a fluorescent protein to the C-terminus of the Tobacco mosaic virus (TMV) coat protein (CP) and also carried an N-terminal Foot-and-mouth disease virus (FMDV) 2A sequence. This enables the fusion protein to be cleaved from TMV.

Potato virus X, in contrast to TMV, has a flexuous rod shape and requires its genomic RNA to self-assemble. PVX has been used extensively as an epitope display system for vaccine research. For example, Uhde-Holzem et al. (2016), reported genetically altered PVX which displayed *Staphylococcus aureus* protein A fragments on its surface, and proved to be easily functionalized with IgG to be used in biosensing plant viruses. VLPs of Papaya mosaic virus (PapMV), of the Potexvirius family, has been engineered for use as a seasonal flu trivalent vaccine (Carignan et al., 2015; Balke and Zeltins, 2020).

CPMV has also been developed as an autonomously replicating virus vector for the expression of either peptides or polypeptides in plants (Shahgolzari et al., 2020). Examples of CPMV used as an epitope presentation system include epitopes from the outer membrane (OM) protein F of *Pseudomonas aeruginosa* which were shown to protect mice against bacterial challenge, and an epitope expressing the 30 amino acid D2 domain of the fibronectin-binding protein (FnBP) from *Staphylococcus aureus*, which has been shown to be able to protect rats against endocarditis (Liu et al., 2005).

Recently, Albakri et al. (2020), explored how CPMV particles can activate human monocytes, dendritic cells (DCs) and macrophages. Monocytes, upon incubation with CPMV *in vitro*, released the chemokines CXCL10, MIP-1α and MIP-1β into cell culture supernatants. Dendritic cells and monocyte-derived macrophages were also activated after incubation with CPMV, this activation is part of SYK signaling. Shukla et al. (2020) were able to demonstrate that CPMV outperformed many other types of VLPs to be a particularly strong immune stimulant.

The capacity for multifunctionality and multivalency makes plant nanoparticle platforms an ideal choice for theranostic applications (Beatty and Lewis 2019; Wang, 2019). Plant nanoparticles are capable of precise molecular imaging to achieve accurate cancer diagnosis and therapy (Ma et al., 2017). Delivery of imaging probes through nanostructures can improve the chances of early-stage cancer diagnosis through the use of multiple modalities to improve resolution, sensitivity, penetration, time, cost and on the top of all clinical relevance compared to the single imaging modalities (Key and Leary, 2014; Shahgolzari et al., 2020). Drug conjugated nanoparticles administered intravenously target tumors, *via* the process of enhanced permeability and retention (EPR) effect depending on the type of tumor (Hansen et al., 2015).

Molecular imaging is an emerging biomedical field which facilitates the visualization, of biological mechanisms *in vivo*. Imaging technologies can include magnetic resonance imaging (MRI), computed tomography (CT), positron emission tomography (PET) and optical imaging, which enable the monitoring of molecular and cellular processes in normal and diseased conditions in living subjects. (Chung et al., 2020). Plant VLPs can be beneficial for molecular imaging technologies than synthetic nanoparticles, due to their short half-life in circulation and their lack of side effects (Steinmetz, 2010). Furthermore, plant VLPs can be developed to carry a wide array of contrast agents and fluorescent labels, as they can be modified with antibodies, peptides and aptamers to enable enhanced targeting to specific tissues and cells.

Magnetic resonance imaging (MRI) is a promising technology for the diagnosis of disease due to its high resolution and deep contrast, however, virus-based nanoparticles have been used to increase sensitivity (Pokorski et al., 2011). TMV can act as a carrier to deliver high payloads of MRI contrast imaging agents to diseased tissues (Michael A. Bruckman et al., 2013) and fluorescent dyes for biosensing and bioimaging (Wen et al., 2015). TMV's biological compatibility and multi-valency enables it to be a suitable carrier of *in vivo* imaging agents. For example, TMV rods have been conjugated to "BF3," a multi-photon absorbing fluorophore which permitted mouse brain imaging over an extended duration without crossing the blood-brain barrier (Niehl et al., 2016). A bimodal contrast agent has been prepared to target integrin α2β1by loading the internal cavity of TMV nanoparticles with the complex of dysprosium (Dy3+) and the near-infrared fluorescence (NIRF) dye Cy7.5, as well as the externally conjugated with an Asp-Gly-Glu-Ala (DGEA) peptide through a linker polyethylene glycol. This nanoparticle (Dy-Cy7.5-TMV-DGEA) was stable, displayed a low cytotoxicity and achieved a high resolution when targeted to PC-3 prostate cancer cells (Hu et al., 2017).

Tobacco Mosaic Virus has been used successfully for CD imaging, targeting atherosclerosis and thrombosis by using an NIR dye as well as a targeting peptide conjugated to TMV [96]. These targeted TMV particles were able to identify atherosclerotic lesions in ApoE−/− mice upon intravenous injection, showing that TMV can be used as a platform to detect at-risk lesions.

VNPs based on PVX have been conjugated to fluorescent reporters as well [135]. As mentioned earlier, the small fluorescent iLOV protein was expressed on the surface of PVX through genetic engineering and served as a fluorescent probe which could be of potential use *in vivo* imaging. Shukla et al. (2018), reportedly produced PVX VNPs that displayed mCherry or GFP on their N-termini in *N. benthamiana* plants. Significantly, fluorescent PVX could successfully be used for *in vivo* particle tracking in an HT-29 murine model, for *in vitro* imaging of HT-29 cells, and for tracing viral infection within plants.

CPMV can also be engineered for intravital imaging (imaging living cells while they are in a multicellular organism) and improved permeability with a retention effect that improves tumor penetration (Beatty and Lewis, 2019). For *in vivo* imaging of tumors, CPMV-based VNPs have been successfully engineered to target specific tissues (Cho et al., 2014). These tumor targeting VNPs also provide biocompatible platforms for cancer therapy and intravital imaging (Beatty and Lewis, 2019).

Clinical treatment for cancer has been routinely addressed by chemotherapy (Hu et al., 2017). Regardless, the high recurrence of cancers as well as the fast clearance of anti-cancer drugs and non-targeted drug delivery necessitate the administration of maximum tolerable doses of drugs in cancer therapy, leading to increased toxicity and lower performance (Cano-Garrido et al., 2021). Therefore, drug delivery technologies that are highly targeted and promote active drug accumulation in tumors, in concert with reductions of dose requirements, could alleviate these concerns and augment treatment outcomes.

Plant virus VLPs have several attractive features that make them appropriate for targeted administration of therapeutic molecules. The anti-cancer drug doxorubicin (DOX), has been successfully delivered using VNPs and VLPs. TMV- and PVX-derived VLPs and VNPs have been successfully used to deliver DOX (Finbloom et al., 2018). In this context, helical plant VNPs such as TMV and PVX, with high aspect ratios, have proven to be of great use in effective drug delivery. VNPs have shown great promise since their cargo-RNA functions as a ruler establishing the length of the virus particle and simple adsorption of DOX on their surface was shown to be effective for reducing tumor growth (Bruckman et al., 2013; Pitek et al., 2016).

TMV can be used as a carrier of peptides with therapeutic or targeting activity against various cancers. Trastuzumab is a cancer cell inhibiting monoclonal antibody that uses the binding sites of human epidermal growth factor receptor 2 (HER2). Trastuzumab-binding peptides (TBP) are immunogenic in nature and capable of initiating production of HER2-inhibiting antibodies to seize the growth of HER2-carrying cancer cells. TMV particles displaying TBP have been created to activate this immunogenicity (Tyulkina et al., 2011). Similarly, a delivery system reported as PhenPt-TMV, with anticancer drug phenanthriplatin loaded into a hollow TMV carrier, serves as an example of stimuli responsive system, as the release of drug is induced in the presence of acidic environment (Czapar et al., 2016). Along these lines, Tian et al. (2018) demonstrated that the Transacting Activation Transduction (TAT) peptide, conjugated to the external surface of TMV, augmented internalization along with an increased ability to escape endo/lysosomal compartments. Most of these VLPS exhibited uptake by dendritic cells and macrophages and proved to be highly immunogenic. Thus, therapeutic nucleic acids can be easily delivered to immune cells during cancer treatments.

Plant virus VNPs have been used for targeted administration of platinum-based drugs against cancer. This is important as 50% of chemotherapy treatments involve the use of these platinum-derived drugs. TMV has been demonstrated to efficiently deliver Cisplatin (Franke et al., 2018) and Phenanthriplatin (Vernekar et al., 2018), both of which are platinum-based drugs. The drugs were loaded into the TMV VNP cavity using charge-driven interactions or by synthesizing stable covalent adducts. Such a TMV-based drug delivery system was proven to enable superior, targeted cytotoxicity as well as increased ease of uptake by cancer cells in in vitro systems using HepG2 and MCF-7 cancer cell lines (Liu et al., 2016).

Another anti-cancer drug, mitoxanthrone (MTO), is a topoisomerase II inhibitor and has been shown to be encapsulated by TMV (Lin and Steinmetz, 2018). VNPs exhibited superior tumor-reduction in mouse cancer models, while precluding severe cardiac outcomes that sometimes accompany direct delivery of MTO. Yet another anti-neoplastic and antimitotic drug, valine-citrulline monomethyl auristatin E (vcMMAE), was bound to the exterior of TMV VNPs which targeted non-Hodgkin's lymphoma. Internalization into endolysosomal compartments was reported (Kernan et al., 2017), most likely accompanied by the protease-mediated release of the drug. This system was efficient in terms of cytotoxicity towards the *in vitro* Karpas 299 non-Hodgkin's lymphoma cell line with an IC50 of 250 nM.

Helical plant virus nanoparticles (VLPs) have also been used as combination therapies to augment their immune efficacy. The PVX-DOX (doxorubicin) (Lee et al., 2017) combination was shown to be highly effective in stimulating cytokine/chemokine levels while prolonging the survival of mice in melanoma models compared to that obtained through the administration of either PVX or DOX alone.

PVX displaying TNF related apoptosis inducing ligand (TRAIL) was used to promote the recruitment and activation of death receptors *in vitro* in HCC-38 primary ductal carcinoma, BT-549 ductal carcinoma and the MDA-MB-231 breast cancer cell lines (Le et al., 2017; Röder et al., 2018). *In vivo* mouse models also demonstrated that the PVX-TRAIL formulation potently inhibited tumor growth. PVX has also been used by displaying tumor necrosis factor (TNF)-related apoptosis inducing ligand (TRAIL) on the surface of VNPs. Multivalent display of TRAIL enabled increased recruitment and stimulation of death receptors expressed on cancer cell lines (Le et al., 2019). Similarly, this formulation was shown to successfully suppress tumor growth in mice breast cancer models.

An efficient and new drug delivery system has been reported for Non-Hodgkin's B cell lymphomas (NHL) based on PVX binding affinity towards malignant B cells. PVX loaded with monomethyl auristatin (MMAE) and administered to tissues harboring malignant B cells lead to inhibition of NHL growth in a mouse model (Shukla et al., 2020). Jobsri et al., 2015 reported a study in which PVX was conjugated to an idiotypic (Id) tumor-associated antigen (TAA) recombinant through a biotin/streptavidin linker, that elicited a 7 times higher anti-Id IgG response compared to Id alone in a mouse B-cell lymphoma model. Cytokine profiling in these mice revealed that the induction of IFN-α and IL-12, also that TLR7 was essential for viral RNA recognition.

PVX nanoparticles are increasingly being used for immunotherapy of tumor microenvironments. The monoclonal antibodies of Herceptin or Trastuzumab can be loaded onto PVX nanofilaments, which successfully induced

apoptosis in breast cancer cell lines (Esfandiari et al., 2016). PVX was used as an expression vector for a mutant form of the HPV16 E7 oncoprotein, by fusing it with lichenase. This elicited protection against tumor progression in mice by inducing a robust cytotoxic T-cell response (Demurtas et al., 2013).

Steinmetz et al. (2009), found that CPMV nanoparticles could bind to vimentin, a protein found on the surface of most cells. Vimentin is upregulated during tumor progression, making it an attractive target for cancer therapy. The fact that surface vimentin expression correlated with CPMV uptake in this study demonstrated the ability of CPMV to detect invasive cancer cells.

The tumor microenvironment poses a great challenge to immune clearance by virtue of being immunosuppressive and favoring immune escape of the tumors through the inhibition of anti-tumor T-cells (Chung et al., 2020). CPMV VLP nanoparticles were shown to decrease tumor growth in murine models of lung melanomas, ovarian, colon and breast tumors (Lizotte et al., 2016; Wang et al., 2019). Mechanistically, CPMV has been shown to reprogram the tumor microenvironment by recruitment of natural killer cells and neutrophils, while enabling the transition of M2 to M1 anti-tumor macrophages. This innate immune cell population subsequently combats the tumor leading to cell lysis. Most recently, Mao et al. (2021) have deduced which TLRs are responsible for these properties.

The icosahedral shape of CPMV capsid can be loaded with precise drug cargos to target tumor and cancer cells. CPMV VNPs have also been formulated as slow-release aggregates along with polyamidoamine generation 4 dendrimers (CPMV-G4) (Czapar et al., 2018), where they were shown to be effective in combating ovarian cancer in murine models, even when provided as a single dosage.

CPMV VLPs have been attached to TAAs (tumor associated antigens) using chemical conjugation, genetic fusion and enzyme-mediated ligation techniques. For example, the human epidermal growth factor receptor 2 (HER2) epitope, when conjugated to the icosahedral CPMV, was successfully delivered to the lymphatic system with enhanced uptake and activation of APCs that led to an augmented anti-HER2 immune response. The CPMV HER2 candidate vaccine slowed tumor progression and metastasis in mouse models, enhancing survival (Shukla et al., 2013). Importantly, CPMV-HER2 stimulated a predominantly Th1 immune response while Sesbania Mosaic Virus-HER2 and CCMV-HER2 induced mostly a Th2 response in mouse models, thus proving that the nature of the epitope carrier itself plays an essential role in regulating the Th1/Th2 bias. This could be due to differences in epitope display on the surface of the VNPs as well as the capsid.

Cancer vaccines against carbohydrate antigens associated with tumors (TACAs) could be useful for diminishing tumor progression. Nevertheless, carbohydrates are weakly immunogenic and therefore, plant viruses used as carriers of these molecules could enhance the immune response to TACAs. CPMV-TACA conjugates targeting the Tn antigen (GalNAc-α-O-Ser/Thr) (Yin et al., 2012) were demonstrated to induce enhanced IgG titers, implicating heightened T-cell mediated immunity and antibody isotype switching in mouse models. IgG binding to the Tn antigens were observed in experiments wherein mice sera were added to breast cancer cell lines.

The chemotherapeutic cyclophosphamide, when used in combination with CPMV VNPs, profoundly elicited tumor cell death, releasing extracellular TAAs and stimulating immune cell invasion in addition to augmenting TAA recognition and antigen presentation (Cai et al., 2019) in mouse tumor models. CPMV VNPs have also been administered in combination with CD47-blocking antibodies (Wang and Steinmetz, 2019) which proved to have synergistic effects in combating tumor growth in murine ovarian tumor models, where it activated phagocytes, leading to stimulation of the adaptive immune response. Similar synergistic effects were observed when CPMV VNPs were used in combination with the anti-programmed cell death-1 checkpoint inhibitor (Lam et al., 2018). In addition to this, CPMV has been used successfully in promoting anti-tumor effects, when combined with radiation therapy. In this instance, CPMV was shown to enhance the recruitment of APCs, which in turn targeted the extracellular TAAs and phagocytosed them to induce a prolonged effectual immune response (Patel et al., 2018) in mice and canine models.

The CPMV-DOX conjugate was developed using eighty molecules of the chemotherapeutic drug doxorubicin (DOX), covalently bound to carboxylates at the external surface of the CPMV nanoparticle. This drug delivery vehicle was found to be more cytotoxic than free DOX when used in low concentration, however, CPMV-DOX cytotoxicity is time-delayed at higher concentrations (Aljabali et al., 2013). Cancer cells manage to resist immunotherapies owing to the immunosuppressive nature of tumors. CPMV nanoparticles have been reported as an *in situ* vaccine to stimulate an anti-tumor response and overcome local immunosuppression (Shukla et al., 2020). CPMV is also shown to be effective for ovarian cancer. The strategy for immunotherapy resulting antitumor efficacy is promising and involved the formation of aggregates of CPMV and polyamidoamine generation 4 dendrimers (CPMV-G4). Administration of CPMV-G4 effectively reduced ovarian cancer (Czapar et al., 2018). CPMV nanoparticles thus provide a therapeutic application for tumor targeting, intravital imaging and cancer therapy (Yildiz et al., 2013). Further exploration into the pharmacology of CPMV nanoparticles will further elucidate its roles in the immune response (Nkanga et al., 2021).

Patel et al. (2018), used CPMV nanoparticles in conjunction with radiotherapy to delay ovarian tumor growth in a mouse model. The treatment was able to result in an increase in tumor infiltrating lymphocytes (TILs), suggesting that this combined treatment could act as a future *in situ* tumor vaccine. Further studies by Wang and Steinmetz (2019) found that a protein known as CD47, that is widely expressed on tumor cells, prevents the action of T cells and phagocytic cells. The authors used a combination therapy of CD47-blocking antibodies and CPMV nanoparticles to act synergistically and elicit an anti-tumor immune response. The same research group also used low doses of cyclophosphamide (CPA) and CPMV nanoparticles as a combination therapy to successfully reduce mouse tumors *in vivo* (Wang and Steinmetz, 2019).

TABLE 1 | Select Examples of Plant Virus Nanoparticles and their Medical Applications.

Plant virus nanoparticle	Architecture	Use in cancer immunotherapy	Reference
Tobacco mosaic virus (TMV)	Rod-shaped	carrier for tumor associated carbohydrate antigens	Yin et al. (2012)
		Carrier of cancer drug phenanthriplatin in inner core of virus nanoparticle	Vernekar et al. (2018)
		In vivo imaging	Chung et al. (2020)
Potato virus X (PVX)	Rod-shaped	*In vivo* imaging	Shukla et al. (2018)
		PVX-DOX (doxorubicin) combination therapy	Lee et al. (2017)
		displays tumor necrosis factor (TNF)-related apoptosis inducing ligand (TRAIL) on the surface	Le et al. (2019)
Cowpea Mosaic virus (CPMV)	Icosahedral shaped	HER2 epitope displayed on virus surface	Shukla et al. (2013)
		combination therapy of CD47-blocking antibodies and CPMV nanoparticles	Wang and Steinmetz, (2019)
		slow-release aggregates comprised of polyamidoamine generation 4 dendrimers (CPMV-G4)	Czapar et al. (2018)

CONCLUSION AND FUTURE DIRECTIONS

The use of plant virus nanoparticles (VNPs) as drug delivery carriers for the treatment of infectious and chronic diseases including cancer are advantageous when compared with naked drugs (Shoeb and Hefferon, 2019; Hefferon, 2018). The most promising nanoparticle systems have been adopted from naturally occurring plant viruses. Plant viruses are ideal for drug delivery as they are safe, non-infectious and nontoxic to humans (Beatty and Lewis, 2019). Cancer cells exhibit specific antigens on the surface of tumor cells which can be identified and targeted by plant-virus based nanoparticles, thus providing a clinical application of diagnosis and therapeutics for cancer. The most promising nano-scale systems have been adopted from naturally occurring plant viruses such as Tobacco mosaic virus (TMV), Cowpea mosaic virus (CPMV), Potato virus X (PVX) and many more. Currently, these new strategies are only applied in small scale production. As these approaches undergo further development, we will witness a spectrum of possible applications in the fields of medicine and biomedical engineering.

In the future, plant virus nanoparticles will need to be developed for high throughput manufacturing. This will require the dedication of facilities that can produce many grams of plant virus nanoparticles using tens of thousands of plants (McNulty et al., 2021). Today, manufacturing facilities have been generated for plant molecular farming, and adaptations could be tailored for nanoparticles (Fausther-Bovendo and Kobiger, 2021). The regulatory pathway will require more exploration to speed the process. More research regarding how plant virus nanoparticles act upon the immune system is underway and will be needed (Mao et al., 2021). Finally, the use of plant virus chimeras or semi-synthetic plant virus nanoparticles with novel properties must be explored, as well as novel modes of administration, such as microneedle patches (Boone et al., 2020).

AUTHOR CONTRIBUTIONS

All authors listed have made a substantial, direct, and intellectual contribution to the work and approved it for publication.

REFERENCES

Adams, M. J., Antoniw, J. F., Bar-Joseph, M., Brunt, A. A., Candresse, T., Foster, G. D., et al. (2004). Virology Division News: The New Plant Virus Family Flexiviridae and Assessment of Molecular Criteria for Species Demarcation. *Arch. Virol.* 149 (5), 1045–1060. doi:10.1007/s00705-004-0304-0

Albakri, M. M., Veliz, F. A., Fiering, S. N., Steinmetz, N. F., and Sieg, S. F. (2020). Endosomal Toll-like Receptors Play a Key Role in Activation of Primary Human Monocytes by Cowpea Mosaic Virus. *Immunology* 159 (2), 183–192. doi:10.1111/imm.13135

Aljabali, A. A. A., Shukla, S., Lomonossoff, G. P., Lomonossoff, N. F., and Steinmetz, D. J. (2013). CPMV-DOX Delivers. *Mol. Pharmaceutics* 10 (1), 3–10. doi:10.1021/mp3002057

Balke, I., and Zeltins, A. (2020). Recent Advances in the Use of Plant Virus-like Particles as Vaccines. *Viruses* 12 (3), 270. doi:10.3390/v12030270

Beatty, P. H., and Lewis, J. D. (2019). Cowpea Mosaic Virus Nanoparticles for Cancer Imaging and Therapy. *Adv. Drug Deliv. Rev.* 145, 130–144. doi:10.1016/j.addr.2019.04.005

Boone, C. E., Wang, C., Lopez-Ramirez, M. A., Beiss, V., Shukla, S., Chariou, P. L., et al. (2020). Active Microneedle Administration of Plant Virus Nanoparticles for Cancer *In Situ* Vaccination Improves Immunotherapeutic Efficacy. *ACS Appl. Nano Mater.* 3 (8), 8037–8051. doi:10.1021/acsanm.0c01506

Bruckman, M. A., Hern, S., Jiang, K., Flask, C. A., Yu, X., and Steinmetz, N. F. (2013). Tobacco Mosaic Virus Rods and Spheres as Supramolecular High-Relaxivity MRI Contrast Agents. *J. Mater. Chem. B* 1 (10), 1482–1490. doi:10.1039/C3TB00461A

Brun, M. J., Gomez, E. J., and Suh, J. (2017). Stimulus-responsive Viral Vectors for Controlled Delivery of Therapeutics. *J. Controlled Release* 267, 80–89. doi:10.1016/j.jconrel.2017.08.021

Byun, D. J., Wolchok, J. D., Rosenberg, L. M., and Girotra, M. (2017). Cancer Immunotherapy - Immune Checkpoint Blockade and Associated Endocrinopathies. *Nat. Rev. Endocrinol.* 13 (4), 195–207. doi:10.1038/nrendo.2016.205

Cai, H., Wang, C., Shukla, S., and Steinmetz, N. F. (2019). Cowpea Mosaic Virus Immunotherapy Combined with Cyclophosphamide Reduces Breast Cancer Tumor Burden and Inhibits Lung Metastasis. *Adv. Sci.* 6 (16), 1802281. doi:10.1002/advs.201802281

Cano-Garrido, O., Álamo, P., Sánchez-García, L., Falgàs, A., Sánchez-Chardi, A., Serna, N., et al. (2021). Biparatopic Protein Nanoparticles for the Precision Therapy of CXCR4+ Cancers. *Cancers* 13 (12), 2929. doi:10.3390/cancers13122929

Carignan, D., Thérien, A., Rioux, G., Paquet, G., Gagné, M.-È. L., Bolduc, M., et al. (2015). Engineering of the PapMV vaccine platform with a shortened M2e peptide leads to an effective one dose influenza vaccine. *Vaccine* 33 (51), 7245–7253. doi:10.1016/j.vaccine.2015.10.123

Cho, C.-F., Shukla, S., Simpson, E. J., Steinmetz, N. F., Luyt, L. G., and Lewis, J. D. (2014). Molecular Targeted Viral Nanoparticles as Tools for Imaging Cancer. *Methods Mol. Biol. (Clifton, N.J.)* 1108, 211–230. doi:10.1007/978-1-62703-751-8_16

Chung, Y. H., Cai, H., and Steinmetz, N. F. (2020). Viral Nanoparticles for Drug Delivery, Imaging, Immunotherapy, and Theranostic Applications. *Adv. Drug Deliv. Rev.* 156, 214–235. doi:10.1016/j.addr.2020.06.024

Czapar, A. E., Tiu, B. D. B., Veliz, F. A., Pokorski, J. K., and Steinmetz., N. F. (2018). Slow-Release Formulation of Cowpea Mosaic Virus for *In Situ* Vaccine Delivery to Treat Ovarian Cancer. *Adv. Sci.* 5 (5), 1700991. doi:10.1002/advs.20170099110.1002/advs.201700991

Czapar, A. E., Zheng, Y.-R., Riddell, I. A., Shukla, S., Awuah, S. G., Lippard, S. J., et al. (2016). Tobacco Mosaic Virus Delivery of Phenanthriplatin for Cancer Therapy. *ACS Nano* 10 (4), 4119–4126. doi:10.1021/acsnano.5b07360

Demurtas, O. C., Massa, S., Ferrante, P., Venuti, A., Franconi, R., Giuliano, G. A., et al. (2013). A Chlamydomonas-derived Human Papillomavirus 16 E7 vaccine induces specific tumor protection. *PLoS One* 23 (8), e61473. doi:10.1371/journal.pone.0061473

Esfandiari, N., Arzanani, M. K., Soleimani, M., Kohi-Habibi, M., and Svendsen, W. E. (2016). A New Application of Plant Virus Nanoparticles as Drug Delivery in Breast Cancer. *Tumor Biol.* 37, 1229–1236. doi:10.1007/s13277-015-3867-3

Farokhzad, O. C. (2008). Nanotechnology for Drug Delivery: the Perfect Partnership. *Expert Opin Drug Deliv.* 5 (9), 927–929. doi:10.1517/17425247.5.9.927

Fausther-Bovendo, H., and Kobinger, G. (2021). Plant-made Vaccines and Therapeutics. *Science* 13, 740–741. doi:10.1126/science.abf5375

FDA Drug Products (2017). *Including Biological Productsd, that Contain Nanomaterials-Guidance for Industry*. Silver Spring, Maryland: FDA Drug Products.

Finbloom, J., Aanei, I., Bernard, J., Klass, S., Elledge, S., Han, K., et al. (2018). Evaluation of Three Morphologically Distinct Virus-like Particles as Nanocarriers for Convection-Enhanced Drug Delivery to Glioblastoma. *Nanomaterials* 8 (12), 1007. doi:10.3390/nano8121007

Franke, C. E., Czapar, A. E., Patel, R. B., and Steinmetz, N. F. (2018). Tobacco Mosaic Virus-Delivered Cisplatin Restores Efficacy in Platinum-Resistant Ovarian Cancer Cells. *Mol. Pharmaceutics* 15, 2922–2931. doi:10.1021/acs.molpharmaceut.7b00466

Hansen, A. E., Petersen, A. L., Henriksen, J. R., Boerresen, B., Rasmussen, P., Elema, D. R., et al. (2015). Positron Emission Tomography Based Elucidation of the Enhanced Permeability and Retention Effect in Dogs with Cancer Using Copper-64 Liposomes. *ACS Nano* 9 (7), 6985–6995. doi:10.1021/acsnano.5b01324

Haynes, J. R., Cunningham, J., von Seefried, A., Lennick, M., Garvin, R. T., and Shen, S.-H. (1986). Development of a Genetically-Engineered, Candidate Polio Vaccine Employing the Self-Assembling Properties of the Tobacco Mosaic Virus Coat Protein. *Nat. Biotechnol.* 4 (7), 637–641. doi:10.1038/nbt0786-637

Hefferon, K. (2018). Repurposing Plant Virus Nanoparticles. *Vaccines* 6 (1), 11. doi:10.3390/vaccines6010011

Hu, H., Zhang, Y., Shukla, S., Gu, Y., Yu, X., and Steinmetz, N. F. (2017). Dysprosium-Modified Tobacco Mosaic Virus Nanoparticles for Ultra-high-field Magnetic Resonance and Near-Infrared Fluorescence Imaging of Prostate Cancer. *ACS nano* 11 (9), 9249–9258. doi:10.1021/acsnano.7b04472

Jobsri, J., Allen, A., Rajagopal, D., Shipton, M., Kanyuka, K., Lomonossoff, G. P., et al. (2015). Plant Virus Particles Carrying Tumour Antigen Activate TLR7 and Induce High Levels of Protective Antibody. *PLoS One* 10 (2), e0118096. doi:10.1371/journal.pone.0118096

Kernan, D. L., Wen, A. M., Pitek, A. S., and Steinmetz, N. F. (2017). Featured Article: Delivery of Chemotherapeutic vcMMAE Using Tobacco Mosaic Virus Nanoparticles. *Exp. Biol. Med. (Maywood)* 242, 1405–1411. doi:10.1177/1535370217719222

Kwon, S.-J., Park, M.-R., Kim, K.-W., Plante, C. A., Hemenway, C. L., and Kim, K.-H. (2005). cis-Acting Sequences Required for Coat Protein Binding and *In Vitro* Assembly of Potato Virus X. *Virology* 334 (1), 83–97. doi:10.1016/j.virol.2005.01.018

Lam, P., Lin, R. D., and Steinmetz, N. F. (2018). Delivery of Mitoxantrone Using a Plant Virus-Based Nanoparticle for the Treatment of Glioblastomas. *J. Mater. Chem. B* 6 (37), 5888–5895. doi:10.1039/C8TB01191E

Le, D. H. T., Commandeur, U., and Steinmetz, N. F. (2019). Presentation and Delivery of Tumor Necrosis Factor-Related Apoptosis-Inducing Ligand via Elongated Plant Viral Nanoparticle Enhances Antitumor Efficacy. *ACS Nano* 13, 2501–2510. doi:10.1021/acsnano.8b09462

Le, D. H. T., Lee, K. L., Shukla, S., Commandeur, U., and Steinmetz, N. F. (2017). Potato Virus X, a Filamentous Plant Viral Nanoparticle for Doxorubicin Delivery in Cancer Therapy. *Nanoscale* 9 (6), 2348–2357. doi:10.1039/c6nr09099k

Leary, J., and Key, J. (2014). Nanoparticles for Multimodal *In Vivo* Imaging in Nanomedicine. *Int. J. Nanomedicine* 9, 711–726. doi:10.2147/ijn.s53717

Lee, K. L., Murray, A. A., Le, D. H. T., Sheen, M. R., Shukla, S., Commandeur, U., et al. (2017). Combination of Plant Virus Nanoparticle-Based *In Situ* Vaccination with Chemotherapy Potentiates Antitumor Response. *Nano Lett.* 17, 4019–4028. doi:10.1021/acs.nanolett.7b00107

Lin, R. D., and Steinmetz., N. F. (2018). Tobacco Mosaic Virus Delivery of Mitoxantrone for Cancer Therapy. *Nanoscale* 10 (34), 16307–16313. doi:10.1039/c8nr04142c

Liu, L., Cañizares, M. C., Monger, W., Perrin, Y., Tsakiris, E., Porta, C., et al. (2005). Cowpea Mosaic Virus-Based Systems for the Production of Antigens and Antibodies in Plants. *Vaccine* 23 (15), 1788–1792. doi:10.1016/j.vaccine.2004.11.006

Liu, X., Wu, F., Tian, Y., Wu, M., Zhou, Q., Jiang, S., et al. (2016). Size Dependent Cellular Uptake of Rod-like Bionanoparticles with Different Aspect Ratios. *Sci. Rep.* 6 (1), 24567. doi:10.1038/srep24567

Lizotte, P. H., Wen, A. M., Sheen, M. R., Fields, J., Rojanasopondist, P., Steinmetz, N. F., et al. (2016). *In Situ* vaccination with Cowpea Mosaic Virus Nanoparticles Suppresses Metastatic Cancer. *Nat. Nanotech* 11 (3), 295–303. doi:10.1038/nnano.2015.292

Ma, Y.-Y., Jin, K.-T., Wang, S.-B., Wang, H.-J., Tong, X.-M., Huang, D.-S., et al. (2017). Molecular Imaging of Cancer with Nanoparticle-Based Theranostic Probes. *Contrast Media Mol. Imaging* 2017, 1–11. doi:10.1155/2017/1026270

Mao, C., Beiss, V., Fields, J., Steinmetz, N. F., and Fiering, S. (2021). Cowpea Mosaic Virus Stimulates Antitumor Immunity through Recognition by Multiple MYD88-Dependent Toll-like Receptors. *Biomaterials* 275, 120914. doi:10.1016/j.biomaterials.2021.120914

Massumi, H., Poormohammadi, S., Pishyar, S., Maddahian, M., Heydarnejad, J., Hosseini-Pour, A., et al. (2014). Molecular Characterization and Field Survey of Iranian Potato Virus X Isolates. *Virus Dis.* 25 (3), 338–344. doi:10.1007/s13337-014-0222-z

McNulty, M. J., Kelada, K., Paul, D., Nandi, S., and McDonald, K. (2021). Introducing Uncertainty Quantification to Techno-Economic Models of Manufacturing Field-Grown Plant-Made Products. doi:10.31224/osf.io/m8gvx

Meshcheriakova, Y., Durrant, A., Hesketh, E. L., Ranson, N. A., and Lomonossoff, G. P. (2017). Combining High-Resolution Cryo-Electron Microscopy and Mutagenesis to Develop Cowpea Mosaic Virus for Bionanotechnology. *Biochem. Soc. Trans.* 45 (6), 1263–1269. doi:10.1042/bst20160312

Moreira, A. F., Dias, D. R., and Correia, I. J. (2016). Stimuli-responsive Mesoporous Silica Nanoparticles for Cancer Therapy: A Review. *Microporous Mesoporous Mater.* 236, 141–157. doi:10.1016/j.micromeso.2016.08.038

Nemykh, M. A., Efimov, A. V., Novikov, V. K., Orlov, V. N., Arutyunyan, A. M., Drachev, V. A., et al. (2008). One More Probable Structural Transition in Potato Virus X Virions and a Revised Model of the Virus Coat Protein Structure. *Virology* 373 (1), 61–71. doi:10.1016/j.virol.2007.11.024

Niehl, A., Appaix, F., Boscá, S., van der Sanden, B., Nicoud, J.-F., Bolze, F., et al. (2016). Fluorescent Tobacco Mosaic Virus-Derived Bio-Nanoparticles for Intravital Two-Photon Imaging. *Front. Plant Sci.* 6, 1244. doi:10.3389/fpls.2015.01244

Nkanga, C. I., and Steinmetz, N. F. (2021). The Pharmacology of Plant Virus Nanoparticles. *Virology* 556, 39–61. doi:10.1016/j.virol.2021.01.012

Nooraei, S., Bahrulolum, H., Hoseini, Z. S., Katalani, C., Hajizade, A., Easton, A. J., et al. (2021). Virus-like Particles: Preparation, Immunogenicity and Their Roles as Nanovaccines and Drug Nanocarriers. *J. Nanobiotechnol* 19 (1), 59. doi:10.1186/s12951-021-00806-7

Park, K. (2019). The Beginning of the End of the Nanomedicine Hype. *J.Control. Release* 305. doi:10.1016/j.jconrel.2019.05.044

Park, M.-R., Kwon, S.-J., Choi, H.-S., Hemenway, C. L., and Kim, K.-H. (2008). Mutations that Alter a Repeated ACCA Element Located at the 5′ End of the Potato Virus X Genome Affect RNA Accumulation. *Virology* 378 (1), 133–141. doi:10.1016/j.virol.2008.05.004

Parker, L., Kendall, A., and Stubbs, G. (2002). Surface Features of Potato Virus X from Fiber Diffraction. *Virology* 300 (2), 291–295. doi:10.1006/viro.2002.1483

Patel, R., Czapar, A. E., Fiering, S., Oleinick, N. L., and Steinmetz, N. F. (2018). Radiation Therapy Combined with Cowpea Mosaic Virus Nanoparticle *In Situ* Vaccination Initiates Immune-Mediated Tumor Regression. *ACS Omega* 3 (4), 3702–3707. doi:10.1021/acsomega.8b00227

Paviolo, C., and Stoddart, P. (2017). Gold Nanoparticles for Modulating Neuronal Behavior. *Nanomaterials* 7, 92. doi:10.3390/nano7040092

Pitek, A. S., Jameson, S. A., Veliz, F. A., Shukla, S., and Steinmetz, N. F. (2016). Serum Albumin 'camouflage' of Plant Virus Based Nanoparticles Prevents Their Antibody Recognition and Enhances Pharmacokinetics. *Biomaterials* 89, 89–97. doi:10.1016/j.biomaterials.2016.02.032

Pokorski, J. K., Breitenkamp, K., Liepold, L. O., Qazi, S., and Finn, M. G. (2011). Functional Virus-Based Polymer-Protein Nanoparticles by Atom Transfer Radical Polymerization. *J. Am. Chem. Soc.* 133 (24), 9242–9245. doi:10.1021/ja203286n

Pokorski, J. K., and Steinmetz, N. F. (2011). The Art of Engineering Viral Nanoparticles. *Mol. Pharmaceutics* 8 (1), 29–43. doi:10.1021/mp100225y

Röder, J., Dickmeis, C., and Commandeur, U. (2019). Small, Smaller, Nano: New Applications for Potato Virus X in Nanotechnology. *Front. Plant Sci.* 10, 158. doi:10.3389/fpls.2019.00158

Röder, J., Dickmeis, C., Fischer, R., and Commandeur, U. (2018). Systemic Infection of Nicotiana Benthamianawith Potato Virus X Nanoparticles Presenting a Fluorescent iLOV Polypeptide Fused Directly to the Coat Protein. *Biomed. Res. Int.* 2018, e9328671. doi:10.1155/2018/9328671

Röder, J., Fischer, R., and Commandeur, U. (2017). Adoption of the 2A Ribosomal Skip Principle to Tobacco Mosaic Virus for Peptide Display. *Front. Plant Sci.* 8, 1125. doi:10.3389/fpls.2017.01125

Rong, J., Niu, Z., Lee, L. A., and Wang, Q. (2011). Self-assembly of Viral Particles. *Curr. Opin. Colloid Interf. Sci.* 16 (6): 441–450. doi:10.1016/j.cocis.2011.09.001

Rybicki, E. P. (2020). Plant Molecular Farming of Virus-like Nanoparticles as Vaccines and Reagents. *WIREs Nanomed Nanobiotechnol* 12 (2), e1587. doi:10.1002/wnan.1587

Sainsbury, F., Cañizares, M. C., and Lomonossoff, G. P. (2010). Cowpea mosaicVirus: The Plant Virus-Based Biotechnology Workhorse. *Annu. Rev. Phytopathol.* 48, 437–455. doi:10.1146/annurev-phyto-073009-114242

Shahgolzari, M., Pazhouhandeh, M., Milani, M., Yari Khosroushahi, A., and Fiering, S. (2020). Plant Viral Nanoparticles for Packaging and *In Vivo* Delivery of Bioactive Cargos. *Wiley Interdiscip Rev Nanomed Nanobiotechnol.* 12 (5), e1629. doi:10.1002/wnan.1629

Shahgolzari, M., Dianat-Moghadam, H., and Fiering, S. (2021). Multifunctional Plant Virus Nanoparticles in the Next Generation of Cancer Immunotherapies. *Semin. Cancer Biol.* 2021, S1044. doi:10.1016/j.semcancer.2021.07.018

Shoeb, E., and Hefferon, K. (2019). Future of Cancer Immunotherapy Using Plant Virus-Based Nanoparticles. *Future Sci. OA* 5 (7), FSO401. doi:10.2144/fsoa-2019-0001

Shukla, S., Ablack, A. L., Wen, A. M., Lee, K. L., Lewis, J. D., and Steinmetz, N. F. (2013). Increased Tumor Homing and Tissue Penetration of the Filamentous Plant Viral Nanoparticle Potato Virus X. *Mol. Pharmaceutics* 10 (1), 33–42. doi:10.1021/mp300240m

Shukla, S., Dickmeis, C., Fischer, R., Commandeur, U., and Steinmetz, N. F. (2018). In Planta Production of Fluorescent Filamentous Plant Virus-Based Nanoparticles. *Methods Mol. Biol.* 1776, 61–84. doi:10.1007/978-1-4939-7808-3_5

Shukla, S., Roe, A. J., Liu, R., Veliz, F. A., Commandeur, U., Wald, D. N., et al. (2020). Affinity of Plant Viral Nanoparticle Potato Virus X (PVX) towards Malignant B Cells Enables Cancer Drug Delivery. *Biomater. Sci.* 8, 3935–3943. doi:10.1039/D0BM00683A

Shukla, S., Wang, C., Beiss, V., Cai, H., Washington, T., Murray, A. A., et al. (2020). The Unique Potency of Cowpea Mosaic Virus (CPMV) *In Situ* Cancer Vaccine. *Biomater. Sci.* 8 (19), 5489–5503. doi:10.1039/D0BM01219J10.1039/D0BM01219J

Singh, P., Prasuhn, D., Yeh, R. M., Destito, G., Rae, C. S., Osborn, K., et al. (2007). Bio-distribution, Toxicity and Pathology of Cowpea Mosaic Virus Nanoparticles *In Vivo*. *J. Controlled Release* 120, 41–50. doi:10.1016/j.jconrel.2007.04.003

Steinmetz, N. F., and Evans, D. J. (2007). Utilisation of Plant Viruses in Bionanotechnology. *Org. Biomol. Chem.* 5 (18), 2891–2902. doi:10.1039/b708175h

Steinmetz, N. F., and Manchester., M. (2009). PEGylated Viral Nanoparticles for Biomedicine: the Impact of PEG Chain Length on VNP Cell Interactions *In Vitro* and *Ex Vivo*. *Biomacromolecules* 10 (4), 784–792. doi:10.1021/bm8012742

Steinmetz, N. F., Shah, S. N., Barclay, J. E., Rallapalli, G., Lomonossoff, G. P., and Evans, D. J. (2009). Virus-templated Silica Nanoparticles. *Small* 5 (7), 813–816. doi:10.1002/smll.200801348

Steinmetz, N. F. (2010). Viral Nanoparticles as Platforms for Next-Generation Therapeutics and Imaging Devices. *Nanomedicine: Nanotechnology, Biol. Med.* 6 (5), 634–641. doi:10.1016/j.nano.2010.04.005

Tian, Y., Zhou, M., Shi, H., Gao, S., Xie, G., Zhu, M., et al. (2018). Integration of Cell-Penetrating Peptides with Rod-like Bionanoparticles: Virus-Inspired Gene-Silencing Technology. *Nano Lett.* 18, 5453–5460. doi:10.1021/acs.nanolett.8b01805

Turpen, T. H., Reinl, S. J., Charoenvit, Y., Hoffman, S. L., Fallarme, V., and Grill, L. K. (1995). Malaria Epitopes Expressed on the Surface of Recombinant Tobacco Mosaic Virus. *Nat. Biotechnol.* 13 (1), 53–57. doi:10.1038/nbt0195-53

Tyulkina, L. G., Skurat, E. V., Frolova, O. Y., Komarova, T. V., Karger, E. M., and Atabekov, I. G. (2011). New Viral Vector for Superproduction of Epitopes of Vaccine Proteins in Plants. *Acta naturae* 3 (4), 73. doi:10.32607/20758251-2011-3-4-73-82

Uhde-Holzem, K., McBurney, M., Tiu, B. D., Advincula, R. C., Fischer, R., Commandeur, U., et al. (2016). Production of Immunoabsorbent Nanoparticles by Displaying Single-Domain Protein A on Potato Virus X. *Macromol. Biosci.* 16, 231–241. doi:10.1002/mabi.201500280

Vernekar, A. A., Berger, G., Czapar, A. E., Veliz, F. A., Wang, D. I., Steinmetz, N. F., et al. (2018). Speciation of Phenanthriplatin and its Analogs in the Core of Tobacco Mosaic Virus. *J. Am. Chem. Soc.* 140, 4279–4287. doi:10.1021/jacs.7b12697

Wang, C., and Steinmetz, N. F. (2019). CD47 Blockade and Cowpea Mosaic Virus Nanoparticle In Situ Vaccination Triggers Phagocytosis and Tumor Killing. *Adv. Healthc. Mater.* 8 (8), e1801288. doi:10.1002/adhm.201801288

Wang, C., Beiss, V., and Steinmetz, N. F. (2019). Cowpea Mosaic Virus Nanoparticles and Empty Virus-like Particles Show Distinct but Overlapping Immunostimulatory Properties. *J. Virol.* 93 (21), e00129–19. doi:10.1128/JVI.00129-19

Wen, A. M., Infusino, M., De Luca, A., Kernan, D. L., Czapar, A. E., Strangi, G., et al. (2015b). Interface of Physics and Biology: Engineering Virus-Based Nanoparticles for Biophotonics. *Bioconjug. Chem.* 26 (1), 51–62. doi:10.1021/bc500524f

Wen, A. M., Wang, Y., Jiang, K., Hsu, G. C., Gao, H., Lee, K. L., et al. (2015a). Shaping Bio-Inspired Nanotechnologies to Target Thrombosis for Dual Optical-Magnetic Resonance Imaging. *J. Mater. Chem. B* 3 (29), 6037–6045. doi:10.1039/c5tb00879d

Wen, J., Xu, Y., Li, H., Lu, A., and Sun, S. (2015b). Recent Applications of Carbon Nanomaterials in Fluorescence Biosensing and Bioimaging. *Chem. Commun.* 51 (57), 11346–11358. doi:10.1039/C5CC02887F

Yildiz, I., Lee, K. L., Chen, K., Shukla, S., and Steinmetz, N. F. (2013). Infusion of imaging and therapeutic molecules into the plant virus-based carrier cowpea mosaic virus: cargo-loading and delivery. *J Control Release* 172 (2), 568–78. doi:10.1016/j.jconrel.2013.04.023

Yin, Z., Nguyen, H. G., Chowdhury, S., Bentley, P., Bruckman, M. A., Miermont, A., et al. (2012). Tobacco Mosaic Virus as a New Carrier for Tumor Associated Carbohydrate Antigens. *Bioconjug. Chem.* 23, 1694–1703. doi:10.1021/bc300244a

Young, M., Debbie, W., Uchida, M., and Douglas, T. (2008). Plant Viruses as Biotemplates for Materials and Their Use in Nanotechnology. *Annu. Rev. Phytopathol.* 46, 361–384. doi:10.1146/annurev.phyto.032508.131939

Zeng, Q., Wen, H., Wen, Q., Chen, X., Wang, Y., Xuan, W., et al. (2013). Cucumber Mosaic Virus as Drug Delivery Vehicle for Doxorubicin. *Biomaterials* 34 (19), 4632–4642. doi:10.1016/j.biomaterials.2013.03.017

Zhang, L., Gu, F., Chan, J., Wang, A., Langer, R., and Farokhzad, O. (2008). Nanoparticles in Medicine: Therapeutic Applications and Developments. *Clin. Pharmacol. Ther.* 83, 761–769. doi:10.1038/sj.clpt.6100400

Zhou, J. C., Soto, C. M., Chen, M.-S., Bruckman, M. A., Moore, M. H., Barry, E., et al. (2012). Biotemplating Rod-like Viruses for the Synthesis of Copper

Nanorods and Nanowires. *J. Nanobiotechnology* 10, 18. doi:10.1186/1477-3155-10-18

Conflict of Interest: The authors declare that the research was conducted in the absence of any commercial or financial relationships that could be construed as a potential conflict of interest.

Publisher's Note: All claims expressed in this article are solely those of the authors and do not necessarily represent those of their affiliated organizations, or those of the publisher, the editors and the reviewers. Any product that may be evaluated in this article, or claim that may be made by its manufacturer, is not guaranteed or endorsed by the publisher.

Advantages of publishing in Frontiers

OPEN ACCESS
Articles are free to read for greatest visibility and readership

FAST PUBLICATION
Around 90 days from submission to decision

HIGH QUALITY PEER-REVIEW
Rigorous, collaborative, and constructive peer-review

TRANSPARENT PEER-REVIEW
Editors and reviewers acknowledged by name on published articles

Frontiers
Avenue du Tribunal-Fédéral 34
1005 Lausanne | Switzerland

Visit us: www.frontiersin.org
Contact us: frontiersin.org/about/contact

REPRODUCIBILITY OF RESEARCH
Support open data and methods to enhance research reproducibility

DIGITAL PUBLISHING
Articles designed for optimal readership across devices

FOLLOW US
@frontiersin

IMPACT METRICS
Advanced article metrics track visibility across digital media

EXTENSIVE PROMOTION
Marketing and promotion of impactful research

LOOP RESEARCH NETWORK
Our network increases your article's readership